Materials Degradation and Failures Series

Materials and Failures in MEMS and NEMS

Edited by **Atul Tiwari and Baldev Raj**

Scrivener Publishing

WILEY

Materials and Failures in MEMS and NEMS

Scrivener Publishing
100 Cummings Center, Suite 541J
Beverly, MA 01915-6106

Materials Degradation and Failure Series

Studies and investigations on materials failure are critical aspects of science and engineering. The failure analysis of existing materials and the development of new materials demands in-depth understanding of the concepts and principles involved in the deterioration of materials The *Material's Degradation and Failure* series encourages the publication of titles that are centered on understanding the failure in materials. Topics treating the kinetics and mechanism of degradation of materials is of particular interest. Similarly, characterization techniques that record macroscopic (e.g., tensile testing), microscopic (e.g., *in-situ* observation) and nanoscopic (e.g., nanoindentation) damages in materials will be of interest. Modeling studies that cover failure in materials will also be included in this series.

Series Editors: Atul Tiwari and Baldev Raj
Dr. Atul Tiwari, CChem
Director, R&D, Pantheon Chemicals
225 W. Deer Valley Road #4
Phoenix, AZ 85027 USA
Email: atulmrc@yahoo.com, atiwari@pantheonchemical.com

Dr. Baldev Raj, FTWAS, FNAE, FNA, FASc, FNASc
Director, National Institute of Advanced Studies
Indian Institute of Science Campus
Bangalore 560 012, India
Email: baldev.dr@gmail.com, baldev_dr@nias.iisc.ernet.in

Publishers at Scrivener
Martin Scrivener(martin@scrivenerpublishing.com)
Phillip Carmical (pcarmical@scrivenerpublishing.com)

Materials and Failures in MEMS and NEMS

Edited by

Atul Tiwari and Baldev Raj

Scrivener Publishing

WILEY

Copyright © 2015 by Scrivener Publishing LLC. All rights reserved.

Co-published by John Wiley & Sons, Inc. Hoboken, New Jersey, and Scrivener Publishing LLC, Salem, Massachusetts.
Published simultaneously in Canada.

No part of this publication may be reproduced, stored in a retrieval system, or transmitted in any form or by any means, electronic, mechanical, photocopying, recording, scanning, or otherwise, except as permitted under Section 107 or 108 of the 1976 United States Copyright Act, without either the prior written permission of the Publisher, or authorization through payment of the appropriate per-copy fee to the Copyright Clearance Center, Inc., 222 Rosewood Drive, Danvers, MA 01923, (978) 750-8400, fax (978) 750-4470, or on the web at www.copyright.com. Requests to the Publisher for permission should be addressed to the Permissions Department, John Wiley & Sons, Inc., 111 River Street, Hoboken, NJ 07030, (201) 748-6011, fax (201) 748-6008, or online at http://www.wiley.com/go/permission.

Limit of Liability/Disclaimer of Warranty: While the publisher and author have used their best efforts in preparing this book, they make no representations or warranties with respect to the accuracy or completeness of the contents of this book and specifically disclaim any implied warranties of merchantability or fitness for a particular purpose. No warranty may be created or extended by sales representatives or written sales materials. The advice and strategies contained herein may not be suitable for your situation. You should consult with a professional where appropriate. Neither the publisher nor author shall be liable for any loss of profit or any other commercial damages, including but not limited to special, incidental, consequential, or other damages.

For general information on our other products and services or for technical support, please contact our Customer Care Department within the United States at (800) 762-2974, outside the United States at (317) 572-3993 or fax (317) 572-4002.

Wiley also publishes its books in a variety of electronic formats. Some content that appears in print may not be available in electronic formats. For more information about Wiley products, visit our web site at www.wiley.com.

For more information about Scrivener products please visit www.scrivenerpublishing.com.

Cover design by Atul Tiwari and Russell Richardson

Library of Congress Cataloging-in-Publication Data:

Materials and failures in MEMS and NEMS / edited by Atul Tiwari and Baldev Raj.
1 online resource.
Includes bibliographical references and index.
Description based on print version record and CIP data provided by publisher; resource not viewed.
ISBN 978-1-119-08387-0 (pdf) -- ISBN 978-1-119-08386-3 (epub) -- ISBN 978-1-119-08360-3 (cloth : alk. paper)
1. Microelectromechanical systems--Design and construction. 2. Nanoelectromechanical systems--Design and construction. I. Tiwari, Atul, editor. II. Raj, Baldev, 1947- editor.
TK7875
621.381--dc23
2015027730

ISBN 978-1-119-08360-3

Printed in the United States of America

10 9 8 7 6 5 4 3 2 1

Contents

1 Carbon as a MEMS Material **1**

Amritha Rammohan and Ashutosh Sharma

1.1 Introduction 1
1.2 Structure and Properties of Glassy Carbon 3
1.3 Fabrication of C-MEMS Structures 4
1.3.1 Mechanism and Features of the Pyrolysis Process 4
1.3.2 Lithographic Processes for the Fabrication of C-MEMS Structures 6
1.3.3 Soft Lithographic Techniques 11
1.3.4 Self-Assembly and Bottom-Up Processes for the Fabrication of C-MEMS Structures 13
1.4 Integration of C-MEMS Structures with Other Materials 15
1.5 Conclusion 18
References 18

2 Intelligent Model-Based Fault Diagnosis of MEMS **21**

Afshin Izadian

2.1 Introduction 21
2.1.1 MEMS Structure and Origins of Fault 22
2.1.1.1 Material Growth Effects 22
2.1.1.2 Lithography and Its Effects 23
2.1.1.3 Effect of Etching Process on Parameters of MEMS 25
2.1.1.4 Effect of Stress, Stress Gradients, Wearing, and Stiction on Deposited Films 26
2.1.1.5 Electrostatic Force 27
2.2 Model-Based Fault Diagnosis 29
2.2.1 Fault and Failure Definitions 30
2.2.2 System Behavior 30
2.2.3 Fault and Model Uncertainty 31
2.2.4 Faulty System Modes and Conditions 31
2.2.5 Fault Diagnosis 31
2.2.6 MEMS Mathematical Model 33
2.2.6.1 Mass Calculations 34
2.2.6.2 Spring Constant Calculations 34
2.2.6.3 Damping Coefficient 35
2.2.6.4 Model of MEMS 36

2.2.6.5 Multiple-Model Estimation Approach 37
2.2.6.6 Multiple Models as Signature Faults 38
2.2.6.7 Kalman Filters 39
2.2.7 Adaptive Estimation 39
2.2.8 Simulation and Experimental Results 41
2.2.9 Experimental Results and Discussion 44
2.2.9.1 Displacement Measurement Technique 44
2.3 Self-Tuning Estimation 49
2.3.1 Estimator Structure 49
2.3.2 Fault Diagnosis Application in MEMS: Simulation and Experiment 50
2.3.2.1 Experimental Results 52
2.3.2.2 Adaptive Self-Tuning Fault Diagnosis 54
2.3.2.3 Discussion 58
References 59

3 MEMS Heat Exchangers 63
B. Mathew and L. Weiss
3.1 Introduction 63
3.2 Fundamentals of Thermodynamics, Fluid Mechanics, and Heat Transfer 67
3.2.1 Thermodynamics 67
3.2.2 Fluid Mechanics 70
3.2.3 Heat Transfer 78
3.2.3.1 Conduction 78
3.2.3.2 Convection 79
3.2.3.3 Thermal Resistance 84
3.3 MEMS Heat Sinks 86
3.4 MEMS Heat Pipes 92
3.6 Need for Microscale Internal Flow Passages 113
Nomenclature 115
Greek Alphabets 116
Subscripts 116
References 117

4 Application of Porous Silicon in MEMS and Sensors Technology 121
L. Sujatha, Chirasree Roy Chaudhuri and Enakshi Bhattacharya
4.1 Introduction 121
4.1.1 Properties of Porous Silicon for MEMS Applications 122
4.1.2 Review of PS for MEMS Applications 122
4.1.3 Formation of PS 123
4.1.3.1 Porous Silicon Formation Setup 123
4.1.3.2 Formation Parameters 124
4.1.3.3 PS Formation Chemistry 124
4.1.3.4 Measurement of Porosity and Thickness of PS Layer 125
4.1.3.5 I–V Characteristics 126

4.1.4 Classification of PS 127
4.1.4.1 Micro PS 127
4.1.4.2 Macro PS 128
4.1.4.3 Meso PS 129
4.1.5 Effect of Formation Parameters on Porosity and Thickness 130
4.1.6 PS Drying Mechanisms 130
4.1.7 Effect of PS Formation on Stiction in MEMS 130
4.2 Porous Silicon in Biosensors 131
4.2.1 PS Cantilever-Based Resonant Frequency Detection 131
4.2.1.1 Antibody–Antigen Binding Detection 132
4.2.1.2 Triglyceride Detection 133
4.2.2 PS-Based Impedance Detection 138
4.2.2.1 Bacteria Detection 138
4.2.2.2 Food Toxin Detection 141
4.2.2.3 DNA Detection 145
4.2.3 PS-Based EISCAP Structure for Capacitive Detection 148
4.2.3.1 Triglyceride Detection 149
4.2.3.2 Penicillin Detection 151
4.2.4 PS-Based Other Electrochemical Biosensors 151
4.2.4.1 Glucose Detection 151
4.2.4.2 DNA Detection 152
4.2.4.3 Bacteria Detection 152
4.2.4.4 IgG Detection 153
4.2.4.5 Other Analytes 153
4.2.5 Reliability 154
4.3 Porous Silicon for Pressure Sensors 155
4.3.1 Pressure Sensor with Silicon/PS Composite Membrane 156
4.3.1.1 Fabrication of Pressure Sensor with Composite Membrane 157
4.3.1.2 Performance of Si/PS Composite Membrane Pressure Sensor 158
4.3.1.3 Temperature and Humidity Effects on Packaged Si/PS Composite Membrane Pressure Sensor 159
4.3.2 Pressure Sensors with Piezoresistive Effect of PS 160
4.3.2.1 Fabrication of the Device 161
4.3.2.2 Experimental Results 162
4.3.2.3 Estimation of Piezoresistive Coefficient 163
4.4 Conclusion 165
References 165

5 MEMS/NEMS Switches with Silicon to Silicon (Si-to-Si) Contact Interface 173
Chengkuo Lee, Bo Woon Soon and You Qian
5.1 Introduction 173
5.1.1 Why Silicon? 174
5.1.2 Electrostatic Switch 174

5.2 Bi-Stable CMOS Front End Silicon Nanofin (SiNF) Switch for Non-volatile Memory Based On Van Der Waals Force 175
5.2.1 Operational SiNF NEMS Switch with Bi-Stable States 176
5.2.2 Van Der Waals Operation and Critical Length 176
5.2.3 Fabrication Process 178
5.2.4 Electrical Characteristics of NEMS Switch Non-volatile Memory 181
5.2.4.1 Non-volatile Memory Array Application 183
5.3 Vertically Actuated U-Shape Nanowire NEMS Switch 184
5.3.1 Dual-Silicon-Nanowires-Based U-Shape NEMS Switch 184
5.3.2 U-Shape Nanowire Fabrication 185
5.3.3 Low-Voltage Operation 185
5.4 A Vacuum Encapsulated Si-to-Si MEMS Switch for Rugged Electronics 187
5.4.1 Three Terminal On–Off with Vacuum Encapsulated Switch 187
5.4.2 Vacuum Encapsulated Si-to-Si Switch 191
5.4.3 Reliability of a Vacuum Encapsulated Si-to-Si Switch 193
5.5 Summary 197
References 197

6 On the Design, Fabrication, and Characterization of cMUT Devices 201
J. Jayapandian, K. Prabakar, C.S. Sundar and Baldev Raj
6.1 Introduction 201
6.2 cMUT Design and Finite Element Modeling Simulation 203
6.3 cMUT Fabrication and Characterization 205
6.3.1 Surface Micromachining Method 205
6.3.2 Wafer Bonding Method 205
6.3.2.1 Dynamic Characterization Using Laser Doppler Vibrometer 208
6.3.2.2 Capacitance Measurement 209
6.3.2.3 Surface Profile and Morphology of cMUT Membrane 209
6.3.2.4 SEM and EDS Analysis 209
6.3.3 Wafer Bonding Method with Isolation Trenches 211
6.3.3.1 Dynamic Characterization Using Nano Vibration Analyzer 212
6.3.3.2 Static Characterization and CV Measurements 214
6.4 Summary and Conclusions 216
Acknowledgments 217
References 217

7 Inverse Problems in the MEMS/NEMS Applications 219
Yin Zhang
7.1 Introduction 219
7.2 Inverse Problems in the Micro/Nanomechanical Resonators 222
7.2.1 Determining the Mass and Position of Adsorbate by Using the Shifts of Resonant Frequencies 222
7.2.2 Determining the Adsorption-Induced Surface Stress and Mass by Measuring the Shifts of Resonant Frequencies 224

7.2.3 Determining the Surface Elasticity and Surface Stress by Measuring the Shifts of Resonant Frequencies 227
7.2.4 Determining the Stiffness and Mass of Biochemical Adsorbates by a Resonator Sensor 230
7.3 Inverse Problems in the MEMS Stiction Test 231
Acknowledgment 234
References 234

8 Ohmic RF-MEMS Control 239
M. Spasos and R. Nilavalan
8.1 Introduction 239
8.1.1 Voltage Drive Control Under Single Pulse 240
8.1.2 Voltage Drive Control Under Tailored Pulse 241
8.1.3 Voltage Drive Control Under Optimized-Tailored Pulse 245
8.1.3.1 Pull-Down Phase 246
8.3.1.2 Release Phase 246
8.2 Charge Drive Control (Resistive Damping) 251
8.3 Hybrid Drive Control 255
8.4 Control Under High-Pressure Gas Damping 258
8.5 Comparison between Different Control Modes 258
References 260

9 Dynamics of MEMS Devices 263
Vamsy Godthi, K. Jayaprakash Reddy and Rudra Pratap
9.1 Introduction 263
9.1.1 Resonant Devices 264
9.1.2 Non-resonant Devices 265
9.2 Modeling and Simulation 266
9.2.1 Design Parameters 266
9.2.2 Multi-physics 268
9.2.3 Simulation Tools 270
9.2.4 Process Flow Simulation 272
9.3 Fabrication Methods 273
9.3.1 Surface Micromachining 273
9.3.1.1 Issues 274
9.3.2 Bonding 275
9.3.2.1 Issues 275
9.4 Characterization 276
9.4.1 Visual 277
9.4.2 Electrical 277
9.4.3 Mechanical 279
9.5 Device Failures 280
9.5.1 Frequency Shifts 280
9.5.2 Wrong Modes 281
9.5.3 Structural Integrity 282
9.5.4 Reliability Failure 282
Acknowledgments 283
References 283

10 Buckling Behaviors and Interfacial Toughness of a Micron-Scale Composite Structure with a Metal Wire on a Flexible Substrate 285
Qinghua Wang, Huimin Xie and Yanjie Li
10.1 Introduction 285
10.2 Buckling Behaviors of Constantan Wire under Electrical Loading 289
10.2.1 Sample and Experiments 290
10.2.1.1 Sample Preparation and Characterization 290
10.2.1.2 Electrical Loading Experiments 291
10.2.1.3 Electrical–Mechanical Loading Experiments 293
10.2.1.4 Temperature Variation under Electrical Loading 293
10.2.2 Buckling Morphologies and Characteristics of Constantan Wire 294
10.2.2.1 Buckling Morphologies under Electrical Loading 294
10.2.2.2 Effects of the Electric Current Form and Current Density 295
10.2.2.3 Buckling Morphologies under Electrical–Mechanical Loading 297
10.2.3 Buckling Mechanism Analysis of Constantan Wire 299
10.2.4 Critical Buckling Analysis of Constantan Wire 300
10.2.5 Post-Buckling Analysis of Constantan Wire 301
10.2.5.1 Derivation of Residual Stress Calculation Formula 301
10.2.5.2 Calculation of Residual Stress in Constantan Wire 303
10.3 Interfacial Toughness between Constantan Wire and Polymer Substrate 305
10.3.1 Interfacial Toughness Formula for Rigid Film and Flexible Substrate 305
10.3.2 Interfacial Toughness Measurement and Discussions 306
10.3.2.1 Measurement of the Interfacial Toughness 306
10.3.2.2 Discussions 308
10.3.3 Applicable Condition of the Electricity-Induced Buckling Method 309
10.4 Buckling Behaviors of Polymer Substrate Restricted by Constantan Wire 310
10.4.1 Sample and Experiments 310
10.4.1.1 Sample Preparation and Characterization 310
10.4.1.2 Experiments 310
10.4.1.3 Sample Temperature Variations during Experiments 311
10.4.2 Micron-Scale Buckling Mode of the Polymer Substrate 312
10.4.2.1 Orthogonal Wave Buckling 312
10.4.2.2 Oblique Wave Buckling and Crumpled Wave Buckling 315
10.4.2.3 Occurrence Conditions of Micron-Scale Buckling Modes 316
10.4.3 Micron and Submicron Cross-Scale Buckling Modes 317
10.4.4 The Buckling Mechanism Analysis of the Polymer Substrate 319
10.4.4.1 Formation Mechanisms of Micron-Scale Wave Buckling Modes 319
10.4.4.2 Formation Mechanisms of Submicron-Scale Wrinkles 320
10.5 Conclusions 321
Acknowledgments 322
References 322

11 Microcantilever-Based Nano-Electro-Mechanical Sensor Systems: Characterization, Instrumentation, and Applications 325
Sheetal Patil and V. Ramgopal Rao
11.1 Introduction 325
11.1.1 General Definitions and Concepts 325
11.2 Operation Principle and Fundamental Models 327
11.3 Microcantilever Sensor Fabrication 330
11.3.1 Si Microcantilevers 331
11.3.2 Bulk Micromachining 331
11.3.3 Polymer Microcantilevers 333
11.3.4 Surface Micromachining 333
11.3.5 Microcantilevers with Integrated Functionality 334
11.4 Mechanical and Electrical Characterization of Microcantilevers 335
11.4.1 Nano-Indentation Techniques 335
11.4.2 Surface and Resonant Frequency Measurements 337
11.4.3 Electrical Characterization 338
11.4.4 Noise and Reliability Characterizations 338
11.5 Readout Principles 339
11.5.1 Integrated Optical Readout 340
11.5.2 Piezo-Resistive Readout 341
11.5.3 Piezoelectric Readout 343
11.5.4 Capacitance Readout 344
11.6 Application of Microcantilever Sensors 344
11.6.1 Vapor Phase/Gas/Chemical Detection 344
11.6.2 Biosensors 346
11.6.3 Agriculture Applications 347
11.7 Energy Harvesting for Sensor Networks 349
11.7.1 Low-Frequency Vibration Energy Harvesting 349
11.7.2 Microwave Energy Harvesting 351
11.7.3 Photo-Voltaic and Thermal Energy Harvesting 351
11.8 Conclusion 351
References 352

12 CMOS MEMS Integration 361
Thejas and Navakanta Bhat
12.1 Introduction 361
12.2 State-of-the-Art inertial Sensor 362
12.2.1 Hybrid Integration-Based Sensors 364
12.2.2 Monolithic Integration-Based Sensors and Actuators 366
12.3 Capacitance Sensing Techniques 366
12.4 Capacitance Sensing Architectures 367
12.5 Continuous Time Voltage Sensing Circuit 368
12.6 CMOS ASIC Design 371
12.7 Test Results of CMOS–MEMS Integration 377
12.8 Electrical Reliability Issues 378
References 380

13 Solving Quality and Reliability Optimization Problems for MEMS with Degradation Data 381
Yash Lundia, Kunal Jain, Mamanduru Vamsee Krishna, Manoj Kumar Tiwari and Baldev Raj
Abbreviations 381
13.1 Introduction 382
13.2 Notations and Assumptions 384
13.2.1 Notations 384
13.2.2 Assumptions 385
13.3 Reliability Model 385
13.3.1 Wear Degradation due to Burn-In Procedure 386
13.3.2 Non-destructive Evaluation 387
13.3.3 Replacement and Failure Cost 388
13.3.3.1 Catastrophic Failures as a Result of Random Shocks 389
13.3.3.2 Soft Failures as a Result of Shocks and Degradation 390
13.3.4 Optimization Model 393
13.3.5 Solution Methodology—Algorithm Description 394
13.4 Numerical Example 395
13.5 Conclusions 397
References 397

Preface

Manufacturing, diagnosis and treatment of biospecies, agriculture, energy and infrastructure, governance, security, etc., need sensors and devices based on well-grounded concepts, engineering and technology. Miniaturization demands new materials, designs and fabrication technologies. The decrease in the size and volume of devices has necessitated the incorporation of a high level of fabrication technologies. There is a priority need to address failures in micro- and nanodevices.

The invention of Microelectromechanical Systems (MEMS) and Nanoelectromechanical Systems (NEMS) fabrication technologies has revolutionized the science and engineering industry. It is estimated that market prospects for MEMS and NEMS will increase rapidly to reach $200 billion in 2025. The key to the success of MEMS and NEMS will be the development of technologies that can integrate multiple devices with electronics on a single chip. Among the technologies available so far, the fabrication of MEMS and/or NEMS has been predominately achieved by etching the polysilicon material. Novel materials and technologies are being explored to overcome the challenges in fabrication or manufacturing processes. In order to meet the ever-increasing demands of MEMS and NEMS, enormous amounts of research, applications and innovations have been explored and exploited. Most of the relevant information originating from such efforts is being treated as confidential or privileged, which seeds extensive barriers to the research, development and aspirational demands of these technologies.

This book includes chapters written by eminent experts in the area of MEMS and NEMS. The opening chapter of this book reviews various C-MEMS fabrication technologies involving patterning of polymeric precursors of carbon such as epoxy photoresists and sol-gel polymers, followed by pyrolysis to generate glassy or semicrystalline carbon. Another chapter discusses the origins of fault in such devices, related mathematical models and utilization of filters in fault diagnosis. Also, the authors have illustrated the structure of a multiple-model adaptive estimator and its application in fault diagnosis simulation. Another chapter provides an overview of the design of MEMS heat exchangers such as heat sinks, heat pipes and two-fluid heat exchangers. The formation of porous silicon devices by elec¬trochemical etching of silicon and the control over the porosity and pore size are discussed in a separate chapter. The use of such porous silicon devices as biosensors is thoroughly investigated by these contributors. Further, a chapter provides an overview on MEMS and NEMS switches using Si-to-Si contact. An interesting chapter discusses the design challenges during fab¬rication and failure analysis of cMUT devices. Investigators have compared the device fabrication by surface micromachining and wafer bonding techniques. Moreover, failure analysis of cMUT using vari¬ous materials characterization techniques and their importance for successful device fabrica¬tion are also investigated.

A successive chapter investigates an effective approach to solve inverse problems in MEMS and NEMS. This chapter describes inverse problems in micro- and nanomechanical resonators and also the stiction test of MEMS and NEMS. Further, there is a chapter in the book dedicated to the control of ohmic RF-MEMS switches operating under different actuation modes, such as single pulse, tailored pulse, and tailored-pulse optimization methods, based on Taguchi's tech¬nique of resistive damping; and the hybrid actuation mode, which is a combination of the tailored pulse, the resistive damping, and Taguchi's optimization technique. Additional challenges involved in design methodologies, and available simulation packages to model and simulate MEMS devices are explored in a separate chapter. To develop MEMS devices and to understand the inception of fabrication defects, researchers have explored fabrication techniques such as surface micromachining and bonding silicon to glass. The use of different characterization techniques, such as visual, electrical and mechanical, for inspecting the defects in these devices has also been demonstrated. An independent chapter systematically investigates the buckling behavior of a typical micron-scale constantan-wire/polymer-substrate structure under electrical loading. Another crucial chapter discusses many important aspects of microcantilever sensors such as operation principles, fabrication of silicon and polymer microcantilevers, mechanical and electrical characterization, readout principles, applications of microcantilever sensors for vapor-phase chemical or gas detection, biosensing and agriculture applications; and nanogenerators for energy harvesting. A chapter in the book elaborates the inherent challenges encountered in CMOS–MEMS along with the possibility of integration at board and chip levels. This chapter also lists various circuit architectures being used in capacitance detection along with a detailed comparison on their merits and demerits. The final chapter proposes a mathematical model to determine strategies for preventive replacement and inspection for MEMS that are subject to multiple dependent competing failure processes as a result of degradation and/or shock loads.

We are confident that this book will constitute a large knowledge bank for students, research scholars and engineers who are involved in the research, development and deployment of advanced MEMS and NEMS for a wide variety of applications. To the best of the editors' knowledge, such a book that addresses the developments and failures in these advanced devices has not yet been available to readers. Comprehensive expertise is mapped out and discussed in this book to advance the knowledge bank of readers in order to enable precise control over dimensional stability, quality, reliability, productivity and life cycle management of MEMS and NEMS.

The editors look forward to constructive suggestions and feedback for improving the next edition of this book on this important, relatively young subject of increasing importance and relevance.

Wishing you a purposeful and wonderful reading experience.

Atul Tiwari, PhD
Baldev Raj, PhD
August 4, 2015

1

Carbon as a MEMS Material

Amritha Rammohan* and Ashutosh Sharma

Department of Chemical Engineering, Indian Institute of Technology, Kanpur, Uttar Pradesh, India

Abstract

Carbon has become a popular material in microelectromechanical (MEMS) applications because of its versatile electrochemical and mechanical properties, as well as the numerous precursor materials and facile fabrication methods available. This review details various C-MEMS fabrication technologies, most of which involve the patterning of polymeric precursors of carbon such as epoxy photoresists and sol–gel polymers followed by their pyrolysis to create glassy or semicrystalline carbon pattern replicas. The structure and properties of glassy carbon, as well as the pyrolysis process and concurrent shrinkage, are also discussed in detail, as these directly affect the applicability of the carbon structures and devices. The integration of carbon structures in MEMS devices by means of surface modification and the incorporation of additives and fillers such as carbon nanotubes and carbon nanofibers to enhance the functional properties are also discussed.

Keywords: Carbon, C-MEMS, pyrolysis, volumetric shrinkage, MEMS integration, lithography

1.1 Introduction

Carbon is one of the most versatile materials in the periodic table. Due to its ability to form *sp*, sp^2, and sp^3 hybridized covalent bonds with various elements including itself, carbon-based compounds and materials are amongst the most adaptable materials available to us. The ability of carbon to form bonds with itself is manifested in the form of many allotropes of carbon including fullerenes, nanotubes, graphite, graphene, and diamond. Even within these allotropes, despite being all made of carbon, the properties such as electrical conductivity, hardness, and strength vary widely with allotrope due to different microstructures in terms of crystallite size, long-range order, anisotropy, *etc*. [1]. Amorphous or glassy carbon, in particular, has a wide window of electrochemical stability as well as high thermal conductivity and excellent biocompatibility, warranting its use in various electrochemical and biological applications [2]. Diamond-like carbon or DLC, another form of carbon, has superior tribological properties and wear

**Corresponding author*: r.amritha@gmail.com

Atul Tiwari and Baldev Raj (eds.), Materials and Failures in MEMS and NEMS, (1–20)
© 2015 Scrivener Publishing LLC

resistance, and anisotropic carbon materials such as nanotubes and nanofibers can be leveraged for their unique and anisotropic electromechanical properties as well [2–4].

When this versatility in functional properties is combined with appropriate micro/nanofabrication techniques, carbon structures become highly viable as elements in micro and nano electromechanical systems (MEMS/NEMS). In order to create micro- and nanosized electromechanical structures such as actuators and microsensors from carbon, appropriate robust and facile micro/nanofabrication techniques have to be adopted. The methods to pattern carbon and its precursors into MEMS structures are divided, like other microfabrication techniques, into top-down and bottom-up techniques. Top-down techniques are subtractive processes such as reactive ion etching (RIE) and lithographic patterning with photons, electrons, or ions. Bottom-up or additive processes include sputtering, evaporation, and chemical vapor deposition (CVD) [5]. While top-down techniques create deterministic patterns with good shape and size control, bottom-up techniques result in increased functionality and have greater capability for three-dimensional (3D) patterns. Self-assembled structures that are formed with very little external guidance or direction also fall in the latter category of bottom-up techniques. Apart from strictly top-down and bottom-up techniques, many fabrication techniques include a combination of these two. For example, hierarchical structures can be achieved by top-down patterning of large-scale structures and bottom-up patterning of smaller, 3D features. Soft lithographic techniques such as micromolding and nanoimprinting are often considered a third classification of microfabrication techniques and have also been used successfully in the patterning of C-MEMS (Carbon MEMS) structures [6].

One process that facilitates the fabrication of amorphous or glassy carbon microstructures involves the pyrolysis of carbon-containing precursor molecules (usually polymers) that have been prefabricated into requisite micro/nanostructures (Figure 1.1). Pyrolysis or carbonization is the method of heating carbon-containing precursors to temperatures upward of 600 °C in an inert atmosphere such as nitrogen

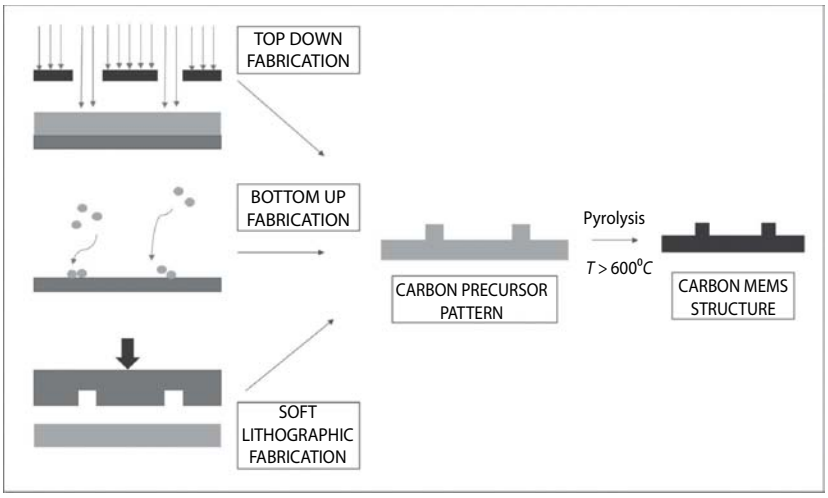

Figure 1.1 Fabrication of Carbon MEMS structures using top-down, bottom-up and soft lithographic techniques.

or argon to remove noncarbonaceous components in a material by volatilizing them into gaseous and hence removable compounds. This method, apart from allowing the creation of any required shape as long as appropriate formable precursors are used, also allows tweaking the properties of the final carbon micro/nanostructures by the rational use of various precursors with different functional groups. Appropriate precursors are those carbon-containing polymers that result in a high enough yield of carbonaceous residue and at the same time do not reflow when subjected to high temperatures during pyrolysis [2]. Thus, the methods to create glassy carbon MEMS structures can be decoupled into various methods to create microstructures in appropriate precursors and the pyrolysis processes (Figure 1.1).

This review is structured as follows. Due to the fact that majority of C-MEMS/NEMS processes involve polymer-derived amorphous or semicrystalline carbon, its properties are reviewed and contrasted with other MEMS materials. The process of pyrolysis for the carbonization is discussed in detail along with methods to address the issue of shrinkage. Then, lithographic techniques and their capabilities and modifications for C-MEMS/NEMS fabrication are discussed. This is followed by a description of bottom-up techniques, in particular self-assembly techniques for C-MEMS/NEMS. Soft lithographic techniques are also briefly covered. Finally, additives and surface modification techniques to improve and expand the applicability of carbon are examined.

1.2 Structure and Properties of Glassy Carbon

Glassy carbon is typically a hard solid prepared by treating polymeric precursors such as copolymer resins at elevated temperatures (600–3000 °C) having increasing amount of graphitic content with increasing temperature. The high temperature removes almost all of the noncarbon elements present in the polymers leaving behind a carbonaceous residue. A fully graphitic material does not develop in usual pyrolysis due to the difficulty in breaking the C–C bonds in the parent polymeric chains as well as other factors such as ratio of sp^2 to sp^3 carbon atoms and amount of hydrogen present in the precursor. The structure is generally understood as entangled ribbons of graphitic planes containing small isolated crystals of graphite. When characterized by Raman spectroscopy, two first-order bands around 1360 cm^{-1} (D band) and 1580 cm^{-1} (G band) are usually observed, which indicate the defect-induced, double-resonance scattering and symmetry in-plane stretching of graphite, respectively. Weak second-order bands related to the 3D ordering of graphite may also be observed between 2700 and 2900 cm^{-1}. It is important to note that the D band mainly arises due to the finite graphite crystallite size and associated defects [7]. As glassy carbon contains smaller crystallites of graphite, its density is less than that of graphite and can be applied in applications requiring lightweight yet chemically inert or thermally stable materials.

While the different preparation methods result in a range of physical properties of glassy carbon, it does have many advantages as a MEMS material. Glassy carbon, for instance, has a lower Young's modulus compared to silicon (10–40 GPa compared to 40–190 GPa for silicon) and a lower surface energy. Thus, carbon can be used in MEMS actuators or other devices where high stiffness is detrimental. The lower surface energy of carbon also solves the problem of stiction in contacting or proximal MEMS elements

where capillary forces cause sticking between close surfaces. Carbon resulting from pyrolysis is also rather inert and impervious in many corrosive chemical environments. It is also possible to tailor the porosity and functionalize the surface of glassy carbon using various carbon chemistry routes as illustrated in Section 1.4.

Glassy carbon is also a model material or gold standard for electrochemists to compare the electrochemical properties of electrodes of other materials as it exhibits excellent electrochemical properties. The electrochemical and physical properties of photoresist material pyrolyzed at temperatures between 600 °C and 1100 °C have been studied in detail, and it has been found that resistance of the material is lower and the electrochemical performance of the carbon material is often found to be better. The pyrolyzed positive photoresist (*eg.* AZ 4330) films have low capacitance as well as background current [8].

Apart from glassy carbon, other carbon-based materials such as DLC, carbon nanotubes (CNTs), and carbon nanofibers (CNFs) have also been applied to great benefit in MEMS devices. However, these materials often lack the capability to form the entire MEMS device by themselves due to fabrication and manipulation constraints. For instance, while DLC is particularly useful as a coating material to improve the wear resistance, reduce friction, and stiction in contacting microcomponents in MEMS devices, the residual stresses that are created in most of the high-energy techniques involved in DLC fabrication often lead to delamination of thicker DLC films precluding their use as structural elements [3]. CNTs and CNFs have unique and anisotropic thermal and electrochemical properties and have been used as structural elements such as cantilevers and microsensors. However, the manipulation and assembly of fabricated CNTs and CNFs on MEMS devices are nontrivial due the possibility of physical damage or morphological changes occurring. Cook and Carter [9] have recently reviewed the effect of different MEMS processes on arc-discharge produced and catalytically grown multiwall CNTs (MWCNTs) and found that while CVD deposition of other materials is compatible with MWCNTs, plasma etching processes tend to cause significant damage. Dau *et al.* [10] have been able to manually maneuver CVD-grown CNT films onto a substrate and pattern it using e-beam lithography into a mechanical sensor. It is also possible to directly synthesize patterned CNT structures for MEMS applications by methods such as CVD on patterned catalyst substrates [11–14], direct or post-synthetic patterning [15–18], templated deposition [19], *etc.* The incorporation of CNTs and CNFs into C-MEMS devices can be as fillers or (surface) additives to enhance useful properties or as structural elements integrated with the rest of the device. Both these uses are discussed in Section 1.4.

1.3 Fabrication of C-MEMS Structures

1.3.1 Mechanism and Features of the Pyrolysis Process

As most C-MEMS processes involve the use of pyrolysis, also known as carbonization, for the conversion of precursors to carbon, a good understanding of this process is a prerequisite for understanding C-MEMS fabrication. Pyrolysis, from the Greek for fire (*pyro*) and separation (*lysis*), is the thermochemical decomposition of a material and in

the context of carbonization refers to the breakdown of carbon-containing precursors at elevated temperatures in an inert or reducing environment. As early as the 1970s, carbon-containing polymers such as phenol formaldehyde, polyacrylonitrile (PAN), and polyimide have been pyrolyzed to amorphous carbon and their electrical properties studied. Jenkins and Kawamura [20] were amongst the first to study the process of pyrolyzing polymers into glassy carbon, where the polymers do not go through a plastic or reflow phase. They have classified the pyrolysis mechanism into four typical stages:

i. Around 300 °C – pre-carbonization stage – polymer turns black.
ii. 300–500 °C – carbonization stage – elements such as nitrogen and oxygen are removed from the material.
iii. 500–1200 °C – dehydrogenation stage – gradual elimination of hydrogen.
iv. 1200 °C and above – annealing stage.

As mentioned earlier, the graphitization of the carbon also occurs when pyrolyzing at elevated temperatures with percentage graphitization increasing with increasing temperatures. At pyrolysis temperatures between 2500 °C and 3300 °C, it is assumed that all nongraphitic regions are annealed out resulting in a near-complete graphitization of the material. Hence, this regime is referred to as graphitization regime.

In the case of lithography-based C-MEMS structures, both positive and negative polymeric photoresists can be used as carbon precursors and have the potential to be carbonized after patterning (Table 1.1). Hsia *et al.* [27] have researched the formation of carbon from SPR-220 (positive photoresist), by heating in Ar atmosphere to 900 °C followed by a second annealing step in a H_2/Ar (reducing) mixture. It was found that this results in a porous carbon with a high surface area, which has been applied as a supercapacitor electrode material for energy storage applications. Negative photoresists, such as SU-8, on the other hand, have a tendency to burn due to the dissolved oxygen present within them [39]. Thicker films of negative photoresist-derived carbon structures can also delaminate from silicon substrate and require ameliorative measures such as slow heating during pyrolysis to minimize thermal stresses and/or an intermediate layer to improve adhesion.

One of the most salient features of the pyrolysis process is the volumetric shrinkage that accompanies it. While this shrinkage can be advantageous in reducing the dimensions of realizable structures [36], it can cause defects such as buckling in constrained structures. In bulk or block structures, where the entire part is unconstrained and shrinks isotropically, the buckling is minimal, however, in the case of devices involving C-MEMS structures integrated with other materials or on a substrate, this is an issue. In self-assembled structures such as xerogels and aerogels, the random orientation and open structure allow their shrinkage and expansion during processing steps such as pyrolysis [40]. Much research has gone into optimizing the pyrolysis process to reduce the defects such as buckling, cracking, and delamination that occur as a result of thermal and shrinkage-related stresses.

To address the issue of shrinkage and related stresses, creating an optimal pyrolysis protocol by modifying heating and cooling rates, temperature of pyrolysis and the atmosphere of carbonization is one of the solutions, and modifying the carbon precursor material with filler material, *etc.*, and creating patterns with lower possibility of buckling

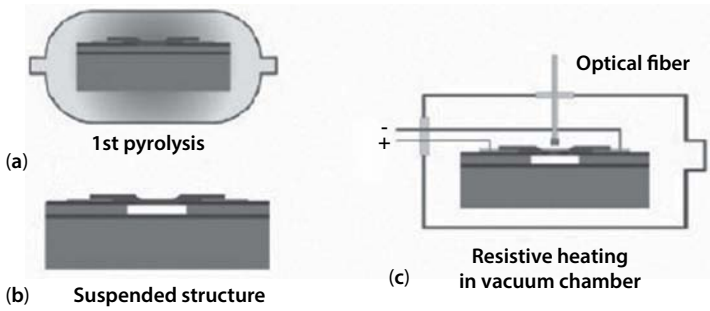

Figure 1.2 Schematic diagram of multistep pyrolysis (a) Preliminary pyrolysis using a quartz furnace (b) fabrication of suspended polymer microstructure, and (c) resistive heating in a vacuum chamber as final pyrolysis. The optical fiber is used to observe the microheater element during resistive heating. (Reproduced with permission from [42]. Copyright 2008 The Japan Society of Applied Physics)

are other techniques. Tang *et al.* [41] have utilized a three-step linear pyrolysis method as well as a mechanical interlocking step, the latter to achieve better bonding and prevent delamination. Naka *et al.* [42] have approached the problem of high-temperature pyrolysis by employing a resistive heating process as the last step of the pyrolysis of a polymeric microstructure on silicon structure. This resistive self-heating is achieved by means of a microheater designed into the microstructure of photosensitive polyimide (Figure 1.2). After initial pyrolysis step, a current is applied to the microheater to complete the carbonization by resistive heating. Since the polymeric structure carbonizes itself by self-heating, the thermal damage of other materials in the MEMS device is prevented.

Wang *et al.* [21] have illustrated a dual use of the pyrolysis process by using a two-step pyrolysis technique with forming gas [H_2 (5%)/N_2 mixture] at 900 °C as a second step to cause the local CVD of CNFs from gases emanating from the polymer during pyrolysis. A gold layer coated on the substrate on which modified SU-8 photoresist was patterned was converted into gold nanoballs at the base of carbon posts. It is also possible to exploit the shrinkage during pyrolysis to create unique shapes as has been shown by deVolder *et al.* [2] who have created canopy shapes connecting carbon pillars by intentionally fabricating an SU-8 topping layer that shrinks and pulls the pillars together as shown in Figure 1.2.

While shrinkage is one of the aspects of pyrolysis, the pyrolysis conditions also affect the functional properties of the MEMS structures. For example, faster heating rates increase the porosity of the pyrolyzed carbon. Teixidor *et al.* [43] have evaluated the effect of pyrolysis conditions on the battery characteristics of a pillar array of epoxy resin and found that pyrolysis at higher temperatures and slower ramping up schedules reduce the irreversible capacity of the carbon electrodes illustrated in Figure 1.3.

1.3.2 Lithographic Processes for the Fabrication of C-MEMS Structures

Lithographic processes are amongst the most pervasive techniques used for C-MEMS devices. So much so that the term "C-MEMS fabrication" is used synonymously with photolithographic patterning followed by pyrolysis. This is in part due to the carbonizable nature of the negative photoresist SU-8 as well as most other photoresist materials

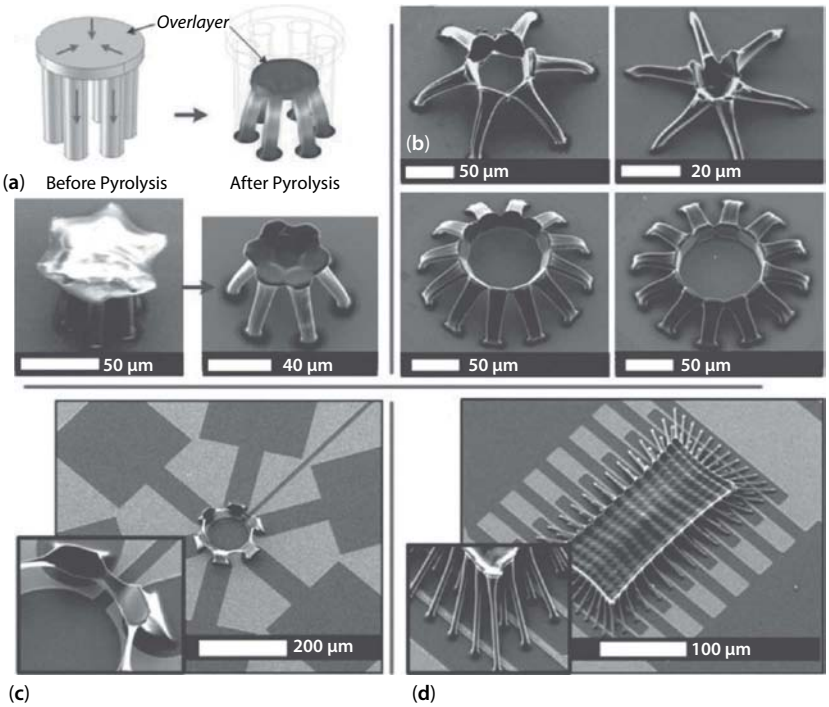

Figure 1.3. Examples of intricate amorphous carbon microarchitectures. (a) FEM simulation and SEM images of the 3D carbon microarchitecture formation by the directed shrinkage of an SU-8 topping layer during pyrolysis. (b) SEM images of six- and 12-legged 3D geometries. Left and right images have a different tilt angle, which is controlled by the pillar height. (c) 3D circular bridge with six legs and integrated pyrolyzed carbon bottom electrodes. (d) 3D arrangement of 180 legs connecting a suspended carbon sheet to interdigitated bottom electrodes. (Adapted with permission from [2], Copyright 2011 American Chemical Society.)

(Table 1.1). SU-8 also falls in the class of chemically amplified photoresist meaning that the cross-linking of the exposed region of the material occurs by means of a self-catalyzed reaction allowing thicker films to be cross-linked completely. This combined with its high transparency, and high contrast allows higher aspect ratio structures in SU-8. Positive photoresists are more challenging to pattern as high-aspect-ratio structures due to the difficulty in using high-thickness films. Multi-exposure and molding are some of the methods used to create high-aspect-ratio structures in positive photoresist.

Lithographic processes result in regular and ordered micropatterns as mentioned before, and Lyons [23] was amongst the first to pyrolyze a patterned photoresist material – novolac resin – in order to understand its electrical properties as a function of the temperature of pyrolysis. He observed the decrease in resistivity of the film upon carbonization. Many researchers since then have used various forms of lithographic processing to pattern C-MEMS structure including conventional UV photolithography [26, 41, 44–47], two-mask lithography [48], five-beam interference lithography [22], and more recently e-beam lithography [30, 49].

The conventional UV photolithography process has been used most extensively, and a detailed explanation of the process steps is warranted. Also, as mentioned earlier, SU-8

Table 1.1. Representative list of carbon precursors.

Material	Chemical composition and properties	Patterning method	References
SU-8	Epoxy resin, negative photoresist	Photolithography, interference lithography, electrospinning	[2, 21, 22] *etc.*
Novolac resin	Phenol formaldehyde polymer	Photolithographic patterning	[23]
EPON SU2.5	Bisphenol-A type novolac epoxy	Photolithographic patterning	[24, 25]
AZ 9260, AZ 4330, etc.	Polymeric resins containing di-azo compounds, positive photoresists	Photolithographic patterning	[26]
SPR 220	Cresol novolac resin and ethyl lactate	Photolithographic patterning	[27]
SC-100	Conventional cyclic polyisoprene photoresist	Photolithographic patterning and buckling-instability-induced patterning	[28]
KMPR 1050	Epoxy, negative photoresist	Photolithographic patterning	[29]
PMMA	Poly methyl methacrylate, e-beam resist	Electron-beam lithography and simultaneous carbonization	[30–32]
Resorcinol diglycidil ether and derivatives	Epoxy resin	Two photon lithography, 3D microtransfer molding	[33]
Copolymers of furfuryl alcohol–phenol	Phenolic resin	Micromolding in capillaries, microtransfer molding	
Resorcinol formaldehyde		Sol–gel, microtransfer molding	[34–36]
Polymer Cirlex	Polyimide	Lithographic patterning	[37]
Parylene	Poly-(p-xylylene)	CVD	[38]

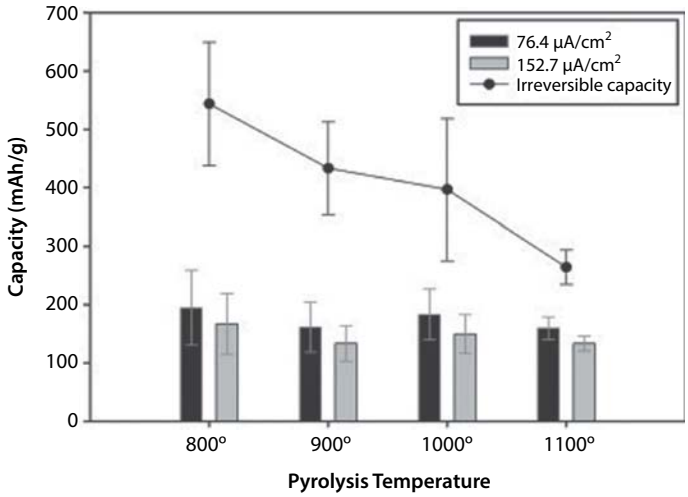

Figure 1.4 Effect of the final pyrolysis temperature in the specific capacity. (Reproduced with permission from Ref. [28], Copyright 2008 Elsevier B.V.)

is the most popular material for C-MEMS fabrication, and the process is explained for this material. A photoresist is a material that is sensitive to photons, and the transformation that occurs in such a material when exposed to light makes it either more or less prone to attack by a developer. Materials that become more prone to attack by developer are called positive photoresists, and those that become more resistant to attack by developer are called negative photoresists. The process of lithography involves the exposure of selective regions of a photoresist and masking other regions either using a physical mask or by other means. The process of lithography for SU-8 typically involves the following steps: (1) coating of SU-8 of desired thickeness by spin coating or other methods, (2) soft baking in which most of the solvent present in SU-8 is evaporated, (3) exposure step in which light from a UV source of wavelength between 300 and 400 nm is incident on the SU-8 surface through appropriate mask, (4) post baking or post exposure bake (PEB) in which the chemical amplification is enhanced by thermal means to create high-aspect-ratio structures, and finally, (5) development step in which the unexposed regions are removed. These steps are illustrated in Figure 1.5.

Conventional lithography is mainly a planar or two-dimensional technique with little control on the height of the patterns fabricated. So, techniques such as five-beam interference lithography as well as combination of e-beam and FIB have been developed to allow 3D patterning that is often required in MEMS structures. Three-dimensional structures such as fractals can improve competing properties such as surface area and transport resistance in a material and within the context of MEMS, engender better electrodes. Yamada and Chung [24] have developed a novel method for the 3D patterning carbon material by including a vaporizable thermoplastic spacer below a carbon precursor epoxy film. Fractal geometries have been synthesized by many techniques including sol–gel synthesis, CVD deposition on carbon posts, doped photoresist method, and 3D carbon microstructures from grayscale lithography of SU-8 [40].

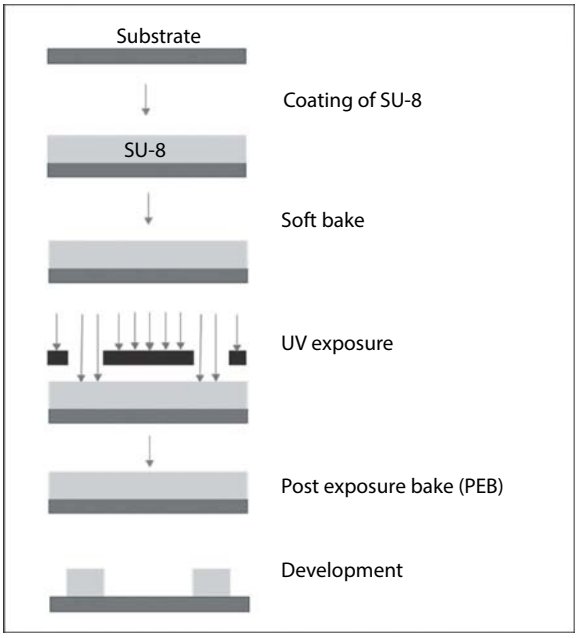

Figure 1.5 Steps involved in the photolithographic patterning of negative photoresist SU-8

Five-beam interference lithography was used by Jin *et al.* [22] to create a woodpile structure with silica shell support (to reduce shrinkage) by the carbonization of patterned SU-8 photoresist. Long *et al.* [50] have tailored the diffraction-induced light distribution of a photolithographic process to fabricate suspended C-MEMS structures. This has been achieved by modeling the light distribution to predict conditions and parameters such as mask pattern dimensions, gap distance between photomask and photoresist, and exposure time for the formation of suspended structures. Interdigitated array electrodes have also been reported by Heo *et al.* [48] as having an increased current amplification factor due to efficient recycling of redox species between carbon nanoelectrodes having 1:1 aspect ratio. Here, a two-mask process was used to fabricate the electrodes.

Poly methyl methacrylate (PMMA), one of the more popular e-beam resists, does not yield high carbonaceous residue [51]. Thus, e-beam lithography has not been used as extensively as UV lithography for C-MEMS applications. Madou and co-workers [52] have modified the process of e-beam lithography for use in SU-8 by coating a thin layer of conductive metal on the nonconductive SU-8 surface. This on pyrolysis gave complex C-MEMS structures such as suspended bridges and networks. Recently, Huigao *et al.* [30] and Gautsch *et al.* [31, 32] have found that the overexposure by e-beam can also carbonize a PMMA resist while simultaneously patterning it giving rise to carbon nanostructures by direct e-beam exposure without development. One of the structures fabricated by this method is shown in Figure 1.6. This patterning and simultaneous carbonization occur due to e-beam-induced collapse of the PMMA macromolecular chains. However, further carbonization and graphitization required a protected annealing step at 600 °C in Ar. The authors have also favorably compared this method to the

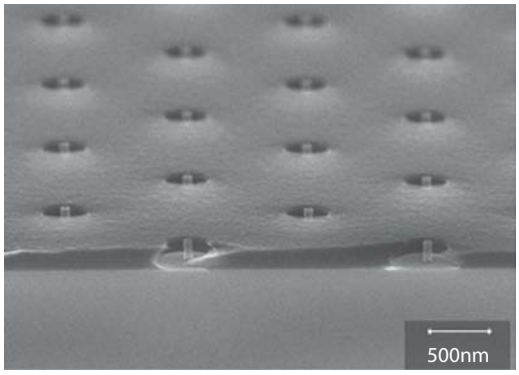

Figure 1.6 SEM image of a carbon nanostructure array fabricated by e-beam induced pyrolysis of PMMA. (Reproduced with permission from Ref. [44], Copyright 2009 Elsevier B.V.)

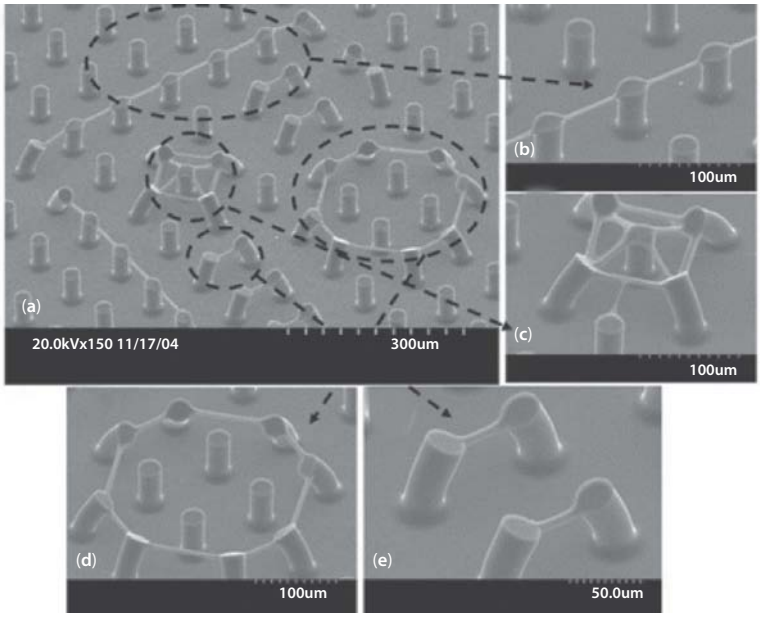

Figure 1.7 Controlled fabrication of CNWs between carbon posts by electron beam writing. (Reproduced with permission from Ref. [42], Copyright 2006 Elsevier B.V.)

electron beam-induced deposition or EBID method of creating carbon nanostructures. Malladi *et al.* [52] have also used the method of e-beam writing to controllably fabricate carbon nanowires that connect carbon pillars (Figure 1.7).

1.3.3 Soft Lithographic Techniques

The materials that can be patterned by lithographic techniques, *i.e.,* sensitive to photons, electrons, or ions, are arguably few, and not all photoresists can be converted to carbon. Furthermore, modified lithographic techniques for 3D patterning are far from

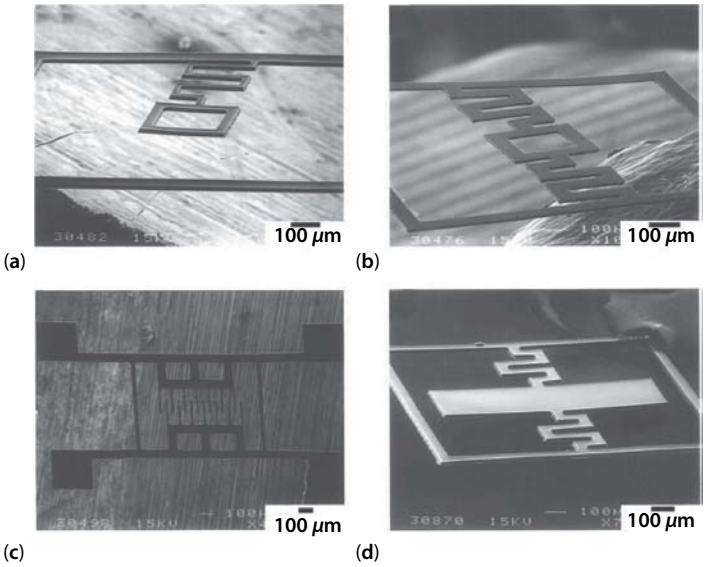

Figure 1.8 Soft lithographic fabrication of carbon MEMS elements such as (a) and (b) accelerometers, (c) precursor to an interdigitated capacitor and (d) optical deflector. (Adapted with permission from Ref. [6], Copyright 1997 American Chemical Society.)

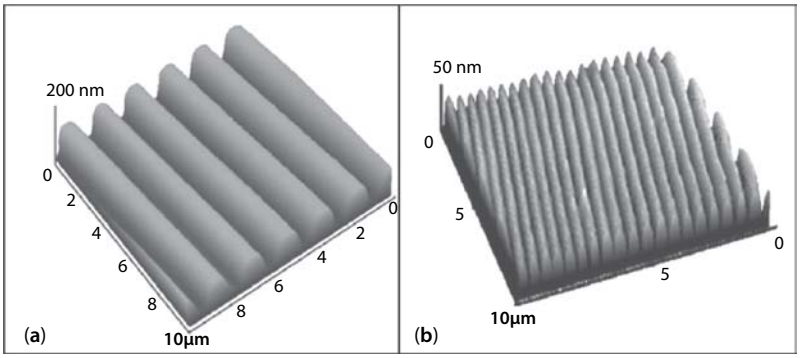

Figure 1.9 Repeated replica miniaturization. (a) Original pattern of periodicity 1.6 μm (b) carbonized pattern after two cycles of replications (periodicity ~379 nm) (Reproduced with permission from Ref. [23], Copyright 2010 American Chemical Society)

simple. Soft lithographic techniques such as molding and imprinting can extend the capability of conventional lithographic techniques in terms of 3D capability and various materials. Schueller *et al.* [53] have replicated MEMS elements such as accelerometers, interdigitated capacitors, and electrostatically actuated optical deflectors using poly (furfuryl alcohol) in an elastomeric mold (Figure 1.8)

Sharma *et al.* [36] have used micromolding and exploited the isotropic volume shrinkage of resorcinol–formaldehyde during drying to repeatedly miniaturize micropatterns. They have been able to achieve down to 379 nm periodicity (Figure 1.9) in C-MEMS

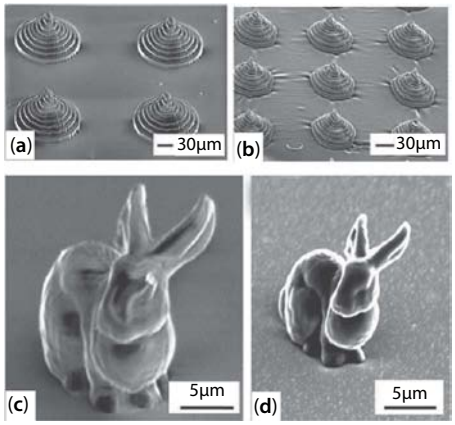

Figure 1.10. Two photon lithography and replica moulding for the fabrication of 3D patterns in (a) and (c) positive photoresist and (b) and (d) carbon. (Reproduced with permission from [33], Copyright The Optical Society (OSA))

patterns which is limited by the wettability of the PDMS (polydimethylsiloxane) intermediate molding material with hydrogel patterns. More recently, Daicho *et al.* [33] have not only developed two new photopolymers based on resorcinol di-glycidyl ether that carbonize during pyrolysis, but they have also illustrated microtransfer molding of 3D patterns (Figure 1.10) fabricated by two-photon lithography using PDMS as a transfer mold. Penmatsa *et al.* [54] have used nanoimrint lithography to pattern an AR-UL-01 photoresist and pyrolyzed it to create carbon micropatterns. Nanoimprint lithography is able to achieve down to 50 nm resolution of features and is relatively inexpensive compared to e-beam or other nanopatterning techniques. However, they have found significant vertical shrinkage which could be an issue for patterning high-aspect-ratio structures.

1.3.4 Self-Assembly and Bottom-Up Processes for the Fabrication of C-MEMS Structures

Lithographic top-down processing involves the directed or guided patterning of the material into useful structures. In contrast, self-assembly and additive bottom-up processes involve the arrangement of the material without active guidance. Electrospinning of fibrous mats which can then be used as sensor platforms is an example of a self-assembly method for MEMS fabrication. CVD (for the fabrication of CNTs or DLC, *etc.*) is an example of a bottom-up technique. Both self-assembly and other bottom-up processes are characterized by reduced control of the MEMS/NEMS feature shape and dimensions due to the absence of any external guidance. However, these techniques have a strong advantage in creating smaller feature sizes with inexpensive equipment. Furthermore, they have better 3D patterning capability thus able to create high-surface-area structures for surface-active applications such as bio/chemical sensing.

Recent research has rediscovered the advantageous aspects of fractal and other 3D geometries in battery applications due to the higher active surface area. Fractal

structures, in particular, reduce the internal resistance of the carbon electrode while maximizing surface area in battery applications [40]. Self-assembly-based fabrication which relies on the intrinsic chemical and physical properties of the material to create ordered structures is better suited to creating such structures. Electrospraying and electrospinning, sol–gel processes, and instability-based self-organization of polymers are some of the examples of self-assembly methods to create fractal and hierarchical structures. Sharma *et al.* [35] in an example of a self-assembly based fabrication, have been able to create carbon xerogel particles and folded fractal-like patterns by the sol–gel polycondensation of resorcinol and formaldehyde followed by pyrolysis.

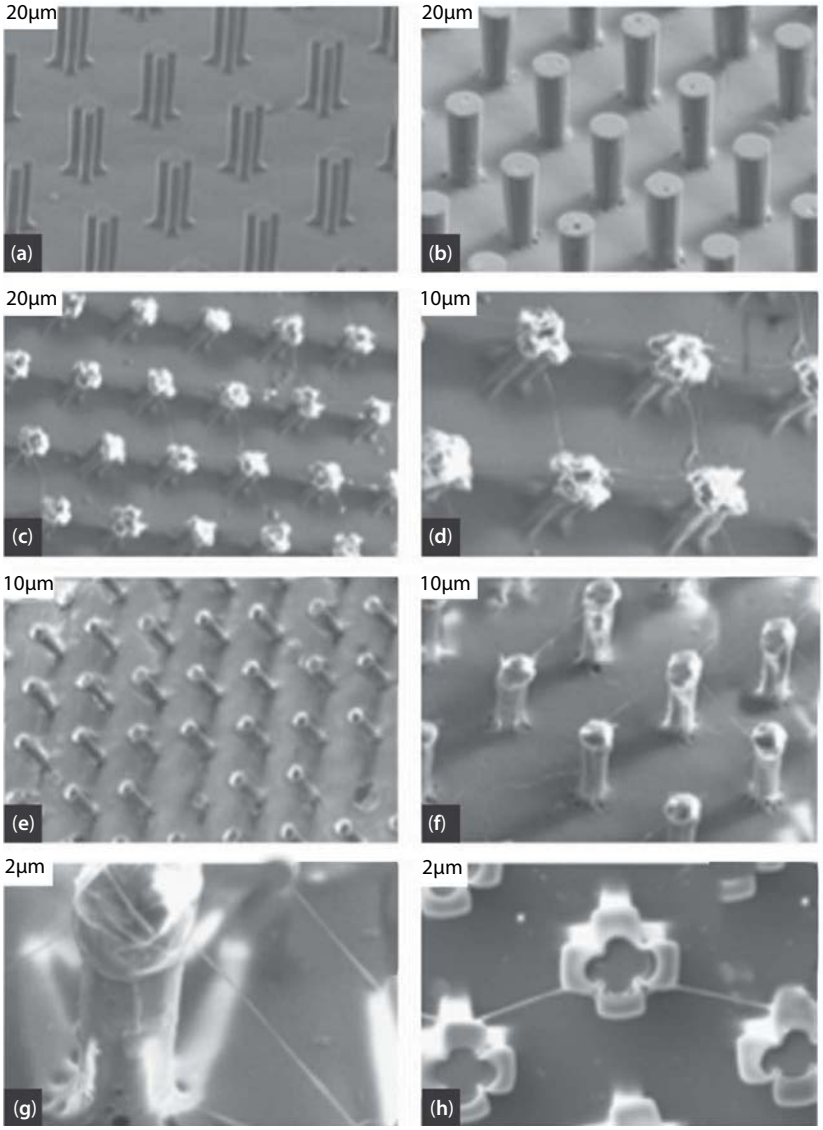

Figure 1.11. Electrospinning based method to create carbon nanowires connected carbon posts. (Reproduced with Permission from Ref. [50], Copyright 2011 Elsevier B.V.)

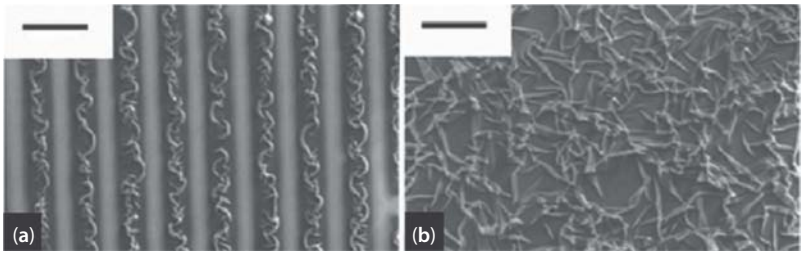

Figure 1.12. SEM images of self-organization based patterning in photoresist. Buckled patterns carbonized at 900 °C (a) UV exposed through equidistand fringe pattern mask and (b) flood UV exposure. (Scale bar:100 μm). (Reproduced from Ref [51], Copyright 2012 Springer)

Electrospinning and electrospraying are techniques where polymeric solutions are squeezed through a nozzle and onto a substrate through an electric field that draws the polymeric solution into fine fibers or particles. While both methods have been used to create carbon structures [55], the electrospinning method has also been employed as a directed self-assembly method in the work by Sharma *et al.* [56], where carbon pillar arrays were used as substrates to alter the electric field such that electrospinning of various carbon precursor polymers such as PAN, SU-8, and RF gel resulted in nanowires connecting the pillars (Figure 1.11). Thus, a substrate fabricated by top-down technique is integrated with a self-assembly technique to create functional structures. This structure is also examined as a setup to measure the electrical properties of single-carbon nanowires.

Another example of a combination of top-down and bottom-up techniques to achieve multiscale patterning of a photoresist films has also been illustrated by a combination of photolithographic patterning and buckling-instability-induced patterning in a Xylene-diluted SC-100 (a conventional cyclic polyisoprene photoresist) [28]. The buckling instability is induced due to the anisotropic swelling and differential shrinkage of the top layer of hard cross-linked photoresist and lower soft native layer during development and subsequent drying. This is an example of a combined top-down and botom-up approach where the photolithographic patterning creates top-down regular patterns, while the self-organization creates smaller patterns superimposed on the larger regular patterns as shown in Figure 1.12. Here, the top-down technique is used to impose control on the features fabricated by a subsequent self-assembly process.

1.4 Integration of C-MEMS Structures with Other Materials

Although carbon is a versatile functional material for various applications, C-MEMS structures often still require integration with other materials and processes to create a complete MEMS device. For example, electrical connections may require the use of gold layers and silicon may be used as substrate or supporting material. However, materials that cannot withstand the high pyrolysis temperatures without physical/chemical transformations cannot be integrated prior to pyrolysis. For example, as illustrated earlier, Madou and co-workers [21] have found that after pyrolysis of an SU-8 pillar array pattern on Au/Ti contact layer, carbon posts with Au balls at the base of the posts are

formed. While using a rigid substrate material places constraints on the shrinkage of the carbon precursor leading to stresses, and in some cases delamination; integration of free-standing carbon structures to other materials after pyrolysis is also difficult due to the nonreactive surface of pyrolyzed carbon. Furthermore, the inert carbon surface also means that to use the glassy carbon in surface-active applications such as biosensing requires the grafting of bio/active moieties on the C-MEMS surface. Thus, in order to incorporate or integrate carbon MEMS/NEMS structures with other materials and functionalities, two methods are available to us: (1) the surface modification of carbon using the versatile carbon chemistry and (2) incorporating appropriate fillers and additives into the carbon precursor not only to address pyrolysis-induced shrinkage but also to also improve the graphitization and electrochemical and mechanical properties.

The nonreactive nature of the glassy carbon surface after pyrolysis is mainly due to the reducing atmosphere of pyrolysis. While this can be an advantage when applying the structures in corrosive or biological environments, in applications requiring active surfaces such as bio-adsorption-based sensing, surface modification becomes indispensable. However, one can exploit the rich chemistry of carbon to modify the surface with active groups for a variety of applications. This modification can be electrochemical such as electrochemically assisted oxidative or reductive processes, or chemical means. Electrochemical modification methodologies can result in, for example, aryl or amine groups on the carbon surface [57]. Bisht *et al.* [58] have fabricated a biofuel cell anode on a C-MEMS structure by electrochemical oxidation of amine linkers on pyrolyzed micropatterned electrodes. Chemical surface modification of carbon microstructures by, for example, oxygen plasma treatment, nitric acid and sulfuric acid treatment has also been achieved. Hirayabashi *et al.* [59] have used all of these techniques as well as 4-amino benzoic acid (4-ABA) treatment for the purposes of improving the attachment affinity of carbon microstructures to DNA and other biomolecules. Positive photoresist AZ9260 derived pyrolyzed carbon surface was also grafted with thrombin aptamers using carbodiimide-mediated chemistry followed by Triton-X 100 and BSA (bovine serum albumin) treatment to function as a thrombin sensor by Lee *et al.* [26]. Here, the BSA treatment reduces the nonspecific binding of thrombin. Using this sensor, they were able to measure thrombin concentrations by electrochemical impedance spectroscopy (EIS) measurement between 0.5 and 500 nM. Yang *et al.* [44] have also demonstrated the surface modification by the direct amination of carbon microstructures for DNA detection. The amination was achieved by UV irradiation in an ammonia gas environment.

Apart from surface modifications, various additives and fillers such as CNTs, CNFs, and nanoparticles can also be incorporated into C-MEMS/NEMS structures. Some of the examples such as silica [22], CNFs [10], and gold [21] have been illustrated in earlier sections. In particular, CNT integration into materials can impart improved and novel functionality such as electrostatic actuation to the system [60]. There are two main methods to achieve the integration of CNTs with a C-MEMS device. The first is the incorporation of CNTs into the carbon precursor before patterning. As CNTs are not significantly modified during the pyrolysis process, the final part becomes a composite of glassy carbon and CNTs. Xi *et al.* [61] have achieved the CNT integration into SU-8 micropattern (post array) by self-assembly-based adsorption during development by adding a CNT-mixed SU-8 developer. More recently, He *et al.* [62] have used a silicon

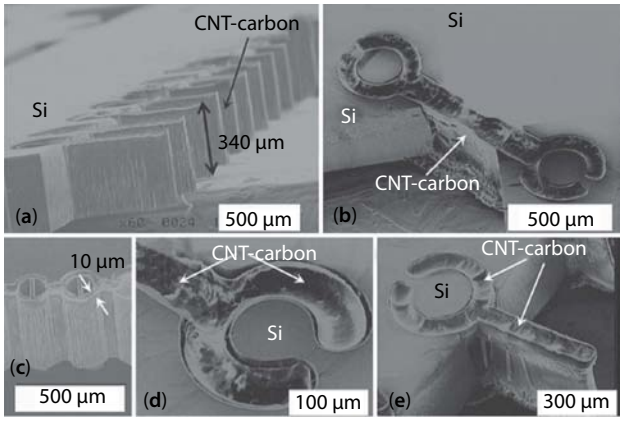

Figure 1.13 SEM images of CNT-carbon composite microstructures. (a), (b) and (c) Tilt views of cantilever, bridge and crossbar ring microstructures, respectively, (d) Surface of the patterned composite microstructure and (e) Magnified view of a single cantilever. (Reproduced with permission from Ref. [57], Copyright Springer)

micromolding technique to pattern a solution of SU-8 mixed with 1 wt% of CNT followed by pyrolysis to result in CNT/carbon composites of with feature sizes between ten and few hundred micrometers (Figure 1.13). The second method of incorporation of CNTs with C-MEMS structure is by the integration of catalyst particles onto the carbon precursor or carbon structure followed by CVD. Such a technique was explored by Chen *et al.* [63] using a conformal coating of Fe catalyst particles by electrostatic spray on a pyrolyzed photoresist 3D C-MEMS structure. The composite material was found to have 20 times higher capacitance than bare C-MEMS and the capacitance could be further improved the functionalization of the composite with oxygen plasma without affecting the structure. However, in complex 3D shapes, uniform conformal coatings are difficult to achieve [40].

Yamada and Chung [24, 25] have demonstrated the ability to integrate carbon structures to alumina substrates with good bonding as well as improve conductivity and reduce shrinkage-induced cracking by including various fillers such as MWCNTs, carbon black, and silver and nickel nanoparticles. They have found that while MWCNT was more effective in reducing the cracking, nickel nanoparticles were more effective in improving conductivity. The percentage of graphitic regions present in the pyrolyzed carbon has a strong effect on its electrochemical properties such as electrical conductivity and irreversible capacity and thus important implications for electrochemical sensing and electrode applications of carbon. By and large, it is advantageous to improve the graphitization during pyrolysis by means of additives and fillers rather than increasing pyrolysis temperatures as the latter method is more expensive and can have unwanted consequences and effects on noncarbon materials in the MEMS device. By using additives that have a catalytic effect on graphitization such as titanium [64], boron [65], zirconia [66], and iron oxide [67, 68], researchers have been able to increase the crystallite size and graphitization of carbon pyrolyzed from various carbon sources.

The research carried out in electrospinning by Maitra *et al.* [69] and Sharma *et al.* [70] illustrates electrospinning as another novel method of incorporating fillers and

increasing graphitization. Using the method of directed electrospinning, *i.e.,* electrospinning PAN/CNT nanofibers between and connecting a pillar pattern which is then converted to a carbon structure, Maitra *et al.* have shown increased graphitization which is proposed to be due to the templating effect of CNTs. Sharma *et al.*, [70] on the other hand, have observed a core–shell structure having a graphitic shell and glassy core which shows increased electrical conductivity.

1.5 Conclusion

In summary, it is evident that carbon-based structures are easily fabricated, integrated, and adapted into a variety of MEMS devices. The process of pyrolysis is a facile technique for converting virtually any patterned precursor including positive and negative photoresists into its miniaturized replica in carbon. While the shrinkage and related stresses and defects associated with pyrolysis is a potential drawback, researchers have created innovative workarounds for this problem by modifying the temperature and atmosphere of pyrolysis and by using filler materials. Lithographic top-down patterning, bottom-up self-assembly techniques, and soft lithographic techniques have been applied successfully to create C-MEMS/NEMS structures which can be further integrated with other materials and substrates.

Some of the applications of the carbon microelements come from the inherent electrochemical and mechanical properties of carbon such as microelectrodes in battery applications, bio/chemical sensing elements and in electrostatic actuation, etc. The surface modification of carbon can also potentially widen the applications where carbon structures can form an integral part such as in tissue engineering, microfluidics, and many others. Using the right combinations of fabrication techniques and precursor materials, carbon-based MEMS devices can be integrated into a wide variety of biochemical, electromechanical, and structural applications.

References

1. R.L. McCreery, *Chem. Rev*, Vol. 108, 2646–2687, 2008.
2. M.F.L. De Volder, R. Vansweevelt, P. Wagner, D. Reynaerts, C. Van Hoof, and A.J. Hart, *ACS Nano*, Vol. 5, 6593–6600, 2011.
3. J.K. Luo, Y.Q. Fu, H.R. Le, J.A. Williams, S.M. Spearing, and W.I. Milne, *J. Micromech. Microeng.*, Vol. 17, S147–S163, 2007.
4. C. Stampfer, A. Jungen, and C. Hierold, *IEEE Sens. J.*, Vol. 6, 613–617, 2006.
5. C. Wang, R. Zaouk, B.Y. Park, and M.J. Madou, *Int. J. Manuf. Technol. Manage.*, Vol. 13, 360–375, 2008.
6. O.J.A. Schueller, S.T. Brittain, and G.M. Whitesides, *Sens. Actuat. A Phys.*, Vol. 72, 125–139, 1999.
7. E. López-Honorato, P.J. Meadows, R.A. Shatwell, and P. Xiao, *Carbon*, Vol. 48, 881–890, 2010.
8. S. Ranganathan, R. Mccreery, S.M. Majji, and M. Madou, *J. Electrochem. Soc.*, Vol. 147, 277–282, 2000.
9. E.H. Cook and D.J.D. Carter, *J. Vac. Sci. Technol. B*, Vol. 29, 2011.

10. V.T. Dau, T. Yamada, D.V. Dao, B.T. Tung, K. Hata, and S. Sugiyama, *Microelectron. J.*, Vol. 41, 860–864, 2010.
11. K.C. Park, J.H. Ryu, K.S. Kim, Y.Y. Yu, and J. Jang, *J. Vac. Sci. Technol. B*, Vol. 25, 1261–1264, 2007.
12. M.H. Park, J.W. Lee, Y.I. Lee, J.H. Lee, J.H. Hwang, H.K. Kim, and C.W. Yang, *J. Nanosci. Nanotechnol.*, Vol. 11, 602–605, 2011.
13. D.J. Yuan, W. Lin, R. Guo, C.P. Wong, and S. Das, *Nanotechnology*, Vol. 23, 215303, 2012.
14. A.B. Kaul, E.W. Wong, L. Epp, and B.D. Hunt, *Nano Lett.*, Vol. 6, 942–947, 2006.
15. J. Chae, H.J. Jin, and K. Jain, *Mat. Lett.*, Vol. 63, 1823–1825, 2009.
16. M.W. Lee, Y.H. Lin, and G.B. Lee, *Microfluid. Nanofluid.*, Vol. 8, 609–617, 2010.
17. Y.H. Yan, M.B. Chan-Park, and Q. Zhang, *Small*, Vol. 3, 24–42, 2007.
18. D. Langheinrich, S. Dorfler, H. Althues, S. Kaskel, and A. Lasagni, *Surf. Coat. Technol.*, Vol. 206, 4808–4813, 2012.
19. S. Lu, J. Chung, and R.S. Ruoff, *Nanotechnology*, Vol. 16, 1765, 2005.
20. G.M. Jenkins, and K. Kawamura, *Nature*, Vol. 231, 175–176, 1971.
21. C.L. Wang, R. Zaouk, and M. Madou, *Carbon*, Vol. 44, 3073–3077, 2006.
22. W.M. Jin and J.H. Moon, *J. Mat. Chem.*, Vol. 21, 14456–14460, 2011.
23. A.M. Lyons, *J. Non-Cryst. Solids*, Vol. 70, 99–109, 1985.
24. Y. Yamada and D.D.L. Chung, *Carbon*, Vol. 46, 1765–1772, 2008.
25. Y. Yamada and D.D.L. Chung, *Carbon*, Vol. 46, 1798–1801, 2008.
26. J.A. Lee, S. Hwang, J. Kwak, S. Il Park, S.S. Lee, and K.C. Lee, *Sens. Actuat. B Chem.*, Vol. 129, 372–379, 2008.
27. B. Hsia, M.S. Kim, M. Vincent, C. Carraro, and R. Maboudian, *Carbon*, Vol. 57, 395–400, 2013.
28. M.M. Kulkarni, C.S. Sharma, A. Sharma, S. Kalmodia, and B. Basu, *J. Mat. Sci.*, Vol. 47, 3867–3875, 2012.
29. T. Moriuchi, K. Morishima, and Y. Furukawa, *Int. J. Precis. Eng. Manuf.*, Vol. 9, 23–27, 2008.
30. D. Huigao, Z. Jianguo, Z. Yongzhe, X. Erqing, and H. Li, *Nanotechnology*, Vol. 20, 135306, 2009.
31. S. Gautsch and N.F. de Rooij, *Microelectron. Eng.*, Vol. 88, 2533–2536, 2011.
32. S. Gautsch, M. Studer, and N.F. de Rooij, *Microelectron. Eng.*, Vol. 87, 1139–1142, 2010.
33. Y. Daicho, T. Murakami, T. Hagiwara, and S. Maruo, *Opt. Mat. Express*, Vol. 3, 875–883, 2013.
34. C.S. Sharma, D.K. Upadhyay, and A. Sharma, *Industrial & Engineering Chemistry Research*, Vol. 48, 8030–8036, 2009.
35. C.S. Sharma, M.M. Kulkarni, A. Sharma, and M. Madou, *Chem. Eng. Sci.*, Vol. 64, 1536–1543, 2009.
36. C.S. Sharma, A. Verma, M.M. Kulkarni, D.K. Upadhyay, and A. Sharma, *ACS Appl. Mat. Interfaces*, Vol. 2, 2193–2197, 2010.
37. Y. Wang, L. Pham, G.P.S. de Vasconcellos, and M. Madou, *J. Power Sources*, Vol. 195, 4796–4803, 2010.
38. M. Liger, T. Harder, Y.-C. Tai, and S. Konishi, Parylene-pyrolyzed carbon for MEMS applications, in: Micro Electro Mechanical Systems, 2004. 17th IEEE International Conference on MEMS, IEEE, pp. 161–164, 2004.
39. C.L. Wang, G.Y. Jia, L.H. Taherabadi, and M.J. Madou, *J. Microelectromech. Syst.*, Vol. 14, 348–358, 2005.
40. B.Y. Park, R. Zaouk, C. Wang, and M.J. Madou, *J. Electrochem. Soc.*, Vol. 154, P1–P5, 2007.
41. Z.R. Tang, T.L. Shi, J.E. Gong, L. Nie, and S.Y. Liu, *Thin Solid Films*, Vol. 518, 2701–2706, 2010.

42. K. Naka, K. Okamoto, and S. Konishi, *Jpn. J. Appl. Phys.*, Vol. 47, 8982–8985, 2008.
43. G.T. Teixidor, R.B. Zaouk, B.Y. Park, and M.J. Madou, *J. Power Sources*, Vol. 183, 730–740, 2008.
44. J.H. Yang, V. Penmatsa, S. Tajima, H. Kawarada, and C.L. Wang, *Mater. Lett.*, Vol. 63, 2680–2683, 2009.
45. L. Zhang, T.L. Shi, Z.R. Tang, D. Liu, and S. Xi, *J. Microelectromech. Syst.*, Vol. 21, 1445–1451, 2012.
46. K. Kinoshita, X. Song, J. Kim, and M. Inaba, *J. Power Sources*, Vol. 81, 170–175, 1999.
47. H.A. Lee, Y.C. Byun, U. Singh, H.J. Cho, and H. Kim, *J. Nanosci. Nanotechnol.*, Vol. 11, 7322–7326, 2011.
48. J.I. Heo, D.S. Shim, G.T. Teixidor, S. Oh, M.J. Madou, and H. Shin, *J. Electrochem. Soc.*, Vol. 158, J76–J80, 2011.
49. R. Kometani, T. Hatakeyama, K. Kuroda, S. Warisawa, and S. Ishihara, *J. Vac. Sci. Technol. B*, Vol. 29, 06FE03, 2011.
50. H. Long, S. Xi, D. Liu, T. Shi, Q. Xia, S. Liu, and Z. Tang, *Opt. Express*, Vol. 20, 17126–17135, 2012.
51. J.A. Lewis, *Ann. Rev. Mater. Sci.*, Vol. 27, 147–173, 1997.
52. K. Malladi, C.L. Wang, and M. Madou, *Carbon*, Vol. 44, 2602–2607, 2006.
53. O.J.A. Schueller, S.T. Brittain, C. Marzolin, and G.M. Whitesides, *Chem. Mater.*, Vol. 9, 1399–1406, 1997.
54. V. Penmatsa, H. Kawarada, and C. Wang, *J. Micromech. Microeng.*, Vol. 22, 045024, 2012.
55. C.S. Sharma, S. Patil, S. Saurabh, A. Sharma, and R. Venkataraghavan, *Bull. Mater. Sci.*, Vol. 32, 239–246, 2009.
56. C.S. Sharma, H. Katepalli, A. Sharma, and M. Madou, *Carbon*, Vol. 49, 1727–1732, 2011.
57. S. Sharma, and M. Madou, *Bioinspired Biomimetic Nanobiomater.*, Vol. 1, 252–265, 2012.
58. G.S. Bisht, S. Holmberg, L. Kulinsky, and M. Madou, *Langmuir*, Vol. 28, 14055–14064, 2012.
59. M. Hirabayashi, B. Mehta, N.W. Vahidi, A. Khosla, and S. Kassegne, *J. Micromech. Microeng.*, Vol. 23, 1, 2013.
60. V.T. Dau, B.T. Tung, T.X. Dinh, D.V. Dao, T. Yamada, K. Hata, and S. Sugiyama, *J. Micromech. Microeng.*, Vol. 23, 075024, 2013.
61. S. Xi, T. Shi, D. Liu, L. Xu, H. Long, W. Lai, and Z. Tang, *Sens. Actuat. a-Phys.*, Vol. 198, 15–20, 2013.
62. L. He, M. Toda, Y. Kawai, H. Miyashita, M. Omori, T. Hashida, R. Berger, and T. Ono, *Microsyst. Technol. Micro- and Nanosyst. Inf. Storage Process. Syst.*, Vol. 20, 201–208, 2014.
63. W. Chen, M. Beidaghi, V. Penmatsa, K. Bechtold, L. Kumari, W.Z. Li, and C.L. Wang, *IEEE Trans. Nanotechnol.*, Vol. 9, 734–740, 2010.
64. Y. Zhang, S.H. Shen, and Y.J. Liu, *Polym. Degrad. Stab.*, Vol. 98, 514–518, 2013.
65. G.P. Yin, Y.Z. Gao, P.F. Shi, X.Q. Cheng, and A. Aramata, *Mater. Chem. Phys.*, Vol. 80, 94–101, 2003.
66. S.A. Steiner, T.F. Baumann, B.C. Bayer, R. Blume, M.A. Worsley, W.J. MoberlyChan, E.L. Shaw, R. Schlogl, A.J. Hart, S. Hofmann, and B.L. Wardle, *J. Am. Chem. Soc.*, Vol. 131, 12144–12154, 2009.
67. W. Che, S.Q. Shi, D. Zhang, D. Jiang, and H.M. Barnes, *Wood Fiber Sci.*, Vol. 46, 237–246, 2014.
68. W. Gao, Y. Wan, Y. Dou, and D. Zhao, *Adv. Energy Mater.*, Vol. 1, 115–123, 2011.
69. T. Maitra, S. Sharma, A. Srivastava, Y.K. Cho, M. Madou, and A. Sharma, *Carbon*, Vol. 50, 1753–1761, 2012.
70. S. Sharma, A. Sharma, Y.K. Cho, and M. Madou, *ACS Appl. Mater. Interfaces*, Vol. 4, 34–39, 2012.

2

Intelligent Model-Based Fault Diagnosis of MEMS

Afshin Izadian*

Energy Systems and Power Electronics Laboratory, Purdue School of Engineering and Technology, IUPUI, Indianapolis, IN, USA

Abstract

Fault in MEMS can originate from local defects, parameter tolerances, design problems, operation, and/or system-level defects. For instance, a fault might happen because of a fracture in different parts of the device, such as suspension springs or fingers. In open-to-air applications, there is a chance that dust and other particles fall on the structure of the device, which may cause a sudden mass change. In addition, the silicon-made structures absorb humidity from air, which results in changes in the mechanical properties of the suspension springs. For devices operating in vacuum conditions, any damage to the container might result in a loss of vacuum and, consequently, change in viscosity. In any of these cases, asymmetries result in behavioral changes and unwanted deviations from the desired output, which can be modeled in mathematical expressions.

In this chapter, the origins of fault are discussed, related mathematical models are obtained, and Kalman filters are developed and utilized in fault diagnosis. The structure of a multiple-model adaptive estimator is illustrated, and its application in fault diagnosis is simulated and experimentally verified. Other model-based diagnosis techniques wherein model parameters are identified and updated automatically are introduced, and their fault diagnosis performances are compared.

Keywords: Mathematical modeling, Kalman filters, model-based diagnosis, fault

2.1 Introduction

The micro-electro-mechanical systems (MEMS) market is predicted to expand to $7 Trillion [1, 2]. MEMS are important for many advanced applications ranging from satellite stabilizers to commercial accelerometers [3]. Their applications include, among others, inkjet printing heads, data storage systems [4], micro surgery applications [5], applications in space, e.g., thermal control of satellites [6], satellite communication [7], space and flight control [8], mirror-based projectors, and HDTV display engines. They are also used in biotech labs on chip drug delivery systems, optical switches, and active heat sinks for integrated circuits (ICs). In all of these applications, they are required to

**Corresponding author*: aizadian@iupui.edu

Atul Tiwari and Baldev Raj (eds.), Materials and Failures in MEMS and NEMS, (21–62)
© 2015 Scrivener Publishing LLC

show a high level of accuracy and functionality. Because of increased complexity and integration level of MEMS in advanced devices and the fact that they do not have an onboard diagnostics, a high-level diagnostics is essential.

2.1.1 MEMS Structure and Origins of Fault

MEMS devices are manufactured with different techniques, one of which is using the sacrificial layers made mainly from silicon oxide. These layers are removed to free each layer from the others. Different manufacturing steps and several machining stages are required for bulk and surface micromachining. Machining procedures on areas larger than 10 μm^2 are called bulk micromachining, and those on smaller areas are called surface micromachining. Layers, parts, joints, and containers in MEMS should possess specific mechanical and electrical characteristics. The problem occurs when there is an imperfection in the machining procedure, which results in different parameters than those expected in the design of the device. Devices with parameters other than those that are expected are hard to control; this matter is even worse when the parameters vary from device to device and are influenced by environmental and operating conditions. In the following sections of this chapter, the effects of the manufacturing steps on the surface, area, sidewall, and body shape are investigated along with their resultant parameter variations.

2.1.1.1 Material Growth Effects

Generally, silicon and other materials in different forms and configurations are widely used in MEMS structures. Depending on the purpose of the MEMS design, there are different materials such as ceramics, plastics, silicon, and glasses. Table 2.1 illustrates some material performance and characteristics [9].

These materials form different parts of a device and are deposited generally in high temperatures and with different deposition rates, resulting in specific mechanical and electrical characteristics. Material growth usually requires high temperatures, which might change the properties of the other deposited parts and their interfacing circuits. Polysilicon, for instance, has close characteristics to Si, such as doping during and after film deposition. SiO2 can be grown or deposited over a broad range of temperatures between 200 °C and 1150 °C to obviate different requirements in different applications. Polysilicon is resistant to SiO2 etchants, so a combination of both is used for surface

Table 2.1. Performance comparison of substrate materials [9].

Substrate	Cost	Metallization	Machinability
Ceramic	Medium	Fair	Poor
Plastic	Low	Poor	Fair
Silicon	High	Good	Very Good
Glass	Low	Good	Poor

micromachining. The polysilicon layer can be deposited in a low-pressure chemical vapor deposition or LPCVD. In this deposition, the relationship between the deposition rate and the substrate temperature is exponential; thus, precise temperature control of the reaction chamber is required. The typical temperature of the chamber is around 580–650 °C under a pressure of 100–400 mtorr when the silane (SiH4) is released to the chamber. For a process at 630 °C, the polysilicon deposition rate is about 100 /min. The characteristics of the deposited silicon layer are functions of the deposition temperature. The temperature along the tube varies about 5–15 °C; thus, there is a non-uniformity of deposition along the tube length.

Polysilicon is made of some small single-crystal domains called grains, which have different orientations, sizes, and alignments. The orientation of these grains results in roughness of the polysilicon. The structure of these grains changes dramatically due to the change in temperature. The size of the grain tends to change due to the thickness of the deposition. The orientation of the grains, like their size, is a function of deposition time. In addition, during the other thermal processes in manufacturing the other parts in MEMS, grain size and orientation will change significantly. Consequently, the roughness of the polysilicon surface increases with an increase in grain size and an undesirable outcome occurs from the microfabrication because "the surface roughness limits the pattern resolution recognized as defects on the surface" [9]. Therefore, the final product contains an unknown grain size and alignment, and consequently, the expected characteristics are different from what is desired.

The LPCVD method can be used to manufacture layers in thicknesses up to $5\mu m$. For layers with a higher thickness, the wafer bonding and etch-back techniques are often used. A deposition technique called *epi-poly* is used to produce a thick layer of polysilicon on sacrificial substrates. The most important point of the deposition is to align the device manufacturing and layer deposition to the crystallographic orientation. Any misalignment can cause a difference and cut the layers, resulting in the defects on the surfaces [10].

The main mechanical parameters that a substance should have to be used in MEMS construction include Young's modulus, yield strength, density, residual stress and stress gradients, electrical and thermal conductivity, and long-term stability [11, 12, 13–17]. Some other types of materials, such as silicon oxide and silicon nitride, can be used to separate the layers and/or mask some parts; however, they need to be protective and/or easy to etch.

The mechanical characteristics of silicon make it widely used in the electronic industry. Silicon is the primary material for bulk micromachining. In addition, silicon in the form of a single crystal can be used as the surface micromachining material of silicon-based MEMS. In addition, the other forms of silicon such as polysilicon, silicon nitride, and silicon oxide are used to form the surface micromachining for the primary structural material, electric insulation, and sacrificial material, respectively.

2.1.1.2 Lithography and Its Effects

Photolithography is one of the key manufacturing steps in the fabrication of MEMS devices, which includes covering specific areas for micromachining. This includes mask alignment, UV exposure, baking, and removing photo resistance for fabrication.

The mask is a pattern that covers some parts of the device for microfabrication. Manufacturing different parts requires different photo masks. For implementing of a symmetric design on the silicon wafer and creating mechanical devices, very accurate techniques are required. Masking as a part of the photolithography process is one of the critical steps to locate the casts of different parts of a mechanical device in the substrate. The quality of the final product and the symmetry of the structure mainly depend on the precision of this step. Figure 2.1 illustrates a catastrophic masking error, which has joined the comb fingers of the stationary part and the shuttle together. In a simpler case, this might be observed as a very small asymmetry in the device, which leaves the lateral displacement unequal on both sides.

In bulk micromachining, when aligning the MEMS device pattern (photo mask) with the crystalline orientation of the substrate, it is also important that the surface of the grown material is smooth. Any rotation from the required orientation will result in a *knife effect*, meaning that the surface will be rough, as if it is chopped. These rough surfaces may contain deep cracks and sharp edges at higher rotation angles. The knife

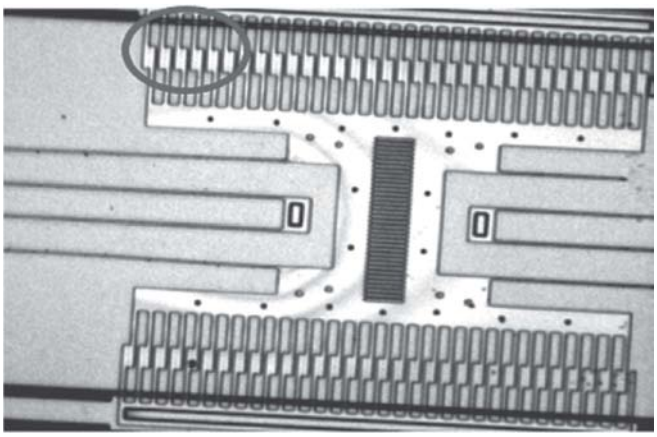

Figure 2.1 The fingers of the stationary part and the lateral shuttle joined together with lithography defects [11].

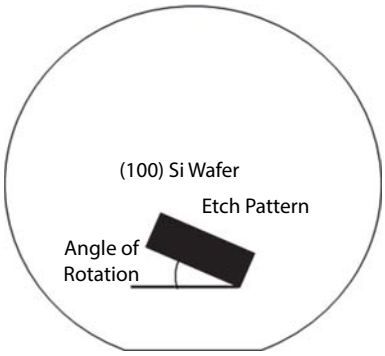

Figure 2.2 The misalignment angle from the wafer orientation [10].

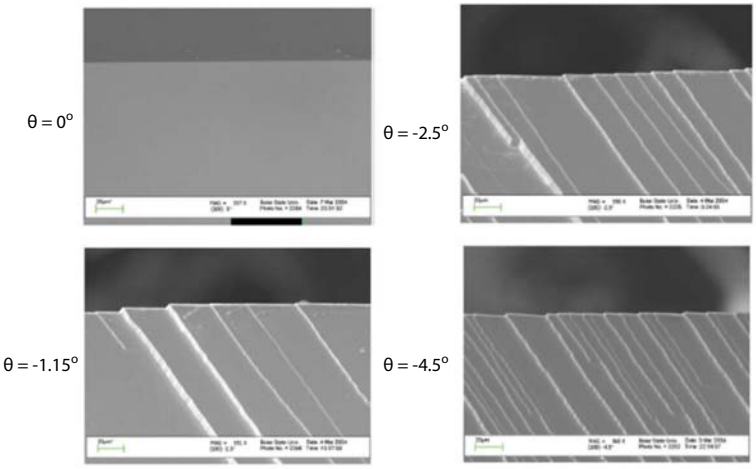

Figure 2.3 The misalignment, or knife effect, in different angles of bulk micromachining [18].

effect is illustrated in Figure 2.2, and the effect of higher rotation angles is shown in Figure 2.3.

In general, lithography can be considered one of the critical steps in manufacturing MEMS devices. Parameters such as the damping coefficient and the spring constant largely vary by small fabrication errors. For instance, a 0.2μm reduction in the size of a 5μm-wide spring beam is a 4% reduction in the width of the spring and results in approximately a 12% change in spring constant, whereas for a 1 μm-wide spring reduced by the same amount, the change is 20%, which results in a 49% spring constant variation [9].

2.1.1.3 Effect of Etching Process on Parameters of MEMS

Etching is defined as removing a specific material in a specific direction/rate and can be done with liquid or gaseous material known as etchants. These materials dissolve the targets in two different ways, isotropic and anisotropic, both of which require that the end of the etching process be recognized. Isotropic etchants are those that etch all the different surfaces at the same rate, whereas anisotropic etchants have different etching rates indifferent directions. In this way, some selective surfaces are etched more.

Anisotropic etchants usually leave a surface too rough in macro-scale. The macroscopic roughness, called notching or pillowing, is observed when the center of the etched area has a slower average etching rate compared to the borders of that area. The difference can be as large as 1–2 μm, which is considerable in a 10–20 μm etch length. Over- and underetching deforms the cantilevers, spring beams, and surfaces and changes the critical values of the microsystem, which for instance, can be observed as a shift in the resonant frequency of the device. Figure 2.4 shows the notching and roughness effects [9].

Since the etching rate has a significant effect on the manufactured device and the main part is to reach to the best etching point, techniques to stop the etching are

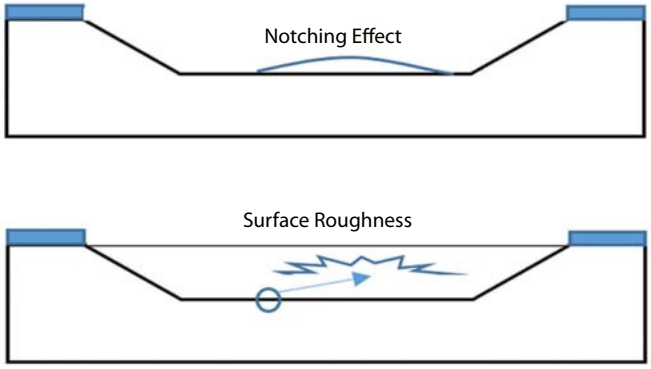

Figure 2.4 Macroscopic and microscopic roughness [9].

required to halt this process. Non-uniformity of the etched surfaces, due to the non-uniformity of the thickness of the silicon wafer, is high. This variation can be 40 μm, and even with the best quality of silicon wafer, this value is not less than 2 μm [9]. This variation may become harmful for some applications.

2.1.1.4 Effect of Stress, Stress Gradients, Wearing, and Stiction on Deposited Films

Stress: One of the most important sources of nonlinearities is the stress in thin films. Stress originates from different sources, such as differences in the thermal expansion coefficient of different layers and materials, specifically when a thin film is deposited at a higher temperature than at other layers. Another source of stress is the difference in the size of dopant atoms in a thin film layer. For example, the differences in size of thermally grown silicon dioxide (SiO_2) cause compression, because the size of the oxide atoms is larger than the lattice size in the substrate of the silicon atoms. Very large stress values may result in the cracking or delaminating of films and layers. Stress in films can be observed as strain or deformation of the microstructures. Another effect of stress is observed as a change of the resonant frequency of the device, as shown in Figure 2.5. In a comb resonator containing different layers that are deposited individually at different annealing and thermal processes, higher stress values are expected. Therefore, temperature variations and environmental conditions might change the device's behavior by directly affecting its parameters.

2.1.1.4.1 Deformation, Stress, and Wear

Forces applied to the body of a MEMS structure will cause a shape deformation. If the body returns to its original when the load is removed, the deformation is called elastic. If there is a residual deformation remaining in the body, it is called plastic or non-elastic deformation. If a material has the same elasticity effect in all directions, it is called isotropic; otherwise, it is anisotropic.

Stress Gradient: Changing the stress values by the thickness of the layers, which is called stress gradient, adds up to the nonlinearity of thin films. High stress gradients on thin plates and gears result in deformation of spiral shape beams.

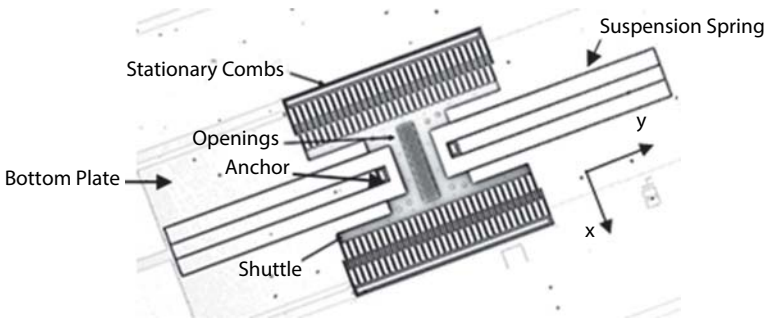

Figure 2.5 MEMS lateral comb resonator [11].

Wearing: When two surfaces rub against each other, the friction between them makes them wear. Friction at the microscopic level is similar to that of macro-sized bodies. If surfaces are made of the same material, they experience more friction and, thus, show wear faster. In conventional designs, surfaces have different materials to reduce the friction. In most of MEMS devices, the surfaces that rub against each other are made of silicon or polysilicon, and most of the time, they operate while dry. Usually, devices operating at frequencies higher than the resonant frequency wear faster. The wear rate is a function of the adhesion of the surfaces rubbing against each other. The wearing of the device accelerates when the surfaces start decaying. Therefore, the lifetime of the device is limited by friction and conditions such as operating frequency and dryness [19].

Stiction: One of the most harmful effects on the MEMS device is stiction, which is the unintended absorption of surfaces and parts. The effect of stiction is shown in Figure 2.6 [20].

The factors that cause stiction are nanoscale surface roughness, large surface areas, electrostatic attraction, humidity, and hydro-absorbent surfaces. Two main forms of stiction are stiction due to the release process and *in-use* stiction [9]. The main cause of stiction in the release process involves the capillary forces of the etchants and other washing liquids that pull the surfaces and parts together as shown in Figure 2.6. Trapped charges on the surfaces can cause electrostatic attraction and increase the stiction. In addition, an extremely humid environment increases the adhesion energy of the parts and elevates the stiction. Water has the same effect as that of the release process on the adhesion of the parts. The stiction effect is increased after the acid releasing process and the dissolving of the sacrificial layers

2.1.1.5 Electrostatic Force

The electrostatic field around the opening areas experiences field fringing, which affects field uniformity and causes forces. The force is affected by the distance between the surfaces and the shape of the bodies facing each other. Much of the related research has neglected the effects of fringing fields, although several researchers have attempted to devise a formula for it, which considers merely the geometry of the plates [18,21,22]. The main effect of fringing is the change of the electrostatic force according to the applied

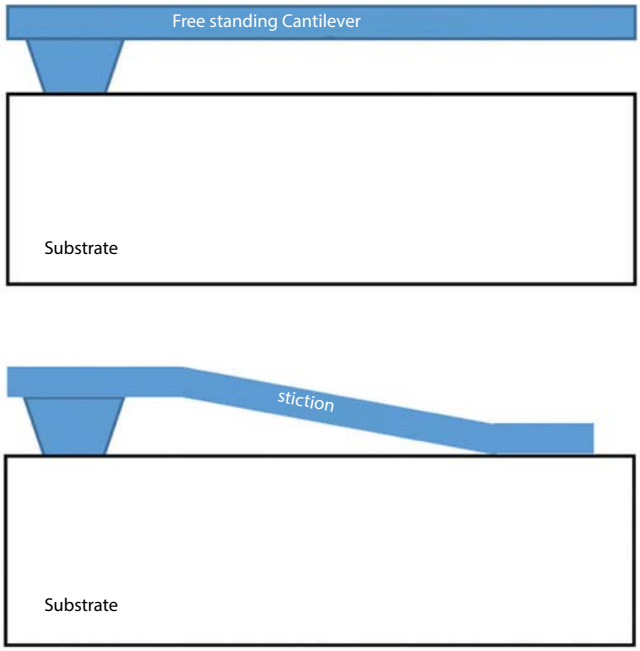

Figure 2.6 Stiction failure: (a) free-standing cantilever and (b) stiction of the same cantilever [20].

Table 2.2. Direct effect of manufacturing process and mechanical effects on the parameters of the device [11].

	Lithography	Material growth	Etching	Mechanical properties	Surface roughness	Stress	Stiction	Aging
Mass		•		•				
Spring Constant	•	•	•	•		•		•
Damping	•		•		•			
Electrostatic Force			•		•		•	

voltages. Another effect in MEMS devices involves the pull-in voltage. According to the inversely proportional relation of the electrostatic force to the distance of the parts, if the parts are placed closer than 67% of the total air gap between them, then the increment rate of electrostatic force becomes greater than that of the suspension spring restoring force, which puts the device into unstable regions of operation. In motion control of MEMS devices, some of the control efforts involve neutralizing the unwanted forces in the device. The asymmetry of the MEMS structure and the devices especially designed for torsion purposes cause the production of unequal electrostatic forces on the bodies. This matter dominates the pull-in voltage effect. However, microscopic

surface roughness in the large distances between the surfaces has no significant effect on the electric field distribution of the surfaces.

Humidity in the air surrounding the device increases the stiction of the plates and contributes to unwanted forces; hence, in microscale devices, the electrostatic force is a nonlinear function of the quality of the interface surrounding the material between the plates, the shape and distance between the fingers, the release process, the roughness of the bulk substrate, and the applied voltage. These effects and the parameter variations cannot be expressed in a lump formulation of the electrostatic force, which results in uncertain variation of the force during operation. Table 2.2 briefly introduces the parameter variations and their causes in the microfabrication processes.

2.2 Model-Based Fault Diagnosis

Faults can be expressed in mathematical model of MEMS [11, 12, 19, 23-31]. They can be modeled by tools such as the contamination and reliability analysis of microelectromechanical layout (CARAMEL) technique, which interprets system structural variations in form of electric circuit elements [32, 33]. In this technique, suitable models containing different fault possibilities can be obtained and used as residual signal generators. Kolpekwar *et al.* modeled up to 4000 types of structural defects using CARAMEL [32]. However, defects such as the change of the environmental and operating conditions, e.g., satellites, fluid control devices, micro-pumps in which the microsystem is under the influence of radiation, rapid environmental changes, and noise, cannot be modeled by CARAMEL [34]. If the displacement of MEMS is monitored, e.g., a laser beam, model-based fault diagnosis can be used. Therefore, a robust modeling technique and compatible with optical monitoring methods is required.

Performance in model-based fault diagnosis of MEMS [35] requires an accurate representation of the faults. The model of the system should represent the dynamics of the observable systems and generate residual signals of the systems under various conditions. However, in noise-contaminated environments, Kalman filters may be required to prevent performance deterioration [14-16]. Other techniques may require proper forgetting-factor techniques to identify accurate and effective models. Slowly varying parameter systems requires system identification techniques to accurately measure the expected output signals, leading to a high-performance diagnosis [14]. The modeling process using Kalman filters or estimation-based techniques require accurate system and measurement noise evaluations or several trials and errors to tune the fixed forgetting factors. Accurate noise evaluation is required in Kalman filters. Noise under- and overestimation resulted in a low-performance residual generation and evaluation process, thus lowering the sensitivity of the fault diagnosis [14-17]. The estimation-based techniques require a manual adjustment of the estimator gains for better results. A history of the variation needs to be selected in parameter estimation blocks. However, the accuracy highly depends on the forgetting-factor gain obtained in a trial and error. The gain has to be re-tuned if the system parameters shift over time or if the noise level changes.

2.2.1 Fault and Failure Definitions

In the beginning, some definitions are necessary to explain the difference between fault and failure. A *fault* in a dynamical system is defined as a change in the construction of the system from normal behavior. Different changes might show the same end effects in the system. A *failure* in the system occurs because of the severe changes in normal operations of the system, and the system becomes dysfunctional and irrecoverable. Parameter variations are the most common type of fault in microsystems. A faulty microsystem can still provide the expected operation by employing a proper control system.

2.2.2 System Behavior

Input/output (I/O) sets define the systems behavior in case of normal or fault conditions. In a system, all sets of possible combination I/O pairs define the space $u \times y$. System behavior is a subset of this space, denoted by β in Figure 2.7. The output of the system due to an input might be placed in the accepted region of the operation, A, or, as result of a change in the system, might be inconsistent with the system dynamics and known as a fault, C. In this case, the system generates a different output for the same excitation.

The system behavior is defined as $y(t) = k_{sys}u(t)$, where k_{sys} is known as the system. The set of possible real numbers that define the system input outputs are the I/O region, and a behavioral region is the possible outputs to the system defined as $\beta = \{(u, y) : y = k_{sys}u\}$. This shows which values of the input and output belong together, and in the case of any false output, the output set would belong to the other regions. Figure 2.8 shows this matter.

If an input is applied to a faultless system, the possible pair of I/O is insets of $A = (U, Y_A)$ and in the case of a faulty system, the same input might result in the output belong to the other region, known as $B = (U, Y_B)$. The faultless and fault regions might overlap

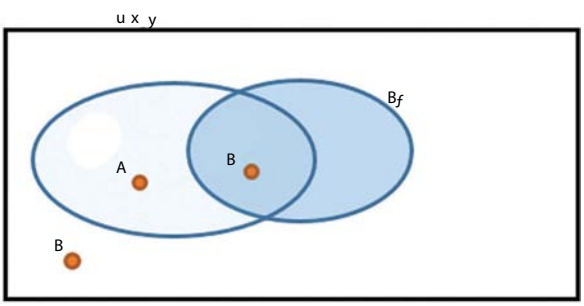

Figure 2.9 Faultless and faulty system output boundaries. β_0 is the faultless system output region.

Figure 2.8 Faultless and faulty system responses to the same input excitation.

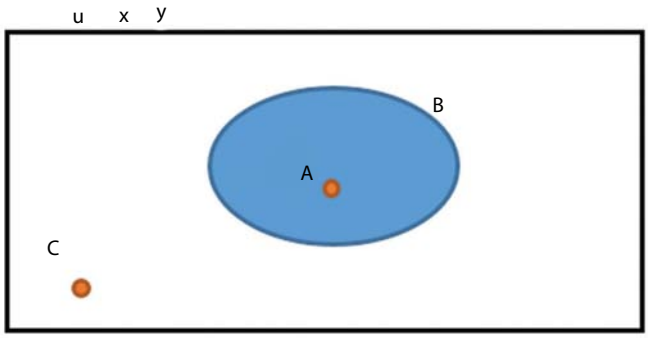

Figure 2.7 I/O set. Healthy and non-healthy system output boundaries.

at some areas. Faults are recognizable by these regions unless they overlap and belong to two regions like point B in Figure 2.9.

2.2.3 Fault and Model Uncertainty

In a second-order differential equation, for instance, an additional external signal to the system or a parameter deviation from the desired value can be identified as a fault. If a signal is added to the input of the system, this can be identified as the additive fault, and in the case of unknown parameters, the system might have a multiplicative fault. Faults are changes that should be detected and their results be removed by a proper action. Model uncertainties and disturbances are those where their effects should be removed by filters or controls.

2.2.4 Faulty System Modes and Conditions

A safe system is one without any harm and is not under any harmful tension. If the safety is provided by a controller, it is called a safe-to-fail system. A reliable system is one that provides the required functions in a period under normal conditions. Fault-tolerant systems cannot change the reliability of the component, but they can enhance the overall reliability of the system by keeping the overall system operational. A fault-tolerant system is a system in which a single fault does not develop to failure of the closed loop system by keeping the performance the same after the fault in the worst case and, if so, the system is fault operational. Fault and recovery processes put the system in different regions of performance. As Figure 2.10 shows, the safe operation of the device is separated from the dangerous region of operation. The safe operation zone is divided into degraded and unacceptable performance operation zones. Fault and recovery change the performance of the operation and put the system into the degraded and required performance regions [36].

2.2.5 Fault Diagnosis

A fault-tolerant controller includes both fault diagnosis blocks and controller redesign. Diagnosis blocks make use of the I/O sets and tests their belonging to the plant model.

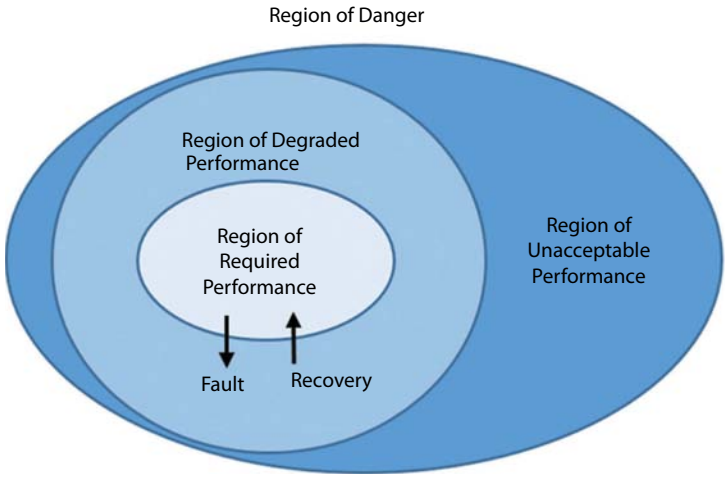

Figure 2.10 Performance categorizing of different system behaviors [36].

These results are used for the controller redesign. In the case of a fault in the system, the fault diagnosis unit identifies the fault and makes the control loop fault tolerant. Some controllers, such as robust and adaptive controllers, provide active fault-tolerant controllers. The fault-tolerant control properties are observed mainly in systems with slowly varying parameters.

If a dynamical system generates pairs of u–y and is subject to the fault, f, the system behavior depends on the type of fault or $f \in F$, where f_0 shows a faultless system. The problem is to identify the fault over a given set of I/O pairs →(U, Y) within a time zone as [37, 38]

$$U = \left(u(0), u(1), \ldots, u(k_h)\right), \tag{2.1}$$

$$Y = \left(y(0), y(1), \ldots, y(k_h)\right). \tag{2.2}$$

Online fault diagnosis requires information from a dynamical model and in a time series of signals, and no physical inspection needs to be done to identify the fault. In control systems, the location and magnitude of the fault are very important and must be identified through the fault diagnosis process. The two main approaches for fault diagnosis are as follows:

- Consistency-based diagnosis
- Diagnosis of continuous variable systems

The idea of consistency-based diagnosis returns to the fact that, for fault diagnosis, the information of I/O (U,Y) is not enough. A reference should exist to define the normal behavior of the plant. For a known system, the reference is determined by the possible sets of I/O that represent the behavior of the system. For instance, in Figure 2.7, at point *A*, in a correct model, the I/O pair (U, Y) would belong to set B; if the system is

faulty it would generate Ŷ as (U, Ŷ) and belong to region C; if so, the fault is detectable. The principle of this type of fault diagnosis is to compare the performance of the current I/O pairs with faultless system behavior B to check the consistency of the current pairs with nominal system behavior. In this case, the fault makes the output behavior inconsistent, except in the same behavior of the system in the case of overlapping areas of healthy and faulty systems. In general, a system should be diagnosable and fault detectable to avoid such uncertainties of decisions.

In conclusion,

- A fault occurs if $(U, Y) \notin B_0$.
- The fault is identified and isolated if $(U, Y) \in B_f$.

2.2.6 MEMS Mathematical Model

As shown in Figure 2.5, a comb resonator consists of a moving shuttle, which resonates between two sets of stationary comb-shaped parts at both sides. The electrostatic force is generated through the interaction of DC and an AC voltages applied to the stationary and shuttle combs, respectively. An opposite sign DC voltage is applied to other set of stationary combs to increase the applied force. The shuttle is suspended on top of the bottom plate by means of suspension springs (manufactured on the anchors). Suspension springs provide enough force to suspend the shuttle and provide a restoring force for returning the shuttle back to the rest position.

The mathematical model of MEMS helps to present a better understanding of behavior of the microsystem. Parameter recognition opens a window to unknown phenomena affecting the performance of the microsystem; however, a complete and precise value of the system's parameters cannot be achieved or presented by mathematical models. MEMS devices in a simple form are modeled as a mass spring damper system, shown in Figure 2.11, with time and condition-varying parameters. A second order differential equation that governs the behavior of the system is

$$F_e = m\ddot{x} + \beta\dot{x} + 2k_s x + F_d, \tag{2.3}$$

where m is mass content of the center comb or shuttle, x is the displacement, k_s is the spring constant on one side of the device, β is the damping coefficient, and F_d is the force of the load.

The main direction of movement is along the x-axis, as shown in Figure 2.11; the effective value of each parameter is calculated along the main direction of displacement (x). The electrostatic force is generated by applying the body and shuttle voltages and is calculated as

$$F_e = -4n\varepsilon\frac{t}{g}\left(V_b \cdot V_s\right) \tag{2.4}$$

Where n is the number of comb fingers, ε is the permittivity of air with, ($\varepsilon_0 = 8.854e{-}12(C^2/N{\cdot}m^2)$) t is the vertical thickness of the fingers, g is the gap between the stator and the translation comb fingers, and V_b, V_s are the DC voltages applied to the stator combs and AC voltage applied to the translation stage (shuttle), respectively. A

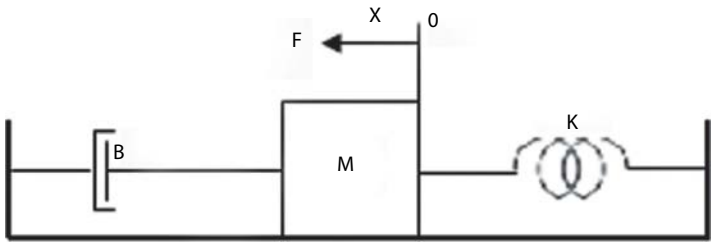

Figure 2.11 Mass-spring-damper system.

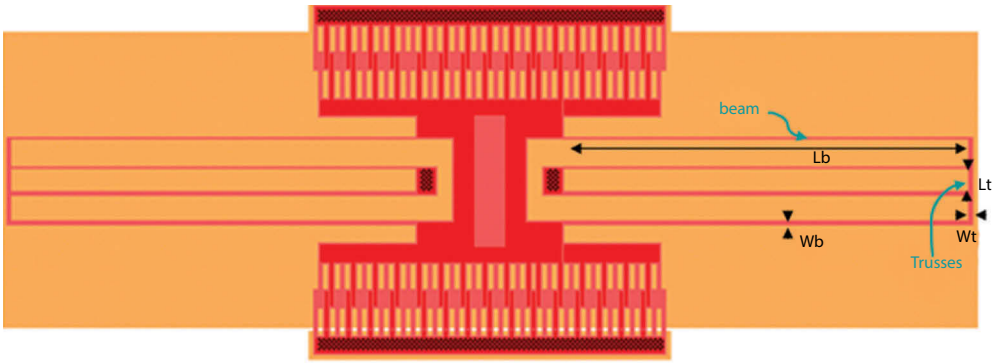

Figure 2.12 MEMS lateral comb resonator with size of suspension springs.

valid model contains accurate values for parameters, but it should be noted that these parameters differ in the fabricated devices from their initial and expected values.

2.2.6.1 Mass Calculations

The mass content of the stage can be calculated, considering of polysilicon deposition density ($2.33e{-}15(kg/\mu m^2)$) and the volume of the shuttle. A more accurate computation considering the effective direction of movement (x-axis) takes more details of the system into account and is expressed as

$$m_x = m_s + \frac{1}{4}m_t + \frac{12}{35}m_b, \tag{2.5}$$

where m_s is the mass of the stage, m_t is the mass of the flexure trusses, and m_b is the mass of the flexure beams. Dimensions and parts are shown in Figure 2.12.

2.2.6.2 Spring Constant Calculations

The folded spring constant of the device is more effective along the x-axis; however, there are components along other directions as well. The effective spring constant in the x-axis can be obtained as

$$k_x = \frac{2Etw_b^3}{L_b^3} \cdot \frac{L_t^2 + 14aL_tL_b + 36a^2L_b^2}{4L_t^2 + 41aL_tL_b + 36a^2L_b^2}, \tag{2.6}$$

and

$$a = \left(\frac{w_t}{w_b}\right)^3, \tag{2.7}$$

where E is Young's modulus, and the other dimensions are shown in Figure 2.12. An average value was used for truss length and a unity value for $a \approx 1$. The resonant frequency of the device considering the mass calculated from (2.7) and the spring constant from (2.6) results in resonant frequency as

$$\omega_R = \sqrt{\frac{k}{m}}. \tag{2.8}$$

2.2.6.3 *Damping Coefficient*

A damping effect arises from the energy dissipations of a moving plate in a viscous material. Damping is modeled by either Couette flow damping or squeeze film damping. The Couette damping effect occurs when two parallel plates are moved laterally on top of one another, as shown in Figure 2.13(a). The squeeze film effect occurs when the plates move toward each other and press the surrounding material out of the volume shown in Figure 2.13(b).

The Couette damping coefficient is computed as

$$\beta_c = \frac{\mu A}{t}, \tag{2.9}$$

where μ is the surrounding gas viscosity, A is the plate area, and t is the distance between the plates or the gas film thickness. The squeeze film is more effective along the direction of movement (x-axis) and is calculated as

$$\beta_x = \mu\left[\left(A_s + \frac{A_t}{2} + \frac{A_b}{2}\right) \cdot \left(\frac{1}{t} + \frac{1}{\delta}\right) + \frac{A_c}{g}\right], \tag{2.10}$$

where A_s is the area of the stage, A_t is the surface area of trusses, A_b is the surface area of the flexure beams, δ is the penetration depth of the airflow above the stage, A_c is

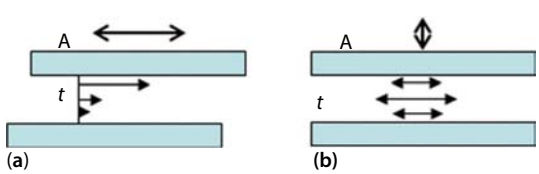

Figure 2.13 The damping coefficient in different movement directions.

the surface area of the comb finger sidewalls, and g is the shuttle-finger to stationary-finger gap.

As illustrated, the effective mass, spring constant, and damping coefficients are related to small details in the structure of the device. The geometry of the device, however, is highly affected by the manufacturing steps. These effects are accelerated when the device operates in open air and is exposed to humidity, dust, and temperature variations. Manufacturing tolerances for specific manufacturer gratings are listed in Table 2.3 as an example.

2.2.6.4 Model of MEMS

These values show that for a fabricated device, both small variations in operating conditions and manufacturing tolerances in the parts of the structure result in parameter variations in the final product. Bode plots of an example system with upper and lower boundary values are shown in Figure 2.14. Upper limits of parameters represent either

Table 2.3. Parameter variation of the lateral comb resonator (LCR) shown in Figure 2.14 [39].

Structure	Bream length (μm)	Mass (10^{10} kg)			Spring Constant K			Resonant frequency (Hz)		
		Min*	Std.	Max*	Min*	Std.	Max*	Min*	Std.	Max*
Grating	350	1.8944	1.9203	1.9506	0.0271	0.0519	0.0905	2482.0	3698.6	4500.2
	400	1.9036	1.9331	1.9675	0.0185	0.0354	0.0618	2046.7	3045.6	3703.6
	450	1.9331	1.9459	1.9844	0.0132	0.0252	0.0441	1724.8	2563.1	3115.3
	500	1.9675	1.9687	2.0013	0.0097	0.0186	0.0325	1478.9	2194.8	2666.3

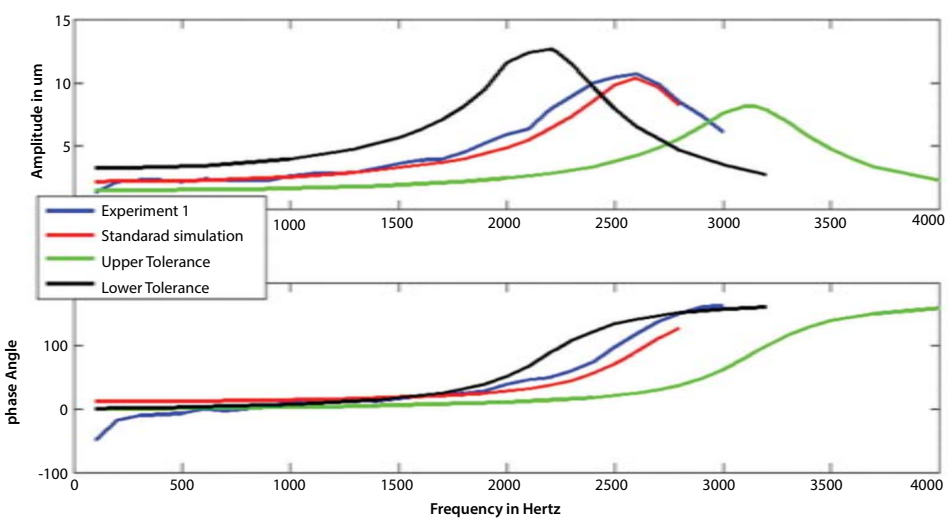

Figure 2.14 The frequency response (bode-plot) of the simulated designed system and the measured values from a fabricated MEMS LCR [39].

stiffer spring constants or massive shuttles, which cause higher resonant frequencies, while lower limit values refer to lower resonant frequencies. In this chapter, the parameters of the device are considered as unknown values, and online parameter identifiers (estimators) are used to estimate the parameters of the system. In this regard, the governing equation of the system is expressed as

$$F_e = m\ddot{y} + \beta\dot{y} + 2k_s y + F_d, \tag{2.11}$$

where m is the mass of the center comb (shuttle), y is the displacement, k_s is the spring constant of one side, β is the damping coefficient, and k_d is the force due to the load. In the driving of microstructure applications (such as connecting the beam to the rotating gears), the load can be applied directly to the shuttle. As mentioned earlier, device parameters are affected by manufacturing processes and operating and environmental conditions. Under these conditions, the model containing uncertainties can be expressed as

$$\hat{F}_e = \hat{m}\ddot{y} + \hat{\beta}\dot{y} + 2\hat{k}_s y + \hat{F}_d, \tag{2.12}$$

where (^) denotes uncertain values of the associated parameters. The desired system should operate similar to (2.11), whereas the manufactured device behaves differently like (2.12). More description on modeling, control, and displacement monitoring techniques for LCRs is introduced in Refs. [11, 14-17,24,25, 39]. This system is represented in the state space form as

$$\begin{cases} \dot{x}_1 = x_2 \\ \dot{x}_2 = \dfrac{1}{\hat{m}}\left(-2\hat{k}_s x_1 - \hat{\beta} x_2\right) + \dfrac{\hat{F}_e - \hat{F}_d}{\hat{m}} \end{cases}$$
$$y = \begin{bmatrix} 1 & 0 \\ 0 & 1 \end{bmatrix} x \tag{2.13}$$

where $A = \begin{bmatrix} 0 & 1 \\ \dfrac{-2\hat{k}_s}{\hat{m}} & \dfrac{-\hat{\beta}}{\hat{m}} \end{bmatrix}, B = \begin{matrix} 0 \\ \dfrac{1}{m} \end{matrix}$, and $C = [1\ 0]$ are the system, input, and output matrices, respectively, $x = [x_1\, x_2]^T$ is the state variable vector, and y is the output of the system. Considering the C matrix elements, one can obtain $y = x_1$. An electrostatic force originates from imperfect manufacturing steps and stiction caused by trapped surface charges, capillary forces, and surface roughness such that they distort the electric field between the very small plates. Environmental conditions such as humidity influence the stiction of the parts. Therefore, the force generated is an uncertain quantity of uncertain parameters in addition to the unknown variables.

2.2.6.5 Multiple-Model Estimation Approach

Multiple-model adaptive estimators generally reveal the behavior of linear time invariant systems by weighting the output of several models simultaneously according to I/O

measurements and evaluating their residual signals. Kalman filters are conventionally used in modeling time invariant systems under different conditions. The history of output variations (in the actual system) also has a considerable effect on the performance of the model-matching core. In uncertain or time-varying parameter systems, techniques other than Kalman filters are required for model matching and weight allocations. The effects of recent data (variations) have to be controlled to accurately identify the parameters of systems and result in a high-performance model-matching unit.

Some of the model-matching units introduce local states for local models and accept possible transients [40]. Graphical structures are also applied to describe the transitions among models, which requires a priori knowledge of the system [41]. Operating systems, however, are modeled by different techniques such as piecewise modeling, spline, and statistical approaches like fuzzy and neural networks [42–46].

In slow time-varying parameter systems, in addition to the model-matching core, there is a need for a unit to identify the model parameters and its variations. The parameter identification unit may be replaced with Kalman filter banks in conventional multiple-model adaptive estimation MMAE configurations. Like Kalman filters, the identification unit has to consider the noise in the system and compute the output deviations to generate residual signals. Since the history of variations (output of the actual system) affects the performance of model matching, the forgetting-factor recursive least square (FFRLS) is applied to weigh the recent data appropriately and to identify the parameters of the system accurately [14, 47]. Thus, MMAE applied in time-varying parameter systems will contain several system identification units and one model-matching core.

2.2.6.6 Multiple Models as Signature Faults

Several distinct models of fault can be obtained by considering different values of m, k_s, and β. A set of these models, $\{f_k \in \Delta \mid f_k = f(m_k, \beta_k, k_{sk}, F_{ek}, F_{dk}), k = 1, 2,...,n\}$, can be selected from the fault domain, Δ, such that it includes all the desired fault models. The parameters of the kth fault-representing model are m_k, β_k, k_{sk}, F_{ek}, F_{dk}. The model can be rewritten as

$$f_k : \begin{cases} x_k(t_i) = \Phi_k x_x(t_{i-1}) + \Gamma_k u(t_{i-1}) + G_k w_k(t_i) \\ z_k(t_i) = H_k x_k(t_i) + v_k(t_i) \end{cases}, \tag{2.14}$$

where x_k is the kth-system state space variable, $\Phi_k = e^{AT}$ is the discrete system matrix, $\Gamma_k = \left(\int_o^T e^{A\tau} d^{\tau} \right)$ and $H_k = C$ is the discrete input matrix, u is the input vector, G_k is the model's input noise matrix, and w_k is the input noise with zero mean and a variance of

$$E\left\{ w_k(t_i) w_k^T(t_j) \right\} = \begin{cases} Q_k, t_i = t_j \\ 0, t_i \neq t_j \end{cases}, \tag{2.15}$$

where z_k is the measurement vector, H_k is the output matrix, and v_k is the output of measurement noise, independent from w_k, with a zero mean value as

$$E\left\{v_k\left(t_i\right)v_k^T\left(t_j\right)\right\}=\begin{cases}R_k, t_i=t_j\\ 0, t_i\neq t_j\end{cases}. \tag{2.16}$$

2.2.6.7 *Kalman Filters*

Modeling of the system with Kalman filters, in the same order as that of the true (healthy) system, takes both structure and system-level noise into account, which is considered a great advantage over the CARAMEL-modeling tool. Having the model outputs compared with the actual output of the microsystem generates the residual signals for fault-representative models in each time interval. The residuals are then evaluated in the hypotheses-testing algorithm to extract the system parameter variation and weight allocations associated with each residual.

Let us consider the Kalman filtering model representation as

$$\hat{x}_k\left(t_i\right)=\Phi_k\hat{x}_x\left(t_{i-1}\right)+\Gamma_k u\left(t_{i-1}\right)+K_e\left(y_k\left(t_i\right)-H_k\hat{x}_k\left(t_i\right)\right), \tag{2.17}$$

where $\hat{x}_k$ is the estimation of the state space variable, y_k is the actual output expected from the model, and K_e is the Kalman filter gain recursively obtained from the following procedure:

$$K_e\left(n\right)=\Phi_k P\left(n\right)H_k^T\left[R+H_k P\left(n\right)H_k^T\right]^{-1}, \text{ where } n=1, 2\ldots \tag{2.18}$$

and where P is the covariance matrix and is updated using

$$P\left(n+1\right)=G_k Q G_k^T+\Phi_k P\left(n\right)\Phi_k^T-\Phi_k P\left(n\right)H_k\left[R+H_k P\left(n\right)H_k^T\right]^{-1}H_k P\left(n\right)\Phi_k^T. \tag{2.19}$$

This value updates the Kalman gain for each iteration. The residual signal is the difference between the output of the Kalman filter and that of the actual system. For each of the models, there is a residual signal defined and used to compute the conditional probability density function. Residuals are computed as

$$r_k\left(t_i\right)=z\left(t_i\right)-H_k\hat{x}_k\left(t_i\right). \tag{2.20}$$

Equation (2.20) explains the differences between the measurements (z) and the Kalman estimated outputs.

2.2.7 Adaptive Estimation

The hypothesis-testing algorithm continuously monitors the residual signal variations. If the output of any of the Kalman filters matches the output of the system, the mean of the residual signal becomes zero and, therefore, the covariance of this residual is computed. Hence, the Kalman filter-generated residual signal, in this case, contains a zero mean white Gaussian sequence with the covariance computable by

$$\psi_k=C_k P_k C_k^T, \tag{2.21}$$

which results in the conditional density function of the output measurement, $z(t_i)$, of the system for the kth Kalman filter over the measurement history of $Z(t_{i-1}) = [z^T(t_1)... z^T(t_{i-1})]$. The conditional density is therefore written as

$$f_{z(t_i)|h,Z(t_{i-1})}\left(z_i \mid h_k, Z_{i-1}\right) = \beta_k \exp\{\bullet\}, \tag{2.22}$$

with

$$\beta_k = \frac{1}{(2\pi)^{1/2}\left|\psi_k\right|^{1/2}}, \tag{2.23}$$

and

$$\{\bullet\} = \{-\frac{1}{2} r_k^T(t_i)\psi_k^{-1} r_k(t_i)\} \tag{2.24}$$

The conditional probability hypothesis for the kth system is defined as

$$p_k(t_i) = \Pr\{h = h_k \mid Z(t_i) = Z_i\}. \tag{2.25}$$

This value can also be computed as

$$p_k(t_i) = \frac{f_{z(t_i)|h,Z(t_{i-1})}\left(z_i \mid h_k, Z_{i-1}\right)\cdot p_k(t_{i-1})}{\sum_{j=1}^{K} f_{z(t_i)|h,Z(t_{i-1})}\left(z_i \mid h_j, Z_{i-1}\right)\cdot p_j(t_{i-1})}. \tag{2.26}$$

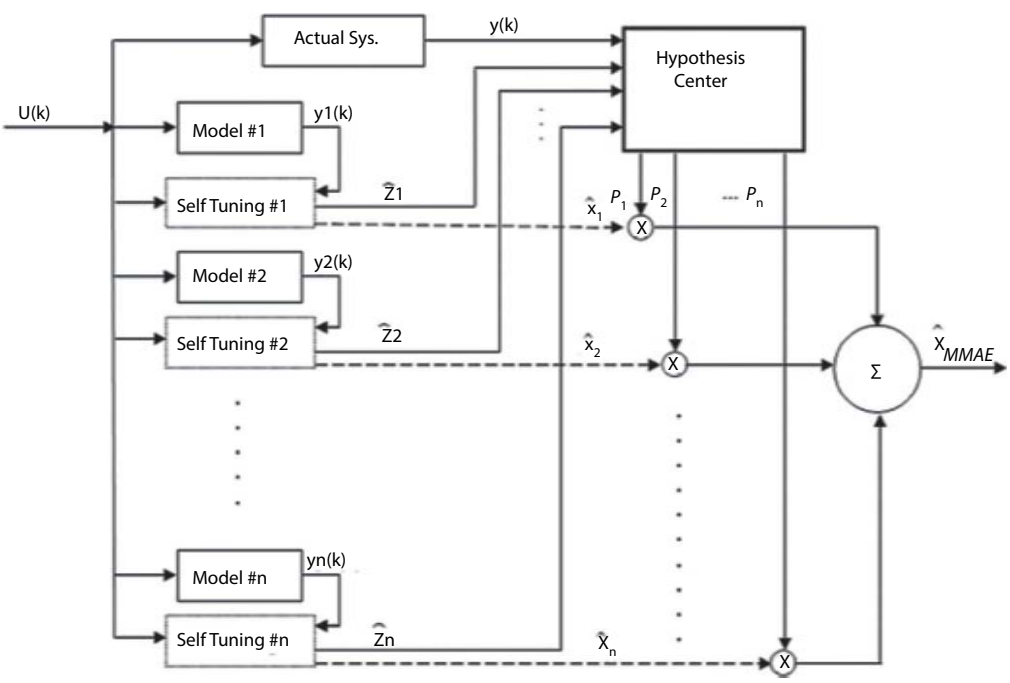

Figure 2.15 Multiple-model adaptive estimator using self-tuning banks.

The conditional probability density function requires a priori samples to compute the current values and is normalized over the complete sum of the conditional probabilities of all systems [24]. The largest conditional probability among all can be used as an indicator of fault in the systems (note that each fault-representing system should be modeled separately). In addition, they can weigh the outputs of the systems and define the weighted output of each fault model. In some applications, where probabilities change rapidly and make the output of the system unpredictable, the output should be compared with a threshold.

Sub-models, shown in Figure 2.15, are connected in parallel with self-tuning banks (containing the system identification algorithm); therefore, each sub-model is represented separately in Figure 2.15. In other words, sub-models are specific representations of the system behavior under different conditions. Parameter identification blocks in self-tuning banks can also estimate the output of these subsystems. Estimated output signals, when compared to the output of the actual system, generate residual signals and are used to compute the weights applied to the estimated state space variables.

2.2.8 Simulation and Experimental Results

To investigate the application of MMAE in fault diagnosis of MEMS devices, a fault scenario consisting of typical parameter variations was designed in seven steps as

1. Healthy operation for 2k samples
2. +5% mass variation for 1k samples
3. +10% mass variation for 1k samples
4. +5% spring constant variation for 1k samples

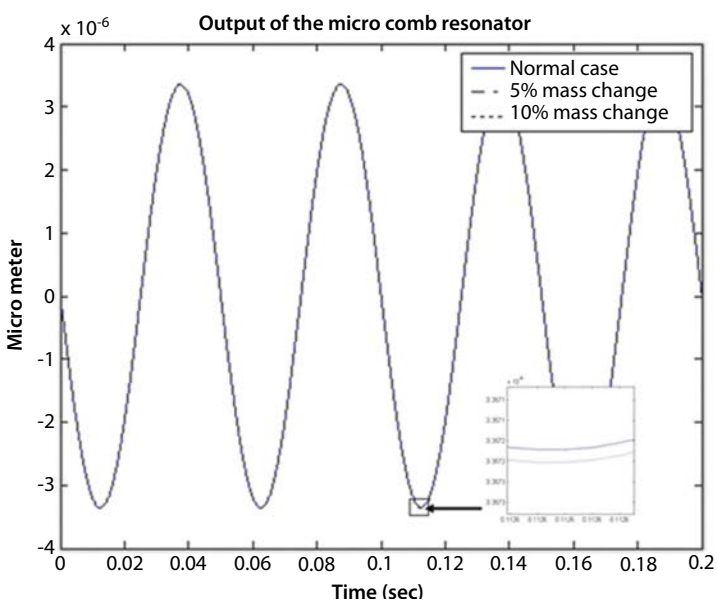

Figure 2.16 Mass change effects on system output. All outputs are very close since the total mass is negligible itself.

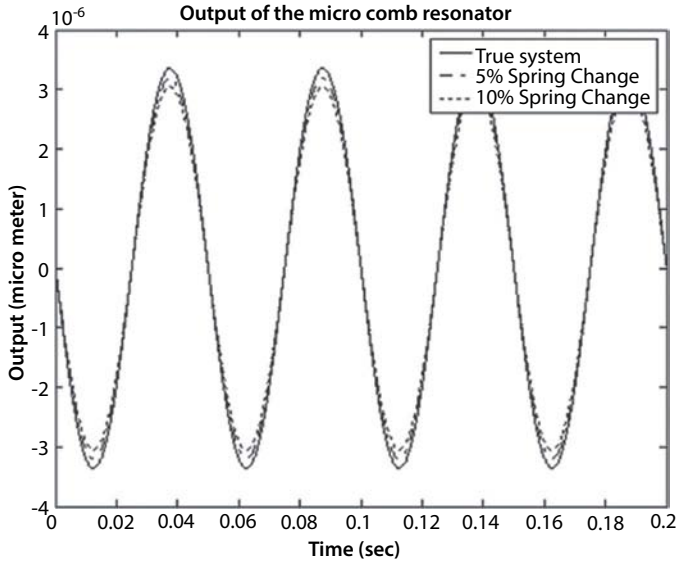

Figure 2.17 Output of the system in the spring constant change of 5% and 10%.

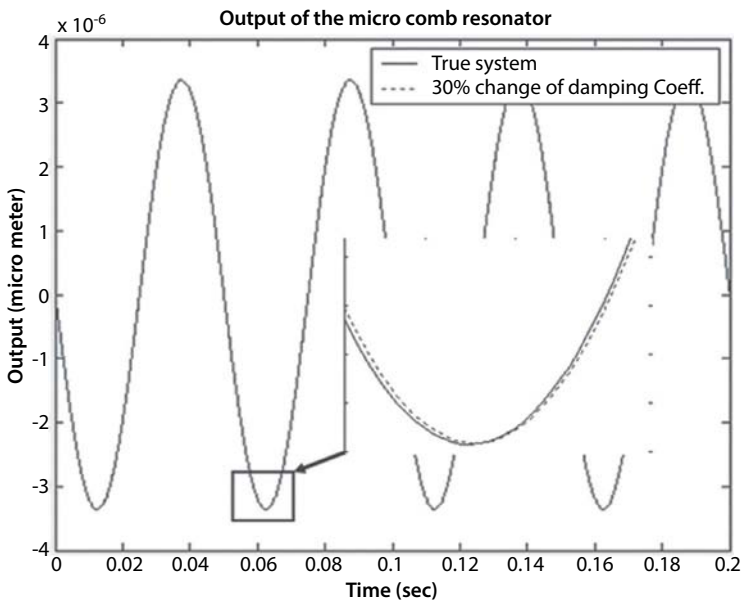

Figure 2.18 The effects of the spring constant change on the lateral comb resonator's output. A 30% change from the true system output.

5. +10% spring constant variation for 1k samples
6. +30% change in damping coefficient for 1k samples
7. Return to normal conditions after 2k samples.

These series of events occur consecutively and cover common types of variations that microsystems undergo during operation. The displacement variations in +5 and

+10% changes of the mass of LCR are shown in Figure 2.16. The displacement resulting from the spring constant variations is shown in Figure 2.17. Any change in spring constant values causes higher displacement variations. Therefore, faults resulting from the spring constant variations are more probable to be diagnosed.

Damping coefficient variations cause a delay from the original waveform. Figure 2.18 shows the phase shift resulting from a 30% change of damping coefficient and matching Step 6 of the fault scenario.

The noise content in the microsystem has a significant effect on the conditional probability functions. The effect of noise in fault diagnosis is studied in two cases of noise under and overestimation in Kalman filter designs. The system contains a zero mean white noise with Q=1e–4, R=1e–4 variances in the measurement signal and system, respectively. Considering the noise content in the system, Kalman gains are computed in each of these models and are shown in Table 2.4.

Running the probability density functions over the steps in the fault scenario designates a weight between 0 and 1 to each system in each time instant. Higher probability numbers indicate the validity of that particular system. Figure 2.19 shows the weights computed by probability density functions in the evaluation of the residual signal in the case of normal noise content in the microsystem. As the figure shows, the highest weight is allocated to the proper system (shown by similar numbers), which matches the same scenario instants.

As Figure 2.19 shows, in each step (also labeled according to the fault sequence), the transition from one step to the next is quick. The fault diagnostic unit accurately identifies the faults as predetermined in the fault scenario.

In case the noise is overestimated in the Kalman gain computations, the fault diagnostic unit identifies the fault rapidly from one type to another, i.e., the transition from mass change to spring constant requires a short time. However, in the same category of fault diagnosis (from 5% to 10% variations) the noise results in a delay in fault recognition, which is also shown in Figure 2.20. A 35% noise overestimation influences the transitions between a 5% and 10% change in mass and spring constants, but still provides a quick switching from mass to spring constant transitions. As the figure shows, delays in transitions from Steps 2 to 3 and 4 to 5 were observed. The existence of noise masking negligible parameter variations is required to be diagnosed.

If the noise content in the system is underestimated, the results show inaccurate diagnosis and random transitions among fault scenario steps, e.g., in transitions from

Table 2.4. Kalman filter gains of the system in different cases as mentioned in the fault scenario.

(Health System)		(5% mass)		(10% mass)		(5% Spring cons)		(10% spring cons.)		(30% damp. coeff)	
1.0e-006*		1.0e-006*		1.0e-005*		1.0e-006*		1.0e-008*		1.0e-008*	
-0.0002	-0.4242	-0.0000	0.0000	0.0000	-0.0000	-00000	0.0000	-0.0022	0.0022	0.0000	0.0000
0.0002	0.4242	-0.3824	0.3824	-0.1116	0.1116	-0.3265	0.3265	-0.5752	0.5752	0.3054	-0.3054

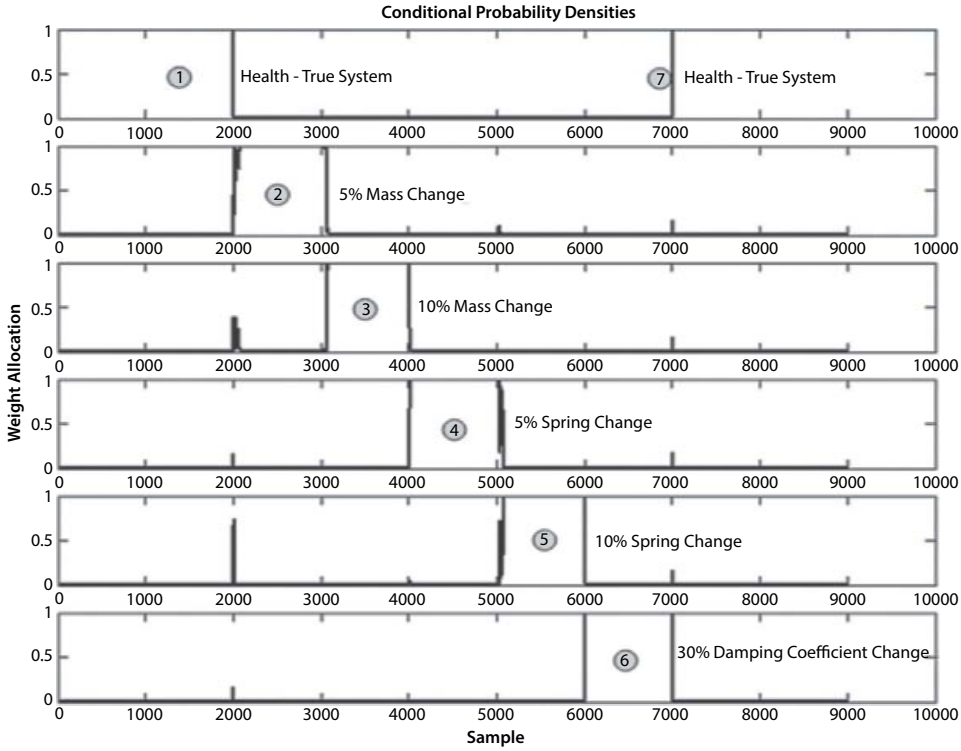

Figure 2.19 Conditional probability density function outputs over different cases of the fault scenario. Higher output values show the validity of the case and, as a result, the diagnosis of the fault. Numbers 1–7 show the different steps of the fault scenario.

Steps 2 to 3, 3 to 4, and 4 to 5. Figure 2.21 shows the noise underestimation results and their consequences on the decision-making process.

2.2.9 Experimental Results and Discussion

In order to experimentally examine the fault diagnosis performance in physical implementations, two MEMS comb resonators were designed and fabricated. The parameters of the systems, shown in Table 2.3, contained almost the same amount of mass, but due to imperfect manufacturing steps, different damping coefficients and spring constants were obtained. In order to measure the displacement of the device, the optical through wafer displacement monitoring technique was utilized.

2.2.9.1 Displacement Measurement Technique

The parameter identification technique utilizes the position signal information acquired from the data obtained by an optical probing of the LCR stage. A Doppler laser velocimeter was used to optically monitor the lateral displacement of the microsystem. The Doppler laser measurement system uses a reference beam and a measurement beam. The variation in the reflected measurement beam phase, relative to that of the reference

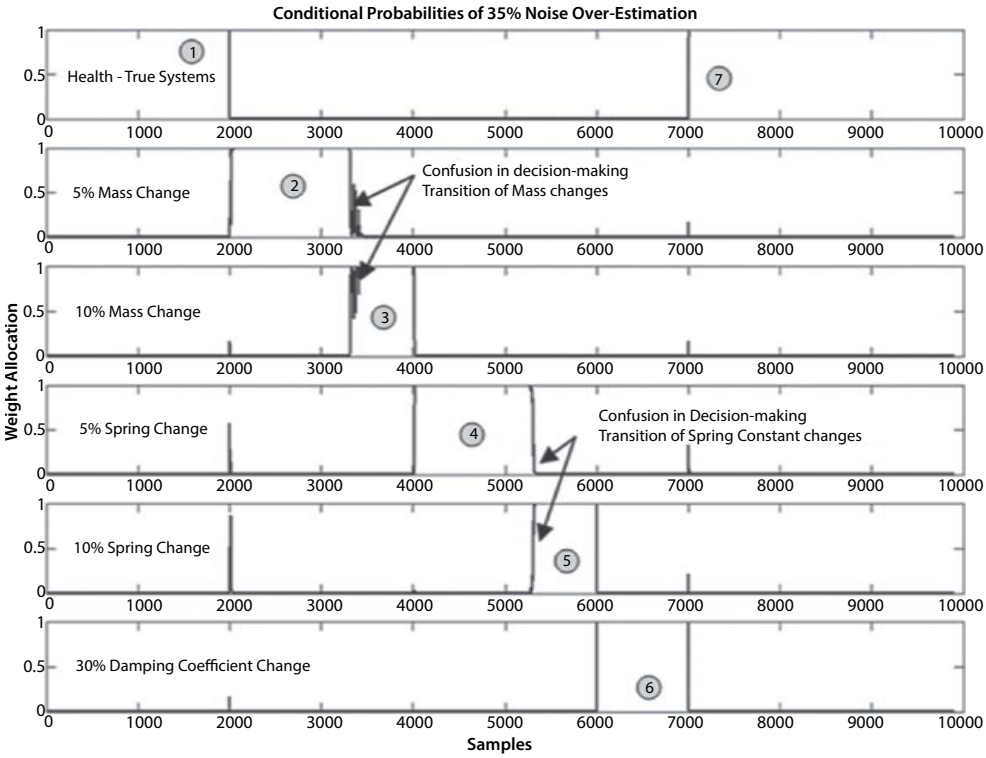

Figure 2.20 Conditional probability function outputs over different cases of the fault scenario in a 35% noise overestimation. Higher output values show the validity of the case and, as a result, the diagnosis of the fault.

beam, returns a signal proportional to the velocity of the surface reflecting the measurement beam relative to the surface reflecting the reference beam.

To infer position information, the changes in the velocimeter signal that arise from the translation of a grating structure in the LCR shuttle through the measurement beam were used. This motion is shown in Figure 2.22(a) and (b), and the optical beam placement on the device is shown in Figure 2.5. Given that the velocity measured by this velocimeter system corresponds to motion in the direction parallel to the beam propagation, prominent transitions in the velocimeter signal occur only as the edges of the released polysilicon layer pass through the measurement beam. This generates the peak-valley points in the optical data and is further used in the optical data recovery unit that measures the shuttle displacement instantaneously.

The control command is then generated by the controller and applied to the device. In this control approach, as mentioned before, the DC voltages are kept constant and the AC voltage applied to the shuttle follows the control command to provide enough force for the shuttle to follow the desired trajectory. The advantage of this method is a high signal-to-noise ratio (SNR), compared to the traditional through-wafer monitoring technique, and an easy laser beam placement on the device, as shown in Figure 2.23. Readers interested in the data recovery technique and instantaneous

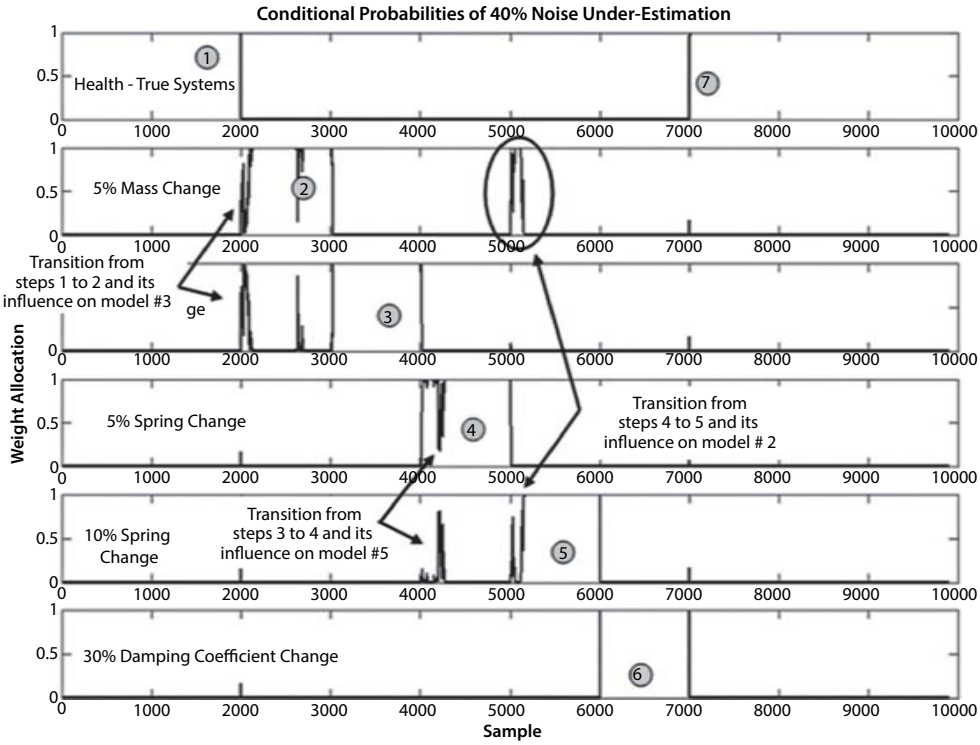

Figure 2.21 Conditional probability function outputs over different cases of the fault scenario in a 40% noise underestimation. Higher output values show the validity of the case and, as a result, the diagnosis of the fault in that.

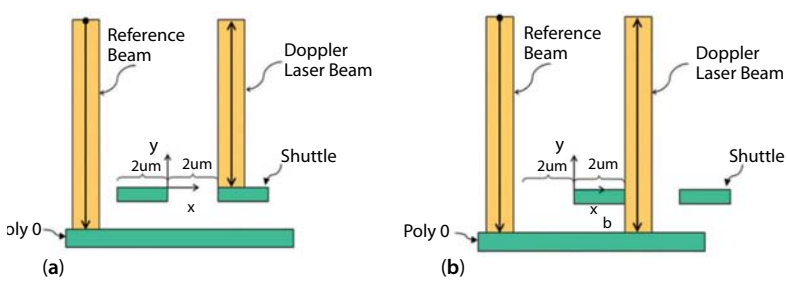

Figure 2.22 Displacement feedback system using Doppler laser for optical displacement monitoring.

displacement monitoring are referred to Ref. [48–50]. As shown in Figure 2.24, the overall experimental setup contains a Doppler laser vibrometer Polytech PSV-300 to generate the optical waveforms, a data recovery component (which forms the displacement feedback loop), a real-time control board type dSPACE PPC DS 1103, and the LCR actuator.

Devices with different parameters result in various displacements even if excited by the same input. For experiments, the fabricated LCRs were excited by the same input and their output was joined together to form the parameter variation (Table 2.5) or fault

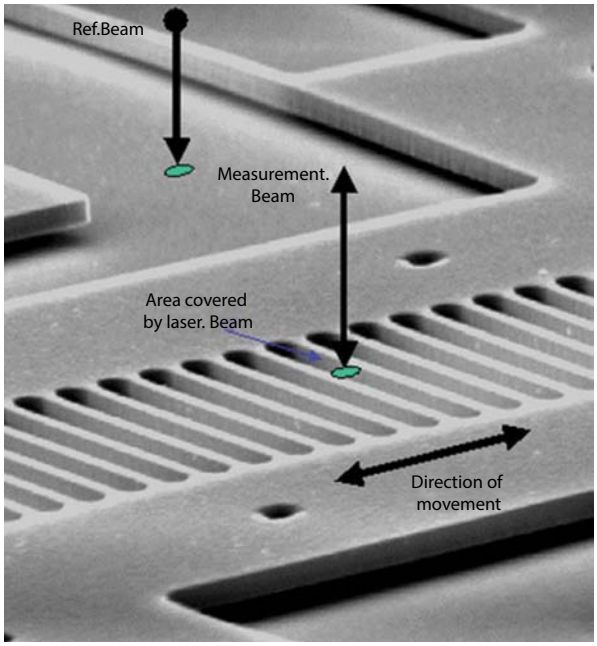

Figure 2.23 Openings on the moving plate (top view).

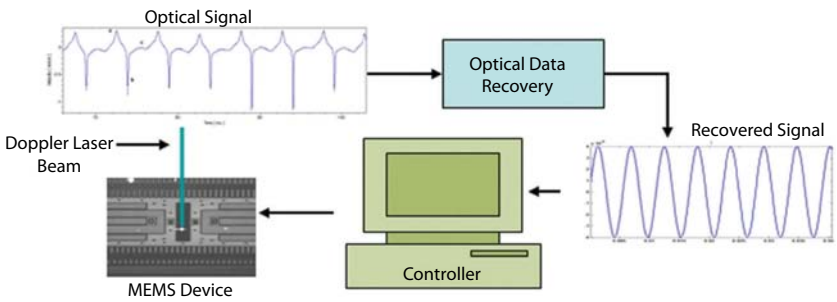

Figure 2.24 The experimental setup and signaling flow. The feedback signal is an electric signal.

Table 2.5. Estimated parameters of two fabricated systems.

	Mass (kg)	**Ks (Nm^{-1})**	**Beta ($Nm^{-1}S$)**
System 1	2.3856e–10	0.0193	7.563e–7
System 2	2.2429e–10	0.0448	1.385e–6

with a transition point at the 1886th sample. The displacement encoded optical data for these devices is shown in Figure 2.25. The recovered displacement signal is shown in Figure 2.26. These devices were excited by a 10V, 2 kHz sine wave voltage at a sampling time of $h = 193e{-}8$ sec.

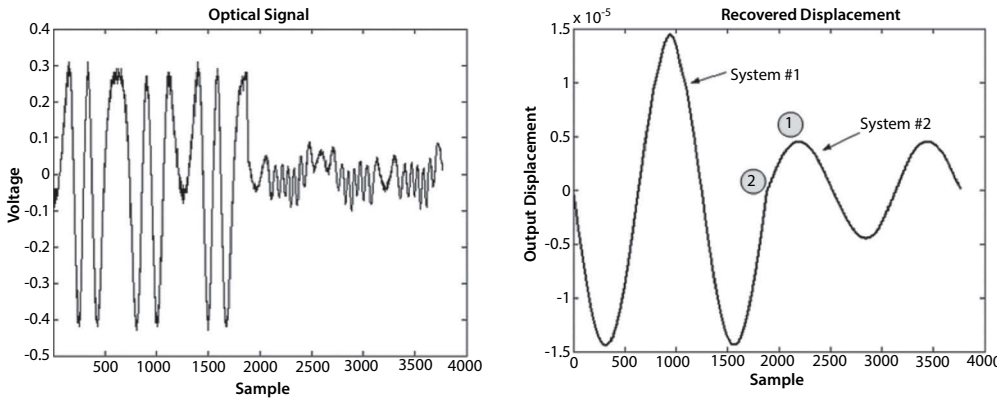

Figure 2.25 Optical signal and grating encoded displacement signals.

Table 2.6. Kalman filtering gains for Systems 1 and 2.

Ke1	Ke2
0.0013 −1.5064	0.0013 −3.5741

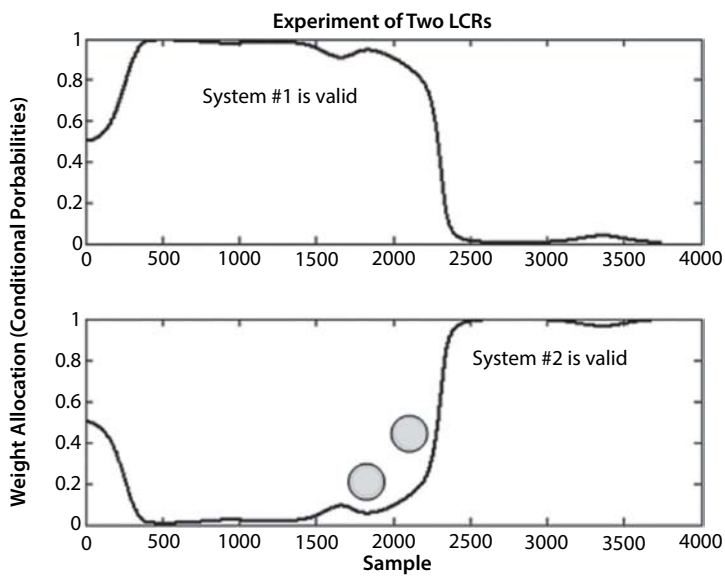

Figure 2.26 Weight allocation and conditional probability densities from tests of two fabricated LCRs. Switching from System 1 to System 2 is shown.

Figure 2.26 illustrates the recovered displacement of LCRs. Point 1 shows the starting of slope change, and Point 2 shows the switching point from System 1 to System 2.

Kalman filters were designed for these devices with their gains shown in Table 2.6. Initial probability density values of these systems were set equally, and their

Kalman gains were computed. Figure 2.26 shows the weight allocation and transitions in the fault diagnostic unit. As Figure 2.26 illustrates, higher probabilities are associated to System 1, making it valid for up to 1886 samples, also marked as Point 1 in Figure 2.26. There is small variation observed in the probability values because of the noise in the system. A quick transition in the probability values is observed when the fault occurs and the weight is shifted to validate the second system (Point 2 in Figure 2.26).

2.3 Self-Tuning Estimation

In this section, the main purpose is to design a system for fault diagnosis of MEMS devices. Since the parameters of MEMS slowly vary over time, the forgetting-factor technique is used. The system identification unit (in the form of self-tuning blocks) and the model-matching core are combined for a second-order mass-spring-damper system (model of MEMS). FFRLS is usually used for single-input single-output systems; however, for multi-input and multi-output systems, a proper number of identifiers can estimate all of the system parameters. The algorithm is implemented for the fault diagnosis of two fabricated lateral comb resonators in the experiments and for intentionally simulated faults during the operation. The results of the system identification and fault diagnosis are compared with those obtained from Kalman filters without application of the system identification unit.

2.3.1 Estimator Structure

The main purpose of a self-tuning unit is to estimate the parameters and output of a system. In slowly varying parameter systems, the recursive least square (RLS) technique is applied. A forgetting factor is utilized where the history of variation affects the performance of estimation.

Consider an auto-regressive moving average (ARMA) system representing the kth subsystem, which is expressed as

$$z_k\left(t_{i+1}\right)=b_0u\left(t_i\right)+\ldots+b_mu\left(t_{i-m}\right)-a_1z_k\left(t_i\right)-\ldots-a_nz_k\left(t_{i-n+1}\right), \tag{2.27}$$

where a_i is the coefficient of the denominator polynomial (input polynomial); b_i is the coefficient of the numerator (output polynomial) of the system; and u, z_k are the input and output signals of the kth subsystem, respectively. The unknown parameter values of the system are listed in a vector as

$$\theta^T=\left[b_0b_1\ldots b_m,a_1a_2\ldots a_n\right]. \tag{2.28}$$

The size of unknown vector is $l = m + n + 1$ where $m + 1$, n represents the order of the numerator and denominator polynomials, respectively. The model's I/O sets can form a regressor matrix as

$$h^T\left(t_i\right)=\left[u\left(t_i\right)u\left(t_{i-1}\right)\ldots u\left(t_{i-m}\right),-z_k\left(t_i\right),-z_k\left(t_{i-1}\right),\ldots,-z_k\left(t_{i-n+1}\right)\right]. \tag{2.29}$$

The ARMA system can then be presented in a compact form as

$$z_k(t_{i+1}) = h^T(t_i)\theta(t_i). \tag{2.30}$$

The estimated output is obtained by substituting an estimate of parameter values $\hat{\theta}(t_i)$ in (30) as

$$\hat{z}_k(t_{i+1}) = h^T(t_i)\hat{\theta}(t_i). \tag{2.31}$$

Estimated parameters of the system are carried out recursively utilizing the RLS identification algorithm as [51]

$$\hat{\theta}(t_{i+1}) = \hat{\theta}(t_i) + \eta(ti)h(ti)\left\{1 + h^T(t_i)\eta(t_i)h(t_i)\right\}^{-1}\left\{z(t_{i+1}) - h^T(t_i)\hat{\theta}(t_i)\right\}, \tag{2.32}$$

where $\eta(t)$ is the covariance matrix, which is defined and updated as

$$\eta(t_{i+1}) = \eta(t_i) - \left\{1 + h^T(t_i)\eta(t_i)h(t_i)\right\}^{-1}\left\{\eta(t_i)h(t_i)h^T(t_i)\eta(t_i)\right\}. \tag{2.33}$$

Applying the FFRLS, time-varying parameters are estimated by introducing the forgetting factor λ as follows [51, 52]:

$$\hat{\theta}(t_{i+1}) = \hat{\theta}(t_i) + \eta(ti)h(ti)\left\{\lambda + h^T(t_i)\eta(t_i)h(t_i)\right\}^{-1}\left\{z(t_{i+1}) - h^T(t_i)\hat{\theta}(t_i)\right\}. \tag{2.34}$$

The covariance matrix, $\eta(t)$ is also updated considering the forgetting factor as

$$\eta(t_{i+1}) = \frac{1}{\lambda}\left[\eta(t_i) - \left\{\lambda + h^T(t_i)\eta(t_i)h(t_i)\right\}^{-1}\left\{\eta(t_i)h(t_i)h^T(t_i)\eta(t_i)\right\}\right], \tag{2.35}$$

where $0 < \lambda < 1$.

Residual signals, which are defined as differences between the actual system's output and those of sub-models, are obtained by

$$r_k(t_i) = y(t_i) - \hat{H}_k\hat{x}_k(t_i) \tag{2.36}$$

2.3.2 Fault Diagnosis Application in MEMS: Simulation and Experiment

The FFRLS estimation algorithm was initialized by *P=1e8*eye(4)* with a forgetting factor of $\lambda = 0.86$. Figure 2.27 demonstrates the performance of the diagnosis in each step of the fault scenario by allocating a probability value to each of the models. Higher probability values (closer to 1) indicate a match of the system to that particular subsystem. For instance, in Step 1 (from the scenario), the system operated under normal conditions, and simulations confirmed this fact by allocating a high probability to the first subsystem.

The speed of transitions from one step to another and the probability variations during the validity of a model indicate the performance of the diagnosis. As Figure 2.27 shows, there is no significant delay observed in the transitions, and the probability is smooth in the validity of the model.

Initializing the system identification at different forgetting factors obtains different diagnosis profiles. At higher forgetting factors, distortions were observed in transitions among models. As illustrated in Figure 2.28, at $\lambda = 0.9$ the diagnosis profile shows distortion in transition from Step 2 to Step 3 of the fault scenario (+5 and +10% mass change cases). The self-tuning banks could estimate the parameters considering the existence of noise in the system, and the fault diagnosis algorithm could identify the rest of the variations properly during a short time. There was no significant delay observed in the transitions among the other steps of the fault scenario.

Increasing the forgetting factor to higher values resulted in a short history of data for the conditional probability density functions and initiated delays in weight computations. As shown in Figure 2.29, the fault diagnosis was completely dysfunctional at $\lambda = 0.98$, wherein a wrong diagnosis was observed in Steps 1, 4, 6, and 7.

According to the level of noise in the system and the rate of parameter variations, satisfactory transitions and precise parameter estimation were observed in the range of $0.86 < \lambda < 0.9$. Values out of this boundary change the history of data and cause

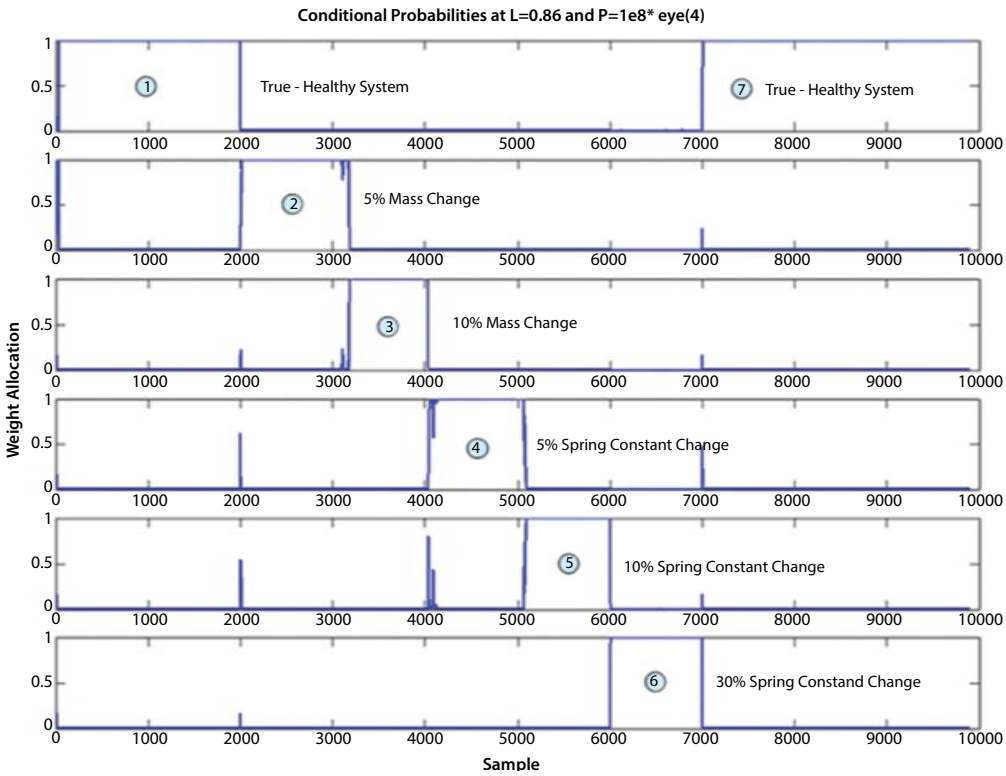

Figure 2.27 Conditional probability values according to the fault scenario with FFRLS at $\lambda = 0.86$, $P = 1e8*I$.

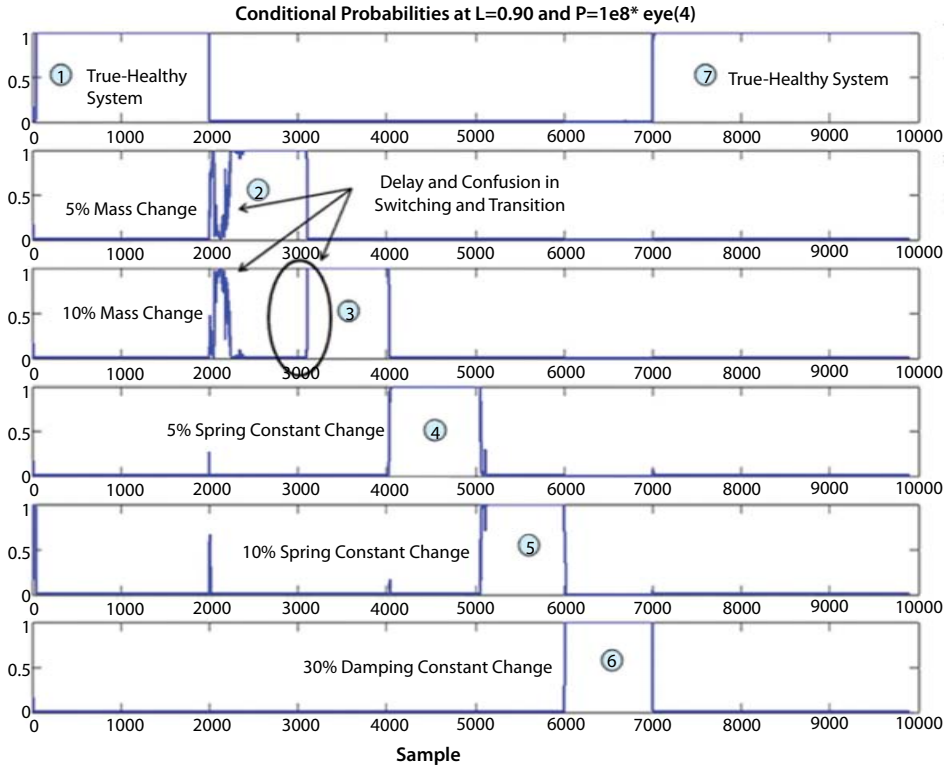

Figure 2.28 Conditional probability values according to the fault scenario with FFRLS at $\lambda = 0.9$, $P = 1e8^{*}I$.

distortions in transitions. Self-tuning banks could successfully estimate the subsystem parameters and output signals at a suitable forgetting-factor value and result in a robust decision making unit under different conditions.

2.3.2.1 Experimental Results

In order to examine the capabilities of the application of self-tuning estimator banks in combination with the MMAE technique to diagnose the type of fault in MEMS devices, two LCRs were designed and fabricated. In the design of these devices, spring constants were intentionally considered different but after fabrication, due to the imperfect manufacturing steps, there was also a variation observed in the damping coefficient of the device. The parameters of the fabricated devices are shown in Table 2.6, which reveal almost the same mass content, a 130% variation in spring constant and an 83% variation in the damping coefficient. LCR devices were excited by the same sine wave, separately, and the resulting output waveforms were attached together resembling the fault occurrence at the 1886th sample point. The recorded optical signals (containing the displacement information) are shown in Figure 2.30, and the devices were excited by a 10 $e^{j\,2\pi\ 2000\,t}$ V signal. Decoding the grating-encoded optical data showed the displacement variation in Figure 2.25.

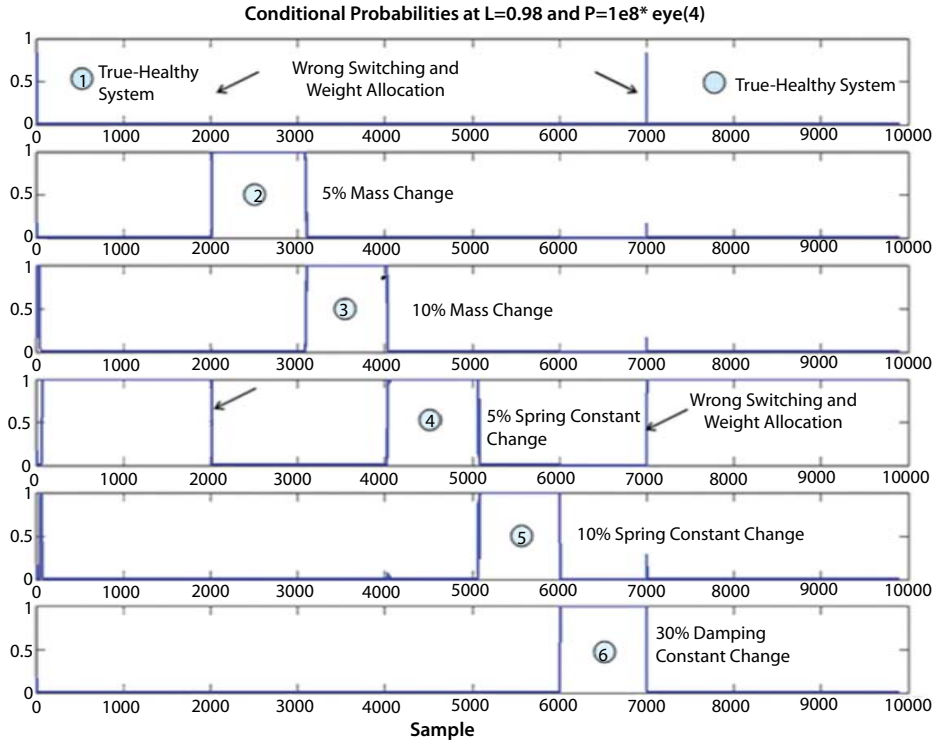

Figure 2.29 Conditional probability values according to the fault scenario with FFRLS at $\lambda = 0.98$, $P = 1e8*I$.

Table 2.7. Self-tuning system identification results for LCR Systems 1 and 2 using forgetting factor $\lambda = 0.8$.

System 1	$\hat{x}(k+1)=\begin{bmatrix}1.9934 & -0.9935\\ 1.0000 & 0\end{bmatrix}\hat{x}(k)+\begin{bmatrix}0.3052e-4\\ 0\end{bmatrix}u(k)$
System 2	$\hat{x}(k+1)=\begin{bmatrix}1.9882 & -0.4944\\ 2.0000 & 0\end{bmatrix}\hat{x}(k)+\begin{bmatrix}0.3052e-4\\ 0\end{bmatrix}u(k)$

Self-tuning banks generated two sets of state space representations for each system at $\lambda = 0.8$, shown in Table 2.7. They contained the same input matrices with similar diagonal elements in their system matrices. The effects of parameter variations are better observed in the off-diagonal values of the system matrix.

Applying the MMAE technique and self-tuning estimators together results in the weight allocations and probability computations shown in Figure 2.30 [53, 54]. As the figure shows, the highest weight was allocated to System 1 in the early steps of the first part, meaning that the actual system behaved similar to Subsystem 1. At the fault point

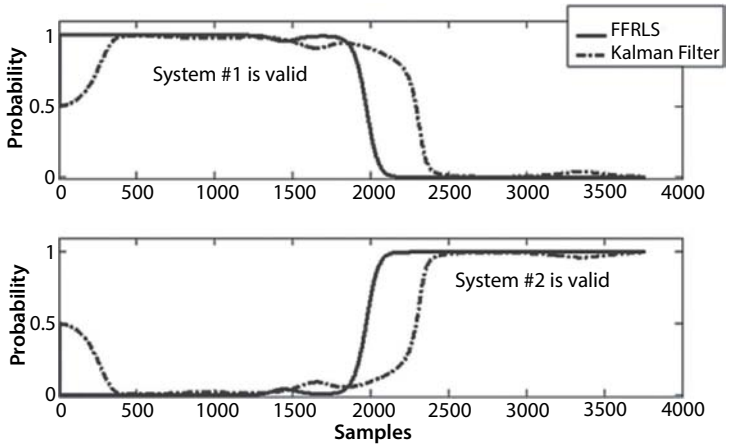

Figure 2.30 Weight allocation and conditional probability densities from the tests of two fabricated LCRs. Switching from System 1 to System 2 is shown at $\lambda = 0.8$.

occurrence (1886th sample), the weight started shifting toward System 2, and the transition was completed in a short time. There was no significant variation observed in the calculated weights before the fault occurrence moment in the first part. After the fault, System 2 had higher weight and probability values, demonstrating the operation under fault in Subsystem 2. The MMAE and self-tuning together could identify the multiple parameter variations resulting from a fault in the system. This demonstrated the successful application of the proposed technique on the MEMS fault diagnosis.

2.3.2.2 Adaptive Self-Tuning Fault Diagnosis [47]

The forgetting factor, λ, can be tuned automatically. This creates the self-tuned forgetting factor, which can be derived according to the following procedure. For optimum forgetting-factor adjustment, consider the level of noise in the system as a white noise with a zero mean and variance as $E\{w(ti)w^T(t_i)\} = \sigma_\omega^2 R_i$, with a normalized variance with respect to σ_ω^2 that can be re-written as

$$R_i = 1 + H_i P'_{i-1} H_i^T. \tag{2.37}$$

In practical implementations, an unbiased estimation of R_i can be obtained from the measurement data [21] as

$$\hat{R}_i = \frac{1}{\sigma_\omega^2}\frac{1}{i-1}\sum_{k=1}^{i} w_k w_k^*, \qquad i = 1,2,\ldots. \tag{2.38}$$

The estimated value can be calculated recursively as

$$\hat{R}_i = \frac{1}{\sigma_\omega^2}\frac{\lambda_{i-1}\hat{R}_{i-1} + w_k w_k^*}{\gamma_i}, \tag{2.39}$$

where

$$\gamma_i = 1 + \lambda_{i-1}\gamma_{i-1}. \tag{2.40}$$

The initial conditions might start at $\lambda_0 = 1, \hat{R}_0 = 0$, and $\gamma_0 = 0$. The value of λ_i, due to the noise in the system, might be larger than 1. There is almost no model that can ensure that the forgetting-factor value under all conditions remains limited within $\lambda \in (0,1)$ [47, 55]. Therefore, in practical implementation, there is a necessity to consider a reasonable limit on λ_i. In this regard, consider the initial value of λ_i as

$$\lambda_i = \frac{\lambda_{i-1}\left(1 + H_i P'_{i-1} H_i^T\right)}{\hat{R}_i}, \tag{2.41}$$

where $P' = \frac{P_i}{\lambda_i}$. To limit the forgetting factor to $\lambda \in (0,1)$, a mapping procedure [18] should be considered as

$$\lambda_i = \lambda_{i-1} + \mu \cdot \mathrm{sgn}\left(\lambda_i - \lambda_{i-1}\right), \tag{2.42}$$

where μ is the step size determined according to the parameter variation rate and the noise, and P is the covariance matrix and is updated using $p(n+1) = G_k Q G_k^T + \Phi_k P(n) \Phi_k^T - \Phi_k P(n) H_k [R + H_k P(n) H_k^T]^{-1} H_k P(n) \Phi_k^T$. For real-time implementation of the self-tuning forgetting factor, there is no need to estimate σ_ω^2 [11, 47, 55]. It can be proven that the forgetting factor can be mapped to the region of $\lambda \in (0,1)$ as follows.

If $\lambda_i \geq 1$, there exists a μ such that $0 < \lambda_{i-1} + \mu \leq 1$. This yields $0 < \lambda_i \leq 1$, which imposes the existence of a negative μ. As $\lambda_{i-1} \geq 1$ and $0 < \lambda_i \leq 1$, this yields sgn $(\lambda_i - \lambda_{i-1}) \leq 0$. Therefore, $\lambda_i = \lambda_{i-1}\ \mu$ sgn $(\lambda_i - \lambda_{i-1})$ guarantees the existence of a bounded forgetting factor and $\lambda_i \in (0,1)$.

If $0 < \lambda_i < 1$, there exists a μ such that $0 < \lambda_{i-1} + \mu \leq 1$. This yields $0 < \lambda_i \leq 1$, which imposes the existence of a positive μ. As $0 < \lambda_i < 1$ and $0 < \lambda_i \leq 1$, this yields sgn $(\lambda_i - \lambda_{i-1}) > 0$. Therefore, $\lambda_i = \lambda_{i-1}\ \mu$ sgn $(\lambda_i - \lambda_{i-1})$ guarantees the existence of a bounded forgetting factor and $\lambda_i \in (0,1)$.

In MEMS fault diagnosis, the initial forgetting-factor value and variance were considered as $\lambda_0 = 1$, $\hat{R}_0 = 0$, with a step size of $\mu = 0.0001$.

2.3.2.2.1 Design of Experiments

The model-based fault diagnosis structure is shown in Figure 2.31. Several models $_{1n}$ can be designed to accurately represent n signature faults for the diagnosis of any system. The is the ith fault-representing model, which can contain unique parameter variations from the original system that result in the output deviation from the desired operation. In a residual generation unit, all models are excited with the same input that drives the actual system. Each fault-representing model generates a different output, which, at a time instant, should not match with any of the other outputs. If there is a fault in the system, the actual system's output will match with the output of one of the fault-representing models. Therefore, the difference between their outputs, the residual signal, becomes a zero mean value. The existence of noise in the actual settings results

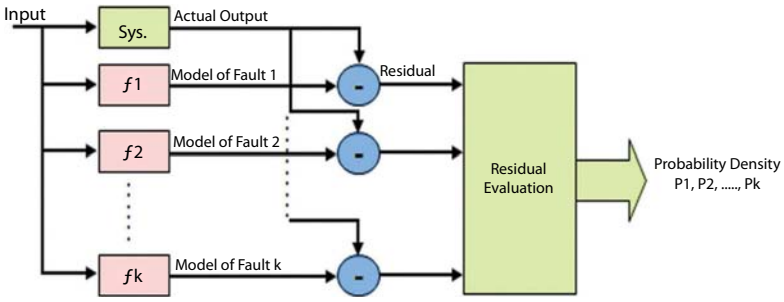

Figure 2.31 Multiple-model residual generation and residual evaluation.

Table 2.8. Estimated parameters of two fabricated systems.

	Mass (kg)	K_s **(Nm^{-1})**	**Beta (Nm^{-1} s)**
Device 1	2.3856e–10	0.0193	7.563e–7
Device 2	2.2429e–10	0.0448	1.385e–6

in the loss of fault information (small SNR ratio). Hence, the fault diagnosis becomes indifferent for small parameter variations, resulting in a low-sensitivity diagnosis. Several modeling techniques have been introduced to estimate the output of the fault models in a noisy environment. In this section, residual generation techniques, such as Kalman filters [15, 56], and output estimation units are used in residual signal generation. Residual signals are used in an evaluation center to determine the mean value, covariance, and probabilities, based on the history of variation.

To create the faults and to demonstrate the effectiveness of self-tuning forgetting-factor-based fault diagnosis, two identical structures of MEMS LCRs with different parameters were designed and manufactured. The parameters of the two MEMS devices are listed in Table 2.8. The fault was created by recording the displacement of the two devices (excited individually) and joining them together to obtain a fault stimulating waveform. The point of fault was created at a zero crossing displacement to emulate a hard-to-diagnose operating point for the diagnosis algorithm evaluation. A Polytech® optical Doppler laser vibrometer was used to measure the displacement of the MEMS LCRs. The data were recorded using dSPACE type DS1103.

The unified displacement waveform resulting from Device 1 and Device 2 while excited by a 10 sin($4000\pi t$) volt signal is shown in Figure 2.25. The fault occurred at Point 1 at the 1886th data sample. Point 2 on this figure indicates the first displacement peak after the fault. The point of fault was created at zero displacement to emulate an extremely difficult operating point for the fault diagnosis algorithm. If the fault occurred at the peak of the displacement, a sudden change would have generated stronger variations and a higher SNR, and the algorithm would be able to diagnose it rapidly. In practical implementation, each MEMS device is monitored individually and has separate signature fault models. The resulting waveform was used to verify the algorithm and evaluate the fault diagnosis performance [57].

To demonstrate the advantages of using the self-tuning forgetting factor in fault diagnosis, the Kalman filter and the fixed forgetting factor were also implemented, and their fault diagnosis profile was recorded for the same set of fault data.

Figure 2.32 illustrates the forgetting-factor generation during the fault diagnosis. As the figure shows, the forgetting-factor value was automatically adjusted to the set of $\lambda_i \in (0,1)$. Accordingly, the residual signals are shown in Figure 2.33. Figure 2.34 shows the probability generation and diagnosis performance resulting from using the Kalman filter, the fixed forgetting factor, and the self-tuning forgetting-factor methods.

Figure 2.33 illustrates the effects of the similar behavior of one model and the actual MEMS. As any model matches the MEMS device, its corresponding residual signal

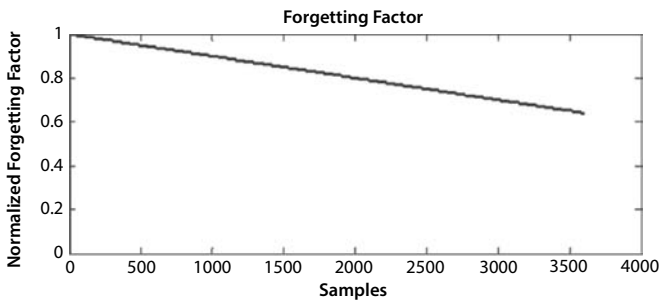

Figure 2.32 Forgetting-factor variation during fault diagnosis.

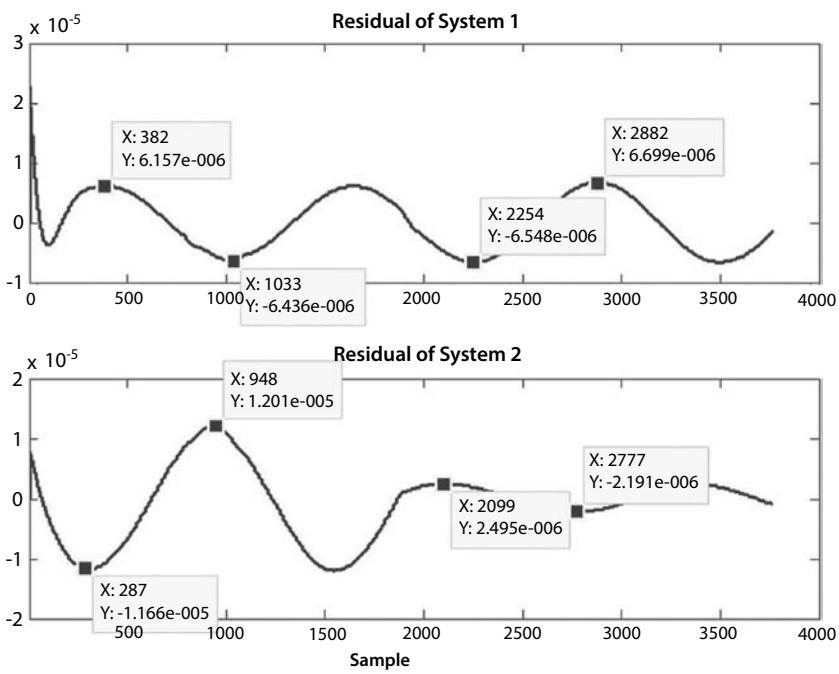

Figure 2.33 Residual signals generated for Devices 1 and 2. A lower residual signal from samples 0 to 1886 was obtained from Device 1 and from samples 1886 to the end from Device 2. The maximum and minimum of each residual section are shown in the figure [47].

generates a zero average and the lowest in-phase variance. This is shown from samples 0 to 1886, where the fault occurs. The residual signals of two systems (models) show variance values of 1.72e–11 (m) and 6.11e–11 (m) for System 1 and System 2, respectively. As the variance of System 1 is lower, the probability generation and evaluation center should assign higher probabilities to System 1.

In data samples 1886 to the end residual, the variance of System 1 remains higher, 2.2 e–11 (m), but System 2 exhibits a lower variance, 2.5e–12 (m). It should be noted that the variance is generated considering a set of recoded data. The instantaneous comparison of two model outputs with that of the system is not an effective system designation. Evaluation of zero crossings and considering a threshold level for the fault will eliminate valuable information. This is more effective if the actual system does not completely match with any of the models. In this case, a linear combination of weighted systems would determine the representative fault model. Hence, the probability density functions and the probability evaluation center are required in this fault diagnosis.

2.3.2.3 Discussion

The self-tuning forgetting-factor equations (2.37–2.42) used in the fault diagnosis of MEMS LCRs were required to be initialized. The initial forgetting-factor value and variance as illustrated earlier were considered as $\lambda_0 = 1$, $\hat{R}_0 = 0$, with a step size of $\mu = 0.0001$. The fault diagnosis performance can be evaluated using several measures.

Starting transition: Compared to the parameter in the estimation-based techniques, the Kalman filters reacted to the fault with a delay. The probability transients in the Kalman filter also showed a significant delay compared to the fixed gain estimation technique. The self-tuning gain provided faster transients in the probability evaluation at the point of fault and required fewer overall data samples to diagnose the faults.

Fault occurrence: The application of Kalman filters, as shown in Figure 2.34, resulted in a delay in the diagnosis of the fault in MEMS. The reaction time in both the fixed and the self-tuning forgetting factor was shorter. The transition time was also shorter

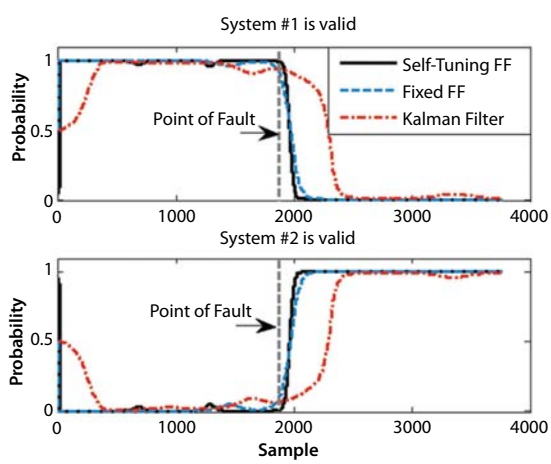

Figure 2.34 Fault diagnosis probability densities for Devices 1 and 2. Transition performance is provided for the Kalman filter, the fixed forgetting factor, and the self-tuning forgetting-factor techniques [47].

in the self-tuning forgetting factor when the second fault was introduced at the 1886th data point sample. The Kalman filter's reaction was slow for this application, running at 4000 rad/sec.

Fault diagnosis: The Kalman filter exhibited smooth probabilities through the diagnosis process. At the point of fault, the Kalman filter showed a delay in the diagnosis of the fault occurrence. The self-tuning forgetting factor resulted in a rapid transition and a stable diagnosis profile. A significant improvement over the Kalman filter and the fixed forgetting factor was achieved by using the self-tuning forgetting-factor technique.

References

1. J. Bryzek, H. Abbott, A. Flannery, D. Cagle, and J. Maitan, "Control issues for MEMS," in *Proceedings of 42nd IEEE Conference on Decision and Control*, pp. 3039–3047, 2003.
2. Available: http://www.meptec.org/Resources/Roadmap to a $Trillion MEMS Market, Meptec.pdf
3. J. W. Judy, "Microelectromechanical systems (MEMS): fabrication, design and applications," *Smart Materials & Structures,* vol. 10, pp. 1115–1134, December 2001.
4. F. Wang, B. Hong, S. A. Brandt, and D. D. Long, "Using MEMS-based storage to boost disk performance," in *22nd IEEE/13th NASA Goddard Conference Proceedings on Mass Storage Systems and Technologies*, pp. 202–209, 2005.
5. K. Ikuta, M. Nokata, and S. Aritomi, "Biomedical micro robots driven by miniature cybernetic actuator," in *IEEE Workshop MEMS'94 Proceedings on Micro Electro Mechanical Systems*, pp. 263–268, 1994.
6. R. Osiander, S. L. Firebaugh, J. L. Champion, D. Farrar, and M. A. G. Darrin, "Microelectromechanical devices for satellite thermal control," *IEEE Sensors Journal,* vol. 4, pp. 525–531, August 2004.
7. S. J. Fiedziuszko, "Applications of MEMS in communication satellites," in *MIKON-2000 13th International Conference on Microwaves, Radar and Wireless Communications*, pp. 201–211, 2000.
8. Q. A. Shams, M. Moniuszko, and J. C. Ingham, "Applying MEMS technology to field, flight and space deployable systems," in *ICIASF 19th International Congress on Instrumentation in Aerospace Simulation Facilities*, pp. 246–255, 2001.
9. M. Gad-el-Hak, *The MEMS Handbook*: CRC Press, 2001.
10. P. S. Reddy and J. R. Jessing, "Pattern alignment effects in through-wafer bulk micromachining of (100) silicon," in *IEEE Workshop on Microelectronics and Electron Devices*, pp. 89–92, 2004.
11. A. Izadian, *Automatic Control and Fault Diagnosis of MEMS Lateral Comb Resonators*: West Virginia University, 2008.
12. R. Rosing, A. Richardson, A. Dorey, and A. Peyton, "Fault simulation for MEMS," *Intelligent and Self-Validating Sensors (Ref. No. 1999/160), IEE Colloquium on* , pp.7/1,7/6, Jun 1999.
13. G. K. Fedder, "MEMS fabrication," in *2013 IEEE International Test Conference (ITC)*, pp. 691–691, 2003.
14. A. Izadian, P. Khayyer, and P. Famouri, "Fault Diagnosis of Time-Varying Parameter Systems With Application in MEMS LCRs," *IEEE Transactions on Industrial Electronics,* vol. 56, pp. 973–978, April 2009.
15. A. Izadian, P. Famouri, "Fault Diagnosis of MEMS Lateral Comb Resonators Using Multiple-Model Adaptive Estimators," *Control Systems Technology, IEEE Transactions on*, vol.18, no.5, pp.1233,1240, Sept. 2010.

16. A. Izadian and P. Famouri, "Reliability enhancement of MEMS lateral comb resonators under fault conditions," *IEEE Transactions on Control Systems Technology,* vol. 16, pp. 726–734, 2008.
17. A. Izadian, L. A. Hornak, and P. Famouri, "Structure rotation and pull-in voltage control of MEMS lateral comb resonators under fault conditions," *IEEE Transactions on Control Systems Technology,* vol. 17, pp. 51–59, January 2009.
18. I. Gyimesi, I. Avdeev, and D. Ostergaard, "Finite-element simulation of micro-electromechanical systems (MEMS) by strongly coupled electromechanical transducers," *IEEE Transactions on Magnetics,* vol. 40, pp. 557–560, 2004.
19. S. Pannu, C. Chang, R. Muller, and A. Pisano, "Closed-loop feedback-control system for improved tracking in magnetically actuated micromirrors," in *2000 IEEE/LEOS International Conference on Optical MEMS*, pp. 107–108, 2000.
20. J. W. Rogers and L. M. Phinney, "Process yields for laser repair of aged, stiction-failed, MEMS devices," *Journal of Microelectromechanical Systems,* vol. 10, pp. 280–285, 2001.
21. V. Leus and D. Elata, "Fringing field effect in electrostatic actuators," *Technion-Israel Institute of Technology Technical Report No. ETR-2004-2,* 2004.
22. X. Wu, J. Zhe, J. Wang, J. Cheng, V. Modi, and K. Farmer, "A generalized capacitance-based model for electrostatic micro-actuators," *Department of Physics, New Jersey Institute of Technology, Newark, NJ,* pp. 07102–1982.
23. L. Wang, J. Dawson, L. Hornak, P. Famouri, and R. Ghaffarian, "Real-time translational control of a MEMS comb resonator," *IEEE Transactions on Aerospace and Electronic Systems,* vol. 40, pp. 567–575, 2004.
24. S. Park, R. Horowitz, and C.-W. Tan, "Adaptive controller design of mems gyroscopes," in *IEEE Proceedings of Intelligent Transportation Systems*, pp. 496–501, 2001.
25. G. K. Fedder and R. T. Howe, "Multimode digital control of a suspended polysilicon microstructure," *Journal of Microelectromechanical Systems,* vol. 5, pp. 283–297, December 1996.
26. W. C. Tang, M. G. Lim, and R. T. Howe, "Electrostatic comb drive levitation and control method," *Journal of Microelectromechanical Systems,* vol. 1, pp. 170–178, 1992.
27. S. Bhansali, A. L. Zhang, R. B. Zmood, P. E. Jones, and D. K. Sood, "Prototype feedback-controlled bidirectional actuation system for MEMS applications," *Journal of Microelectromechanical Systems,* vol. 9, pp. 245–251, 2000.
28. Y. Li and R. Horowitz, "Active suspension vibration control with dual stage actuators in hard disk drives," in *Proceedings of the American Control Conference*, pp. 2786–2791, 2001.
29. M. Rodrigues, D. Theilliol, M. Adam-Medina, and D. Sauter, "A fault detection and isolation scheme for industrial systems based on multiple operating models," *Control Engineering Practice,* vol. 16, pp. 225–239, February 2008.
30. X. O. Kai, L. A. Tang, and Y. J. Lei, "Multiple model Kalman filter for attitude determination of precision pointing spacecraft," *Acta Astronautica,* vol. 68, pp. 843–852, April–May 2011.
31. Y.-Y. Guo and B. Jiang, "Multiple model-based adaptive reconfiguration control for actuator fault," *Acta Automatica Sinica,* vol. 35, pp. 1452–1458, 2009.
32. A. Kolpekwar, C. Kellen, and R. D. Blanton, "MEMS fault model generation using CARAMEL," in *International Test Conference Proceedings*, pp. 557–566, 1998.
33. A. Kolpekwar and R. D. Blanton, "Development of a MEMS testing methodology," in *International Test Conference Proceedings*, pp. 923–931, 1997.
34. L.P. Schanwald, J.R. Schwank, J.J. Sniegowsi, D.S. Walsh, N.F. Smith, K.A. Peterson, M.R. Shaneyfelt, P.S. Winokur, J.H. Smith, B.L. Doyle, B.L., "Radiation effects on surface micromachined comb drives and microengines," *Nuclear Science, IEEE Transactions on* , vol.45, no.6, pp.2789,2798, Dec 1998
35. R. Isermann, "Supervision, fault-detection and fault-diagnosis methods—an introduction," *Control Engineering Practice,* vol. 5, pp. 639–652, 1997.

36. M. Blanke and J. Schröder, *Diagnosis and Fault-Tolerant Control,* vol. 2: Springer, 2006.
37. F. Nejjari, R. Perez, and T. Escobet, "Diagnosability analysis using quasi-static models," in *IECON 2006-32nd Annual Conference on IEEE Industrial Electronics*, pp. 519–524, 2006.
38. R. J. Patton, P. M. Frank, and R. N. Clarke, *Fault Diagnosis in Dynamic Systems: Theory and Application*: Prentice-Hall, Inc., 1989.
39. L. Wang, J. Dawson, J. Chen, P. Famouri, and L. Hornak, "Stroke-length control of a MEMS device," in *Proceedings of the 2000 IEEE International Symposium on Industrial Electronics*, pp. 535–539, 2000.
40. B. Kuipers and K. Åström, "The composition and validation of heterogeneous control laws," *Automatica,* vol. 30, pp. 233–249, 1994.
41. J. Whittaker, *Graphical Models in Applied Multivariate Statistics*: Wiley Publishing, 2009.
42. R. Bellman, R. E. Bellman, R. E. Bellman, and R. E. Bellman, *Adaptive Control Processes: A Guided Tour,* vol. 4: Princeton University Press, Princeton, 1961.
43. V. Opoitsev, "Identification of static plants by means of piecewise-linear functions," *Automation and Remote Control, vol. 31,* pp. 809-815 1970.
44. J.-E. Strömberg, F. Gustafsson, and L. Ljung, "Trees as black-box model structures for dynamical systems," in *Proceedings of the First European Control Conference*, pp. 1175–1180, 1991.
45. G. Wahba, *Spline Models for Observational Data,* vol. 59: Siam, 1990.
46. M. J. Powell, "Radial basis functions for multivariable interpolation: a review," in *Algorithms for Approximation*, pp. 143–167, 1987.
47. A. Izadian, "Self-tuning fault diagnosis of MEMS," *Mechatronics,* vol. 23, pp. 1094–1099, 2013.
48. D. Laurent, G. Olivier, and N. De Rooij, "Microsystems for diverse applications using recently developed microfabrication techniques," in *Proc SPIE*, p. 16, 2000.
49. M. E. Motamedi, M. C. Wu, and K. S. Pister, "Micro-opto-electro-mechanical devices and on-chip optical processing," *Optical Engineering,* vol. 36, pp. 1282–1297, 1997.
50. J.-G. Guo and Y.-P. Zhao, "Influence of van der Waals and Casimir forces on electrostatic torsional actuators," *Journal of Microelectromechanical Systems,* vol. 13, pp. 1027–1035, 2004.
51. X. Zhang and W. C. Tang, "Viscous air damping in laterally driven microresonators," in *MEMS'94, IEEE Workshop Proceedings on Micro Electro Mechanical Systems*, pp. 199–204, 1994.
52. H. W. Sorenson, "Least-squares estimation: from Gauss to Kalman," *Spectrum, IEEE,* vol. 7, pp. 63–68, 1970.
53. M. Vaezi and A. Izadian, "Multiple-model adaptive estimation of a hydraulic wind power system," in *IECON 2013-39th Annual Conference of the IEEE on Industrial Electronics Society*, pp. 2111–2116, 2013.
54. A. Edalatnoor, A. Izadian, and M. Vaezi, "Indirect adaptive control of droplet dispensing in digital microfluidic systems," in *IECON 2013-39th Annual Conference of the IEEE on Industrial Electronics Society*, pp. 3580–3585, 2013.
55. W. Zhuang, "RLS algorithm with variable fogetting factor for decision feedback equalizer over time-variant fading channels," *Wireless Personal Communications,* vol. 8, pp. 15–29, 1998.
56. P. D. Hanlon and P. S. Maybeck, "Multiple-model adaptive estimation using a residual correlation Kalman filter bank," *IEEE Transactions on Aerospace and Electronic Systems,* vol. 36, pp. 393–406, 2000.
57. P. M. Frank, "Analytical and qualitative model-based fault diagnosis—a survey and some new results," *European Journal of Control,* vol. 2, pp. 6–28, 1996.

3

MEMS Heat Exchangers

B. Mathew[1]* and L. Weiss[2]

[1]*Mechanical Engineering Department, College of Engineering, Khalifa University of Science, Technology and Research, Abu Dhabi, UAE*
[2]*Mechanical Engineering Department, College of Engineering and Science, Louisiana Tech University, Ruston, Louisiana, USA*

Abstract
This chapter provides an overview of MEMS heat exchangers, specifically state of the art and design. The MEMS heat exchangers considered in this chapter include heat sinks, heat pipes, and two-fluid heat exchangers. The chapter starts by introducing several fundamental concepts of thermodynamics, fluid mechanics, and heat transfer that are relevant to MEMS heat exchangers. This is followed by sections specifically dedicated to each of the three MEMS heat exchanger types. Equations for preliminary design of the different MEMS heat exchangers are provided in sections dedicated to the same. The last section of this chapter provides an in-depth analytical treatment that demonstrates the merits of employing microscale internal flow passages in heat transfer devices.

***Keywords*:** Analytical equations, capillary effect, heat pipes, heat sinks, two-fluid heat exchangers, MEMS, microchannels, modeling, one-dimensional equations

3.1 Introduction

Heat exchangers are devices used for exchanging heat between two entities in thermal contact but at different temperatures. The entities could be fluids, or one could be a fluid and the other could be a solid [1]. Irrespective of the nature of the entities associated with a heat exchanger, heat transfer initiates from the higher temperature to the colder as dictated by the second law of thermodynamics [2]. Heat exchangers in which fluid(s) thermally interacts with a solid are often addressed as heat sinks; on the other hand, those heat exchangers in which two fluids are in thermal contact are termed as two-fluid heat exchangers. In situations where fluid(s) are used in heat exchangers, the fluid(s) could be transported through the heat exchanger either with or without undergoing phase change. Thus, heat exchangers may be further divided into single-phase or two-phase type. Single-phase exchangers house working fluid that does not undergo phase change as a result of operation. Two-phase exchangers contain working fluid that

**Corresponding author*: bmathew9791@gmail.com

Atul Tiwari and Baldev Raj (eds.), Materials and Failures in MEMS and NEMS, (63–120)
© 2015 Scrivener Publishing LLC

does change phases during energy absorption and transfer. Heat exchangers have been used extensively for a very long time and can be found in diverse applications ranging from chemical processing, general building thermal management, or electronic chip temperature control.

Microscale heat exchangers can be broadly categorized as those heat exchangers employing microscale internal flow passages; thus, these heat exchangers have surface area density greater than 4000 m^2/m^3 [1]. MEMS heat exchangers can be classified as a subset of microscale heat exchangers; MEMS heat exchangers are those microscale heat exchangers with foot print comparable to that of an electronic chip. Microscale internal flow passages are referred to as microchannels if they are continuous over the entire length of the heat exchanger as shown in Figure 3.1. It is possible to micromanufacture

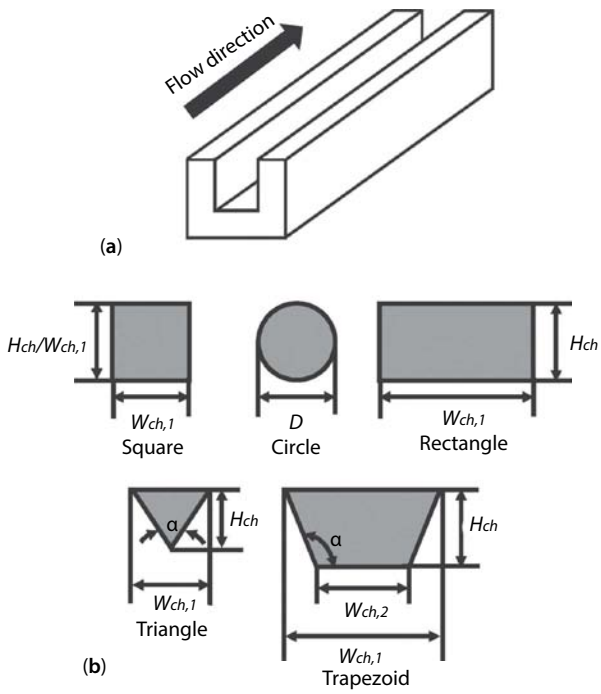

Figure 3.1 (a) Typical microchannel and (b) microchannel profiles

Table 3.1. Classification of continuous internal flow passages according to Mehendale *et al.* [3].

Type	Hydraulic diameter
Conventional heat exchanger	$D_{hy} > 6$ mm
Compact heat exchanger	6 mm $\geq D_{hy} >$ 1 mm
Meso heat exchanger	1 mm $\geq D_{hy} >$ 100 μm
Micro heat exchanger	100 μm $\geq D_{hy} >$ 1 μm

Table 3.2. Classification of continuous internal flow passages as per Kandlikar and Grande [4].

Type		**Hydraulic diameter**
Conventional Channels		$D_{hy} > 3$ mm
Minichannels		3 mm $\geq D_{hy} > 200$ μm
Microchannels		200 μm $\geq D_{hy} > 10$ μm
Transitional channels	Microchannels	10 μm $\geq D_{hy} > 1$ μm
	Nanochannels	1 μm $\geq D_{hy} > 0.1$ μm
Nanochannels		0.1 μm $\geq D_{hy}$

the microchannels with different cross-sectional profiles including rectangular, square, circular, triangular, and trapezoidal, Figure 3.1. Mehendale *et al.* [3] and Kandlikar and Grande [4] categorized continuous internal flow passages employed in heat exchangers as provided in Tables 3.1 and 3.2, respectively. As there is little overall consensus on the classification of continuous internal flow passages provided in Tables 3.1 and 3.2, it is common in literature to address sub-millimeter continuous flow passages as microchannels [5, 6]. Thus, in this chapter, all heat exchangers employing sub-millimeter flow passages are referred to as MEMS heat exchangers.

MEMS heat exchangers employ both active and passive pumping mechanisms. MEMS heat exchangers such as heat sinks and two-fluid heat exchangers employ active pumping mechanisms; passive pumping mechanism is employed in MEMS heat pipes or heat spreaders. Active pumping mechanisms are realized through auxiliary equipment such as pumps and compressors that are external to the MEMS heat exchangers. By contrast, passive pumping mechanisms are based on capillary action generated within the devices themselves. Irrespective of the nature of the pumping mechanism, the available pumping power/pressure is an important factor in the design of MEMS heat exchangers. While MEMS heat exchangers have found many applications, thermal management of microelectronics may be the first application for which MEMS heat exchangers were considered. Tuckerman and Pease [7] developed the first MEMS heat exchanger in silicon in 1981 for thermal management of microelectronics. Since that time, MEMS heat exchangers have been proposed as well as used for thermal management of several on-chip energy devices. Little [8] developed the first two-fluid MEMS heat exchanger in glass, as part of a Joule-Thomson micro cryocooler, for recuperating heat from the hot fluid to the cold fluid. Delsman *et al.* [9] developed a portable fuel processor by integrating three two-fluid MEMS heat exchangers for carrying out functions including heat recuperation as well as thermal management of the chemicals. Similarly, Hill *et al.* [10] integrated a two-fluid MEMS heat exchanger with a microreactor for purposes of cooling the products. Ashwani *et al.* [11, 12] have developed several microscale combustors for energy applications; structurally, these consist of a microreactor surrounded by a MEMS heat exchanger for heat recuperation between reactants and products. MEMS heat exchangers have been realized in a wide range of materials

such as silicon, glass, ceramic, and metals [8–15]. Several firms have developed and commercialized MEMS heat exchangers, primarily for thermal management applications [16–19]. Asetek developed a liquid cooling system employing MEMS heat sinks for personal computers and data centers [17]. Similarly, Kalaydzhyan at Microflexis and Mikro Manufacturing, Inc., have independently developed coldplates, with microscale features, for thermal management applications [18, 19]. Northrop Grumman employs MEMS heat sinks for thermal management of their commercially available laser diode arrays [20]. Pacific Northwest National Labs (PNNL) has developed a MEMS heat exchanger for thermal management applications [21]. Images of a few MEMS heat exchangers described in literature are provided in Figure 3.2 [9, 11, 13–17, 20]. MEMS heat exchangers enjoy several merits such as increased portability, enhanced heat and mass transfer coefficients, and increased surface area density [21].

This chapter is dedicated to MEMS heat exchangers such as heat sinks, heat pipes, and two-fluid heat exchangers. Fundamental concepts of thermodynamics, fluid mechanics, and heat transfer that enable the reader to understand these MEMS heat exchangers are explained in Section 3.2 of this chapter. Section 3.2 is subdivided with Section 3.2.1 detailing the related thermodynamics topics. Section 3.2.2 is dedicated to

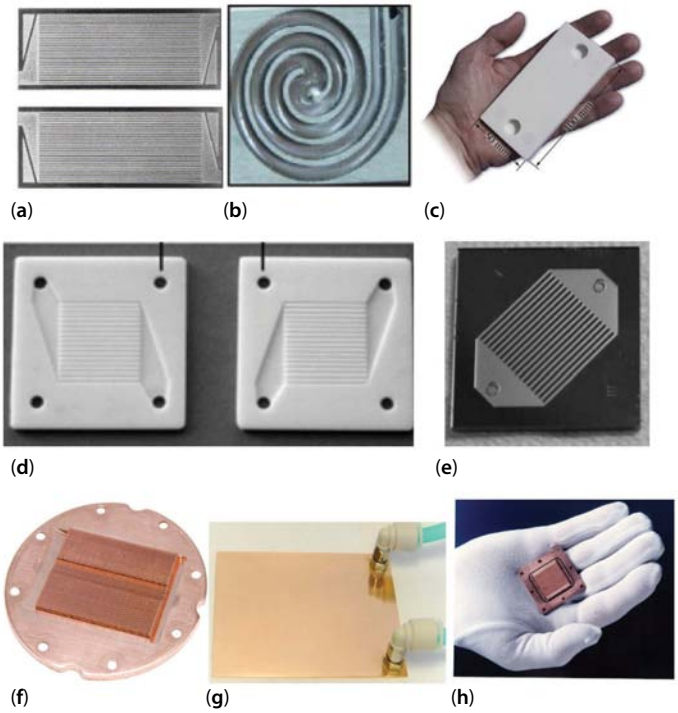

Figure 3.2 Representative images of MEMS heat exchangers: (a) microchannel heat exchanger of portable fuel cell [9], (b) microcombustor (microreactor coupled with two-fluid MEMS heat exchanger) [11], (c) ceramic two-fluid MEMS heat exchanger [13], (d) ceramic two-fluid MEMS heat exchanger [14], (e) MEMS heat sink [15], (f) coldplate, employing microchannels, developed by Asetek [16], (g) coldplate developed by Kalaydzhyan at Microflexis and Mikro Manufacturing, Inc. [17] and (h) microchannel heat exchanger for heat pump applications, developed at PNNL [20]

the subject of fluid mechanics, and Section 3.2.3 describes relevant heat transfer concepts. Section 3.3 is dedicated to MEMS heat sinks, while MEMS heat pipes are considered in Section 3.4. Section 3.5 specifically deals with two-fluid MEMS heat exchangers. Sections 3.3–3.5 include design equations as well as literature review of corresponding MEMS heat exchangers.

3.2 Fundamentals of Thermodynamics, Fluid Mechanics, and Heat Transfer

This section is dedicating to providing a brief overview of thermodynamics, heat transfer, and fluid mechanics relevant to MEMS heat exchangers.

3.2.1 Thermodynamics

Thermodynamics is fundamental to all fields of engineering including the topic of MEMS heat exchangers. The base concepts of thermodynamics are not effected by the small size of the MEMS components but remain the same as those of macroscale devices. Most MEMS heat exchangers are open systems for the obvious reason that there is mass transfer across the exchanger boundary, specifically the inlet and outlet. Governing the basic operation of the MEMS exchangers is the First Law, relating incoming and outgoing energy from the control volume (CV) [2]. This is schematically depicted in Figure 3.3. The first law can be mathematically stated as shown in Equation (3.1) for CVs.

$$\frac{dE_{CV}}{dt} = \dot{E}_{in} - \dot{E}_{out} \tag{3.1}$$

The different forms of energy associated with any CV include kinetic, potential, and internal energies. For CVs, energy transfer across its boundary can be in the form of heat and work as well as that associated with mass transfer across its boundary. The energy associated with mass transfer includes kinetic, potential, internal energies as well as flow work. The different entities (energy and mass) crossing the boundaries of a CV is schematically depicted in Figure 3.4. The final form for the first law for an open system can be mathematically stated as in Equation (3.2).

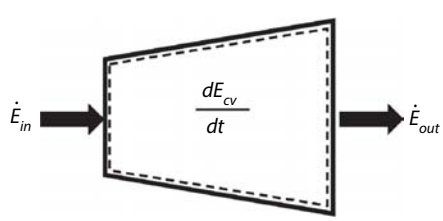

Figure 3.3 Energy transfers and change associated with a control volume

$$\dot{W}_{in} + \dot{Q}_{in} + \dot{m}_{in}\left(pe + ke + u + \frac{P}{\rho}\right) - \dot{W}_{out} - \dot{Q}_{out} - \dot{m}_{out}\left(pe + ke + u + \frac{P}{\rho}\right)$$

$$= \frac{d}{dt}\left(KE_{CV} + PE_{CV} + U_{CV}\right) \tag{3.2}$$

For all situations analyzed with respect to MEMS heat exchangers, it is assumed that operation is under steady-state conditions. This allows the transients of Equation (3.2) to be neglected. Thus, the final form of the first law for a MEMS heat exchanger can be written as in Equation (3.3).

$$\dot{W}_{in} + \dot{Q}_{in} + \dot{m}_{in}\left(pe + ke + u + \frac{P}{\rho}\right) - \dot{W}_{out} - \dot{Q}_{out} - \dot{m}_{out}\left(pe + ke + u + \frac{P}{\rho}\right) = 0 \tag{3.3}$$

The exact mathematical form of kinetic, potential, and internal energies is provided in Equations (3.4)–(3.6) [2]. The equations are based on the state variables such as velocity, elevation, and temperature of the mass being transferred across the boundary of the CV; Equation (3.6) is valid only for single-phase flows.

$$ke = \frac{1}{2}V^2 \tag{3.4}$$

$$pe = g\,z \tag{3.5}$$

$$u = C_p T \tag{3.6}$$

Another topic of thermodynamics that is of importance to MEMS heat exchangers, specifically those involved with phase change, is the properties of pure substances. This subject considers the relationship between pressure, volume, and temperature of pure substances at different thermodynamic states [2]. All coolants employed in MEMS heat exchangers can be classified as pure substances. The T–v relationship of pure substances assumes the shape shown in Figure 3.5 [2]. The path ***abcd*** is the T–v curve for a specific pressure. The path defined between states ***a*** and ***b*** of the T–v curve represents sub-cooled liquid. Along this path, the substance remains as liquid irrespective

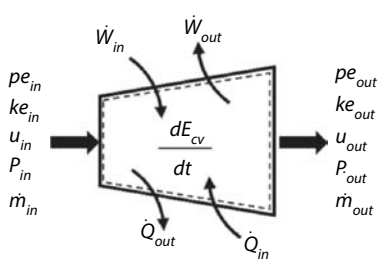

Figure 3.4 Different energies associated with a control volume

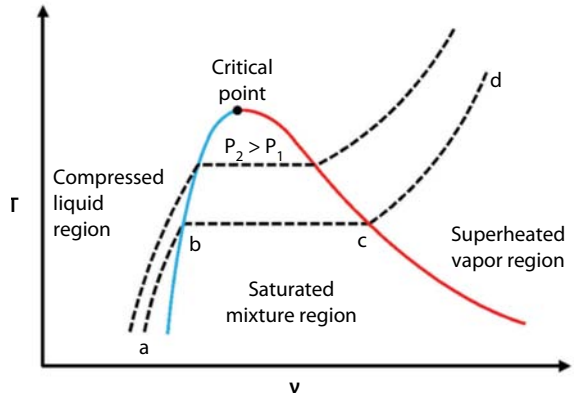

Figure 3.5 *T-v* diagram of pure substances

of the temperature and specific volume for a particular pressure. The path of the *T–v* curve between states ***c*** and ***d*** constitutes the superheated region; during this process the substance remains as vapor irrespective of the temperature and specific volume for a particular pressure. The path of the *T–v* diagram between states ***b*** and ***c*** thus represents liquid–vapor mixture of the substance. As a substance transitions from state ***b*** to state ***c***, it transitions from being 100% liquid to 100% vapor. When a substance is at state ***b*** and state ***c***, it is often referred to as saturated liquid and saturated vapor, respectively. Thus, the path between states ***b*** and ***c*** represents phase change during which the temperature remains constant. Though the temperature remains constant, energy is required to yield phase change. The specific energy required for phase change is referred to as enthalpy of vaporization [2].

T–v curves similar to ***abcd***, of Figure 3.5, can be generated by changing the pressure. If the pressure is increased above that associated with ***abcd*** the *T–v* curve generated would lie above ***abcd*** as shown in Figure 3.5. Also, with increase in pressure, there is reduction in the path between the saturated liquid and saturated vapor states; this path reduces to zero for a particular pressure termed as critical pressure. *T–v* curves corresponding to every pressure below the critical pressure will have a distinct saturated liquid and saturated vapor state. The curve obtained by joining the statured liquid states is referred to as saturated liquid line, while that obtained by joining the saturated vapor states is termed as saturated vapor line. In Figure 3.5, the blue line represents the saturated liquid line, while the red line represents the saturated vapor line. The saturated liquid line lies to the right of the many sub-cooled states of a substance; the saturated vapor line is located to the left of the superheated vapor region of the substance.

From Figure 3.5, it can be seen that in the region enclosed by the saturated liquid and vapor lines, of a pure substance, there is one-to-one relationship between pressure and temperature. For every pressure, there is a single temperature at which phase change will occur and vice versa. This pressure and temperature are referred to as saturation pressure and temperature, respectively [2]. Saturation pressure is interchangeably referred to as vapor pressure [2].

3.2.2 Fluid Mechanics

Fluids are continuously transported through MEMS heat exchangers either via active or passive flow mechanisms. For most of the first two decades since Tuckerman and Peace [7] presented their seminal work, considerable research on fluid mechanics at the microscale has been conducted. During the latter half of the past decade, the physics associated with fluid mechanics at the microscale was irrevocably established to be the same as that at the macroscale [22]. In this sense, flows and general operation can be described using standard Continuum Mechanics relationships. The use of small-scale features does present specific points for consideration in MEMS heat exchangers, however. These specific points of interest are detailed in this section [23].

Consider an internal flow passage as shown in Figure 3.6; an incompressible fluid continuously enters this internal flow passage from an external reservoir. The velocity of the liquid across any cross section of the reservoir is assumed uniform and is the same as the velocity of the liquid entering the internal flow passage. This corresponds to a flat velocity profile at the inlet as shown in Figure 3.6. Immediately after moving beyond the inlet of the internal flow passage, the layer of liquid in contact with the wall that is confining the fluid is subject to the surface friction from the wall and will come to rest. The remaining fluid, internal to the walls, will continue to move at velocities greater than that at the inlet so as to keep constant the flow rate. After the layer of the liquid at the interface, between the liquid and wall, is brought to rest, this layer will slow the layer of liquid adjacent to it due to viscosity and resulting internal friction; the remaining layers will move at velocities higher than the velocity at the inlet in order to maintain the flow rate constant. This scenario is represented by the second and third velocity profiles in Figure 3.6. This slowing down of a layer by its adjacent layer progresses from the interface between the liquid and the wall to the center of the internal flow passage. The velocity of layers increases from zero at the interface between the liquid and the wall and reaches a maximum at the center of the internal flow passage. In laminar flows, this results in a parabolic profile; the last velocity profile represented in Figure 3.6. No change occurs in the velocity after it attains the parabolic profile. Flow is said to be hydrodynamically fully developed beyond the axial location of the internal flow passage at which flow attains parabolic velocity profile [24, 25]. Hydrodynamically developing flow exists between the inlet and the axial location at which the velocity of flow attains parabolic profile [24–26]. The axial length over which developing flow exists is referred as hydrodynamic entrance length [24–26]. The average velocity at any location in the internal flow passage is the same as that at the inlet in order to maintain constant flow rate through the internal flow passage.

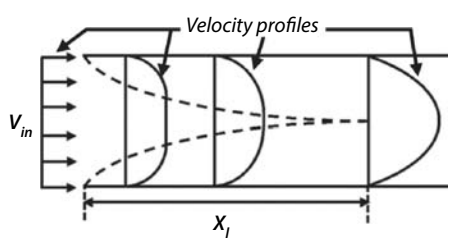

Figure 3.6 Evolution of velocity profile along axial direction in an internal flow passage

In the field of fluid mechanics, the most important geometric parameter is hydraulic diameter. It is proportional to the cross-sectional area of the internal flow passage and inversely proportional to the wetted perimeter of the same as mathematically stated in Equation (3.7) [24–26]. Table 3.3 lists the hydraulic diameter of different profiles of internal flow passages [24–26]. The most prominent independent parameter in the field

Table 3.3. Hydraulic diameter and fully developed friction factor and Nusselt number of different microchannels.

Profile	D_{hy}	α	f	Nu_H	Nu_T
Circle	D	–	$\frac{16}{Re}$	4.36	3.66
Square	$W_{ch,1}$	–	$\frac{14.2}{Re}$	3.61	2.98
Rectangle	$\frac{2(W_{ch,1}H_{ch})}{(W_{ch,1}+H_{ch})}$	–	Equation (R1)	Equation (R2)	Equation (R3)
Triangle	$\frac{2W_{ch,1}H_{ch}}{\left(W_{ch,1}+2\frac{H_{ch}}{\sin\alpha}\right)}$	60°	$\frac{13.3}{Re}$	3	2.35
		70.6°	$\frac{13.35}{Re}$	3.121	–
Trapezoid	$\frac{4(W_{ch,1}+W_{ch,2})H_{ch}}{\left(W_{ch,1}+2\frac{H_{ch}}{\sin\alpha}+W_{ch,2}\right)}$	125.3°	Equation (Trp1)	Equation (Trp2)	–

$$f=\frac{24}{Re}\left(1-1.3553\,AR+1.9467\,AR^2-1.7012\,AR^3+0.9564\,AR^4-0.2537\,AR^5\right) \quad \text{(R1)}$$

$$Nu_H=8.235\left(1-2.0421\,AR+3.0853\,AR^2-2.4765\,AR^3+1.0578\,AR^4-0.1861\,AR^5\right) \quad \text{(R2)}$$

$$Nu_T=7.541\left(1-2.610\,AR+4.970\,AR^2-5.119\,AR^3+2.702\,AR^4-0.548\,AR^5\right) \quad \text{(R3)}$$

$$AR=\frac{\min\{W_{ch,1},H_{ch}\}}{\max\{W_{ch,1},H_{ch}\}} \qquad \textit{for Equations } (R1),(R2) \textit{ and } (R3)$$

$$f=\frac{1}{Re}\left(13.35+10.74\exp\left\{-\exp\left[-0.85\left(\ln AR-1.25\right)\right]\right\}\right) \qquad \textit{for } 0\le AR\le 1100 \quad \text{(Tpr1)}$$

$$Nu_H=\begin{cases}3.121 & \textit{for } 0\le AR<0.1\\ 3.265+5.075\exp\left\{-\exp\left[-0.9041\left(\ln AR-1.3496\right)\right]\right\} & \textit{for } 0.1\le AR<200\\ 8.235 & \textit{for } 200\le AR<\infty\end{cases} \quad \text{(Trp2)}$$

$$AR=\frac{W_{ch,2}}{H_{ch}} \qquad \textit{for Equations } (Tpr1) \textit{ and } (Tpr2)$$

of fluid mechanics is dimensionless Reynolds number (Re). It is defined as the ratio of inertial force to viscous force of the fluid; the mathematical form of Reynolds number is shown in Equation (3.8) [24–26]. The Reynolds number signifies the importance of inertial forces relative to viscous forces: a higher Reynolds number shows flow characteristics of greater inertial forces relative to viscous forces. For Reynolds numbers below 2000, the flow is referred to as laminar [24]. For Reynolds number above 2300–2400, the flow is turbulent [24]. The region of Reynolds numbers between these two flow regimes is typically referred to as transition flow where either fluid state may be present [24]. Due to factors such as channel dimensions, flows are laminar in all MEMS heat exchangers and thus information on fluid mechanics detailed in this section is limited to that pertaining to laminar flow.

$$D_{hy} = 4\frac{A_{cr}}{p} \tag{3.7}$$

$$Re = \frac{\rho D_{hy} V}{\mu} = \frac{\rho D_{hy} \dot{V}}{\mu A_{cr}} \tag{3.8}$$

The hydrodynamic entrance length associated with continuous internal flow passage of any cross section can be approximated using the correlation provided in Equation (3.9) [25]. This correlation is valid even for microscale internal flow passages despite its original development for macroscale channels. Recently, Ahmad and Hassan [27] experimentally concluded that conventional correlations of hydrodynamic entrance length are valid even in microscale continuous internal flow passages for Reynolds number greater than 10.

$$x_l \approx 0.06\, Re\, D_{hy} \tag{3.9}$$

Figure 3.7 graphically represents the influence of Reynolds number and hydraulic diameter on the hydrodynamic entrance length based on Equation (3.9). For microscale

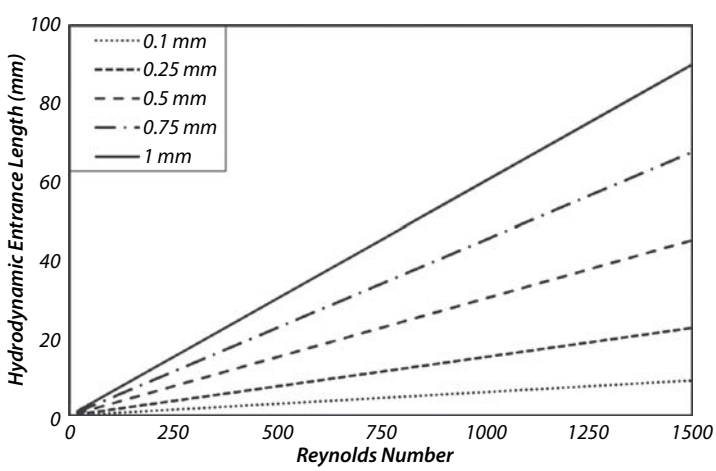

Figure 3.7 Influence of Reynolds number and hydraulic diameter on hydrodynamic entrance length

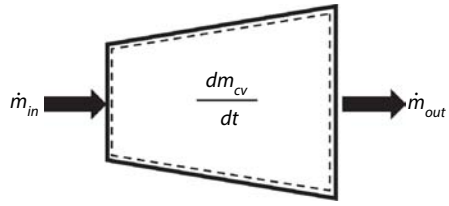

Figure 3.8 Mass transfers and change associated with a control volume

internal flow passages, the hydrodynamic entrance length can vary significantly as shown in Figure 3.7. MEMS heat exchangers operate over a wide range of Reynolds number and hydraulic diameter; generally, the Reynolds number ranges between 50 and 300 with hydraulic diameter smaller than 500 μm. The length is on the order of a couple of centimeters as the footprint is maintained similar to that of a microelectronic chip. Thus, the existence of hydrodynamically developing flow in microscale internal flow passages cannot be neglected.

While the Thermodynamic First Law governs the basic energy exchange of a MEMS heat exchanger, conservation of mass represents the primary equation describing internal fluid flows [24, 25]. This law relates the mass entering and leaving a CV to the mass accumulated/consumed within the same; this is schematically depicted in Figure 3.8. The differential form of this law can be mathematically represented as shown in Equation (3.10) [24, 25].

$$\frac{dm_{CV}}{dt} = \dot{m}_{in} - \dot{m}_{out} \tag{3.10}$$

Because transients are not considered in this chapter, the right hand side of Equation (3.10) is zero. This allows the simplified form of the equation represented in Equation (3.11). In many instances, it is beneficial to represent mass flow rate in terms of density, velocity, and cross-sectional area. Thus, Equation (3.11) can be rewritten as shown in Equation (3.12); Equation (3.12) assumes uniform flow across the cross sections as shown in Figure 3.9. In addition, when liquids are employed in MEMS heat exchangers, it is possible to neglect changes in density between the inlet and outlet. This helps simplifying Equation (3.12) further to Equation (3.13). However, when gases are employing in MEMS heat exchangers, such a simplification is not justified.

$$\dot{m}_{in} = \dot{m}_{out} \tag{3.11}$$

$$\left(\rho V A_{cr}\right)_{in} = \left(\rho V A_{cr}\right)_{out} \tag{3.12}$$

$$\left(V A_{cr}\right)_{in} = \left(V A_{cr}\right)_{out} \text{ (applicable only in the case of liquids)} \tag{3.13}$$

The second law of great importance in fluid mechanics is the law of conservation of momentum. This law can be thought of as the application of Newton's second law to fluids. The law of conservation of momentum can be mathematically stated as in Equation (3.14) for a CV [24, 25].

$$\frac{dM_{CV}}{dt} = \dot{M}_{in} - \dot{M}_{out} + \sum F_{ext} \tag{3.14}$$

External forces, i.e., the term on the right hand side of Equation (3.14), represent the forces imposed on the CV by external sources and can be classified as either surface or body forces. Surface forces act on the CV through the surface of the CV and include forces such as pressure and stress. By contrast, body forces are forces that act on the entire bulk of the CV. Examples include gravitational and magnetic force. In the case of MEMS heat exchangers, the only volume force that must be considered is gravitational force. It should be recognized, however, that the influence of gravitational force is limited because of the small volumes of fluid utilized. When considering solid materials, the first and second terms on the right hand side of Equation (3.14) are absent; however, in the case of any CV of fluids, these two terms are relevant because of the fact that there is transfer of momentum with the transfer of mass across the inlets and outlets of the CV. As before, transients are not considered, and thus Equation (3.14) is simplified as shown in Equation (3.15)

$$\dot{M}_{out} - \dot{M}_{in} = \sum F_{ext} \tag{3.15}$$

It is beneficial to represent momentum in terms of density, velocity, and cross-sectional area. Equation (3.15) is written in terms of these parameters as applicable to Figure 3.10. For the case presented in Figure 3.10, the surface forces include those due to pressure acting on the inlet and outlet as well as shear stress acting on the boundary between the wall and the CV. It is assumed that the pressure and velocity are uniform across the inlet and outlet surfaces. The final form of Equation (3.15) as applicable to Figure 3.10 is Equation (3.16).

$$\left(\rho A_{cr} V^2\right)_{out} - \left(\rho A_{cr} V^2\right)_{in} = \left(PA_{cr}\right)_{in} - \left(PA_{cr}\right)_{out} - \left(\tau A\right)_w \tag{3.16}$$

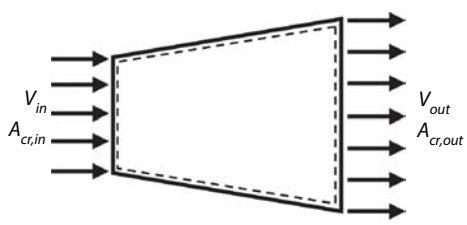

Figure 3.9 Uniform velocity distribution at the inlet and outlet of a control volume

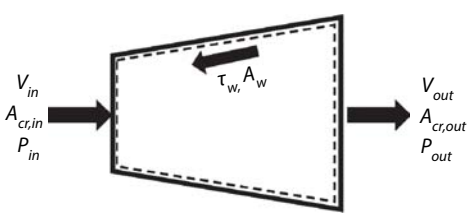

Figure 3.10 Components of momentum and forces associated with control volume

In situations where the momentum entering and exiting the CV is the same, the left hand side of Equation (3.16) reduces to zero. This situation exists for all single-phase MEMS heat exchangers where the flow area remains constant and the flow is hydrodynamically fully developed; the law of conservation of momentum for this case can be presented as in Equation (3.17). Equation (3.17) allows the calculation of pressure drop experienced by the fluid while moving through the internal flow passage. For two-phase MEMS heat exchangers, the phase change causes momentum entering the CV to be different from that exiting the CV even when the flow area remains constant. Shear stress is always defined using Fanning friction factor, a dimensionless parameter, as shown in Equation (3.18) [26, 28].

$$\Delta P = P_{in} - P_{out} = \frac{(\tau A)_w}{A_{cr}} \tag{3.17}$$

$$f = \frac{\tau}{\rho V^2 / 2} \tag{3.18}$$

Determination of friction factor, including Fanning friction factor, has been a prominent research topic in microfluidics as evidenced by the many publications in literature [22]. The Fanning friction factor depends on the cross-sectional profile of the internal flow passage as well as nature of flow, i.e., developing or developed. Figure 3.11 represents the relationship between Fanning friction factor and the distance along the length of the internal flow passage [26, 28]. As can be observed from the figure, the factor remains constant once the flow becomes fully developed. The Fanning friction factor is well documented in literature for fully developed flow; Fanning factor values for different profiles of internal flow passages are listed in Table 3.3 [26, 28, 29]. Equation (3.17) can be written in terms of the Fanning friction factor as shown in Equation (3.19); this is the most relevant conclusion of the momentum equation for those single-phase MEMS heat exchangers with constant cross-sectional area. Equation (3.19) represents the pressure drop required to overcome the viscous forces [25]. The pumping power can in turn be determined using Equation (3.19) and volumetric flow rate as presented in Equation (3.20).

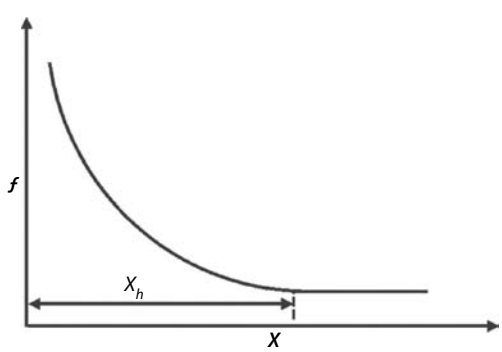

Figure 3.11 Axial variation of friction factor

$$\Delta P = 2\frac{f\,\rho V^2 L}{D_{hy}} \tag{3.19}$$

$$PP = \Delta P \dot{V} \tag{3.20}$$

The third law of conservation in the field of fluid mechanics deals with energy and is the same as that presented for thermodynamics. For completeness of these conservation laws, the energy equation is presented here, Equation (3.3) [2, 24].

$$\dot{W}_{in} + \dot{Q}_{in} + \dot{m}_{in}\left(pe + ke + u + \frac{P}{\rho}\right) - \dot{W}_{out} - \dot{Q}_{out} - \dot{m}_{out}\left(pe + ke + u + \frac{P}{\rho}\right) = 0 \tag{3.3}$$

$\dot{Q}_{in}$ represents volumetric heat generation as well as heat entering the CV across the surface of the same; $\dot{Q}_{out}$ is the combination of volumetric heat consumption and heat leaving the CV through the surface of the same. $\dot{W}_{in}$ constitutes the work added to the bulk of the CV which in most cases represent the work associated with a pump. Similarly, $\dot{W}_{out}$ constitutes the work removed from the bulk of the CV, specifically via a turbine, as well as that required for overcoming friction.

Capillary flow (capillarity) is a topic in fluid mechanics that is of importance to microfluidics devices, specifically those employing passive pumping mechanisms [30]. Capillary flow simply refers to the transport of liquids, in capillaries or similar-sized tubes, solely driven by surface tension and influenced by wettability associated with liquids [31, 32]. Figure 3.12 provides a schematic of capillary flow with respect to a capillary tube vertically held in a liquid bath. In the case shown in Figure 3.12, liquid rises through the capillary tube until the force due to surface tension is balanced by the weight of the liquid column in the capillary tube. The net upward force, due to surface tension, is given by Equation (3.21). Force analysis of just the liquid–vapor interface will reveal the need for existence of a pressure jump across the same for balancing the force due to surface tension provided in Equation (3.21) [31, 32]. The pressure difference across the liquid–vapor interface is mathematically represented as in Equation (3.22).

$$F = F_\sigma \cos(\gamma) = \sigma\, p \cos(\gamma) \tag{3.21}$$

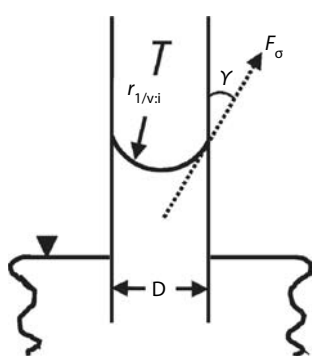

Figure 3.12 Capillarity and surface tension force

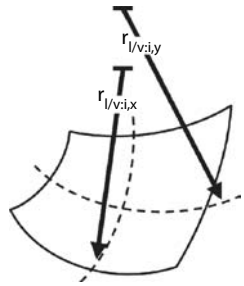

Figure 3.13 Radii of two-dimensional random interface

$$\Delta P = 4\frac{\sigma\cos(\gamma)}{D} = 2\frac{\sigma}{r_{l/v:i}} \tag{3.22}$$

Equation (3.22) represents the pressure jump specific to liquid–vapor interface associated with a column of liquid as shown in Figure 3.12. The generic form of pressure jump across a liquid–vapor interface as shown in Figure 3.13 is given in Equation (3.23) with the pressure greater on the concave side of the interface; this is the Young–Laplace equation [31]. The generic form of the pressure jump equation is beneficial when dealing with MEMS heat exchangers where microscale flow passages perform the function of capillaries.

$$\Delta P = \sigma\left(\frac{1}{r_{l/v:i,x}} + \frac{1}{r_{l/v:i,y}}\right) \tag{3.23}$$

At the beginning of this section, it was noted that the theory of fluid flow at the microscale is identical to that at the macroscale given that the continuum hypothesis is valid. The validity of the continuum hypothesis at any length scale for gaseous flow can be checked using the Knudsen number (Kn). The Knudsen number is defined as the ratio of molecular mean free path to the characteristic flow dimension; it is mathematically represented in Equation (3.24) [4, 33, 34]. For flow through internal flow passages, the characteristic flow dimension is hydraulic diameter.

$$Kn = \frac{\lambda}{L} \tag{3.24}$$

Based on the magnitude of Knudsen number, flow has been classified into three cases as shown in Table 3.4 [4, 33, 34]. The continuum hypothesis is valid for all cases of internal flow if the Knudsen number is less than 10^{-3}.

The upper limit of Knudsen number for continuum flow indicates the lower limit of the hydraulic diameter for which the continuum hypothesis holds for different gases. This lower limit of the hydraulic diameter for common gases is provided in Table 3.5 [4, 33]. It can be deduced from Table 3.5 that continuum hypothesis is valid for most practical cases of MEMS heat exchangers.

Table 3.4. Flow regime vs. Knudsen number range.

Flow regime	Range
Continuum flow	$Kn < 10^{-3}$
Slip flow	$10^{-3} \leq Kn \leq 10^{-1}$
Transition flow	$10^{-1} \leq Kn \leq 10$
Free molecular flow	$Kn > 10$

Table 3.5. Hydraulic diameter above which continuum hypothesis is valid.

Gas	Hydraulic diameter (μm)
Air	68
Argon	72
Helium	194
Hydrogen	123
Nitrogen	66
Oxygen	72

3.2.3 Heat Transfer

Following the seminal work of Tuckerman and Peace [7], heat transfer investigations were conducted as related to microscale flow passages as well [35]. As with fluid flow findings, heat transfer research has indicated no differences in fundamentals between micro- and macroscales [35]. Heat transfer occurs due to temperature gradient. There are three modes associated with heat transfer, specifically conduction, convention, and radiation. Conduction and convection are most relevant to MEMS heat exchangers and thus discussed in this section.

3.2.3.1 Conduction

Conduction refers to the transfer of heat either between parts of the same body at different temperature or between two bodies, in physical contact, at different temperatures. Heat conduction is a phenomenon that occurs at the molecular/atomic level [25, 28]. Vibration of molecules/atoms is associated with temperature; higher the temperature greater the associated vibration. Heat conduction, between two regions at different temperature, occurs via transfer of energy from molecules/atoms at a greater degree of vibration (associated with maximum of the two temperatures) to molecules/atoms at lesser degree of vibration (associated with minimum of two temperatures). Heat conduction exists in solids, liquids, and gases as they all are composed on atoms/molecules. Heat conduction is the only mode of heat transfer in solids; however, in liquids and

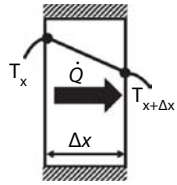

Figure 3.14 One dimensional heat conduction

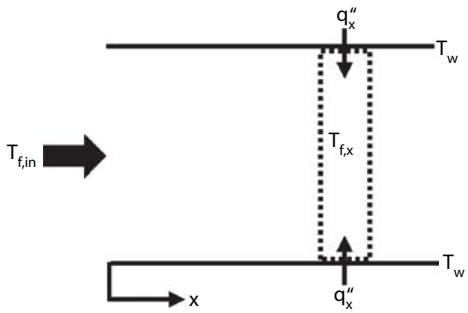

Figure 3.15 Fluid flow through a heated internal flow passage

gases, other modes of heat transfer exist because they are loosely packed with constituent atoms/molecules and not rigidly held at specific locations as in solids. For the solid shown in Figure 3.14, heat conduction between any two faces of the same is given by Equation (3.25); the temperature varies linearly between the two faces [25].

$$\dot{Q}'' = -k_w \frac{dT}{dx} \tag{3.25}$$

3.2.3.2 Convection

Convection refers to the heat transfer between a solid and a fluid (liquid or gas). Consider an internal flow passage transporting a fluid as shown in Figure 3.15. The walls of the internal flow passage are maintained at constant temperature, and the fluid enters the internal flow passage at a temperature different from that of the wall. As the walls of the internal flow passage and the fluid are at different temperatures, there is heat transfer between the two and this thermal energy is in turn carried away by the fluid. This process of transfer and transport of heat is collectively referred to as convection and is a combination of conduction and advection. Heat is transferred via conduction from the surface of the wall to the fluid layer in contact with it as well as between all adjacent fluid layers. This heat is then transported along with the flow, in the axial direction, which constitutes advection. Convection heat transfer is influenced by the temperature difference, geometry of the internal flow passage, properties of the fluids and wall, flow velocity, and type of flow (laminar or turbulent). The influence of several of these parameters is coupled into a single parameter termed as the heat transfer

coefficient [1]. Thus, heat transfer via convection at any location x along the length of the internal flow passage can be quantified in Equation (3.26) [25, 26].

$$q''_x = h_x\left(T_w - \overline{T}_{f,x}\right) \tag{3.26}$$

As was the case with fluid flows, developing and fully developed flow exists with respect to heat transfer between flowing fluid and the confining internal flow passages. Consider an internal flow passage with conditions similar to that of Figure 3.15. Fresh fluid continuously enters the internal flow passage at a uniform temperature as shown in Figure 3.16. Upon entering the internal flow passage, heat from the wall is added to the layer of the fluid in contact with the wall, thereby leading to change in temperature of this layer. The other layers of the fluid do not experience any temperature change and remain at the same temperature as the inlet temperature. As the fluid progresses further along the internal flow passage, heat is transferred from the layer of fluid adjacent to the wall to the next layer and in the process alters the temperature of that particular layer. The other layers of the fluid do not experience any temperature change and remain at the same temperature as that at the inlet. This process continues as fluid moves further into the internal flow passage resulting in several fluid layers with altered temperature and several layers with original temperature. The second and third temperature profiles in Figure 3.16 are representative of this situation. At some distance from the inlet, the thermal energy from the wall will alter the entire temperature of the fluid flow; the fourth temperature profile in Figure 3.16 is representative of this situation. The region between the inlet, of the internal flow passage, and the location at which the temperature of all layers is altered is classified as thermally developing flow. The axial length over which this thermally developing flow exists is referred to as thermal entrance length [25]. Flow in the region beyond the thermal entrance length is referred to as thermally developed flow. This situation is very similar to that described with respect to fluid flow; however, unlike velocity profile which remains unaltered beyond the hydrodynamic entrance length, the temperature profile continues to change beyond the thermal entrance length as the fluid continuous to be heated. It can be noticed from Figure 3.16 that the temperature is not uniform at any axial location of the internal flow passage even when the wall temperature is maintained constant; thus, the average temperature at the cross section of interest is used for calculations such as those represented by Equation (3.26).

Thermal entrance length associated with internal flow passages can be approximated using Equation (3.27) [25]. It can be seen from Equations (3.9) and (3.27)

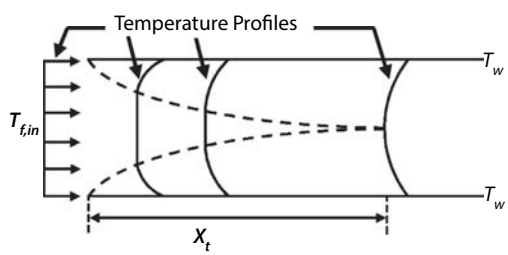

Figure 3.16 Evolution of temperature profiles along axial direction in an internal flow passage

that the thermal entrance length is related to hydrodynamic entrance length through the Prandtl number. For liquids with Prandtl number lower than unity, the thermal entrance length is smaller than the hydrodynamic entrance length; on the other hand, the thermal entrance length is larger than the hydrodynamic entrance length for liquids with Prandtl number greater than unity [25]. The two entrance lengths are equal when the Prandtl number is unity [36]. For gases, the Prandtl number is smaller than unity, while for fluids, it is greater than unity. Figures 3.17 and 3.18 provide a graphical representation of the variation of thermal entrance length with Reynolds number and hydraulic diameter for air and water, respectively. For MEMS heat exchangers the influence of thermal entrance length cannot be neglected.

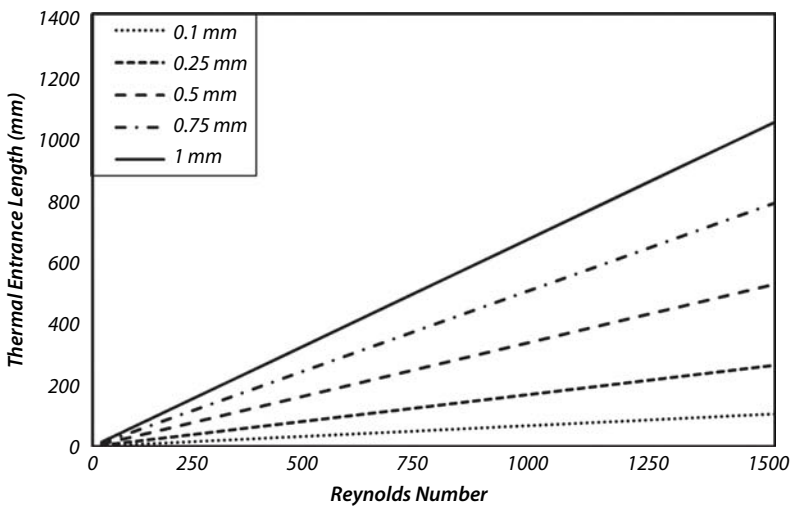

Figure 3.17 Influence of Reynolds number and hydraulic diameter on thermal entrance length of water

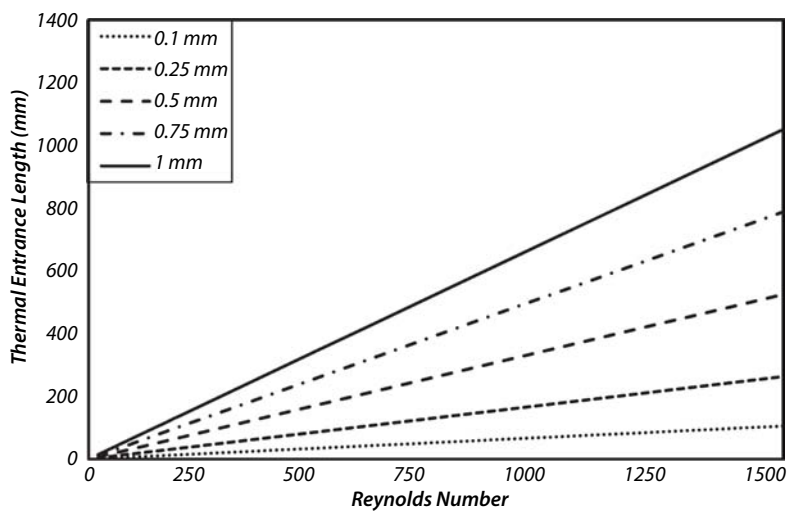

Figure 3.18 Influence of Reynolds number and hydraulic diameter on thermal entrance length of air

$$x_t \approx 0.06\, Re\, Pr\, D_{hy} = x_l\, Pr \tag{3.27}$$

The heat transfer coefficient varies in the thermally developing region of an internal flow passage; however, it remains constant when the flow is thermally developed, Figure 3.19. It is common to define heat transfer coefficient in terms of Nusselt number, a non-dimensional parameter, as provided in Equation (3.28); this is irrespective of whether the flow is developing or developed [25, 26]. The Nusselt number for different internal flow passages operating under thermally developed flow conditions is provided in Table 3.3 [26, 28, 29].

$$h = \frac{Nu\, k_f}{D_{hy}} \tag{3.28}$$

With respect to convection, two situations are commonly encountered. In one scenario, the wall of the internal flow passage is maintained at a constant temperature, while in the other case, the wall is maintained at constant heat flux [25]. In both situations, the average fluid and wall temperatures as well as the total heat transfer are determined by combining Equation (3.3) with Equation (3.26). The first scenario is represented in Figure 3.20. The average fluid temperature at any axial location can be calculated using Equation (3.29). The outlet temperature can be determined by substituting the length of the internal flow passage for the axial distance parameter [25].

$$\frac{\overline{T}_{f,x} - T_w}{T_{in} - T_w} = exp\left(-\frac{\overline{h} A_s}{\dot{m} C_p L} x \right) \tag{3.29}$$

Figure 3.21 is a schematic of the variation of temperatures with axial distance. The temperature of the wall remains constant over the entire length of the internal flow

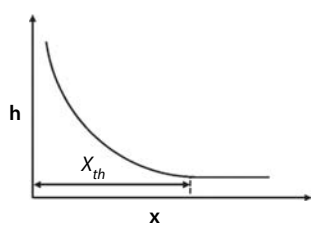

Figure 3.19 Axial variation of heat transfer coefficient

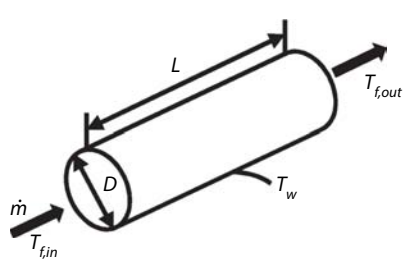

Figure 3.20 Internal flow passage subjected to constant wall temperature

passage, while the average temperature of the fluid varies in an exponential manner between the inlet and outlet of the same. In this situation, the temperature difference is a function of axial location. The average temperature difference, between the fluid and the wall, can be calculated as shown in Equation (3.30), and it is commonly referred to as **l**og **m**ean **t**emperature **d**ifference (LMTD) [25]. The total heat transfer can be determined using Equation (3.31) [25].

$$LMTD = \frac{\Delta T_{in} - \Delta T_{out}}{ln\left(\frac{\Delta T_{in}}{\Delta T_{out}}\right)} \text{ where } \Delta T_{in} = T_{w,in}(= T_w) - \overline{T}_{f,in} \text{ and} \tag{3.30}$$

$$\Delta T_{out} = T_{w,in}(= T_w) - \overline{T}_{f,out}$$

$$\dot{Q} = \overline{h}\, A\, LMTD \tag{3.31}$$

The second scenario is represented in Figure 3.22. In this situation, the temperature of the fluid as well as the wall varies in the axial direction. The total heat transfer between the fluid and wall is determined as in Equation (3.32) without the need for knowledge of the fluid and the wall temperatures.

$$\dot{Q} = \dot{Q}''_w A \tag{3.32}$$

The average temperature of the fluid at any axial location from the inlet of the internals flow passage can be determined using Equation (3.33) [25]. The average outlet

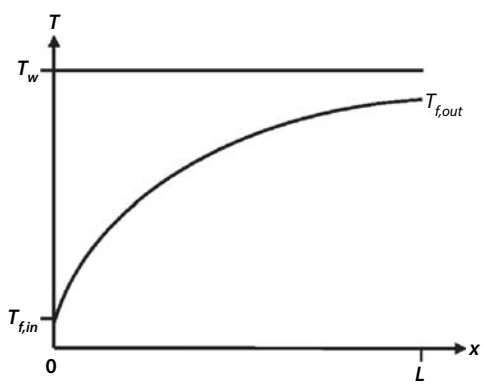

Figure 3.21 Temperature variation of fluid and wall in axial direction

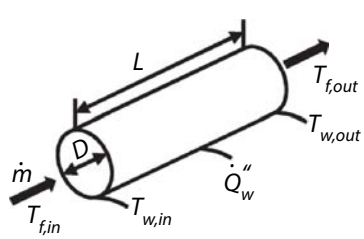

Figure 3.22 Internal flow passage subjected to constant heat flux

temperature of the fluid can be determined from Equation (3.33) by replacing the axial distance parameter by the length of the internal flow passage. The average temperature of the wall can be determined using Equation (3.33) as shown in Equation (3.34) [25]. Equation (3.34) will provide the average temperature of the wall at the outlet section of the internal flow passage when the temperature of the fluid used in the same corresponds to that at the outlet.

$$\overline{T}_{f,x} = \overline{T}_{f,in} + \frac{\dot{Q}_w'' A}{\dot{m} C_p L} x \tag{3.33}$$

$$\overline{T}_{w,x} = \overline{T}_{f,x} + \frac{\dot{Q}_w''}{\overline{h}} \tag{3.34}$$

From Equation (3.33), it can be noticed that the temperature of fluid varies in a linear fashion between the inlet and outlet of the internal flow passage, Figure 3.23. The average temperature of the wall varies linearly only in the thermally developed region. In the thermally developing region, linear variation of the wall temperature is not observed because of the axial variation of heat transfer coefficient as previously described. If the thermally developing region can be neglected, then the average temperature difference between the wall and the fluid remains constant over the entire length of the internal flow passage and can be determined form Equation (3.34); otherwise, the same can be determined using Equation (3.30).

3.2.3.3 Thermal Resistance

Thermal resistance has an electrical engineering corollary in the form of electrical resistance. Temperature difference provides the potential for heat transfer similar to voltage difference creating potential for current flow. Thus thermal resistance, temperature

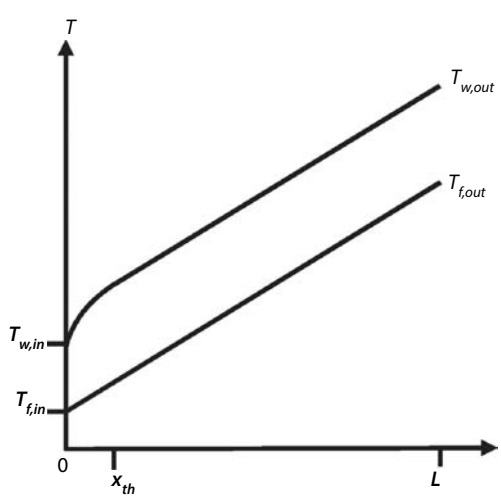

Figure 3.23 Temperature of fluid and wall in the axial direction

difference, and heat transfer can be related through Equation (3.35); it is similar in form as Kirchhoff's equation in electrical engineering [36].

$$\Delta T = R_{th}\dot{Q} \tag{3.35}$$

Thermal resistance associated with conduction heat transfer is given by Equation (3.36); it is obtained by comparing Equation (3.25) and Equation (3.35) [36]. Similarly, the thermal resistance associated with convection heat transfer can be determined by comparing Equations (3.26) and (3.35) and is provided in Equation (3.37) [36].

$$R_{th,cond} = \frac{\Delta x}{k_s A} \tag{3.36}$$

$$R_{th,conv} = \frac{1}{hA} \tag{3.37}$$

A third thermal resistance termed calorific thermal resistance also exists. Calorific thermal resistance relates the influence of mass flow rate and specific heat capacity of a body on its temperature change while absorbing or rejecting heat. The equation for this process can be formulated by substituting Equation (3.6) into Equation (3.3) to generate Equation (3.38). The associated thermal resistance is provided in Equation (3.39); the product of mass flow rate and specific heat capacity is as termed heat capacity.

$$\dot{m}C_p\left(T_{in} - T_{out}\right) = \dot{Q}_{out} - \dot{Q}_{in} = \Delta\dot{Q} \tag{3.38}$$

$$R_{th,cal} = \frac{1}{\dot{m}C_p} = \frac{1}{C_f} \tag{3.39}$$

Just like electrical resistances, thermal resistances can be added as part of an overall thermal "network." When thermal resistances are in parallel, the temperature difference remains constant across each of the resistances, but heat transfer varies across each. The equivalent thermal resistance can be determined as shown in Equation (3.40) [36]. By contrast, whenever thermal resistances are arranged in series, the heat transfer through each remains the same while the temperature change across each is different. The equivalent thermal resistance of resistances in series is provided in Equation (3.41) [36].

$$R_{th} = \sum_{i=0}^{n} \frac{1}{R_i} \tag{3.40}$$

$$R_{th} = \sum_{i=0}^{n} R_i \tag{3.41}$$

Thermal conductance is another parameter that is relevant to MEMS heat exchangers; it is the inverse of thermal resistance.

3.3 MEMS Heat Sinks

MEMS heat sinks are one of type of MEMS heat exchanger that have caught the interest of researchers globally. The primary application of MEMS heat sinks is thermal management of microelectronics, though it can be used for thermal management of other chip-scale energy systems such as micro fuel cells, microcombustors, microreactors, solar cells, and laser diode arrays. The working of MEMS heat sinks can be explained using Figure 3.24 [34]. The MEMS heat sink is kept in thermal contact with the electronic chip that is to be cooled. The coolant, at a prescribed temperature, enters the MEMS heat sink through the section labeled inlet. The electronic chip generates heat which is equivalent to the power required for its operation. The heat generated by the electronic chip travels in the direction perpendicular to its surface. This heat travels through the heat sink substrate material and crosses the interface, between coolant and the microchannel, into the coolant. The thermal energy that enters the flowing coolant is carried to the outlet of the MEMS heat sink. Heat transfer through the heat sink substrate material is via conduction (black arrows in Figure 3.24a), and that between the substrate material and the coolant is via convection (grey arrows in Figure 3.24b). As billions of transistors (heat sources) are present on the surface of an electronic chip, the heat generated by the chip is assumed to be uniform across its surface similar to the constant heat flux scenario mentioned in Section 3.2.3; this fact has been confirmed by researchers [37, 38]. The temperature of the coolant and the substrate increases in the direction of the coolant flow just as depicted in Figure 3.23.

The self-explanatory design approach is detailed in the flowchart provided in Figure 3.25. The constraints associated with the design of MEMS heat sinks include power consumption and maximum allowable junction temperature of the electronic chip, inlet temperature of the coolant, maximum allowable pressure drop, and pumping power as well as overall dimensions. The design variables include the dimensions of microchannel as well as volumetric flow rate and inlet temperature of the coolant. The output parameters include the outlet temperature of the coolant, the maximum junction temperature of the electronic chip, pressure drop, and pumping power. The most common approach of designing MEMS heat sinks is presented in this section, and it utilizes analytical equations. This is a simplified approach based on certain assumptions. The assumptions include uniform flow rate through each internal flow passage

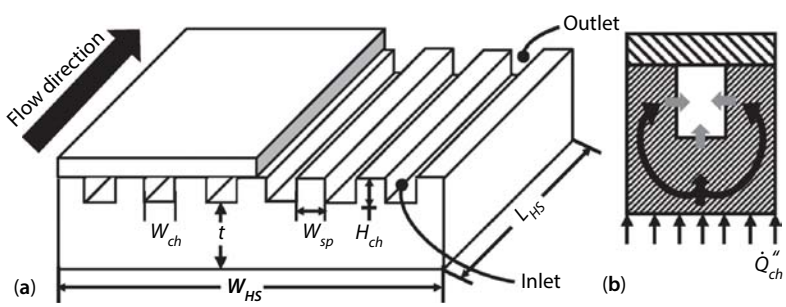

Figure 3.24 (a) Typical microchannel heat sink (top exposed to show microchannel) and (b) cross-sectional of heat sink

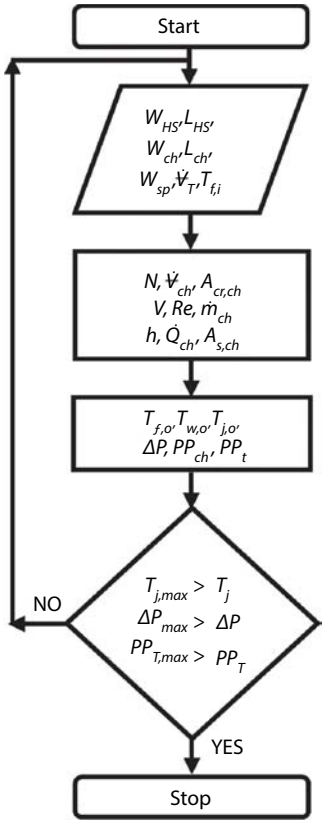

Figure 3.25 Design process of MEMS heat sinks

of the heat sink, no heat conduction through the substrate in the axial direction, uniform temperature at any cross section along the length, constant coolant properties, and straight internal flow passages [39]. The analytical equations listed in Table 3.6 are same as that introduced in Sections 3.2.2 and 3.2.3. This table demonstrates how the fundamental concepts of fluid mechanics and heat transfer are applied to the design of a MEMS heat sink. These equations are applicable to all microchannels irrespective of the cross-sectional profile.

The detailed thermal design approach listed earlier is not always warranted as maximum chip temperature, pressure drop, and power are the primary parameters of interest for a designer. For determining the maximum chip temperature, the related equations can be coupled into one using the concept of thermal resistance. The total thermal resistance associated with a MEMS heat sink is the combination of the conduction, convective, and calorific thermal resistances. These three resistances are in series and can be added to establish the total thermal resistance, Equation (3.59). The maximum chip temperature can in turn be determined using Equation (3.60).

$$R_{th,T} = \frac{1}{\dot{m}_{ch} C_p} + \frac{1}{\bar{h} A_{s,ch}} + \frac{t}{k_w A_{s,ch}} \tag{3.59}$$

$$T_j = T_{f,in} + R_{th,T}\dot{Q}_{ch} \tag{3.60}$$

It was mentioned earlier that the temperature is assumed to be uniform across any cross section, of the MEMS heat sink, in the axial direction. In reality, this is not true and is justifiable only because the temperature gradient in the axial direction is much greater than that in the transverse direction. Several researchers have improved upon the basic model of MEMS heat sinks by also including the effect of temperature variation in the transverse direction [39]. Table 3.6 provides the total thermal resistance of two models specifically for MEMS heat sinks employing microchannels with square/rectangular cross sections [39]. The first model accounts for the axial as well as transverse variation of temperature in the wall while considering only the axial variation of temperature in the coolant. On the other hand, the second model considers axial and transverse variation in the wall and coolant. For both models, the governing equation of the liquid is the differential form of Equation (3.3) in which all terms except those associated with internal energy and heat addition are equated to zero. Equation (3.6) is used in both models to quantify internal energy in terms of temperature. For the second model, the heat added to the fluid is quantified using Equation (3.26) as the heat transfer between the fluid and the wall is via convection. The maximum chip temperature based on any of the thermal resistances of Table 3.7 can be determined using Equation (3.60).

The very first work reported on MEMS heat sinks was that of Tuckerman and Pease [7]. The MEMS heat sink they developed was in silicon, consisted of rectangular microchannels, employed water as the coolant and dissipated 730 W of heat at a total thermal resistance of 0.1°C/W. Considerable research has taken place since, focused on fundamental aspects of fluid flow and heat transfer in microchannels or development of MEMS heat sinks with improved thermal performance. Improvements in thermal performance of MEMS heat sinks can be achieved by positively altering each of the parameters influencing the thermal resistance in Equation (3.59). One means of performance improvement currently under investigation is through the use of nanofluids [40, 41]. Nanofluids are a mixture of nanoparticles typically of high thermal conductance, suspended in conventional coolants such as water, ethylene glycol, and engine oil. The thermal conductivity of nanofluids is better than that of the coolant in which the nanoparticles are dispersed; the enhanced thermal conductivity acts to enhance the heat transfer coefficient as dictated by Equation (3.28) [40, 41]. Several combinations of nanoparticles and coolants have been developed to date. Nanoparticles of oxides (aluminum and copper oxide), carbides (silicon carbide), nitrides (aluminum and silicon nitrides), and metals (copper, aluminum, and iron) have been used as additives to the typical coolants [40, 41]. In addition, popular nanomaterials such as carbon nanotubes and graphite have also been investigated for this purpose. Several studies can be found in literature confirming the effectiveness of nanoparticles in enhancing the heat transfer coefficient [40, 41]. Townsend and Christianson [42] proved, through experiments, that nanofluids can reduce the junction temperature of electronic chips. Recently, Hodes *et al.* [43] theoretically investigated the usefulness of Galinstan as coolant in MEMS heat sinks. Galinstan is a gallium, indium, and tin eutectic with a melting temperature of −19 °C and has unique properties. The thermal conductivity of Galinstan is

Table 3.6. Design equations of MEMS heat sinks.

Total number of microchannels	$N = \dfrac{W_{HS}}{W_{ch} + W_{sp}}$	(3.42)
Length of microchannel	$L_{ch} = L_{HS}$	(3.43)
Volumetric flow rate through each microchannel	$\dot{V}_{ch} = \dfrac{\dot{V}_T}{N}$	(3.44)
Cross-sectional area associated with each microchannel	$A_{cr,ch} = H_{ch} W_{ch}$	(3.45)
Average velocity of coolant through each microchannel	$\overline{V} = \dfrac{\dot{V}_{ch}}{A_{cr,ch}}$	(3.46)
Reynolds number associated with each microchannel	$Re = \dfrac{\rho D_{hy} V}{\mu}$	(3.47)
Total mass flow rate	$\dot{m}_T = \rho \dot{V}_T$	(3.48)
Mass flow rate through each microchannel	$\dot{m}_{ch} = \dfrac{\dot{m}_T}{N}$	(3.49)
Heat added to each microchannel	$\dot{Q}_{ch} = \dfrac{\dot{Q}_T}{N}$	(3.50)
Temperature of the fluid at the outlet section of each microchannel	$\overline{T}_{f,out} = T_{f,in} + \dfrac{\dot{Q}_{ch}}{\dot{m}_{ch} C_p}$	(3.51)
Heat transfer coefficient	$\overline{h} = \dfrac{Nu k_f}{D_{hy}}$	(3.52)
Heat transfer area of each microchannel	$A_{s,ch} = \left(2H_{ch} + W_{ch}\right) L_{ch}$	(3.53)
Temperature of the wall of microchannel at the outlet section	$\overline{T}_{w,out} = \overline{T}_{f,out} + \dfrac{\dot{Q}_{ch}}{\overline{h} A_{s,ch}}$	(3.54)
Temperature of the electronic chip at the outlet section of the microchannel	$\overline{T}_{j,out} = \overline{T}_{w,out} + \dfrac{\dot{Q}_{ch}}{\dfrac{k_w A_s}{t}}$	(3.55)

(*Continues*)

Table 3.6 (Cont.)

Pressure drop through each microchannel	$\Delta P_{ch} = \dfrac{2 f \rho V^2 L_{ch}}{D_{hy}}$	(3.56)
Pumping power associated with each microchannel	$PP_{ch} = \Delta P_{ch} \dot{V}_{ch}$	(3.57)
Pumping power associated with MEMS heat sink	$PP_T = \Delta P_{ch} \dot{V}_T = N \Delta P_{ch} \dot{V}_{ch}$	(3.58)

Table 3.7. Advanced models of MEMS heat sinks employing microchannels.

Model 1		
Solid	Governing equation $$\frac{d^2 T_w}{dy^2} = \frac{2\bar{h}}{k_s W_{sp}}\left(T_w - T_f(x)\right)$$ Boundary conditions $$-k_w \left.\frac{dT_w}{dy}\right\|_{y=0} = \left(\frac{2\alpha}{2\alpha+1}\right)\left(\frac{W_{ch}+W_{sp}}{W_{sp}}\right)\dot{Q}''_{ch}$$ $$\left.\frac{dT_w}{dy}\right\|_{y=H_{ch}+t} = 0$$	
Liquid	Governing equation $$\dot{m}_{ch} C_p \frac{dT_f}{dx} = \left(W_{ch}+W_{sp}\right)\dot{Q}''_{ch}$$ Boundary condition $$T_f\Big\|_{x=0} = T_{f,in}$$	
Total resistance	$$R_{th,T} = \left(\frac{1}{m k_w}\right)\left(\frac{W_{ch}+W_{sp}}{L_{HS} W_{HS} W_{sp}}\right)\left(\frac{2\alpha}{2\alpha+1}\right)\frac{\cosh\left(m H_{ch}\right)}{\sinh\left(m H_{ch}\right)} + \left(\frac{1}{W_{HS}}\right)\left(\frac{W_{ch}+W_{sp}}{\dot{m}_{ch} C_p}\right)$$ $$m = \sqrt{\frac{2\bar{h}}{k_s W_{sp}}}$$	(3.61)

Table 3.7 (Cont.)

Model 2		
Solid	Governing equation $$\frac{\partial^2 T_w}{\partial y^2} = \frac{2\bar{h}}{k_s W_{sp}}\left(T_w - T_f(x,y)\right)$$ Boundary conditions $$-k_w \left.\frac{dT_w}{dy}\right\|_{y=0} = \left(\frac{2a}{2a+1}\right)\left(\frac{W_{ch}+W_{sp}}{W_{sp}}\right)\dot{Q}''_{ch}$$ $$\left.\frac{dT_w}{dy}\right\|_{y=H_{ch}+t} = 0$$	
Liquid	Governing equation $$\dot{m}_{ch} C_p \frac{dT_f}{dx} = 2\bar{h}\left(T_w - T_f(x,y)\right)$$ Boundary condition $$T_f\Big\|_{x=0,y} = T_{f,in}$$	
Total resistance	$$R_{th,T} = \left(\frac{J\lambda^2}{k_w \bar{H}_{ch} a}\right)\left[1 + \frac{L_{ch}}{a} + \frac{1}{3}\frac{a^2}{\lambda^2}\bar{H}_{ch}^2\right]\left(\frac{1}{L_{HS}W_{HS}}\right)$$ $$J = \left(\frac{2a}{2a+1}\right)\left(\frac{W_{ch}+W_{sp}}{W_{sp}}\right)\dot{Q}''; a = \frac{2\dot{m}_{ch}}{H_{ch}\bar{h}}; \lambda^2 = \frac{k_w W_{sp}}{2\bar{h}}$$	(3.62)

two orders of magnitude greater than that of water; however, its specific heat capacity is one order of magnitude lower than that of water. Nevertheless, the calculated total thermal resistance of MEMS heat sinks with Galinstan as coolant was lower than that employing water by 40% [43].

From Figure 3.19, it can be noted that the heat transfer coefficient is high in the thermally developing flow regime in comparison with that in the thermally developed flow regime. Thus, a higher-average heat transfer coefficient can be realized by maintaining thermally developing flow over the entire length of the microchannel. The common approach adopted for maintaining thermally developing flow over the entire length of the microchannel is that of physically disrupting the flow at regular intervals between the inlet and outlet of the microchannel [44–46]. Wavy and "zig-zag" microchannels are continuous microchannels that can achieve periodic disruption of flow. This in turn maintains the thermally developing flow regime over the length of the microchannel.

Little information is available on the total thermal resistance of MEMS heat sinks employing wavy and zig-zag microchannels as studies involving such microchannels have concentrated on estimating friction factor and Nusselt number [44–46].

It can also be concluded from Equation (3.59) that one approach to improving the thermal performance is by increasing the area associated with conduction heat transfer. However, simultaneous increase in footprint of the MEMS heat sink and electronic chip is not possible; increase in footprint of the electronic chip would lead to degradation in its electrical performance. When only the footprint of the MEMS heat sink is increased, there would be spreading of heat from the electronic chip to the MEMS heat sink. Thermal spreading introduces additional resistance in the heat flow path between the electronic chip and MEMS heat sink; the thermal resistance associated with thermal spreading is not included in Equation (3.59). Thus, this approach would be beneficial only if the reduction in conduction thermal resistance overshadows the resistance due to the thermal spreading. Missagia *et al.* [47] were one of the first ones to implement this approach for cooling a laser diode. The planar dimensions of the MEMS heat sink were 10 mm by 8 mm; the planar dimensions of the laser diode were approximately 1 mm by 4 mm [47]. The MEMS heat sink was fabricated in Si and employed water as the coolant. The thermal resistance was determined to be 0.04 °C/W. They did not conduct tests with same footprint for the MEMS heat sink and laser diode; however, based on extrapolated data, they concluded that the thermal resistance of such an arrangement would be 0.07 °C/W, thereby indicating the success of their approach [47].

3.4 MEMS Heat Pipes

Micro heat pipes are miniaturized versions of conventional heat pipes; thus, the working principle is the same irrespective of length scale [48–52]. The operation of a heat pipe is explained below with respect to conventional cylindrical heat pipes. Figure 3.26 provides the schematic of a simplified cylindrical heat pipe. Every heat pipe consists of three sections, namely evaporator, condenser, and adiabatic region. The evaporator is located at one extreme, while the condenser is located at the other. The evaporator is the section that absorbs heat from the electronic chip. This process forces the coolant to

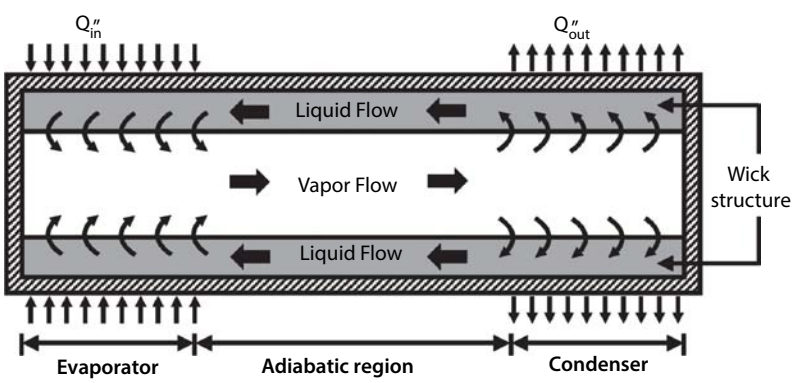

Figure 3.26 Cross-sectional view of cylindrical heat pipe

undergo phase change from liquid to vapor, via evaporation, which is then transported to the condenser section where it undergoes phase change from vapor to liquid via condensation. This rejects heat to the surroundings, ideally equal to the amount absorbed in the evaporator section. These two sections are thermally isolated from one another but physically connected via the adiabatic region where the coolant does not undergo phase change. The coolant is circulated between the evaporator and condenser yielding continuous operation of the heat pipe, Figure 3.26. Evaporation causes the curvature of the liquid–vapor interface to increase in the evaporator, along the direction of liquid flow, while condensation leads to reduction in the curvature of the liquid–vapor interface in the condenser, along the direction for vapor flow [48]. Thus, the transverse pressure jump and capillary force associated with the liquid–vapor interface vary in the axial direction. It is this difference in the transverse capillary force between the evaporator and condenser that causes the coolant to move from the condenser to the evaporator; the vapor moves from the evaporator to the condenser in response to the movement of liquid coolant [48]. An additional attraction of heat pipes is that these devices operate at near-isothermal conditions as heat transport is by phase change processes, i.e., evaporation and condensation [48].

The study and operation of the capillary forces and resulting fluid motion within MEMS heat pipes are especially important. In general, micro heat pipes have been defined as those heat pipes which satisfy the criterion listed in Equation (3.63) [49, 51]. Accordingly, the radius of curvature of the liquid–vapor interface is comparable to the hydraulic diameter of the internal flow passage in micro heat pipe. For all practical situations, heat pipes that employ internal flow passages smaller than 1 mm can be referred to as micro heat pipes [48, 51]. In addition, if the foot print of micro heat pipes is comparable to that of an electronic chip, then they are labeled as MEMS heat pipes in this chapter.

$$\frac{r_{l/v:i}}{r_{hy}} \geq 1 \tag{3.63}$$

Figure 3.27 provides the schematic of a typical MEMS heat pipe array; the design consists of multiple microscale internal flow capillary passages arranged in parallel with each functioning as an individual heat pipe, Figure 3.27a. Typically MEMS heat pipe arrays are embedded in the substrate. Figure 3.27b represents the cross-sectional profile of an individual MEMS heat pipe.

Figure 3.28 provides the perspective view of an individual MEMS heat pipe as well as the cross section of a MEMS heat pipe at different locations along the length [52, 53]. There are several points of significance to the capillary channels and resulting fluid interaction that are reviewed here. First, for most of the length of the heat pipe, liquid coolant occupies only the corners of the internal flow passage where capillary forces promote fluid movement. The liquid coolant is transported between the condenser and evaporator through these corners, thus establishing the wicking structure in MEMS heat pipes [50, 52, 53]. As determined by heat transfer to the evaporator section, the area occupied by the vapor increases along the axial length from the condenser to the evaporator and vice versa. This implies that the interface recedes into the channel corners along the length of the heat pipe and is accompanied with a reduction in radius

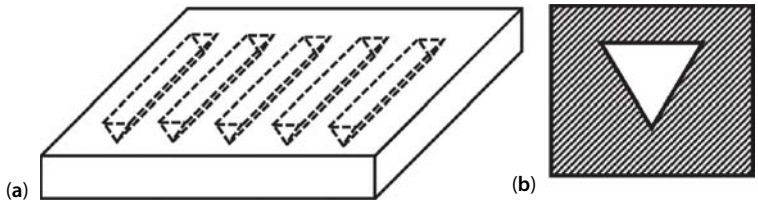

Figure 3.27 (a) MEMS heat pipe array and (b) cross-section of individual MEMS heat pipe

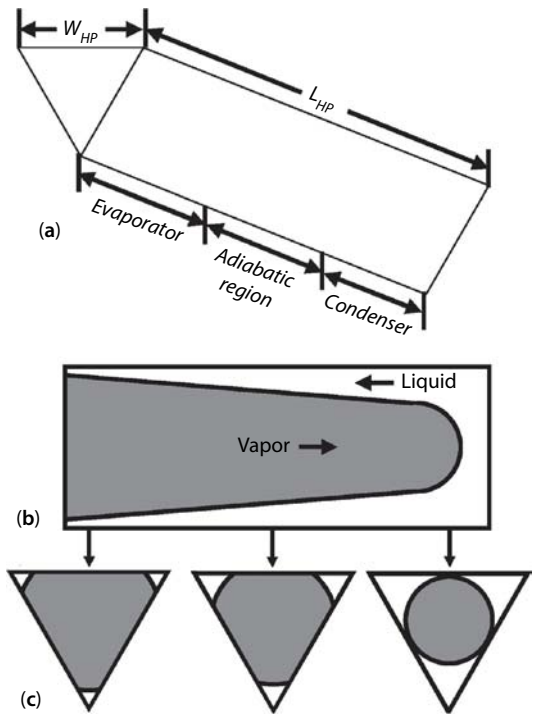

Figure 3.28 Triangular MEMS heat pipe (a) perspective view and (b) top view and (c) cross-sectional profile at three axial locations.

of curvature. The angle of contact remains a constant along the length irrespective of the radius of curvature as this is a base fluid surface tension property [53, 54]. Due to evaporation in the evaporator section, the corresponding liquid–vapor interface has a greater curvature, i.e., smaller radius of curvature, than that in the condenser which promotes condensation [53, 54]. The curvature of the interface is maximum and minimum at the end of the evaporator and condenser, respectively.

Figure 3.29 shows the axial variation of pressure associated with liquid and vapor phases of the coolant in a typical heat pipe [48]. It can be seen that the pressure drop in the evaporator and condenser are non-linear for both liquid and vapor phases of the coolant. This is due to the changing mass flow rate as phase change transition occurs. By contrast, the vapor and liquid pressure drop in the adiabatic region is linear. It can be

concluded from Figure 3.29 that for operation of heat pipes, irrespective of size, the difference in capillary pressure, between the evaporator and condenser, should be greater than the sum of the total vapor and liquid pressure, Equation (3.64) [48–51]. The third term on the right hand side of Equation (3.64) accounts for gravitational force; it is not taken into account in Figure 3.29 [48–51].

$$\Delta P_c \geq \Delta P_l + \Delta P_v + \Delta P_g \tag{3.64}$$

The changing profiles (radii) and contact area of the working fluid within the operating heat pipe imply that the pressure jump across the liquid–vapor interface at the end of the evaporator is greater than that at the end of the condenser. It is this fundamental difference in capillary pressure that provides the driving force for the liquid in the axial direction between these two sections of the heat pipe. The Young–Laplace equation provided in Section 3.2.2 can be used for determining the capillary pressures in the evaporator as well as condenser; the two capillary pressures can then be combined to determine the net capillary pressure available for driving the liquid in the axial direction. The location in the evaporator where the curvature of the interface attains its maximum is referred to as dry point, while the location in the condenser where the curvature is minimum is termed as wet point [48]. The radius of curvature, along the length of the MEMS heat pipe, of the interfaces at the dry as well as wet point is assumed to be infinite and thus do not contribute to the capillary pressure at these locations [48]. Therefore, only the radius of curvature, in the transverse direction, of the interfaces at these locations is considered for determining the capillary pressure at the respective locations.

The procedure for designing MEMS heat pipes is provided in Figure 3.30 [48, 49, 51, 52]. It involves estimating the geometric and operating parameters suitable for satisfying the pressure constraint, Equation (3.64), at a particular temperature without compromising the space and heat input requirements. The influence of temperature and total thermal absorption capability is introduced to the design process through the coolant liquid enthalpy of vaporization. The design approach enlists several of the analytical equations which were listed in Section 3.2 in the form applicable to MEMS heat pipes. The necessary equations for performing the different equations associated with Figure 3.30 are listed in Table 3.8 [48, 49, 51, 52].

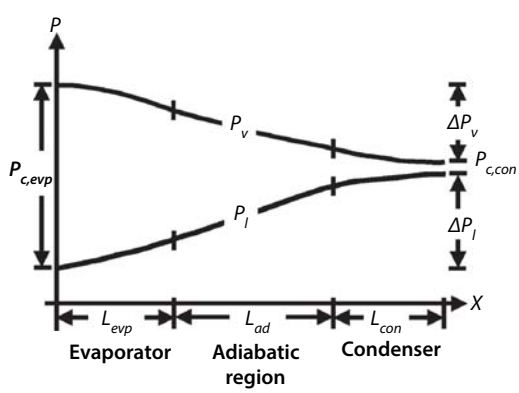

Figure 3.29 Pressure variation in a typical heat pipe

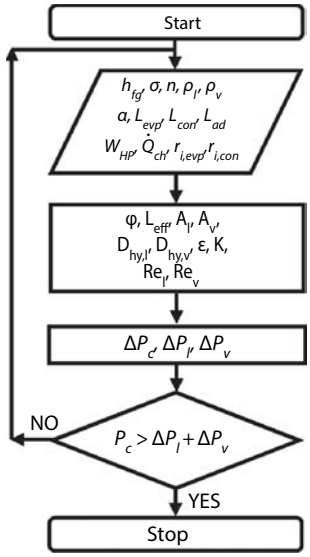

Figure 3.30 Design process of MEMS heat pipes

For purposes of calculation, it is assumed that mass transfer associated with evaporation and condensation occurs in a linear manner in the evaporator and condenser, respectively [48, 49, 51, 52]. Thus, only half the length of the evaporator and condenser is considered in calculating pressure drop. The porosity for MEMS heat pipes shown in Figure 3.27 is unity [49]. As seen in Figure 3.27, the space, occupied by the vapor and liquid phases, changes with axial location of the MEMS heat pipe and for this matter the associated hydraulic diameter, cross-sectional area, and Reynolds number also change with axial location. However, the relationship between the axial location and parameters of liquid and vapor phases such as hydraulic diameter, cross-sectional area, and Reynolds number are not known a priori which in turn complicates the estimation of liquid and vapor pressure. Nevertheless, the pressures can be conservatively estimated using the equations provided in Table 3.7 if it is assumed that the hydraulic diameter and area associated with the liquid and vapor regions remains constant over the entire length. To utilize this approach, the hydraulic diameter and area of the liquid phase should be calculated at the start of the condenser section, where these parameters are maximum. Vapor-phase properties should be determined at the end section of the evaporator. The maximum radius of curvature of the interface occurs at the start of the condenser as given in Table 3.10. On the other hand, the minimum radius of curvature of the interface occurs at the end of the evaporator; at maximum heat transfer capacity, this radius should be zero as all fluid is evaporated [55]. For design purposes, the radius of curvature of the interface at the end of the evaporator can be selected from this maximum to minimum range. Because the space occupied by liquid-phase coolant in MEMS heat pipes resembles a triangle, the corresponding friction factor is used in the associated pressure drop equation [56].

Several researchers [51, 55–57] have used alternative techniques to arrive at analytical equations for calculating the maximum heat transport capability of a MEMS heat

Table 3.8. Design equations for MEMS heat pipes.

Capillary pressure difference	$P_c = \sigma\left[\frac{1}{r_{l/v:i,evp}} - \frac{1}{r_{l/v:i,con}}\right]$	(3.65)
Heat transfer per channel	$\dot{Q}_{ch} = \frac{\dot{Q}_T}{N_{ch}} = \dot{m}_{ch} h_{fg}$	(3.66)
Liquid pressure per channel	$\Delta P_l = \frac{\mu_l \dot{Q}_{ch} L_{eff}}{K A_l h_{fg} \rho_l}$ $K = \frac{\varepsilon D_{hy,l}^2}{2\left(f_l Re_l\right)}$ $Re_l = \frac{D_{hy,l}\dot{Q}_{ch}}{\mu_l A_l h_{fg}}$ $L_{eff} = 0.5 L_{evp} + L_{ad} + 0.5 L_{con}$	(3.67)
Vapor pressure per channel	$\Delta P_v = \frac{2\left(f_v Re_v\right)\mu_v \dot{Q}_{ch} L_{eff}}{D_{hy,v}^2 A_v h_{fg} \rho_v}$ $Re_v = \frac{D_{hy,v}\dot{Q}_{ch}}{\mu_v A_v h_{fg}}$	(3.68)

pipe while satisfying Equation (3.64); few analytical equations are provided in Table 3.9. In these models, the minimum radius is taken to be zero. Analytical equation by Suman and Kumar [56] is applicable to all regular polygons.

In many instances, it is necessary to have a deeper understanding of the operation of MEMS heat pipes and for this, one-dimensional models have been developed. Using one-dimensional equations, it is possible to understand the axial variation of parameters associated with MEMS heat pipes. Several one-dimensional equations have been developed; in this chapter, the simplest model is reviewed [58]. The equations that constitute the model are based on the laws of fluid mechanics as applied to the liquid and vapor phases of MEMS heat pipes. Figure 3.31 provides a schematic of the corner region of a MEMS heat pipe. The equations developed by Suman *et al.* [58] are listed in this section. These equations are based on several assumptions that enable neglecting the axial variation in liquid and vapor cross-sectional area, vapor pressure and

Table 3.9. Analytical equations for determining maximum heat transfer capability of MEMS heat pipes.

Model	$Q_{ch,max}$	
Babin *et al.* [51]	$\frac{0.16\beta\sqrt{K_l K_v}}{8\pi H(L_{HP})}\frac{\sigma h_{fg}}{\nu_l}\sqrt{\frac{\nu_l}{\nu_v}}\frac{A_{ch,cr}^{0.75}}{L_{HP}}$ $\beta = 2.044, H(L_{HP}) = 0.5, K_l = 0.6, K_v = 0.975$	(3.69)
Ma and Peterson [55]	$\frac{0.16\beta\sqrt{K_l K_v}}{8\pi H(1)}\frac{\sigma h_{fg}}{\nu_l}\sqrt{\frac{\nu_l}{\nu_v}}\frac{A_{ch,cr}^{1.5}}{L_{HP}}$ $\beta = 1.1343, H(1) = 0.8226, K_l = 0.5, K_v = 0.94$	(3.70)
Suman and Kumar [56]	$\frac{2B_1\sigma\rho_l h_{fg} R_{max}^3}{3B_2(L_{HP}+L_{ad})}$ $B_1 = n\left[\cot(\varphi+\gamma)+(\varphi+\gamma)-\frac{\pi}{2}+\frac{\cot(\varphi+\gamma)\cos(\varphi+\gamma)\sin\gamma}{\sin\theta}\right]$ $B_2 = \frac{\mu f\cos^2(\varphi+\gamma)}{2\text{in}^2\varphi\left[\frac{\cot(\varphi+\gamma)\cos(\varphi+\gamma)\sin\gamma}{\sin\varphi}+\cot(\varphi+\gamma)+(\varphi+\gamma)-\frac{\pi}{2}\right]^2}$ $R_{max} = \frac{W_{HP}}{2}\left[\frac{\sin\varphi}{\cos(\varphi+\gamma)}\right]$ $\varphi = \frac{(n-2)}{n}\frac{\pi}{2}$	(3.71)
Shukla [57]	$\left(\frac{\pi r_i^3\beta^2}{8L_{HP}}\right)\left(\frac{\sigma h_{fg}}{\nu_v}\right)\left[\left(1-\frac{2}{3}\beta^2+\frac{1}{5}\beta^4\right)+\frac{P_v r_i}{2\beta^2\sigma}\left(1+\gamma_v Ma_v^2\right)\left(1-\beta^2\right)^2\right]$ $\beta = 0.6533$ *for equilateral triangle*	(3.72)

vapor velocity as well as shear stress at the liquid–vapor interface. The liquid velocity is assumed to be uniform at any cross section along the axial length of the MEMS heat pipe. In addition, the device is assumed to be operated under isothermal conditions, and thus the energy equation is not considered for this model. Thus, the operating

Table 3.10. Geometric parameters of one-dimensional model.

$r_{max} / r_{l/v:i,con}$	$p_{l/v:i}$	$A_{cr,l}$
$\frac{W_{HP}}{2}\left[\frac{\sin\varphi}{\cos(\varphi+\gamma)}\right]$	$r_{l/v:i}\left[\pi-2(\varphi+\gamma)\right]$ $\varphi=\frac{(n-2)}{n}\frac{\pi}{2}$	$\left[\cot(\varphi+\gamma)+(\varphi+\gamma)-\frac{\pi}{2}+\frac{\cot(\varphi+\gamma)\cos(\varphi+\gamma)\sin\gamma}{\sin\theta}\right]r_{l/v:i}^2$

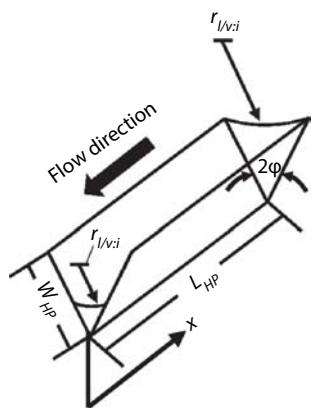

Figure 1.31 Computational domain (corner of a MEMS heat pipe)

temperature of the MEMS heat pipe is set a priori as per the design requirements. The vapor pressure is constant over the entire length of the MEMS heat pipe; it is equal to the saturation pressure of the coolant corresponding to the temperature at which the device is operated. Equation (3.73) is the continuity equation, while Equation (3.74) is the momentum equation. These equations represent the differential form of those listed in Section 3.2 and are associated with each corner of the MEMS heat pipe.

$$\left(\rho A_{cr}\right)_l \frac{dV_l}{dx}+\frac{\left(\dot{Q}p\right)_{l/v:i}}{h_{fg}}=0 \text{ where } \dot{Q}_{l/v:i}=\frac{\dot{Q}_{ch}W_p}{p_i}/0/-\frac{\dot{Q}_{ch}W_p}{p_i} \tag{3.73}$$

$$\left(\rho A_{cr}V\right)_l \frac{dV_l}{dx}+A_{cr,l}\frac{dP_l}{dx}+2\left(\tau p\right)_{l/w:i}=0 \tag{3.74}$$

Heat transferred across the liquid–vapor interface is positive for the evaporator, zero for the adiabatic section, and negative for the condenser. Shear stress in Equation (3.74) is defined in terms of friction factor exactly as in Equation (3.18); friction factor for triangular cross-sectional profile is appropriate for MEMS heat pipes as the cross-sectional profile of space occupied by liquid in each corner resembles a triangle. Liquid flow through the corners is laminar. The cross-sectional area of the liquid region as well as the liquid–vapor interface length are functions of the radius of curvature of the

liquid–vapor interface. The differential form of the Young–Laplace equation, Equation (3.75), is taken as the third equation necessary to solve the model.

$$\frac{dP_l}{dx} = \frac{\sigma}{r_i^2}\frac{dr_{l/v:i}}{dx} \tag{3.75}$$

The boundary conditions associated with the model are described in Equations (3.76)–(3.78) [58]. The liquid velocity at the end of the evaporator is zero, and this is used as one of the boundary conditions. The liquid pressure at the inlet of the condenser is related to the vapor pressure through Young–Laplace equation, forming the second boundary condition. The third boundary condition is the radius of curvature at the inlet of the condenser; the radius of curvature is maximum at the start of the condenser. The different geometric relationship associated with the model is provided in Table 3.10 [58]. The set of governing equations can be solved using various numerical techniques like finite-difference methods and Runge–Kutta solutions.

$$V_l\left(x=0\right)=0 \tag{3.76}$$

$$P_l\left(x=L_{HP}\right)=P_v-\frac{\sigma}{r_{l/v:i}\left(x=L_{HP}\right)} \tag{3.77}$$

$$r_i\left(x=L_{HP}\right)=r_{max}=r_{l/v:i,con} \tag{3.78}$$

In these MEMS heat pipes, the vapor region is bounded by the liquid region. However, there exists another type of MEMS heat pipe in which the vapor region is located above the liquid region rather than bounded by it. The cross section of such a MEMS heat pipe is shown in Figure 3.32. In these MEMS heat pipes, the internal flow passages are kept open at the top for purposes of mass transfer via evaporation and condensation. Only a single vapor region exists, and it occupies the space over multiple liquid-filled microscale flow passages. Because of difference in fluid and vapor interaction, the coolant fills the microchannels more completely and is not limited to the corners as with typical heat pipes. The radius of curvature of the liquid–vapor interface reduces as the liquid progresses along the MEMS heat pipe evaporator as represented in Figure 3.33. The contact angle of the interface reduces, as its radius reduces, with the minimum contact angle occurring at the end of the evaporator [59–61]. It is widely

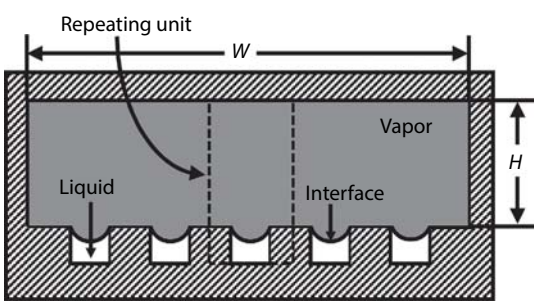

Figure 3.32 Cross-section of MEMS heat pipe

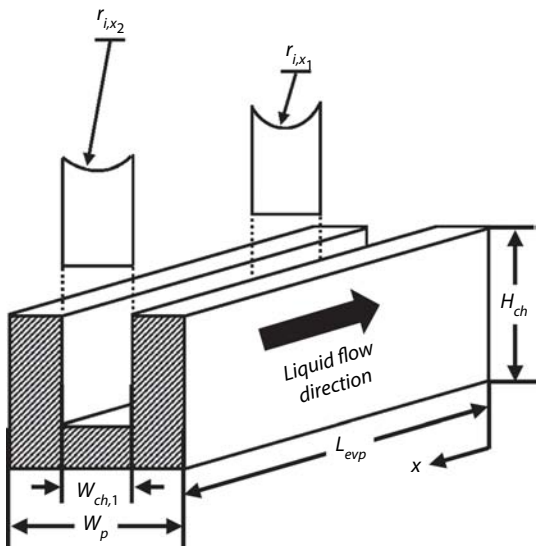

Figure 3.33 Variation of interface radius of curvature along microchannel length

reported that the interface remains attached to the top edges of the passages and any recession of the interface into the depth of the passage is neglected, Figure 3.33 [59–63]. This avoids dry-out, a condition where all working fluid from the microchannel has been evaporated due to thermal input. As with other MEMS exchangers, laminar flows result in the microchannels. The friction factor corresponding to rectangular cross section is used for approximating the pressure drop associated with vapor flow [62, 63]. The analytical equations listed in Table 3.8 are applicable to MEMS heat pipes of this type as well. These analytical equations have been successfully applied to the MEMS heat pipes shown in Figure 3.32 by Cao *et al.* [64], Zaghdoudi [65], and Shi *et al.* [66]. The equations necessary for determining the parameters associated with the models are provided in Table 3.11 [48, 59, 60, 62–67]. The section enclosed by the dashed line constitutes a repeating unit of the MEMS heat pipe, and only it needs to be considered in the design.

Several one-dimensional equations have been developed for this type of MEMS heat pipe, or heat spreader as they are sometimes referred. The simplest one, as detailed by Rullière *et al.* [68], is listed in the following. This model consists of continuity and momentum equations of the liquid and vapor regions. Equations (3.91) and (3.92) represent the continuity equations of the liquid and vapor regions, respectively; Equations (3.93) and (3.94) are the momentum equations of the liquid and vapor regions, respectively. As with the previous one-dimensional model, this model also assumes that the microdevice is operating under isothermal conditions. In addition, the effect of condensation on the channel spacing is neglected in this model. In this model, the x-coordinate starts at the dry point.

$$\frac{d\left(A_{cr}V\right)_l}{dx}dx = \left(pV\right)_{l/v:i}dx \text{ where } V_{l/v:i} = -\frac{\dot{Q}_{i,ch}}{\rho_l h_{fg}} \tag{3.91}$$

Table 3.11. Equations of parameters associated with equations in Table 3.8.

Hydraulic diameter of liquid region		
Rectangle	$\dfrac{4W_{ch}H_{ch}}{(W_{ch}+2H_{ch})}$	(3.79)
Triangle	$\dfrac{2W_{ch,1}H_{ch}}{(2H_{ch}/\cos(\alpha/2))}$	(3.80)
Trapezoid	$\dfrac{2\left(W_{ch,1}+W_{ch,2}\right)H_{ch}}{(W_{ch,2}+2H_{ch}/\sin\alpha)}$	(3.81)
Hydraulic diameter of vapor region		
	$\dfrac{2WH}{(W+N_{ch}H)}$	(3.82)
Minimum radius of curvature (radius of curvature in evaporator for maximum heat transport)		
Rectangle	$\dfrac{W_{ch,1}}{2\cos(\gamma)}$	(3.83)
Triangle	$\dfrac{W_{ch,1}}{2\cos\left(\gamma+\alpha\right)}$	(3.84)
Trapezoid	$\dfrac{W_{ch,1}}{2\cos\left(\gamma+\alpha\right)}$	(3.85)
Porosity		
Rectangle	$\dfrac{W_{ch,1}}{W_p}$	(3.86)
Triangle	$\dfrac{W_{ch,1}}{2W_p}$	(3.87)
Trapezoid	$\dfrac{\left(W_{ch,1}+W_{ch,2}\right)}{2W_p}$	(3.88)

Table 3.11. (Cont.)

Friction factor for vapor region		
Equation (R1)		
Friction factor for liquid region		
Rectangle	$$(fRe)_l = (fRe)_{l0}\left[1+\frac{W_{ch}^3}{6\pi D_{hy,v}^3}(fRe)_v\frac{\nu_v}{\nu_l}\left(1-1.971exp^{\left(\frac{-\pi H_{ch}}{W_{ch}}\right)}\right)\right]$$ $$(fRe)_{l0} = \frac{8H_{ch}^2 h}{\left\{\frac{W_{ch}^2}{4}\left(1+\frac{2H_{ch}}{W_{ch}}\right)^2\left[\frac{1}{3}-\frac{32W_{ch}}{\pi^5 H_{ch}}\tanh\left(\frac{\pi H_{ch}}{W_{ch}}\right)\right]\right\}}$$	(3.89)
Triangle and trapezoid	$$(fRe)_l = A_1(fRe)_{l0}\left[1-(fRe)_v\frac{H_{ch}^2}{6W_{ch,1}^2 D_{hy,v}}\frac{\mu_v\rho_v A_v}{\mu_l\rho_l A_l}\left(1-1.971exp^{\left(\frac{\pi H_{ch}}{W_{ch,1}}\right)}\right)A_2\right]$$ $$A_1 = 1.44-\frac{0.84}{1+\sin\gamma}\left(1-0.19\sqrt{1-\left(\frac{W_{ch,2}}{W_{ch,1}}\right)^2}\right)$$ $$A_2 = -1.2+1.1\frac{W_{ch,1}}{H_{ch}}+1.6exp^{\left(\frac{W_{ch,2}}{W_{ch,1}}\right)^3}-0.45\sqrt{\frac{W_{ch,1}}{W_v/N}}+\frac{H_{ch}}{H_v}\left(1.6-0.77\frac{W_{ch}}{H_{ch}}-1.6exp^{\left(\frac{W_{ch,2}}{W_{ch,1}}\right)^3}+1.3\gamma\right)$$	(3.90)

$$\frac{d\left(A_{cr}V\right)_v}{dx}dx = -\frac{\rho_l}{\rho_v}\left(pV\right)_{l/v:\,i}dx \tag{3.92}$$

$$\rho_l\frac{d\left(A_{cr}V^2\right)_l}{dx}dx = -A_{cr,l}\frac{dP_l}{dx}dx + \left(P_v - P_l\right)\frac{dA_{cr,l}}{dx}dx + \left(\tau p\right)_{l/w:i}dx + \left(\tau p\right)_{l/v:i}dx \tag{3.93}$$

$$\rho_v\frac{d\left(A_{cr}\right)_v}{dx}dx = -A_{cr,v}\frac{dP_v}{dx}dx + \left(P_l - P_v\right)\frac{dA_{cr,v}}{dx}dx - \left(\tau p\right)_{v/w:i}dx - \left(\tau p\right)_{l/v:i}dx \tag{3.94}$$

$$\frac{dP_v}{dx} - \frac{dP_l}{dx} = \frac{d\left(\sigma / r_{l/v:i}\right)}{dx} \tag{3.95}$$

The shear stress, at the liquid-wall and vapor-wall interface, in the preceding equations can be evaluated through friction factor. Though shear stress at the liquid–vapor interface was included in the governing equation, it was neglected by Rullière *et al.* during calculation [68]. The parameters such as cross-sectional area of liquid and vapor as well as interfacial length are functions of the radius of curvature of the interface. The boundary conditions are listed in the following. The boundary conditions include liquid and vapor velocities and pressures as well as radius of curvature. In this model, radius of curvature at the start of the condenser is an input; Do *et al.* [62] assumed this to be equivalent to half of the hydraulic diameter of the vapor space that exists when the MEMS heat pipe is not operational.

$$V_l\left(x = L_{HP}\right) = V_v\left(x = L_{HP}\right) = 0 \tag{3.96}$$

$$P_v\left(x = L_{HP}\right) = P_{v,sat}\left(T_{sat}\right) \tag{3.97}$$

$$P_l\left(x = L_{HP}\right) = P_v\left(x = L_{HP}\right) - \frac{\sigma}{r_{l/v:i}\left(x = L_{HP}\right)} \tag{3.98}$$

$$r_{l/v:i}\left(x = L_{HP}\right) = r_{max} \tag{3.99}$$

MEMS heat pipes similar to the standard design represented in Figure 3.27 were initially envisioned by Cotter [69]. Cotter's [69] vision of MEMS heat pipes spurred growing interest; both experiment- and model-based research efforts resulted with the latter taking precedence. Researchers have developed analytical as well as numerical models of MEMS heat pipes. Peterson and co-workers [51, 52, 54] developed several analytical models of MEMS heat pipes. They developed analytical equations for calculating the maximum heat that can be transported between the evaporator and condenser sections of the MEMS heat pipe based on the dimensions and thermophysical properties of the

coolant. These analytical equations were also of use in understanding the influence of different geometric and operating parameters on the maximum heat transferring capacity of a MEMS heat pipe. Similar analytical equations have been developed by other researchers as well [55, 56]. Though these models were developed for similar MEMS heat pipes, there exists minor variation between each primarily because of the differences in the set of assumptions considered while developing the model. As all models have been satisfactorily validated against experimental data, no one model can claim superiority over the rest. Numerical models have primarily been one dimensional, comprising of the continuity and momentum equations of either just the fluid phase or both phases. Khrustalev and Faghri [53] and Longtin *et al.* [54] developed a one-dimensional model of triangular heat pipes. The model developed by Khrustalev and Faghri [53] was unique in that it accounts for the influence of liquid blocking that occurs in the condenser of MEMS heat pipes as well as the influence of different regions of the interface on evaporation. It has long been observed that the wet point occurs between the beginning and end of the condenser rather than at the end of the condenser. The space between the wet point and the end of the condenser is, in fact, completely filled with liquid coolant; this is a condition referred to as liquid blocking. Suman *et al.* [55, 58, 70, 71] developed several one-dimensional models of MEMS heat pipes similar to that shown in Figure 3.27. Most models developed by Suman *et al.* [55, 58, 70, 71] were considerably simpler in form than those developed by others as only the fluid phase was considered; additionally, these models considered only the axial gradient in pressure, velocity, and radius of curvature and neglected liquid blocking. One of the one-dimensional models developed by Suman and Kumar [55] additionally considers the heat transfer in the substrate.

All numerical models in literature have similar purpose; the models, if implemented, can be used for parametric study of the different geometric and operating parameters. The models developed by Suman *et al.* [55, 58, 70, 71] are easier to implement in comparison with the models developed by other researchers. Most studies have dealt with MEMS heat pipes with triangular profile; however, MEMS heat pipes with star and rhombus profiles have been developed and characterized [72, 73]. The star and rhombus profiles have a greater number of corner regions; these increase pumping pressure and enhance the heat transfer capability. More recently, researchers have introduced arteries in MEMS heat pipes with triangular cross section for enhancing the thermal performance [74, 75]. Arteries are smaller internal flow passages placed parallel to the main flow passage, handling evaporation and condensation, for the purpose of transporting additional coolant to the evaporator from the condenser. The availability of the additional coolant helps enhance the heat transfer capability. An in-depth review of this type of MEMS heat pipes can be found elsewhere [76–78].

Considerable research has also been conducted with regard to the other MEMS heat pipes and spreaders described in this section with efforts primarily focused on modeling. The models associated with the MEMS heat pipes shown in Figure 3.31 were one dimensional and solved using numerical techniques. As this type of MEMS heat pipe resemble axially grooved macroscale heat pipes, the analytical models originally developed for the same have been used with little modification. Most of the numerical models consider both the fluid and vapor phases. Complexity of the models has varied from researcher to researcher. Advanced models have accounted for the effect of condensation on the spacing separating internal flow passages, in addition to that occurring in

the internal flow passage, on the overall performance of the MEMS heat pipes. For this type of MEMS heat pipes, nanofluids have been proposed as coolants as well. This would achieve improvement in thermal performance; however, no experimental work has yet been reported as validation [79]. In recent years, there has been interest in scavenging thermal energy from the vapor phase of the coolant. For purposes of energy scavenging, the MEMS heat pipe shown in Figure 3.32 is better suited over that depicted in Figure 3.27 for the obvious reason that the vapor phase is present above the liquid phase. Richards *et al.* [80] and Weiss *et al.* [81] have successfully coupled a MEMS heat pipe-like structure with piezoelectric membrane for thermal energy scavenging.

3.5 Two-Fluid MEMS Heat Exchanger

Two-fluid MEMS heat exchangers, as the name suggests, handle two fluids that are at different temperatures. The temperature difference between the two fluid leads to heat transfer between the two. The two fluids are not in physical contact, though they are in thermal contact. The fluid that loses heat is referred to as the "hot" fluid. The fluid absorbing the heat is termed the "cold" fluid. These two fluids may be thought of as the heat source and heat sink, respectively. Depending on the application the same fluid can function as the hot and cold fluid. In addition, the fluids can have equal or unequal heat capacity depending on the application. If the fluids have equal heat capacity then the two-fluid MEMS heat exchanger is said to be operating under balanced flow conditions [1]. On the other hand, the microdevice is said to be operating under unbalanced flow conditions if the heat capacity of the fluids are different [1]. As there are two fluids associated with this microdevice, three configurations are possible with regard to relative direction of flow. If the fluids are flowing parallel to one another in the same direction, then the microdevice is referred to as parallel-flow MEMS heat exchanger. On the other hand, the heat exchanger is termed counter-flow MEMS heat exchanger if the fluids are flowing parallel to each other but in opposite directions. In the third configuration, the directions in which the fluids flow are orthogonal and this configuration is termed as cross flow MEMS heat exchanger. Figure 3.34 provides the schematic of the different flow configurations along with typical temperature profiles.

This section discusses only counter and parallel-flow two-fluid MEMS heat exchangers. A set of one hot and one cold fluid microchannels comprises the repeating unit of

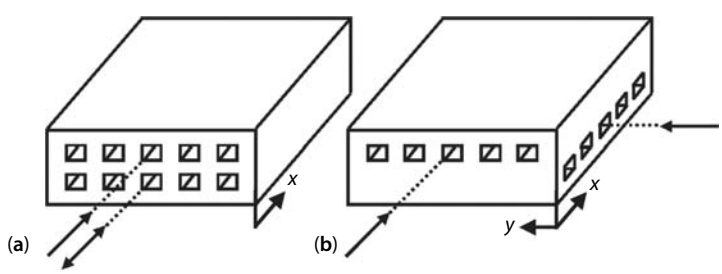

Figure 3.34 (a) Counter/parallel flow ad (b) Cross flow MEMS two-fluid heat exchanger (arrows represent the direction of fluid flow)

counter and parallel-flow two-fluid MEMS heat exchangers. For purposes of design, only the repeating unit needs to be considered for parallel- and counter-flow two-fluid MEMS heat exchanger. Two-fluid MEMS heat exchangers work in a manner very similar to that of MEMS heat sinks. In these devices, the hot fluid is the heat source and cold fluid is the heat sink. Heat from the hot fluid travels through an initial wall–liquid interface via convection and then through the substrate of the MEMS heat exchanger via conduction. Thermal energy is ultimately absorbed by the cold fluid after crossing the second wall–liquid interface via convection. This process occurs continuously over the entire space between the inlet and outlet associated with each of the fluids of the microdevice. Thus, the hot fluid loses thermal energy as it moves from its inlet to outlet, while the cold fluid gains heat as it is transported from its inlet to outlet. Figure 3.35 provides a schematic of the cross section of a repeating unit of two-fluid MEMS heat exchanger. The arrows in grey represent convection, while the arrows in black represent conduction. A typical temperature profile of the counter- and parallel-flow MEMS heat exchanger is provided in Figure 3.36; the arrows represent the direction of flow [36].

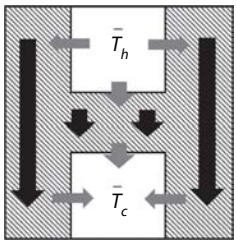

Figure 3.35 Cross-section of two-fluid MEMS heat exchanger

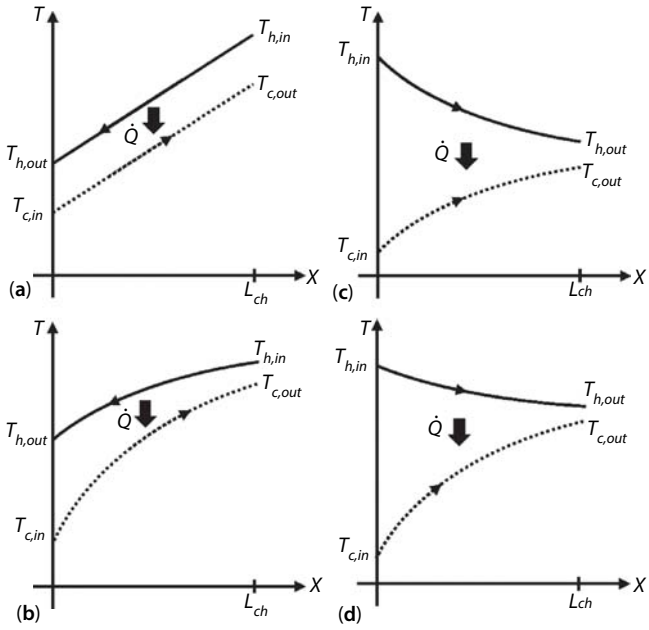

Figure 3.36 Representative temperature profiles of counter flow, (a) and (b), and parallel flow, (c) and (d), two-fluid MEMS heat exchangers

Unlike a MEMS heat sink which functions to cool the hot surface, a two-fluid MEMS heat exchanger can act to either heat the cold fluid or cool the hot fluid. Thus, the inlet and outlet temperatures of one of the fluids are known a priori. The purpose of the design is then to size the two-fluid MEMS heat exchanger that would satisfy the heat transfer requirements set by the fluid that must be processed. The design process is illustrated in the flow chart provided in Figure 3.37. The equations necessary for carrying out the design process is provided in Table 3.12. In textbooks on heat exchanger, this process of sizing heat exchangers is carried out using the concept of *LMTD* as the temperature difference, between the fluids, does not remain constant over the length of the microdevice, Figure 3.36; *LMTD*, Equation (3.30) provides the average temperature difference between the two fluids [21]. The design constraints include the inlet temperatures of the fluids as well as the flow rate and the outlet temperature of the fluid that needs to be processed. In addition, the allowable pressure drop for both the fluids is a constraint. Unlike with a MEMS heat sink, the overall dimensions of the two-fluid

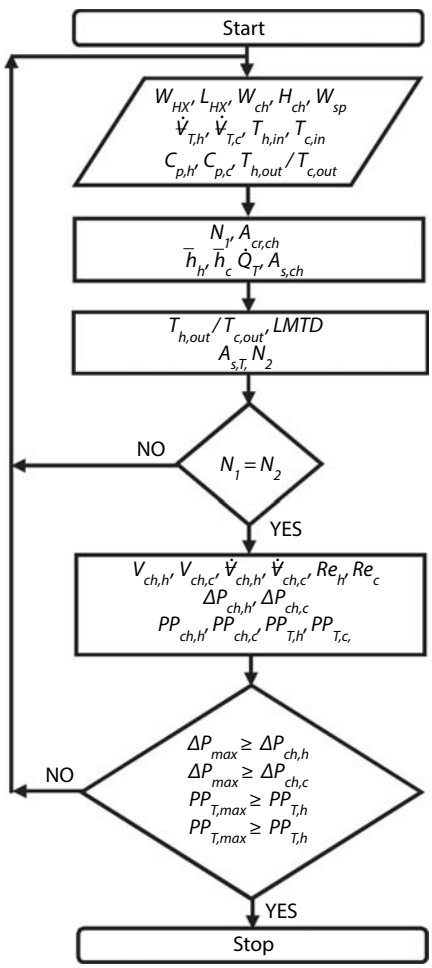

Figure 3.37 Design process of two-fluid MEMS heat exchangers

Table 3.12. Design equations for two-fluid MEMS heat exchanger.

Maximum and minimum heat capacity	$C_{max} = max\{C_h, C_c\}$ $C_{min} = min\{C_h, C_c\}$	(3.100)
Heat capacity ratio	$C_R = \frac{C_{min}}{C_{max}}$	(3.101)
Total heat transfer	$\dot{Q}_T = C_h \Delta T_h = C_c \Delta T_c$	(3.102)
Unknown temperatures	$\overline{T}_{h,out} = T_{h,in} - \frac{\dot{Q}_T}{C_h}$ or $\overline{T}_{c,out} = T_{c,in} + \frac{\dot{Q}_T}{C_h}$	(3.103)
LMTD	Parallel flow $LMTD = \frac{(T_{h,in} - T_{c,in}) - (\overline{T}_{h,out} - \overline{T}_{c,out})}{ln\left(\frac{T_{h,in} - T_{c,in}}{\overline{T}_{h,out} - \overline{T}_{c,out}}\right)}$ Counter flow $C_R < 1$ $LMTD = \frac{(T_{h,in} - \overline{T}_{c,out}) - (\overline{T}_{h,out} - T_{c,in})}{ln\left(\frac{T_{h,in} - \overline{T}_{c,out}}{\overline{T}_{h,out} - T_{c,in}}\right)}$ $C_R = 1$ $LMTD = (T_{h,in} - \overline{T}_{c,out}) = (\overline{T}_{h,out} - T_{c,in})$	(3.104)
Total thermal conductance	$UA_{T,s} = \frac{\dot{Q}_T}{LMTD}$	(3.105)
Heat transfer coefficient of each microchannel	Hot fluid $\overline{h}_h = \frac{Nu k_{f,h}}{D_{hy}}$ Cold fluid $\overline{h}_c = \frac{Nu k_{f,c}}{D_{hy}}$	(3.106)
Overall heat transfer coefficient	$\frac{1}{U} = \frac{t A_{ch,s}}{k A_{ch,cr}} + \left(\frac{1}{\overline{h}}\right)_h + \left(\frac{1}{\overline{h}}\right)_c$	(3.107)

(*Continues*)

Table 3.12. (Cont.)

Total surface area	$A_{T,s} = \dfrac{\dot{Q}_T}{U\,LMTD}$	(3.108)
Total number of microchannels	$N_1 = \dfrac{W_{HX}}{W_{ch} + W_{sp}}$	(3.109)
Total number of microchannels	$N_2 = \dfrac{A_{T,s}}{A_{ch,c}}$	(3.110)
Volumetric flow rate through each microchannel	Hot fluid $\dot{V}_{ch,h} = \dfrac{\dot{V}_{T,h}}{N_2} = \dfrac{\dot{m}_{T,h}}{N_2 \rho_h}$ Cold fluid $\dot{V}_{ch,c} = \dfrac{\dot{V}_{T,c}}{N_2} = \dfrac{\dot{m}_{T,c}}{N_2 \rho_c}$	(3.111)
Average flow velocity through each microchannel	Hot fluid $\overline{V}_h = \dfrac{\dot{V}_{ch,h}}{A_{cr,ch}}$ Cold fluid $\overline{V}_c = \dfrac{\dot{V}_{ch,c}}{A_{cr,ch}}$	(3.112)
Pressure drop through each microchannel	Hot fluid $\Delta P_h = \dfrac{2 f \rho_h \overline{V}_h^2 L_{ch}}{D_{hy}}$ Cold fluid $\Delta P_c = \dfrac{2 f \rho_c \overline{V}_c^2 L_{ch}}{D_{hy}}$	(3.113)
Pumping power associated with each microchannel	Hot fluid $PP_{ch,h} = \Delta P_h \dot{V}_{ch,h}$ Cold fluid $PP_{ch,c} = \Delta P_c \dot{V}_{ch,c}$	(3.114)
Pumping power associated with each fluid	Hot fluid $PP_{T,h} = \Delta P_h \dot{V}_{T,h}$ Cold fluid $PP_{T,c} = \Delta P_c \dot{V}_{T,c}$	(3.115)

MEMS heat exchanger are maintained as a design variable. Additional design variables include the dimensions of the microchannel as well as the flow rate of the fluid with the unknown outlet temperature. The output parameters are the unknown outlet temperature and the number of microchannels. The design approach provided in Figure 3.37 determines the microchannel geometry and operating parameters to match the number of required microchannels given geometric/space constraints with what is needed to satisfy heat transfer requirements. Subsequently, the constraints on pressure drop and pumping power are checked for the design parameters that satisfied the constraint on number of microchannels. These equations are applicable to all microchannels irrespective of the profile.

As with other reviewed MEMS heat exchangers, one-dimensional models are available for two-fluid MEMS devices. One-dimensional models are necessary for determining the temperature of the fluids at any axial location along the length of the two-fluid heat exchanger. The analytical equations associated with two-fluid MEMS heat exchangers cannot provide information about the temperature at axial locations as the heat transfer between the fluids is not known a prior and it varies in the axial direction. This is in contrast to MEMS heat sinks where the heat transfer is a known parameter and remains constant, in the axial direction, thereby enabling analytical equations to predict the temperatures at any axial location between the inlet and outlet. Shah and Sekulić [1] have constructed a one-dimensional model for both counter- and parallel-flow configurations. Shah and Sekulić [1] have generated this model in non-dimensional form which is listed in the following in Equation (3.116) corresponding to the hot fluid while Equation (3.117) is that of the cold fluid. Equation (3.116) is the same for both configurations. Equation (3.117) represents the counter-flow configuration when the parameter j is set equal to +1; when j is set equal to –1, Equation (3.117) represents parallel-flow configuration [1]. The operating parameter of these equations is NTU; it is a function of thermal conductance and minimum heat capacity. The governing equation for the hot fluid can be developed by differentiating the energy equation, i.e. Equation (3.3), with respect to the axial coordinate after expressing change in internal energy as well as the outward heat transfer in terms of fluid temperatures in addition to setting other terms of Equation (3.3) to zero. The governing equation of the cold fluid can be developed from Equation (3.3) in a similar manner. The momentum equations do not provide any additional information in the case of two-fluid MEMS heat exchangers. Application of the momentum equation to each of the fluids will generate an equation for pressure drop which is exactly same as Equation (3.17). The boundary conditions as provided by Shah and Sekulić [1] are also listed in the following; Equations (3.118) and (3.119) are the boundary conditions for counter-flow two-fluid MEMS heat exchangers, while that for parallel-flow two-fluid MEMS heat exchangers are listed in Equations (3.118) and (3.120). The boundary conditions are the inlet temperatures of the fluids. When non-dimensionalized, the inlet temperature of the hot fluid is equivalent to unity while that of the cold fluid is equivalent to zero. It is possible to realize an analytical solution for the one-dimensional model provided in Equations (3.121) and (3.122).

$$\frac{d\theta_h}{d\xi}+NTU\left(\theta_h-\theta_c\right)=0 \tag{3.116}$$

$$\frac{d\theta_c}{d\xi} - jNTU\frac{C_h}{C_c}\left(\theta_h - \theta_c\right) = 0 \tag{3.117}$$

$$\theta_h\left(\xi = 0\right) = 1 \quad \text{for counter/parallel flow} \tag{3.118}$$

$$\theta_c\left(\xi = 1\right) = 0 \quad \text{for counter flow} \tag{3.119}$$

$$\theta_c\left(\xi = 0\right) = 0 \quad \text{for parallel flow} \tag{3.120}$$

$$\left.\begin{aligned} \theta_h &= \frac{1 - \exp\left[-\xi NTU\left(1 - \frac{C_h}{C_c}\right)\right]}{1 - \frac{C_h}{C_c}\exp\left[-NTU\left(1 - \frac{C_h}{C_c}\right)\right]} \\ \theta_c &= \frac{1 - \frac{C_h}{C_c}\exp\left[-\xi NTU\left(1 - \frac{C_h}{C_c}\right)\right]}{1 - \frac{C_h}{C_c}\exp\left[-NTU\left(1 - \frac{C_h}{C_c}\right)\right]} \end{aligned}\right\} \tag{3.121}$$

$$\left.\begin{aligned} \theta_h &= \frac{1 - \exp\left[-\xi NTU\left(1 + \frac{C_h}{C_c}\right)\right]}{1 + \frac{C_h}{C_c}} \\ \theta_c &= \frac{1 + \frac{C_h}{C_c}\exp\left[-\xi NTU\left(1 + \frac{C_h}{C_c}\right)\right]}{1 + \frac{C_h}{C_c}} \end{aligned}\right\} \tag{3.122}$$

Equation (3.121) is applicable for all cases except balanced flow condition. For balanced flow condition, the temperatures of the fluids are given by Equations (3.123) and (3.124) [1]. Equation (3.122) is applicable to both balanced and unbalanced flow conditions.

$$\theta_h = \frac{\xi NTU}{1 + NTU} \tag{3.123}$$

$$\theta_c = \frac{1 + \xi NTU}{1 + NTU} \tag{3.124}$$

3.6 Need for Microscale Internal Flow Passages

Based on the reviewed work of this chapter, there is obviously great interest in MEMS heat exchangers. The devices themselves have taken multiple forms for different applications. There is good reason for this prior and ongoing research interests. Two of the most frequently cited reasons for employing microscale internal flow passages in general are enhanced heat transfer coefficient and increased surface area density [21]. Heat transfer coefficient in internal flow passages is inversely proportional to the thickness of the boundary layer and it in turn is proportional to the size of flow passage [25]. Therefore, with reduction of flow passage the thickness of the associated boundary layer reduces, leading to enhancement in heat transfer coefficient. Under the laminar flow conditions of MEMS heat exchangers, the relationship between heat transfer coefficient and hydraulic diameter of the flow passage is given by Equation (3.28). The enhanced heat transfer coefficient can lead to either increased heat transfer for a specific surface area and log mean temperature difference or reduced log mean temperature difference for a specific heat transfer and surface area. These two scenarios can be observed by rewriting Equation (3.31), after neglecting thermal resistance associated with the wall, as shown in Equations (3.124) and (3.125).

$$\dot{Q}=\left(\frac{Nu\,k_f}{D_{hy}}\right)A\,LMTD \tag{3.124}$$

$$LMTD=\left(\frac{D_{hy}}{Nu\,k_f}\right)\frac{1}{A}\dot{Q} \tag{3.125}$$

Surface area density of an internal flow passage implies surface area per unit volume of the same. Regarding surface area density, it increases with reduction in the size of the flow passages because volume scales at a greater rate than surface area. The relationship between surface area density and the size of the internal flow passages is provided in Equation (3.126).

$$\beta=\frac{S.A}{V}=\frac{\pi D_{hy}L}{\frac{\pi D_{hy}^2 L}{4}}=\frac{4}{D_{hy}} \tag{3.126}$$

Increase in surface area density, by reducing size of a single internal flow passage, will either enhance the heat transfer for a specific log mean temperature difference or reduced log mean temperature difference for a specific heat transfer; these can be clearly inferred from Equations (3.127) and (3.128).

$$\dot{Q}=\overline{h}\left(\beta V\right)LMTD \tag{3.127}$$

$$LMTD = \frac{1}{\bar{h}}\left(\frac{1}{\beta V}\right)\dot{Q} \tag{3.128}$$

The individual influence of enhanced heat transfer coefficient and surface area density, associated with reduction in size of a single internal flow passage, on heat transfer and log mean temperature difference of a single internal flow passage can be assessed as already shown. However, analysis of a single internal flow passage is of limited value as heat exchangers generally consist of multiple passages. Moreover, change in size of the internal flow passages can simultaneously change both heat transfer coefficient and surface area density. The influence of multiple internal flow passages and simultaneous change in heat transfer coefficient and surface area density on heat transfer and log mean temperature difference is analyzed in the following. In order to perform this analysis, consider that a circular internal flow passage is replaced by multiple, smaller circular internal flow passages without change in volume. Based on the fact that the volumes are maintained equal, a relation between diameters can be determined, Equation (3.129). Based on the relation between the overall heat transfer areas, Equation (3.130), it is possible to show that the heat transfers can be related as in Equation (3.131).

$$\frac{D_{hy}}{D_{N,hy}} = \sqrt{N\frac{L_N}{L}} \tag{3.129}$$

$$\frac{A_T}{A_{N,T}} = \frac{1}{N}\frac{L}{L_N}\sqrt{N\frac{L_N}{L}} = \sqrt{\frac{1}{N}\frac{L}{L_N}} \tag{3.130}$$

$$\frac{\dot{Q}_T}{\dot{Q}_{N,T}} = \left(\frac{1}{N}\frac{L}{L_N}\right)\frac{LMTD}{LMTD_N} \tag{3.131}$$

Depending on the engineering application, it might be necessary to keep either the heat transfer constant, i.e., $\dot{Q}_T = \dot{Q}_{N,T}$, or the log-mean-temperature-difference constant, i.e., $LMTD = LMTD_N$. Based on the first scenario, it can be deduced that $LMTD_N$ will reduce below $LMTD$, Equation (3.132), if the length ratio is smaller than the number of channels. For the second scenario, $\dot{Q}_{N,T}$ can be greater than $\dot{Q}_T$, Equation (3.133), if the length ratio is smaller than the number of channels.

$$LMTD_N = \left(\frac{1}{N}\frac{L}{L_N}\right)LMTD \tag{3.132}$$

$$\dot{Q}_{N,T} = \left(N\frac{L_N}{L}\right)\dot{Q}_T \tag{3.133}$$

The importance of employing microchannels in heat exchangers is clearly identifiable from the two equations for meeting the two scenarios described. It is interesting to recognize that MEMS heat exchangers operate via laminar flows due to restricted

channel size. For this reason, heat transfer coefficients are reduced below what would be associated with a turbulent flow exchanger. Because of this, other factors and benefits are driving the development and understanding of this exchanger. These include the shrinking space availability and weight requirements of modern systems.

Nomenclature

A	: area (m^2)
AR	: aspect ratio (Tables 3.3)
C	: heat capacity (J/k)
C_p	: specific heat capacity (J/kg.K)
D_{hy}	: hydraulic diameter (m)
D	: diameter (m)
f	: Fanning friction factor
H	: height (m)
h	: local heat transfer coefficient ($W/m^2.K$)
$\overline{h}$	: axially averaged heat transfer coefficient ($W/m^2.K$)
h_{fg}	: enthalpy of vaporization (J/kg.K)
j	: flow direction indicator
KE	: kinetic energy (J)
K	: permeability
ke	: specific kinetic energy (J/kg)
k	: thermal conductivity (W/m.K)
L	: length of internal flow passage (m)
$LMTD$	: log mean temperature difference (K)
M	: momentum (kg.m/sec)
$\dot{M}$	: momentum transfer rate (N)
Ma	: Mach number
$\dot{m}$	: mass flow rate (kg/sec)
N	: number of internal flow passages
n	: number of sides of a regular polygon
P	: pressure (Pa)
ΔP	: pressure difference (Pa)
PE	: potential energy (J)
PP	: pumping power (W)
Pr	: Prandtl number
p	: perimeter (m)
pe	: specific potential energy (J/kg)
$\dot{Q}$	: heat transfer (W)
$\dot{Q}''$	: heat flux (W/m^2)
r	: radius of curvature (m)
$S.A$	: surface area (m^2)
T	: temperature (K)
$\overline{T}$	: temperature averaged across cross section (K)
U	: internal energy (J)

u	: specific internal energy (J/kg)
V	: average velocity (m/sec)
$\forall$	: volume (m^3)
$\dot{V}$	: volumetric flow rate (m^3/sec)
v	: volume per unit mass (m^3/kg)
W	: width (m)
x	: axial distance variable (m)

Greek Alphabets

α	: angle between adjacent sides of a microchannel (Figure 3.1, Tables 3.3 and 3.11)
β	: surface area density (m^2/m^3)
ρ	: density (kg/m^3)
μ	: viscosity (Pa.sec)
τ	: shear stress (N/m^2)
Δx	: thickness (m)
θ	: non-dimensional temperature
φ	: half-angle between adjacent sides of a regular polygon (Figure 3.31, Tables 3.8, 3.9 and 3.10))
σ	: surface tension (N/m)
γ	: contact angle
ν	: kinematic viscosity (m^2/sec)
ε	: porosity
ξ	: non-dimensional axial length ($=x/L_{ch}$)

Subscripts

ad	: adiabatic region of heat pipe
avg	: average
CV	: control volume
con	: condenser of heat pipe
cr	: cross-section
ext	: external
evp	: evaporator of heat pipe
H	: constant heat flux condition
HS	: heat sink
f	: fluid
fg	: liquid–vapor transition
i	: inlet
l	: liquid
l/v:i	: liquid–vapor interface
l/w:i	: liquid–wall interface
max	: maximum

min	: minimum
N	: identifies all parameters associated with multiple microchannels
out	: outlet
p	: pitch
sat	: saturation
s	: surface
sp	: spacing
T	: total/constant temperature condition
V	: volume
v/w:i	: vapor–wall interface
v	: vapor
w	: wall
x	: coordinate in the axial direction
y	: coordinate in the transverse direction

References

1. R.K. Shah, and D.P. Sekulić, *Fundamentals of Heat Exchanger Design*, Hoboken, New Jersey, USA, John Wiley & Sons, Inc., 2003.
2. Y. çengal, and M. Boles, *Thermodynamics: An Engineering Approach*, New York, USA, McGraw-Hill, 2010.
3. S.S. Mehendale, A.M. Jacobi, and R.K. Shah, *Applied Mechanics Reviews*, Vol. 53, p. 175, 2000.
4. S.G. Kandlikar, and W.J. Grande, *Heat Transfer Engineering*, Vol. 24, p. 3, 2003.
5. P. Fernando, B. Palm, T. Ameel, P. Lundqvist, and E. Granryd, *International Journal of Refrigeration*, Vol. 31, p. 669, 2008.
6. Z. Wu, and B. Sunden, *Renewable and Sustainable Energy Reviews*, Vol. 40, p. 11, 2014
7. D.B. Tuckerman, and R.F.W. Pease, *IEEE Electron Device Letters*, Vol. 2, p. 125, 1981.
8. W.A. Little, *Review of Scientific Instruments*, Vol. 55, p. 661, 1984.
9. E.R. Delsman, M.H.J.M. De Croon, A. Pierik, G.J. Kramer, P.D. Cobden, Ch. Hofmann, V. Cominos, and J.C. Schouten, *Chemical Engineering Science*, Vol. 59, p. 4795, 2004.
10. T.F. Hill, L.F. Velasquez-Garcia, B.A. Wilhite, W.T. Rawlins, S. Lee, S.J. Davis, K.F. Jensen, A.H. Epstein, and C. Livermore *Journal of Microelectromechanical Systems*, Vol. 16, p. 1492, 2007.
11. V. Vijayan, and A.K. Gupta, *Applied Energy*, Vol. 87, p. 2628, 2010.
12. T.A. Wierzbicki, I.C. Lee, and A.K. Gupta, *Applied Energy*, Vol. 118, p. 41, 2014.
13. R.J. Kee, B.B. Almand, J.M. Blasi, B.L. Rosen, M. Hartmann, N.P. Sullivan, H. Zhu, A.R. Manerbino, S. Menzer, W.G. Coors, and J.L. Martin, *Applied Thermal Engineering*, Vol. 31, p. 2004, 2011.
14. B. Alm, U. Imke, R. Knitter, U. Schygulla, and S. Zimmermann, *Chemical Engineering Journal*, Vol. 135, p. S179, 2008.
15. T.-L. Liu, B.-R. Fu, and C. Pan, *International Journal of Heat and Mass Transfer*, Vol. 56, p. 20, 2013.
16. Asetek, www.asetek.com.
17. Microflexis, www.microflexis.com.
18. Mikros Manufacturing, Inc., www.mikros.com.
19. Cutting Edge Optronics, Northrop Grumman, www.northropgrumman.com.

20. Pacific Northwest National Laboratories (PNL), www.pnl.gov.
21. S. Kakac, H. Liu, and A. Pramuanjaroenkij, *Heat Exchangers: Selection, Rating, and Thermal Design*, 3rd Eds., Boca Raton, FL, USA, CRC Press, 2012.
22. M.E. Steinke, and S.G. Kandlikar, *International Journal of Thermal Sciences*, Vol. 45, p. 1073, 2006.
23. P. Rosa, T.G. Karayiannis, and M.W. Collins, *Applied Thermal Engineering*, Vol. 29, p. 3447, 2009.
24. G. Hauke, *An Introduction to Fluid Mechanics and Transport Phenomena*, the Netherlands, Springer, 2008.
25. G. Nellis, and S. Klein, *Heat Transfer*, New York, USA, Cambridge University Press, 2009.
26. A. Bejan, "Forced Convection: Internal Flows" in A. Bejan, and A.D. Kraus, eds. *Heat Transfer Handbook*, John Wiley & Sons, Inc., pp. 395–438, 2003.
27. T. Ahmad, and I. Hassan, *Journal of Fluids Engineering*, Vol. 132, p. 041102-1, 2010.
28. W.M. Rohsenow, J.P. Hartnett, and Y.I. Cho, *Handbook of Heat Transfer,* 3rd Eds., New York, USA, McGraw-Hill, 1998.
29. J.P. McHale, and S.V. Garimella, *International Journal of Heat and Mass Transfer,* Vol. 53, p. 365, 2010.
30. N.S. Lynn, and D.S. Dandy, *Lab on a Chip*, Vol. 9, p. 3422, 2009.
31. F.M. White, *Fluid Mechanics,* 6th Eds., New York, USA, McGraw-Hill, 2007.
32. Y.A. Cengal, and J.M. Cimbala, *Fluid Mechanics: Fundamentals and Applications*, 2nd Eds., New York, USA, McGraw-Hill, 2010.
33. S, Kakac, L.L. Vasiliev, Y. Bayazitoglu, and Y. Yener, *Microscale Heat Transfer: Fundaments and Applications*, the Netherlands, Springer, 2004.
34. Y. Zohar, "Microchannel Heat Sinks" in M. Gad-el-Hak, eds., *The MEMS Handbook*, CRC Press, pp. 12-1–12-29, 2001.
35. M.E. Steinke, and S.G. Kandlikar, *ASME International Conference on Nanochannels, Microchannel and Minichannels*, pp. 667–678, 2005.
36. J.P. Holman, *Heat Transfer,* 10th Eds., New York, USA, McGraw-Hill, 2010.
37. D. Liu, and S.V. Garimella, *International Journal of Numerical Methods in Heat & Fluid Flow*, Vol. 15, p. 7, 2005.
38. R.J. Phillips, *Lincoln Laboratory Journal*, Vol. 1, p. 31, 1988.
39. P-S. Lee, and S.V. Garimella, *International Journal of Heat and Mass Transfer*, Vol. 49, p. 3060, 2006.
40. L. Godson, B. Raja, D.M. Lal, and S. Wongwises, *Renewable and Sustainable Energy Reviews*, Vol. 14, p. 629, 2010.
41. A. Ijam, and R. Saidur, *Applied Thermal Engineering*, Vol. 32, p. 76, 2012.
42. J. Townsend, and R.J. Christianson, *ASME Journal of Thermal Science and Engineering Applications*, Vol. 1, p. 031006-1, 2009.
43. M. Hodes, R. Zhang, L.S. Lam, R. Wilcoxon, and N. Lower, *IEEE Transactions on Components, Packaging and Manufacturing,* Vol. 4, p. 46, 2014.
44. M.E. Steinke, and S.G. Kandlikar, *Heat and Technology*, Vol. 22, p. 3, 2004.
45. G. Xia, L. Chai, H. Wang, M. Zhou, and Z. Cui, *Applied Thermal Engineering*, Vol. 31, p. 1208, 2011.
46. Y. Sui, P.S. Lee, and C.J. Teo, *International Journal of Thermal Sciences,* Vol. 50, p. 2473, 2011.
47. L.J. Missaggia, J.N. Walpole, Z.L. Liau, and R.J. Phillips, *IEEE Journal of Quantum Electronics*, Vol. 25, p. 1988, 1989.
48. J.M. Ochterbeck, "Heat Pipes," in A. Bejan, and A.D. Kraus, eds. *Heat Transfer Handbook*, John Wiley & Sons, Inc., pp. 1181–1230, 2003.

49. H. Ma, "Micro Heat Pipes" in D. Li, eds., *Encyclopedia of Microfluidics and Nanofluidics*, Springer, pp. 1245–1253, 2008.
50. H.S. Lee, *Thermal Design: Heat Sinks, Thermoelectrics, Heat Pipes, Compact Heat Exchangers, and Solar Cells*, Hoboken, New Jersey, John Wiley & Sons, 2010.
51. B.R. Babin, G.P. Peterson, and D. Wu, *Journal of Heat Transfer*, Vol. 112, p. 595, 1990.
52. G.P. Peterson, and C.B. Sobhan, "Micro Heat Pipes and Micro Heat Spreaders" in M. Gad-el-Hak, eds., *The MEMS Handbook*, CRC Press, pp. 11-1–11-37, 2001.
53. D. Khrustalev, and A. Faghri, *ASME Journal of Heat Transfer*, Vol. 116, p. 189, 1994.
54. J.P. Longtin, B. Badran, and F.M. Gerner, *ASME Journal of Heat Transfer*, Vol. 116, p. 709, 1994.
55. J.M. Ha, and G.P. Peterson, *Journal of Heat Transfer*, Vol. 120, p. 1064, 1998.
56. B. Suman, and P. Kumar, *International Journal of Heat and Mass Transfer*, Vol. 48, p. 4498, 2005.
57. Shukla, *Journal of Electronic Packaging*, Vol. 131, p. 024502-1, 2009.
58. B. Suman, S. De, and S. DasGupta, *International Journal of Heat and Fluid Flow*, Vol. 26, p. 495, 2005.
59. D. Khrustalev, and A. Faghri, *ASME Journal of Heat Transfer*, Vol. 117, p. 1048, 1995.
60. D. Khrustalev, and A. Faghri, *ASME Journal of Heat Transfer*, Vol. 118, p. 261, 1996.
61. R. Hopkins, A. Faghri, and D. Khrustalev, *ASME Journal of Heat Transfer*, Vol. 121, p. 102, 1999.
62. K.U. Do, S.J. Kim, and S.V. Garimella, *International Journal of Heat and Mass Transfer*, Vol. 51, p. 4637, 2008.
63. F. Lefèvre, R. Rullière, G. Pandraud, and M. Lallemand, *International Journal of Heat and Mass Transfer,* Vol. 51, p. 4083, 2008.
64. Y. Cao, M. Gao, J.E. Bean, and B. Donovan, *AIAA Journal of Thermophysics and Heat Transfer*, Vol. 11, p. 158, 1997.
65. M.C. Zaghdoudi, C. Tantolin, and C. Godet, *AIAA Journal of Thermophysics and Heat Transfer*, Vol. 18, p. 430, 2004.
66. P.Z. Shi, K.M. Chua, S.C.K. Wong, Y.M. Tan, International MEMS Conference 2006, *Journal of Physics: Conference Series*, Vol. 34, p. 142, 2006.
67. J-S. Suh, R. Grief, and C.P. Grigoropoulous, *International Journal of Heat and Mass Transfer*, Vol. 44, p. 3103, 2001.
68. R. Rullière, F. Lefèvre, and M. Lallemand, *International Journal of Heat and Mass Transfer*, Vol. 50, p. 1255, 2007.
69. T.P. Cotter, *5th International Heat Pipe Conference,* p. 328,Tsukuba, Ibaraki, Japan, 14–18 May 1984.
70. B. Suman, and N. Hoda, *International Journal of Heat and Mass Transfer*, Vol. 48, p. 2090, 2005.
71. B. Suman, *International Journal of Heat and Mass Transfer*, Vol. 49, p. 3957, 2006.
72. S-W. Kang, and D. Huang, *Journal of Micromechanics and Microengineering*, Vol. 12, p. 525, 2002.
73. Y.M. Hung, and Q. Seng, *International Journal of Heat and Mass Transfer*, Vol. 54, p. 1198, 2011.
74. S. Launay, V. Sartre, and M. Lallemand, *Applied Thermal Engineering*, Vol. 24, p. 233, 2004.
75. W. Liu, J. Kang, X. Fu, C. Stefanini, and P. Dario, *Microelectronic Engineering*, Vol. 88, p. 2255, 2011.
76. A. Faghri, *Annual Review of Heat Transfer*, Vol. 12, p. 1, 2002.
77. C.B. Shoban, R.L. Rag, and G.P. Peterson, *International Journal of Energy Research*, Vol. 31, p. 664, 2007.

78. B. Suman, *Advances in Heat Transfer*, Vol. 41, p. 1, 2009.
79. K.H. Do, and S.P. Jang, *International Journal of Heat and Mass Transfer*, Vol. 53, p. 2183, 2010.
80. S. Whalen, M. Thompson, D. Bahr, C. Richards, and R. Richards, *Sensors and Actuators A: Physical*, Vol. 104, p. 290, 2003.
81. L. Weiss, C.D. Richards, and R.F. Richards, *Journal of Microelectromechanical Systems,* Vol. 20, p. 1287, 2011.

4

Application of Porous Silicon in MEMS and Sensors Technology

L. Sujatha[1], Chirasree Roy Chaudhuri[2] and Enakshi Bhattacharya[3*]

[1]*Department of Electronics and Communication Engineering, Rajalakshmi Engineering College, Thandalam, Chennai, Tamil Nadu*
[2]*Department of Electronics and Telecommunication Engineering, Indian Institute of Engineering Science and Technology, Shibpur, Howrah*
[3]*Department of Electrical Engineering, IIT Madras, Chennai, India*

Abstract
Porous silicon (PS), which is derived from silicon, is a viable material option for microelectro mechanical systems (MEMS) and sensors due to its unique properties. The pore size, from nano- to micrometers, can be controlled by varying the formation conditions and decide the mechanical properties and the increased functionality of PS. In this chapter, we discuss the applications of PS in MEMS and sensors. We begin with a discussion on PS formation by electrochemical etching of silicon and the control over the porosity and pore size. Applications of PS for various biosensors, in which the large surface-to-volume ratio of PS helps in improving the sensor performance, are discussed. Silicon/PS composite cantilevers show higher sensitivity as biosensors due both to changes in mechanical properties of the cantilever beam as well as enhanced reaction rate due to larger surface area. The low Young's modulus of PS has also been utilized to improve the sensitivity of MEMS pressure sensors with silicon/PS composite membranes. Experimental results as well as models to understand them have been discussed touching upon the instability of PS and reliability issues with techniques to reduce them.

Keyword: Porous silicon, porosity, pressure sensor, biosensors, cantilevers

4.1 Introduction

The material porous silicon (PS) is generally formed by the electrochemical etching of silicon in hydrofluoric (HF) acid-based electrolytes. It consists of silicon filaments and voids with an appearance of spongy structure. PS is not a new material. It was discovered in 1956 by Ulhir at Bell Labs, USA while he was working on electropolishing of silicon wafers with HF [1–3]. Though PS can be formed easily at room temperature, due to its fragile and highly reactive nature, not much research work was carried out for

**Corresponding author*: enakshi@ee.iitm.ac.in

Atul Tiwari and Baldev Raj (eds.), Materials and Failures in MEMS and NEMS, (121–172)
© 2015 Scrivener Publishing LLC

many years. In 1981, Imai has reported a new method of dielectric isolation for silicon on insulator (SOI) structures called full isolation by porous oxidized silicon (FIPOS) technology [4–5]. In 1990, a strong and visible photoluminescence (PL) was discovered from electrochemically etched silicon at room temperature [6,7]. This is followed by reports on electroluminescence (EL) from PS [8–11]. These observations are extremely important in silicon material research and show that PS can have optoelectronics applications like III–V semiconductor systems [12]. For the past two decades, lot of research work has been carried out on PS resulting in various techniques in formation process, oxidation, proper drying mechanisms, etc. to improve the mechanical strength of PS [12–14]. The unique morphology of PS has become very attractive in the field of surface sciences. It has been extensively used in the fabrication of chemical sensors due to its good adhesion and high reaction rate [15]. Due to the large surface-to-volume ratio, PS finds lot of application in biosensors [16–18]. Lehmann [3] reported the formation of regular PS arrays for biochips. Also, being a derivative of silicon, PS is highly compatible with silicon IC technology. Due to its many unique features, PS has become an interesting material in the field of optics [19,20], surface science [21–23] and also in microelectro mechanical systems (MEMS) [24–28]. The basic concepts of the nanocrystalline silicon as compared to crystalline silicon for recent applications in different areas of science and technology have been highlighted [29].

4.1.1 Properties of Porous Silicon for MEMS Applications

The possibility of tailoring the porous structure of PS, as required, leads to many new applications. In recent years, PS has been recognized as an interesting material in different MEMS applications where it has been used as sacrificial layer, structural layer or functional layer [30,31]. New applications where PS is used as the active part of a device are possible by an improved understanding of pore initiation and formation process, which enables us to tailor the porous structure according to its application.

For MEMS, the most important properties of PS are: Low thermal conductivity (down to 1 W/mK), drastic reduction in Young's modulus from 83 GPa at 20% porosity to 0.87 GPa at 90% porosity (for crystalline silicon, this ranges from 160 to 190 GPa), large surface-to-volume ratio, selective formation of PS, high piezoresistive co-efficient, highly reactive nature to form thick oxides and easy dissolution in 1% KOH.

4.1.2 Review of PS for MEMS Applications

PS can be used as a multifunctional material for different applications in the field of MEMS [32]. Highly reactive nature and compatibility with IC technology make PS an important and versatile material in the field of MEMS. PS can be oxidized very fast at low temperatures due to the porous structure. This feature had been used [33] to realize SOI structures called FIPOS technology in applications to LSIs. ELTRAN (epitaxial layer transfer) wafers are the first commercially available SOI wafers in which the splitting within the PS layer by water jet allows the seed wafer to be reused several times and hence reduces the manufacturing cost [34]. Electrochemical etching can have large aspect ratio and deep trenches with the depth of 42 μm and diameter of 0.6 μm have

been reported [35,36]. The surface-to-volume ratio of PS is very high, of the order of 1000, 100 and 1 $m^2\,cm^{-3}$ for micro PS, Meso PS and macro PS, respectively [37,38]. Based on this, a novel capacitor concept due to the large electrode surface and superior dielectric property of PS were reported [38]. A high-temperature micro hot plate with minimum power consumption for the purpose of integrated gas sensors was realized using the features of selective formation and low thermal conductivity of PS [39]. High adsorption property of PS has been used to fabricate a capacitive PS humidity sensor with PS as functional layer [40]. Fabrication of freestanding mobile 3D PS microstructures was reported by Lammel and Renaud [41]. PS has been usually used as the sacrificial layer in most of the MEMS applications due to its high reaction rate with chemicals. The use of PS in micromachining technologies as a sacrificial material with the advantages of formation of thick and thin sacrificial layers, selective sacrificial etching for applications such as cantilevers, vertical, and horizontal accelerometers and other types of microsensors have been reported [42]. The fabrication of membranes and cantilevers with c-Si structures using PS as sacrificial layer have been reported [43]. PS and its combination with a variety of filling materials (metals and ferromagnetic metals) lead to nanocomposites with specific physical properties caused by the nanometric size and its potential applications in spintronics, magnetic, and magneto-optic devices, nutritional food additives have been reviewed [44].

4.1.3 Formation of PS

PS has unique morphological features with wide variation and the formation of PS is a very complex function of numerous factors. Better understanding of formation of PS is necessary before using PS for any new application. Some of the common facts about formation theory and most accepted formation mechanisms of various types of PS are discussed in this section.

4.1.3.1 Porous Silicon Formation Setup

A simple apparatus can be used to form PS by electrochemical etching. The anode is the silicon sample itself. The cathode is an HF resistant and conducting material – usually platinum. The cell body is usually made of Teflon which is a highly acid-resistant polymer. The Teflon cell is filled with the required electrolyte (aqueous or organic). A clean silicon surface is hydrophobic in nature. Hence, electrolyte dilution in this way increases the wettability of silicon surface and it also removes the bubbles formed during etching. The process is controlled by controlling the anodic current or potential. PS is formed on the wafer exposed to HF. Figure 4.1 shows the setup used for PS formation on p-type silicon substrate [45]. Aluminum metallization is done at the back of the silicon wafer to get ohmic contact. The silicon sample is placed on a stainless steel base and sealed through an O-ring. In this setup, only the front side of the silicon sample is exposed to the electrolyte. Constant current is passed during the electrochemical etching to have better control over pore formation and to get better reproducibility. The surface area to be etched is 1.2 cm^2 decided by the inner diameter of the O-ring, which is 1.23 cm. The sample size that can be loaded into the cell is 2 cm × 2 cm.

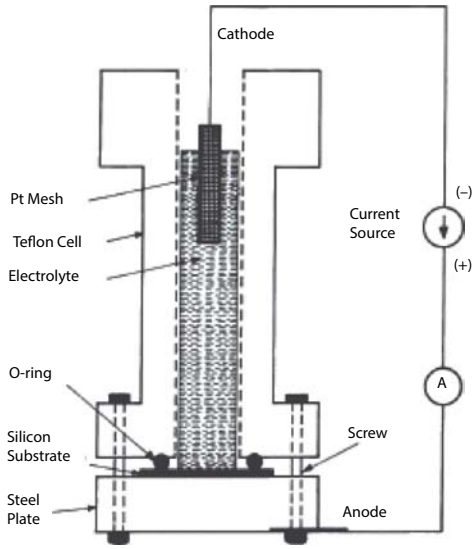

Figure 4.1 Set-up for electrochemical etching of p-type silicon.

4.1.3.2 Formation Parameters

The formation parameters that can be varied during the electrochemical etching are HF concentration, substrate type and level of doping, anodization time, current density, illumination state in the case of n-type substrate, temperature, and orientation of the wafer. The pore geometry and morphology of PS can be varied by controlling the above formation parameters. These formation parameters also control the porosity and the thickness of the PS layer.

4.1.3.3 PS Formation Chemistry

In order to understand the formation of PS, it is necessary to look at the silicon dissolution chemistry that takes place during the electrochemical etching. Though the exact silicon dissolution chemistry is in dispute, it is generally accepted that holes are required for silicon dissolution [46]. The electrochemistry was well explained by Smith and Collins (1992) [47]. Figure 4.2 shows the sequence of reaction steps involving electron and hole exchanges and the hydride and fluoride coverage taking place at the surface during silicon electrode dissolution in HF acid. The dissolution reaction begins at the defects of silicon surface. The silicon surface saturated by hydrogen is in inert state as long as no holes (h^+) are present. If a hole reaches the surface, a fluoride ion attacks a Si-H bond and the Si-H bond is replaced by a Si-F bond. Due to the polarizing influence of the bonded F, another F^- ion can attack another Si-H bond and form Si-F bond with the generation of a H_2 molecule and injection of one electron into the substrate. The inner Si-Si bonds are weakened and these are attacked by HF, H or O. The resultant product is H_2SiF_6 which decomposes into SiF_6 and hydrogen and these byproducts can dissolve in the electrolyte. When a silicon atom is removed by this reaction, an atomic size dip is formed. This changes the electric field distribution in such a way that the holes are preferentially collected at the pore tips and dissolution further takes place at the pore tips.

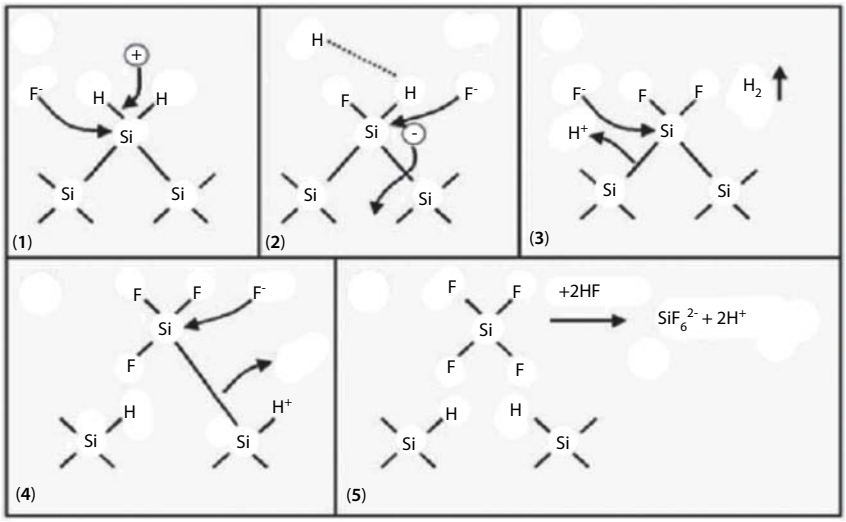

Figure 4.2 Electro-chemical reaction during PS formation (1–5) shows the sequence of reactions [12].

The chemical reactions for silicon dissolution are given by Equations (4.1) and (4.2) [12]. During pore formation,

$$Si + 6HF \rightarrow H_2SiF_6 + H_2 + 2H^+ + 2e^- \tag{4.1}$$

During electropolishing,

$$Si + 6HF \rightarrow H_2SiF_6 + H_2 + 4H^+ + 4e^- \tag{4.2}$$

The difference in chemical reactions during pore formation and electropolishing is the number of electrons required to remove one silicon atom which is two and four respectively.

The conditions for pore formation are: (i) The pore tips must be active in dissolution reaction and the pore walls must be passivated from dissolution and (ii) The current density should be less than the critical current density (J_{PS}). Different types of pore formation mechanisms and models explaining the passivation of pore walls against dissolution on p, n, p^+ and n^+ substrates have been reported by many authors [7,48–50].

4.1.3.4 Measurement of Porosity and Thickness of PS Layer

Porosity is defined as the fraction of void within the PS layer and can be easily determined by gravimetric method [12]. The wafer is weighed before anodization (m_1), just after anodization (m_2) and after a rapid dissolution of the whole porous layer in a 3% KOH solution (m_3). The porosity (P) is given by the following equation:

$$P(\%) = \frac{(m_1 - m_2)}{(m_1 - m_3)} \times 100 \tag{4.3}$$

PS layer thickness (d) can be defined by the equation:

$$d = \frac{(m_1 - m_3)}{S_a \rho_d} \tag{4.4}$$

where ρ_d is the silicon density and S_a is the area of etched surface.

4.1.3.5 I–V Characteristics

Current–voltage (I–V) relationship is one of the best techniques to understand the PS formation. Figure 4.3 shows the typical I–V characteristics obtained on p and n-type silicon substrates during electrochemical etching reported [47]. The current-voltage curves show similarities to Schottky diode characteristics in both the anodic and cathodic regions by the silicon-electrolyte interface behavior. But the reverse current in dark is three times higher than the reverse current in Schottky diodes. In electrochemical etching, though the majority carriers are different in p and n type silicon, the chemical reactions remain same at the interface. Under cathodic potentials, both p and n type silicon wafers are stable and no dissolution takes place. Silicon dissolution takes place only under anodic potentials. At higher anodic potentials, electropolishing takes place. Pore formation takes place only at low anodic potentials. The current density corresponding to the first peak is known as critical current density (J_{PS}). The region to the left of the first peak (shaded by crossed lines) is the pore formation region and the region to the right of the first peak is the electro-polishing region. In the region beyond the second peak of the curve, the current oscillates and anodic oxidation takes place [12].

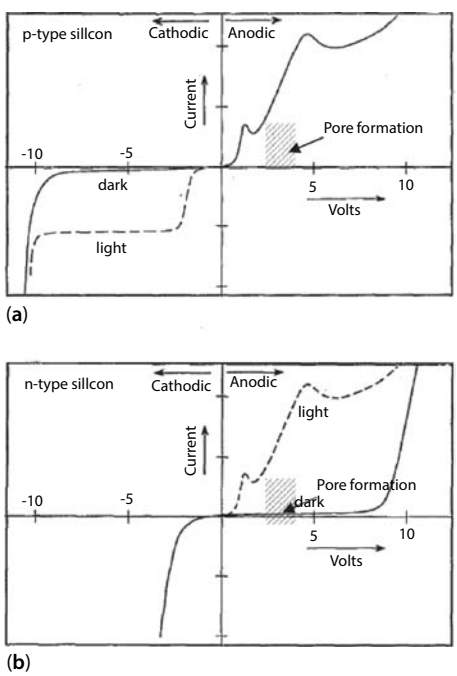

Figure 4.3 Current–voltage (I–V) characteristics: (a) on p-type silicon and (b) on n-type silicon [47].

The I–V characteristics in the PS formation region for four different silicon samples p, p^+, n and n^+ anodized under similar conditions are shown in Figure 4.4. The I–V curves for each sample type are displaced to the right in the general order $n^+ < p^+ < p < n$. It is understood that the PS formation depends on the type of doping and also the level of doping. During PS formation, the etching behavior is doping-sensitive and there is good selectivity between n-type and p-type silicon and between low-doped p-type (p^-) and degenerately doped p-type (p^+) silicon. With this preferential etching property, silicon microstructures such as membranes, beams and cantilevers have been realized [51]. This room temperature etching process is IC-compatible. Also, this is better than KOH etching of silicon which requires additional clean-up process for the wafers.

4.1.4 Classification of PS

Based on the geometry of pores, PS is classified into three types according to IUPAC standards as follows (Foll *et al.* 2002) [26]: (i) micro PS – average pore diameter less than 10 nm, (ii) Meso PS – average pore diameter between 10 nm and 50 nm (iii) macro PS – average pore diameter more than 50 nm

4.1.4.1 Micro PS

The PS formation setup is as shown in Figure 4.1. When the silicon wafer is p-type, holes are the majority carriers which are involved in the etching of silicon. Etching goes on till the structures reach the smaller size of around 2 or 3 nm. The mechanism of passivation of pore walls is by quantum confinement. The charge carriers are confined in the thin silicon quantum wires which increase the band gap and hence the holes can no longer enter into the pore walls. The resultant pore structure is known as micro PS. The increase in energy band gap feature is highly advantageous to use micro PS for optical applications.

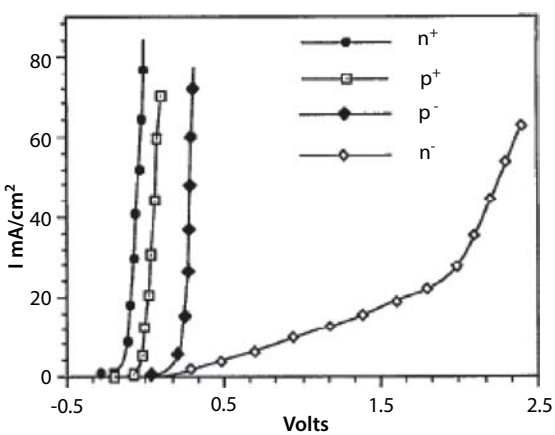

Figure 4.4 Current–voltage plot for n^-, p^-, n^+, and p^+ samples. All samples were anodized in 49% HF in the absence of illumination. Dopant concentrations were chosen so as to show all data clearly on same graph [47].

Micro PS with average pore diameters of few nm can be easily formed on moderately doped p-type substrate (10^{15}-10^{18} cm^{-3}) with aqueous electrolyte in the dark. As the doping concentration increases the pore diameters and interpore spacings increase resulting in meso PS with side branches. P-type substrate with doping concentration of 10^{16} - 10^{17} cm^{-3} is best suited for formation of purely micro PS layers.

4.1.4.2 Macro PS

The n-macro PS was first reported by Lehmann and Foll (1990) [36]. Holes are minority carriers in n-type semiconductors, and that passivates them against dissolution in HF acid under anodic bias. At room temperature, the number of thermally generated holes is very small, but hole generation can be enhanced if the n-type electrode is illuminated. Holes generated by this mechanism are collected by the pore tips and they promote dissolution there. Perfect pores with large aspect ratios can be obtained in this method. It gives smooth pore walls, smooth cross sections, and constant diameter throughout the depth. Lehmann has explained the pore formation in n-type substrate with back illumination [52]. Recently reports were made on formation of macro PS on p-type substrate using organic electrolyte [53–56].

4.1.4.2.1 Formation of Macro PS on n-Type Substrate

The most common method of forming macro PS is using n-type substrate with aqueous electrolyte [49,52]. The pore diameters in n-type silicon are considerably larger than p-type silicon and form straight channels at low dopant concentrations rather than the randomly directed pores of p-type silicon. The etching technique allows producing pores with aspect ratios of up to 250 and a constant pore density. This helps in fabrication of three-dimensional microstructures with trenches [57]. Since in n-type silicon the majority carriers are the electrons, the holes required for electrochemical reaction are supplied by the photogeneration. The backside of the sample is illuminated by light from a halogen lamp as shown in Figure 4.5. The holes

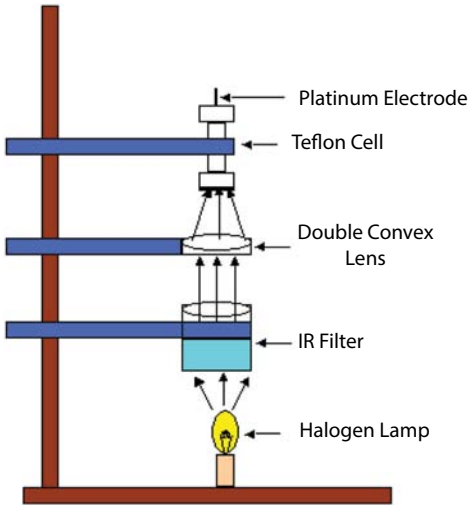

Figure 4.5 Setup for electrochemical etching of n-type silicon.

generated by the photocurrent diffuse from the bottom of the substrate to the surface and actively participate in the chemical reaction. By varying the intensity of the light the anodization current can be varied. The PS formation mechanism and the effect of formation parameters on the resultant pore diameter and pore wall thickness have been derived [52].

The setup for PS formation on n-type substrate requires an electrochemical cell similar to the p-type but it also requires illumination from the back, which is provided by a 120 V, 300 W Halogen lamp as shown in Figure 4.5. To make an n^+ ohmic contact to the n-type silicon, phosphorous diffusion has been carried out at the back of the wafer after protecting the top surface with an oxide. Aluminum metal contacts have been made only at the edges so as the light does not get blocked. To allow the light to pass, the stainless steel base has a hole at the center. A double convex lens with a focal length of 5 cm is used to focus the light on the back of the wafer. The photocurrent is varied by varying the illumination level by an autotransformer. Copper Sulfate solution is used to filter the IR to prevent the heating of the sample. A fan is also used to remove the heat on the sample and hence to avoid the thermal generation of carriers.

4.1.4.2.2 Formation of Macro PS on p-Type Substrate

Advantages when compared to n-macro PS are the simpler cell design (no back side illumination is necessary) and no need for additional process steps required for back metal contact. A perfect macro PS on p-type substrate can be obtained with organic electrolytes. Major organic compounds used so far are acetonitrile (MeCN), dimethylformamide (DMF), formamide (FA), dimethylsulfoxide (DMSO), hexamethylphosphoric triamide (HMPA), and dimethylacetamide (DMA) [26]. The formation of macro PS with average pore diameter of around 1 μm on p-type substrate with resistivity of 1–10 ohm-cm using an organic electrolyte containing DMF and HF has been reported [55]. We have followed this procedure in our experiments for formation macro PS. Uniform pores equivalent to that of n-macro PS have been obtained on p-type substrates with organic electrolyte (HF + DMF) and this avoids the complication in the setup due to back illumination and the additional process steps necessary to get ohmic contact. Figure 4.6 shows the SEM images of (a) micro PS (p-substrate), (b) macro PS (n-substrate), and (c) macro PS (p-substrate) [58,59].

4.1.4.3 Meso PS

Meso PS is formed on heavily doped substrates with aqueous electrolytes by increasing the potential to values more than the breakdown potential. In highly doped substrates (both p- and n-type), the width of the depletion region (DR) at the silicon - electrolyte interface is very thin and hence the charge transfer is dominated by tunneling of the carriers. The pore size reflects the width of the DR, being typically around 10 nm. The width of the pore wall (d) is less than twice the width of DRs formed by the silicon electrolyte interface and hence they are depleted due to the overlapping of the DRs. The resulting pore morphology has the branches on the pores and the shape of the pore is like a star. In many cases, meso PS structures are preferred because they have better mechanical stability in comparison to micro PS [26].

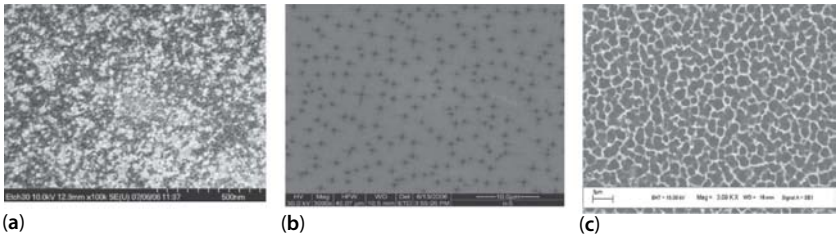

Figure 4.6 SEM pictures of (a) micro PS formed on p-substrate, (b) macro PS formed on n-substrate and (c) macro PS formed on p-substrate. HF conc. = 33%; anodization time = 10 min; current density = 10 mA/cm^2.

4.1.5 Effect of Formation Parameters on Porosity and Thickness

Porosity and thickness for varying formation parameters such as HF concentration, anodization time, and current density have been measured by gravimetric method. The variation in porosity and thickness depends on the chemical dissolution during PS formation. Both porosity and thickness increase linearly with increase in anodization time for a constant current density because of the dissolution that takes place for a longer time. Increasing HF concentration reduces the thickness of the space-charge layer and increases the pore tip current density, which results in smaller pores and thicker wall. Hence, porosity decreases with increase in HF concentration [60,61]. Increase in current density increases the rate of PS formation and hence porosity increases [3,62]. The effects of formation parameters on porosity and thickness have been well investigated and reported [12,61–63]. The mechanism and the effect of formation parameters of PS layer growth during electrochemical etching on n-silicon with aqueous electrolyte were investigated and reported [3,64,65].

4.1.6 PS Drying Mechanisms

PS films can be dried by allowing the electrolyte in the pores to evaporate at atmospheric pressure and temperature. But, when wet porous material is allowed to dry by evaporation, the liquid vapor interfaces formed inside the pores can generate enormous capillary tensions. If the material skeleton is not strong enough, these forces can induce cracking and disintegration. Hence, drying of PS layers, especially those of high porosities, is a crucial step. The magnitude and effects of capillary forces can be significantly reduced by rinsing PS layers in drying liquids of lower surface tension. Pentane has a very low surface tension and shows no chemical interaction with PS. Using pentane as the drying liquid enables us to reduce the capillary tension, but since water and pentane are non-miscible liquids, ethanol or methanol have to be used as intermediate liquids [12].

4.1.7 Effect of PS Formation on Stiction in MEMS

Stiction, or adhesion of components to one another, is a major failure mechanism in surface micromachined MEMS. Surface micromachined structures, mostly with

polysilicon as the structural layer, are particularly susceptible to autoadhesion or "stiction" – a word coined from static friction – because the structural members are in close proximity to each other; are highly compliant due to their extreme length-to-thickness aspect ratio, and have large surface-to-volume ratios which increase the relative importance of adhesive surface forces. A possible method to prevent stiction is to modify the contacting surfaces by reducing the real contact area (RCA). This can be achieved by either providing bumps [66] or by making the surface rough by selective etching. The RCA can be reduced by intentional roughening like texturing [67] of the contacting surfaces so that actual contact occurs at the asperities of the textured surface. Since electrochemical etching on released surface micromachined structures may be difficult, Bhattacharya *et al.* [68] have shown that formation of PS by stain etching on the surface of the polysilicon structural layer reduces the stiction force in surface micromachined structures.

4.2 Porous Silicon in Biosensors

PS has been identified as a promising platform for biosensing applications for its surface roughness and microstructure leading to higher capture of biomaterials [69–71]. Nanoporous silicon is formed by anodic etching of p-type or n-type silicon in HF acid and ethanol solution as an electrolyte [72,73]. On the other hand, macroporous silicon is fabricated by using mostly organic solvents, usually mixed with HF [74–78]. Both nanoporous silicon and macroporous silicon have been reported to possess greater sensitivity as biosensors than planar silicon owing to their large surface area of adsorption [79–82]. A proper pore size distribution helps to achieve an efficient biosensor by immobilization of biomolecules depending upon their molecular size. PS, with pore diameter of the order of a few nm, is suitable only for very small biomolecules while PS with pore diameter of the order of a few μm may accommodate larger molecules [83]. PS has been reported to detect a wide variety of biomolecules like food toxins, virus, DNA, proteins, bacteria, and others and also analytes like urea, triglycerides, glucose, and others both by optical and electrochemical methods. In this section, we will highlight primarily the various electrochemical techniques reported using PS.

4.2.1 PS Cantilever-Based Resonant Frequency Detection

Microcantilevers are sensitive biosensors mainly due to their ability to transduce a variety of chemical and physical phenomena into mechanical movements on a micrometer scale [84–89]. These cantilevers have been used as transducers for detecting cells, proteins, heavy metals, and other chemical and biological species with high selectivity and sensitivity [84–90]. Capabilities of current microfabrication technology allow the development of arrays of cantilevers making it possible for simultaneous detection of multiple species. The miniaturization of cantilevers, however, leads to the decrease of the sensing area. One method to increase the sensing area could be to form a porous layer on the surface of the cantilevers. PS is a unique material for immobilization of biomolecules due to a huge fractal surface area within a small volume [91–95].

4.2.1.1 Antibody–Antigen Binding Detection

Stolyrova *et al.* [96] reported the use of PS by the stain etching process using vapor-phase technique on c-Si cantilevers [97–99]. They have employed commercial cantilever arrays from Protiveris Ltd. [100] since these cantilevers were tailored to an elaborate measurement system for monitoring natural frequencies and quality factors. The Protiveris cantilevers were made from SOI wafers with approximately 1 μm thick p-type (1 0 0) device layer and cantilever size of 150 μm × 500 μm. The Protiveris cantilevers were coated by around 30 nm gold layer to enhance the reflectivity required for measuring the natural frequency. The schematic is shown in Figure 4.7. The cantilever surface was exposed to vapors generated by the dissolution reaction of a sacrificial piece of silicon in HF (49%)/HNO_3 (65%) mixture with volume ratio 4:1 with addition of small amount of acetic acid as a surfactant. The vapors produced a PS layer of 50–100 nm in 10–20 s. Figure 4.8 shows the general view of the micro cantilever array before and after the formation of the PS layer and Figure 4.9 shows the detailed morphology of the porous layer. It is observed from Figure 4.9 that, in contrast to traditional PS obtained by electrochemical etching, the morphology of vapor-phase etched silicon exhibits a dual macro and nano superposed structure of the porous layer similar to the report in Ref. [101].

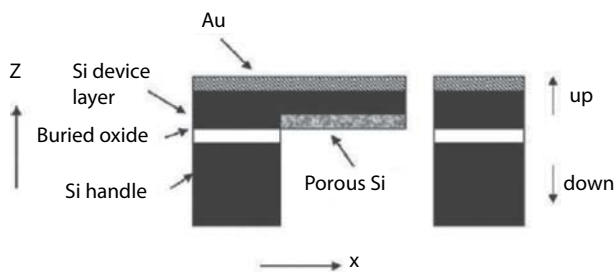

Figure 4.7 Schematic view of the cross section (not in scale) of unbent composite porous silicon–silicon cantilever. The BOX (buried oxide) is 1 μm; the handle wafer is 300 μm. The silicon device layer is 1.5 μm. The porous silicon layer is about 100 nm. The Au layer (optional) is 30 nm.

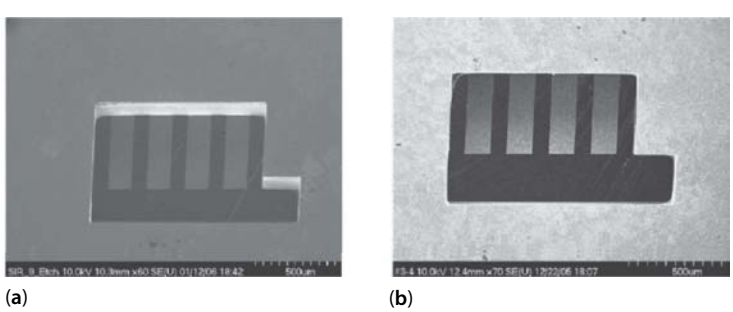

Figure 4.8 SEM overall view of an array of SOI cantilevers, each cantilever 150 μm × 500 μm, before and after the formation of the porous silicon layer. (a) The c-Si cantilevers with smooth surfaces and (b) the composite porous silicon–silicon cantilever with the structured surface layer of the porous silicon. The inner surface of cantilevers is shown through the DRIE openings made in SOI wafer handle (termed the down side as shown in Figure 4.7).

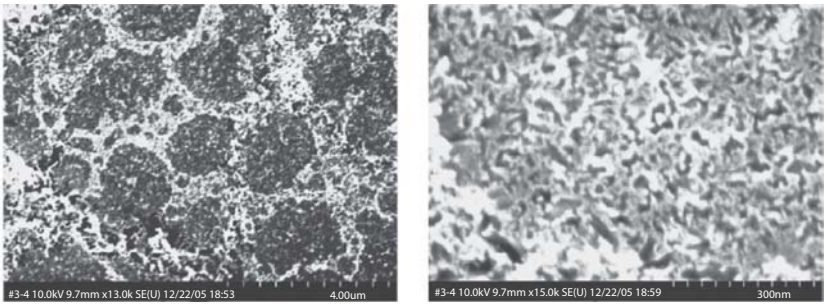

(a) (b)

Figure 4.9 SEM images of the detailed morphology of the achieved porous silicon surface layer, imaged at the same spot with increasing magnification; (a) magnification 13,000. The macrostructure formed by the drop condensation of the reactive vapor is clearly seen; (b) magnification 150,000. The detailed nanostructure of the porous silicon is shown.

The natural frequency of the commercial cantilevers is of the order of 5000 Hz and the quality factor is of the order of 100 under ambient pressure conditions. The natural frequency is reduced by around 40–200 Hz while the quality factor either increases or decreases by approximately 20% after the formation of the PS layer. The observed reduction in the natural frequency corresponds to a slight increase of the overall mass due to the presence of the oxidized PS surface. Due to the small thickness of the PS (50–100 nm), it is assumed that the effective spring constant of the cantilever is the same before and after the formation of the PS. The PS surface is next immobilized using APTES-glutaraldehyde protocol shown in Figure 4.10. The specificity and activity of the antibody immobilized on PS was tested using the Pharos FX scanner, BioRad and the results confirmed the successful immobilization. The immune recognition reaction was carried out by incubating the mAb-modified cantilevers with antigen – the HSA-FITC conjugate (albumin labeled with fluorescein isothiocyanate, synthesized using a standard procedure). The fluorescent label allows tracking of the formation of immune complex. To evaluate the extent of binding of biomolecules, the deflection of cantilevers was measured by a sensitive 3D optical profilometer with an accuracy of 10 nm [102] and the obtained values are summarized in Table 4.1.

Measurements were carried out on four dies. Deflections corresponding to immobilization of antibody on the PS were 5 and 3.8 μm for the specific (die 2, AL01) and non-specific (die 4, E2G2) antibodies, respectively. More importantly, the immune affinity reaction with the HSA-FITC antigen resulted in a higher response for the specific compared to the non-specific antibody, the deflection shifts were from 5 to 3.5 μm and from 3.8 to 3.3 μm, respectively.

4.2.1.2 Triglyceride Detection

Fernandez *et al.* have reported novel composite PS/polysilicon silicon microcantilevers for sensing of triglycerides [103]. The oxide anchored cantilever beams of length 100–200 μm, width 10–20 μm and thickness 2 μm as shown in Figure 4.11 were fabricated

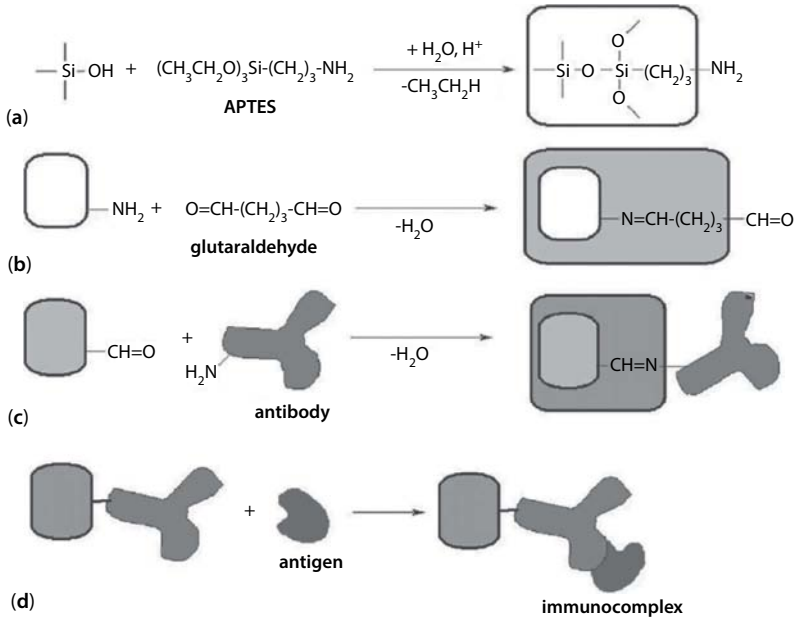

Figure 4.10 Scheme of modification of the silicon surface initially (a) the surface is silanized using aminopropyltriethoxysilane, thus generated amino groups are further (b) activated using glutaraldehyde and finally (c) the molecule of antibody is covalently attached; either AL01 or E2G2 antibody clones were used. The obtained immune-specific surface is allowed to react (d) with the molecule of antigen (fluorescently labeled albumin) providing the antibody–antigen immune complex which becomes attached on the sensing surface.

Table 4.1 Summary of deflection changes in (μm) of the composite cantilevers with porous silicone surface after immobilization of antibodies and immunoreactions steps.

Die #	Cantilever surface modification	Porous silicon deflection δZ (μm)
Die 1	AL01 + HSA-FITC	3.5
Die 2	AL01	5
Die 3	E2G2+ HSA-FITC	3.3
Die 4	E2G2	3.8

AL01, immobilized specific anti-HSA mAb; E2G2, immobilized non-specific mAb control; +HSA-FITC, after immunoreactions with the HSA-FITC conjugate.

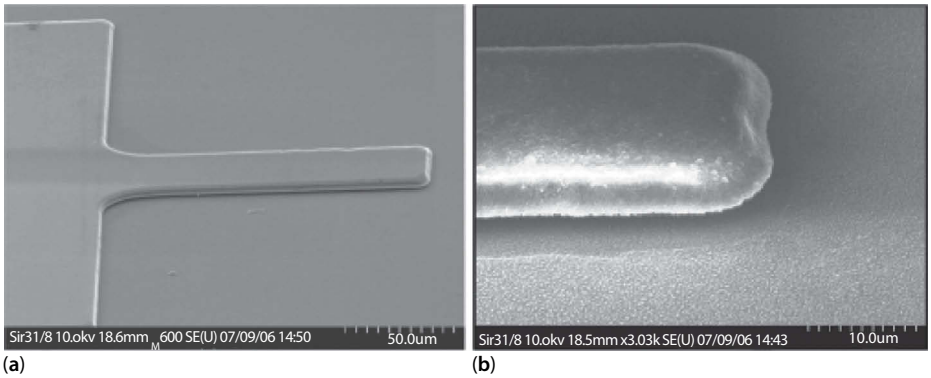

Figure 4.11 A top view of typical released polysilicon cantilever taken by SEM: (a) × 600 and (b) × 3000.

by surface micromachining. Crystalline silicon, p-type, oriented wafers of resistivity 1–10 Ωcm were used as the substrate for the surface micromachined cantilevers. Polysilicon layer of thickness 2 μm was deposited by Low Pressure Chemical Vapor Deposition (LPCVD) on 1.6 μm thermal oxide which was used as the sacrificial layer [104]. The polysilicon was patterned using wet chemical etching and the sacrificial oxide was etched using buffered HF with typical etch times being 90 min. Formation of the porous layer on the surface of these cantilevers is a major challenge for two reasons. First, being oxide anchored there is no electrical contact to the beam through the substrate and standard electrochemical etching cannot be used. Second, the polysilicon layer becomes very fragile after the formation of the PS layer and cannot withstand the long release etch of the sacrificial layer. The approach pursued here was to form the PS layer after the release of the beams. A new approach for the formation of porous layer on polysilicon cantilevers after release was found by applying a novel technique: reaction induced vapor-phase stain etch (RIVPSE) [105]. A sacrificial piece of silicon was put in a mixture of HF:HNO_3 in the ratio of 8:1 with a small addition of surfactant and the sample containing the cantilever beams was exposed to the fumes emerging from it for a certain period of time which resulted in the formation of PS layer. The surface morphology of the cantilevers before and after the formation of the PS layers is shown in Figure 4.12. Before biosensing application, the resonant frequency of the cantilever beams had been characterized in air and water. It was observed that in presence of water, the resonant frequency decreased since a liquid medium being denser than air contributed extra mass to the cantilever. Further, the viscosity also reduced the quality factor Q.

For triglyceride detection, immobilization of enzyme on the cantilevers was carried out as shown in Figure 4.13. The activity and the amount of active enzyme immobilized on the samples were estimated using *para*-nitrophenolpalmitate (pNPP) assay [106], as well as by measurement of resonance frequency shift. With both the methods, it was observed that the nonporous sample adsorbed 96 μg of enzyme, while the 2 and 5 s etched PS sample had 168 and 215 μg, respectively, which can be attributed to the larger surface area. For triglyceride sensing, the cantilever sensor was first calibrated using different concentrations of butyric acid: glycerol (3:1) solutions. Glycerol, being denser than butyric acid, contributes more to the density changes. The experiments were repeated using enzymatically hydrolyzed tributyrin solutions. Normal level of

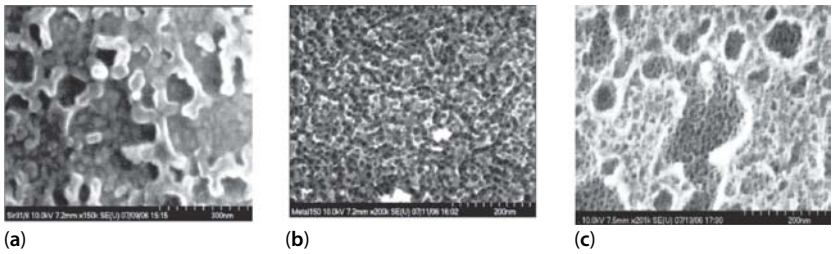

Figure 4.12 SEM patterns of detailed morphology of polysilicon cantilever surface before [(a) × 150,000] and after formation of porous silicon layer by 2 s; [(b) × 200,000] and 5 s [(c) × 200,000] vapour-phase etching.

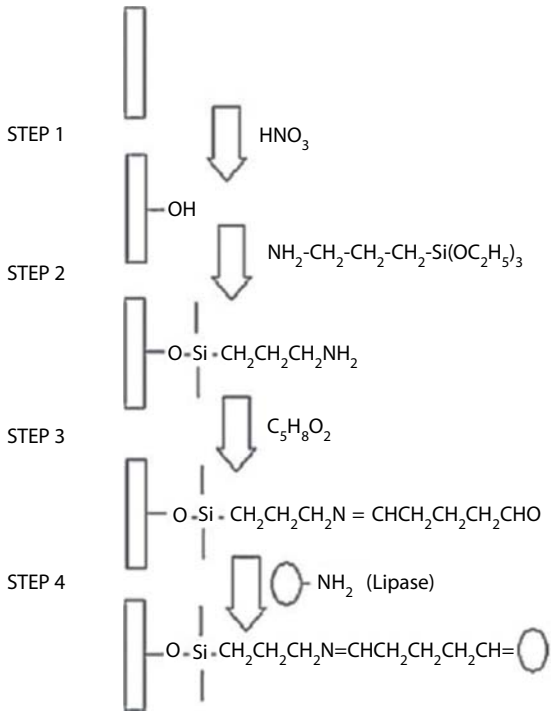

Figure 4.13 Various stages of immobilization of lipase. (STEP 1: Treatment with HNO3, STEP 2: Treatment with APTES, STEP 3: Treatment with glutaraldehyde, STEP 4: Treatment with Lipase)

triglycerides in human blood is in the range of 150–250 mg/dL [107]. To compare the performance of the composite beams with polysilicon beam, the tributyrin solution was added to the three kinds of the polysilicon beams with immobilized enzyme: (a) without vapor etching and with vapor etching for (b) 2 s and (c) 5 s and the response was observed during the course of hydrolysis.

Table 4.2 and Figure 4.14 show the absolute and relative variations in normalized resonance frequency of the cantilever beams over a period of time in solution. The improved response of porous cantilever beams can be attributed to its enhanced surface

Table 4.2 Change of resonance frequency during enzymatic hydrolysis reaction.

Time (min)	Resonance frequency R_f (kHz) (non-porous)	Resonance frequency R_f (kHz) (2 sec etched)	Resonance frequency R_f (kHz) (5 sec etched)	ΔR_f (kHz) (non-porous)	ΔR_f (kHz) (2 sec etched)	ΔR_f (kHz) (5 sec etched)
1	46.2	47.7	44.2	0	0	0
5	44.4	44.1	39.8	−1.8	−3.6	−4.4
10	41.3	42.2	36.7	−4.9	−5.5	−7.5
20	39.5	40.8	33.9	−6.7	−6.9	−10.3
30	38.8	39.3	31.1	−7.4	−8.4	−13.1

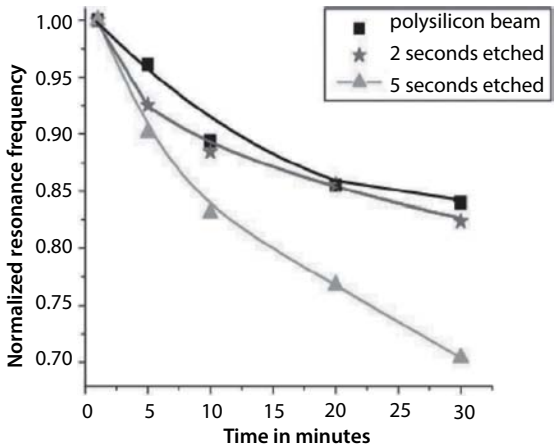

Figure 4.14 Normalized resonance frequency versus time during the course of tributyrin hydrolysis for polysilicon cantilever beam and composite beams etched for 2 and 5 s.

area which, in turn, enables it to accommodate a larger amount of the enzyme leading to the higher hydrolysis rate.

Bhat *et al.* [108,109] reported on the measurement of resonance frequency on composite PS and Si/polysilicon beams. The PS layer was formed on the Si/polysilicon beams of length 200, 300, and 350 μm by vapor etching [110] for 5 and 10 s. Resonance frequency measured using a Doppler vibrometer before and after pore formation shows contradictory results. In the case of 5 s etching, all beams show the same trend of increase in resonance frequency. However, in the case of 10 s etching, the 200 μm beam showed a decrease in the resonance frequency, while the 300 and 350 μm beams showed an increase. Possible effects due to the porous layer formation are: i) Mass reduction due to pore formation increases the frequency and ii) porous layer reduces Young's modulus which will decrease the resonance frequency. Using the expression for the resonance frequency of a multilayer beam [111],

$$f = \frac{\lambda^2}{L^2}\sqrt{\frac{\sum_i E_i I_i}{\sum_i m_i}} \tag{4.5}$$

Bhat extracted Young's modulus of PS from the resonance frequency data. The measurements and simulations showed that the pore location, depth, and size play an important role in determining the resonance frequency. A pore located at the anchor–beam junction can have a higher effect on the spring constant (k) than on mass (m), thus leading to reduction in resonance frequency. If the pore is located away from the junction, it should affect the mass more than spring constant leading to increase in frequency. Uniformity in the porous layer formation, both in pore size and distribution is important for the correct estimation.

4.2.2 PS-Based Impedance Detection

Micro impedance affinity biosensors using interdigitated electrodes have been extensively employed for label-free and rapid detection of a wide variety of biomolecules. Interdigitated micro electrode (IDE) array is one of the most common patterns for impedance-based biosensors [112–117]. But they suffer from low sensitivity and poor specificity. To improve the performance, PS may replace the conventional substrates. However, the formation of reproducible electrical contacts is essential since impedance measurements will be erroneous if the metal semiconductor contact is noisy. For PS-based impedance biosensors, the contacts have to be fabricated on PS oxide rather than only PS. As the metal–silicon oxide–silicon junction is primarily capacitive in nature like the gate oxide capacitance in a Metal Oxide Semionductor Field Effect Transistor (MOSFET), impedance biosensor fabricated on PS is expected to overcome the apparent limitations of noisy metal contact junctions in PS [118–120].

4.2.2.1 Bacteria Detection

Das *et al.* have reported the use of macroporous silicon for bacteria detection [121]. The expected advantages of impedance detection by macroporous silicon trapping array are: (a) natural trapping of bacteria in the self-assembled optimum size pores near the electrodes without using dielectrophoresis, (b) localization of the electrical field lines through the pores adjacent to the electrodes filled up with bacterial analyte solution permitting much wider spacing of electrodes, and (c) sensitivity at a significantly lower processing cost compared to the IDE structures. Further, the oxidized macroporous silicon substrate provides a high-resistance hydrophilic platform essential for achieving high-Q capacitance required for reliable impedance measurement. The etching was carried out under constant current source of current density 2 mA/cm^2 with an electrolyte mixture of HF acid (48 wt %) in dimethyl sulfoxide (DMSO) in the ratio of 1:9. The time of etching was kept at 30, 60, and 90 min to obtain different porous layer thickness of around 3, 8, and 12 μm, respectively. The top and cross-sectional view of SEM pictures of the macroporous silicon layer formed for 30 and 90 min is shown in Figure 4.15. For contacts on oxidized macroporous silicon layer, metal electrodes of

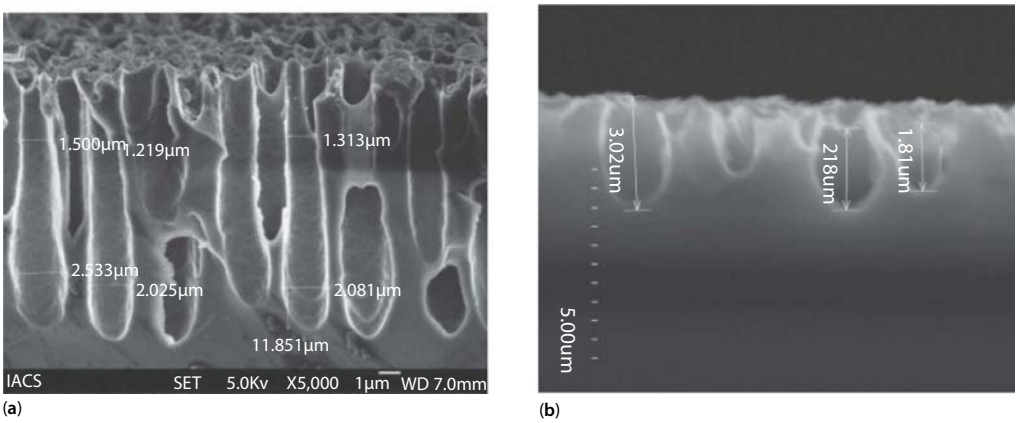

Figure 4.15 (a) SEM cross section of macro PS formed for 90 min and (b) SEM cross section of macro PS formed for 30 min.

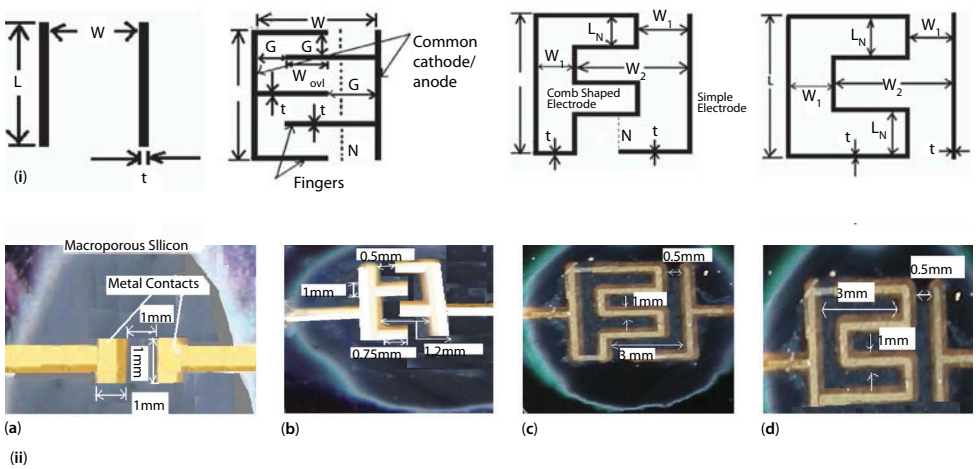

Figure 4.16 (i) Schematic of electrode configurations and (ii) Picture of electrode.

aluminum paste were fabricated with minimum dimension of 500 µm (much larger than the conventional electrodes) using screen printing technique. Four different patterns of electrodes shown in Figure 4.16 had been selected with coplanar rectangular geometries since rectangular geometries are least sensitive to sample depth which is an important criterion for obtaining stable readings in a low cost, portable sensor since the volume of the applied analyte may vary slightly from one test to another [122]. The oxidized samples were next immobilized with antibodies using the covalent silanization protocol by MTS-GMBS method shown in Figure 4.17 [123].

The stability of the sensors had been tested in the presence of control phosphate buffer solution (PBS). For testing with bacteria solution, initially impedance readings with control PBS had been recorded using Inductance-Capacitance-Resistance (LCR) bridge of Agilent 4284A. This was followed by the application of bacteria solution for 10–15 min for binding with the antibodies. The remaining solution was then washed off and the sensor surface was exposed again to control PBS for calculation of the fractional change in impedance in percentage which had been termed as sensitivity. The

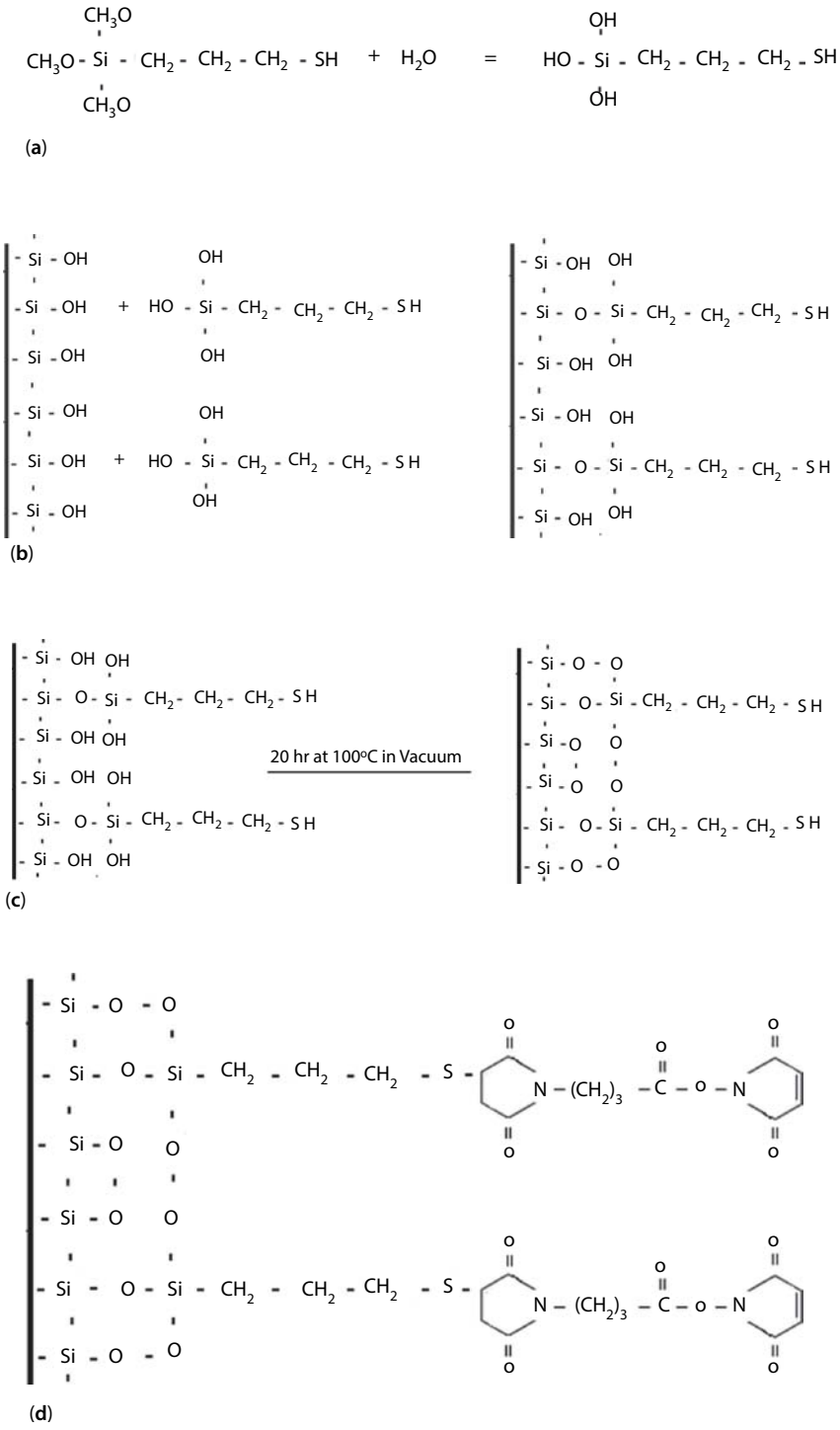

Figure 4.17 (a) Hydrolysis reaction of MTS silane, (b) Reaction of hydroxylated silane with silicon, (d) Reaction of MTS silane with GMBS and (e) Reaction of antibody molecules with GMBS. (*continued*)

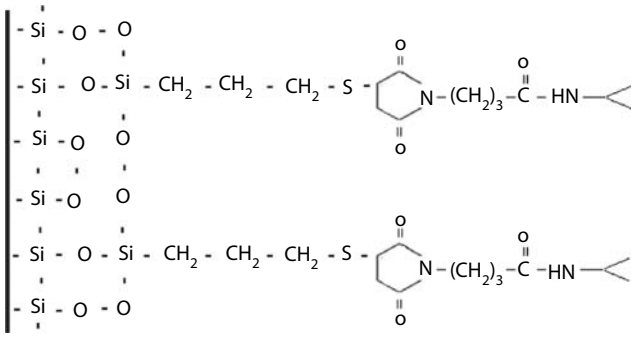

Figure 4.17 (*continued*)

sensors had been tested with both *Salmonella typhimurium* and *Escherichia coli* O157. The impedance decreased with frequency for all the cases which was similar to conventional substrates. But the sensitivity varied significantly with porosity as well as electrode design as shown in Figure 4.18. The sensitivity was found to be maximum around 1 kHz for 8 μm thick layer. This was attributed to the fact that around 1 kHz the overall impedance is primarily due to the double-layer impedances at the electrode–electrolyte and SiO_2–electrolyte interfaces and that the fractional change in the double-layer impedance at the SiO_2–electrolyte interface after bacteria capture is maximum for the 8 μm thick macroporous silicon sensor. This is probably due to the optimum current line confinement in 8 μm thick macroporous silicon sample such that a greater fraction of the distributed double layers at the SiO_2–electrolyte interface get modified by the bacteria cells. Further, the sensitivity was found to be maximum for the electrode design shown in Figure 4.16(ii)(b) with the dimensions of L=1 mm and W=0.5 mm. This was attributed to the optimum area utilization factor (AUF) of the electrode which was calculated as the ratio of the effective area occupied by captured bacterial cells (A_{beff}) to the effective exposed area available for capture between the electrodes. It is observed from Figure 4.18(c) that the detection limit was 100 CFU/ml with the optimized macroporous silicon sensor which is better than most of the label-free impedance sensors.

This had been attributed to the fact that the macroporous silicon substrate with pore dimensions of the order of 1–2 μm is an efficient trapping medium for bacteria. Due to the presence of short pores (~10 μm length), the solution enters through the pores and comes in contact with the bottom silicon substrate which provides a relatively low impedance parallel path compared to the lateral current path through the solution. This causes the field lines to scan only a small length of the solution near the electrode (~10 μm) irrespective of the horizontal and vertical spread above the surface of the applied solution unlike in planar substrates. This channeling of the field lines contributes greatly to the sensitive detection even with a wider spacing of electrodes. The detailed explanation with equivalent model has been reported in Refs. [124,125].

4.2.2.2 Food Toxin Detection

The presence of toxins in food and water is a serious public health concern. Among the various toxins, aflatoxin B1 (AfB1) has been classified as a class-1 human carcinogen

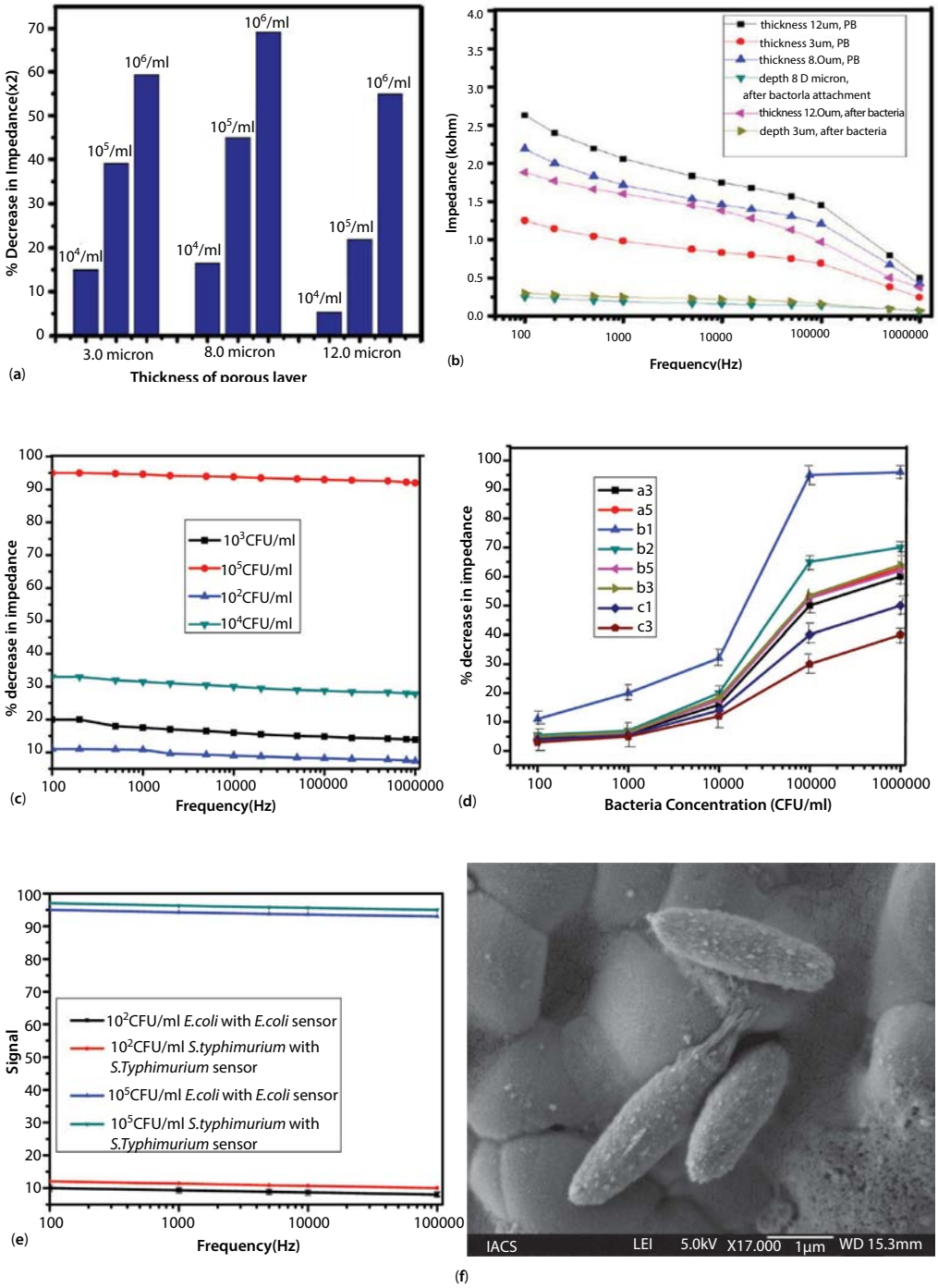

Figure 4.18 (a) Percent change in impedance for different concentration of *E. coli O157* with thickness of porous silicon, (b) Impedance variation with frequency for all samples at .10^5CFU/ml *E.coli O157,* (c) Percent change in impedance with frequency for pattern b1 with different *E. coli O157* concentration, (d) Percent decrease in impedance for different patterns at 100 Hz frequency with *E. coli O157* concentration [$(a–c)_i$ represents the patterns in 10 (i) with different dimensions], (e) Optimized sensor output for selectivity testing, (f) SEM of macro PS after *E. coli O157* capture.

by the International Agency for Research on Cancer [126]. Nanostructured substrate for toxin detection not only improves the binding efficiency of the analyte due to large surface area to volume ratio but also shows a possible catalytic effect in the diffusion of the analyte molecules within the nanopores [127]. However, the lowest detection limit achievable by electrochemical method using the various nanostructures is around 100 fg/ml or equivalently 100 fM [128–131]. Ghosh *et al.* [132] reported an immune sensor on electrochemically fabricated nanoporous silicon oxide structure and showed experimentally that it was capable of ultrasensitive label-free detection of AfB1 through antibody–antigen interactions not only by change in impedance values but also by a different mechanism of shift in peak frequency corresponding to maximum sensitivity. Fabrication was carried out by anodic etching of p-type silicon <100> wafers of 10–20 Ωcm resistivity in a double pond electrochemical bath for 30 min under a constant current density of 2.35 mA/cm^2 with an electrolyte mixture of HF acid (48 wt%) in DMSO in the ratio of 1:9 by volume. The nanopores formed were of about 100 nm thickness and 200–400 nm diameter as observed in Figure 4.19. The sensors were then thermally oxidized with suitable parameter to maintain an opening of 100 nm. For metallization, lateral metal contacts with aluminum paste were screen printed on nanostructured silicon oxide column which was followed by immobilization of antibodies by the method shown in Figure 4.17.

The measurement method was same as that in previous section for bacteria detection. Figure 4.20 shows the sensitivity with frequency for different AfB1 concentration. Interestingly, it is observed that the maximum change occurs at different frequencies for different AfB1 concentration. Usually in most of the reported impedance biosensors on AfB1 detection, the sensitivity gradually decreases, increases, or remains almost constant with frequency. In this case, we observe that the shift of the peak frequency is quite significant with AfB1 concentration. Also for every AfB1 concentration, the maximum impedance sensitivity at the peak frequency is almost three times than that of the lowest value which indicates that the measurement is not

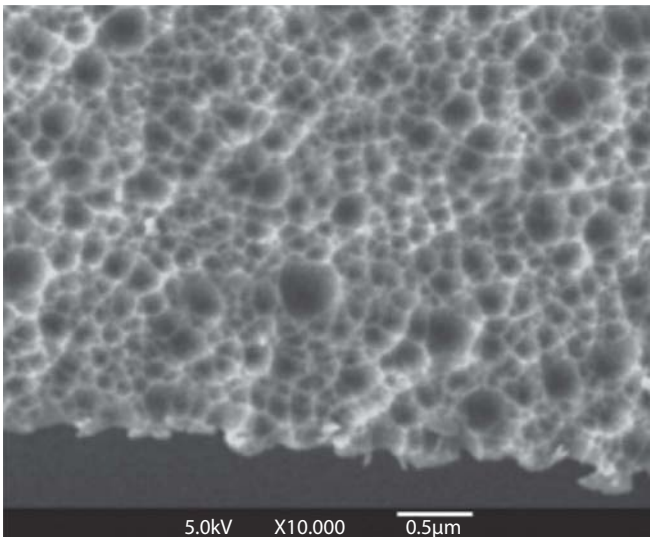

Figure 4.19 (a) SEM of silicon nanopores.

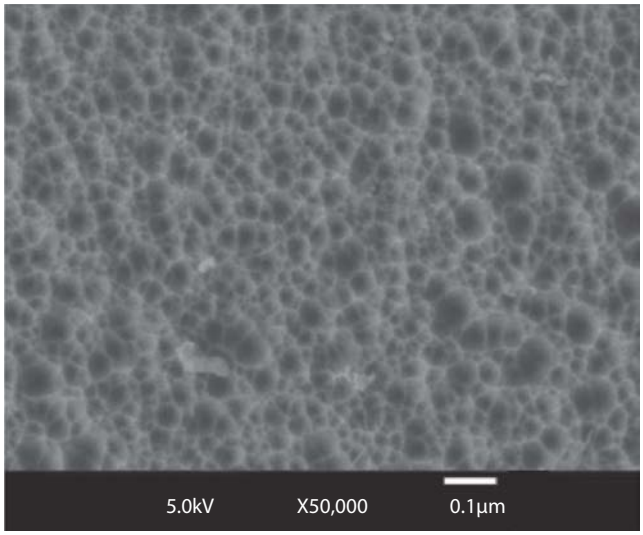

Figure 4.19 (b) SEM of silicon nanoporous oxide.

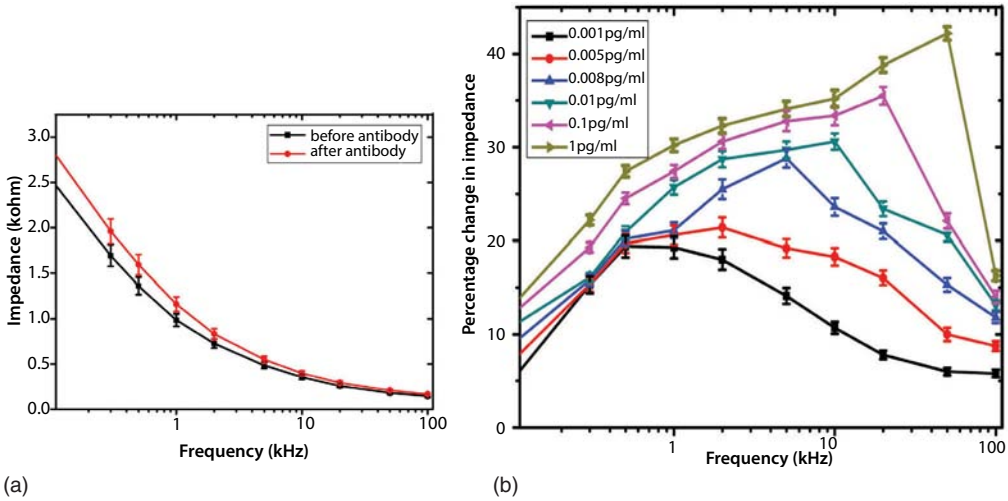

Figure 4.20 (a) Impedance spectroscopy before and after antibody immobilization and (b) Sensitivity for different AfB1 concentration.

noisy. The percentage change in impedance is around 19% for 1 fg/ml and around 40% for 1 pg/ml which is only twice but the peak frequency shifts from 500 Hz to 50 kHz for the same change in concentration and hence is significantly less susceptible to noise.

The observations were explained on the basis of an equivalent circuit model of the nanoporous silicon oxide structure shown in Figure 4.21. The total impedance (Z_t) between the metal contacts is given by Equation (4.6a):

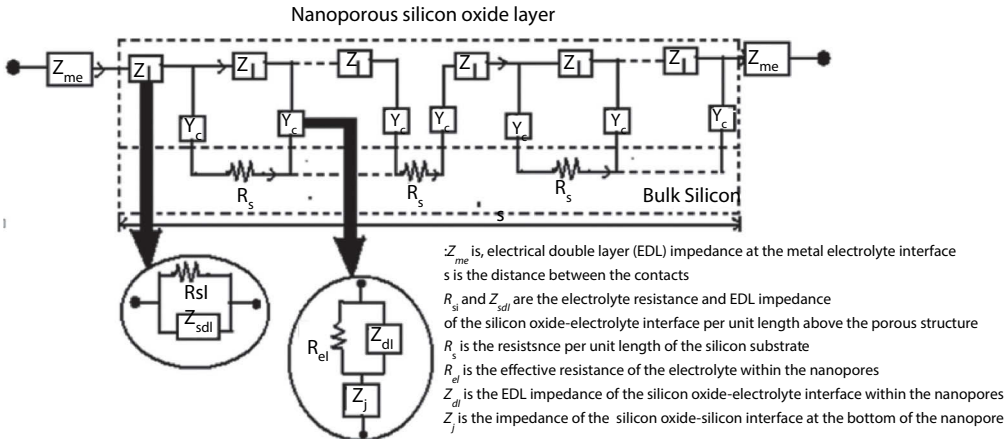

Figure 4.21 Equivalent circuit.

$$Z_t = Z_{me} + 2\sqrt{\frac{Zi + Rs}{Y_c}}coth\left(\frac{S}{2L_T}\right) + 2R_{S'} \quad L_T = \sqrt{\frac{1}{Y_c(Z_i + R_s)'}}$$

$$Z_l = \frac{R_{sl}Z_{dl}}{\mathrm{R}_{\mathrm{e}l} + Z_{dl}}, \frac{1}{Y_c} + Z_j \tag{4.6a}$$

$$Z_{dl} = K_1\omega^{-a_1}, Z_j = K_2\omega^{-a_2}, Z_{me} = K_3\omega^{-a_3} \tag{4.6b}$$

The symbols are explained in Figure 4.21. To summarize, two reasons were hypothesized for the observation of such behavior. First, the change in Z_{dl} and Z_j were of opposite nature. Second, the narrow pore dimensions were such that it allowed the target molecules surrounded by its screened charges to penetrate the bottom of the pore and at the same time, the electrolyte resistance, R_{el} was greater than or equal to the Electric double layer (EDL) impedance at the pore walls.

4.2.2.3 DNA Detection

Archer *et al.* [133] have reported the use of macroporous silicon for impedance-based DNA hybridization detection. PS layers were fabricated on 10–20 Ωcm resistivity p-type silicon under constant current density of 4 mA/cm^2 with 4% HF in DMF. The thickness of the porous layer was varied from 20 to 150 μm. Self-supporting layers were also fabricated under the same conditions and the detachment of the porous layer from the crystalline silicon substrate was performed in two steps. Figure 4.22 shows the SEM of a heterostructure and a self-supporting layer. The PS layers were then thermally oxidized in 30% wt boiling hydrogen peroxide for 150 s. This process results in very hydrophilic oxide helping in the infiltration of water molecules. The oxide on the back side was stripped and two metal contacts were fabricated 700 μm apart as shown in Figure 4.23. To attach DNA probes, standard silanization process was carried out as discussed in previous sections.

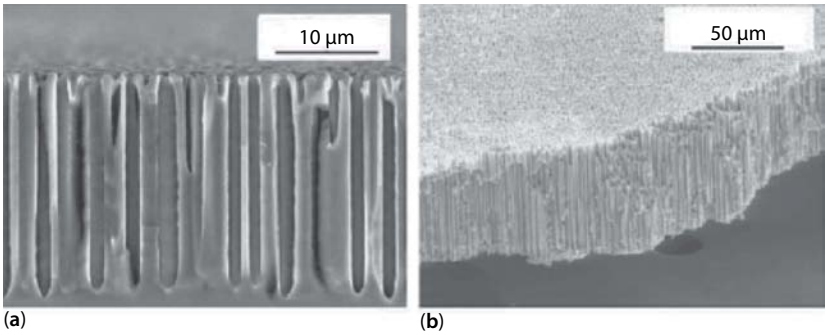

Figure 4.22 SEM cross-sectional view of (a) macroporous silicon heterostructure and (b) self-supporting layer.

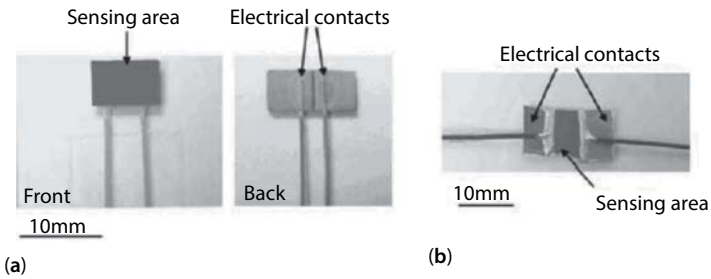

Figure 4.23 Pictures of the (a) front side and back side of the heterostructure. (b) Top picture showing the self-supporting layer.

Three different synthetic oligonucleotides were used as a model for DNA binding as shown in Table 4.3. A non-complementary sequence was used in control experiments to address selectivity. Experiments were performed on different layers by adding 10 µl of pDNA1 (probe), allowing the sensor to dry and then adding 10 µl of either cDNA1 (complementary) or ncDNA (non-complementary). An additional control experiment consisted in the addition of a NaCl hybridization buffer following probe infiltration. Experiments were also performed with peptide nucleic acid (PNA). The methodology followed was the same for DNA experiments.

The responses to DNA binding were addressed using the 150 µm thick PS samples and 10 µl each of 25 µM probe and target molecules. Figure 4.24 shows the impedance and phase angle change with time when pDNA1 is infiltrated followed by cDNA1. It is observed that addition of cDNA generates a larger effect than pDNA. The reduction in the impedance and the increase in the phase angle indicate the hybridization of the two sequences. The selectivity was also tested to be satisfactory. Similar experiments were performed using PNA and the results of both of them were explained based on the space charge region model. Further, the effect of the thickness of the PS was also observed as shown in Figure 4.25. The percentage change in impedance and phase increased with increasing thickness owing to the increased surface area. The experiment was carried out for different concentration also. These results show that the impedance change of the 20 µm device increase as the DNA concentration is reduced. In comparison, the response of the thicker layers is slightly reduced with a lower target concentration. The

Table 4.3a Identification name and base pair DNA sequences used for the DNA experiments.

Identification name (ID)	Base sequence
pDNA1 (probe DNA1)	5'-TAG CTA TGG AAT TCC TCG TAG GCA-3'
cDNA1 (complementary DNA1)	5'-GCC TAC GAG GAA TTC CAT AGC T-3'
ncDNA (non-complementary DNA)	5'-TCG ATA CCT TAA GGA GCA TCC G-3'

Table 4.3b Identification name of the DNA and PNA sequences used for the PNA experiments.

Identification name (ID)	Base sequence
pPNA (probe PNA)	5'-GTA GCA TAC GCA GCC-3'
cPNA (complementary PNA)	5'-GGC TGC GTA TGC TAC-3'
pDNA2 (probe DNA2)	5'-GTA GCA TAC GCA GCC-3'
cDNA2 (complementary DNA2)	5'-GGC TGC GTA TGC TAC-3'

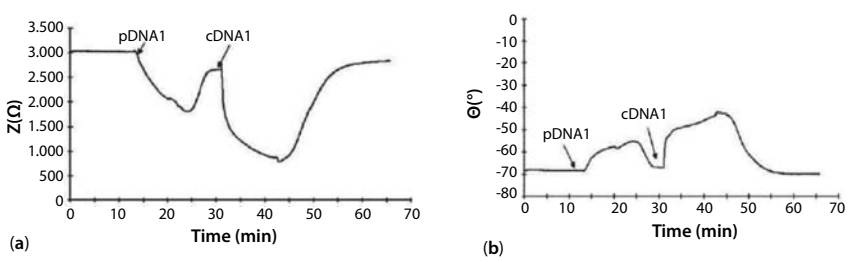

Figure 4.24 Real-time (a) impedance (Z) and (b) phase angle (θ) of the porous silicon sensor when the probe is exposed to its complement.

response of the thicker layers can be explained by considering that a lower target concentration implies a smaller number of binding sites contributing to the response. The enhancement of the response in the 20 μm samples, even at a lower concentration, suggested that the sensitivity was affected also by the charged backbone of DNA. In fact, there is a trade-off between the surface area and the number of binding sires that can be accommodated without affecting the hybridization. Experiments were performed using self-supporting membranes and the results are shown in Figure 4.26. In this case, the change in the dielectric constant inside the pores changes the capacitance. The difference in the range of values of the impedance and phase angle between the heterostructures and the self-supporting membranes is due to the differences in the electric

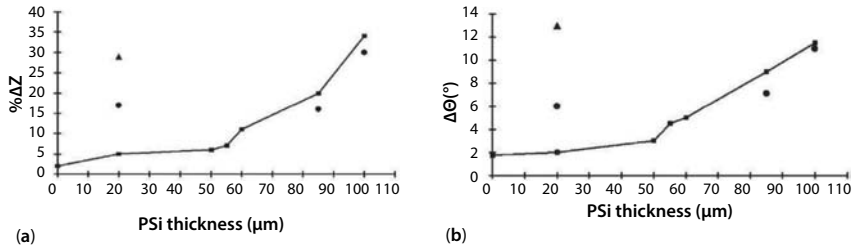

Figure 4.25 Maximum change in (a) impedance (%ΔZ) and (b) phase angle shift (Δθ) for porous silicon sensors of various thicknesses. The zero thickness point corresponds to planar c-Si. The connected data points correspond to pDNA1 and cDNA1 concentration of 25 μM. Solid circles correspond to a 25 μM vs 10 μM (pDNA1 vs cDNA1) concentration and the solid triangle to a 5 μM vs 5 μM (pDNA1 vs cDNA1) concentration on a 20 μm thick layer.

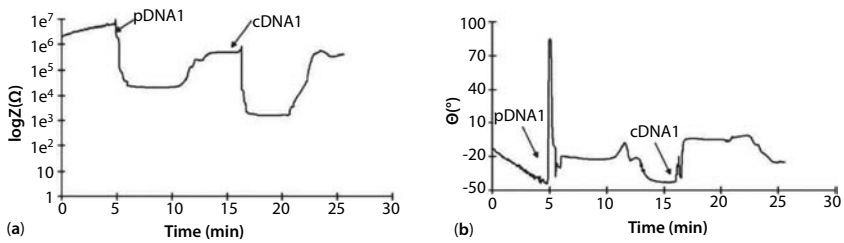

Figure 4.26 Real-time (a) impedance (log Z) and (b) phase angle (θ) of self-supporting porous silicon layers when pDNA1 is exposed to its cDNA1 at 10 μM concentration.

field propagation. Although the self-supporting membranes produced larger signal, it was difficult to fabricate and handle.

Vamvakaki and Chaniotakis [134] also developed electrochemical impedance-based DNA hybridization PS biosensor. Pores ranging from 20 to 40 nm size on p-type boron-doped silicon wafers were created using electrochemical etching. PS surface was functionalized by anodic oxidation and 21-mer oligonucleotide (50-GAG GAG TTG GGG GAG CAC ATT-30) was attached on it thereafter. It was observed that the dielectric constant of PS increased on attachment of such highly negative nucleotides on the surface. This increase in dielectric constant led to decrease in impedance of the designed system. Complimentary DNA sequence (50-AAT GTG CTC CCC CAA CTC CTC-30) hybridization forms double helix leading to a decrease in hydrated sphere and thus the amount of electrolyte surrounding the initial ss-DNA. It has been proposed that formation of duplex on hybridization results in lesser interface charge density following decrease in capacitance and increase in impedance measurements.

4.2.3 PS-Based EISCAP Structure for Capacitive Detection

Electrolyte-Insulator-Semiconductor Capacitor (EISCAP) is electrolyte insulator semiconductor-based capacitive structure whose theory was developed by Bergveld

[135,136] and Siu *et al.* [137]. The working principle of EISCAP is the flat band voltage shift in response to the pH of the electrolyte and is explained in great detail with different dielectrics [138–140]. The EISCAP basically serves as a pH sensor working on the principle of the thermodynamic equation, "Nernst response" [133]. Interfacial potential, flat-band voltage across the sensor would change with the pH of the electrolyte used in the sensor. Many biological reactions, especially enzyme-mediated ones, involve change in the pH of the electrolyte. Hence, an EISCAP can be effectively used as a biosensor [94]. In this section, we discuss the use of PS in such structures for biosensing.

4.2.3.1 Triglyceride Detection

Reddy *et al.* first reported on a PS-based potentiometric sensor for tributyrin, a short-chain triglyceride, where SiO_2 was the insulator in the EISCAP [141,142]. Silicon nitride has advantages over SiO_2 as an insulator because it offers better pH sensitivity [143] and also it is stable in basic solutions in contrast to SiO_2. Hence, with silicon nitride as the insulator, the detection can be extended to the basic range. Using a stacked PECVD silicon nitride on thermal SiO_2 insulator on single crystal silicon a higher-sensitivity biosensor that can be used to detect both triglycerides as well as urea was reported [144]. Figure 4.27(a) and (b) shows C–V measurements taken using PBS at a signal frequency of 10 kHz on a PS sample and an identically processed crystalline silicon substrate. Due to the much larger surface area of the PS sample, there is a 34.5 times increase in accumulation capacitance over the single crystalline silicon sample. The responsivity of PS as well as the dissipation factor is better at lower frequencies. Hence, the CV measurements to determine the pH sensitivity of PS samples were done at 1 kHz.

Since the pH sensitivity is decided by the electrolyte–nitride interface, we expect higher pH sensitivity as compared with an oxide dielectric. This was not seen presumably because the PECVD nitride is unable to conformally cover the entire surface area of the oxidized PS and did not change when the pore size was increased. Even though the improvement in pH sensitivity with silicon nitride on PS as compared to using oxide as the dielectric was not seen, a comparison of the final calibration plot for the two showed a much larger detection range of 0.5–20 mM of tributyrin concentration

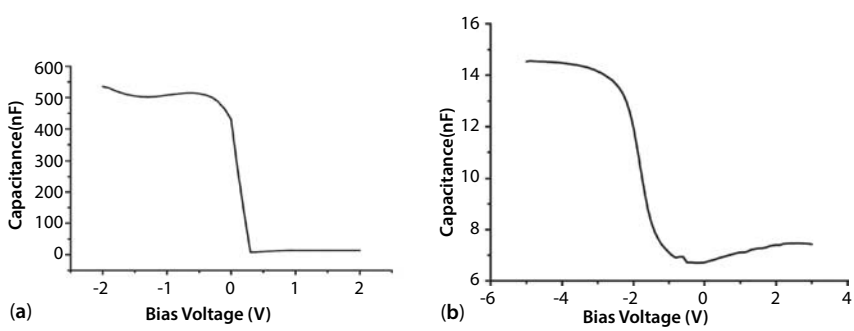

Figure 4.27 CV at 10 kHz for identically processed (a) porous silicon and (b) crystalline silicon substrate.

for the nitride sample as compared to the range of 5–40 mM for the oxide sample. Arun *et al.* [145] used silicon and PS-based EISCAPs for several applications.

Vemulachedu *et al.* [146] have reported the miniaturization of EISCAP sensors on crystalline silicon and PS substrates. Fabrication steps are shown in Figure 4.28. To make PS-based mini-EISCAP device, the PS formation step was introduced in the fabrication protocol after the removal step of passivating SiO_2 layer in Figure 4.28. Electrochemical etching was carried out for 10 min. The sensor surface was then immobilized with lipase as shown in Figure 4.13.

A probe station was used to characterize the devices and a platinum electrode with a diameter of 300 μm was used to make contact with the electrolyte. Back contact was made from the probe station bottom plate. The volume of the electrolyte corresponding to dimensions of the device was 0.1 μl. Different solutions of known pH (pH = 2, 4, 7, 9, and 11) in 1 M KCl in 10 mM phosphate buffer were used to determine the pH sensitivity of the sensor which was found to be 55 mV/pH. The pH sensitivity of the PS-based mini-EISCAP device, measured in a similar manner was found to be 33 mV/pH. For the detection of triglyceride concentration, five millimolar of triglyceride solutions in buffer electrolytes were used to fill the lipase immobilized mini-EISCAP cells using a micro-syringe. The immobilized lipase hydrolyzed the triglyceride producing butyric acid and glycerol. The C–V curves shifted toward the left as the hydrolysis progressed with time. The PS-based sensor, with a higher surface area and capacity to bind more enzymes showed a little power shift than its silicon based counterpart. The smaller shift for the PS mini-EISCAP could be due to the lower sensitivity of PS (33 mV/pH) as compared to the crystalline based sensor (55 mV/pH). We found that, even though PS binds more enzyme, the abundance of enzyme alone does not necessarily correspond to a higher triglyceride sensitivity as the triglyceride concentration is the limiting factor for the miniaturized EISCAPs. In addition, reproducibility was found to be a problem for the PS EISCAPs.

Triglyceride sensing has also been carried out by potentiometric method using PS. In such structure, PS acts as an electrode of electrochemical cell where it forms the pathway for transducing electrolytic solution in a detectable electric signal. Potential difference between cathode which was the platinum electrode and anode which was PS electrode of the electrochemical cell was determined to estimate tributyrin concentration in blood [147–151]. In one of the reports [152], the active surface area of

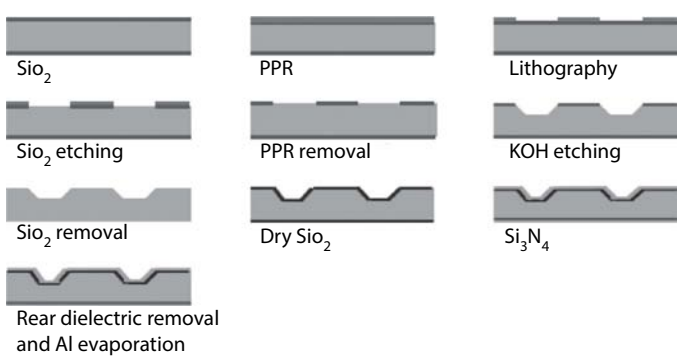

Figure 4.28 Fabrication steps for miniature EISCAP.

the planar electrode was approximately 0.16 cm^2 and that of the porous electrode was approximately 0.5 cm^2. The sensitivities were 0.085 μA/mM for the planar sensor and 0.265 μA/mM or the porous sensor.

4.2.3.2 Penicillin Detection

Similar structure of PS EIS with a mean pore diameter of about 1 μm and a mean pore depth of about 2 μm were realized for capacitive pH sensors [153]. An average penicillin sensitivity of about 90 mV/mM in the concentration range from 0.01 to 1 mM was obtained with the help of penicillinase enzyme and showed a potential stability of more than 1 week in the long term. The longevity was further improved to 1 year by the introduction of macro PS [154].

4.2.4 PS-Based Other Electrochemical Biosensors

Various other electrochemical biosensors based on potentiometric measurements, conductivity changes, dc I–V characteristics, capacitive change, and electron transfer kinetics using cyclic voltammetry measurements have been reported. In this section, we attempt to highlight some of them.

4.2.4.1 Glucose Detection

The basic concept of the glucose biosensor is based on the oxidation of β-D-glucose by molecular oxygen producing gluconic acid and hydrogen peroxide. Hydrogen peroxide is further oxidized at the electrode which can recognize the number of electrons transferred. This electron flow is proportional to the number of glucose molecules present in the blood [71]. PS-based glucose sensors have been very successful in detecting glucose selectively as shown in Figure 4.29. It has been observed that the activity of enzyme glucose oxidase increases by a factor of 100 and is more sensitive to small concentration of

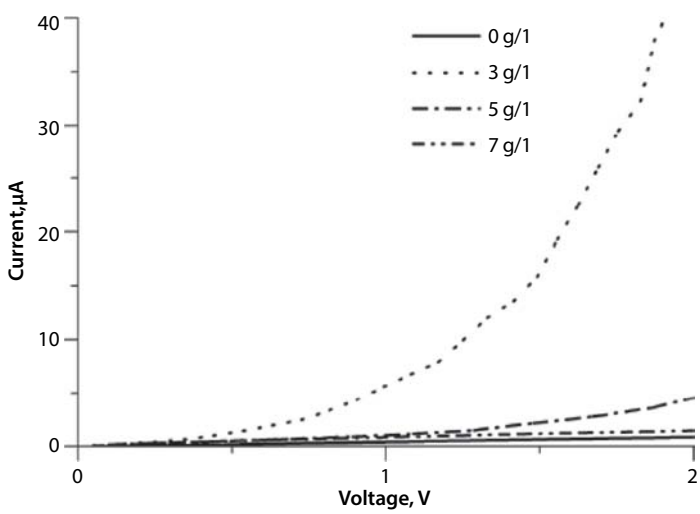

Figure 4.29 Current–voltage characteristics at different glucose concentration.

glucose when it is immobilized on PS surface [155]. Similar electrical characteristics for both longitudinal and transversal conduction through PS structure for glucose detection have been reported by other groups [156].

4.2.4.2 DNA Detection

Electrochemical biosensor for the detection of DNA involves conversion of some electroactive compound where the single strand of oligonucleotide is attached on PS surface. Duplex formation has been detected by employing reversible redox reaction of guanine base present in DNA with ruthenium bipyridine in PS. This reaction showed that the catalytic effect on the anodic peak current could be directly related to the concentration of target DNA. The anodic peak current of was linearly related to the target DNA sequence in the range 0.5×10^{-10}–500×10^{-10} M with a detection limit of 0.5×10^{-10} M. In addition, the ruthenium bipyridine indicator was able to selectively discriminate against different DNA sequences; a necessary property for sensing applications. Figure 4.30 shows the typical cyclic voltammograms for different concentrations of target DNA [157]. Jin and co-workers [158] fabricated and electrochemically characterized a label-free DNA sensor based on PS substrate on which polypyrrole film was directly electro polymerized. Intrinsic negative charge of the DNA backbone was exploited to electrostatically adsorb 26 base pairs of probe DNA into the polypyrrole film by applying positive potential. Results show that the *Salmonella enteric* serovar Enteritidis DNA (tDNA) concentration is inversely related to the peak current at 0.2 V vs Ag/AgCl. The current density decreases by 29 $\mu A/cm^2$ per hour of incubation time.

4.2.4.3 Bacteria Detection

Bacteria detection has been carried out using metal/nano PS/metal devices fabricated by making metallic contacts on PS wafer. PS was functionalized with APTES and immobilized with *E. coli* antibodies and the results showed a strong variation of the current as a function of the presence/absence of *E. coli* bacterium and surface concentration [159]. Zhang and Alocilja [160] developed a label-free DNA electrochemical biosensor on

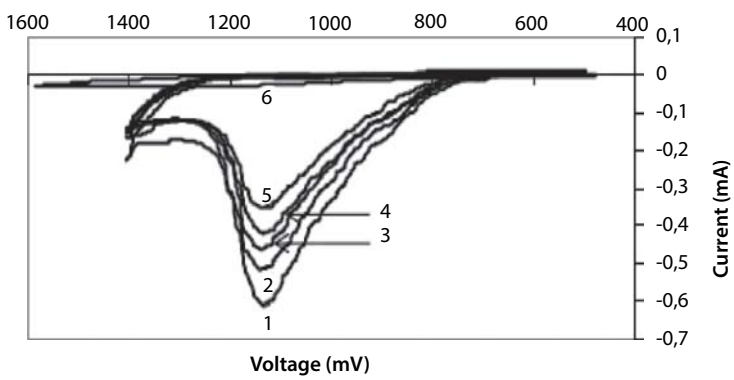

Figure 4.30 Cycled voltammograms of different concentrations of target DNA: (2) 0.5×10^{-10} M, (3) 100×10^{-10} M, (4) 200×10^{-10} M, and (5) 500×10^{-10} M. Curve 1 shows the CV for the probe-mismatch target DNA sequence (0.5×10^{-10} M) and curve 6 for the probe DNA sequence (0.5×10^{-10} M).

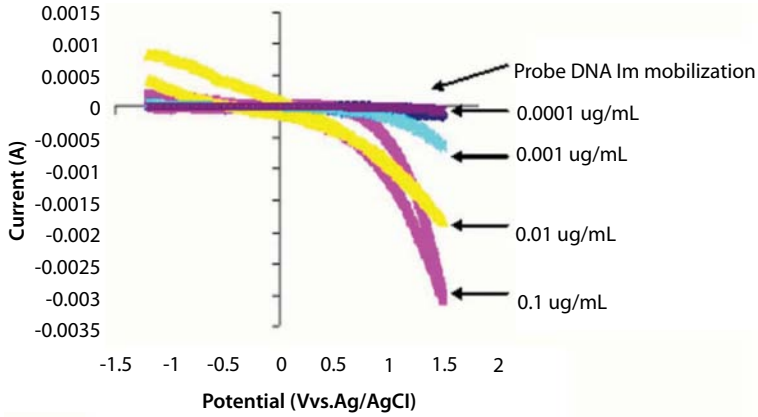

Figure 4.31 Cyclic voltammograms of non-biotinylated DNA samples on PS biosensor (0.01 W cm) in a 5 mM K4 Fe(CN)6 solution with 1 M KCl. Scanrate is 50 mV/s.

nanoporous silicon chips for the determination of *Salmonella enteritidis*. Their experiments revealed that the PS had four times higher surface area than crystalline silicon and higher DNA probe selectivity and affinity to the target DNA with a 1 mg/ml detection limit. Figure 4.31 shows the cyclic voltammograms of DNA samples on PS.

4.2.4.4 IgG Detection

PS has been employed for the detection of antigen by measuring the shift in the capacitance voltage characteristics with a detection limit of 10 ng/ml [161]. In other reports, macros had been used for the capacitive detection of antigen [162–164]. It was observed that the magnitude and nature of the capacitance change after antibody–antigen binding varied with many factors such as the silane used, process of grafting, the surface area of the substrate, length and thickness of the columns in the porous structure. The increase in sensitivity observed with higher frequency for the squat irregular columnar structure was of the same order as that of the increase in surface area. The constraints on the length and size of the columns in order to have maximum capacitance change at the measurement frequencies are: the columns should not get fully depleted at the measurement voltage and the length should be optimum enough to allow complete penetration of the electrical signal in the electrolyte in the pore. Figure 4.32 shows the CV characteristics of squat type columnar structure of PS at 7 kHz.

4.2.4.5 Other Analytes

PS biosensor has been employed for rapid and integrated measurement of alanine aminotransferase (ALT) and aspartate aminotransferase (AST) which indicates an abnormal symptom of the liver. The biosensor array consisted of two glutamate sensors and was constructed with platinum electrodes and a PDMS microchannel and device sensitivities of 0.145 μA/(U/l) for ALT and 0.463 μA/(U/l) for AST over a range of 1.3–250 U/l [165]. Integrated three electrode system module composed of PS base sensing electrode, an Ag/AgCl reference electrode and a Pt thin-film counter electrode

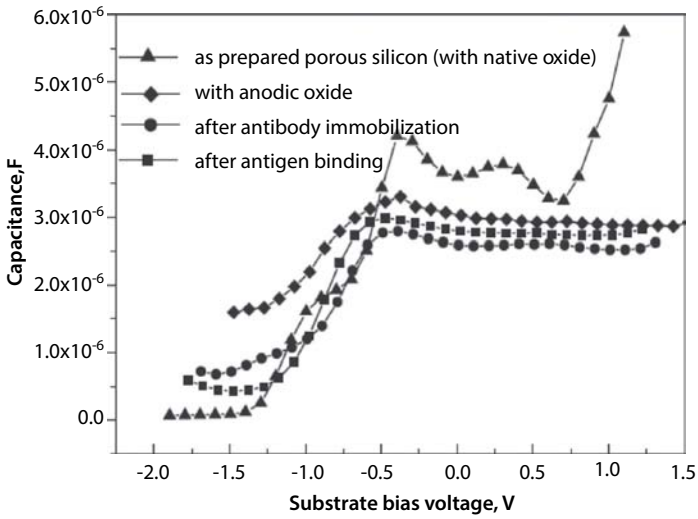

Figure 4.32 CV characteristics at 7 kHz.

was developed by other groups for monitoring urea level of artificially prepared body fluid [166]. After electro polymerization of the conductive poly (3-methylthiophene) (P3MT) on the PS-based Pt thin film, urease molecules were electro statically doped into the P3MT film by applying positive bias. Amperometric calibration curves showed that urea concentration in the range of 0.1–125 mM could be detected. Urea detection has also been reported by amperometric method using nano PS by urease enzyme with a sufficiently high sensitivity [167]. Conductivity based catechol sensor using tyrosinase enzyme has also been reported with PS where the current voltage characteristics were obtained to be proportional to the analyte concentration [168]. In a similar manner, bilirubin was also detected by PS biosensor with a current sensitivity of 0.153 mA/mM [169].

4.2.5 Reliability

Apart from the various advantages, there are certain challenges which control the reliability of such sensors. The chemical stability of the PS sensors needs to be considered. Nanostructured or macrostructured PS prepared from HF organic electrolytes like DMSO or DMF have been observed to be more reproducible and stable as the pores formed are more ordered and regular than those prepared from HF and ethanol or methanol. However, for biosensor applications, the oxidation followed by surface derivatization reduces the surface activity of PS structure and hence the problem of instability, in general is much less compared to other chemical sensors. To partially overcome the problem posed by reproducibility or time related drifts, suitable electronic interface may be developed as reported in Ref. [170]. Whenever measurements will be carried out, a control measurement needs to be recorded first and then the test reading will be recorded. The sensitivity is estimated by the relative change and hence the reliability issue can be minimized. Also, Wheatstone bridge configuration of sensors can be deployed to minimize the effects of internal changes of PS caused by

temperature and humidity [171]. Reliability issues from stable electrical contacts in capacitive biosensors on PS are better than their resistive counterparts. This is primarily because, the effect of flicker noise due to the presence of interface states at the junction of PS and metal contacts is lower in capacitive measurement. However, for commercialization of PS biosensors, more rigorous investigations using real-life samples like blood, urine and others need to be carried out.

4.3 Porous Silicon for Pressure Sensors

The use of PS for pressure sensor has been successfully introduced by Bosch Research Centre in commercial sensors in which the PS is used to form a cavity with reference pressure [172]. Here, PS has been formed on the surface of silicon wafer by electrochemical etching and a monocrystalline silicon layer (membrane) is deposited on the top of the PS layer. When the PS is subsequently heated to 1000 °C, it collapses like soapsuds and forms a cavity with a reference pressure of less than one millibar. In this section, we discuss about the techniques of improving the sensitivity of pressure sensor by using Si/PS composite membrane where the mechanical properties and piezoresistive properties of PS enhance the sensitivity.

PS is very attractive due to its amazing optical, electrical, and thermal properties. But the mechanical properties of PS have not been much studied. Young's modulus (E) is a material property that describes its stiffness and is therefore one of the most important properties in engineering design. The elastic properties of porous materials drastically vary with porosity and Young's modulus of porous materials is lower by an order of 3 or 4 compared to nonporous materials [173]. It is difficult to predict the mechanical properties of porous materials because many factors other than porosity such as morphology, pore diameter and pore spacing affect the mechanical properties. Measurement of the elastic properties of porous materials such as thin PS layer using conventional mechanical testing methods is difficult and it may give erroneous results or damage the samples.

Measurement of mechanical properties of PS by acoustic technique has been proposed [174] and in this method acoustic microscopy and microechography were used to characterize the PS layer such as thickness and porosity dependence of Young's modulus and elastic properties. Young's modulus of PS (on p^+ substrates) derived from the acoustic measurements and empirical constants, drastically reduces with increase in porosity as shown in Figure 4.33.

Measurement of Young's modulus by nanoindentation technique on PS layers showing drastic variation with porosities has been reported along with the comparisons of X-ray diffraction method and acoustic method [175,176]. We found that the measured Young's modulus of micro PS formed on p-type (100), 1–10 ohm-cm is 22.11 GPa with 50% porosity reducing to 5.51 GPa for 70% porosity. Young's modulus of 70% porosity has been reported as 2.2 GPa by Bellet *et al.* (1996) [175]. For isotropic PS, Young's modulus (E_{ps}) can be written [177] as

$$E_{ps} = E_{Si}\left(1-P\right)^3 \tag{4.7}$$

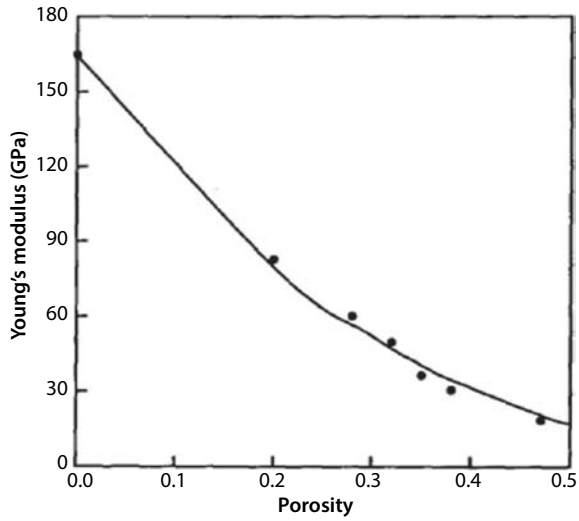

Figure 4.33 Young's modulus of PS layer as a function of porosity on p^+ samples. *Source*: Da Fonseca *et al.* (1995).

where P is the porosity and E_{si} is Young's modulus of silicon.

Using Equation (4.7), Young's modulus for 50% and 70% PS work out to be 23.75 and 5.13 GPa and are quite close to the measured values given above. The variation in Young's modulus with porosity in n-type substrates is larger compared to p-type substrates. Reports and our measurements show Young's modulus of PS is much lower than Young's modulus of single crystalline silicon and it drastically reduces with increase in porosity.

4.3.1 Pressure Sensor with Silicon/PS Composite Membrane

MEMS pressure sensors are the first successful MEMS devices and there are many commercial products available [178]. Bulk micromachined pressure sensors are fabricated with a silicon membrane and polysilicon piezoresistors on an oxide layer that exhibit good sensitivity and temperature tolerance [179]. In these pressure sensors, the deformation of the membrane depends strongly on its thickness, and higher sensitivity can be achieved by reducing the thickness of the membrane. But pressure sensors with very thin membranes are nonlinear and difficult to handle during processing. The sensitivity of the pressure sensors can be improved by fabricating the membrane with a material of low Young's modulus. PS has very low Young's modulus that reduces with increase in porosity. When a part of the silicon membrane is converted into PS, the effective Young's modulus of the membrane reduces which gives more deformation with the application of pressure. Since the deformation is greater, the strain is also greater compared to single crystalline silicon and hence the sensitivity is higher. In this section, we discuss the fabrication and testing of pressure sensors with composite membranes of Si/micro PS and Si/macro PS. The effect of temperature and humidity on PS is expected to be worse due to its large surface area, and we have investigated this on packaged pressure sensors with composite membranes.

4.3.1.1 *Fabrication of Pressure Sensor with Composite Membrane*

Silicon membranes of 16 μm thickness were fabricated by potassium hydroxide etching. After Radio Corporation of America (RCA) standard cleaning, aluminum evaporation was done on top of the wafer to provide electrical contact for the formation of PS. The wafer was scribed into 2 cm × 2 cm samples to enable loading into the electrochemical cell. PS was formed on the back of the membrane by electrochemical etching using the optimized formation conditions and the specified electrolyte. Samples were prepared with composite membranes of Si/micro PS and Si/macro PS with the same thickness of PS layer of 6 μm and porosities of 50%, 70%, and 90%. The other fabrication steps such as oxidation of composite membrane, formation of poly piezoresistors and metal contacts were as reported earlier [176]. Figure 4.34 shows the cross section of the fabricated pressure sensor with Si/PS composite membrane. The surface profiler view (using WYKO NT1000) of the device showing the poly piezoresistors connected as Wheatstone bridge is shown in Figure 4.35.

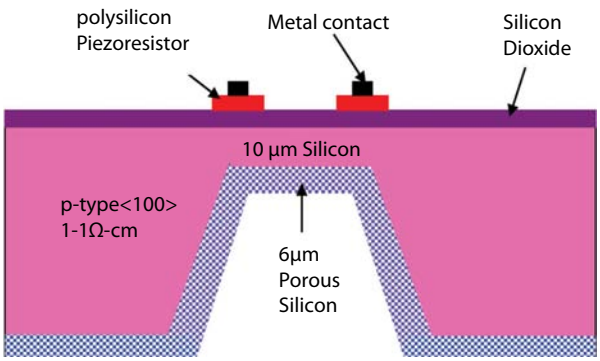

Figure 4.34 Cross section of the fabricated pressure sensor with Si/PS composite membrane.

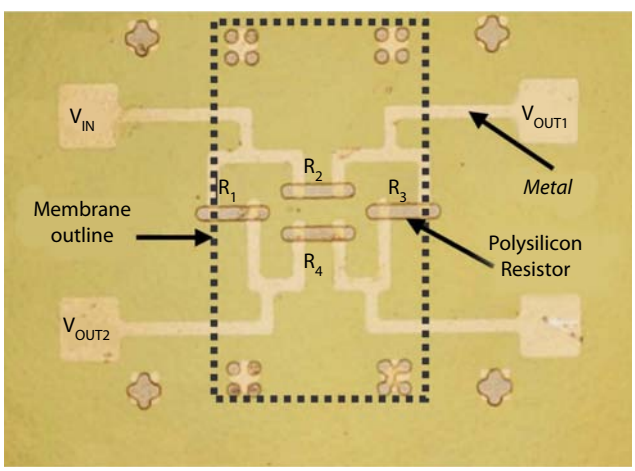

Figure 4.35 Top view of the device showing the poly piezoresistors connected as Wheatstone bridge.

4.3.1.2 *Performance of Si/PS Composite Membrane Pressure Sensor*

Figure 4.36 shows the sensitivity obtained on composite membranes of Si/micro PS and Si/macro PS with varying porosity on membrane sizes of 500 μm × 500 μm and 1000 μm × 500 μm. The points corresponding to zero percent porosity represent the sensitivity obtained on membranes of silicon alone. We can see the sensitivity of composite membrane with Si/micro PS is higher than that of Si/macro PS. The random structure of pores in micro PS makes the material spongier than the regular pore structure of macro PS increasing the deflection. This is also borne out by the nanoindentation measured Young's modulus on micro and macro PS with 70% porosity which were 5.51 and 7.4 GPa, respectively. It is also reported in literature that for a given porosity, a micro PS sample made from p-type silicon is less stiff than a meso PS sample made from p^+ silicon [175].

We can see that in both Si/micro PS and Si/macro PS composite membranes, the output voltages are linear with the applied pressure at pressures less than 1 bar. The sensors were also found to behave linearly at pressures less 1 bar for the other porosities [59]. We also observed the offset voltage is higher in composite membranes compared to single crystalline membranes. The higher offset voltage in Si/PS composite membrane implies that there is deformation of the composite membrane even without applied pressure and could be caused by internal stress developed during the formation of PS. The offset voltage increases exponentially with the increase in porosity in both types of membranes but for the same porosity, it is higher in the case of Si/micro PS than Si/macro PS for same porosity indicating that the formation stress is greater in the case of micro PS. The formation of PS by electrochemical etching develops a compressive stress due to lattice mismatch which makes the deformation. The

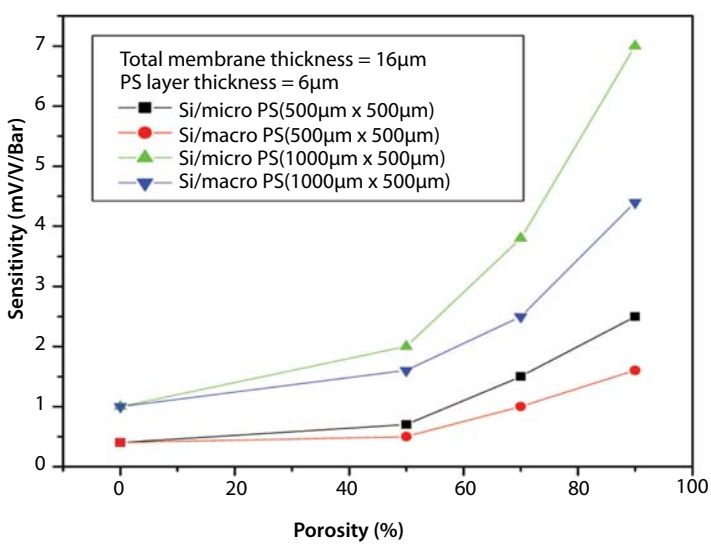

Figure 4.36 Sensitivity of Composite membranes with Si/micro PS and Si/macro PS for varying porosity.

measurement of compressive stress developed on the Si/PS composite membrane has been reported [180].

Figure 4.37 shows the deformations of silicon and composite membranes of Si/micro PS and Si/macro PS at high pressures applied from a nitrogen cylinder. In both types of composite membranes, the deformations are higher than that of silicon membranes and the magnitude of deformation increases with increase in porosity. Both types of composite membranes deform linearly at low pressures, but the linear range reduces with the increase in porosity. The range of linearity is larger in the case of Si/macro PS than that of Si/micro PS composite membranes – both showing irreversible deformation at higher pressures. We have seen that for the same porosity, Young's modulus of the macro PS is greater than that of micro PS. Also, the average pore diameter of macro PS is three orders higher than that of micro PS. It is possible that at high pressures, the walls of the pores collapse and come in contact with each other. The resulting surface adhesive forces continue to hold them together even after the removal of the applied pressure [181]. Thus, the macro PS with wider pores can withstand higher applied pressures. The improvement in the linear range of operation in Si/macro PS composite membrane pressure sensor with the formation of self-assembled monolayer has also been reported [182].

4.3.1.3 Temperature and Humidity Effects on Packaged Si/PS Composite Membrane Pressure Sensor

The fabricated pressure sensor devices were diced out and packaged into a TO 39 header [183]. The packaged pressure sensor has been mounted on a specially fabricated jig to apply pressure. A DC input voltage of 1V was given to the input terminals of the Wheatstone bridge on the pressure sensor and the output voltage from the pressure sensor was measured using a digital multimeter. Pressure was applied from a nitrogen cylinder. The applied pressure was varied using a control valve and measured by using

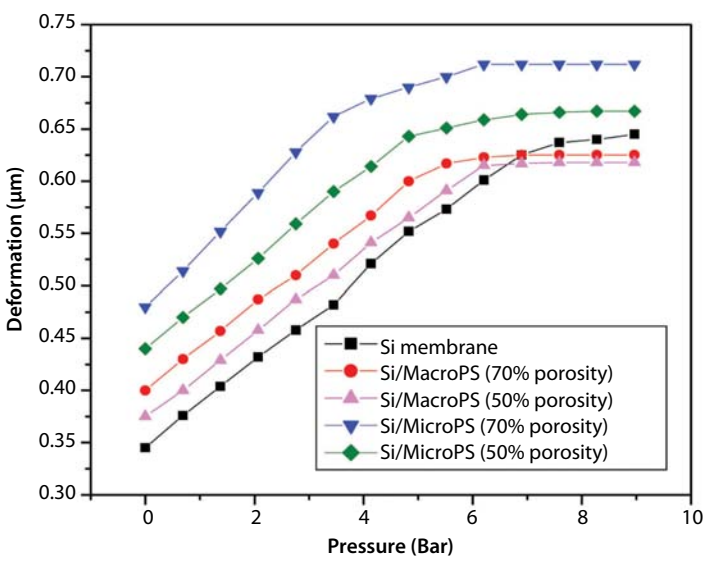

Figure 4.37 Deformation on silicon and composite membranes at high pressure range.

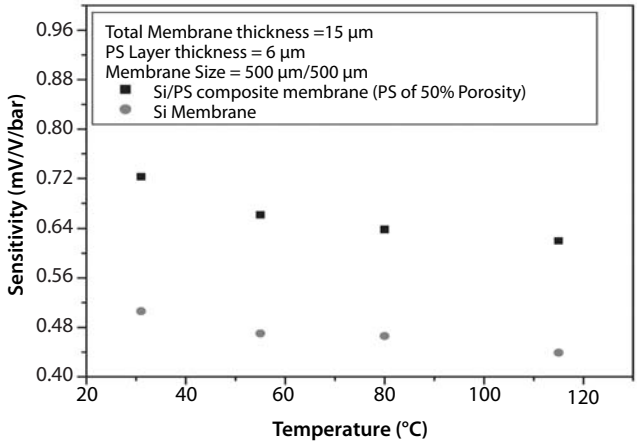

Figure 4.38 Sensitivity of silicon and Si/PS composite membranes for varying temperatures.

a digital pressure gauge. The packaged sensors were subjected to different temperatures ranging from 30 °C to 115 °C.

The measured sensitivity at different temperatures for silicon membrane and Si/PS composite membrane are given in Figure 4.38. Sensitivity decreases with temperature in both types of membrane and percentage change in sensitivity due to temperature variation from 30 °C to 115 °C is 14.25% for Si/PS composite membrane sensor and is 13.25% for Si membrane sensor. Hence, the effect of temperature on composite membrane is almost the same as that of silicon membrane and it is due to the change in resistance of polysilicon piezoresistors with temperature.

PS is very sensitive to humidity due to its high surface-to-volume ratio leading to greater adsorption [184,185]. In our devices, we can see that the wafer level (unpacked) devices are sensitive to humidity showing a reduction in the sensitivity. But the packaged device shows only slight variation in offset voltage and there is no change in sensitivity. Hence, there is no effect of humidity in packaged device since the porous side is sealed on the die mount with a strong adhesive and is not exposed to water vapor [186].

4.3.2 Pressure Sensors with Piezoresistive Effect of PS

Nanoporous Silicon being essentially nanocrystalline may have greater piezoresistivity than bulk monocrystalline silicon. Further, Young's Modulus of PS is less than that of bulk silicon. Both these factors, together, lead to higher pressure sensitivity of PS piezoresistor [187]. The idea is supported by the fact that PS is natural nanomaterial with silicon columns confined between silicon dioxide and voids and it has been observed theoretically and experimentally that in quantum-well structures formed by other semiconductors like GaAs [188], the sensitivity toward pressure is much greater compared to that of bulk material. Also, the sensitivity may be easily tailored by changing the porosity, uniformity and thickness of the PS layer. The piezoresistive coefficient has been estimated from experimental results for various thicknesses of the PS layer.

4.3.2.1 *Fabrication of the Device*

PS pressure sensors are fabricated in the following manner. On a P-type monocrystalline silicon wafer (100) of resistivity 1–3 ohm-cm, oxidation is done in a dry-wet–dry sequence to form a thick oxide (0.6 μm) layer. The sample is next micromachined by wet etchant at room temperature to the desired thickness. This is followed by PS formation by anodic etching method in a two-pond cell. The area of the PS layer is 2 mm × 2 mm. Contacts on top of PS layer are formed by vacuum evaporation of aluminum and its subsequent heat treatment at around 500 °C for about 40–45 s. Contact area is 1 mm × 1 mm. The back contact metallization is done by screen printing of silver aluminum paste and its subsequent firing at 700 °C for 45 s. The thickness of the PS layer has been restricted at 20 μm on a p-type wafer since it has been found that on increasing the thickness further, the porosity increases and fabrication of ohmic and stable metal contacts becomes difficult. Thus the bulk silicon gives mechanical support to the structure. Also, it provides the desired PS-silicon hetero junction needed for integrated temperature sensing and compensation. SEM and cross-sectional views of the PS sensor are shown in Figure 4.39(a) and (b). Sandwich contact geometry is chosen so that the current lines are forced to pass through PS in order to observe its electrical behavior on application of pressure. In the case of lateral contacts, the current lines pass almost entirely through the underneath bulk silicon, since PS is much more resistive compared to bulk silicon and hence the response of PS will be masked. The thickness of the PS layer has been restricted to 20 μm on a p-type wafer, since it has been found that on increasing the thickness further, the porosity increases and fabrication of ohmic and stable metal contacts becomes difficult.

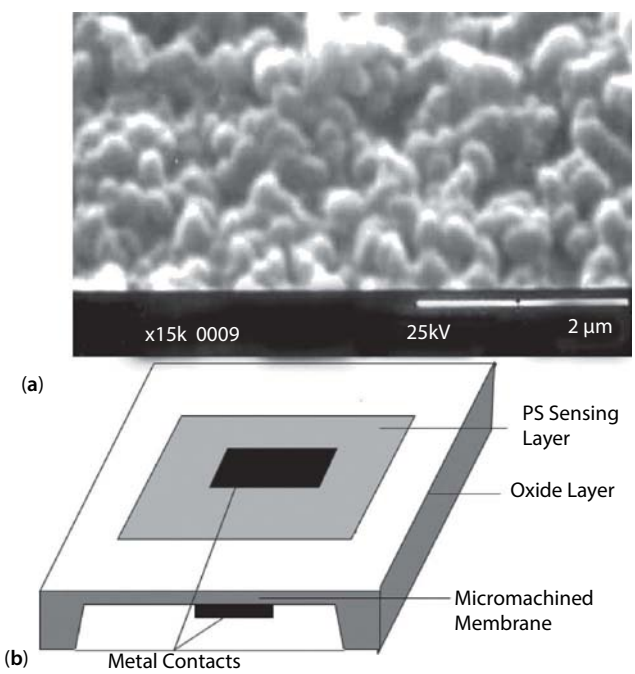

Figure 4.39 (a) SEM of porous silicon layer and (b) cross-sectional view of the sensor.

4.3.2.2 Experimental Results

On application of pressure on PS samples of various porosities and thicknesses, the following results were obtained, which are displayed in Figures 4.14 and 4.15. The results have been found to be highly reproducible. One observes from Figure 4.14 that the sensitivity increases with porosity. However, there is an optimum porosity required. In

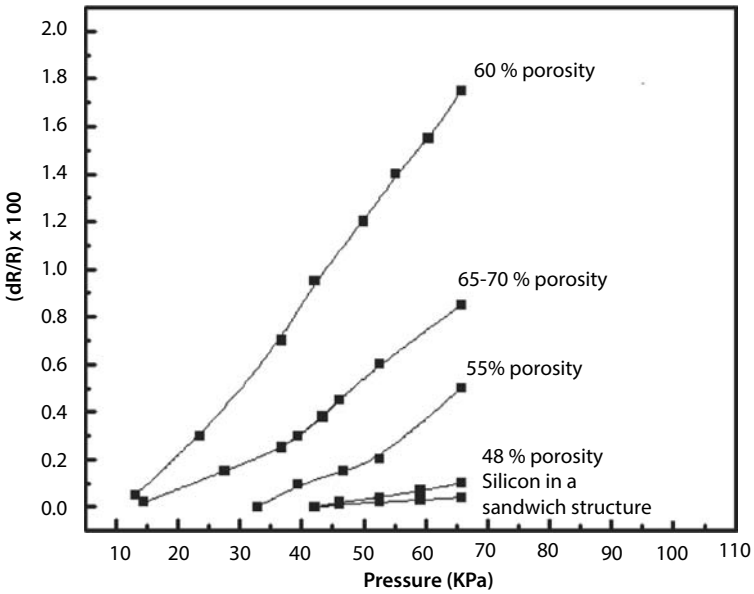

Figure 4.40 Variation of fractional change in resistance of porous silicon layer of thickness 20 μm and various porosities.

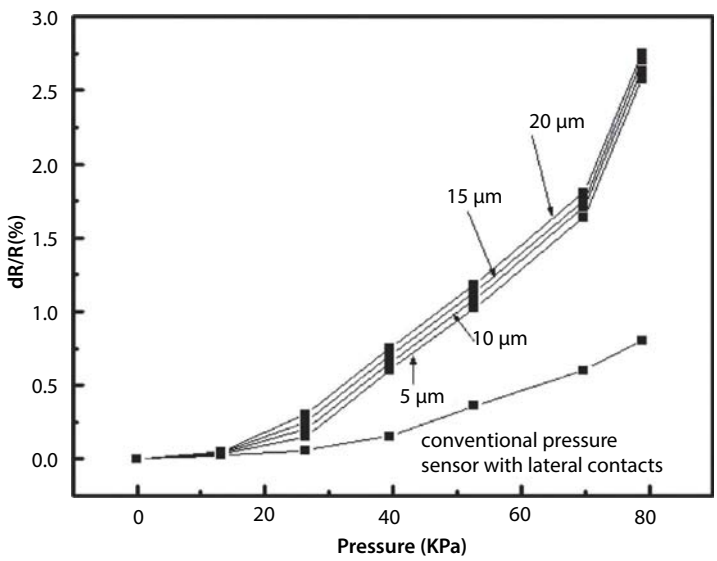

Figure 4.41 Fractional change in resistance for different thicknesses of porous silicon and a fixed porosity of 60% with affixed diaphragm of 100 μm.

this case, for a 100-μm-thick diaphragm, the optimum porosity is 60%. As the porosity increases, the conductivity decreases and the resistance increases. The carrier density (pnw) in the nanocrystallites will be affected by the quantum confinement, due to which the band gap of PS is enlarged, leading to a reduction in carrier density compared to that of bulk silicon (pb). The reduction in carrier density accompanied by the quantum-confinement effect leads to an increase in the piezoresistive coefficient [189]. However, porosity also affects the mobility of the carriers in the nanocrystallites, which becomes dominant above 65% porosity. As long as the porosity is below 60%, the decrease in mobility is not significant compared to the decrease in carrier concentration. Thus, the increase in piezoresistive coefficient, which depends only on carrier concentration, dominates over the increase in resistance, which results in a higher value of fractional change in resistance dR/R with increasing porosity (below 60%). When porosity exceeds 60%, the interconnecting silicon network is drastically reduced, leading to a significant reduction in its mobility, so that the resistance R increases at a much faster rate compared to the increase in dR, which ultimately causes the ratio dR/R to decrease.

4.3.2.3 Estimation of Piezoresistive Coefficient

The piezoresistive coefficient can be calculated from the fractional change in resistance R according to the following equation:

$$\frac{dR}{R} = \pi_l \sigma_t + \pi_t \sigma_l \tag{4.8}$$

where σ_l is the longitudinal stress, which is in the direction perpendicular to the surface of the diaphragm for sandwich metal configuration, σ_t is the transverse stress, and π_l and π_t are the longitudinal and transverse piezoresistive coefficients, respectively. The stress perpendicular to the surface of the diaphragm is negligible and can be ignored [84]. Thus, Equation (4.8) reduces to

$$\frac{dR}{R} = \pi_l \sigma_t \tag{4.9}$$

The transverse stress depends on the distance from the neutral axis and is given by [190]

$$\sigma_t = \frac{3}{4}\left(qz/h^3\right)[a^2(1+\gamma) - r^2(3+\gamma)] \tag{4.10}$$

where γ is Poisson's ratio of the composite medium, a is the radius of the diaphragm, r is the radial distance from the center of the diaphragm, z is the distance from the neutral line, q is the pressure applied, and h is the thickness of the diaphragm. Poisson's ratio of the composite medium is calculated from the following equation [190]:

$$K_{eff} = \frac{E_{eff}}{2(1-2\gamma)} \tag{4.11}$$

where K_{eff} is the composite bulk modulus, and E_{eff} is the composite Young's modulus, given by

$$K_{eff} = \frac{(V_{Ps} + V_{Si})K_{Si}K_{Ps}}{V_{Ps}V_{Si} + K_{Si}K_{Ps}} \tag{4.12}$$

$$E_{eff} = \frac{(V_{Ps} + V_{Si})K_{Si}K_{Ps}}{V_{Ps}V_{Si} + K_{Si}K_{Ps}} \tag{4.13}$$

where L_{Ps}, V_{Ps} are the length and volume of the PS layer, respectively, L_{Si}, V_{Si} are the length and volume of the silicon layer, respectively, E_{Si}, K_{Si} are Young's modulus and bulk modulus of silicon, respectively, and E_{Ps}, K_{Ps} are Young's and bulk modulus of PS, respectively, for 60% porosity [84]. The variation of Young's modulus, bulk modulus and Poisson's ratio with different thicknesses of PS layer and a diaphragm thickness of 100 μm have been estimated and reported [191]. Thus, the change in sensitivity with thickness can be attributed to the change in Poisson's ratio. The total resistance R of the diaphragm is given by

$$R = R_{Ps} + R_{Si} \tag{4.14}$$

where R_{Ps} is the resistance of the PS layer at 60% porosity, and R_{Si} is the resistance of the silicon. The change in resistance dR is given by

$$dR = dR_{Ps} + dR_{Si} = R_{Ps}\pi_{Psl}\sigma_{Pst} \pm R_{Si}\pi_{Sil}\sigma_{Sit} \tag{4.15}$$

where $\sigma_{Pst,}$ and σ_{Sit} are the stresses on PS and silicon layer, respectively, and they depend on the thickness of the PS layer. The ± sign indicates that the resistance of silicon can increase or decrease, depending on whether it is above or below the neutral axis. The part of the silicon above the neutral axis experiences compressive stress, and that below the neutral axis experiences tensile stress. Thus, from Equations (4.8) through (4.15) and from the experimental values of the fractional change in resistance we can calculate the piezoresistive coefficient for different porosities of the PS layer, as shown in Figure 4.42.

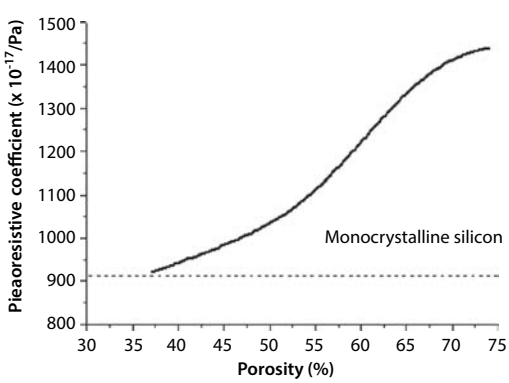

Figure 4.42 Variation of piezoresistive coefficient with porosity of porous silicon layer at constant thickness of PS layer.

The sensitivity of a PS membrane toward pressure has been studied and observed to be three times greater than that of monocrystalline silicon, since there is the possibility of improvement in piezoresistance due to quantum confinement in the PS nanostructure.

4.4 Conclusion

In this paper, we have discussed the viability of PS for applications in MEMS and sensors. PS can be easily derived from silicon with good control over the thickness of the porous layer, the porosity and the pore size. The porosity determines the mechanical and electrical properties of the material. While the large surface-to-volume ratio makes it attractive for sensor applications, it also renders the material to be unstable and prone to surface effects. However, proper packaging and surface treatments can mitigate these problems to a large extent facilitating the exploitation of its unique properties.

References

1. D. R. Turner, *Journal of Electrochemical Society,* vol. 105, 7, pp. 402–408, 1958.
2. G. Hodes, *Electrochemistry of Nanomaterials*, Wiley-VCH, Weinheim, 2001.
3. V. Lehmann, *Electrochemistry of silicon – Instrumentation, Science, Materials and Applications*, Wiley-VCH, Weinheim, 2002.
4. K. Imai, *Solid State Electronics*, vol. 24, pp. 159–164,1981.
5. K. Imai and H. Unno, *IEEE Transaction on Electron Devices*, vol. 31, 3, pp. 297–302, 1984.
6. L. T. Canham, *Applied Physics Letters,* 57, 10, pp. 1046–1048, 1990.
7. V. Lehmann and U. Gosele, *Applied Physics Letters*, vol. 58, 8, pp. 856–858, 1991.
8. A. Halimaoui, C. Oules, G. Bomchil, A. Bsiesy, F. Gaspard, R. Herino, M. Ligeon and F. Muller, *Applied Physics Letters*, 59, 3, pp. 304–306, 1991.
9. N. Koshida and H. Koyama, *Applied Physics Letters*, 60, 3, pp. 347–349, 1992.
10. P. Steiner, F. Kozlowski and W. Lang, *IEEE Electron Device Letters*, vol. 14, 70, pp. 317–319, 1993.
11. A. Bsiesv, F. Muller, M. Ligeon, F. Gaspard, R. Herino, R. Romestain and J. C. Vial, *Applied Physics Letters*, 71, pp. 637–640, 1993.
12. S. Osscini, L. Pavesi and F. Priolo, *Light Emitting Silicon for Microphotonics*, 1st Ed., Springer Publications, 2004.
13. A. Bsiesy, F. Gaspard, R. Herino, M. Ligeon, F. Muller and J. C. Oberlin, *Journal of The Electrochemical Society*, vol. 138, 11, pp. 3450–3456, 1991.
14. A. M. Rossi, G. Amato, V. Camarchia, L. Boarnio and S. Borini, *Applied Physics Letters*, 78, 20, pp. 3003–3005, 2001.
15. R. C. Anderson, R. S. Muller and C. W. Tobias, *Sensors and Actuators A*, vol. 23, pp. 835–839, 1990.
16. J. Drott, L. Rosengren, K. Lindstrom and T. Laurell, *Thin Solid Films*, 330, pp. 161–166, 1998.
17. S. P. Michael and J. M. Buriak, *Advanced Materials*, vol. 12, 12, pp. 859–869, 2000.
18. R. R. K. Reddy, A. Chadha and E. Bhttacharya, *Biosensors & Bioelectronics*, 16, pp. 313–317, 2001.

19. U. Gruning, V. Lehmann, S. Ottow and K. Busch, *Applied Physics Letters*, 68, 6, pp. 747–749, 1996.
20. M. Thonissen, S. Billat, M. Kruger, H. Luth, M. G. Berger, U. Frotscher and U. Rossow, *Journal of Applied Physics*, 80, 5, pp. 2990–2993, 1996.
21. L. Seals, J. L. Gole, L. A. Tse and P. J. Hesketh, *Journal of Applied Physics*, vol. 91, 4, pp. 2519–2523, 2002.
22. E. Galeazzo, H. E. M. Peres, G. Santos, N. Peixoto and F. J. Ramirez-Fernandez, *Sensors and Actuators B*, 93, pp. 384–390, 2003.
23. S. E. Lewis, J. R. DeBoer, J. L. Gole and P. J. Hesketh, *Sensors and Actuators B*, 110, pp. 54–65, 2005.
24. V. Lehmann, IEEE The ninth annual international workshop on Micro Electro Mechanical Systems, MEMS'96, San Deigo, CA, USA, pp. 1–6, 1996.
25. U. M. Mescheder, A. Kovacs, W. Kronast, I. Barsony, M. Adam and Cs. Ducso, Proceedings of the 1st IEEE conference on nanotechnology 2001, Maui, HI, USA, pp. 483–488, 2001.
26. H. Foll, M. Christophersen, J. Carstensen and G. Hasse, *Materials Science and Engineering R*, 39, pp. 93–141, 2002.
27. Y. Ding, Z. Liu, L. Liu and Z. Li, *Microsystem Technologies*, 9, pp. 470–473, 2003.
28. K. Takahashi, I. Tatsuya, D. Yoichiro, N. Kunihito and K. Masahiro, Proc. of the 23rd Sensor Symposium, Kagawa, Japan, pp. 513–516, 2006.
29. Sukumar Basu and Jayita Kanungo, Nanocrystalline Porous Silicon, Crystalline Silicon – Properties and Uses, http://www.intechopen.com/books/crystalline-silicon-properties-and-uses/nanocrystalline-porous-silicon 2011.
30. W. Kronast, B. Muller, W. Siedel and A. Stoffel, *Sensors and Actuators*, A87, pp. 188–193, 2001.
31. O. Garel, C. Breluzeau, E. Dufour-Gergam, A. Bosseboeuf, B. Belier, V. Mathet and F. Verjus, *Journal of Micromechanics and Microengineering*, 7, 7, p. 164, 2007.
32. A. Santos, Helder, L. M. Bimbo, Luis Lehto Vesa-Pekka, A. J. Airaksinen, J. Salonen and J. Hirvonen, *Current Drug Discovery Technologies*, 8, 3, pp. 228–249, 2011.
33. Imai, Unno and Takaoka, *Journal of Crystal Growth*, 63, 3, pp. 547–553, 1983.
34. T. Yonehara and Kiyofumi Sakaguchi, *JSAP International,* 4, pp. 10–16, 2001.
35. H. Ohji, P. J. Trimp and P. J. French, Technical Digest of the Eleventh IEEE International Workshop on Micro Electro Mechanical Systems (MEMS-98), Heidelberg, Germany, pp. 246–250, 1998.
36. V. Lehmann and H. Foll, *Journal of The Electrochemical Society*, 137, 2, pp. 653–659, 1990.
37. G. R. Bassam, M. H. Mouhsen and M. A. W. Shanon, *Journal of Engineering & Technology*, 28, 9, pp. 1728–1734, 2010.
38. V. Lehmann, W. Honlein, H. Reisinger, A. Spitzer, H. Wendt and J. Willer, *Thin Solid Films*, 276, pp. 138–142, 1996.
39. Cs. Dusco, E. Vazsonyi, M. Adam, I. Szabo, I. Barsony, J. G. E. Gardeniers, A. V. Berg, *Sensors and Actuators A*, 60, pp. 235–239, 1997.
40. Z. M. Rittersma, A. Splinter, A. Bodecker and W. Benecke, *Sensors and Actuators B*, 68, pp. 210–217, 2000
41. G. Lammel and Ph. Renaud, *Sensors and Actuators,* 85, pp. 356–360, 2000
42. T. E. Bell, P. T. J. Gennissen, D. DeMunter and M. Kuhl, *Journal of Micromechanics and Microengineering*, 6, pp. 361–369, 1996.
43. A. Kovacs and U. Mescheder, Proceedings of the Transducers 01, Munich, Germany, June 2001, pp. 620–623, 2001.
44. G. Petra and R. Klemens, *Materials*, 3, pp. 943–998, 2010.
45. R. R. K. Reddy, R. I. Basu, Enakshi Bhttacharya and Anju Chadha, *Current Applied Physics*, 3, pp. 155–161, 2003.

46. F. Ronkel and J. W. Schultze, *Journal of Porous Materials*, 7, pp. 11–16, 2000.
47. R. L. Smith and S. D. Collins, *Journal of Applied Physics*, 71, 8, pp.R1–R22, 1992.
48. Unagami, *Journal of The Electrochemical Society: Solid State Science and Technology*, vol. 127, 2, pp. 476–483, 1980.
49. M. J. J. Theunissen, *Journal of The Electrochemical Society: Solid-State Science and Technology*, vol. 119, 3, pp. 351–360, 1972.
50. M. I. J. Beale, N. G. Chew, M. J. Uren, A. G. Cullis and J. D. Benjamin, *Applied Physics Letters,* vol. 46, 1, pp. 86–88, 1985.
51. J. Branebjerg, C. J. M. Eijkel, J. G. E. Gardeniers and F. C. M. Van de Pol, Proc. MEMS IEEE, Nara, Japan, pp. 221–226, 1991.
52. V. Lehmann, *Journal of The Electrochemical Society*, vol. 140, 10, pp. 2836–2843, 1993.
53. P. K. Eric and P. A. Kohl, *Journal of The Electrochemical Society*, vol. 141, 4, pp. 1006–1013, 1994.
54. A. Vyatkin, V. Starkov, V. Tzeitlin, H. Presting, J. Konle and U. Konig, *Journal of The Electrochemical Society*, 149, 1, pp.G70–G76, 2002.
55. Lust Sandra and Claude Levy–Clement, *Journal of The Electrochemical Society*, 149, 6, pp. C338–C344, 2002.
56. E. V. Astrova, T. N. Borovinskaya, A. V. Tkachenko, S. Balakrishnan, T. S. Perova, A. Rafferty and Y. K. Gunko, *Journal of Micromechanics and Microengineering*, 14, pp. 1022–1028, 2004.
57. S. Ottow, V. Lehmann and H. Foll, *Journal of Applied Physics A*, 63, pp. 153–159, 1996
58. L. Sujatha and E. Bhattacharya, SPIE Photonics West 2008, 19–24 January 2008, San Jose, California, USA, pp. 68820H1–7, 2008.
59. L. Sujatha, V. S. Kale and E. Bhattacharya, *Journal of Micro/Nanolithography, MEMS, and MOEMS*, vol. 8, pp. 033070, 2009.
60. L. Sujatha and Enakshi Bhattacharya, International Symposium for Research Scholars on Metallurgy, Materials Science and Engineering (ISRS-2006), IITM, pp. 734–739, 2006.
61. P. Kumar and Patrick Huber, *Journal of Nanomaterials*, vol. 2007, Article ID 89718, pp. 1–4, 2007.
62. V. Labunov, I. Baranov and V. Bondarenko, Investigation of porous silicon formation during anodic treatment in aqueous HF, *Thin Solid Films*, 64, pp. 479–483, 1979.
63. X. Zhang Gregory, *Modern Aspects of Electrochemistry*, 39, Vayenas CG, White, RE, Springer, New York XXI, pp. 65–133, 2005.
64. S. Ronnebeck, S. Ottow, J. Cartensen and H. Foll, *Journal of Porous Materials*, 7, pp. 353–356, 2000.
65. V. P. Parkhutik, L. K. Glinenko and V. A. Labunov, *Surface Technology*, 20, pp. 265–277, 1983.
66. N. Tas, T. Sonnenberg, H. Jansen, R. Letenberg and M. Elwenspoek, *Journal of Micromechanics and Microengineering*, 6, p. 385, 1996.
67. R. L. Alley, P. Mai, K. Komvopoulos and R. T. Howe, Proc. 7th Int. Conf. On Solid-State Sensors and Actuators, Transducers '93, Yokohama, p. 288, 1993.
68. E. Bhattacharya, L. H. A. Rani, U. V. Babu, P. R. S. Rao, K. N. Bhat and J. Martin, *Physica Status Solidi (a)*, vol. 202, pp. 1482–1486, 2005.
69. A. Salis, S. Setzu, M. Monduzzi and M. Guido, *Biosensors-Emerging Materials and Applications*, InTech. Publisher, Chapter 17, pp. 334–352, 2011.
70. S. Dhanekar and S. Jain, *Biosensors and Bioelectronics*, vol. 41, pp. 54–64, 2013.
71. G. Palestino, R. Legros, V. Agarwal, E. Perez and C. Gergely, *Sensors and Actuators B: Chemical*, vol. 135, pp. 27–34, 2008.
72. C. Steinhauer, A. Ressine, G. M. Varga, T. Laurell, C. A. K. Berrebaeck and C. Wingren, *Analytical Biochemistry*, vol. 341, pp. 204–213, 2005.

73. J. Saarinen, S. M. Weiss, P. M. Fauchet and J. E. Sipe, *Journal of Applied Physics*, vol. 104, p. 013103–7, 2008.
74. J. Das, S. Dey, S. M. Hossain, Z. M. Rittersma and H. Saha, *IEEE Sensors*, vol. 3, pp. 414–420, 2003.
75. M. Archer, M. Christophersen and P. M. Fauchet, *Sensors and Actuators B*, vol. 106, pp. 347–357, 2005.
76. J. Z. Wallner, N. Nagar, C. R. Friedrich and P. L. Bergstrom, *Physica Status Solidi (a)*, vol. 204, pp. 1327–1331, 2007.
77. J. Z. Wallner and P. L. Bergstrom, *Physica Status Solidi (a)*, vol. 204, pp. 1469–1473, 2007
78. H. Contopanagos, D. N. Pagonis and A. G. Nassiopoulou, *Physica Status Solidi (a)*, vol. 250, pp. 2548–2551, 2008.
79. C. A. Prestidge, T. J. Barnes, A. Mierczynska-Vasilev, I. Kempson , F. Peddie, C. Barnett, *Physica Status Solidi (a)*, vol. 205, pp. 311–315, 2008.
80. A. Jane, R. Dronov, A. Hodges and N. H. Voelcker, *Trends in Biotechnology*, vol. 27, pp. 230–239, 2009.
81. K. A. Kilian, T. Boecking and J. J. Gooding, *Chemical Communications*, vol. 6, pp. 630–640, 2009.
82. B. Gupta, Y. Zhu, B. Guan, P. J. Reece and J. J. Gooding, Analyst**,** vol. 138, pp. 3593–3615, 2013.
83. C. RoyChaudhuri, J. Kanungo, R. D. Das, S. K. Dutta, S. RoyChaudhuri, S. Majhi, and H. Saha, *Lecture Notes Electrical Engineering*, Springer–Verlag, vol. 20, pp. 101–116, 2008.
84. N. V. Lavrik, M. J. Sepaniak and P. G. Datskos, *Review of Scientific Instruments*, vol. 75, pp. 2229–2253, 2004.
85. M. D. Antonik, N. P. D. Costa and J. H. Hoh, *IEEE Engineering in Medicine and Biology Magazine*, vol. Mar./Apr., pp. 66–72, 1997.
86. R. Raiteri, M. Grattarola, H-J. Butt and P. Skládal, *Sensors and Actuators B*, vol. 79, pp. 115–126, 2001.
87. A. W. McFarland, M. A. Poggi, M. J. Doule, L. A. Bottomley and J. S. Colton, *Applied Physics Letters,* vol. 87, pp. 053505-1–053505-3, 2005.
88. M. Spletzer, A. Raman, A. Q. Wu, X. Xu and R. Reifenberger, *Applied Physics Letters,* vol. 88, pp. 254102-1–254102-3, 2006.
89. S. Cherian and T. Thundat, *Applied Physics Letters,* vol. 80, pp. 2219–2221, 2002.
90. L. M. Lechuga, J. Tamayo and M. Alvarez *et al.*, *Sensors and Actuators B*, vol. 118, pp. 2–10, 2006.
91. Cahnam, "Properties of Porous Silicon," ser. Emis Data Review Series, L. T. Cahnam, Ed., N18, pp. 371–376, 1997.
92. J. Drott, K. Lingstrom, L. Rosengren and K. Laurell, *Journal of Micromechanics and Microengineering*, vol. 7, pp. 14–23, 1997.
93. N. E. Chayen, E. Saridakis, A. El-Bahar and Y. Nemirovsky, *Journal of Molecular Biology*, vol. 312, pp. 591–595, 2001.
94. M. Thust, M. J. Schoning, S. Prohnhoff, R. Arens-Fisher, P. Kordos and H. Luth, *Measurement Science and Technology*, vol. 7, pp. 26–29, 1996.
95. S. Stolyarova, E. Baskin, N. E. Chayen and Y. Nemirovsky, *Physica Status Solidi (a)*, vol. 202, pp. 1462–1466, 2005.
96. S. Stolyarova, S. Cherian, R. Raiteri, J. Zeravik, P. Skladal and Y. Nemirovsky, *Sensors and Actuators B*, vol. 131, pp. 509–515, 2008.
97. S. Kalem and O. Yavuzcetin, *Optics Express*, vol. 6,pp. 7–11, 2000.
98. M. Saadoun, N. Mliki, H. Kaabi, K. Daoubi, B. Bessais, H. Ezzaouia and R. Bennaceur, *Thin Solid Films*, vol. 405, pp. 29–34, 2002.

99. E. A. deVasconcelos, EF da Silva, BECA dos Santos, WM de Azevedo, J. A. K. Freire Jr., *Physica Status Solidi (a)*, vol. 202, pp. 1539–1542, 2005.
100. Protiveris Ltd., 15010, Broschart Road, Rockville, MD 20850, United States
101. S. Stolyarova, S. Weiss, M. Levy and Y. Nemirovsky, *Physica Status Solidi C*, vol. 4, p. 2054, 2007.
102. Veeco Optical Profiler, model Wyko NT1100D, http://www.veeco.com.
103. R. E. Fernandez, S. Stolyarova, A. Chadha, E. Bhattacharya and Y. Nemirovsky, *IEEE Sensors Journal*, vol. 9, pp. 1660–1666, 2009.
104. S. Bhat and E. Bhattacharya, *Journal of Micro/Nanolithography, MEMS, and MOEMS*, vol. 6, pp. 043013–043019, 2007.
105. E. A. de Vasconcelos, J. A. K. Freire, V. N. Freire, B. E. C. A. dosSantos, W. M. de Azevedo and E. F. da Silva, Jr, *Physica Status Solidi (c)*, vol. 1, pp. S287–S290, 2004.
106. R. E. Fernandez, E. Bhattacharya and A. Chadha, *Applied Surface Science*, vol. 254, pp. 4512–4519, 2008.
107. http://mens-health.health-cares.net/triglycerides.php.
108. Somasekara Bhat, PhD thesis, IIT Madras, India, 2008.
109. S. S. Bhat, R. E. Fernandez, S. Stolyarova and E. Bhattacharya, 8th World Congress on Computational Mechanics (WCCM8) and 5th. European Congress on Computational Methods in Applied Sciences and Engineering (ECCOMAS 2008), June 30–July 5, 2008.
110. M. Saadoun, N. Mliki, H. Kaabi, K. Daoudi, B. Bessais, H. Ezzaouia and R. Bennaceur, *Thin Solid Films*, vol. 405, 1–2, pp. 29–34, 2002.
111. D. Herman, M. Gaitan and D. DeVoe, MEMS Test Structures for Mechanical Characterization of VLSI Thin Films. Proceedings of SEM Conference, Portland, Oregon, pp. 1–5, June 4–6, 2001.
112. RoyChaudhuri C and R. D. Das, *Sensors and Actuators A*, vol. 157, pp. 280–289, 2010.
113. S. M. Radke and EC ALocilja, *IEEE Sensors Journal*, vol. 4, pp. 434–440, 2004.
114. O. Laczka, E. Baldrich, F. X. Munoz and F. J. D. Campo, *Analytical Chemistry*, vol. 80, pp. 7239–7247, 2008.
115. M. M. Varshney, Y. Li, B. Srinivasan and S. Tung, *Sensors and Actuators B*, vol. 128,pp. 99–107, 2007.
116. Z. Zou, S. Lee and C. H. Ahn, *IEEE Sensors Journal*, vol. 8, pp. 527–535, 2008.
117. Z. Zou, J. Kai, M. J. Rust, J. Han, C. H. Ahn, *Sensors and Actuators A*, vol. 136, pp. 518–526, 2007.
118. L. A. Balagurov, S. C. Bayliss, V. S. Kasatochkin, E. A. Petrova, B. Unal and D. G. Yarkin, *Journal of Applied Physics,* vol. 90, p. 1, 2001.
119. S. Dhar and S. Chakraborti, *Applied Physics Letters*, vol. 68, p. 1392, 1996.
120. H. Saha and C. Pramanik, *Materials and Manufacturing Processes*, vol. 21, p. 239, 2006.
121. D. R. Das, C. RoyChaudhuri, S. Maji, S. Das and H. Saha, *Biosensors and Bioelectronics*, vol. 24, pp. 3215–3222, 2009.
122. L. H. Dengll, S. H. Karagiannoglou, W. I. Sakkas and J. C. Barbenel, Proceedings of the Second Joint EMBS/BMES Conference IEEE, pp. 1667–1668, 2002.
123. D. R. Das, S. Maji, S. Das and C. RoyChaudhuri, *Applied Surface Science*, vol. 256, pp. 5867–5875, 2010.
124. D. R. Das, A. Dey, S. Das and C. RoyChaudhuri, *IEEE Sensors*, vol. 11, pp. 1242–1252, 2011.
125. D. R. Das, N. Mondal, S. Das and C. RoyChaudhuri, *IEEE Sensors*, vol. 12, pp. 1868–1877, 2012.
126. K. R. N. Reddy, C. S. Reddy and K. Muralidharan, *Food Microbiology*, vol. 26, p. 27, 2009.
127. S. Park, H. C. Kim and T. D. Chung, *Analyst*, vol. 137, p. 3891, 2012.

128. P. Kalita, J. Singh, M. K. Singh, P. R. Solanki, G. Sumana and B. D. Malhotra, *Applied Physics Letters*, vol. 100,p. 093702, 2012.
129. P. Actis, O. Jejelowo and N. Pourmand, *Biosensors and Bioelectronics*, vol. 26, p. 333, 2010.
130. M. Campas, D. Garibo and B. P. Simon, *Analyst*, vol. 137, p. 1055, 2012.
131. G. Bacher, S. Pal, L. Kanungo and S. Bhand, *Sensors and Actuators B*, vol. 168, p. 223, 2012.
132. H. Ghosh and C. RoyChaudhuri, *Applied Physics Letters*, vol. 102, p. 243701–4, 2013.
133. M. Archer, M. Christophersen, P. M. Fauchet, *Biomedical Microdevices*, vol. 6, pp. 203–211, 2004.
134. V. Vamvakaki and N. A. Chaniotakis, *Electroanalysis*, vol. 20, pp. 1845–1850, 2008.
135. P. Bergveld, *IEEE Transactions on Biomedical Engineering*, vol. 17, p. 70, 1970.
136. P. Bergveld, *IEEE Transactions on Biomedical Engineering*, vol. 19,p. 342, 1972.
137. W. M. Siu and R. S. C. Cobbold, *IEEE Transactions on Electron Devices*, vol. 26, p. 1805, 1979.
138. I. R. Lauks and J. N. Zemel, *IEEE Transactions on Electron Devices*, vol. 26, p. 1959, 1979.
139. P. R. Barabash and R. S. C. Cobbold, *IEEE Transactions on Electron Devices*, vol. 29, p. 102, 1982.
140. L. Bousse, N. F. De Rooij and P. Bergveld, *IEEE Transactions on Electron Devices*, vol. 30, p. 1263,1983.
141. R. R. K. Reddy, I. Basu, E. Bhattacharya and A. Chadha, *Current Applied Physics*, 3, pp. 155–161, 2003.
142. R. R. K. Reddy, A. Chadha and E. Bhattacharya, *Biosensors and Bioelectronics*, 16, pp. 313–317, 2001.
143. C. Cane, I. Gracia and C. A. Merlos, *Microelectronics Journal*, 28, p. 389, 1997.
144. B. Indranil, R. Venkata Subramanian, M. Arun, A. M. Kayastha, A. Chadha and E. Bhattacharya, Sensors and Actuators B: Chemical**,** vol. 107, 1, pp. 418–423, 2005.
145. Arun Mathew, Ganesh Pandian, Enakshi Bhattacharya and Anju Chadha, *Physica Status Solidi (a)*, vol. 206, 6, pp. 1369–1373, 2009.
146. H. Vemulachedu, R. E. Fernandez, E. Bhattacharya and A. Chadha, *Journal of Materials Science: Materials in Medicine*, vol. 20, pp. S229–S234, 2009.
147. M. Thust, M. J. Schoning, S. Frohnhoff, R. Arens-Fischer, P. Kordos and H. Luth, *Measurement Science and Technology*, vol. 7, pp. 26–29, 1996.
148. R. R. K. Reddy, I. Basu, E. Bhattacharya and A. Chadha, *Current Applied Physics*, vol. 3, pp. 155–161, 2003.
149. R. R. K. Reddy, A. Chadha and E. Bhattacharya, *Biosensors and Bioelectronics*, vol. 16, pp. 313–317, 2001.
150. M. J. Schöning, F. Ronkel, M. Crott, M. Thust, J. W. Schultze, P. Kordos and H. Lüth, *Electrochimica Acta*, vol. 42, pp. 3185–3193, 1997.
151. S. Setzu, S. Salis, V. Demontis, A. Salis, M. Monduzzi and G. Mula, *Physica Status Solidi A*, vol. 204, pp. 1434–1438, 2007.
152. M. J. Song, D. H. Yun, J. H. Jin, N. K. Min and S. I. Hong, *Japanese Journal of Applied Physics*, vol. 45, pp. 7197–7202, 2006.
153. M. J. Schöning, A. Kurowski, M. Thust, P. Kordos, J. W. Schultze and H. Lüth, *Sensors and Actuators B*, vol. 64, pp. 59–64, 2000.
154. A. Simonis, C. Ruge, M. Müller-Veggian, H. Lüth and M. J. Schöning, *Sensors and Actuators B*, vol. 91, pp. 21–25, 2003.
155. G. A. Melikjanyan and K. S. Martirosyan, *Armenian Journal of Physics*, vol. 4, pp. 225–22, 2011.
156. L. J. García and M. R. J. Palma, *Sensors and Actuators B*, vol. 126, pp. 82–90, 2007.

157. J. E. Lugo, M. Ocampo, A. G. Kirk, D. V. Plant and P. M. Fauchet, *Journal of New Materials for Electrochemical Systems*, vol. 10, pp. 113–116, 2007.
158. J. H. Jin, E. C. Alocilja and D. L. Grooms, *Journal of Porous Materials*, vol. 17, pp. 169–176, 2010.
159. R. Sánchez, G. D. Canizares, M. Manso, I. Preda, V. T. Costa, A. Gutierrez, L. Soriano and R. J. M. Palma, *Current Nanoscience*, vol. 7, pp. 178–182, 2011.
160. D. Zhang and E. C. Alocilja, *IEEE Sensors Journal*, vol. 8, pp. 775–780, 2008.
161. O. Meskini, A. Abdelghani, A. Tlili, R. Mgaieth, N. Jaffrezic-Renault and C. Martelet, *Talanta*, vol. 71, pp. 1430–1433, 2007.
162. C. A. Betty, R. Lal, D. K. Sharma, J. V. Yakhmi and J. P. Mittal, *Sensors and Actuators B*, vol. 97, pp. 334–343, 2004.
163. C. A. Betty, R. Lal, J. V. Yakhmi and S. K. Kulshreshtha, *Biosensors and Bioelectronics*, vol. 22, pp. 1027–1033, 2007.
164. C. A. Betty, R. Lal and J. V. Yakhmi, *Electrochimica Acta*, vol. 54, pp. 3781–3787, 2009.
165. M. J. Song, D. H. Yun and S. I. Hong, *Bioscience, Biotechnology, and Biochemistry*, vol. 73, pp. 474–478, 2009.
166. J. H. Jin, S. I. Hong and N. K. Min, *Journal of Porous Materials*, vol. 8, pp. 1593–1597, 2008.
167. D. Yun, M. J. Song, S. Hwang and S. I. Hong, *Japanese Journal of Applied Physics*, vol. 51, p. 06FG02, 2012.
168. S. Tembe, P. S. Chaudhari, S. V. Bhoraskar, S. F. D'Souza and M. S. Karve, *IEEE Sensors Journal*, vol. 8, pp. 1593–1597, 2008.
169. M. J. Song, D. H. Yun, N. K. Min and S. I. Hong, *Journal of Bioscience and Bioengineering*, vol. 103, pp. 32–37, 2007.
170. N. Samanta, O. Kundu and C. RoyChaudhuri, *IEEE Sensors*, vol. 13, pp. 4716–4724, 2013.
171. C. Maedler, S. Erramilli, L. J. House, M. K. Hong and P. Mohanty, *Applied Physics Letters*, vol. 102, p. 043112(1–4), 2013.
172. Bosch Research Info. (2003) 1, http://researchinfo.bosch.com/en/research/download/briE1_2003.pdf.
173. Adachi T and Sumio Sakka, *Journal of Materials Science*, 25, pp. 4732–4737, 1990.
174. R. J. M. Da Fonseca, J. M. Saurel, A. Foucaran, J. Camassel, E. Massone, T. Taliercio and Y Boumaiza, *Journal of Materials Science*, 30, pp. 35–39, 1995.
175. D. Bellet, P. Lamagnere, A. Vincent and Y. Brechet, *Journal of Applied Physics*, 80, 7, pp. 3772–3776, 1996.
176. L. Sujatha and E.i Bhattacharya, *Journal of Micromechanics and Microengineering*, 17, pp. 1605–1610, 2007.
177. Ch. Populaire, B. Remaki, V. Lysenko, D. Barbier, H. Artmann and T. Pannek, *Applied Physics Letters,* vol. 83, 7, pp. 1370–1372, 2003.
178. S. D. Senturia, *Microsystem Design,* Kluwer, Dordrecht, 2001.
179. K. N. Bhat and E. Bhattacharya, Proc. Int. Symp. Smart Materials and Systems, Chennai, pp. 41–51, 2004.
180. L. Sujatha and E. Bhattacharya, International Workshop on Physics of Semiconductor Devices IWPSD 2007 at Indian Institute of Technology Bombay, pp. 737–739, 2007.
181. A. S. Tadigadapa, Private communication, 2007.
182. L. Sujatha, R. Goswami and E. Bhattacharya, SPIE MOEMS-MEMS, San Francisco, USA, pp. 7592–31, 2010.
183. S. V. Kale, M.Tech. Project Report, Indian Institute of Technology Madras, 2008.
184. V. Strikha, V. Skryshevsky, V. Polishchuk, E. Souteyrand and J. R. Martin, *Journal of Porous Materials*, 7, pp. 111–114, 2000.

185. E. J. Connolly, G. M. OHalloran, H. T. M. Pham, P. M. Sarro and P. J. French, *Sensors and Actuators A*, 99, pp. 25–30, 2002.
186. L. Sujatha, V. S. Kale and E. Bhattacharya, International Conference on MEMS (ICMEMS) at IIT Madras, pp. 1–4, 2009.
187. C. Pramanik and S. Hiranmay, *IEEE Sensors Journal*, vol. 6, 2, pp. 301–309, 2006.
188. K. L. Kolokolov, A. M. Savin, S. D. Benrslavski, N. Ya. Minima and O. P. Hansen, *Physical Review B*, vol. 59, p. 7537, 1999.
189. T. Toriyama and S. Sugiyama, *Sensors and Actuators A*, vol. 108, p. 244, 2003.
190. S. Timoshenko, *Theory of Plates and Shells*, McGraw Hill, 1940.
191. U. Gangopadhyay, C. Pramanik, H. Saha, K. Kyunghae and J. Yi, *Journal of the Korean Physical Society*, vol. 47, November, pp. S450–S453, 2005.

5

MEMS/NEMS Switches with Silicon to Silicon (Si-to-Si) Contact Interface

Chengkuo Lee*, Bo Woon Soon and You Qian

Department of Electrical and Computer Engineering, National University of Singapore, Singapore

Abstract

This chapter provides an overview on microelectromechanical system (MEMS)/nanoelectromechanical system (NEMS) switches using Si-to-Si contact. The basic background of MEMS/NEMS switches is briefly described first. In the following parts, devices are discussed in terms of several aspects including fabrication process, electrical measurement, and failure analysis. The applications of MEMS/NEMS with Si-to-Si contact interface are demonstrated as non-volatile memory and logic computation. Meanwhile, High-temperature environment operation under 300 °C and 400 °C for vacuum-encapsulated Si-to-Si MEMS switches is presented as sound evidence of reliable operation.

Keyword: Microelectromechanical system (MEMS) switches, nanoelectromechanical system (NEMS) switches, silicon to silicon contact, non-volatile memory (NVM), logic switch

5.1 Introduction

Microelectromechanical system (MEMS) and nanoelectromechanical system (NEMS) switch is a micro/nanosize device able to alter between two or more states and usually made of multiple movable and fixed electrodes. Unlike its bulk version, MEMS/NEMS switch is not a human hand operated and can be categorized into two major types: passive and active switch. Passive switch is triggered though environmental energy transduction (e.g. magnetic reed switch [1,2], latching shock switch [3,4]) while active switch's state is configurable by deliberately applying known triggering signal (e.g. RF MEMS switch [5–7], logic switch [8–10]). The requirement of MEMS/NEMS switch is usually application specific, depending on the device functions, nature of operations as well as its working surroundings. These often call for different prerequisites such as in memory, form factor is a major consideration, and on the other hand, low voltage is much more favorable in logic operation. While in harsh environment, reliability of switching is a crucial factor when device is exposed to catastrophic level of pressure, temperature, radiation and more. The operating condition has rendered the simplest on–off structure into complex switching

**Corresponding author*: elelc@nus.edu.sg

Atul Tiwari and Baldev Raj (eds.), Materials and Failures in MEMS and NEMS, (173–200)
© 2015 Scrivener Publishing LLC

mechanism, focusing on different parameters to achieve reasonable performance. In this chapter, active switch will be emphasized and discussed further, comprises Si-to-Si contact switch in non-volatile memory (NVM), low-voltage and harsh environment operation.

5.1.1 Why Silicon?

Report suggests that high current density, hot switching, and high impact velocity may causes switch micro-welding, fracture, contact surface degradation, and oxidation that eventually leads to failure [11–14]. Under these circumstances, material selection is a critical factor to reduce contact resistance, increasing heat conduction and be able to withstand contact degradation due to force. Silicon has high melting point of 1414 °C, Mohs hardness scale of 7 and relatively high Young's modulus of 130–188 GPa, which makes it one of the most appropriate material in terms of reliability, adequately hard material and suitable in low operating voltage design. Besides CMOS compatibility, Si is one of the most established platforms in micromachining fabrication, where most of the process technologies are developed surrounding Si material, making Si the most shapeable material in MEMS/NEMS micromachining. One of the major disadvantages by choosing Si perhaps is the material resistivity. Some may think that the semiconductor resistance can be reduced significantly by highly doping the semiconductor material with corresponding impurities, so that it behaves like metal or degenerate semiconductor. However, the non-ideal case would be rather challenging to determine the doping concentration and its uniformity distribution near the contact point in switch design.

5.1.2 Electrostatic Switch

Amongst various types of switching mechanism, electrostatic-based NEMS switches have recently generated considerable amount of interest as an alternative to the CMOS transistor in both computing and memory applications. Typical reported electrostatic switch's characteristics, including ideally zero standby power, high sub-threshold slope, and ability to withstand harsh environments [15–19]. This has been reinforced by numerous reports as a possible solution to the limitations of CMOS scaling [8,20]. Properties as mentioned above enables further scaling as well as low-power computing, showing a power consumption much lower than that of CMOS transistors [21,22]. NEMS switches have also been suggested for NVM applications, where they can offer write/erase speeds several orders of magnitude faster than NAND Flash [23]. A good example shown in Table 5.1 summarizes the comparison between NEMS switch and existing Flash technology.

Furthermore, MEMS/NEMS switches have the advantage of being able to withstand harsh environments [24,25], and such properties may prove invaluable for computing or memory, especially in the area of rugged electronics, where machines and devices operates in harsh environments and usually requires higher reliability than standard conditions. In this chapter, both examples of in-plane and out-of-plane actuated NEMS/MEMS switch are discussed. With the aim of addressing different nature of operation, several forms of latest reported Si-to-Si contact MEMS/NEMS switch are shown. In the early part of the chapter, applications such as NVM and logic computation are deemed

Table 5.1 Comparison of NEMS switch with major Flash technology.

Properties	NAND Flash SLC	NAND Flash MLC	NOR Flash	NEM Switch
Cell size (F is feature size)	$4F^2$	$4F^2$	$10F^2$	$4F^2$
Program (time)	30 μSec	100 μSec	1 mSec	<20 nSec
Erase (time)	2 mSec	2 mSec	900 mSec	<20 nSec
Read (time)	25 μSec (random) 50 nSec (serial)	25 μSec (random) 120 nSec (serial)	20 nSec	<20 nSec
Operating voltage	16–20 V (read/ write)	16–20 V (write) 6 V(read)	6–8 V (read/write)	5 V (write) 2 V (read)
Endurance (cycles)	10^5–10^6	10^4–10^5	10^5–10^6	10^3–10^9
Temperature stability	<150 °C	<150 °C	<150 °C	<400 °C

viable through different physical phenomenon. For instance, a bi-stable two terminal NEMS NVM application that leverage on van der Waals force to produce contact surface latching mechanics and sub-1 V ultra-low operation voltage that is enabled by U-shape nanowire, resulting in low-power devices [26,27]. In the later part of the chapter, Si-to-Si contact reliability in vacuum encapsulation as well as its failure mechanism is discussed, to provide an overall performance for Si material used in NEMS/MEMS switch [15].

5.2 Bi-Stable CMOS Front End Silicon Nanofin (SiNF) Switch for Non-volatile Memory Based On Van Der Waals Force

A high aspect ratio nanoelectromechanical (NEM) Silicon Nanofin (SiNF) switch has been fabricated and measured as a potential alternative to solid-state NVM for application such as storage in harsh environments [28,29]. Flash memory degrades rapidly in such environment due to increased activity of hot carrier injection and standby leakage results. Reported maximum memory retention of such device is estimated to be approximately 250 °C [30,31]. NEM switches can overcome this problem [17] thanks to their mechanical switching properties and possibility of leveraging on van der Waals force to demonstrate hysteresis behavior [11]. To make it suitable to be rugged electronics, silicon material was chosen because it has relatively high melting temperature. [32] Measurement results show bi-stable hysteresis behavior with pull-in voltage at 12 V with the mean temperature drift of 24 mV/ °C from 50 °C to 150 °C, depending on switch's dimensions.

5.2.1 Operational SiNF NEMS Switch with Bi-Stable States

A sketch of the bi-stable two-terminal SiNF switch is shown in Figure 5.1. A SiNF based cantilever beam with thickness t_f and length h is flanked by gate and drain electrodes on either side, separated by gaps of g_d, respectively. To actuate the switch, an electrostatic force is applied via a voltage at the gate electrode. If the applied voltage exceeds the pull-in voltage V_{PI}, the SiNF is actuated and comes into contact with the drain electrode. Possible contact between the beam and gate electrode is avoided by having a larger gap between the beam and gate. This mitigates the problem of capacitive discharge between two surfaces held at different potentials, which might cause the beam to melt and result in device failure. If the SiNF length exceeds the critical length h_c, adhesive surface forces, dominated by van der Waals interactions, can overcome the elastic restoring force and allow the cantilever to retain switch contact after pull-in when the actuation voltage is removed, thus functioning as NVM. To switch the SiNF to the other side, a voltage is applied to the opposite gate electrode, and the minimum voltage at which the SiNF pulls in to the other side is the pull-out voltage V_{PO}.

5.2.2 Van Der Waals Operation and Critical Length

The presented model follows a methodology presented by Mastrangelo and Hsu [33]. The profile of an actuated SiNF is shown in Figure 5.2, with the beam sticking to the drain electrode at distance c, the contact length. The adhesion area is modeled as a region held flat against the drain electrode. The contact length is determined by the balance of beam elastic energy, van der Waals adhesion energy and electrostatic energy, with the total energy of the system being minimized at equilibrium. Unit width of the SiNF is assumed throughout the analysis. Assuming the electrostatic force is being applied from the opposite side via a voltage V across $0 \le x \le s$, the beam deflection y in this region is given by the Euler–Bernoulli beam Equation (5.1).

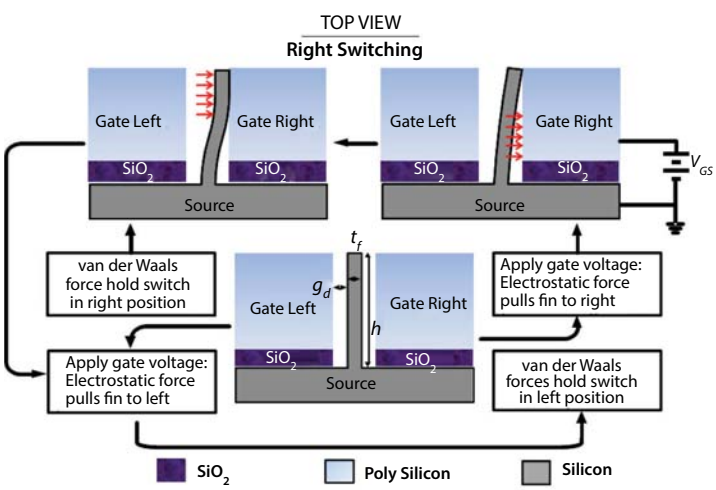

Figure 5.1 Schematics of the switching operation of the SiNF. When $V_{GS} > V_{PI}$, switch is on. When $V_{GS} < V_{PI}$. van der Waals force will hold the fin in contact.

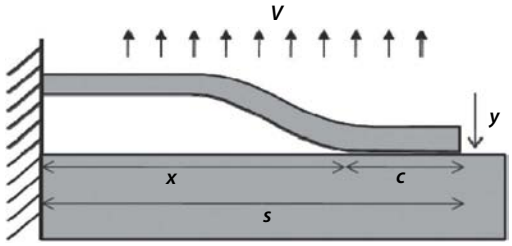

Figure 5.2 Side view of SiNF structure stick to bottom substrate.

$$EI\frac{d^4y}{dx^4} = -\frac{\varepsilon_0 V^2}{2\left(y+g_g\right)2\left(y+g_g\right)^2} \tag{5.1}$$

Where the area moment of inertia I is given by Equation (5.2).

$$I = \frac{Wt^3}{12} \tag{5.2}$$

Thus, the elastic energy stored in the beam is described in Equation (5.3).

$$U_E = \frac{El}{2}\int_0^s \left(\frac{d^2y}{dx^2}\right)^2 dx \tag{5.3}$$

While the van der Waals adhesion energy is given by Equation (5.4), where H is Hamaker's constant of Si [34].

$$U_{vdw} = \frac{H}{12\pi r^2} \tag{5.4}$$

The electrostatic energy can be expressed as (5.5).

$$U_{electrostatic} = -\frac{\varepsilon_0 v^2}{2}\int_{\varepsilon 1}^{\varepsilon 2} \frac{1}{\left(y+g_g\right)} dx \tag{5.5}$$

The total energy U_T is given by (5.6).

$$U_T = U_E + U_{electrostatic} - U_{vdw} \tag{5.6}$$

The equilibrium is found by setting its derivative to zero. Pull-out occurs as c approaches 0 and the equation yields critical length as follows.

$$Lc = \left(\frac{9\pi Et^3 gd^2 r^2}{2H}\right)^{\frac{1}{4}} \tag{5.7}$$

An expression for the critical length of the SiNF as well as a closed-form solution for the pull-out voltage can be obtained through a series expansion of fourth order. This closed-form solution enables rapid analysis of wide ranges of design parameters, reducing the reliance on finite element simulations which can be time consuming. If cantilever length exceeds the critical length L_c, adhesive surface forces, dominated by van der Waals interactions, can overcome the elastic restoring force and allow the cantilever to retain switch contact after pull-in even after the actuation voltage is removed, thus functioning as NVM. In contrast, if the SiNF length is shorter, the restoring force will dominate and the beam will break the contact and operates like a logic switch. Such demonstration is shown in the next part by a NVM using silicon nanofin (SiNF). The device is fabricated and characterized to show bi-stable states non-volatility properties. Its critical length is estimated with earlier equation and it shows that surface forces can be leveraged to realize bi-stable non-volatile mechanical device.

5.2.3 Fabrication Process

While silicon (Si) process technology has grown tremendously, defining NEMS device remains a huge challenge, where performance of devices is much related to physical dimensional processing capability such as aspect ratio, surface roughness, and device release. In the SiNF NEMS memory, process requirements are repeatedly optimized to provide a high aspect ratio and smooth surface to the main structure: The moving Si beam. Structurally Si has good reliability and implantation can be performed to reduce the resistivity of the material. Other than that, nanosize electromechanical device can be realized without much intrinsic stress when it is made out of single crystal Si, which is the standard case of for Si-on-insulator (SOI) wafer platform. However, the conductance of Si is still incomparable to metal no matter how much impurity density can be implemented. Figure 5.3 shows the fabrication process flow: (a) starting from SOI wafer, (b) a layer of SiO_2 is thermally grown as a hard mask for the first layer etching, (c) hard mask is etched followed by silicon deep reactive ion etching (DRIE), (d) further oxidation is performed to reduce the overall fin dimension to nanoscale size < 100 nm, (e) poly Si is overfilled as the gate electrode to the SiNF, (f) the wafer is planarized so that the fin is exposed, (g) an insulation layer of SiO_2 is deposited followed by opening to the gate and Al is deposited as contact, and (h) finally, the device is release in dry hydrofluoric acid vapor (VHF) to remove the SiO_2, leaving the SiNF suspended. Heavy implantation and activation are performed at steps (a) and (e) in order to make the silicon as conductive as possible to reduce the resistance of the Si. More details on the fabrication process will be given in the following.

Fabrication of nanoscale device is very challenging and the process is carried out at Institute of Microelectronics, Agency of Science and Technology Singapore (A*STAR) where 248-nm-deep UV lithography tool is available. Multiple steps of CMOS compatible processes are leveraged to create the SiNF two terminal NVM. First, eight inch SOI wafer with 3.5 μm N-type device layer and 1 μm BOX is used. A high-dosage phosphorous implantation of 5×10^{16} ion/cm^2 at 80 keV is performed to make the device layer more conductive. Next, 300 nm of thin SiO_2 is thermally grown at 1050 °C in O_2 ambient to create hard mask for the first etching step. For the first layer, patterning of SiNF is performed with Nikon KRF 248-nm excimer laser scanner. After that, the hard mask is etched in optimized C_4F_8 + Ar-based recipe using high-density plasma etcher. The rest of the steps is shown in scanning electron micrograph (SEM) in Figure 5.4, these steps include (a)

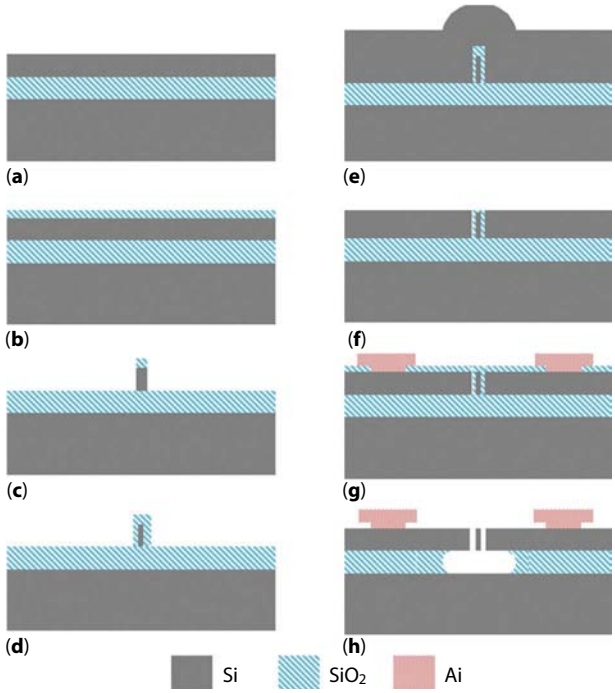

Figure 5.3 CMOS-based process flow for SiNF switch.

BOSCH high aspect ratio DRIE, this recipe is modify with extremely short 6 seconds passivation cycle of C_4F_8, alternating earlier with a longer 30 seconds etching cycle of SF_6, this results in a smooth sidewall, this step is crucial because reducing sidewall roughness will enhance the van der Waals adhesion force. (b) Local oxidation of 1050 °C is later performed to further reduce the fin width by consuming the Si to SiO_2, increasing the aspect ratio to thickness/height of 1:37.5, the dimensions of the fin ranges from 80 to 110 nm. This can be measured accurately by the thickness grown using a ellipsometry measurement (c and d). The thermally grown SiO_2 can be conveniently defined as the sacrificial layer and the insulation layer. The area near the actuation gap has to be etched partially by creating a smaller gap for the electrostatic actuation. In order to do this, first the thickness of the SiO_2 is measured with ellipsometer, since the gap target is approximately 80 nm, any excess SiO_2 has to be etched way. This is done by time etch using diluted hydrofluoric (HF) acid of (1:25), the etch rate is about 35 nm/min, using photoresist as a mask. (e) Next 4-μm-thick poly-silicon is deposited, this process naturally over-fills the entire SiNF, after that, poly-Si CMP is performed to planarize the entire wafer, until the SiNF emerged from the overfilled poly-Si. At this stage, the SiNF can be released but there will be no interconnect. (f) To re-distribute the electrodes, an insulating 300-nm LPCVD TEOS SiO_2 is deposited and etches back on release area, this layer serves as the insulation to the metallization path. After that, 500 nm aluminum is sputtered and patterned to provide contact to the SiNF and poly-Si gate. (g) To further prevent the possibility of leakage current, isolation trench is patterned and etched stop on buffered oxide layer (BOX) to isolate the SiNF and the gate electrodes. Lastly, the device is released in VHF and is shown in Figure 5.5. Dry release is capable of providing a non-stiction suspended

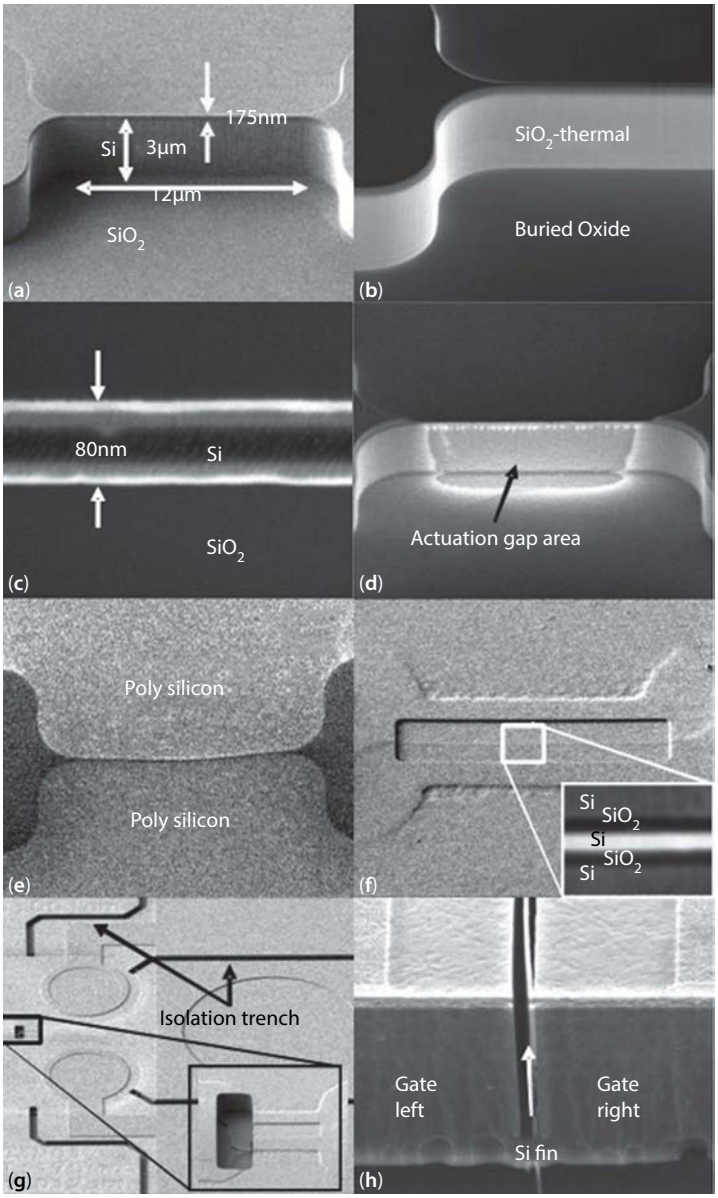

Figure 5.4 SEM pictures of the SiNF NEMS switch fabrication process flow. (a) High aspect ratio silicon fin etch of 1:17. (b) Further oxidation to thin down the fin width to aspect ratio of 1:37.5 (80 nm), at the same time smoothing the silicon's surface. (c) Removal of SiO_2 around the fin. (d) Deposition of SiO_2 dielectric for insulation for overall area followed by reduction etches around the fin area to create 100 nm gap for electrostatic actuation. (e) Top view after thick poly-silicon deposition followed by planarization until SiNF surface. (f) Overall SiO_2 dielectric deposition for insulation of metallization. This layer is reduced at the toggle-fin area so that the release etching for this area is faster. (Inset) Top scan shows silicon fin, silicon gate electrodes and sacrificial SiO_2 layers. (g) Isolation trench stop on buried oxide (BOX) layer to isolate the SiNF and the gate-electrodes. (Inset) Etch away one anchor of the clamped–clamped bridge to become cantilever structure. (h) Release etching of SiNF using VHF.

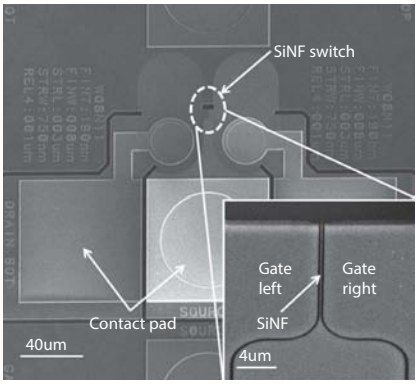

Figure 5.5 SEM of a switch device of 8 μm length × 90 nm thick SiNF. (Inset) Zoom in view of the SiNF in the centre of the device.

structure, resulting SiNF initially in neutral position before testing. Figure 5.5 shows the SEM of a device with 8-μm-long and 90-nm-thick SiNF. Inset shows the high magnification of the lateral actuated SiNF between two gate electrodes.

5.2.4 Electrical Characteristics of NEMS Switch Non-volatile Memory

As the total electrostatic force is proportionate to V_{GS}, electrostatic pull-in of the SiNF to the gate happens when V_{GS} is increased beyond the pull-in voltage (V_{PI}), $V_{GS} = V_{PI}$. To show this, with the SiNF (source) grounded, a voltage sweep (V_{GS}) is applied across left gate and right gate from negative region (0 to –30 V) to positive region (0–30 V). Figure 5.6(b) shows the SEM of SiNF actuated by contacting the left gate. It is interesting to note that the device inspected in SEM is not biased but the switch remains in contact and the direction agrees well with where V_{GS} is applied. Similarly, Figure 5.6(c) shows the SEM of the same device with reversed V_{GS} applied across source and right gate. Electrostatic force is negligible when the switch is turned off, thus the dominating force that holds the contact is the van der Waals attraction. Despite electrostatic force can arise from the electron beam scanning in SEM microscope and may cause the SiNF to switch [30], the results are reliable due to multiple device tested are verified.

The measured hysteresis loop of set and reset operation (Figure 5.7) where the ground measurement point is omitted for illustration purpose is demonstrated. Electrical measurement of three devices with thicknesses, h (70, 80, 90 nm) × 2 μm length SiNF measured as a bi-stable NVM. As the thickness scales down, less electrostatic energy is required to actuate SiNF due to reduced spring constant, V_{PI} is proportional to $h^{3/2}$. The pull-in phenomenon is represented by an abrupt increase in I_G, usually between two voltage steps. To achieve non-volatile hysteresis curve, the following criteria has to be fulfilled, $E_{VDW} > (E_{SPRING} – E_{ELECTROSTATIC})$. Continuous flow of I_G after pull-in shows that the relay maintains its contact by van der Waals surface force, since $E_{ELECTROSTATIC} < E_{SPRING}$ and there is no sign of SiNF pull-out. Note that at 0 V, I_G returns to near pA as there is no voltage applied by the analyzer. This point is omitted for illustration purpose. The abrupt jump in I_G corresponds to I_{on}/I_{off} of 10^2 is considered far from ideal due to the

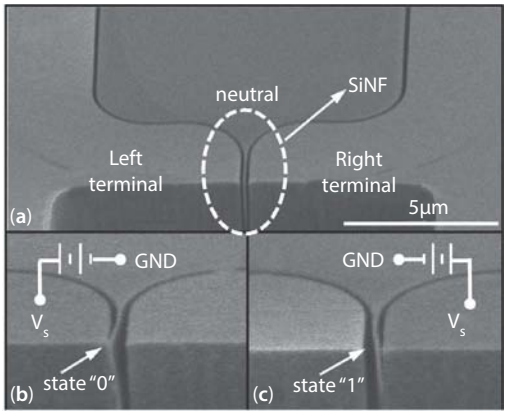

Figure 5.6 SEM showing a 2 μm × 80 nm relay in operation. (a) When no bias voltage is applied, SINF remains at neutral position. (b) SiNF is pulled in to left gate when V_{GS} is applied between left gate and source. The contact remains on hold even after V_{GS} is reduced below V_{PI}, this provide the device state "0". (c) Reversely, SiNF is pulled in by opposite gate when V_{GS} is applied between right gate and source, providing the device state "1".

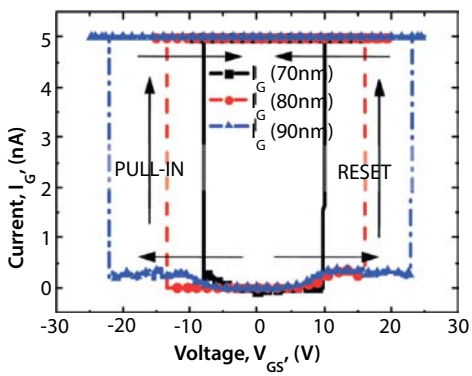

Figure 5.7 Measured I_G–V_{GS} curve, showing V_{PI} = 8.4, 13.8, 22.6 V and V_{RESET} = 10.1, 16.2, 24.4 V for 2-μm-long SiNF device with varying thickness of 70, 80, and 90 nm. The measured hysteresis curve shows bi-stability in device. Note: 0 V point is omitted for illustration purpose.

compliance current setting of 5 nA. Low I_G compliance prevents excessive current from flowing through SiNF that may cause device failure due to fusing and oxidation of Si. Even so, the hysteresis condition is mostly repeatable for 5–10 cycles. This may improve if the testing is done under vacuum condition [31]. The device displays clear bi-stable characteristics when voltage is sweep from one terminal to the other.

Figure 5.8 shows that temperature decreases the pull-in voltage, causing a voltage drift. One notable observation is the pull-in voltage in shorter fin actually increases with temperature. Besides that, 2 μm SiNF experiences the largest pull-in voltage difference due to elevated temperature, while 8 and 12 μm SiNF are less affected. This also suggests that by optimizing fin length it would be possible to design a memory cell free from temperature drift.

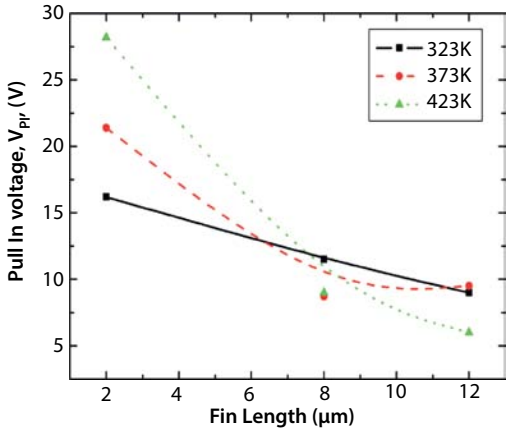

Figure 5.8 Pull-in voltage at varying temperature of 50 °C, 100 °C, and 150 °C. The results reflect mean temperature drift of 24 mV/ °C.

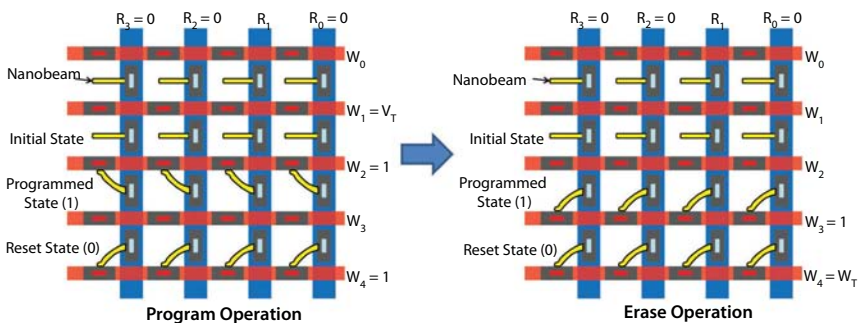

Figure 5.9 Proposed 2^3 bit memory array implemented by two terminal SiNF relay. Each device consists of two states, namely state "0" and state "1". Write and reset operation can be executed by turning on both read and write line. Meanwhile, read operation is performed by low current measurement where device are subjected to a read potential ($V_{read} < V_{PI}$).

The SiNF NEMS switch demonstrates low-power operation while exhibiting non-volatile hysteresis loop with two bi-stable states. It is also the first measured result of two way bi-stable hysteresis curve based on VDW force for application in NVM memory. The material used is single crystal Si, which resistance is significantly higher than metal. Nevertheless, this material is stress free and its process technology is very established. However, the current fabrication process produce very low yield and the current device possess very low reliability, due to fusing/micro-welding because of Joule heating during switching. Advanced packaging to provide vacuum environment is a dire need before this device is able to perform at more dynamic application.

5.2.4.1 Non-volatile Memory Array Application

To realize an array of devices with a small footprint, an array structure is proposed such that each gate electrode is shared between two SiNF, as shown in Figure 5.9. To program

or erase the device in an array without affecting other cells, a threshold holding voltage V_T needs to be defined such that it is sufficient to prevent the SiNF from switching when a program voltage is applied to the other electrode, yet insufficient to cause switching itself. For instance, to erase the programmed state (1) in Figure 5.9, V_{RESET} is applied to W_3 while V_T needs to be applied to W_4 to hold the already reset state (0) where $0 < V_T < V_{RESET}$.

5.3 Vertically Actuated U-Shape Nanowire NEMS Switch

Among the different actuation mechanisms which can be realized by CMOS process, electrostatic actuation is favored for its low-power consumption, fast switching speed and simple fabrication process. The typical pull-in voltage is 5–30 V from the recent reports [35,36], which makes it incompatible with the modern CMOS circuit. There are various approaches to deal with the high pull-in voltage issue and the most effective way is to scale down the dimension. Silicon nanowires are easy to be actuated with their sub 100 nm cross section, but it also reduces the electrostatic force it received.

5.3.1 Dual-Silicon-Nanowires-Based U-Shape NEMS Switch

A dual-silicon-nanowires-based U-shape NEMS switch is designed to demonstrate its low actuation voltage. The schematic diagram of the NEMS switch is shown in Figure 10(a). Two silicon nanowires are fixed at one end and connected with a movable capacitive paddle on the other end. The cross-section of the SiNW is close to a length of 90 by 90 nm. Once voltage is applied between the capacitive paddle and the substrate, the electrostatic force would bend the SiNWs down and make the capacitive paddle have an electrical contact with the substrate. The combination of large capacitive paddle and flexible SiNWs makes the U-shape structure bending more effectively under electrostatic actuation. After the release process, the NEMS switch is checked under the SEM (Figure 5.10b). No stiction or deflection could be found, as the whole movable structure is made from single crystal silicon.

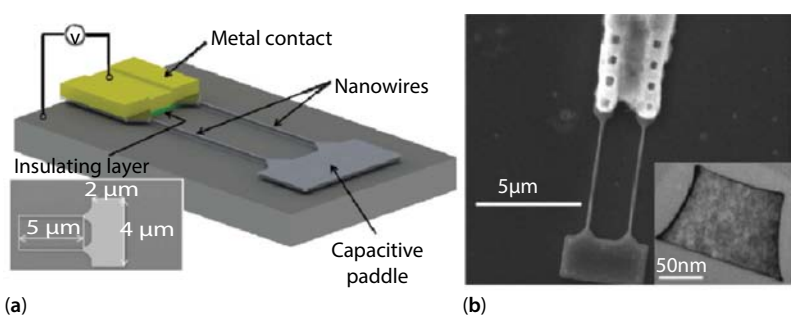

Figure 5.10 (a) A schematic illustration of the U-shape NEMS switch. (b) SEM photo of a U-shape NEMS switch after HF vapor releasing, Inset: TEM image of a SiNW cross section.

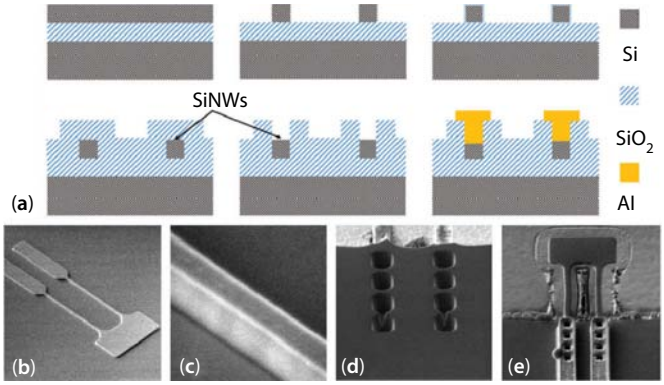

Figure 5.11 (a) Process flow for U-shape nanowire fabrication. SEM photos taken during the process (b) after silicon etch, (c) zoom in view of the nanowire, (d) via opening, and (e) after metallization.

5.3.2 U-Shape Nanowire Fabrication

The fabrication process of the U-shape NEMS switch starts with an SOI (100) wafer, with a device layer of 117 nm and BOX layer of 145 nm. After the first photolithography, which defines the SiNWs and capacitive paddle, the photoresist is trimmed, and the critical dimension is decreased to around 100 nm. The SiNW is then patterned along (110) directions. To further shrink down the dimension of SiNW, thermal oxidation is conducted with the final cross section of the SiNW being 90 nm × 90 nm. To increase the conductivity of the Si device layer, a p-type implantation process using BF_2 with a dosage of 1×10^{14} ion/cm^2 is done, followed by annealing for dopant activation. Measurement result shows that the SiNW has a resistivity of 0.021 Ωm, and the resistance per SiNW is 130 kΩ. Next, an extra SiO_2 layer of 400 nm is deposited for protection. After via opening and Al metal patterning, the device is released by hydrogen fluoride (HF) vapor, with the HF etching away the BOX layer between U-shape NEMS switch and the silicon substrate. Therefore, the gap of the switch is defined by the thickness of the BOX layer.

5.3.3 Low-Voltage Operation

Figure 5.12 shows the COMSOL simulation performed to estimate the effect on the variation of SiNW length. The size of the capacitive paddle and the gap are fixed in the simulation. When the length of SiNW equals to zero, which means the movable part becomes a simple fix-free cantilever. The pull-in voltage of cantilever type of switch increases to as high as 26.5 V. When a very short SiNW with a length of 0.2 μm is included in the simulation, the pull-in voltage dramatically decreases to 6.97 V. In addition, simulation result has shown that our design has great effectiveness in reducing the pull-in voltage as SiNW length increasing to 5 μm. Once the length of SiNW exceeds 5 μm, the pull-in voltage become saturated, without significant improvement in the performance in term of pull-in voltage, and the paddle with a softer support structure suggests it would be easier to collapse.

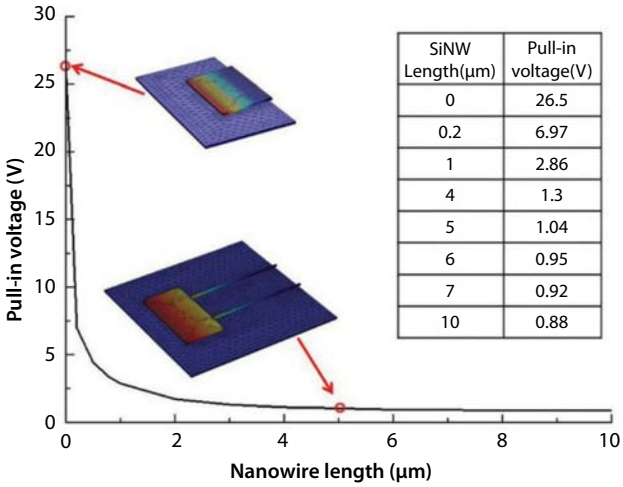

SiNW Length(μm)	Pull-in voltage(V)
0	26.5
0.2	6.97
1	2.86
4	1.3
5	1.04
6	0.95
7	0.92
10	0.88

Figure 5.12 Simulated result of the influence on nanowire length versus pull-in voltage, as the length of SiNW varies from 0 to 10 μm.

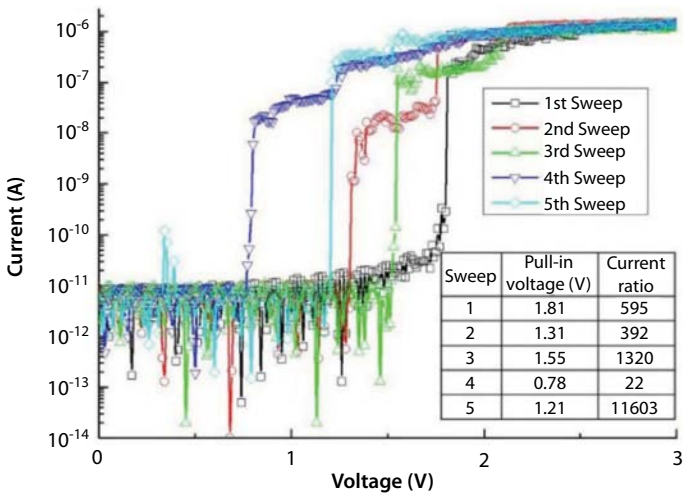

Sweep	Pull-in voltage (V)	Current ratio
1	1.81	595
2	1.31	392
3	1.55	1320
4	0.78	22
5	1.21	11603

Figure 5.13 I–V characteristic of the device shown in Figure 5.10(b) for the first five switching cycles. The current ratio indicates the change in current that occurs within 10 mV of the pull-in voltage.

Figure 5.13 shows the I–V plots of the fabricated U-shape NEM switch. Since it operates as a two-terminal switch, the voltage applied is between the U-shape structure and the substrate. The voltage is swept from 0 to 3 V, with no compliance being set for the current. The measured off current is around 10 pA, which is equivalent to the noise level of the test setup. The first pull-in happens at 1.81 V, causing the current to increase rapidly to 0.1 μA. Based on the applied voltage step of 10 mV, this abrupt switching slope is less than 4 mV/decade. With higher voltage applied after the initial pull-in, the physical contact area enlarged and the current passing through has a few jumps until 3 μA. Considering the resistance of two SiNWs is around 65 kΩ, the total resistance is mainly from the contact, which should be in the range of few hundreds of kΩ.

The following switching cycles also show a good switching behavior. The ON/OFF state current maintains at the same level. The average pull-in voltage is 1.12 V. The pull-in voltage varies in a wide range of about 1 V. One possible reason for such pull-in voltage variation is the charging effect on the native oxide that has grown on the contact surface. During the electrical measurement, charges can be stored on these surfaces and an additional electrostatic force is formed to decrease the initial gap. It also explains the reason why the first pull-in voltage is much larger than all the following sweeps after it. Such kind of phenomenon cannot be avoided after HF vapor releasing for Si-to-Si contact working in ambient air condition. However, adding process to cover the contact with metal before release would improve the performance of the U-shape NEMS switch largely, as it could avoid the charging issue and provide a much lower contact resistance. Another possible solution is using the vacuum level encapsulation process to protect the devices from oxidation, which will be discussed in the next section.

5.4 A Vacuum Encapsulated Si-to-Si MEMS Switch for Rugged Electronics

An attempt to fabricate silicon-based vacuum encapsulated curved switch is made to investigate its capability to operate in harsh environment. Extremely clean vacuum encapsulation process is performed to seal the switch after release process, providing pristine operating surroundings for switching operation. Besides that, curved beam designs of the actuation mechanism has enhanced the overdrive voltage tolerance, as no gate voltage (V_G) breakdown is observed when this voltage is swept up to 100 V, resulting in robust voltage overdrive. Meanwhile, preliminary reliability study of such switch is investigated and shown here. Failure analyses are performed to show that the reliability is temperature dependent. 10^6 on–off cycling test is performed and achieved under room ambient and at least 10^4 cycles at elevated temperature of 300°C, with measured consistent contact resistance of approximately 30 kΩ. Micro-welding is presumably happening beyond 400 °C, causing a lower reliability and this is discussed in the later part.

5.4.1 Three Terminal On–Off with Vacuum Encapsulated Switch

A Si-to-Si MEMS switch, consists of all Si material, which is defined on single crystal silicon as stress free and homogenous is fabricated and characterized. Entire moving structure is encapsulated in vacuum environment with only electrical terminal interconnects are fanned out on the chip surface and metalized by aluminum. These terminals consist of drain (movable curve beam), gate (fixed) and source (fixed) are shown in SEM in Figure 5.14. The curved beam's dimension, radius and width, is represented by *r* and *w* in the same figure, where the beam is defined on the circle of the radius. To test this switch, an arbitrary signal can be applied continuously between source and drain, this signal is detected when drain source makes contact by pulling the curved beam toward the gate. Such operation is achieved by another potential difference applied across drain and gate, which leads to electrostatic attraction between the two. This is

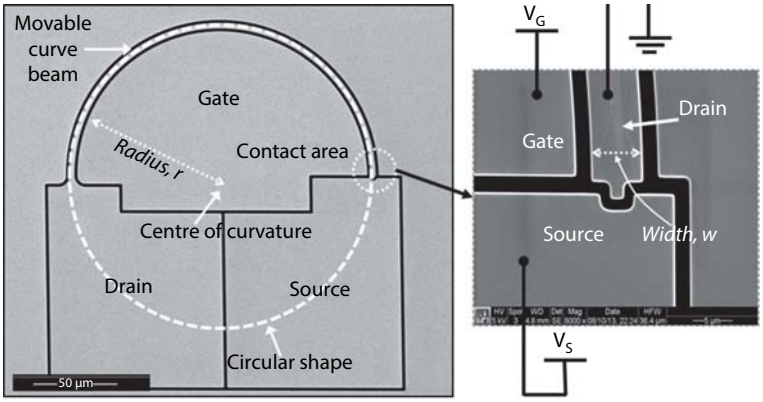

Figure 5.14 SEM of a curved beam Si-to-Si MEMS switch. The operation of the switch is shown where V_G is used to control the actuation with gate terminal and V_S is used to detect signal from source to drain. Parameter radius r and width w of beam are shown.

also referred as the pull-in phenomenon [37]. In order to increase the device's reliability through prevention of mainly oxidation of contact, the switch is encapsulated in vacuum of a few Pa. Besides that, ultra-clean environment is created and is part of the Epi-Seal process [38,39], as the wafer is exposed to high temperature >900 °C with presence of hydrogen, silicon, and chlorine. In addition to vacuum encapsulation, curve beam design provides robust overdrive pull-in voltage, resulting in high tolerance to gate voltage overshooting. As drain is in contact with source, the source acts as a natural stopper to the curve beam, preventing the beam from further deformation due to the arch-like structure, resulting in a rigid configuration that is able to sustain high gate voltage. This is proven to be valuable for rugged electronics such as down-hole operation, automotive and aerospace application. This also serves as surge protection application in some cases of high overshoot in gate voltage pulse.

The curved beam is designed to withstand higher operating voltage and served as a voltage overshoot protection. This is due to its spring constant modification during operation. When the beam is pulled in, the beam (drain) is trapped by the contact (source). This exerts a large spring constant increment to the beam. According to simulation performed in Coventorware, the spring constant increases by approximately 16× of the initial value. Figure 5.15 shows the multiple finite element model (FEM) simulated pull-in voltage of different beam length and width.

On the other hand, the pull-in voltage of such device can be determined numerically by evaluating the spring constant of the curved beam. The spring constant of a semicircular curvature can be evaluated by Equation (5.8).

$$Kc = \frac{2EI}{3\pi R^3\left(1 - a + \frac{\beta}{3}\right)}; \quad a = \frac{I}{AR^2}, \beta = \frac{6EI}{5GAR^2} \tag{5.8}$$

Where E is the Si Young's modulus, I is the second area moment of inertia, R is the radius of curvature from centroid, A is the cross-sectional area of the beam, and G is the

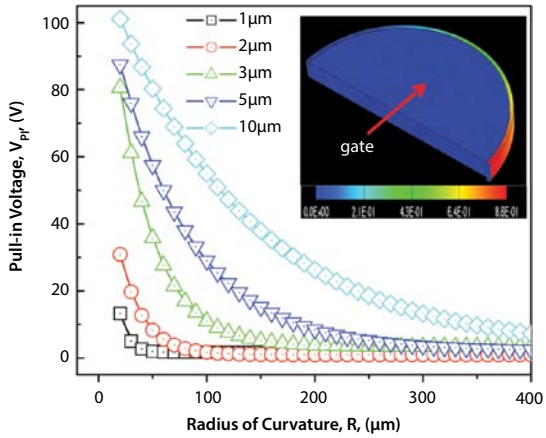

Figure 5.15 Simulation result of pull-in voltage versus radius of curvature for curved beam with varying widths. Inset: 3D model of curved switch (displacement: 0–0.86 μm).

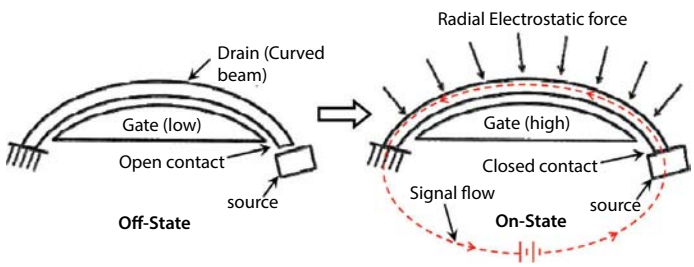

Figure 5.16 Illustration of radial electrostatic force exerted on the curved beam when gate potential is changed from high to low. (Condition for pull-in: $V_{GATE} > V_{PI}$.)

shear modulus of elasticity. Note that the force acting on the beam is a centripetal force thus the electrostatic forces acting on the beam are considered radial forces as shown in Figure 5.16. In order for the switch to be turned on, the potential applied across gate and drain has to overcome the curved beam spring restoration force ($V_G > V_{PI}$), where V_{PI} is the pull-in voltage. In most ideal case, pull-in voltage due to parallel capacitance can be approximated by Equation (5.9).

$$V_{PI} = \left(\frac{8}{27} \frac{K_C d^3}{\varepsilon A} \right)^{\frac{1}{2}} \tag{5.9}$$

where d is the separation gap between the gate and the drain, ε is the relative permittivity of vacuum, A is the effective capacitive area between gate and drain. Note that the equation is accurate for parallel capacitive actuator with proper aspect ratio where the fringing field is negligible. For devices where fringing effect is not negligible, V_{PI} has to be approximated according to different capacitive force generated by different aspect ratio [40].

To realize or simulate the most ideal environment, pristine vacuum level encapsulation is a requirement to investigate the Si-to-Si contact. Such process flow is shown in Figure 5.17. Initial SOI wafer of 40-μm-thick device layer with 1 μm BOX is used. First, DRIE is processed to etch 40 μm deep trenches into thick silicon device layer, stopping on SiO_2 layer. After that, sacrificial SiO_2 is low pressure chemical vapor deposited to overfill the trenches. In this context the etching gap of the initial DRIE has to be limited so overfill can completely seal the etched trench. Next, the SiO_2 layer is etched to define where the electrode should be interfaced, at the same time the opening area serves as the anchor area for the following Si epitaxy capping. The release hole is patterned and etches in the Si capping layer to provide access to the SiO_2 underneath. Then, isotropic vapor hydrofluoric acid is used release the beam. Subsequently the release hole is sealed by second layer of Si epitaxy. This process is also referred as the Epi-Seal where a few Pa of pressure level can be achieved [41]. During the sealing, the wafer is exposed to high temperature with hydrogen gas content and this process removes most impurities and polymers as reported [42]. Subsequently, top Si is isolated with SiO_2 and finally the contact pads are open and metalized with aluminum. The finish chip has flat topography and only the metal pads are visible under optical microscope.

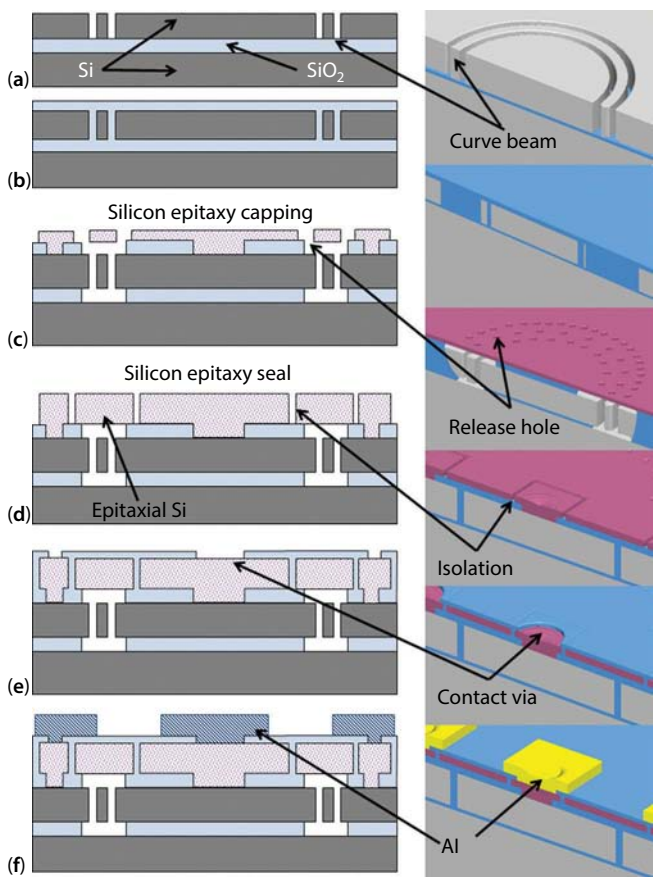

Figure 5.17 Fabrication process flow of encapsulated curve switch. (a) Si deep trench etching, (b) SiO_2 overfill to seal trench, (c) via definition with device release, (d) Si epitaxy sealing and electrode isolation, (e) passivation opening, and (f) Al metallization.

5.4.2 Vacuum Encapsulated Si-to-Si Switch

Similar to earlier section but more ruggedized switching characterization is performed on the vacuum encapsulated Si-to-Si switch. Besides standard switching cycling with more details, the switch is also tested under higher operating voltage and elevated temperature. Figure 5.18 shows the measured typical pull-in and pull-out of a 5 μm thick × 95 μm radius curve beam switch. Gate voltage (V_G) is swept from 0 to 25 V. Pull-in phenomenon is represented by abrupt drain (I_D) and source current (I_S) rise as indicated during the voltage increment sweep, while pull-out voltage is represented by the abrupt drop in both current during voltage decrement sweep. In this switch, the pull-in voltage (V_{PI}) is 20 V and pull-out voltage (V_{PO}) is 4.77 V. In this measurement, all three terminals: drain, source, and gate current are measured, where gate is connected to sweeping voltage, DC bias of 2.5 V is applied to source and drain is subjected to ground. As compared to two terminal devices discussed in previous section, three terminal switch distinctively separate gate control signal from drain and source terminal, resulting in advantages such as low- and high-power gating and power logic application.

Through this experiment, three terminal device is demonstrated with low gate current (I_G) throughout the measurement (fA range). As drain contact source, positive current will flow through drain and negative current flow through source. Typical current on–off ratio (I_{on}/I_{off}) is approximately 10^6 and approximately 6.25 mV/decade. V_{PO} can be measured by sweeping the gate voltage from 25 to 0 V. Note that gate current measurement is important to measure a three terminal device, as experimental error may not be detected when device is still able to produce abrupt rise in current even sometimes when gate is shorted to drain. Hysteresis window in pull-in and pull-out voltage is related to the surface adhesion and the imposed electrostatic force. In order to break off from the contact, the spring restoration force has to overcome surface adhesion and electrostatic force. Trade-off between V_{PI} and spring constant is inevitable to make the switch behaves between a logic and a onetime programmable device. Gap between the pull-in and pull-out can be seen as a measure of the balance between spring constant

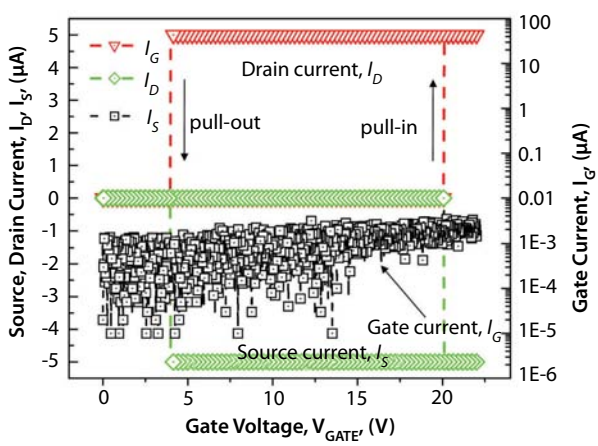

Figure 5.18 Three terminal testing of I_D, I_S, I_G–V_G. I_G remains low at fA range during switching after switch is turned on.

and surface adhesion force. In other mean, curved beam design can be optimized further to operate at lower voltage; however, surface contact has to be considered carefully to compensate lower restoration force. Despite one time programmable application can be realized as reported [43], the reliability or memory retention characteristics of such contact-based memory are unknown.

A constant DC bias is applied across source drain, and the amount of current flow depends on the contact resistance. This current (I_{DS}) is measured and the measurement is shown in Figure 5.19. In this setup, current compliance set to the maximum so that the current flow is uncontrolled. Upon contact, I_{DS} is restricted immediately and rises gradually. This current flow is represented by the slope after the near infinite threshold rise, which in turns shows the resistance of the contact, predominantly determined by the contact asperity and the area of contact. In this figure, the extracted resistance is approximately 42 kΩ for Si-to-Si MEMS contact switch. It is important to show that the switch is still able to pull-out the contact when the spring restoration force overcomes the electrostatic force under vacuum encapsulation. In some cases, pull-out cannot be obtained when the switch's contact is fused after pull-in. This is caused by micro-welding, as a result of Joule's heating when a large current flowing through the contact.

High overdriving voltage can impose large contact force to the switch's contacts. Such electrostatic pull-in generates an exponential force over small gate voltage increment and may result in mechanical degradation at the contact surface, causing early fatality in switching. However, the relatively tough hardness of Si material (Mohs hardness: 7) attributed to the mechanical durability in Si-to-Si MEMS switch. In the Si-to-Si contact switch, there is no obvious adverse effect using large gate over drive voltage such as shown in Figure 5.20. This is shown when pull-out is still obtainable when the beam retracts as the spring restoration force overcomes the electrostatic and adhesion force. Note that the beam does not collapse and contact with gate despite high gate voltage

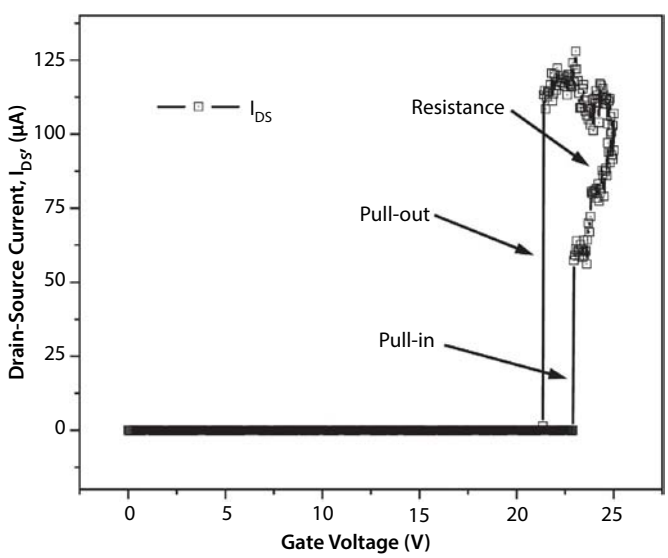

Figure 5.19 Pull-in and pull-out characteristics of a 5 μm × 95 μm device showing a contact resistance measurement without current compliance.

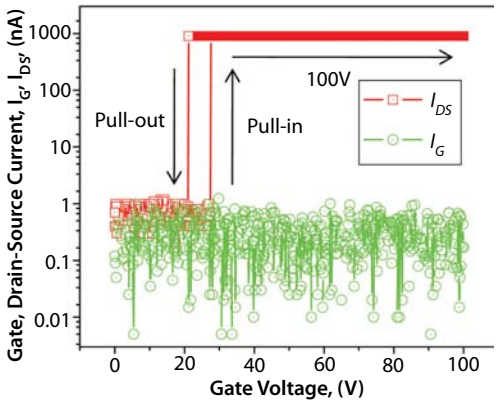

Figure 5.20 Pull-in and pull-out characteristics of a 5 μm × 95 μm device with voltage over drive from 0 to 100 V.

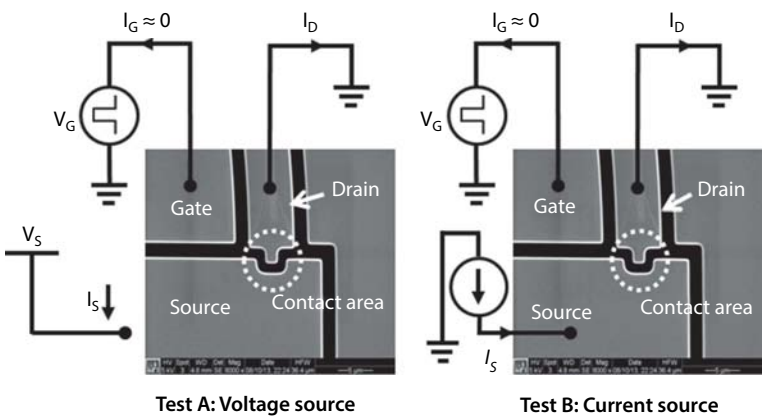

Figure 5.21 Cycling test setup for Si-to-Si reliability test.

is applied, as gate current, I_G remains low throughout the voltage sweep. This is due to the curved beam design which naturally turns into arch-like structure that is extremely resilient to secondary gate pull-in, thus allowing robust gate voltage control.

5.4.3 Reliability of a Vacuum Encapsulated Si-to-Si Switch

Any mechanical or electronics switch has contact lifetime and this is no exception to MEMS switch. In the authors' opinion, MEMS switches operating lifetime can be experimentally measured by alternating the switch's on–off until it fails. Two different cycling experiment setups are carried out to measure the lifetime of the Si-to-Si vacuum encapsulated switch, i.e. voltage source or current source signal can be performed as shown in Figure 5.21. In Test A, a constant voltage source, V_S is applied between drain and source while gate is biased with an alternating signal, V_G. This signal continuously turns the device on and off, while drain and source current, I_D and I_S are measured in every on and off cycle and is used to determined the contact resistance. Similarly, in Test B,

instead of voltage source, a current source, I_S is applied from drain to source while the potential drop between both terminals is measured. This potential drop between the terminals depicts the contact resistance as the constant current source is constricted by the contact area and surface asperities. The advantage by performing Test B over Test A is excessive heating can be mitigated by I_S compliance current setting.

A vacuum encapsulated Si-to-Si switch is experimented with Test A under room temperature and the result is shown in Figure 5.22. The device operates for approximately 3.2 million on–off cycles before a sudden breakdown in contact resistivity during the last cycle. After device fail, low off resistance depicts that drain (beam) is permanently in contact with source as shown in Figure 5.22(b). The unusually low resistance (milliohms) in both on and off cycle means that there is a breakdown in contact resistance. The entire phenomenon can be explained by contact area degradation, as number of cycle increases, surface asperities further degrades which leads to higher contact resistance. This is indicated in the overall on-resistance curve in Figure 5.22(a). At some point, the resistance reaches a threshold where excessive Joule heating happens due to current flow between contact asperities and this may result in a catastrophic breakdown. Oxidation of contact surface is deemed to be negligible in the case of a vacuum encapsulated Si-to-Si MEMS switch. Despite vacuum encapsulation, contact asperities

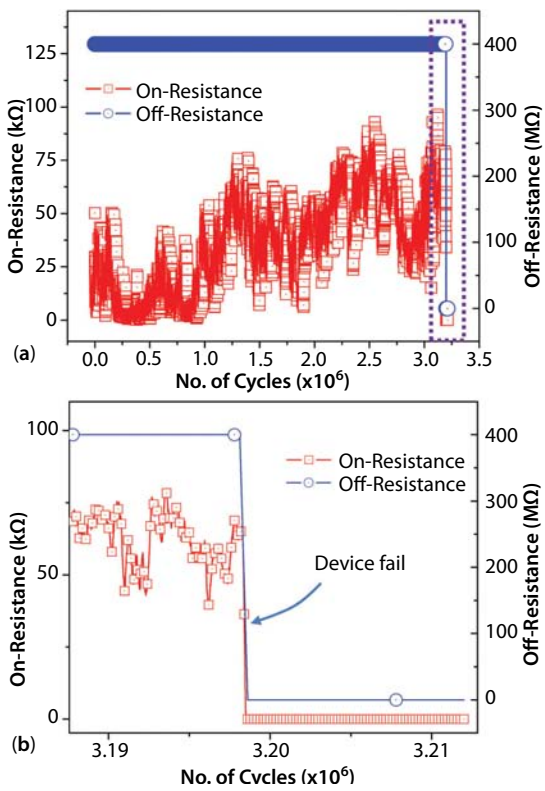

Figure 5.22 Contact resistance versus number of cycles at room temperature. (a) Approximately 3.2 million cycles achieved for Si-to-Si switch encapsulated in vacuum. (b) Zoom-in to the last few cycles showing that device fail.

temperature may increase drastically when surface roughness increase due to number of cycling.

To show that MEMS contact switch has the advantage to operate in higher temperature, another Si-to-Si device is verified to work with Test B for at least 10^4 cycles at elevated temperature of 300 °C. The measured result is comparable to the initial cycling condition of cycling results under room temperature condition. Instead of voltage source, a current source of 5 μA is applied to source terminal as signal, and voltage bias is uncontrolled. As the switch turns on, a constant current of 5 μA flows through source-drain terminal and there will be a potential drop across the contact resistance. This potential is measured by the source monitoring unit and the contact resistance can be determined merely by ohm's law. Current compliance setting is important in this experiment as too high current allowance may cause excessive Joule heating and the switch may fail earlier. Figure 5.23 shows the measured contact resistance versus no. of cycles of this device. Contact resistance shows average contact resistance of approximately 28kΩ through cycling testing. Note that when device is turned off, the contact resistance reach maximum of 1 MΩ, which the limit setting in the configuration to show clear plotting results. The actual open circuit resistance is known to be in hundreds of gigaohm. Within 10^4 cycles, there is no clear sign of increase in contact resistance despite higher range of standard deviation.

Lastly, accelerated life testing of Si-to-Si MEMS switch was carried out at 400 °C with Test A. The result is shown in Figure 5.24, similar failure to Figure 5.22(b) is observed at lower number of cycles. A total of approximately 47,000 cycles verified before device suddenly breakdown, again, unusually low resistance similar to device tested in room temperature shows that likely a permanent joint is formed due to excessive Joule heating.

As expected, device fails earlier due to severe mechanical degradation in high temperature environment. This is further elaborated by the four different modes of failure

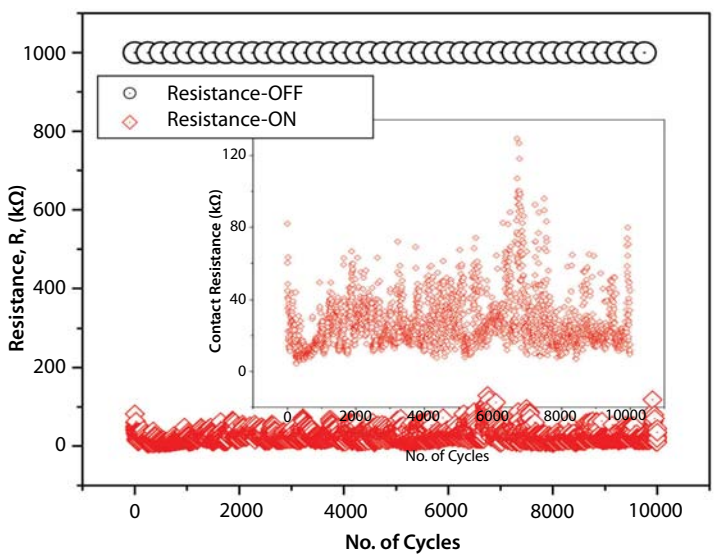

Figure 5.23 Contact resistance versus no. of cycles under 300 °C elevated temperature.

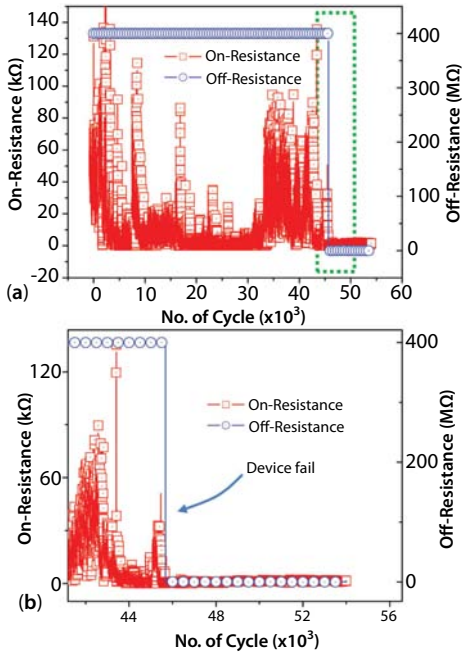

Figure 5.24 Contact resistance versus number of cycles at 400 °C. (a) Approximately 47,000 cycles achieved for Si-to-Si switch encapsulated in vacuum. (b) Zoom-in to the last few cycles showing that device fail.

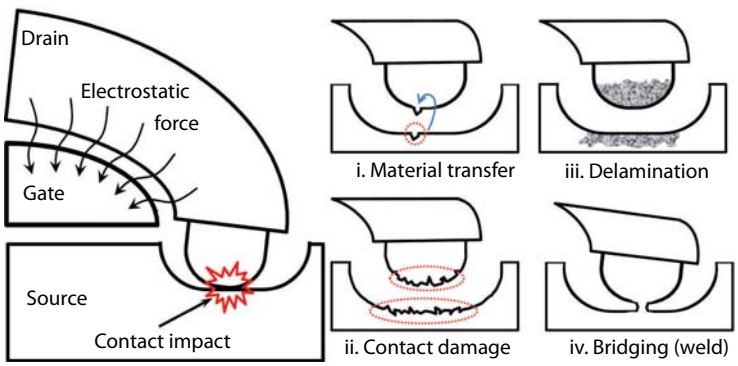

Figure 5.25 Failure mechanisms of contact switches. Repeated push and pull by turning on and off electrostatic force can results in four major mechanics of contact degradation.

mechanism, i.e. material transfer, contact damage, delamination, and bridging as shown in Figure 5.25 [44,45]. Delamination is not considered in the Si-to-Si contact since the contact material is homogenously Si. However, material transfer and damaging of contact after repeated push and pull operation can lead to damage of contact surface. In the vacuum encapsulated Si-to-Si switch, the effect of contact surface damage is clearly demonstrated by the increase in contact resistance. This effect is more apparent when the temperature is elevated from room temperature to 400 °C, where device's lifetime expectancy is greatly reduced from million to thousands. Eventually, contact asperities

modification causes high current conduction between the terminals, resulting in excessive Joule heating which leads to micro-welding and bridge formation. One possible way to enhance the switch lifetime is to limit the current compliance that conducts from source to drain, similar to Test B in Figure 5.21. Currently, no commercial CMOS integrated device available that can work under harsh environment temperature above 250 °C. Such device can be very valuable to be designed as logic switching and used under harsh environment application such as down-hole operation, automotive and aerospace industry.

5.5 Summary

Through different devices' examples, Si-to-Si contacts seem to be a good candidate for MEMS switching device. This interface has demonstrated both NVM and logic computation application. Repeatable operation in high-temperature environment such as 300 °C and 400 °C has been demonstrated in vacuum encapsulation Si-to-Si MEMS switch where such temperature is usually devastating to the current state-of-art CMOS devices. To lower the resistivity and amplify the range of usage, the production and design of such device requires development in the field of thin-film coatings. Metallic layer such as titanium nitride (TiN), ruthenium (Ru), and molybdenum (Mo) is deemed to be a good add-on to the contact area to enhance the reliability of the device. Even after that, vacuum encapsulation or non-oxidizing working environment is desired to prolong the lifetime of MEMS switch, as well as providing a pristine environment for the switch to operate in harsh environment.

References

1. R. Meichun, J. Shen, and C.B. Wheeler, *Journal of Microelectromechanical Systems*, Vol. 10, 511–517, 2001.
2. M. Tang, E. Liao, K.C. Cheng, D. Lee, R. Kumar, Y.H. Lee, R. Shankar, O. Le Néel, G. Noviello, and F. Italia, *Journal of Microelectromechanical Systems*, Vol. 10, pp. 511–517, 2010.
3. Z.Y. Guo, Q.C. Zhao, L.T. Lin, H.T. Ding, X.S. Liu, J. Cui, Z.C. Yang, H. Xie, and G.Z. Yan, *Journal of Micromechanics and Microengineering*, Vol. 20, 055006, 2010.
4. J.S. Go, Y.-H. Cho, B.M. Kwak, and K. Park, *Sensors and Actuators A: Physical*, Vol. 54, 579–583, 1996.
5. S.P. Pacheco, L.P. Katehi, and C.-C. Nguyen, Design of low actuation voltage RF MEMS switch, in: *2000 IEEE MTT-S International Microwave Symposium Digest*, IEEE, pp. 165–168, 2000.
6. G.M. Rebeiz and J.B. Muldavin, *IEEE Microwave Magazine*, Vol. 2, 59–71, 2001.
7. E.R. Brown, *IEEE Transactions on Microwave Theory and Techniques*, Vol. 46, 1868–1880, 1998.
8. E. Alon, F. Chen, T.-J.K. Liu, H. Kam, D. Markovic, and V. Stojanovic, Integrated circuit design with NEM relays, in: *Computer-Aided Design, 2008. ICCAD 2008. IEEE/ACM International Conference on IEEE*, pp. 750–757, 2008.
9. B.W. Soon, E. Jiaqiang Ng, Y. Qian, N. Singh, M. Julius Tsai, and C. Lee, *Applied Physics Letters*, Vol. 103, 053122, 2013.

10. F. Chen, M. Spencer, C.C. Wang, R. Nathanael, H. Fariborzi, A. Gupta, H. Kam, V. Pott, J. Jeon, T.-J.K. Liu, D. Markovic, V. Stojanovic, and E. Alon, *IEEE Journal of Solid-State Circuits*, Vol. 46, pp. 308–320, 2011.
11. V.X.H. Leong, E.J. Ng, J.B.W. Soon, N. Singh, N. Shen, T. Myint, V. Pott, and J.M. Tsai, Vertical silicon nano-pillar for non-volatile memory, in: *Solid-State Sensors, Actuators and Microsystems Conference (TRANSDUCERS), 2011 16th International*, pp. 649–652, 2011.
12. S.W. Lee, D.S. Lee, R.E. Morjan, S.H. Jhang, M. Sveningsson, O.A. Nerushev, Y.W. Park, and E.E.B. Campbell, *Nano Letters*, Vol. 4, 2027–2030, 2004.
13. C. Ke and H.D. Espinosa, *Small*, Vol. 2, 1484–1489, 2006.
14. V.V. Deshpande, H.Y. Chiu, H.W.C. Postma, C. Mikó, L. Forró, and M. Bockrath, *Nano Letters*, Vol. 6, 1092–1095, 2006.
15. B.W. Soon, E.J. Ng, V.A. Hong, Y. Yang, C.H. Ahn, Y. Qian, T.W. Kenny, and C. Lee, *Journal of Microelectromechanical Systems*, Vol. 23, pp. 1121–1130, 2014.
16. O.Y. Loh and H.D. Espinosa, *Nature Nanotechnology*, Vol. 7, 283–295, 2012.
17. T.H. Lee, S. Bhunia, and M. Mehregany, *Science*, Vol. 329, 1316–1318, 2010.
18. P. Schmid, F. Hernandez-Guillen, and E. Kohn, *Diamond and Related Materials*, Vol. 12, 418–421, 2003.
19. Y. Qian, B.W. Soon, P. Singh, H. Campanella, and C. Lee, *Nanoscale*, Vol. 6, 5606, 2014.
20. S. Bhunia, M. Tabib-Azar, and D. Saab, Ultralow-Power Reconfigurable Computing with Complementary Nano-Electromechanical Carbon Nanotube Switches, in: *Proceedings of the 2007 Asia and South Pacific Design Automation Conference, IEEE Computer Society*, pp. 86–91, 2007.
21. K. Akarvardar and H.-S.P. Wong, *IEEE Electron Device Letters*, Vol. 30, pp. 1143–1145, 2009.
22. S.W. Lee, S.J. Park, E.E.B. Campbell, and Y.W. Park, *Nature Communications*, Vol. 2, 220–226, 2011.
23. A.B. Kaul, E.W. Wong, L. Epp, and B.D. Hunt, *Nano Letters*, Vol. 6, 942–947, 2006.
24. W.W. Jang, J.O. Lee, J.-B. Yoon, M.-S. Kim, J.-M. Lee, S.-M. Kim, K.-H. Cho, D.-W. Kim, D. Park, and W.-S. Lee, *Applied Physics Letters*, Vol. 92, 103110, 2008.
25. J.O. Lee, M.-W. Kim, S.-D. Ko, H.-O. Kang, W.-H. Bae, M.-H. Kang, K.-N. Kim, D.-E. Yoo, and J.-B. Yoon, 3-Terminal nanoelectromechanical switching device in insulating liquid media for low voltage operation and reliability improvement, in: *Electron Devices Meeting (IEDM), 2009 IEEE International, IEEE*, pp. 1–4, 2009.
26. B.W. Soon, E.J. Ng, Y. Qian, N. Singh, M.J. Tsai, and C. Lee, *Applied Physics Letters*, Vol. 103, 053122, 2013.
27. Y. Qian, L. Lou, M. Julius Tsai, and C. Lee, *Applied Physics Letters*, Vol. 100, 113102, 2012.
28. W. Young Choi, T.-J.K. Liu, H. Kam, D. Lee, and J. Lai, Compact nano-electro-mechanical non-volatile memory (NEMory) for 3D integration, in: *Electron Devices Meeting, 2007. IEDM 2007. IEEE International, IEEE*, pp. 603–606, 2007.
29. J. Rubin, R. Sundararaman, M. Kim, and S. Tiwari, *IEEE Electron Device Letters*, Vol. 32, pp. 414–416, 2011.
30. V. Pott, G.L. Chua, R. Vaddi, J.M.-L. Tsai, and T.T. Kim, *IEEE Transactions on Electron Devices*, Vol. 59, pp. 1137–1143, 2012.
31. R. Gaddi, C. Schepens, C. Smith, C. Zambelli, A. Chimenton, and P. Olivo, Reliability and performance characterization of a MEMS-based non-volatile switch, in: *2011 IEEE International Reliability Physics Symposium (IRPS), IEEE*, pp. 2G. 2.1–2G. 2.6, 2011.
32. C. Glassbrenner and G.A. Slack, *Physical Review*, Vol. 134, A1058, 1964.
33. C. Mastrangelo and C. Hsu, *Journal of Microelectromechanical Systems*, Vol. 2, 33–43, 1993.
34. J. Visser, *Advances in Colloid and Interface Science*, Vol. 3, 331–363, 1972.

35. M.-W. Kim, Y.-H. Song, and J.-B. Yoon, *Journal of Micromechanics and Microengineering*, Vol. 21, 115009, 2011.
36. W. Xiang and C. Lee, *Applied Physics Letters*, Vol. 96, 193113, 2010.
37. R.K. Gupta, Electrostatic pull-in test structure design for in-situ mechanical property measurements of microelectromechanical systems (MEMS), in: *Citeseer*, 1998.
38. M. Hopcroft, R. Melamud, R.N. Candler, W.-T. Park, B. Kim, G. Yama, A. Partridge, M. Lutz, and T.W. Kenny, Active temperature compensation for micromachined resonators, *Solid-State Sensor, Actuator and Microsystems Workshop*, pp. 364–367, 2004.
39. R.N. Candler, M.A. Hopcroft, K. Bongsang, P. Woo-Tae, R. Melamud, M. Agarwal, G. Yama, A. Partridge, M. Lutz, and T.W. Kenny, *Journal of Microelectromechanical Systems*, Vol. 15, 1446–1456, 2006.
40. V. Leus and D. Elata, *Technion-Israel Institute of Technology Technical Report No. ETR-2004-2*, 2004.
41. E.J. Ng, H.K. Lee, C.H. Ahn, R. Melamud, and T.W. Kenny, Stability measurements of silicon MEMS resonant thermometers, in: *Sensors, 2011 IEEE, IEEE*, pp. 1257–1260, 2011.
42. V. Hong, B. Lee, D. Christensen, D. Heinz, E. Ng, C. Ahn, Y. Yang, and T. Kenny, XY and Z-axis capacitive accelerometers packaged in an ultra-clean hermetic environment, in: *Solid-State Sensors, Actuators and Microsystems, 2013 Transducers & Eurosensors XXVII: The 17th International Conference on IEEE*, pp. 618–621, 2013.
43. P. Singh, C.G. Li, P. Pitchappa, and C. Lee, *Electron Device Letters, IEEE*, Vol. 34, 987–989, 2013.
44. Z. Yang, D. Lichtenwalner, A. Morris, J. Krim, and A.I. Kingon, *Journal of Micromechanics and Microengineering*, Vol. 20, 105028, 2010.
45. T. Ishida, K. Kakushima, and H. Fujita, *Journal of Microelectromechanical Systems*, Vol. 22, 828–834, 2013.

6

On the Design, Fabrication, and Characterization of cMUT Devices

J. Jayapandian[1]*, K. Prabakar[1], C.S. Sundar[1] and Baldev Raj[2]

[1]*Materials Science Group, Indira Gandhi Centre for Atomic Research, Kalpakkam, Tamil Nadu, India*
[2]*National Institute of Advanced Studies, Bangalore, India*

Abstract

MEMS-based capacitive micromachined ultrasonic transducers (cMUTs) are the devices used to transmit and receive ultrasonic waves in air, and they have potential to be an alternative to piezo transducers. This chapter provides an overview about the design, challenges during fabrication, and failure analysis of cMUT devices. Device fabrication by surface micromachining method, and wafer bonding technique are compared. The failure analysis of cMUT using various materials characterization techniques and their importance for successful device fabrication are discussed in detail. Dynamic characterization using laser Doppler vibrometer and nano vibration analyzer and CV measurements on successful devices are also presented.

Keywords: cMUT MEMS devices, fabrication challenges, failure analysis, characterization

6.1 Introduction

Ultrasonic transducers are the devices used to transmit and receive ultrasonic waves. These are used in various research areas such as materials science, nondestructive testing (NDT), defense, and medical diagnostics [1]. Conventional ultrasonic transducers are made of piezoelectric materials. However, these transducers have complications like reduced efficiency in fluid-coupled applications because of impedance mismatch. In air-borne applications, it is difficult to produce ultrasound because the acoustic impedance of air (400 kg/m^{2}s) is much smaller than that of the piezoelectric material (30×10^6 kg/m^{2}s) [2]. This larger impedance mismatch shows that it is very difficult to generate ultrasonic waves because of two reasons: First, matching layer with necessary characteristics is rarely available. Second, for high-frequency waves, a very thin layer is required, practically which is very difficult [2].

Capacitive micromachined ultrasonic transducer (cMUT) has proved to be better alternative to piezoelectric ultrasonic transducers for various applications. cMUT is

**Corresponding author*: jjp@igcar.gov.in

Atul Tiwari and Baldev Raj (eds.), Materials and Failures in MEMS and NEMS, (201–218)
© 2015 Scrivener Publishing LLC

made directly on silicon wafers by means of standard micromachining techniques and potentially shows many attractive characteristics such as larger bandwidth, good capabilities to make high-frequency arrays, possibilities to integrate on the same wafer, the front-end electronics, and finally, low cost for mass production [3]. cMUT technology uses integrated circuit (IC) processing techniques to fabricate arrays of ultrasonic transducers in different forms and sizes. Basic micro-lithography and batch processing techniques allow thousands of arrays to be fabricated at once on each production run. Arrays with different operating frequencies, different numbers of elements, and even different geometries can be fabricated [3] on a single silicon wafer, resulting in both uniform quality and reduced cost.

Capacitive ultrasonic transducers use the electrostatic principle, in which electrostatic force is responsible for inducing the vibration in membrane to transmit the waves in surrounding medium. In the receiving mode, deflection of membrane is due to the pressure of ultrasonic waves, which results in the change of capacitance between conducting membrane and rigid back plate of the device.

Three different cMUT operating regimes have been reported so far: conventional, collapse, and collapse snapback [4]. In the conventional operation, the cMUT is biased at a voltage close to the collapse voltage. The sum of the DC bias and the AC excitation are adjusted so that the membrane does not make contact with the substrate. The DC bias causes a deflection in the membrane and induces stress within the membrane to balance the electrostatic attraction. Driving the membrane with an AC voltage superimposed on the DC bias voltage generates ultrasound. If the biased membrane is subjected to ultrasound, a current output is generated by the capacitance change under constant bias voltage. The amplitude of this output current is a function of the frequency of the incident wave, the bias voltage, and the capacitance of the device [2]. In this mode, the maximum AC displacement occurs at the center of the membrane.

Significant progress in cMUTs has been demonstrated in the early 1990s. Moving from the first functional device in 1994 [5] to first full-scale, phased-array imaging results in 2002 [6] took less than a decade. It has high impact in the area of ultrasonic imaging and expected to be an excellent transducer in biomedical applications, hence rapidly progressing, transducer technology. Ultrasonic scanners using two-dimensional cMUT arrays recently have demonstrated with clinical-quality images [7,8]. However, cMUT being a complex MEMS structure, fabrication technology is not yet matured and is in the process of moving from R&D studies to commercial area.

A program on the development and fabrication of cMUT was initiated at Indira Gandhi Centre for Atomic Research (IGCAR) for in-service inspection of the main and safety vessels of the prototype fast breeder reactor (PFBR) in collaboration with Indian Institute of Science (IISc), Bangalore and Central Electronics Engineering Research Institute (CEERI), Pilani, India. The envisaged application requires a higher dynamic range and working temperature. Design of cMUT devices was carried out at IISc, and fabrication of cMUT was performed at CEERI, Pilani, using surface micromachining and wafer bonding techniques. IGCAR played a crucial role in device characterization and failure analysis making use of in-house characterization tools and providing effective and useful feedback about the failure of fabricated devices. This chapter shares some of these experiences.

6.2 cMUT Design and Finite Element Modeling Simulation

The device consists of hexagonal silicon membrane suspended 1.0 μm above the silicon substrate which serves as the bottom electrode (see Figure 6.1). The membrane is fixed along its edges, and the cavity thus formed is vacuum-sealed during the fabrication process. This is done to reduce the transducer losses and improve the dynamic range of the device which enables a better signal-to-noise ratio leading to the detection of smaller defects in materials.

A layer of aluminum, 1 μm thick, is deposited over the silicon membrane, and this serves as the top electrode. The frequency of the device is selected on the basis of the size of the smallest crack (or imperfection) to be detected, which in turn decides the geometrical parameters, such as thickness and the edge length of the hexagonal membrane. The edge length of the hexagonal membrane is designed to be fixed at 50 μm with a uniform thickness of 1 μm. The wavelength, in a material like steel, corresponding to a frequency of 2.35 MHz is about 2 mm, which is the desired resolution of the device. Finite element modeling (FEM) has been an important aid in the evolution of cMUT like MEMS sensors [9,10]. In the present work, FEM was performed to find out the design parameters like natural frequency, pull in voltage, etc., of the cMUT membrane using Intellisuite—a commercial MEMS computer-aided design (CAD) tool [11]. Intellisuite was used to calculate membrane characteristics including maximum displacement, equivalent mechanical impedance, and frequency response. The required input parameters for these simulations include thickness and edge length of the membrane, Young's modulus, Poisson's ratio, material density, dielectric constant, environmental pressure, tension force, electrode thickness, air gap thickness, DC bias source, AC signal, and ratio of AC to DC voltages. Some of the design parameters are shown in Table 6.1 [12].

The shape of the poly silicon membrane was regular hexagon with an edge length of 50 μm and thickness of 1 μm. On top surface, Al electrode was selected with a dimension of 50 μm edge length and 1 μm in thickness. All the edges were fixed using boundary conditions, and frequency analysis was performed.

Figure 6.2 shows the first two modes of vibrations of the capacitive membrane. First mode of vibration was found to be at 2.4 MHz. Frequency analysis was performed for various materials with different thickness, and the results are shown in Figure 6.4. It is clear from Figure 6.3(a) that natural frequency increases linearly with increase in

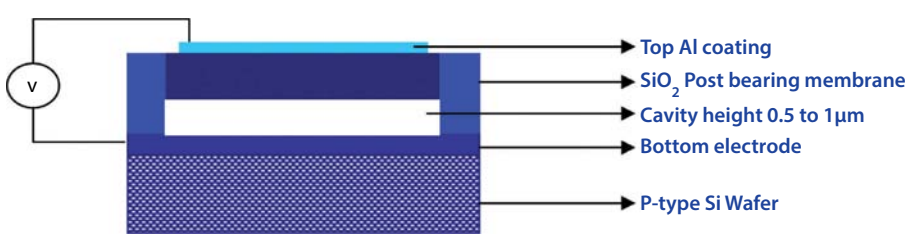

Figure 6.1 Schematic diagram of a single cMUT cell with 1-μm-thick membrane coated with Al electrode, with an air or vacuum cavity of height 0.5–1 μm. Bottom substrate coated with Al electrode separated with the top membrane by an SiO_2 insulator posts.

Table 6.1 Design parameters of cMUT device.

S. No.	Parameter	Value
1.	Shape of the membrane	Regular hexagon
2.	Thickness	50 μm edge length × 1.0 μm
3.	Cavity height	1.0 μm
4.	Residual stress of membrane	200 MPa
5.	Pull-in voltage of the structure	90 V DC
6.	Natural frequency	2.4 MHz
7.	Maximum displacement	0.16 μm at 50 V DC + 10 V AC
8.	Maximum stress in membrane	256 MPa

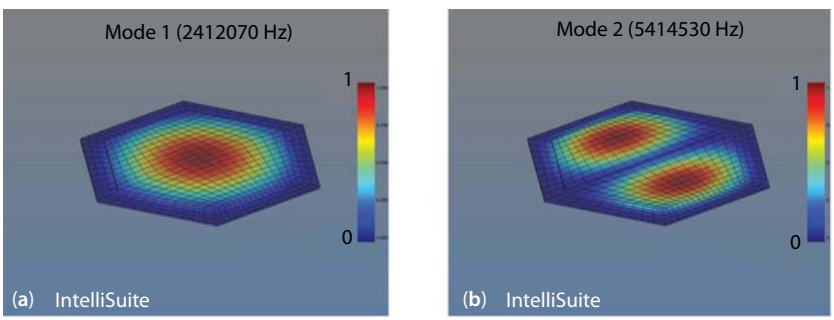

Figure 6.2 Vibration modes of single cMUT cell: (a) First mode of vibration was found to be at 2.4 MHz and (b) in Mode 2 the vibration was found to be 54.14 MHz.

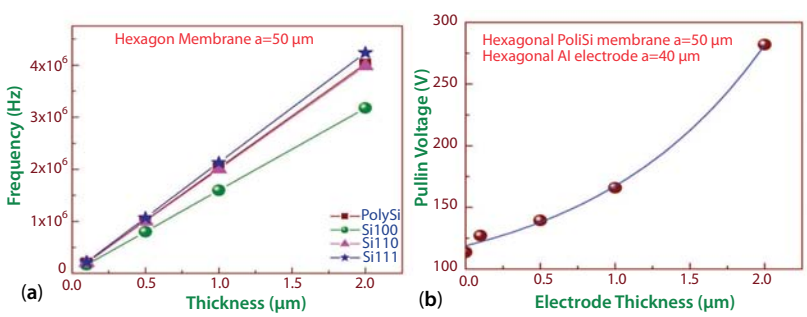

Figure 6.3 (a) Variation of natural frequency versus frequency plot for four different materials. (b) Variation of Pull-in voltage versus thickness plot for poly Si membrane.

thickness for all the materials studied. The DC bias at which the top membrane touched the bottom plate is known as pull-in voltage and is an important parameter in the design of a cMUT. To determine the optimum pull-in voltage value for the designed cMUT, static analysis was performed. Figure 6.3(b) shows the variation of pull-in voltage with electrode thickness, and it is evident from this figure that pull-in voltage increases with increase in electrode thickness [10]. Dynamic analysis of the device revealed that the acoustic power radiated by a single cell is of the order of 0.05 μW [13]. This necessitates the use of these cells in the form of arrays to couple more power into the medium being investigated. Hence, the arrays of 1×1, 5×1, 5×5, and 10×10 are proposed in the design of cMUT.

6.3 cMUT Fabrication and Characterization

Fabrication of the micromachined capacitive ultrasonic transducer was performed using both the techniques, viz. surface micromachining [3] and wafer bonding techniques [14]. Both the fabrication processes with their results are discussed in the subsequent sections.

6.3.1 Surface Micromachining Method

In this fabrication technique, double-side-polished, 4-inch, p-type, <100>, 500–550-μm-thick silicon wafer with resistivity 10–20 Ohm-cm were used. After standard wafer cleaning, thermal 1.0 μm silicon dioxide was grown on silicon wafer for cavity formation and for phosphorus diffusion to make bottom electrode/plate. Low Pressure Chemical Vapor Deposition (LPCVD) nitride of thickness 1500 Å was deposited after diffusion for isolation. Nitride deposition is followed by Atmospheric Pressure Chemical Vapor Deposition (APCVD) PSG (Phosphosilicate Glass) deposition as sacrificial layer [15].

After PSG deposition and planarization, LPCVD polysilicon was deposited as active layer of membrane and top electrode. Membrane patterning was followed by phosphorus diffusion for top electrode. Once electrode was formed, sacrificial layer was removed using hydrofluoric (HF) solution. Contact window was opened, and aluminum was deposited followed by metal patterning for top and bottom electrode contact. Micro photograph of a fabricated single cell is shown in Figure 6.4 [15].

cMUT devices fabricated by surface micromachining did not respond to any excitation. To know the cause of the device failure, a cross-sectional SEM was carried out on the devices at wafer level and is shown in Figure 6.5. From this figure, it is clear that cMUT membrane did not release completely. One can clearly see the residual sacrificial layer.

6.3.2 Wafer Bonding Method

To overcome the issues in the surface micromachined fabrication, the conventional wafer bonding fabrication technique was implemented for the next batch of cMUT device fabrication at CEERI, Pilani, India [15].

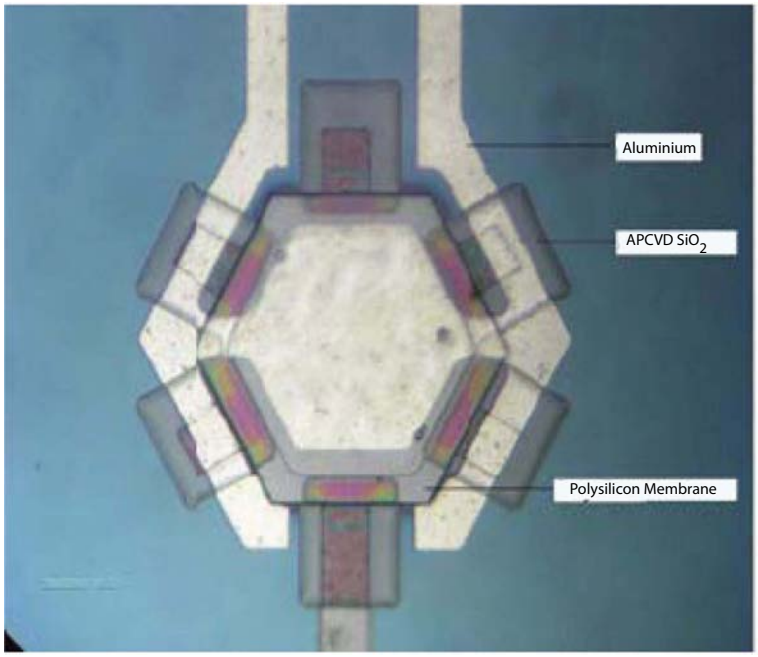

Figure 6.4 Single element of cMUT device with poly silicon membrane and aluminum coated top electrode.

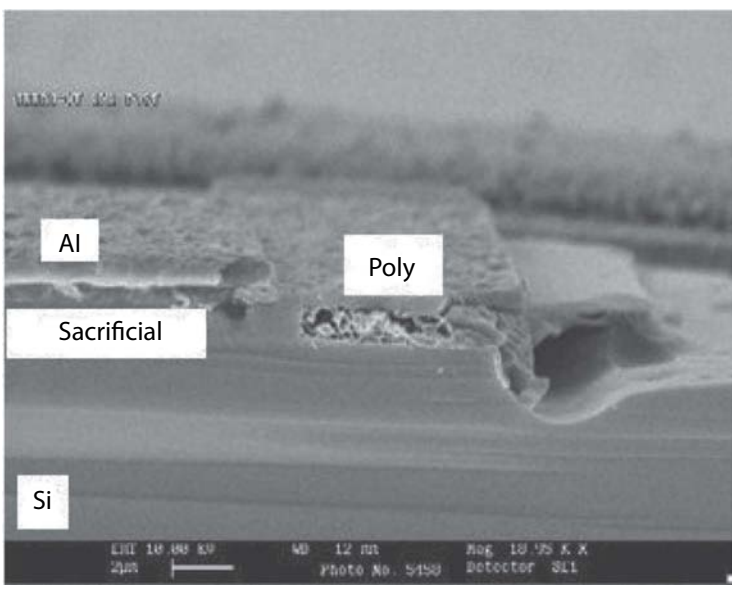

Figure 6.5 SEM image of a single cMUT cell. Sacrificial layer was not completely removed to release the membrane.

In this fabrication technique, two wafers were used. One is single-side-polished, 4-inch, p-type, <100>, and 500–550-μm-thick silicon wafer with resistivity 10–20 $\times 10^9$ cm, which was used for bottom plate and the cavity formation. Second wafer was silicon on insulator (SOI) with device thickness 2.0±0.5 μm, handle thickness 500±5 μm, and device resistivity of 2–5 $\times 10^9$ cm. Standard wafer cleaning was used, and thermal 1.0 μm silicon dioxide was grown on silicon wafer for cavity formation and for support (posts) of membrane. Lithography was done to pattern the cavity for each cell. Mask with different arrays of elements was used for lithography for cavity formation. Dry etching of silicon dioxide was performed to achieve 1.0 μm cavity height [15].

Bottom silicon electrode of the cells was heavily doped by $POCl_3$ to achieve resistivity of 1–2 Ohm-cm. A 1500 Å layer of LPCVD silicon nitride was deposited to act as insulating layer. The wafer was ready for wafer bonding with SOI. The surface finish and cleanliness of both SOI and patterned silicon wafers play an important role for wafer bonding. Therefore, prior to the bonding, the wafer surface was cleaned and activated. The wafer bonding was done with a commercial wafer bonder (M/s EVG, Austria) at pressure in the range of 10^{-4} mbar and temperature of 400 °C. After this, the handle wafer from bonded SOI etched away (using TMAH - Tetramethylammonium hydroxide) up to the buried oxide layer of the SOI wafer to form the membrane.

This oxide layer was removed with 10% HF solution. Remaining device wafer of 2.0 μm thick was oxidized, and this oxide was etched to make 1.0-μm-thick silicon membrane. The transferred silicon layer (from SOI) was phosphorous doped and patterned by photolithography followed by plasma etching by Reactive Ion Etching (RIE) and Al deposition for top plate and wire bonding pads. A typical diced and packaged cMUT device is shown in Figure 6.6.

To verify the membrane release by present method, focused ion beam milling was used to cut open a window for imaging the cross section of the device. Figure 6.7 shows

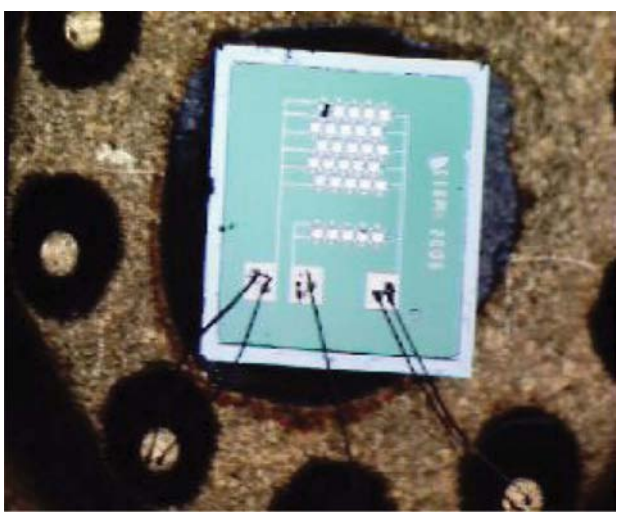

Figure 6.6 Diced and packaged 5×5 arrays and 1×5 arrays of cMUT device.

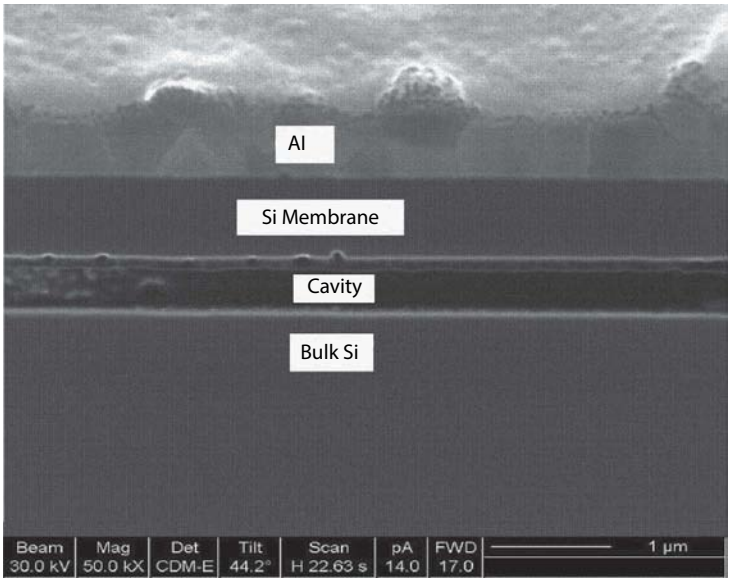

Figure 6.7 Cross-sectional SEM image of a single cMUT cell shows cavity properly etched out during fabrication process. However, cavity height appears to be less than the designed value.

cMUT single-cell cross-sectional view, which shows a clear cavity and confirms the successful release of the membrane. However, the cavity height appears to be less than 1 µm.

6.3.2.1 Dynamic Characterization Using Laser Doppler Vibrometer

Since the membrane was released, dynamic characterization of the device was carried out using laser Doppler vibrometer (LDV) at IISc. LDV is a noncontact vibration measurement technique using the Doppler effect. It measures the back-scattered light from a vibrating structure to determine its vibrational velocity and displacement. LDVs are typically two beam interferometric devices which detect the phase difference between an internal reference and the measurement beam. The measurement beam is focused on the target and scattered back to the interferometer [16].

The frequency response of the device was determined (see Figure 6.8), and the natural frequency of the single-cell cMUT was found to be at 2.24 MHz, which is close to the design value of about 2.4 MHz. The frequency response function was determined by applying a 9 V periodic chirp sweeping the frequency from 0 to 3 MHz [16]. The displacement response of the cMUT cells was determined by applying a 3 V AC signal together with a DC bias of 6 V.

At resonance, the impedance will be maximum, and this can be observed using a network analyzer. An Agilent make network analyzer (Model No. E5100A) was used to plot the frequency spectrum (from 10 kHz to 180 MHz) of .cMUT devices (not shown here). But none of the devices has shown the impedance peak at the expected resonance frequency.

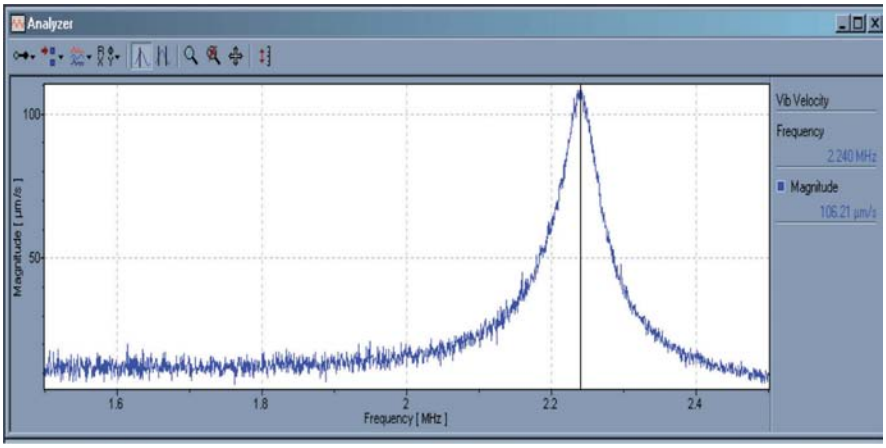

Figure 6.8 Frquency response of single-cell cMUT device measured using LDV. From this figure natural frequency of the device was estimated.

6.3.2.2 Capacitance Measurement

To study the electrical response of the device, capacitance measurements were carried out on 5 × 1 and 5 × 5 arrays using precision LCR (Inductance – L, Capacitance – C and Resistance – R) meter (Quadtech, Model No. 1920). Unfortunately, none of the devices was showing any constant *C* value and showed unexpected low resistance value [17]. This clearly implies that there is an Ohmic short between top and bottom electrodes of the device. To identify this Ohmic short, further characterization was carried out using surface profiler and SEM.

6.3.2.3 Surface Profile and Morphology of cMUT Membrane

Dektak Stylus Profiler was used to study the surface profile of cMUT array and membrane deformation during the application of pull-in DC voltage. Figure 6.9(a) shows the surface profile of a single cMUT cell. Although the expected height of membrane (1 μm) from the substrate is seen in these figures, the surface roughness of the electrode coating is large (≈1 μm) [17]. This is also evident from Figure 6.9(b) which shows the AFM image of the Al electrode. Figure 6.9(a) also shows the surface life profile when a DC voltage was applied to the device. It is clear from this figure that there is no deformation taking place in the membrane due to the applied DC voltage further confirming the nonfunctionality of the device.

6.3.2.4 SEM and EDS Analysis

SEM and energy-dispersive X-ray spectrometer (EDS) studies were undertaken on a cMUT using scanning electron microscopy (Philips, Model No. ESEM XL-30). Figure 6.10(a) and (b) shows the SEM image of one cell of 5×1 array and the interface between Al electrode and Si, respectively. Inset of Figure 6.10(b) shows the EDS spectra recorded on Al and has the expected characteristic peaks of Al and Si. From these figures, one can observe that the Al electrode coating is not centered on the membrane

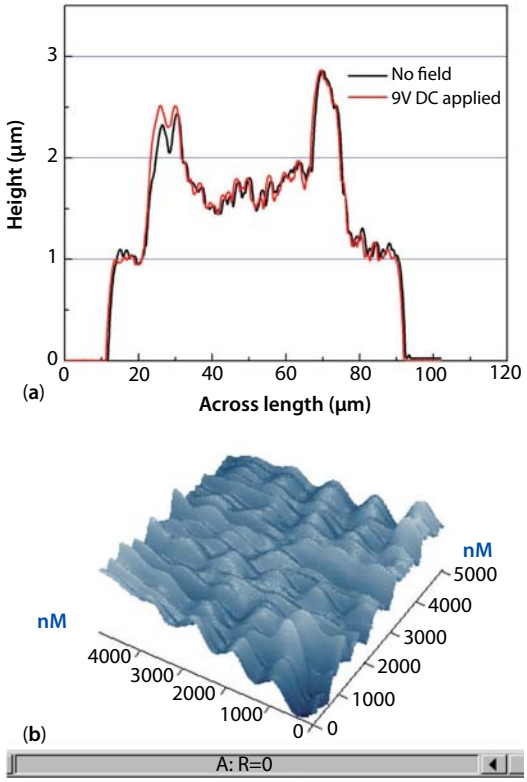

Figure 6.9 (a) Surface line profile of a single cMUT cell with and without DC voltage and (b) surface morphology of cMUT cell.

and is not uniform. Also, micro cracks are seen at several places on the device (shown by arrow).

With the various analyses and testing described earlier of the cMUT devices with in-house characterizing tools, it has been observed that only cavity has been successfully cleared in the cMUT device fabrication compared to earlier fabrication. The aforementioned tests establish that the offset in Al electrode coating was the reason for the nonfunctionality of the devices. Also, the micro crack in the top membrane permitted the Al material inside the cavity during the process of electrode coating, which causes a short between top membrane and bottom substrate of the cMUT device. The aforementioned analysis clearly confirms that only cavity has been successfully cleared in the second batch of cMUT device fabrication compared to first batch of fabrication [17,18].

The reasons for the failure of the wafer bonding process was identified as follows: (1) large bow in the silicon wafers caused weak joints of the SOI wafer after fusion bonding, and (2) misalignment of the metal interconnections has caused shift in the displacement peak of the membrane.

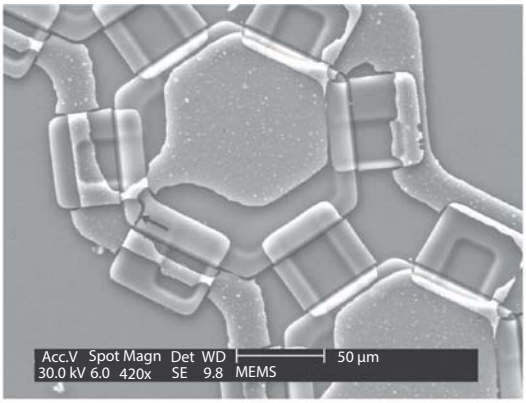

(a)

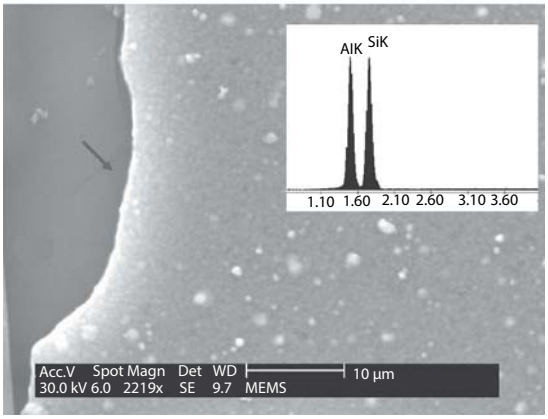

(b)

Figure 6.10 (a) SEM image of the (a) cMUT cell and (b) Al electrode and Si interface. It is clear from these figures that top Al electrode of the fabricated device is not centered. Also several micro cracks are seen and are shown by arrows.

6.3.3 Wafer Bonding Method with Isolation Trenches

To avoid these difficulties, next batch of cMUT devices were fabricated with isolation trench using anodic bonding technique. The developed fabrication process is easy, low temperature (<400 °C), stiction free, repeatable, reliable, and gives high yield (>90%) [19]. The cMUT device is designed and fabricated successfully using the developed process, which requires SOI wafer for membrane and cavity formation, and Pyrex glass wafer for cavity and bottom electrode formation. The process is used for single cell as well as for development of 1×5, 5×5, and 10×10 cMUT arrays. Figure 6.11 shows the photograph of the wafer containing the cMUT devices fabricated by present method. Now, the characterization of these devices will be presented.

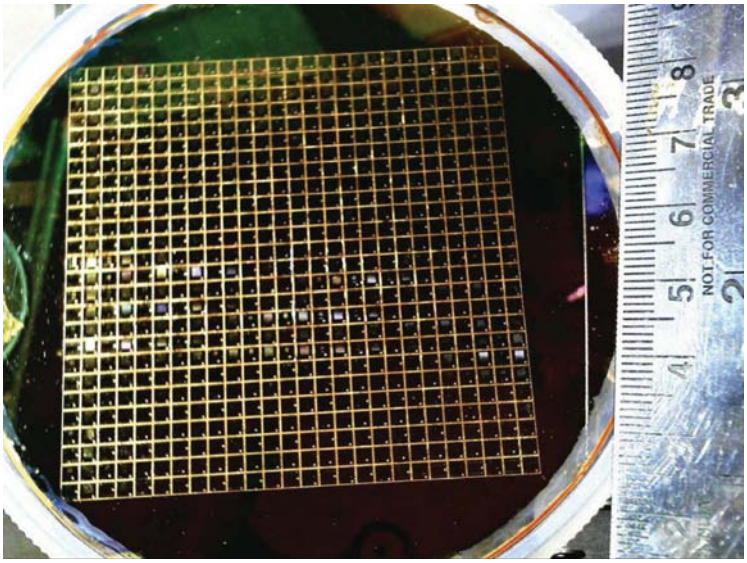

Figure 6.11 Photograph of the fabricated 4″ wafer containing cMUT devices fabricated by anodic bonding technique.

6.3.3.1 Dynamic Characterization Using Nano Vibration Analyzer

A laser-based interferometric system (Nano Vibration Analyser—M/s SIOS, GmbH make) was used for characterizing the frequency response of the cMUT devices. It is a compact, fiber-coupled laser-interferometric vibrometer integrated with a precision microscope and works in noncontact mode. This interferometric vibrometer can precisely measure the vibration displacement or changes in length with a high accuracy of ~ 0.1 nm over a wide range of frequencies up to 10 MHz [20].

Figure 6.12(a) and (b) shows the block diagram and photograph of the experimental setup, used for the dynamic characterization of the cMUT devices, respectively. NVA comprises of a He–Ne laser (λ = 632.8 nm), a compact fiber optic-coupled sensor head with a built-in miniaturized interferometer and an interface with a PC, including software, which controls the instrument and displays measurement results. The measuring laser beam is focused onto the cMUT device under test, with a microscope objective and the back-reflected signal interferes with the reference signal inside the interferometer [20]. The wafer containing cMUT devices were placed on an X–Y stage (see Figure 6.12(c)). Two tungsten microprobes, monitored through another USB camera, were used to apply the biasing voltage to the cMUT under characterization. This was done by precisely placing the tungsten tips on contact pads of the device (see Figure 6.12(d)). AC signal was applied using a function generator (BK Precision make, model 4086 AWG) and a high-voltage power supply (SRS make, Model: PS325) was used to provide the DC biasing. For simultaneous application of AC signal and DC bias voltage to the device, a simple bias T-circuit was used. By varying the function generator frequency in required steps, amplitude of vibration was recorded at each frequency and resonance frequency of each cMUT device was estimated from the plot of frequency versus amplitude.

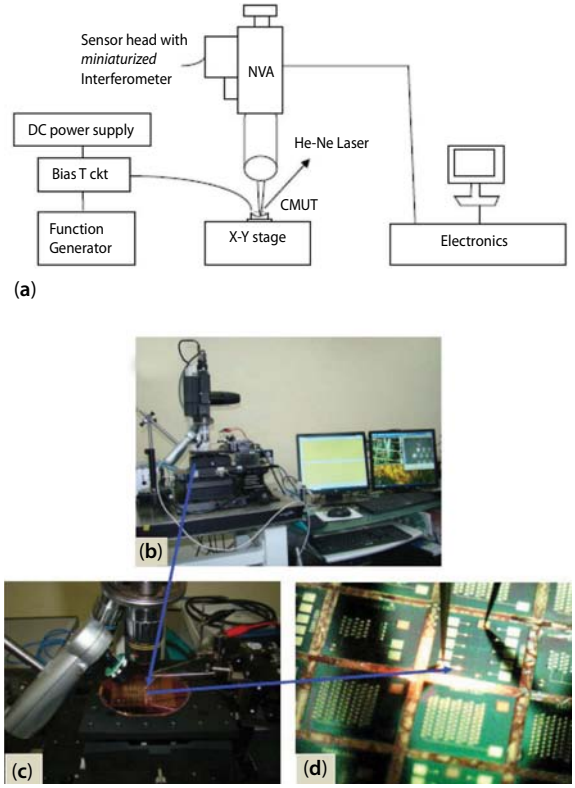

Figure 6.12 (a) Block diagram and (b) photograph of the experimental setup for dynamic characterization of cMUT devices, (c) wafer containing cMUT devices along with micromanipulators and digital camera, and (d) a single cMUT cell being biased with tungsten probes.

A typical frequency response of a cMUT cell is shown in Figure 6.13(a). It is recorded by applying an AC excitation signal of 4V superimposed with a DC bias of 100 V. From this plot, it is clear that it has a resonant frequency at ~1.54 MHz with a bandwidth of 48.5 kHz leading to a Q-factor of 31. Also, a typical response of an array of 1×5 cells is shown in Figure 6.13(b). Inset of these figures also shows the displacement plots measured using LDV for comparison. Resonance frequency of these cMUT devices is around ~1.6 MHz (at 150V DC + 5V AC). Similar measurements were carried out on about 45 elements, and it is found that the resonance frequency of the measured cells is mostly centered around 1.5 MHz with a variation of ~100 Hz. Also, the average Q-factor was about ~28 [20].

Effect of the magnitude of the applied DC bias and AC signal on the resonance frequency of the cMUT cells is also studied. Figure 6.14(a) shows the variation of resonance frequency with increasing DC voltage for a fixed AC voltage. Inset of the figure shows the variation of resonance frequency with the applied DC voltage. It is clear from this figure that with increasing DC voltage, both amplitude of vibration and resonant frequency also increases. cMUT natural frequency generally decreases as the electric field increases, reaching a value of zero at pull-in and is explained on the basis of 'spring softening' [3]. However, strain-hardening effects can cause the frequencies to increase

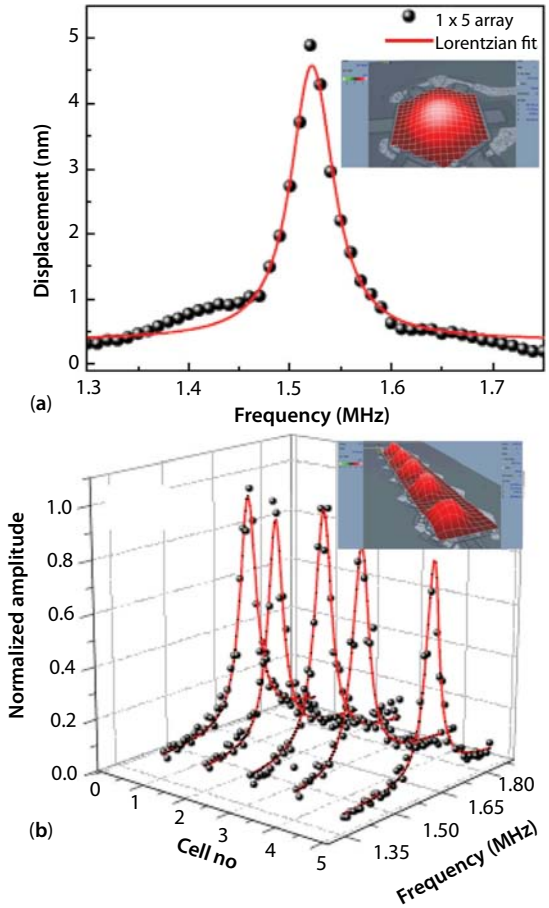

Figure 6.13 Frequency response of (a) single cMUT cell and (b) 1×5 array. Resonance frequency of the cells is ~1.5 MHz with an average Q-factor of ~28.

with voltage. cMUT devices are always fully clamped at the edge. Therefore, the nonlinear and nonuniform electrostatic forces are generated due to the presence of residual stress and the strain energy in the middle of the membrane. For a large diameter, large gap membrane with large deflection, nonlinear behavior known as the 'spring hardening' effect may be seen [21] and might be the reason for increase in frequency with increasing DC voltage. Figure 6.14(b) shows the effect of AC signal voltage on resonance frequency of cMUT cells. Amplitude of vibration was found to increase linearly with increase in the AC signal magnitude (see inset). However, as expected, resonant frequency did not change.

6.3.3.2 Static Characterization and CV Measurements

For studying the static response, DC voltage alone was applied across the cMUT device and the deflection of the membrane was monitored using NVA. Incremental DC voltage in the range of 0–120V was applied to the device and corresponding displacement of the cMUT membrane was noted down. For measuring CV data, again bias T-circuit was

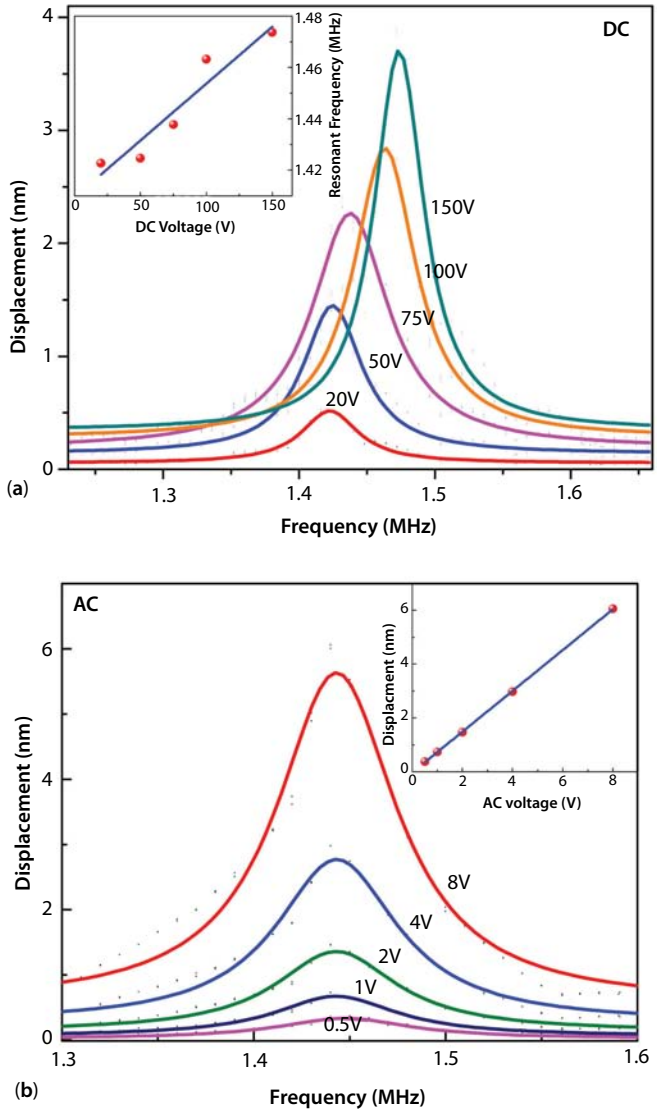

Figure 6.14 Shift in resonance spectrum of cMUT with increasing (a) DC bias voltage and (b) AC signal. Frequency was found to increase linearly with increasing DC voltage where as it was independent of AC signal amplitude.

used, but instead of function generator, a precision LCR meter (M/s Agilent Technologies, Model No. E 4980A) was connected in the capacitor arm. LCR meter was connected to a personal computer through USB interface. A labVIEW-based program has been implemented and used to set the LCR meter measurement parameters to capacitance (C) and voltage (V), collect the data *in situ* and store it for off-line analysis. The AC signal amplitude and frequency of C measurement was set at 1V and 1 KHz, respectively.

Figure 6.15(a) shows a typical static deflection versus voltage response of cMUT device. From this figure, it is clear the deflection (toward the bottom electrode) increases

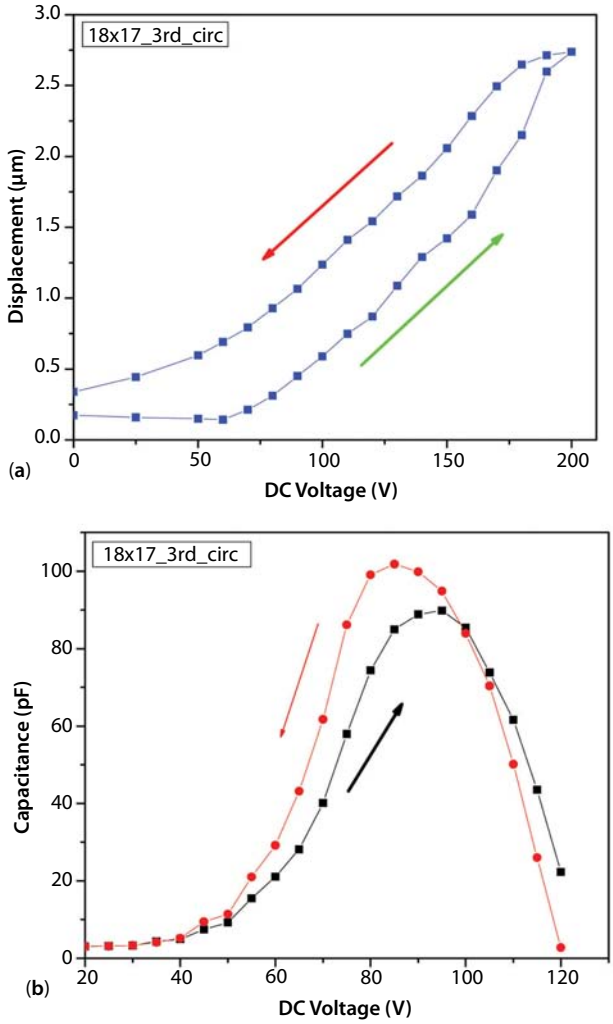

Figure 6.15 (a) Static deflection data of a typical cMUT membrane measured using NVA. (b) CV measurement of a cMUT device.

with increasing DC voltage. However, the deflection does not seem to saturate (pull-in), and there is a hysteresis in the response. Figure 6.15(b) shows the CV response of a typical device. Although, the C value was found to increase with increasing DC voltage until 100V, after which it started decreasing. This peculiar behavior needs further investigation.

6.4 Summary and Conclusions

Design and characterization of cMUT has been presented. Various aspects design like membrane thickness, material, electrode material, etc., are discussed. The difficulties in fabricating these devices by surface micromachining technique and how they were

overcome using wafer bonding technique are explained. Failure analysis of the device at various fabrication steps is detailed, and the role of these crucial feedbacks in successful fabrication of the device is pointed out. It is concluded that the failure analysis of cMUT device is a major part of the device fabrication process.

Acknowledgments

The work presented in this chapter is an outcome of a collaborative project between IGCAR, Kalpakkam, India; IISc, Bangalore, India; and CSIR-CEERI, Pilani, Rajasthan, India. The authors would like to acknowledge the contributions and constant support from the colleagues at IISc and CEERI.

References

1. *Ultrasonic transducers: Materials and Design for Sensors, Actuators and Medical Applications*, Edited by Nakamura, Woodhead Publishing, 2012.
2. X. Jin, I. Ladabaum and B. T. Khuri-Yakub, "The microfabrication of capacitive ultrasonic transducers", *IEEE/ASME J. Microelectromech. Syst*., Vol. 7, no. 3, pp. 295–302, 1998.
3. I. Ladabaum, X.C. Jin, H. T. Soh, A. Atalar, and B.T. Khuri-Yakub, "Surface micromachined capacitive ultrasonic transducers," *IEEE Trans. Ultrason., Freq. Contr.*, Vol. 45, pp. 678–690, 1998.
4. Omer Oralkan, *et.al.* "Experimental characterization of collapse-mode cMUT operation," *IEEE Trans. Ultrason. Ferroelectr. Freq. Contr.,* Vol. 53, No. 8, pp. 1513–1523, August 2006.
5. M. I. Haller and B. T. Khuri-Yakub, "A surface micromachined electrostatic ultrasonic air transducer," in *Proc. IEEE Ultrason. Symp.*, pp. 1241–1244, 1994.
6. O. Oralkan, A. S. Ergum, J. A. Johnson, M. Karaman, U. Demirci, K. Kaviani, T. H. Lee, and B. T. Khuri-Yakub, "Capacitive micro-machined ultrasonic transducers: next-generation arrays for acoustic imaging?," *IEEE Trans. Ultrason. Ferroelectr. Freq. Contr.*, Vol. 49, No. 11, pp. 1596–1610, 2002.
7. Ö. Oralkan, A. S. Ergum, C. H. Cheng, J. A. Johnson, M. Karaman, T. H. Lee, and B. T.Khuri-Yakub, "Volumetric ultrasound imaging using 2-D CMUT arrays," *IEEE Trans. Ultrason. Ferroelectr. Freq. Contr.*, Vol. 50, No. 11, pp. 1581–1594, 2003.
8. D. M. Mills, "Medical imaging with capacitive micromachined ultrasound transducer (cMUT) arrays," *in Proc. IEEE Ultrason. Symp.*, pp. 384–390, 2004.
9. Y. Roh and B. T. Khuri-Yakub, "Finite element analysis of underwater micromachined ultrasonic transducers," *IEEE Trans. Ultrason. Ferroelectr. Freq. Contr.*, Vol. 49, pp. 293–298, 2002.
10. K. Prabakar, J. Jayapandian, and C.S. Sundar, Influence of membrane and electrode dimensions on the performance of a cMUT. *Workshop on Nanosensors and Devices*, IITD, New Delhi, 22–23, 2008.
11. MEMS design CAD tool Intellisuite V 8.5. 2009.
12. Aravind Pathak, "Design of a Single Cell of Capacitive Micromachined Ultrasonic Transducer", M.E. thesis, IISc, 2004.
13. Babar Ahmad and Rudra Pratap, "Static and dynamic analysis of a capacitive micromachined ultrasonic transducer", *Conference on Applications and Design in Mechanical Engineering*, Malaysia, 2007.

14. Y.Huang, A.S. Ergun, E. Haeggström, M.H. Badi, and B.T. Khuri-Yakub, "Fabricating capacitive micromachined ultrasonic transducers with wafer-bonding technology," *IEEE/ASME J. Microelectromech. Syst.*, Vol. 12, No. 2, pp. 128–137, 2003.
15. Development and fabrication of MEMS based ultrasonic transducer, Progress report submitted to IGCAR, Kalpakkam by CEERI, Pilani, 2012.
16. Rudra Pratap, "Progress report on cMUTs," Progress report submitted to IGCAR, Kalpakkam by IISc, 2007.
17. J. Jayapandian, C.S. Sundar, and K. Prabakar, "Report on the recent batch of fabricated cMUT Devices", IGCAR Internal Report, 2009.
18. T.Jayakumar, C. Babu Rao, John Philip, C.K. Mukhopadhyay, J. Jayapandian, and C. Pandian. "Sensors for monitoring components, systems and processes." *Int. J. Smart Sens. Intell. Syst.,* Vol. 3, No. 1, pp. 61–74, 2010.
19. R. Mukhiya, Aditi K. Prabakar, M. Raghuramaiah, J. Jayapandian, R. Gopal, V. K. Khanna, and M. Chandra Shekar, "Fabrication of Capacitive Micromachined Ultrasonic Transducer 2D Arrays with Isolation-trench using Anodic Wafer Bonding," MS under preparation.
20. M. Raghuramaiah, K. Prabakar, J. Jayapandian, and C.S. Sundar, "A Report on Capacitive micromachined ultrasonic transducers (cMUT) characterization," IGCAR Internal Report, 2012.
21. M. Wang, "Capacitive Micromachined Ultrasonic Transducer Arrays for Blood Flow Ultrasound Doppler and Photoacoustic Imaging Applications", Ph.D. thesis, University of New Mexico, 2010.

7

Inverse Problems in the MEMS/NEMS Applications

Yin Zhang*

State Laboratory of Nonlinear Mechanics, Institute of Mechanics, Chinese Academy of Sciences, Beijing, China

Abstract

As a structure is scaled down, the ratio of surface to volume increases and the surface effects thus stand out, which may result in the different material properties from those of bulk. Therefore, some key parameters such as Young's modulus and adhesion energy, which concern the performance and reliability of the micro/nano-electro-mechanical systems (MEMS/NEMS), are unknown. Sometimes, the direct measurements of some parameters are extremely difficult if not impossible, for example, measuring the position of an adsorbate as small as a molecule or an atom. How to use the measured quantities such as resonant frequencies and deformation to determine those key parameters forms an inverse problem. Every inverse problem requires a particular approach. In this chapter, we present some effective approaches of solving the inverse problems in the MEMS/NEMS applications. The chapter consists of two major parts: the inverse problems in (1) micro/nano mechanical resonator and (2) the stiction test of MEMS/NEMS.

Keywords: Inverse problem, MEMS/NEMS, resonator, sensor, stiction

7.1 Introduction

"*Most mathematical problems in science, technology and medicine are inverse problems*" [1]. For example, in geophysics and medicine, the inverse problem arises as the determination of properties of some inaccessible regions from the observations on the boundary of those regions [1]. In the applications of MEMS/NEMS, many physical parameters are not subject to direct measurements and the effects induced by these parameters are then the only measurable quantities.

Solving the inverse problems is to relate the (measured) effects with those (intrinsic) physical parameters. For practical applications, the interpretation of experimental findings is of fundamental importance and studying inverse problems is the only complete way of analyzing experimental results [1]. Because the micro/nanomechanical sensor can provide a label-free, high-throughput, and rapid detection of biological and

**Corresponding author*: zhangyin@lnm.imech.ac.cn

Atul Tiwari and Baldev Raj (eds.), Materials and Failures in MEMS and NEMS, (219–238)
© 2015 Scrivener Publishing LLC

chemical molecules [2,3], it has become increasingly important in detecting tiny force or mass [4–8]. Depending on the nature of the input stimuli, micromechanical sensor can be categorized as physical, chemical, or biological sensor [7].

The adsorbed analytes on a micromechanical sensor surface can cause the changes of mass, damping, stiffness changes and surface stress, etc. [7,8]. These changes can result in the deflection and resonant frequency shifts of a micromechanical sensor, which are also the mechanisms used for sensing. For example, the self-assembly of alkanethiols [5] and the ligand-receptor binding [6] on a microcantilever surface can induce surface stress, which bends the beam. The bending of beam can be related with the surface stress by the following Stoney formula:

$$\Delta\sigma = \frac{Eh^2}{6R(1-\upsilon)} \tag{7.1}$$

where E, υ, and h are the microcantilever Young's modulus, Poisson's ratio, and thickness, respectively. $R = 2L^2 / (3\Delta x)$ is the radius of curvature (L and Δx are the microcantilever length and deflection at the free end as shown in Figure 7.1). $\Delta\sigma$ is the differential surface stress, which has the unit of Nm^{-1} rather than pascal. Here, Δx is the measured quantity, which determines the surface stress ($\Delta\sigma$) by Eq. (7.1). The ligand-receptor binding is highly selectively [6,9], $\Delta\sigma$ can thus be used as an effective criterion to determine what a ligand material is in Fritz's experiment [6].

In the earlier applications of micromechanical sensor using surface stress as the sensing mechanism, surface stress $\Delta\sigma$ has the one-to-one relation with the measured quantity Δx. In general, such one-to-one relation does not hold in many micromechanical sensor

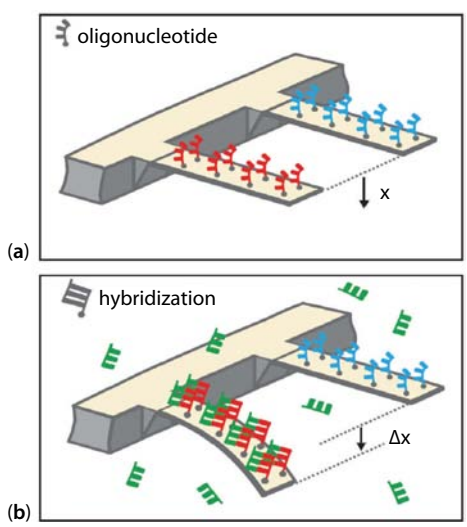

Figure 7.1 Scheme illustrating the hybridization experiment. A different oligonucleotide base sequence (red or blue) is immobilized on one side of cantilever as the receptor materials. (a) The differential signal is set to zero. (b) After injection of the first complementary oligonucleotide (green) as the ligand material, hybridization (ligand-receptor binding) occurs on the cantilever that provides the matching sequence (red), increasing the differential signal of the cantilever free end displacement (Δx). Adapted from Ref. [6].

applications. As mentioned earlier, the mass, damping, and stiffness of sensor change when adsorption occurs. The system resonant frequency changes as follows [4,7]:

$$f' = \frac{1}{2\pi}\sqrt{\frac{K+\Delta K}{M+\Delta M}}\sqrt{1-\frac{(C+\Delta C)^2}{4MK}} \tag{7.2}$$

Where f' is the resonant frequency after adsorption. K, M, and C are the effective spring stiffness, mass, and damping of a micromechanical sensor, respectively. ΔK, ΔM, and ΔC are those corresponding changes due to adsorption. In the real application, f', K, and M are the (known) measured quantity. As the sensor motion is recorded in an experiment, C and ΔC can also be easily determined from the frequency response curve by the half-power method [10]. ΔK and ΔM are the unknowns to be determined. In the forward problem (or alternatively called the direct problem [1]) in which ΔK, ΔM, and ΔC are given, f' is uniquely determined by Eq. (7.2). However, for a measured/given f', there are infinite combinations of ΔK and ΔM. The intrinsic material properties of adsorbate are embodied in ΔK and ΔM, which induce the effects of the resonant frequency changes. Therefore, a natural inverse problem arises in the application of the micromechanical resonator sensor: *How to use the changes of the resonant frequencies to determine the changes of mass and stiffness induced by adsorbates?* The effective mass (ΔM) changes due to two things: the mass of adsorbate and its position, which are the two convolving factors of determining the shifts of the resonant frequencies [11–13]. The stiffness change ΔK is mainly caused by two mechanisms: the stiffness of adsorbate [14,15] and surface stress [4–6,16,17]. When the adsorbate material vibrates with the micromechanical resonator as a whole, the system behaves as a composite structure [14,15] and the stiffness of adsorbate material always cause the system resonant frequencies to increase. As shown in the adsorption tests of *Escherichia coli* (*E. coli*) bacteria on a silicon resonator by Ramos *et al.* [14,15], the system resonant frequencies increase due to the fact that the adsorbate stiffness effect outweighs its mass effect. As surface stress can be either compressive or tensile [4,16,17], it can either decrease or increase the system resonant frequencies. On the other hand, the mechanism for damping (C) for the micromechanical resonator, which indicates the energy dissipation of the system, is a complex one though it can be measured. Various mechanisms and models have been proposed [18]; a clear physics picture still remains elusive.

Another inverse problem arises in the stiction test of MEMS structure. Stiction is a major failure mechanism for MEMS structures [19–25]. The competition between the adhesive force and the microstructure restoring force determines whether the stiction occurs and how the structure deforms [23]. The presence of residual stress changes the structure stiffness and thus leads to the change of the restoring force. The previous models of arc-shape [20,21] and S-shape [24,25] correspond to the zero residual stress case, which also prescribes the stiction shape. When the residual stress becomes large, arc-shape and S-shape significantly deviate from the actual stiction shape of a slender beam. With the assumed stiction shape of arc and S, suspension length is the only parameter needed to characterize the stiction shape and suspension length can also be used to uniquely determine the adhesion energy. However, there are infinite combinations of residual stress and adhesion energy which can result in the same suspension length. The residual stress and adhesion energy are the two key parameters concerning

the performance and reliability of the MEMS/NEMS devices and the stiction test is such an experiment designed to extract these two parameters. However, the residual stress and adhesion energy are the quantities which are extremely difficult to be measured directly. In a stiction test, the measured quantity is the structure deformation shape. Therefore, the inverse problem arises as follows: *How to use the stiction shape of MEMS/NEMS devices to determine the residual stress and adhesion energy?*

7.2 Inverse Problems in the Micro/Nanomechanical Resonators

7.2.1 Determining the Mass and Position of Adsorbate by Using the Shifts of Resonant Frequencies

For a micro/nanomechanical resonator, the resonance change due to adsorption as given in Eq. (7.2) is the sensing mechanism. The ultimate limit for a micro/nanomechanical resonator sensitivity is imposed by the thermodynamic fluctuation [26,27]. For the mass sensing, the theory proved that the limit is well below a Dalton (1 Dalton ≈ 1.65×10^{-24} g is approximately the mass of a proton), which leaves enough room for the development of the micro/nanomechanical resonator. Based on the NEMS technology, Hanay *et al.* [11] developed the resonator sensor capable of detecting a single protein with the mass of approximately one mega-Dalton. Jensen *et al.* [12] developed a carbon nanotube (CNT)-based mechanical resonator sensor capable of detecting one single gold atom with the mass of approximately 197 Dalton. The sensitivity of the CNT-based resonator has recently been pushed by Chaste *et al.* [13] to achieve the capability of detecting the mass of one Dalton. There are three major approaches to push the sensitivity of a micro/nanomechanical resonator sensor toward its ultimate limit. Because the resonant frequency is proportional to $h / L^2 \times \sqrt{E / \rho}$ (h and L are the resonator thickness and length; E and ρ are the Young's modulus and mass density) [28], the first approach is to scale down the resonator size, which is to make the factor h / L^2 large and at the same time fractional change due to a same adsorbate is also larger in a smaller resonator [29]. The second one is to use the materials with large E / ρ , such as silicon [11], silicon carbide [30], CNT [12,13], and graphene [31]. Both approaches are to increase the resonant frequencies. With very large resonant frequencies, a tiny fractional change in the resonant frequencies is still absolutely large enough to be detected [29]. In 2003, a clamped–clamped beam fabricated by the NEMS-based technology achieved the fundamental resonant frequency of around 1 GHz (10^9 Hz), which is a breakthrough as the mechanical vibration frequency enters the microwave range [30]. The third one is to increase the quality factor of a micro/nanomechanical resonator. Quality factor (Q) indicates the sharpness of resonance, which is inversely proportional to damping and has the approximate relation as follows [28,32]:

$$Q \approx \frac{1.09 f_o}{\Delta f} \tag{7.3}$$

where f_o is the resonant frequency (with no adsorbate) and $\Delta f = f' - f_o$ is its shift. For a given resonant frequency f_o, larger Q means smaller Δf can be detected as clearly indicated by Eq. (7.3). The in-plane tension has been shown to be effective on enhancing

quality factor by both simulation [33] and experiment [34]. At the same time, it is always effective to increase quality factor by setting the resonator in a vacuum environment, which reduces or even eliminates the damping due to ambient air [35].

The ultimate goal of any detection method is to achieve the level of resolving a single quantum of a measured entity [36]. For the micro/nanomechanical resonator sensor, the progresses toward this goal are clearly indicated by the improvement of the sensitivity. The resonator sensors with the capability of detecting the presence of a biomolecule [3], a protein [11], a cell [37], a virus [38], a gold atom [12], and a proton [13], have been developed. Although those achievements are very impressive, there is a fundamental problem remained in those mass resonators: all those frequency shift measurements actually cannot give the mass of individual atom, molecule, or nanoparticle [11]. As demonstrated by Jensen *et al.* [12], their CNT-based mass resonator actually does not measure the mass of a gold atom, even though the resonator has the capability of detecting a smaller frequency shift induced by the adsorption of a gold atom. The atom/molecule/particle mass and its position are the two (major) convolving factors of determining the resonant frequency shift of a resonator. To know the position, there are three major experimental approaches: (1) measuring the trajectory of a sprayed particle [26], (2) occluding some portions of resonator so that the particle must land at a specific location [12], and (3) direct measurement of the position of an adsorbate [39]. These measurement approaches not only require extra experimental setup but also (sometimes) are extremely difficult if not impossible to be applied. For example, Dohn *et al.* determined the position of a particle with the size of a micron by using optical image [39]. However, in Burg's resonator with an embedded microfluidic channel where the biomolecules are pumped in [3] as shown in Figure 7.2, the optical method cannot work because the smaller size of a biomolecule and small contrast between a biomolecule and solution. The exact position of the biomolecule is thus a major uncertainty in

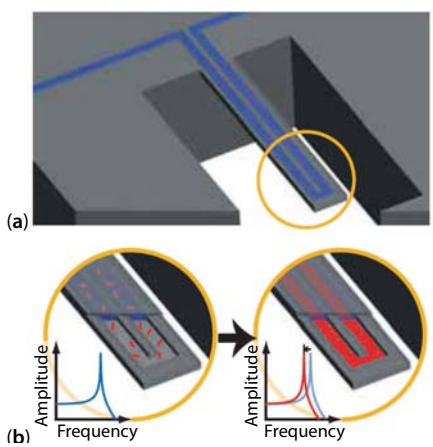

Figure 7.2 Illustration of two mass measurement modes enabled by a fluid-filled microcantilever. (a) The microcantilever is the resonator, and a microfluidic is embedded in the microcantilever. The microchannel translates mass changes into changes in resonance frequency. Fluid continuously flows through the channel and delivers biomolecules, cells, or synthetic particles. (b) Because the biomolecules, cells, or synthetic particles have different mass densities with that of solution, the resonant frequency shown as the blue and red lines changes when biomolecules pass through the microchannel. Adapted from Ref. [3].

Burg's experiment [3]. Knobel [29] gave the following comment: before a practical mass spectrometer can be made, the most important problem to be solved is to determine the atom/molecule/particle position.

In the earlier experiments of mass sensing, an inverse problem is encountered: *How to use the measured resonant frequencies to determine the adsorbate mass and position?* The methods of using multiple resonant frequencies to determine the mass and position of a single adsorbate have been developed [11, 40]. However, unlike the method of probability density function [11] or a minimizing procedure which requires at least four resonant frequencies to be measured [40], the author developed a straightforward method to tackle the problem for a circular membrane resonator made of graphene [28]. The inverse problem solved in Ref. [28] is based on the following two mechanisms: (1) the adsorbate mass and position have different impacts on the same resonant frequency; (2) for a circular membrane which has infinite resonant frequencies, the same adsorbate mass and position have different impact on different resonant frequencies [28,39].

7.2.2 Determining the Adsorption-Induced Surface Stress and Mass by Measuring the Shifts of Resonant Frequencies

As indicated by Eq. (7.2), the adsorption can induce (1) the mass addition, which results in ΔM and always reduces the resonant frequencies, and (2) surface stress, which results in ΔK and can either increases or decreases the resonant frequencies [4]. For a given/measured resonant frequency f', there are infinite possible combinations of ΔM and ΔK. One strategy is to find out either ΔM or ΔK first by a different measurement method and then use the dynamic mode to find the other. For example, by measuring the concentration of adsorbed analyte (ΔM is thus found), ΔK can then be found from Eq. (7.2) [16]; or by localizing the adsorption areas at the terminal end of cantilever to minimize the surface stress effect on the spring stiffness, $\Delta K = 0$ can be assumed [41,42], then ΔM can then be found by applying Eq. (7.2). Obviously, the drawback of this strategy is that extra efforts on device and design, which is not trivial at all, are needed. Another strategy is to use the static mode to measure surface stress to find out ΔK first [e.g., by the Stoney formula of Eq. (7.1)] and then use the dynamic mode to find out ΔK [41,43]. While, the problem of this strategy is that adsorption is a dynamic process. The adsorption-induced mass and surface stress vary not only with time [41,44] but also with how they are measured [44]. In chemical sensors, adsorption and desorption of gas molecules often occur at the same time [45]; in biological sensor, the receptor–ligand such as biotin–streptavidin and biotin–avidin also experiences a dynamic process of bonding–debonding due to the competition between the barrier of mechanical energy, dissociation kinetics, and effect of thermal activation [46]. One vivid example on the difference of the static and dynamic modes is that the adsorption of water on the microcantilever coating layer of polymethylmethacrylate (PMMA) saturates in the static mode, whereas no saturation is observed in the dynamic mode [44]. The reason is that in the dynamic mode, the diffusion of water within the polymer and the dissolution of the polymer occur simultaneously [44]. In other words, the static mode and dynamic mode may not measure the same adsorption-induced mass and surface stress. Ref. [4] presents a general method of

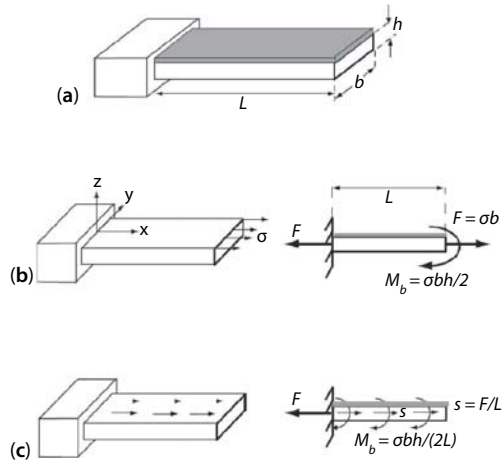

Figure 7.3 (a) Schematic of a cantilever with a uniform layer of adsorption on its upper surface. The cantilever is with the length L, width b, and thickness h. (b) The concentrated load modeling: σ is the surface stress induced by the adsorption; $F = \sigma b$ and $M_b = \sigma bh / 2$ are the concentrated load and moment exerted at the beam free end, respectively. (c) The distributed load modeling: $s = F / L = \sigma b / L$ and $M_b = \sigma bh / (2L)$ are the uniformly distributed load and moment along the length direction, respectively. Adapted from Ref. [4].

using the shifts of two resonant frequencies to uniquely determine the mass and surface stress induced by adsorption.

Figure 7.3(a) is a schematic of a cantilever with a uniform layer of adsorption on its upper surface. Figure 7.3(b) is a schematic of the concentrated load modeling, in which a concentrated load F and a concentrated moment M_b are applied at the cantilever free end. For brevity, the governing equation of the concentrated load modeling and the boundary conditions are given as follows [47–49]:

$$(m + \Delta m)\frac{\partial^2 w}{\partial t^2} + c\frac{\partial w}{\partial t} + E^* I\frac{\partial^4 w}{\partial x^4} - F\frac{\partial^2 w}{\partial x^2} = 0 \tag{7.4}$$

where m is the beam mass per unit length, and Δm is the adsorption mass per unit length, which is assumed to have a uniform distribution all over the cantilever and is thus treated as a constant. In the applications of chemical and biological sensors, an adsorbed mass spanning the entire cantilever surface is preferred instead of an adsorbed at a selected area [50], which prevents the need for selective activation of surface and avoids unspecific binding. w is the beam deflection, and c is damping. E^*I is the beam bending stiffness. The concentrated load $F = \sigma b$ (σ is the adsorption induced surface stress, and b is the beam width) [47]. Clearly, in Eq. (7.4), one of the surface effects is modeled as an axial force (F), which can influence the resonant frequencies of the beam. The Stoney formula of Eq. (7.1) is to model the surface stress as a concentrated moment applied at the beam free end [47], which will not result in any resonant frequency change [4]. There are still some debates on how to model the surface stress. Besides the aforementioned Stoney formula and concentrated load modeling, there is following one called the distributed load modeling [4,47]:

$$(m+\Delta m)\frac{\partial^2 w}{\partial t^2}+c\frac{\partial w}{\partial t}+E^*I\frac{\partial^4 w}{\partial x^4}-s(L-x)\frac{\partial^2 w}{\partial x^2}+s\frac{\partial w}{\partial x}=0 \tag{7.5}$$

where $s = F / L = \sigma b / L$ is the distributed load as shown in Figure 7.3(c), and L is the beam length. As the experiments show that the surface stress is directly related with the coverage density of adsorbate [5] or areal density of ligand–receptor binding [6], Zhang *et al.* [47] and Finot *et al.* [51] argued that surface stress should be viewed as the sum of two contributions: one is an axial force per unit length, and the other is a moment per unit cross section. In Ref. [4], the distributed load model of Eq. (7.5) is used. However, the inverse problem solving technique presented in Ref. [4] can also be applied to the concentrated load model of Eq. (7.4).

By introducing $\xi = x / L$, $W = w / L$, and $\tau = \sqrt{E^*I/(mL^4)}t$, Eq. (7.5) has the following dimensionless form [4]:

$$(1+a)\frac{\partial^2 W}{\partial \tau^2}+C\frac{\partial W}{\partial \tau}+\frac{\partial^4 W}{\partial \xi^4}-\Lambda(1-\xi)\frac{\partial^2 W}{\partial \xi^2}+\Lambda\frac{\partial W}{\partial \xi}=0 \tag{7.6}$$

where $a=\frac{\Delta m}{m}$, $C=c\sqrt{\frac{L^4}{E^*I\,\mathrm{m}}}$, $\Lambda=\frac{\sigma b L^2}{E^*I}$. Clearly, a indicates the ratio of the adsorption mass to the beam mass, and Λ indicates the ratios of the surface stress to the beam stiffness per unit width. C is the dimensionless damping. Again, in the real sensor application, a and Λ are unknown; the resonant frequencies are extracted from the beam frequency response curves [41]. Therefore, using the resonant frequencies (shifts) to determine a and Λ forms an inverse problem. For a given $(a, \Lambda) = (10^{-3}, 10^{-2})$, the first two resonant frequencies can be calculated from Eq. (7.6) as a direct problem as $\omega_1 = 3.516491$ and $\omega_2 = 22.025444$. Now, how to use these two (measured) resonant frequencies to determine a and Λ is presented in Figure 7.4.

Figure 7.4(a) plots the variation of the first eigenfrequency, ω_1, as a function of Λ and a, which is a titled plane. ω_1 increases monotonically with the increase of Λ and decreases monotonically with the increase of a. The level plane is the one with the fixed first eigenfrequency value of $\omega_1 = 3.516491$. The intersection of these two planes is all the combinations of Λ and a, which result in the same first eigenfrequency of $\omega_1 = 3.516491$. The intersection is a line marked in Figure 7.4(a). This line also indicates that the combinations resulting in a same eigenfrequency are infinite. Figure 7.4(b) plots the second eigenfrequency of ω_2 as a function of Λ and a. The level plane is the one with the fixed value of $\omega_2 = 22.025444$. Again, the intersection line of the two planes indicates the combinations of Λ and a resulting in $\omega_2 = 24.628$. Clearly, for any given values of Λ and a, each eigenfrequency is uniquely determined by Eq. (7.6). As an inverse problem, there are infinite combinations of Λ and a for a given eigenfrequency. However, as shown in Figure 7.4(c), for two given eigenfrequencies, their combinations of Λ and a, which are two lines, intersect. Physically, this intersection is used to uniquely determine the combination of Λ and a. In Figure 7.4(c), the intersection of the combinations of Λ and a for $\omega_1 = 3.516491$ and $\omega_2 = 22.025444$ is marked as a circle, which happens to be exactly $(a, \Lambda) = (10^{-3}, 10^{-2})$. Physically, that the inverse problem can be solved is due to

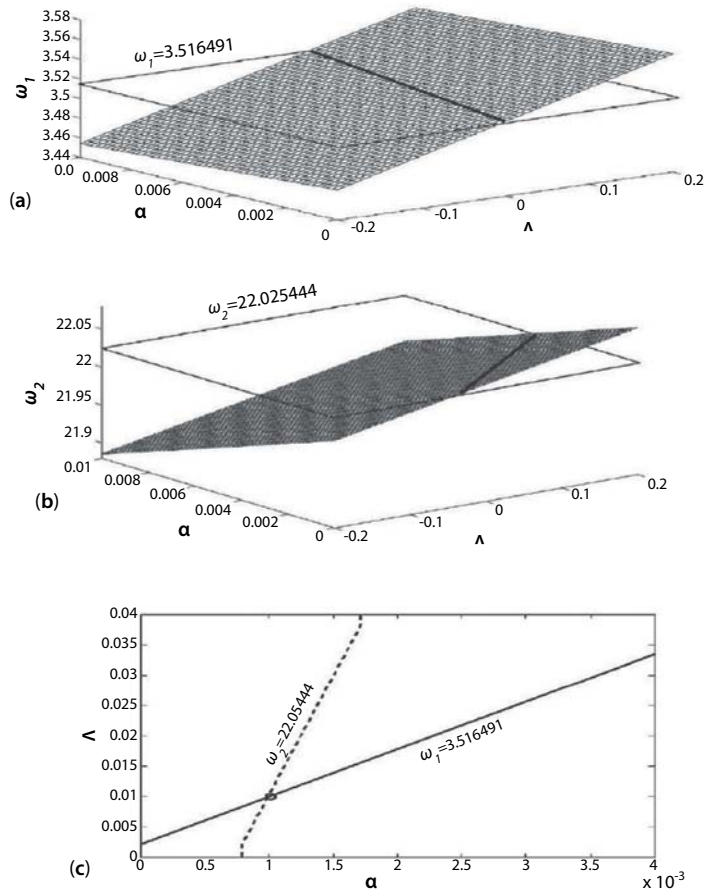

Figure 7.4 (a) Variation of the first resonance frequency (ω_1) as a function of α and Λ. The level plane is the one with a fixed resonance frequency of ω_1 = 3.516491. The intersection of the two planes is marked with a solid line. (b) Variation of the second resonance frequency (ω_2) as a function of α and Λ. The level plane is the one with a fixed resonance frequency of ω_2 = 22.025444. The intersection of the two planes is marked with a solid line. (c) The combinations of α and Λ for the resonant frequencies of ω_1 = 3.516491 and ω_2 = 22.025444, which are two lines marked in Figures 7.3 and 7.4. The intersection is marked with a circle, which corresponds to (α, Λ)= (10^{-3}, 10^{-2}). Adapted from Ref. [4]

the fact that surface stress and mass have different impacts on the resonant frequencies, which is also reflected mathematically in Eq. (7.6). Here, the inverse problem is solved by using the first two resonant frequencies. As a higher resonant frequency has a higher sensitivity, the method can be easily extended to this application scenario by choosing to calculate two other different resonant frequencies in Eq. (7.6).

7.2.3 Determining the Surface Elasticity and Surface Stress by Measuring the Shifts of Resonant Frequencies

One of the motivations to solve the inverse problem of using the shifts of resonant frequency to determine surface elasticity and surface stress is ascribed to a debate in 1970s

[17]. In 1975, Lagowski *et al.* [52] found that the resonant frequencies of a microcantilever deviate significantly from those predicated by the axial load-free beam theory; they proposed that surface stress is the mechanism causing the resonant frequencies shifts. Subsequently, Gurtin *et al.* [53] disputed Lagowski's explanation; they argued that the resonant frequency is independent of surface stress and surface elasticity is the only mechanism responsible for the resonant frequency shifts. Lagowski's essential argument is that surface stress behaves as residual stress, which has the axial load effect and thus changes the resonant frequencies [52]; Gurtin's argument is that as the surface stress is induced inside a surface layer, there will be a corresponding force generated inside bulk due to constraint [53]. According to Newton's third law, the force inside the bulk has the same magnitude but opposite direction as the product of surface stress and the thickness of surface layer. Therefore, the total amount of the axial load inside a micro/nanostructure is zero, and the resonant frequencies are independent of surface stress, which is the same scenario of the bending of a bimetallic beam due to temperature studied by Timoshenko [54]. The application of ansatz that nanostructure=bulk + surface [55] in continuum mechanics leads to the so-called core–shell model [56–58], in which the core is bulk and the shell is surface layer. In a surface layer, the total surface stress (τ) is given as follows [56–58]:

$$\tau = \sigma + C_s \varepsilon \tag{7.7}$$

where ε is the dimensionless strain, and C_s is the surface modulus. Here, τ is the result of charge redistribution as the electrons response to the effects of terminating a solid at a surface [59]. By the thermodynamics definition, τ is a tensor associated with the reversible work to elastically stretch a pre-existing surface [60]. We find that τ consists of two parts: σ and $C_s\varepsilon$; σ, which is strain independent, is often referred to as surface stress [52]; $C_s\varepsilon$, which is strain dependent, is often referred to as surface elasticity [53]. Surface elasticity is due to the formation of surface layer which has a different elastic property from that of a bulk [58,61]. Surface relaxation [61] and sometimes surface reconstruction [59] are the two profound mechanisms responsible for the formation of a surface layer. Both σ and C_s have the unit of force per unit length (Nm^{-1}) compared with that of force per unit area (Nm^{-2}) for the bulk stress and modulus. Here, σ and C_s can be either positive or negative [55], which can thus either stiffen or soften a micro/nanostructure. In dynamics, the effect of the structure stiffness change (either stiffening or softening) is embodied in the shifts of the structure resonant frequencies.

Lagowski *et al.* [52] and McFarland *et al.* [62] found surface stress by measuring the shifts of one resonant frequency and by assuming zero surface elasticity. Similarly, Gurtin *et al.* [53] found surface elasticity by proving that surface stress has no impact on the resonant frequency. Gavan *et al.* [63] are the first to use the two resonant frequencies of a microcantilever to determine the effects of surface elasticity and surface stress. Again, Gavan *et al.* [63] extracted the fitting value of surface stress/surface elasticity by assuming that of surface elasticity/surface stress to be zero, which excludes the general case that both surface elasticity and surface stress are non-zero [55]. Recently, many theoretical investigations [64–66] show that both surface elasticity and surface stress have the impact on the structure stiffness; however, the effect of surface elasticity is too small to explain the experimental observations for a slender structure. The reason

is geometrical, as shown in Ref. [17], the surface stress effect is amplified by a factor of $(L / D)^2$ (L and D are the length and diameter of a cylinder-like nanowire, respectively). For slender structure, because this $(L / D)^2$ factor is large, the surface stress effect is dominant if σ and C_s have the same order of magnitude [17]. However, for chunky structure or some materials whose C_s is significantly larger than σ, the surface elasticity effect must be considered [17]. Atomistic simulation is often used to obtain σ and C_s, which are determined by the underlying lattice structure and interatomic potential [55,67,68]. It is noted that σ and C_s calculated by atomistic simulation can be significantly different for the same material depending on what kind of interatomic potential is taken during the computation [17]. According to Song *et al.* [69], there is no experimental method that can determine both non-zero surface elasticity and surface stress at the same time. The goal of Ref. [17] is twofold: by solving the inverse problem, it provides (1) a viable experimental scheme to determine both non-zero surface elasticity and surface stress by measuring two (arbitrary) resonant frequencies; (2) an alternative method/theory other than atomistic simulation.

Actually, solving the inverse problem is very similar to the one of using the shifts of two resonant frequencies to determine the mass and surface stress [4] as presented in the last section. Here, we outline the procedures. The dimensionless governing equation is given as follows:

$$(1+\Delta)\frac{\partial^4 W}{\partial \xi^4} - N(1-\xi)\frac{\partial^2 W}{\partial \xi^2} + N\frac{\partial W}{\partial \xi} + \frac{\partial^2 W}{\partial \tau^2} = 0 \tag{7.8}$$

where dimensionless parameters Δ and N indicate the effect s of surface elasticity and surface stress, respectively. Eq. (7.8) is similar to Eq. (7.6). The same inverse problem solving technique is applied: finding the all possible combinations of Δ and N for two given resonant frequencies and then find the intersection of these two infinite combinations, which uniquely determine Δ and N [17]. Again, this technique works. The physical reason is that surface elasticity and surface stress have different impacts on different resonant frequency [17].

Finally, we give our comment on the debate between Lagowski *et al.* [52] and Gurtin *et al.* [53] on whether surface stress can induce the stiffness/resonant frequency change. We are prone to the opinion that surface stress should be viewed as residual stress [70,71]. The experiment by Chen *et al.* [72] shows that an adsorbate can significantly increase the resonant frequencies of a monolayer graphene resonator. For a monolayer graphene, there is no room to form a surface layer which has a different mechanical property. Chen *et al.* [72] ascribed the increase of resonant frequencies as the adsorption-induced tension, which in essence is also surface stress. The atomistic simulations [73,74] also show that adsorption can induce electronic and mechanical distortion of a graphene structure. The adsorption-induced distortion, which is responsible for the presence of surface stress, is similar to the doping in semiconductor materials. The doped impurities inside a semiconductor material distort its lattice structure, which makes residual stress prevalent in many MEMS devices [75,76]. For the argument of the Newton third law to apply for a bi-material composite case, the ideal interface condition is (implicitly) assumed. In an ideal interface, the interface has no zero thickness, and displacement/strain is continuous across the interface [54]. However,

in reality, the interface is non-ideal or say, flawed, which has finite thickness and slips. The interfacial slip causes the discontinuity of displacement/strain at the interface and this non-ideal interface effect amplifies with the decreasing dimension of a structure [77–79]. Here, the essential idea is that for a micro/nano bi-material composite structure, Newton's third law does not apply for the two layers, which means that the force inside one layer does not has the same magnitude but the opposite direction as that of the other layer. In a micro/nano "bi-material" composite structure, the correct modeling should be three layers, i.e., layer 1–interface–layer 2 [77,79]. Of course, we have no intention to challenge Newton's third law; it still applies between layer 1 and interface, and between layer 2 and interface [77,79], but NOT between layer 1 and layer 2. Quite often, defects such as dislocation, twin and cavity are localized and accumulate at an interface [77,80], which makes the stress around the interface very high. The stressed state of a micro/nanostructure is balanced externally as a whole through boundaries, which equivalently adds the axial load or bending moment on the micro/nanostructure [75,76]. And, the axial load is responsible for the structural stiffness change [4,17].

7.2.4 Determining the Stiffness and Mass of Biochemical Adsorbates by a Resonator Sensor

Surface stress is an effective sensing mechanism for many receptor-based sensors [5,6]. However, the receptor–ligand binding is highly selective for identifying an adsorbate/ligand; the challenges for developing robust and stable recognition methods through functionalized coatings (i.e., the receptor materials) and even interpreting the responses of receptor-based sensor still remain [9]. The development for the receptorless or receptor-free sensors, which bypass the chemistry of receptor–ligand binding and capitalize on the intrinsic material properties of adsorbate, has been called for [9]. The mass density (related with mass) and Young's modulus (related with stiffness) are the intrinsic material properties, which can be used to identify the material of an adsorbate. Solving the inverse problem of using resonant frequencies to determine the stiffness and mass of adsorbates can provide an alternative method of mass identification. The mass information only is insufficient to provide fundamental insights into the resonator-based molecular detection [81]. In general, the appropriate properties of a detected material including its mechanical properties as well as the mass must be considered when interpreting the resonator data [82]. The adsorption tests of *E. coli* bacteria on a silicon resonator by Ramos *et al.* [14,15] show that the system resonant frequencies increase. According to Eq. (7.2), the mass addition due to adsorption can only decrease the resonant frequency. At same time, the surface of resonator is not functionalized and surface stress is thus very small because of the high selectivity as discussed earlier [14,15]. The increase of resonant frequency can only mean that the stiffness of the bacteria plays a more important or even a dominant role [14,15].

In the experiment [14,15], the shifts of resonant frequencies are recorded. To solve the inverse problem, Ramos *et al.* [14] counted the total *E. coli* bacteria number (about 4200) and calculated the mass; the bacteria stiffness was then obtained by curve-fitting, which is a laborious work. They changed the adsorption location to try to "uncouple" the effects of stiffness and mass of the bacteria [14]. Our study [83] shows that the methods including shifting adsorption location, multiple resonant frequencies, and

changing the adsorption length cannot be used to solve the inverse problem. By varying the adsorbate thickness and utilizing a geometric approximation, a solution method to the inverse problem can be presented [83]. Here, we have a brief discussion on why the multiple resonant frequencies method, which solves the two inverse problems [4,17] as presented above, cannot work for this inverse problem. When the resonator surface is fully covered by an adsorbate layer, the (circular) resonant frequency is given as follows [83]:

$$\omega_i = \sqrt{\frac{1+\alpha}{1+\beta}}\omega_i^o \tag{7.9}$$

where ω_i is the ith resonant frequency with the presence of an adsorbate layer, and ω_i^o is the ith resonant frequency with no adsorbate layer. The dimensionless parameters α and β indicate the effects of the stiffness and mass of an adsorbate layer, respectively [83]. It is worth pointing out that Eq. (7.9) applies to all resonant frequencies, which is somewhat surprising and this is also the exact reason why the multiple resonant frequencies method cannot work. According to Eq. (7.9) for the full coverage scenario, no matter how many ω_i are measured, they all lead to the same one equation of Eq. (7.9) and mathematically, two unknown variables (α and β) cannot be solved by one equation. By varying the thickness of adsorbate layer, two independent equations can be derived from Eq. (7.9), from which α and β can be solved. Therefore, the inverse problem-solving method [83] requires to measure the thickness of adsorbate layer. However, the thickness measurement is much easier than that of stiffness (Young's modulus) or mass. For example, the adsorbate layer thickness of alkanethiol [5] and DNA [6] was measured by ellipsometry; the thickness of a membrane protein (FhuA) [84] and gold film [85] was measured by atomic force microscope (AFM). It can be even much simpler in a well-controlled inkjetting deposition procedure, in which the volume and spreading shape/area are precisely controlled/monitored [86] and the thickness can thus be easily calculated. Once α and β are solved, the mass density and Young's modulus of an adsorbate layer can be readily found out by a simple relation [83], which can be used to identify the material of adsorbate.

7.3 Inverse Problems in the MEMS Stiction Test

Suspended micromechanical structures are extensively used in varieties of microsensors and microactuators. In general, it is desirable to make sensors and actuators that have a minimum gap distance and a large surface area [87]. Smaller gap distance requires smaller actuation voltage, less power consumption, and less amount of energy stored in the system. If the stored energy is large, the discharge current densities during the contact of suspended structure and substrate can be so large to ablate the active element or damage the electrode, which is the so-called burn-out phenomenon [88]. A straightforward solution to burn out is the smaller gap distance. However, such solution comes at the expense of favoring the stiction failure mode. Use of dimples or cavities [87] to reduce contact area, or hydrophobic surface coating to reduce surface energy [88], or to operate the device in dry or vacuum environment to reduce capillary force,

can not completely prevent stiction from occurring because of the presence of van der Waals (vdW) force [89].

Stiction is a major failure mechanism for the MEMS structures, and extensive studies have been done on this topic. Stiction is the competition result of the microstructure elastic energy and microstructure–substrate interfacial energy, i.e., the work of adhesion or say, adhesion energy [19–23]. The presence of residual stress and its gradients in a microstructure, which in essence changes the stiffness and elastic energy of the microstructure [75,76], is a common phenomenon. As a direct outgrowth of silicon-based microelectronics, the manufacturing technique of using successively patterned deposition of thin-film polysilicon and sacrificial oxide layers is applied to fabricate those MEMS structures [24]. Polysilicon is prone to have residual stress/gradients, which is strongly dependent on the deposition process and heating cycles, including doping or annealing [90]. For a clamped–clamped microstructure [19–23], the axial thermoelastic stress due to the temperature variation also has the impact on the microstructure stiction [90]. Even for a cantilever, when the stiction occurs with the S-shape configuration, which in essence is also a clamped–clamped configuration [20,22,24], thermoelastic stress is also shown to have an influence on the microstructure stiction [91]. Residual stress can be the dominant factor in the microstructure deflection and stiction [92]. The previous studies on the stiction of a microstructure either assume the zero residual stress [19–24,93], or the residual/thermoelastic stress is known as a measured quantity [91,92], or a control parameter [94]. However, residual stress/gradients and thermoelastic stress in general are not known *a priori*. Thermoelastic stress is obtained by measuring the material coefficient of thermal expansion (CTE) and the temperature variation [90,91]. When the residual stress gradients are asymmetric along the microstructure thickness, which generates bending moment and thus deflection, the residual stress and its gradients can be characterized as a function of the microstructure dimensions [75,76]. By any standard, measuring the residual stress and its gradients or thermoelastic stress inside a microstructure is not a trivial thing. Extra experimental setup to monitor the temperature variation and heating devices are often needed in the thermoelastic stress measurement [91]. Multiple special specimens are needed; the extraction of residual stress and its gradients often involves complex numerical simulation [75,76]. Besides the residual stress/gradients and thermoelastic stress, the nominal adhesion energy is another unknown material property in a stiction test. The nominal adhesion energy is found by minimizing the system total energy with respect to the suspension length [19–24,87,90,93]. The total energy is the sum of the elastic energy and surface energy. The residual stress and thermoelastic stress generate axial force; the residual stress gradients generate bending moment. They all result in the change of the microstructure elastic energy. When the residual stress/gradients and thermoelastic stress are (assumed) zero or measured, the elastic energy can be calculated and the total energy minimization gives the relation of adhesion energy and detachment length. Such relation is given as follows for a cantilever beam with zero axial stress:

$$\gamma_s = C\frac{EH^2t^3}{S^4} \tag{7.10}$$

where γ_s is the nominal adhesion energy, E and t are the beam Young's modulus and thickness, respectively. H is the gap distance; S is called the suspension length or the detachment length. C is a constant, $C = 3/8$ for the arc-shaped stiction [21] and $C = 3/2$ for the S-shaped stiction [24]. Clearly, Eq. (7.10) presents a one-to-one relationship of adhesion energy and suspension length: once the suspension length is measured, the adhesion energy is uniquely determined. Similarly, if the non-zero residual axial stress/strain is measured, the adhesion energy can also be uniquely determined by the suspension length [90]. When the axial stress is unknown, as shown in this study, the one-to-one relationship can no longer hold: there are infinite combinations of the axial stress and adhesion energy which can result in the same suspension length. Here, the inverse problem is encountered as: *How to use the stiction shape to determine the axial stress and adhesion energy?*

The arc- and S-shapes of stiction are shown in Figure 7.5. Eq. (7.10) actually does not tell us how to choose between these two shapes and only the following vague rule applies: generally speaking, slender beam forms an S-shape, and its unstuck/suspension length is appreciably shorter than the beam length; chunky beam forms an arc-shape, and its unstuck/suspension length is approximately equal to the beam length. The arc- and S-shapes are the assumed deflection shapes [22,23,95]. The contact mechanics model [22,95] shows that when axial load is zero, S-shape indeed is a very good approximation shape for the stiction shape of a slender beam; arc-shape is an idealized one which deviates significantly from that of a chunky beam. The contact mechanics model [22,95] also shows that Eq. (7.10) can result in the significant error on the evaluation of adhesion energy. As listed in Ref. [22], the difference of the measured adhesion energy for polysilicon in the stiction tests using Eq. (7.10) is more than one thousand times. Hariri *et al.* [96] commented that "the inconsistency and unreliability of the experimental data" are the main deficiencies of those experiments; some of data are even observed to be in contradiction with one another. More explicitly, van Spengen *et al.* [97] concluded that "the surface interaction energy measurement using stuck beams needs considerable research before we can conclude anything definite about the precise magnitude of the measured surface interaction energy". Adhesion energy can be measured other than

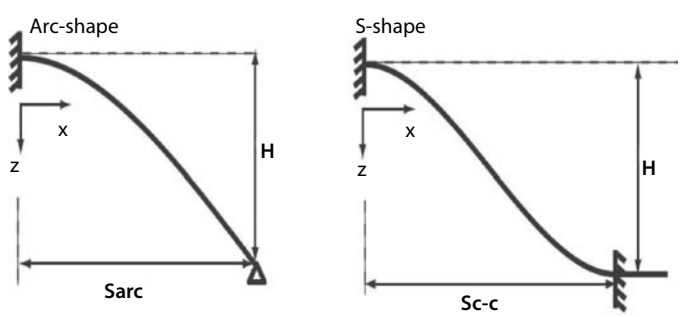

Figure 7.5 Schematics of arc-shape and S-shape stiction. For arc-shape, the boundary conditions are the clamped–hinged ones; for S-shape, the boundary conditions are the clamped–clamped ones. Adapted from Refs. [22,23].

the stiction test, for example, the measurement of the pull-off force [98,99]. However, it is extremely difficult to exert a pull-off force on a suspended MEMS device. The goal of the contact mechanics model [22,95] is to improve the evaluation on adhesion energy on the modeling aspect. Ref. [23] adopts the contact mechanics model [22,95] to solve the inverse problem. Furthermore, the axial load effect can be easily implemented in the contact mechanics model [23]. In contrast, arc- and S-shapes are for the zero axial load scenario, and they deviate significantly when axial load is large [23]. In stiction test, the mature measurement technique of Michelson interferometer is often used [22,24, 100], and the out-of-plane deflection of a stuck microstructure can be measured with the high accuracy of nanometer scale [100]. The deflection profile of a stuck microbeam is used to identify the structural nonidealties such as the compliance of support post [89,100]. Ref. [23] is to use the deflection profile to determine the axial stress and adhesion energy. To be more specific, two parameters are taken from the deflection profile, which are the suspension length and rise above substrate (at a given location) [23]. The axial stress and adhesion energy determine the stiction shape. For a given suspension length or rise, there are infinite combinations of the axial stress and adhesion energy. However, when the suspension length and rise are both given, the axial stress and adhesion energy are uniquely determined.

Acknowledgment

The work has been supported by the National Natural Science Foundation of China (NSFC Nos. 11023001 and 11372321).

References

1. G. Anger, *Inverse Problems in Differential Equations*, Plenum Press, New York, 1990.
2. T.P. Burg and S.R. Manalis, *Appl. Phys. Lett.*, Vol. 83, 2698–2700, 2003.
3. T.P. Burg, M. Godin, S.M. Knudsen, W. Shen, G. Carlson, J.S. Foster, K. Babcock, and S.R. Manalis, *Nature*, Vol. 446, 1066–1069, 2007.
4. Y. Zhang, *Sens. Actuator A-Phys.*, Vol. 194, 169–175, 2013.
5. R. Berger, E. Delamarche, H.P. Lang, Ch. Gerber, J.K. Gimzewski, E. Meyer, and H.J. Guntherodt, *Science*, Vol. 276, 2021–2024, 1997.
6. J. Fritz, M.K. Baller, H.P. Lang, H. Rothuizen, P. Vettiger, E. Meyer, H.J. Guntherodt, Ch. Gerber, and J.K. Gimzewski, *Science*, Vol. 288, 316–318, 2000.
7. N.V. Lavrik, M.J. Sepaniak, and P.G. Datskos, *Rev. Sci. Instrum*. Vol. 75, 2229–2253, 2004.
8. S.T. Koev, M.A. Powers, H. Yi, L.Q. Wu, W.E. Bentley, G.W. Rubloff, G.F. Payne, and R. Ghodssi, *Lab. Chip*, Vol. 7, 103–111, 2007.
9. R.H. Farahi, A. Passian, L. Tetard, and T. Thundat, *ACS Nano.*, Vol. 6, 4548–4556, 2012.
10. L. Meirovitch, *Analytical Methods in Vibrations*, Prentice Hall, New York, 1967.
11. M.S. Hanay, S. Kelber, A.K. Naik, D. Chi, S. Hentz, E.C. Bullard, E. Colinet, L. Duraffourg and M.L. Roukes, *Nat. Nanotechnol.*, Vol. 7, 602–608, 2012.
12. K. Jensen, K. Kim, and A. Zettl, *Nat. Nanotechnol.*, Vol. 3, 533–537, 2008.
13. J. Chaste, A. Eichler, J. Moser, G. Ceballos, R. Rurali, and A. Bachtold, *Nat. Nanotechnol.*, Vol. 7, 301–304, 2012.

14. D. Ramos, J. Tamayo, J. Mertens, M. Calleja, and A. Zaballos, *J. Appl. Phys.*, Vol. 100, 106105, 2006.
15. J. Tamayo, D. Ramos, J. Mertens, and M. Calleja, *Appl. Phys. Lett.*, Vol. 89, 224104, 2006.
16. S. Cherian and T. Thundat, *Appl. Phys. Lett.*, Vol. 80, 2219–2221, 2002.
17. Y. Zhang, L. Zhuo, and H. Zhao, *Proc. R. Soc. A*, Vol. 469, 20130449, 2013.
18. P. Mohanty, D.A. Harrington, K.L. Ekinci, Y.T. Yang, M.J. Murphy, and M.L. Roukes, *Phys. Rev. B*, Vol. 66, 085416, 2002.
19. R. Legtenberg, T. Tilmans, J. Elders, and M. Elwenspoek, *Sens. Actuat. A Phys.*, Vol. 43, 230–238, 1994
20. C.H. Mastrangelo and C.H. Hsu, *J. Microelectromech. Syst.*, Vol. 2, 33–43, 1993.
21. C.H. Mastrangelo and C.H. Hsu, *J. Microelectromech. Syst.*, Vol. 2, 44–55, 1993.
22. Y. Zhang and Y.P. Zhao, *Int. J. Solids Struct.*, Vol. 49, 2203–2214, 2012.
23. Y. Zhang and Y.P. Zhao, *Microsyst. Technol.*, 2014 (DOI: 10.1007/s00542-014-2127-6).
24. M.P. de Boer and T.A. Michalske, *J. Appl. Phys.*, Vol. 86, 817–827, 1999.
25. M.P. de Boer, J.A. Knapp, T.M. Mayer, and T.A. Michalske, "The role of interfacial properties on MEMS performance and reliability", in: C. Gorecki, eds., *Microsystems Metrology and Inspection*, Spie-Int Soc, Optical Engineering, Bellingham, pp. 2–15, 1999.
26. A.K. Naik, M.S. Hanay, W.K. Hiebert, X.L. Feng, and M.L. Roukes, *Nat. Nanotechnol.*, Vol. 4, 445–450, 2009.
27. K.L. Ekinci, Y.T. Yang, and M.L. Roukes, *J. Appl. Phys.*, Vol. 95, 2682–2689, 2004.
28. Y. Zhang and Y.P. Zhao, *Proc. R. Soc. A*, Vol. 470, 2014.
29. R.G. Knobel, *Nat. Nanotechnol.*, Vol. 3, 525–526, 2008.
30. X. Huang, C.A. Zorman, M. Mehregany, and M.L. Roukes, *Nature*, Vol. 421, 496–496, 2003.
31. J.S. Bunch, A.M. van der Zande, S.S. Verbridge, I.W. Frank, D.M. Tanenbaum, J.M. Parpia, H.G. Craighead, and P.L. McEuen, *Science*, Vol. 315, 490–493, 2007.
32. A. Eichler, J. Moser, J. Chaste, M. Zdrojek, I. Wilson-Rae, and A. Bachtold, *Nat. Nanotechnol.*, Vol. 6, 339–342, 2011.
33. S.Y. Kim and H. Park, *Nanotechnology*, Vol. 21, 105710, 2010.
34. A. Jockel, M.R. Rakher, M. Korppi, S. Camerer, D. Hunger, M. Mader, and P. Treutlein, *Appl. Phys. Lett.*, Vol. 99, 143109, 2011.
35. X. Xia and X. Li, *Rev. Sci. Instr.*, Vol. 79, 074301, 2008.
36. F. Schedin, A.K. Geim, S.V. Morozov, E.W. Hill, P. Blake, M.I. Katsnelson, and K.S. Novoselov, *Nat. Mater.*, Vol. 6, 652–655, 2007.
37. W.H. Grover, A.K. Bryan, M. Diez-Silva, S. Suresh, J.M. Higgins, and S.R. Manalis, *Proc. Natl. Acad. Sci. USA*, Vol. 108, 10992–10996, 2011.
38. A. Gupta, D. Akin, and R. Bashir, *Appl. Phys. Lett.*, Vol. 84, 1976–1978, 2004.
39. S. Dohn, R. Sandberg, W. Svendsen, and A. Boisen, *Appl. Phys. Lett.*, Vol. 86, 233501, 2005.
40. S. Dohn, W. Svendsen, A. Boisen, and O. Hansen, *Rev. Sci. Instr.*, Vol. 78, 103303, 2007.
41. G.Y. Chen, T. Thundat, E.A. Wachter, and R.J. Warmack, *J. Appl. Phys.*, Vol. 77, 3618–3622, 1995.
42. T. Thundat and L. Maya, *Surf. Sci.*, Vol. 430, L546–L552, 1999.
43. A.W. McFarland, M.A. Poggi, L.A. Bottomley, and J.S. Colton, *J. Micromech. Microengr.*, Vol. 15, 785–791, 2005.
44. F.M. Battiston, J.P. Ramseyer, H.P. Lang, M.K. Baller, Ch. Gerber, J.K. Gimzewski, E. Meyer, and H.J. Guntherodt, *Sens. Actuat. B Chem.*, Vol. 77, 122–131, 2001.
45. K.L. Ekinci and M.L. Roukes, *Rev. Sci. Instrum.*, Vol. 76, 061101, 2005.
46. R. Merkel, P. Nassoy, A. Leung, K. Ritchie, and E. Evans, *Nature*, Vol. 397, 50–53, 1999.
47. Y. Zhang, Q. Ren, and Y.P. Zhao, *J. Phys. D Appl. Phys.*, Vol. 37, 2140–2145, 2004.

48. J. Dorignac, A. Kalinowski, S. Erramilli, and P. Mohanty, *Phys. Rev. Lett.*, Vol. 96, 186105, 2006.
49. Q. Ren and Y.P. Zhao, *Microsyst. Technol.*, Vol. 10, 307–314, 2004.
50. M.K. Ghatkesar, V. Barwich, T. Braun, J. Ramseyer, Ch. Gerber, M. Hegner, H.P. Lang, U. Drechsler, and M. Despont, *Nanotechnology*, Vol. 18, 445502, 2007.
51. E. Finot, A. Passian, and T. Thundat, *Sensors*, Vol. 8, 3497–3541, 2008.
52. J. Lagowski, H.C. Gatos, and E.S. Sproles, *Appl. Phys. Lett.*, Vol. 26, 493–495, 1975.
53. M.E. Gurtin, X. Markenscoff, and R.N. Thurston, *Appl. Phys. Lett.*, Vol. 29, 529–530, 1976.
54. S. Timoshenko, *J. Opt. Soc. Am.*, Vol. 11, 233–255, 1925.
55. V.B. Shenoy, *Phys. Rev. B*, Vol. 71, 094104, 2005.
56. P. Lu, H.P. Lee, C. Lu, and S.J. O'Shea, *Phys. Rev. B*, Vol. 72, 085405, 2005.
57. J. He and C.M. Lilley, *Appl. Phys. Lett.*, Vol. 93, 263108, 2008.
58. J. He and C.M. Lilley, *Nano Lett.*, Vol. 8, 1798–1802, 2008.
59. H. Ibach, *Surf. Sci. Rep.*, Vol. 29, 193–263, 1999.
60. R.C. Cammarata, K. Sieradzki, and F. Spaepen, *J. Appl. Phys.*, Vol. 87, 1227–1234, 2000.
61. J.G. Guo and Y.P. Zhao, *Nanotechnology*, Vol. 18, 295701, 2007.
62. A.W. McFarland, M.A. Poggi, M.J. Doyle, L.A. Bottomley, and J.S. Colton, *Appl. Phys. Lett.*, Vol. 85, 053505, 2005.
63. K.B. Gavan, H.J.R. Westra, E. van der Drift, W.J. Venstra, and H.S.J. van der Zant, *Appl. Phys. Lett.*, Vol. 94, 233108, 2009.
64. X. Yi and H.L. Duan, *J. Mech. Phys. Solids*, Vol. 57, 1254–1266, 2009.
65. H.L. Duan, *Acta Mech. Solida Sin.*, Vol. 23, 1–11, 2010.
66. D.W. Dareing and T. Thundat, *J. Appl. Phys.*, Vol. 97, 043526, 2005.
67. H.S. Park and P.A. Klein, *J. Mech. Phys. Solids*, Vol. 56, 3144–3166, 2008.
68. W. Haiss, *Rep. Prog. Phys.*, Vol. 64, 591–648, 2001.
69. F. Song, G.L. Huang, H.S. Park, and X.N. Liu, *Int. J. Solids Struct.*, Vol. 48, 2154–2163, 2011.
70. Y. Li, B. Fang, J. Zhang, and J. Song, *J. Appl. Phys.*, Vol. 110, 114303, 2011.
71. Y. Li, J. Song, B. Fang, and J. Zhang, *J. Phys. D, Appl. Phys.*, Vol. 44, 425304, 2011.
72. C. Chen, S. Rosenblatt, K.I. Bolotin, W. Kalb, P. Kim, I. Kymissis, H.L. Stormer, T.F. Heinz, and J. Hone, *Nat. Nanotechnol.*, Vol.4, 861–867, 2009.
73. M. Chi and Y.P. Zhao, *Comput. Mater. Sci.*, Vol. 46, 1085–1090, 2009.
74. M. Chi and Y.P. Zhao, *Comput. Mater. Sci.*, Vol. 56, 79–84, 2012.
75. Y. Zhang, *J. Micromech. Microeng.*, Vol. 17, 753–762, 2007.
76. Y. Zhang and Y.P. Zhao, *Microsys. Technol.*, Vol. 12, 357–364, 2006.
77. Y. Zhang, *J. Appl. Mech.*, Vol. 75, 011008, 2008.
78. I.C. Noyan, C.E. Murray, J.S. Chey, and C.C. Goldsmith, *Appl. Phys. Lett.*, Vol. 85, 724–726, 2004.
79. C.E. Murray and I.C. Noyan, *Philos. Mag. A*, Vol. 82, 3087–3117, 2002.
80. Y. Zhang, *J. Mater. Sci.*, Vol. 43, 88–97, 2008.
81. K. Eom, H.S. Park, D.S. Yoon, and T. Kwon, *Phys. Rep.*, Vol. 503, 115–163, 2011.
82. H. Craighead, *Nat. Nanotechnol.*, Vol. 2, 18–19, 2007.
83. Y. Zhang. *Sens. Actuat. B Chem.*, Vol. 202, 286–293, 2014.
84. T. Braun, M.K. Ghatkesar, N. Backmann, W. Grange, P. Boulanger, L. Letellier, H.P. Lang, A. Bietsch, Ch. Gerber, and M. Hegner, *Nat. Nanotechnol.*, Vol. 4, 179–185, 2009.
85. D. Lee, S. Kim, N. Jung, T. Thundat, and S. Jeon, *Nanotechnology*, Vol. 106, 024310, 2009.
86. A. Bietsch, J. Zhang, M. Hegner, H.P. Lang, and Ch. Gerber, *Nanotechnology*, Vol. 15, 873–880, 2004.
87. F. Yang, *J. Appl. Phys.*, Vol. 100, 124511, 2006.
88. O.Y. Loh and H.D. Espinosa, *Nat. Nanotechnol.*, Vol. 7, 283–295, 2012.

89. F.W. Delrio, M.P. De Boer, J.A. Knapp, E.D. Reedy, P.J. Clews, and M.L. Dunn, *Nat. Mater.*, Vol. 4, 629–634, 2005.
90. Y. Yee, M. Park, and K. Chun, *J. Microelectromech. Syst.*, Vol. 7, 339–344, 1998.
91. J.W. Rogers, T.J. Mackin, and L.M. Phinney, *J. Microelectromech. Syst.*, Vol. 11, 512–520, 2002.
92. M.F. Wong, G. Duan, and K.T. Wan, *J. Appl. Phys.*, Vol. 101, 024903, 2007.
93. Y. Zhang and Y.P. Zhao, *Acta Mech. Solida Sin.*, Vol. 17, 104–112, 2004.
94. C.S. Majidi, R.E. Groff, and R.S. Fearing, *J. Appl. Phys.*, Vol. 98, 103521, 2005.
95. Y. Zhang and Y.P. Zhao, *Sens. Actuat. A Phys.*, Vol. 17, 381–390, 2011.
96. A. Hariri, J.W. Zu, and R. Ben Mrad, *J. Micromech. Microeng.*, Vol. 16, 1195–1206, 2006.
97. W.M. van Spengen, R. Puers, and I. De Wolf, *J. Micromech. Microeng.*, Vol. 12, 702–713, 2002.
98. Y. Zhang, *J. Adhes. Sci. Technol.*, Vol. 22, 699–715, 2008.
99. Y. Zhang, *J. Adhes. Sci. Technol.*, Vol. 25, 1435–1464, 2011.
100. B.D. Jensen, M.P. de Boer, N.D. Masters, F. Bitsie, and D.A. LaVan, *J. Microelectromech. Syst.*, Vol. 10, 336–346, 2001.

8

Ohmic RF-MEMS Control

M. Spasos[1] and R. Nilavalan[2]*

[1]*Department of Electronics, Alexander T.E.I. of Thessaloniki, Thessaloniki, Greece*
[2]*Electronics & Computer Engineering, College of Engineering, Design and Physical Science, Brunel University, Uxbridge, Middlesex, UK*

Abstract
Efficient control of Radio Frequency Microelectromechanical Switches (RF-MEMS) is a very important issue as it is correlated to main failure mechanisms/modes such as the impact force and bouncing phenomena that degrade their dynamic performance and longevity. This chapter presents the control of ohmic RF-MEMS switches under different actuation modes: single pulse; tailored pulse; tailored-pulse optimization method based on Taguchi's technique (voltage mode actuation control methods); resistive damping (charge mode actuation control method); and finally, the hybrid actuation mode, which is a combination of the tailored pulse, the resistive damping, and Taguchi's optimization technique. The control mechanisms are presented through case studies where analytical approaches are used to understand behavior and simulations based on Coventorware© software are used to evaluate performance. Finally, this chapter presents the comparison between different control methods.

Keywords: RF-MEMS, ohmic MEMS, voltage drive control, tailored-pulse control, charge drive control

8.1 Introduction

A reliable ohmic RF-MEMS switch should be capable of switching very fast without settling periods to be necessary due to bouncing phenomena. Additionally, the contact force should be sufficient and constant as soon as the switch closes. During the release phase, the switch should return to its null position as fast as possible in order to be ready for the next actuation pulse. In reality, there is always a trade-off between switching speed, settling time, and contact force. Fast switching under a voltage step pulse can be achieved by increasing the amplitude of the actuation pulse. Nevertheless, one of the main problems associated with electrostatic actuation under open-loop voltage control is the pull-in instability, a saddle-node bifurcation phenomenon wherein the cantilever snaps through to the underneath contact area once

**Corresponding author*: rajagopal.nilavalan@brunel.ac.uk

Atul Tiwari and Baldev Raj (eds.), Materials and Failures in MEMS and NEMS, (239–262)
© 2015 Scrivener Publishing LLC

its displacement exceeds a certain fraction (typically 1/3) of the full gap. Increased cantilever pull-in velocity implies bouncing, and settling time is necessary for the switch to perform its best. Moreover, the contact force during the settling period is not constant, reaching undesirable peak values when cantilever touches its corresponding contact area for the first time. That results in unstable contact resistance, power loss, and arcing as far as the signal is concerned and induces local hardening, pitting, or dislocations in the metal crystal structures of the materials used, reducing the reliability and the longevity of the switch [1]. Although a lot of effort has been invested in developing materials capable of maintaining high electrical contact conductance while keeping structural failures low, it still remains one of the major reasons for device failure [2]. Different control modes (open-loop and closed-loop) have been introduced by researchers in order to control MEMS electrostatic actuation, [3–5]. Unlike macro mechanical systems, where the implementation of feedback for closed-loop scheme is relatively simple, in the MEMS case the feedback design is challenging, due to the limited availability of sensor data, the presence of sensor dynamics and noise, and the typically fast actuator dynamics.

In terms of the complexity for the driving and sensing electronics, an open-loop approach has advantages over closed-loop control, as it uses only driving circuits. On the other hand, open-loop driving is sensitive to parameter uncertainties. The closed-loop control approach is significantly less sensitive to changes in system parameters and generates oscillation-free response. Nevertheless, closed-loop produces relatively slow response and needs complicated hardware. In terms of application requirements, when an ohmic cantilever type RF-MEMS switch is used, only two signal levels (ON and OFF) are of interest; its switching time usually varies between 2 and 20 μs and the best way to drive it is by using open-loop control. Generally, there are four main ways for open-loop switching control of RF-MEMS switches, using voltage drive, charge drive, hybrid drive and high-pressure gas damping control.

8.1.1 Voltage Drive Control Under Single Pulse

The analysis of the electrostatic actuated switch is based on the model of the variable capacitor with two parallel plates, as shown in Figure 8.1. In this simplified one-dimensional switch model, the lower plate is anchored, while the upper plate of mass m can move attracted by an electrostatic force working against a linear restoring force, represented by an elastic constant k, in a medium represented by a linear viscous damping coefficient b.

This is essentially a mass-spring system actuated by a voltage source in series with a low-value bias resistor, and the electrostatic force is depended on the amplitude of V and the remaining gap between the surfaces of the capacitor g. The co-energy (U^*) for this system is given by:

$$U^* = \frac{C(x)V^2}{2} \tag{8.1}$$

and the electrostatic force (F_{el}) at a constant voltage is

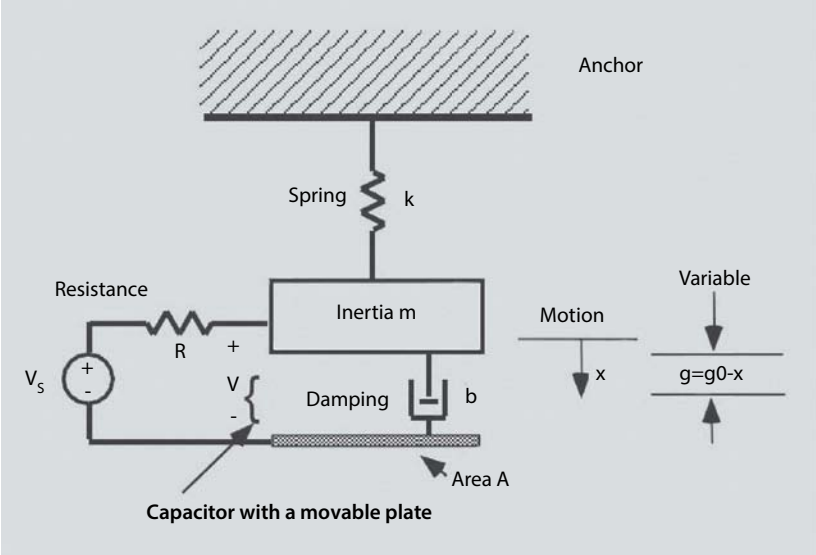

Figure 8.1 Model of an electrostatically actuated variable capacitor [5].

$$F_{el} = -\left.\frac{\partial U^*}{\partial x}\right)_V = -\frac{\partial}{\partial x}\left(\frac{1}{2}C(x)V^2\right) = \frac{e_0 A V^2}{2(g_0 - x)^2} = \frac{e_0 A V^2}{2g^2} \tag{8.2}$$

The preceding equation states that the electrostatic force applied is always attractive and increases as the plates of the capacitor get closer. Under these circumstances, the static equilibrium is reached when the electrostatic force equals the mechanical force (F_m):

$$F_m = k(g_0 - g) \tag{8.3}$$

and the system is stable at

$$\frac{d}{dg}(F_e - F_m) < 0 \Rightarrow -k + \frac{e_0 A V^2}{g^3} < 0 \tag{8.4}$$

From the preceding equation, the system is unstable for $g \le \frac{2}{3} g_0$ and the pull-in voltage (V_{pi}), where the cantilever collapses to the substrate is given by:

$$V_{pi} = V\left(\frac{2}{3} g_0\right) = \sqrt{\frac{8kg_0^3}{27e_0 A}} \tag{8.5}$$

8.1.2 Voltage Drive Control Under Tailored Pulse

Observing the operation of an ohmic RF-MEMS switch under step pulse implementation at the moment the contact is made, the contact force is very high due to the

high impact velocity of the cantilever. The conductance becomes very high but unstable due to the bouncing of the cantilever which follows the first contact (due to the elastic energy stored in the deformed contact materials and in the cantilever), and it needs time to develop a stable contact force and thereof a stable conductance. This bouncing behavior increases the effective closing time of the switch. Additionally, bouncing affects the opening time (ON to OFF transition) since the cantilever needs time to settle on its null position. That behavior introduces system noise as the distance between cantilever, and its corresponding contact point is not constant. Meanwhile, the contact may get damaged by the large impact force which can be much greater than the high static contact force necessary for low contact resistance. This instantaneous high impact force may induce local hardening or pitting of materials at the contact. Besides, it may facilitate material transfer or contact welding, which is not desirable for a high-reliability switch. All the above increase the adhesive force, which is a function of the maximum contact force and they result contact stiction.

Instead of using a continuous step command to control the electrode, a tailored pulse [6] with different levels of applied voltages and time intervals can be applied, as shown in Figure 8.2. The entire operation can be classified in two phases: the "pull-down" phase and the "release phase". The pull-down phase mainly refers to the actuation of a contact switch from its original null position to the final contact position.

In the past few years, several efforts have been made to tailor the shape of the actuation pulse using either analytical equations on a simplified single-degree-of-freedom (SDOF) model (parallel-plate capacitor) on their own [7,8], or in combination with Simplex optimization algorithms [3,9]. All these efforts focused on the minimization

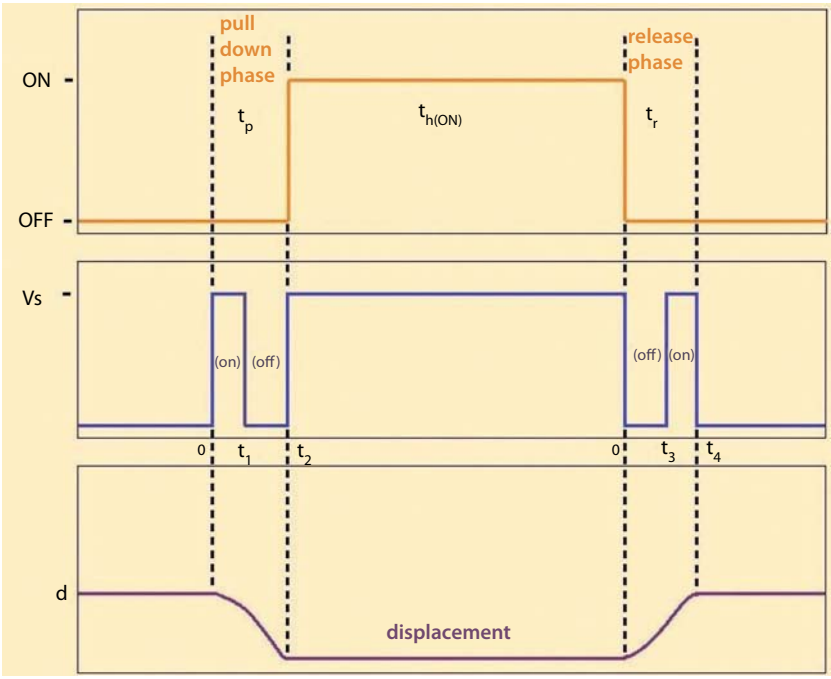

Figure 8.2 Different phases of the tailored actuation pulse.

of the impact force and bouncing during the pull-down phase of the switch but without taking into account damping or adhesion forces. Recently, new publications presented a more accurate solution that includes all the involved parameters [6, 10–12]. Nevertheless, the SDOF model is not considered as an accurate method to describe efficiently a nonlinear system like an RF-MEMS switch during its ON–OFF operation. Besides, it is not possible to obtain an analytical expression for damping, with the exception for a linear system with viscous damping. This implies that in all cases which are mentioned earlier, the tailored pulse which has been created under analytical implementation needs to be manually fine tuned in order to fulfill the requirements for soft landing and bouncing elimination.

A proper design must achieve a rapid and low impact response (ideally zero velocity) at the time of contact and fast settling once the switch is released from its contact position toward the null position. Special effort must be paid in the release phase due to the fact that considerable residual vibration at null position could be generated before settling, reducing switching rate during a repeated operation and producing undesirable noise, as the isolation of the switch is unstable, during hot switching operation [13].

For an initial estimation of the tailored pulse, the analytical method [6] is followed in order to calculate voltage amplitudes and time intervals. The sum of potential energy, U, and kinetic energy of the switch must be equal to the applied electrostatic energy. For the system shown in Figure 8.1, the energy conservation argument can be written as

$$\frac{1}{2}mv^2 + \frac{1}{2}kx^2 = F_{el} = \frac{e_0 A V^2}{2(g_0 - x)^2} \tag{8.6}$$

In order to achieve the condition of zero contact velocity at the moment of contact, all the electrostatic energy must be converted to potential energy at the moment the contact occurs. To achieve this goal, the applied force must be turned off once the displacement exceeds a particular middle point (x_1). By equaling the potential energy and the applied electrostatic energy, the distance x_1 can be computed by

$$\int_0^{x1} F_{el} dx = \int_0^{x_{max}} kx\, dx \tag{8.7}$$

$$x_1 = \frac{g_0^2 U\big|_{x=x_{max}}}{H_1 + g_0 U\big|_{x=x_{max}}} \tag{8.8}$$

where

$$H_1 = \frac{A e_0 V_1^2(t)}{2} \tag{8.9}$$

V_1 is the selected applied voltage, which must exceed the pull-in voltage V_{PI} with a factor of about 1.4 for correct operation of the device [13]. Next, the time intervals of the pulse have to be calculated. In order to achieve this, consider that

$$v = \frac{dx}{dt} = \sqrt{\frac{2}{m}(W - U)} \tag{8.10}$$

where the potential energy U equals $kx^2/2$ and the work done by the external force W is defined as

$$W = \int_0^x F_{el} dx = \frac{Hx}{g_0(g_0 - x)} \tag{8.11}$$

and the time interval, t_1, can be found from

$$t_1 = \int_0^{x1} \frac{1}{\sqrt{\frac{2}{m}\left(\frac{Hx}{g_0(g_0 - x)} - \frac{1}{2}kx^2\right)}} dx \tag{8.12}$$

Following the same approach, the time t_2 when the mass reaches the target can be calculated as

$$t_2 = t_1 + \int_{x_1}^{x_{max}} \frac{1}{\sqrt{\frac{2}{m}\left(\frac{Hx}{g_0(g_0 - x)} - \frac{1}{2}kx^2\right)}} dx \tag{8.13}$$

For determination of V_2, the condition is not unique, since the only requirement is to ensure the contact between the switch and substrate. In general, an increase in V_2 will not increase the impact force, but instead it enhances the contact pressure and thus decreases the electrical contact resistance. For simplicity and ease of implementation, let $V_2 = V_1 = V_s$.

The same strategy discussed in the previous section can be used in the release phase. The proposed command history is schematically shown in Figure 8.2. First, at t=0, a constant voltage V_1 is applied to actuate the switch. The switch then accelerates and moves toward the substrate. This input voltage is then ceased when t=t_1. The switch decelerates but still continuously moves toward the substrate. At the moment of $t = t_2$, the switch finally contacts the substrate at a negligible speed. At this moment, an input $V = V_2$ immediately kicks in to counteract the elastic restoring force and to ensure the final contact. Thu, a voltage-pulse train actuation scheme, defined by the attributes listed in the following, has been used to improve the dynamic response of the microswitch.

These attributes are

- The amplitude of the actuation voltage (V_s),
- The pull-down actuation time (t_p), which consists of the on time ($t_{p(on)}$) and the off time ($t_{p(off)}$),
- The hold-on time ($t_{h(on)}$),
- The release time (t_r) which consists of the off time ($t_{r(off)}$) and the on time ($t_{r(on)}$).

Making use of this open-loop control technique the bouncing of the switch after the initial contact can be eliminated and the impact force during contact can be minimized while maintaining a fast closing time. The main drawback of the aforementioned procedure is that there are many parameters that have to be modified in order to reach a good convergence to the targets. Due to the large number of parameters and the non-linear structure of the problem, it is very difficult to work it through analytically. Thus, the only solution is the implementation of an optimization method.

8.1.3 Voltage Drive Control Under Optimized-Tailored Pulse

Recently, thanks to the rapid development of computer technology, several stochastic optimization techniques that incorporate random variation and selection such as genetic algorithms (GA) [14], particle swarm optimization (PSO) [15], and statistic such as Taguchi's optimization [16] have been implemented via computer codes to solve various problems. These global optimization methods are capable of handling multidimensional, discontinuous and non-differentiable objective functions with many potential local maxima while they are highly independent of initial conditions.

Applying a stochastic or statistic method to optimize the actuation pulse of an ohmic RF-MEMS switch allows soft landing (low impact force), without the expense of more switching speed as well as eliminating the bouncing phenomena. The appropriate magnitude of voltages and time intervals of the actuation pulse train can be calculated by combining an optimization algorithm and a simulation program such as Architect module of Coventorware®.

The "Hammerhead" RF-MEMS switch [17] and the statistic Taguchi's optimization technique are presented in the following as a case study in this chapter. Results from this optimized performance are compared with step and tailored-pulse methods. The optimization procedure begins with the problem consideration, which includes the initial conditions, the selection of a proper orthogonal array (OA) and an appropriate expression of the *fitness function* (*ff*). The selection of an OA depends on the number of input parameters and the number of levels for each parameter. The *ff* is a particular mathematical function and is developed according to the nature of the problem and the optimization goals.

The procedure followed toward the design of the switch and the optimization of the tailored pulse used for its actuation is described in a few steps in the following.

- Initially, a step actuation pulse has been applied to the switch to observe its switching characteristics and verify that there are considerable weaknesses as far as the impact force and the bouncing phenomena are concerned.
- A tailored pulse has been applied next, instead of the single step pulse [6]. The performance of the switch got better but there was still plenty of room for further improvement.
- Finally, Taguchi's optimization technique has been applied to modify the actuation pulse in order to further improve the behavior of the switch.

The objective of Taguchi's algorithm is the minimization of the *ff*. According to the nature of the problem two separate optimization procedures have to be realized within two different switching operation phases: the pull-down phase ($ff_{p\text{-}d}$) and the release phase (ff_r).

8.1.3.1 Pull-Down Phase

The ff_{p-d} is suitably determined according to the next three conditions.

- Lowest contact time (highest switching speed)
- Lowest contact force (lowest conductance)
- Existence or non existence of a gap (bouncing) after the first contact up to the end of the time interval.

Thus a weighted ff_{p-d} has been chosen with the form:
Search for time **gap** between the contact force measurements

If **yes** then $\rightarrow ff_{p-d} = 10^6 \cdot t_{(\text{impact})} + 10^5 \cdot F_{(\max)} + 10$

If **no** then $\rightarrow ff_{p-d} = 10^6 \cdot t_{(\text{impact})} + 10^5 \cdot F_{(\max)}$

$$ff_{p-d(\text{Log})} = 20Log_{10}(ff_{p-d})$$

where $t_{(\text{impact})}$ is the time needed for the first contact to occur, and $F_{(\max)}$ is the maximum impact force measured during the pull-down phase.

8.3.1.2 Release Phase

The ff_r is suitably determined according to the difference between maximum and minimum cantilever's displacement, after a predefined time, which includes the pull-down time, the switch-on time and the time that the cantilever needs to reach its zero position after the switch-off.

Thus a weighted ff_r has been chosen with the form:

$$t_{(\text{initial})} > 163\mu\text{s}$$

$$ff_r = 10^4 \cdot (\text{Displacement}_{\max} - \text{Displacement}_{\min})$$

$$ff_{r(\text{Log})} = 20\text{Log}_{10}(ff_r)$$

where the $t_{(initial)} > 163\mu\text{s}$ includes the pull-down phase time, the hold-down time (ON) and the time that the switch needs to reach its null position (OFF) (these time intervals have been investigated during the step pulse implementation). The weight factors (10^4, 10^5, 10^6) are used according to the magnitude (in micron) of the factors and factor 10 indicates the penalty that has to be paid in the case of bouncing during the pull-down phase, otherwise the *ff* could be driven to false results.

Table 8.1 Pull-down phase (t_p) levels.

V_p (Volts)	48	60	72
$t_{p(on)}$ (μs)	5.6	7	8.4
t_f (μs)	1.6	2	2.4
$t_{p(off)}$ (μs)	8.8	11	13.2
t_r (μs)	1.6	2	2.4

Table 8.2 Release phase (t_r) levels.

V_p (Volts)	48	60	72
$t_{r(on)}$ (μs)	3.2	4	4.8
t_r (μs)	1.6	2	2.4
$t_{r(off)}$ (μs)	6.4	8	9.6
t_r (μs)	1.6	2	2.4

Taguchi's method is accurate within a well defined initial area. Thus, taking into account the magnitudes of the tailored actuation pulse of the previous step and considering a ±20% deviation from these predefined values, the initial levels of the parameters for Taguchi optimization can be created, as shown in Tables 8.1 and 8.2.

The numbers of parameters of the actuation pulse which will be calculated through the optimization process are 5 with 3 initial levels each and are considered for the two actuation phases as follows:

Pull-down phase (t_p)

A. The magnitude of the pull-down pulse $V_p(V)$
B. The ON state of the pulse $t_{p\text{-}on}$ (μs)
C. The fall time of the pulse $t_{p\text{-}f}$ (μs)
D. The OFF state of the pulse $t_{p\text{-}off}$ (μs)
E. The rise time of the pulse $t_{p\text{-}r}$ (μs)

Release phase (t_r)

A. The magnitude of the release pulse V_r (V)
B. The OFF state of the pulse $t_{r\text{-}off}$ (μs)
C. The rise time of the pulse $t_{r\text{-}r}$ (μs)
D. The ON state of the pulse $t_{r\text{-}on}$ (μs)
E. The fall time of the pulse $t_{r\text{-}f}$ (μs)

For an OA with 5 parameters and 3 levels for each parameter, a configuration with at least $n_{\text{rows}} = 1 + (k \cdot DOF_m) = 1 + (5 \cdot 2) = 11\text{rows}$ are needed.

Where $DOF_m = m-1$ represents the degrees of freedom, and in statistical analysis, it is equal to the number of the levels of a parameter minus 1.
The optimization procedure graphs, shown in Figures 8.3 and 8.4 present the curves of mean and optimum values for the pull-down and release phase, as they converged through Taguchi's process, respectively.

The results for optimum dimensions extracted through Taguchi's optimization method after 20 iterations (less than 1 hour of processing time), for the pull-down and release switching phases of the ohmic RF-MEMS switch are illustrated in Table 8.3.

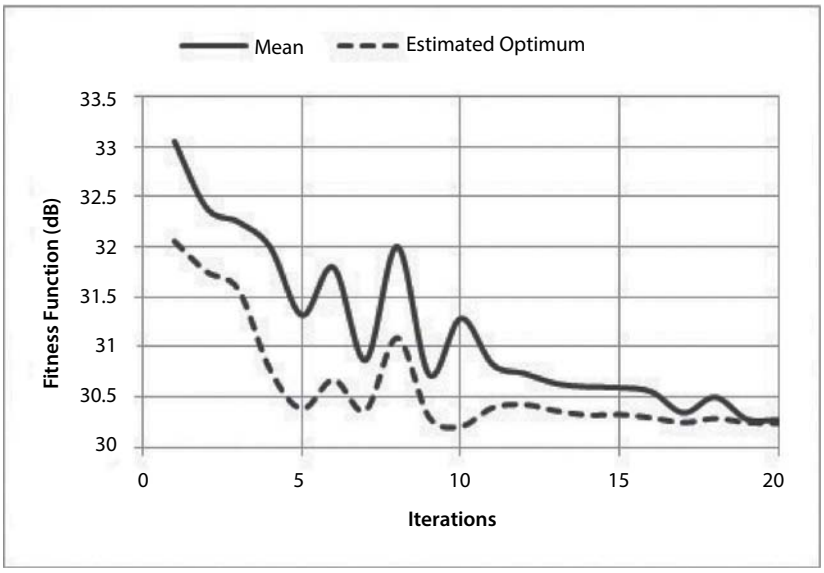

Figure 8.3 Progress of optimization process for the pull-down phase of the switch.

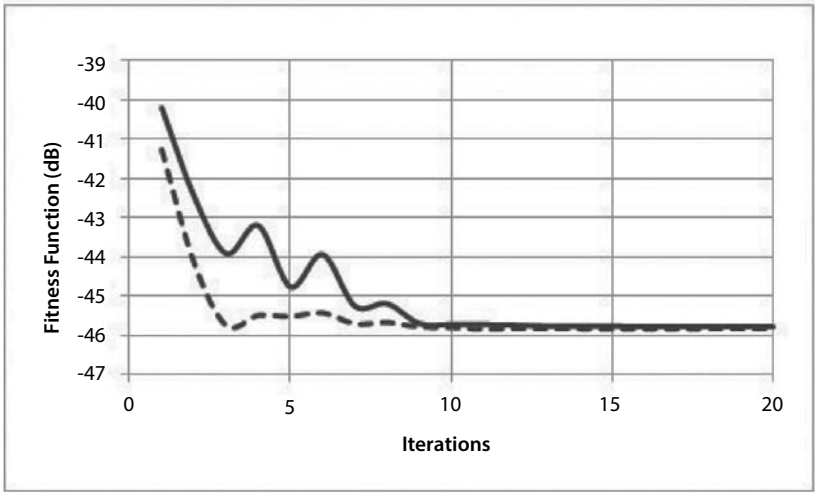

Figure 8.4 Progress of optimization process for the release phase of the switch.

Table 8.3 Voltage and time intervals of the optimized-tailored pulse.

Pull-down phase (t_p)					Release phase (t_r)				
$V_{p\text{-}d}$	$t_{p\text{-}on}$	$t_{p\text{-}f}$	$t_{p\text{-}off}$	$t_{p\text{-}r}$	V_r	$t_{r\text{-}off}$	$t_{r\text{-}r}$	$t_{r\text{-}on}$	$t_{r\text{-}f}$
61.5 V	7.3 μs	1.6 μs	10.2 μs	2.2 μs	61.5 V	4.9 μs	1.9 μs	9.3 μs	1.9 μs

Table 8.4 Step pulse voltage and time values.

t (μs)	0	2	150	152
V (V)	0	60	60	0

Table 8.5 Tailored pulse voltage and time values.

t (μs)	0	2	9	11	22	24	150	152	156	158	166	168
V (V)	0	60	60	0	0	60	60	0	0	60	60	0

Table 8.6 Optimized-tailored pulse voltage and time values.

t (μs)	0	2	9.3	10.9	21.1	23.3	150	152	156.9	158.8	168.1	170.
V (V)	0	61.5	61.5	0	0	60	60	0	0	61.5	61.5	0

Continuing with the analysis, the switch is examined under transient conditions in Coventorware Architect environment. Simulations have been carried out using, initially, a step pulse as an actuation pulse, a tailored pulse and finally the optimized pulse, as described in Tables 8.4, 8.5, and 8.6, respectively.

Simulating then, the behavior of the switch under the optimized-tailored pulse, the results show great improvement with respect to impact velocity (3.6 cm/sec instead of 31 cm/sec of the step pulse and 5.1 cm/sec of the tailored pulse), which implies true "*soft landing*" of the cantilever, reducing dramatically the impact force (138 μN instead of 349 μN of the step pulse and 174 μN of the tailored pulse), as shown in Figure 8.5.

In the pull-down phase, the bouncing phenomena have been eliminated and the switching speed, is kept high (17 μs), around 1.7 μs slower than the step pulse (15.3 μs), but around 1.5 μs faster than the tailored pulse (18.5 μs) as shown in Figure 8.6.

Similar behavior is also observed during the release phase with ON–OFF switching time of 13.2 μs, around 0.5 μs slower than step pulse method (12.7 μs), but around 1.7 μs faster than the tailored pulse method (14.9 μs). Additionally, bouncing phenomena have practically eliminated (instead of max. deviation of 3.59 μm for the step pulse and 0.37 μm for the tailored pulse) during the release phase, as presented in Figure 8.7.

A comparison between the results implementing different actuation pulses is shown in Table 8.7.

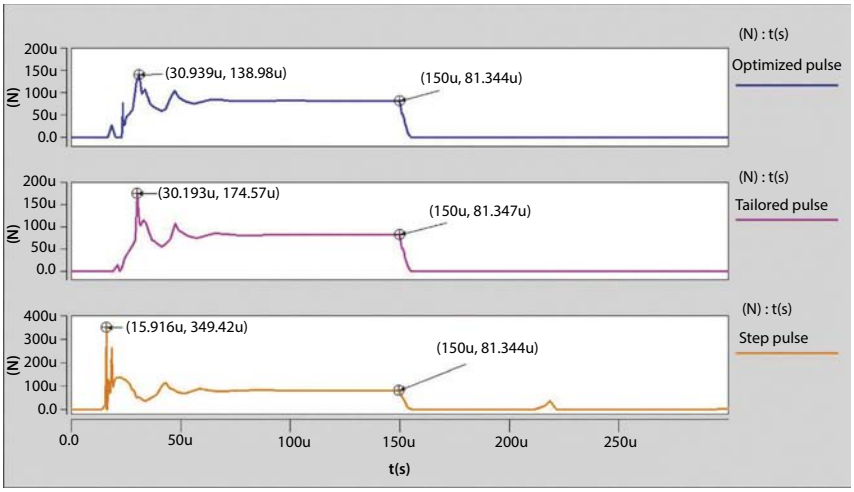

Figure 8.5 Comparison of the contact forces for voltage control methods.

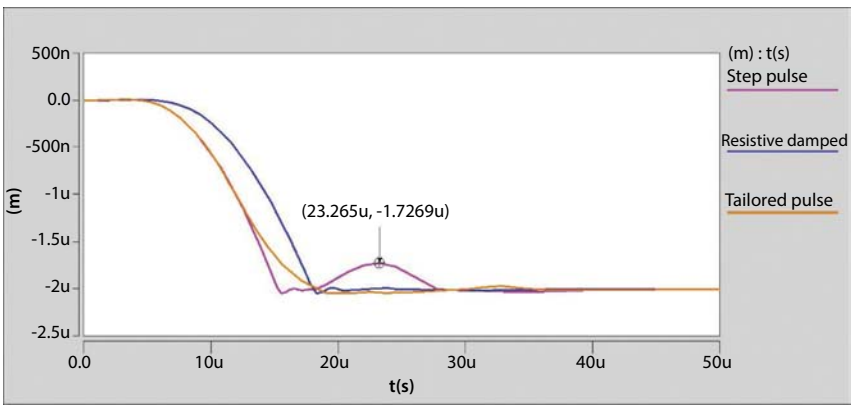

Figure 8.6 Comparison of the switching behavior during the pull-down phase for voltage control methods.

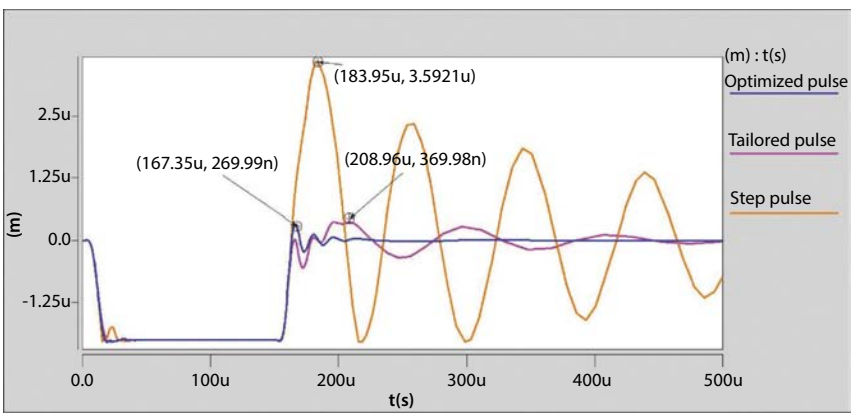

Figure 8.7 Comparison of the switching behavior during the release phase for voltage control methods.

Table 8.7 Comparison of switching characteristics under different actuation modes.

	Impact velocity (cm/s)	Impact force (μN)	Switching (pull down) (μs)	Switching (release) (μs)	Max. bouncing displacement (μm)
Step pulse	31	349	15.3	13.2	3.59 to –2
Tailored pulse	5.1	174	18.5	14.9	0.37 to –0.33
Optimized-tailored pulse	3.6	138	17	13.7	0.11 to –0.09

8.2 Charge Drive Control (Resistive Damping)

Resistive damping is another way to control the impact velocity in order to achieve soft landing and fewer bouncing phenomena. This control method is also referred as charge drive [18]. Under charge control the pull-in phenomenon of the constant voltage controlled electrostatic actuators does not exists while, if the current drive is ideal, any position across the gap is stable. The main reason for this behavior is that the applied electrostatic force is always attractive and is independent of the remaining gap of the actuator.

Charge drive control using constant current sources is mostly preferred to extend the travel range of electrostatic micro-actuators. Recently, there are also few references in the literature that use charge drive control on RF-MEMS [19–21].

In case, a constant voltage source V increase, the electrostatic force is increased due to an increase in the charge (Q).

$$F_e = \frac{QV}{2g} \tag{8.14}$$

Simultaneously, the increased force decreases the beam height (g), which, in turn, increases the capacitance and its charge. In other words the electrostatic energy provided by a constant voltage source V is converted to kinetic energy, accelerating the beam [22].

$$E_k = \frac{mv^2}{2} \tag{8.15}$$

At $g = 2/3g_0$, the increase in the electrostatic force is greater than the increase in the restoring force, resulting in an unstable condition and a collapse of the cantilever beam to the CPW line. This behavior creates a high impact force and bouncing phenomena. When a voltage source with a large series bias resistance is used instead, the behavior of the switch is not the same. The presence of the high bias resistor changes the behavior of the source, to a rather constant capacitor current charge, which mainly depends on the resistor's value. Under these conditions the source behave like a current source and reduces the kinetic energy of the MEMS switch near the point of contact by causing

the voltage across the switch to drop in case of a rapid change in the capacitance of the electrode area.

$$V_C = V_S\left(1 - e^{-\frac{t}{RC}}\right) \tag{8.16}$$

For series ohmic RF-MEMS switches the capacitance created by the electrode area of switches in the open state is in the order of 0.02–1 pF, with a final remaining gap of g>0.4 μm in the down-state position. The current drown out of the source by the variable capacitor during the transition time is very small (2–20 μA) and a bias resistance R_B=10–50 MΩ is needed for an appreciable voltage drop. The maximum initial charging current of the capacitor which is created under resistive damping between the electrode area and the cantilever during the transition time of the actuation pulse is given by

$$i_C = C_{el}\frac{dV_C}{dt} \tag{8.17}$$

where
C_{el} is the capacitance between the electrode and the cantilever in its initial position.
dV_C is the voltage drop in the capacitor
dt is the rise time of the actuation pulse

The value of the appropriate bias resistance for reducing the velocity of the cantilever through the gradual raise of the actuation voltage is calculated through Ohm's law as

$$R_B = \frac{V_C}{I_C} \quad \text{or} \quad R_B = \frac{t_r}{C_{el}} \tag{8.18}$$

Such a bias resistance cause soft landing with less bouncing phenomena, lower initial impact force but is also introduces additional delay to the switching time. All the aforementioned considerations are valid only for the case that the rise time (t_r) of the pulse is much smaller than the switching time $t_r << t_s$, which means that during the rise time of the pulse the cantilever has not started to move yet and its initial capacitance remains stable. To eliminate bouncing phenomena, during the release phase of the switch, when the cantilever oscillates in the resonance frequency, the $R_B C_{el}$ product must be equal to the period of the resonance frequency [22] and the R_b for this case is calculated as

$$R_B = \frac{t_{res}}{C_{el}} \tag{8.19}$$

Two kinds of ohmic RF-MEMS switches are considered next for a case study in this section. A relatively long and slow switch as the "Hammerhead" RF-MEMS switch [23] and a stiff one such as the North-Eastern University (NEU) switch [12].

Beginning with the Hammerhead switch, for the pull-down phase the value of the damping resistance R_B depends on the values of the capacitance created between the

electrode area and the cantilever when the cantilever is in its initial position and the rise time t_r of the applied pulse as shown in the following:

$$R_b C_{el} = t_r = 2\mu\text{m} \Rightarrow R_b \approx 17\,\text{M}\Omega \tag{8.20}$$

where C_{el}=118 fF, the capacitance created in the electrode area.

Figure 8.8 illustrates the characteristics of the switch under step pulse implementation with resistive damping. The results show excellent switch response during the pull-down phase. Elimination of the bouncing is observed with significant reduction in settling time (35 from 55 μN) and reduction in the initial impact force (169 from 349 μN) with only a small increase in the switching time (18 from 15 μN). In the contrary, very poor response is observed during the release phase. Although the delay in the switching time is 3 μm (15 from 12) the effect on the bouncing is very small (3.09 from 3.59 μm). This phenomenon is due to the fact that the movement of the cantilever is governed by different forces.

In the release phase the free move is due to the restoring force and the mechanical resonance frequency of the cantilever and depends only on its elastic properties. Thus, a resistance that can be effective at this phase has to be proportional to the period of the resonance frequency of the cantilever. The resonance frequency of this switch is about 12.3 kHz with the period around 80 μs and the resulted resistance, calculated for this time, is about R_b=680 MΩ, which unavoidably, is inappropriate for the pull-down phase.

In a very stiff device like the "NEU" switch, the actuation control under resistive damping is the only solution. Due to the small switching time as well as the high actuation voltage, it is not practical to implement a tailored control pulse, i.e., time intervals

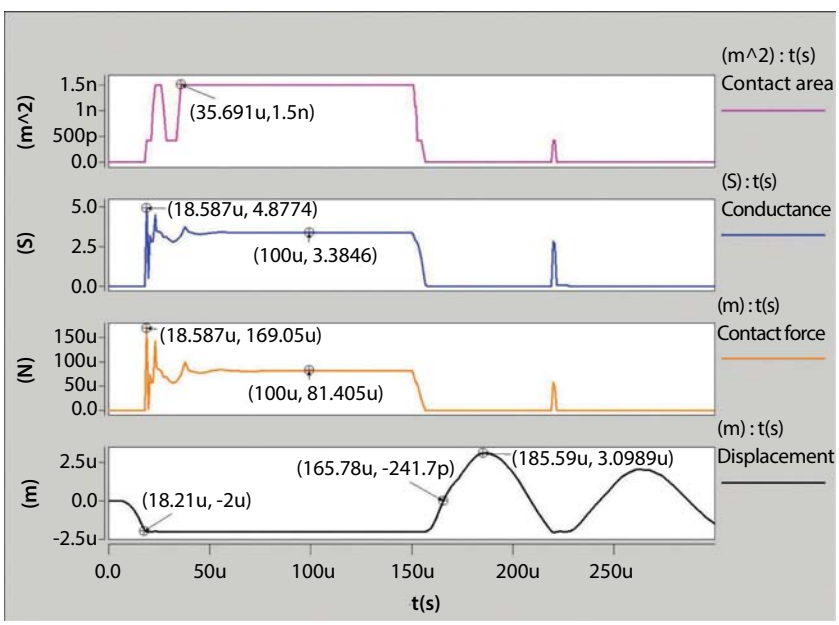

Figure 8.8 Performance characteristics of the switch under resistive damping.

smaller than 1 μs and pulses with slew-rate greater than 200 V/μs are needed in order to shape a tailored pulse for this switch, as the switching time is about 1.24 μs when an actuation pulse with 83 *V* is applied. Even if a fast and high-voltage pulse can be generated, there are other issues like overshooting that can render problematic for the control of the switch.

Another reason that make resistive damping control appropriate for this kind of switch is that the time constant RC calculated for the pull-down phase is near the period of the mechanical resonance frequency, achieving significant improvement in both switching operation phases of the switch. Concluding, control under resistive damping is the only practical solution for very fast RF-MEMS switches where the switching time and the period of the resonance frequency are of the same order.

Actuating the "NEU" switch with a voltage pulse with amplitude of 83 *V* and t_r=1 μs, the correct bias resistance can be calculated as

$$R_b C_{el} = t_r = 1\mu\text{m} \Rightarrow R_b \approx 33\text{M}\Omega \tag{8.21}$$

where C_{el}=30 fF, the capacitance which created within the electrode area.

Figure 8.9 illustrates the characteristics of the switch under step pulse implementation with resistive damping. The simulation results with R_b=33 MΩ shows excellent response of the switch during the pull-down phase as they presents elimination of the bouncing and the initial impact force (the high impact velocity has been reduced to 13.2 from 65.9 cm/sec), with only a small increase in the switching time (3.47 from 2.38 μN). During the release phase, a significant reduction of the amplitude of bouncing is observed, too (174 from 255 nm).

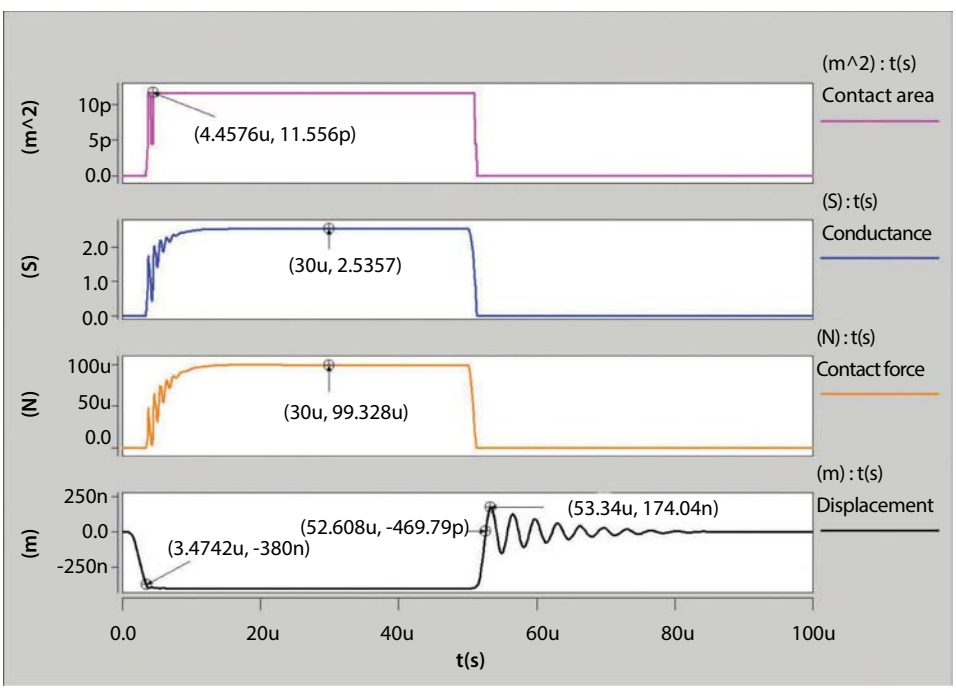

Figure 8.9 Contact area and conductance of the switch with R_B = 33 MΩ.

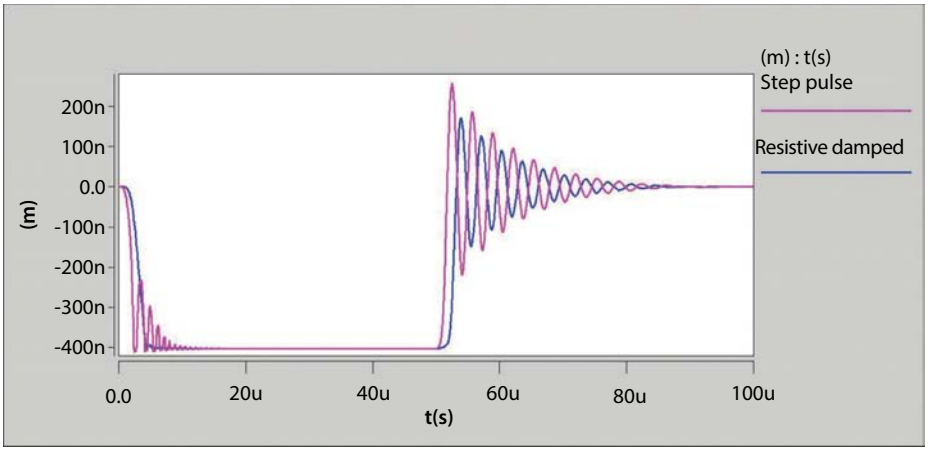

Figure 8.10 Displacement comparison between step pulse and resistive damping actuation modes.

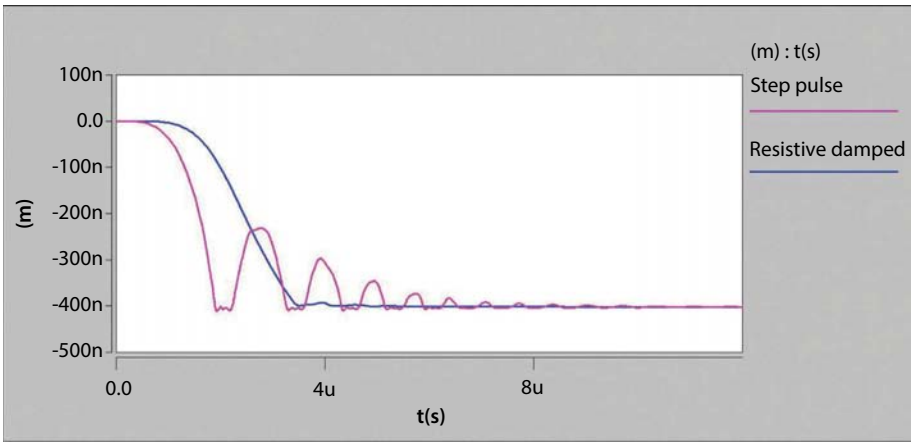

Figure 8.11 Displacement comparison between different actuation modes during the pull-down phase.

A comparison between step-pulse and step-pulse with resistive damping actuation modes that have been used is illustrated in Figure 8.10. It is obvious that the control of the switch under resistive damping excels that of the step-pulse in both OFF–ON and ON–OFF transitions with only a slight increase of the switching times.

In Figure 8.11, a more detailed view of the pull-down phase displacement of the cantilever between step pulse and resistive damped pulse implementation is shown.

8.3 Hybrid Drive Control

Another control method for cantilever type RF-MEMS consists of a combination of the two aforementioned techniques (optimized tailored and resistive). The required steps for applying the Hybrid control mode for a given switch are the following.

- Consider the initial optimization procedure as in Section 8.1.3.
- Consider the procedure for Resistive damping as in Section 8.2.
- Consider an optimization procedure for a switch controlled by a tailored actuation source in series with a large bias resistor.

The "Hammerhead" RF-MEMS switch is considered for the case study [24]. As the two first steps have already implemented in the two previous paragraphs, only the implementation of the third step remains. Taguchi's optimization method is implemented taking as central values the magnitudes of the optimized-tailored actuation pulse of the Section 8.1.3 and considering a ±20% deviation from these predefined values, the initial levels of the parameters can be created, as shown in Tables 8.8 and 8.9.

The optimization procedure graphs shown in Figures 8.12 and 8.13 present the curves of mean and optimum values for the pull-down and release phases, as converged through Taguchi process, respectively.

The results for optimum dimensions extracted through Taguchi's optimization method after 20 iterations (less than 1 hour of processing time), for the pull-down and release switching phases of the ohmic RF-MEMS switch are illustrated in Table 8.10.

Continuing the analysis, the switch is examined under transient conditions in Coventorware Architect environment. Simulations have been carried out using a voltage source with the characteristics of the optimized pulse, as described in Table 8.11, in series with a bias resistor of 17 MΩ.

Figure 8.14 illustrates the characteristics of the "Hammerhead" switch under hybrid control mode. The results show excellent response during both switching phases with

Table 8.8 Pull-down phase (t_p) levels (hybrid mode).

V_p (Volts)	49.2	61.5	73.8
$t_{p(on)}$ (μs)	5.84	7.3	8.76
t_f (μs)	1.28	1.6	1.92
$t_{p(off)}$ (μs)	8.16	10.2	12.24
t_r (μs)	1.76	2.2	2.64

Table 8.9 Release phase (tf) levels (hybrid mode).

V_p (Volts)	49.2	61.5	73.8
$t_{r(on)}$ (μs)	3.92	4.9	5.88
t_r (μs)	1.52	1.9	2.28
$t_{r\ (off)}$ (μs)	7.44	9.3	11.16
t_r (μs)	1.52	1.9	2.28

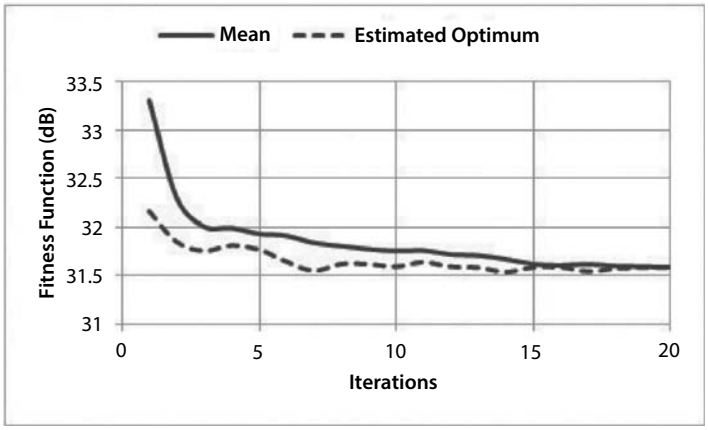

Figure 8.12 Optimization procedure graph for the pull-down phase of the switch.

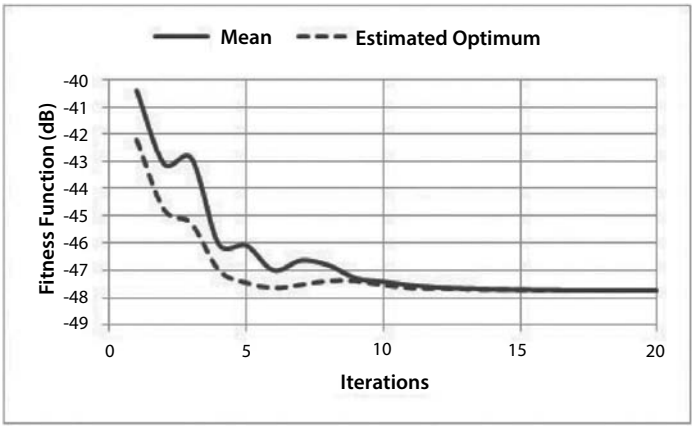

Figure 8.13 Optimization procedure graph for the release phase of the switch.

Table 8.10 Voltage and time intervals of the optimized-tailored pulse (hybrid mode).

Pull-down phase (t_p)					Release phase (t_r)				
$V_{p\text{-}d}$	$t_{p\text{-}on}$	$t_{p\text{-}f}$	$t_{p\text{-}off}$	$t_{p\text{-}r}$	V_r	$t_{r\text{-}off}$	$t_{r\text{-}r}$	$t_{r\text{-}on}$	$t_{r\text{-}f}$
66 V	7.5 µs	1.9 µs	9.7 µs	1.9 µs	61 V	6.5 µs	2.2 µs	8.6 µs	2.2 µs

Table 8.11 Optimized-tailored pulse voltage and time values (hybrid mode).

t (µs)	0	2	9.5	11.4	21.1	23	150	152	158.5	160.7	169.3	171.5
V (V)	0	66	66	0	0	60	60	0	0	61	61	0

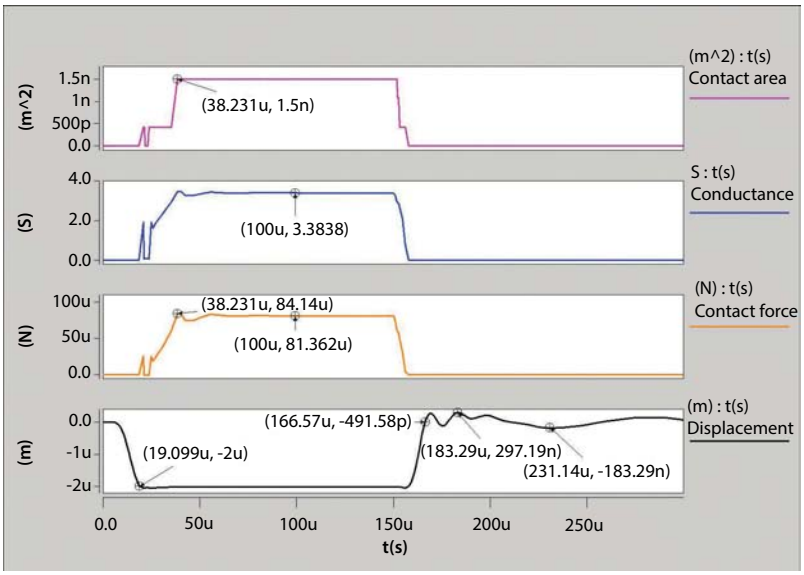

Figure 8.14 Characteristics of the "Hammerhead" switch under hybrid control mode.

elimination of the bouncing and impact force in the pull-down phase and elimination of the bouncing in release phase.

8.4 Control Under High-Pressure Gas Damping

Another way to control the ohmic RF-MEMS switches is the damping of the cantilever movement by increasing the pressure of the gas [12,25]. High pressure results in increased viscosity, damping force, and spring force. With the increase in damping force the switching time is increased, but bouncing and settling times are decreased. This behavior is because at high ambient pressure, the squeeze film acts more like an incompressible layer rather than a compressible one. The increase in pressure also affects the cleanliness of the contact surfaces as at high pressures, contaminant films are formed at the switch contacts and increase the contact resistance [25]. It has to be mentioned that the method of using high pressure to increase damping force on RF-MEMS switches in order to control them, presents a lot of difficulties and it is not a practical solution for real life applications [12].

8.5 Comparison between Different Control Modes

A comparison between the four actuation modes (step pulse, step pulse with resistive damping, Taguchi's optimized-tailored pulse, and hybrid) that have been used is illustrated in Figure 8.15. It is obvious that the control of the switch with optimized-tailored pulse mode as well as with hybrid mode is much better during the release phase as the swing of the cantilever is about 6–7 times smaller.

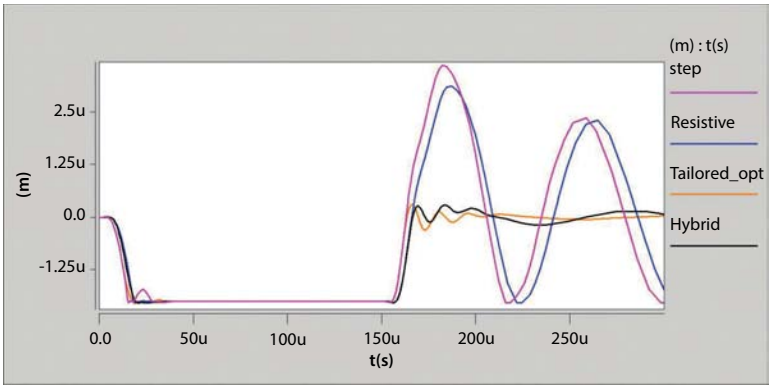

Figure 8.15 Comparison between different actuation modes.

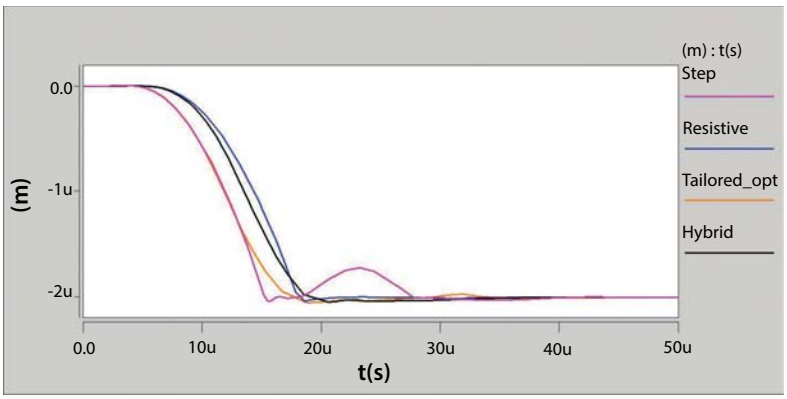

Figure 8.16 Comparison between different actuation modes during the pull-down phase.

In Figure 8.16, a more detailed view of the pull-down phase is shown, where the actuation of the switch under optimized-tailored pulse, resistive damping or hybrid mode presents very good behavior, around 17–19 μs switching time and almost no bouncing. Under step pulse actuation, the switch is faster, roughly 15 μs, but with much more initial impact force and with a bounce of about 270 nm high.

Comparing the impact force of the switch under the four control modes, the results show great improvement with respect to impact velocity for all three modified actuation modes 9.4 cm/sec for the resistive, 3.6 cm/sec for the optimized tailored and 1.4 cm/sec for the hybrid, instead of 31 cm/sec of the step pulse. The hybrid mode excels all the others and implies true *"soft landing"* of the cantilever, reducing dramatically the impact force (84 μN instead of 139 μN of the optimized tailored, 317 μN of the resistive and 349 μN of the step pulse), as shown in Figure 8.17.

A comparison between the results implementing the four different actuation pulses, are shown concentrated in Table 8.12.

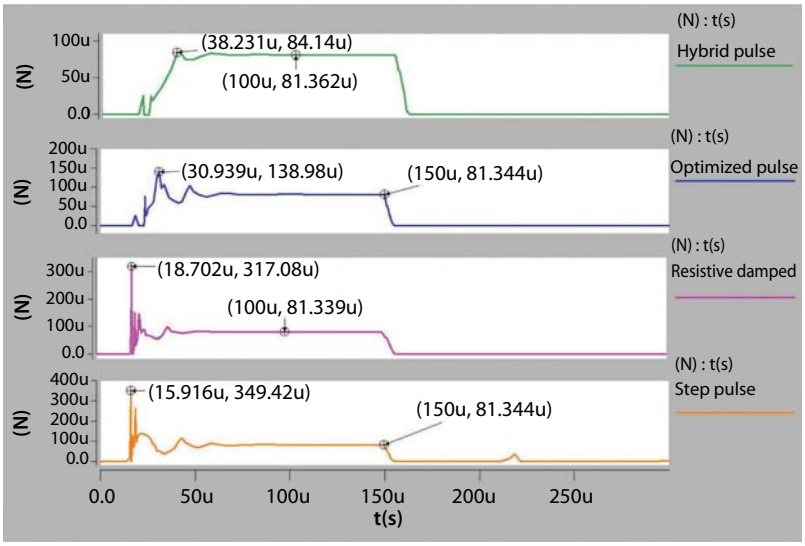

Figure 8.17 Comparison of the contact forces.

Table 8.12 Comparison of switching characteristics under different control modes.

Mode	Impact velocity (cm/s)	Impact force (μN)	Switching (pull down) (μs)	Switching (release) (μs)	Max. bouncing displacement (μm)
Step pulse	31	349	15.3	13.2	3.59–2
Optimized-tailored pulse	3.6	138	17	13.7	0.11–0.09
Resistive damped	9.4	317	18.2	15.78	3–2
Hybrid	1.4	84	19	16.57	0.18–0.18

References

1. H. Newman, J. L. Ebel, D. Judy, and J. Maciel, Lifetime measurements on a high-reliability RF-MEMS contact switch, *IEEE Microwave and Wireless Component Letters,* Vol. 18, pp. 100–102, 2008.
2. D. Czaplewski, C. Nordquist, C. Dyck, G. Patrizi, G. Kraus, and W. Cowan, Lifetime limitations of ohmic, contacting RF MEMS switches with Au, Pt and Ir contact materials due to accumulation of 'friction polymer' on the contacts, *Journal of Micromechanics And Microengineering*, Vol. 22, No 10, 2012. http://iopscience.iop.org/0960-1317/22/10/105005/pdf/0960-1317_22_10_105005.pdf
3. H. Sumali, J. Massad, D. Czaplewski, and C. Dyck, Waveform design for pulse-and-hold electrostatic actuation in MEMS, *Journal of Actuators and Sensors*, Vol. 134, pp. 213-220, 2006.
4. B. Borovic, A. Q. Liu, D. Popa, H. Cai, and F. L. Lewis, Open-loop versus closed-loop control of MEMS devices: choices and issues, *Journal of Micromechanics and Microengineering*, Vol. 6, pp. 1917–1924, 2005.

5. L. Castaner, Drive methods for electrostatic MEMS switches, *UIC Seminar*, Barcelona, Spain, 2005.
6. K. S. Ou, K. S. Chen, T. S. Yang, and S. Y. Lee, A command shaping approach to enhance the dynamic performance and longevity of contact switches, *Journal of Mechatronics*, Vol.13, pp. 375–389, 2008.
7. D. A. Czaplewski, C. W. Dyck, H. Sumali, J. E. Massad, J. D. Kuppers, I. Reines, W. D. Cowan, and C. P. Tigges, A Soft-landing waveform for actuation of a single-pole single-throw ohmic RF-MEMS switch, *IEEE Journal of Microelectromechanical Systems*, Vol. 15, pp. 1586–1594, 2006.
8. J. Massad, H. Sumali, D. Epp, and C. Dyck, Modeling, simulation, and testing of the mechanical dynamics of an RF-MEMS switch, *International Conference on MEMS, NANO and Smart Systems* (*ICMENS'05*), Banff, Alberta, Canada, pp. 237–240, 2005.
9. M. Allen, R. Field, and J. Massad, Modeling and input optimisation under uncertainty for a collection of RF-MEMS devices, *ASME International Mechanical Engineering Congress and Exposition*, Chicago, USA, 5–10 November 2006.
10. M. F. Daqaq, C. K. Reddy, and A. H. Nayfeh, Input-shaping control of nonlinear MEMS, *Journal of Nonlinear Dynamics*, Vol. 54, pp. 167–179, 2008.
11. C. Do, C. Marcin, L. Maryna, and D. Kieran, Dual-pulse control to eliminate bouncing of ohmic RF-MEMS switch. In *Proceedings of ISSC 2010*, Cork, Ireland June 23–24, pp. 36–41, 2010.
12. Z. Guo, N. McGruer, and Adams, Modeling, simulation and measurement of the dynamic performance of an ohmic contact, electrostatically actuated RF-MEMS switch, *Journal of Micromechanics and Microengineerin*g, Vol. 17, No. 9, pp. 1899–1909, 2007.
13. G. Rebeiz, *RF MEMS: Theory, Design, and Technology*, John Wiley & Sons, 2003
14. M. Donelli, S. Caorsi, F. De Natale, M. Pastorino, and A. Massa, Linear antenna synthesis with a hybrid Genetic Algorithm, *Progress in Electromagnetics Research*, PIER, Vol. 49, pp. 1–22, 2004.
15. K. Deligkaris, Z. Zaharis, D. Kampitaki, S. Goudos, I. Rekanos, and M. Spasos, Thinned planar array design using Boolean PSO with velocity mutation, *IEEE Transactions on Magnetics*, Vol. 45, pp. 1490–1493, 2009.
16. G. Taguchi and Y. Yokoyama, *Taguchi Methods: Design of Experiments, Quality Engineering*, Vol. 4, Amer Supplier Institute, 1993.
17. M. Spasos, N. Charalampidis, K. Tsiakmakis, and R. Nilavalan, RF-MEMS switch actuation pulse optimisation using Taguchi's method, *Microsystems Technologies*, Vol. 17, pp. 1351–1359, 2011.
18. L. Castaner and S. Senturia, Speed-energy optimisation of electrostatic actuators based on pull-in, *IEEE Journal of Microelectromechanical Systems*, Vol. 8, pp. 290–298, 1999.
19. J. Lee and C. Goldsmith, Numerical simulations of novel constant-charge biasing method for capacitive RF-MEMS switch, In *Proceedings of NanoTech Conference*, San Francisco, CA, USA, pp.396–399, 2003.
20. J. Blecke, D. Epp, H. Sumali, and G. Parker, A simple learning control to eliminate RF-MEMS switch bounce, *IEEE Journal of Microelectromechanical Systems*, Vol. 18, pp. 458–465, 2009.
21. M. Spasos and R. Nilavalan, Resistive damping implementation as a method to improve controllability in stiff ohmic RF-MEMS switches, *Microsystems Technologies Journal*, Vol. 19, pp 1935-1943, 2013.
22. M. Varehest, R. Amantea, D. Sauer, and S. Senturia, Resistive damping of pulse-sensed capacitive position sensors, transdusers '97, In *Proceedings of International Conference on Solid-state Sensors and Actuators*, Chicago, USA, June 16–19, 1997.

23. M. Spasos, K. Tsiakmakis, N. Charalampidis, and R. Nilavalan, An easy to control all-metal in-line-series ohmic RF-MEMS switch, *Journal of Analog Integrated Circuits and Signal Processing*, Vol. 65, pp. 87–97, 2010.
24. M. Spasos and R. Nilavalan, On the investigation of a reliable actuation control method for ohmic RF MEMS switches, *Microelectronics Journal*, Vol. 42, pp. 1239–1251, 2011.
25. C. Brown, Thesis: Impact of Environmental Conditions on the Contact Physics of Gold Contact RF Microelectromechanical Systems (MEMS) Switches, North Carolina State University, 2008.

9

Dynamics of MEMS Devices

Vamsy Godthi, K. Jayaprakash Reddy and Rudra Pratap*

Centre for Nano Science & Engineering, Indian Institute of Science, Bangalore, India

Abstract

MEMS devices have gained prominence and are replacing conventional devices in various applications such as mass/vibration/rate sensors, Radio Frequency (RF) switches, microphones, and speakers. Most MEMS devices use released structures in the form of beams, flexible plates, rigid plates, or a combination of these structures. The operation of these devices essentially involves some mechanical response to the applied signal or stimulus. The response is typically some static deflection or structural vibration. We focus our discussion here on vibrating MEMS devices. Such devices can be broadly classified into two categories: resonant devices and broadband devices. Devices such as mass sensors and gyroscopes operate at the resonant frequency of the structure, and therefore, achieving the designed resonant frequency is critical to their efficient operation. Other devices such as accelerometers and microphones are designed to operate over a wide band of frequencies, and achieving a linear broadband response is essential for their successful operation. In this chapter, we briefly explain the challenges involved, design methodologies used, and simulation packages available to model and simulate such MEMS devices. We then discuss two fabrication techniques to realize MEMS devices: surface micromachining and bonding silicon on glass. We explain the fabrication defects that arise with each process. We also discuss different characterization steps—visual, electrical, and mechanical—used to check for defects in these devices. With examples, we explain different failure states of resonant and broadband MEMS devices such as loss of structural integrity of the structure, resonant frequency shift, unintended modes of vibration of the structure, and reliability failure of the structure.

Keywords: Dynamics, resonant devices, multi-physics, squeeze film, acoustic radiation, fabrication defects, dynamic MEMS device failures

9.1 Introduction

MEMS devices, as the name suggests, involve mechanical elements [1]. The most commonly found mechanical elements are 1D and 2D structures such as beams, membranes, and rigid or flexible plates. These micromechanical structures are designed to respond to the intended stimulus or signal by deforming statically as in the case of pressure sensors, temperature sensors, or switches, or dynamically with desired vibration characteristics as in the case of microphones, accelerometers, etc. Based on the mode

**Corresponding author*: pratap.mems@gmail.com

Atul Tiwari and Baldev Raj (eds.), Materials and Failures in MEMS and NEMS, (263–284)
© 2015 Scrivener Publishing LLC

of operation of these devices, they can be classified as—resonant and non-resonant devices. This classification is essential as the chosen mode of operation dictates design, fabrication, electronics interface, and characterization. The basic design philosophy of the two devices differs significantly as the main performance parameters—sensitivity and resolution—are quite different in the two cases.

9.1.1 Resonant Devices

Various MEMS devices operate at the resonance of their structure. Devices such as mass sensors use resonance for sensing [2]. Mass sensors use a resonating structure, usually a beam, to measure a very small mass. When a mass adheres to the cantilever, the resonant frequency decreases due to the added mass. This shift in resonant frequency is used to determine the added mass (assuming surface effects are neglected). Devices for distance sensing such as micromachined ultrasonic transducers (MUT) operating as transceivers also use resonance to boost transmission and to improve receiver sensitivity. The ultrasonic waves generated by actuating membranes at their resonant frequency are transmitted out and at an obstruction these waves get reflected back and are sensed by the membranes. Since ultrasonic waves attenuate in the medium and at reflections, using an array of transmitting membranes such that the waves interfere constructively increases the range of these devices. Hence, the critical parameter in these devices is to achieve same resonance frequency across all the membranes.

Inertial sensors such as MEMS vibratory rate gyroscopes operate at resonance to improve their sensitivity. The vibratory gyroscope usually consists of a proof mass suspended on beams (Figure 9.1). The suspending beams are designed to have very close stiffness in two perpendicular directions: actuation and sensing. The proof mass is set into vibration at the resonance of the device along the actuation direction. When the vibrating proof mass subjected to some rotation in a direction perpendicular to the direction of vibration, then the proof mass experiences a coriolis acceleration in

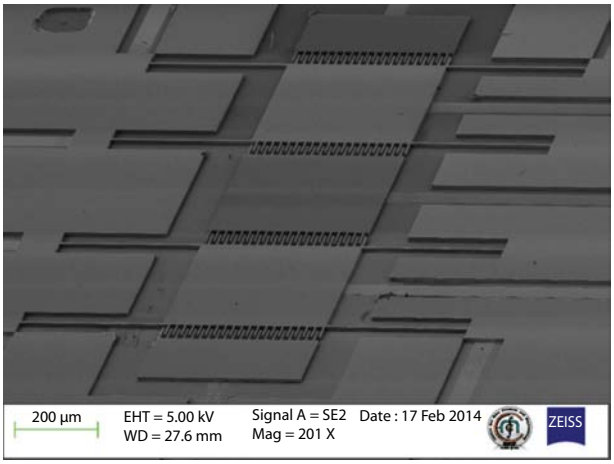

Figure 9.1 Resonant device—MEMS vibratory gyroscope.

the direction orthogonal to both actuation and rotation axis. The coriolis acceleration induced vibration in the third direction is used for sensing and this particular direction is called sense direction. This coriolis acceleration is proportional to the rate of rotation and is at the same frequency as the actuation frequency. The vibration along the sense direction is used to determine the rate of rotation. If the resonance frequencies in the drive and sense directions are close, then for the same rate of rotation, the magnitude of vibration is higher in the sense direction resulting in better sensitivity. Hence, the critical parameter is to achieve mode matching in both actuation and sense directions.

9.1.2 Non-resonant Devices

Other MEMS devices need to operate linearly over a range of frequencies—called bandwidth of the device. These devices operate at frequencies far below the resonance of their structure. A MEMS accelerometer is an inertial sensor, which is used to sense acceleration over a bandwidth of frequencies. It usually consists of a proof mass suspended by beams (Figure 9.2a). When the device experiences acceleration, the proof mass experiences a force proportional to the acceleration. This force causes the proof mass to deflect or vibrate, which is sensed. In order to measure acceleration of unknown frequency and magnitude, the response of the device should be linearly proportional to the acceleration over the desired frequency bandwidth. This is possible by keeping the resonance frequency far away from the bandwidth of operation. But the trade-off of increasing resonance frequency is the reduction in sensitivity of the device. Hence, the critical parameter is to place the resonance of the structure such that the response of the device is linear in the desired bandwidth, while achieving the maximum possible sensitivity. A MEMS audio microphone—usually consisting of a flexible plate (Figure 9.2b)—is used to measure sound pressure in the audio frequency range [3]. In order to accurately record sound, the device response should be linearly proportional to the sound pressure over the entire audio frequency range. Hence, as in the case of an accelerometer, the critical parameter is to place the resonance of the structure at an appropriate value.

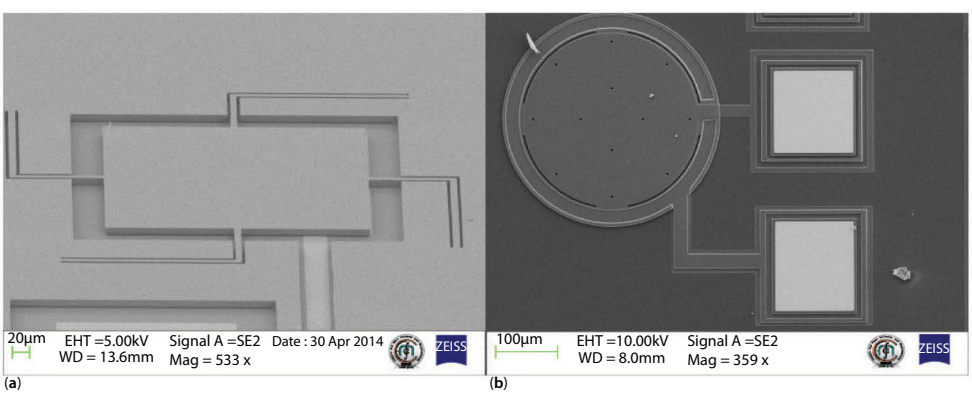

Figure 9.2 Non-resonant devices: (a) accelerometer and (b) microphone.

9.2 Modeling and Simulation

We saw in the previous section that various MEMS devices have some critical parameters based on their mode of operation. We will look at the design parameters for different devices. These parameters—based on the application—are used to design the device. MEMS devices are modeled either analytically or using finite element (FE) tools. Simple devices involving only structural modeling can be easily modeled analytically. But most of the devices involve multiple physics—mechanical, electrical, fluid, and acoustics—coupled to each other and hence the model becomes very complex. We will briefly look at the challenges involved in modeling devices involving multi-physics. Once the device is designed, the device model is simulated to check if the device performs as designed. We will discuss some of the simulation tools available. The microfabrication itself is a multi-step process involving many mask designs. We will discuss fabrication process flow simulation to check the validity of the mask designs.

9.2.1 Design Parameters

All mechanical elements in MEMS devices have inertia and elasticity. During mechanical vibrations, kinetic energy stored in the inertia of the system gets converted into potential energy stored in the elasticity of the system and vice versa. The simplest form of a mechanical system undergoing mechanical vibrations can be represented using a spring and a mass. From Newton's second law of motion, the equation of motion of such a system can be easily derived as

$$m\ddot{x} + kx = 0. \tag{9.1}$$

Any system governed by Eq. 1 undergoes a simple harmonic motion with a frequency $\omega_0 = \sqrt{k/m}$ that is specific to the system. But this system is an ideal model; real systems have dissipation (usually represented by a viscous damping term $c\dot{x}$) that has to be accounted for. The equation of motion of the system with damping driven by an external force $F(t)$ is given by

$$m\ddot{x} + c\dot{x} + kx = F(t). \tag{9.2}$$

When $F(t) = 0$, the system undergoes free vibrations at a characteristic frequency (called natural frequency) $\omega_d = \omega_0\sqrt{1-\zeta^2}$, where $\zeta = c/2\sqrt{mk}$. When the system is driven by a periodic forcing $F(t) = F_0 \sin(\omega t)$, the steady state response when plotted at various forcing frequencies gives the *frequency response graph*.

Figure 9.3 shows the frequency response of a MEMS accelerometer. The frequency response of the system can be divided into three regions: pre-resonance, resonance, and post-resonance. In the pre-resonance region, the response is stiffness controlled and is linear over a range of forcing frequencies. Hence, the non-resonant devices are designed to operate in this region and the sensitivity of these devices is stiffness controlled. In the resonance region, the response of the system is damping controlled. The lower the damping, the larger is the response of the system at resonance. Hence, reducing damping is crucial for resonant devices. Simple continuum structures like beams and plates of regular geometry can easily be represented by a corresponding lumped

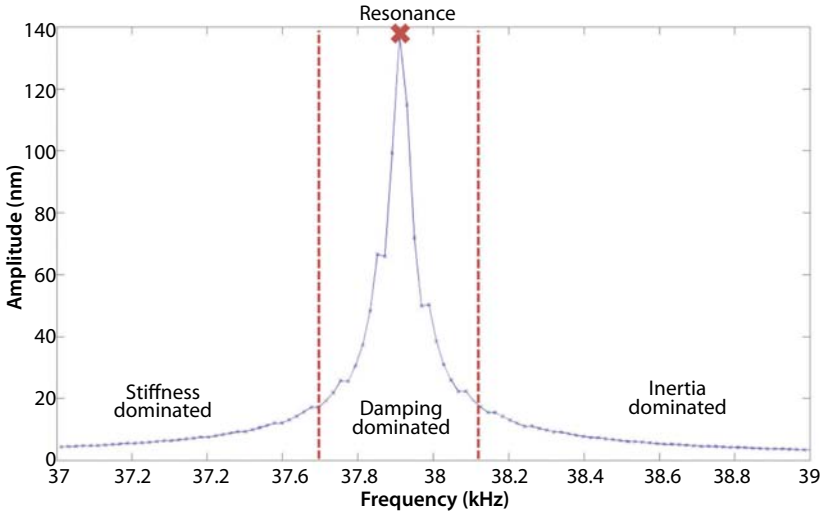

Figure 9.3 Experimentally obtained frequency response plot of a MEMS accelerometer structure.

quantity of stiffness and mass and Eq. 2 can be used to model the structures {for more details refer [4]}.

In the design of non-resonant devices, the main design drivers are sensitivity and bandwidth of operation. In the case of a MEMS accelerometer, the sensitivity (S) is defined as the amplitude of vibration of the proof mass for a unit acceleration input and is related to the stiffness (k) and mass (m) of the structure as $S \propto m/k \propto 1/\omega_0^2$. The bandwidth is defined by the linear region in the frequency response before the onset of resonance. Hence, higher the mass of the proof mass and lower the stiffness of the suspending beams, the better the sensitivity (since sensitivity is inversely proportional to the resonant frequency) of the device but with a reduction in the bandwidth. In the design of resonant devices, the design parameters are resonant frequency and damping ratio. The resonant frequency is related to the stiffness and mass of the mechanical structure as $\omega_0 = \sqrt{k/m}$. The damping ratio is computed as the ratio of the energy dissipated to the energy stored in a cycle of vibration of the structure. The higher the damping ratio, the greater is the energy dissipation. Since, resonant devices such as mass sensors detect the added mass by change in resonant frequency, their resolution—the smallest detectable mass change—is limited by the damping ratio. The highest mass sensing resolution is obtained by having the lowest possible damping in the structure. But for other resonant devices such as MUT's and gyroscopes, some amount of damping is necessary to quickly bring the system into steady state response. With very low damping, the structure "rings" for a long time once set into motion. Hence, modeling damping during the design is necessary for successful design of resonant devices.

The damping in the system is due to various mechanisms that can be classified as fluid–structure interaction damping and structural damping. The fluid–structure interaction damping dominates when the mechanical structure is in contact with a viscous fluid (air at atmospheric pressure) and is proportional to the surface area in contact. Fluid–structure interaction damping can occur due to *squeeze film* and acoustic radiation. Squeeze film damping is due to the compression of a thin film of fluid (between

the structure and the bottom substrate) in contact with the vibrating structure. Acoustic radiation into the surrounding fluid (due to the vibration of the structure) also causes damping. Analytical methods to model squeeze film damping [5] and acoustic radiation damping [6] are available for simple geometries. In the absence of fluid, structural damping becomes important. Structural damping includes thermoelastic damping and damping at clamped boundaries [7].

For surface micromachined MEMS structures, another constraint that limits the operation of the device is the maximum amplitude of oscillation, which is governed by the gap between the structure and the bottom substrate. In devices where electric potential is applied between the structure and the bottom substrate, this limit is even lower. Due to the nature of electrostatic force, the system becomes unstable as the amplitude of oscillation of the structure exceeds one-half of the gap and the structure gets pulled-in (called *dynamic pull-in phenomenon*) [8] and sticks to the bottom due to forces of adhesion.

9.2.2 Multi-physics

As seen in the previous section, the successful design of MEMS devices requires accounting for the effect of multiple physics coupled with the mechanical structure of the device—electrical (electrostatic actuation, pull-in, capacitive sensing), fluid (squeeze film effects), acoustic (MEMS microphone/speaker modeling, acoustic damping), piezoelectric (actuation/sensing), etc. For some of the coupled multi-physics with very simple geometry of the structure, analytical methods can be used to model the effect of the physics on the structural response. But, in reality, most MEMS structures cannot be modeled with the simpler analytical models. The assumptions such as small amplitude oscillations, parallel-plate motion, standard/periodic geometries, and ideal boundary conditions are not valid in many MEMS designs. Hence, a real system with realistic boundary conditions is taken and converted into an equivalent spring mass network containing a finite number (n) of degree of freedom. This n-degree-of-freedom system converts the complex system into a simple set containing n number of coupled differential equations that can be easily solved. This set of differential equations further transforms into a generalized eigenvalue problem of the form $\omega_n^2 [M]\{v_n\} = [K]\{v_n\}$, where ω_n is the eigenvalue (natural frequency) with the corresponding eigenvector (mode shape) v_n, M is the $(n \times n)$ inertial matrix, and K is the $(n \times n)$ stiffness matrix. This approach of dividing the system into a finite number of (spring mass) elements is called discretization and is used in modeling complex systems with FE method (FEM).

Electrostatic actuation and capacitive sensing are commonly used in MEMS devices. Coulomb's inverse-square law states that the interaction force between electrical charges is inversely proportional to the square of the distance between them. Since the separation is very small in MEMS devices, electrostatic forces are used to actuate the MEMS structures. Similarly, as the distance between two charged surfaces is varied, the capacitance (inversely proportional to the distance) varies and the change in capacitance is used to sense the amplitude of oscillation of MEMS structures. For standard geometries and parallel-plate motion of the surfaces, analytical models exist (discussed in detail in Ananthasuresh et al. [9]). But for modeling real cases such as a plate vibrating in flexural mode, comb-drive actuators (Figure 9.5a), and unequal size of top and bottom surface,

FEM is used. While the structure is discretized with FEM, the fluid domain may be is discretized with finite difference method. The coupling between various domains usually involves iterative steps. For example, in the case of electrostatic structure coupling the electrostatic domain is solved for electric field and the electric forces on the structure are computed, then the structural solution to the electrical forces is computed that gives the changed geometry of the electrostatic domain, and the cycle is repeated till the solution converges. During the electrostatic simulation, the open boundaries (where there is no structure) have to be modeled to have zero potential at infinity (Neumann boundary). Various simulation tools that are able to model electrostatics and coupled elasto-electrostatics are discussed in the following section.

Most of the vibratory MEMS structures oscillate over a bottom substrate separated by a small gap, which causes the air in the gap to get squeezed resulting in added stiffness and damping on the structure. The squeeze film stiffness and damping are functions of the frequency of vibration of the structure and hence change the frequency response of the structure over a range of frequencies. Thus, to successfully realize a vibratory MEMS device, squeeze film stiffness and damping have to be accounted for during the design of the MEMS device. The influence of squeeze film on MEMS structures has been extensively studied and several analytical models exist to estimate the squeeze film forces [5]. All these models involve solving the linearized (for small oscillations) form of the compressible Reynolds equation for the fluid trapped between the top and the bottom substrate. Analytical solutions to estimate squeeze film forces exist for simple cases—rigid plate with fluid vented on all sides (see Blech [10]), rigid plate with different fluid boundary conditions (see Darling et al. [11]). But real MEMS devices have perforations on the structure either for sacrificial release or to reduce the squeeze film effects. For symmetrically arranged perforations, there are analytical models to estimate the squeeze film forces (see Mohite et al. [12] and Pandey et al. [13]). Analytical models also exist to model the effect of flexural modes of the structure on the squeeze film (see Pandey & Pratap [14]). But the effect of squeeze film on structures with non-trivial geometries, unsymmetrical perforations, and mixed boundary conditions have to be modeled numerically using FEM. The structure is discretized with 3D structural elements and the area of the structure in contact with the fluid is discretized with 2D squeeze film elements (discretized Reynolds equation). There are two strategies by which the coupled analysis is performed: mode superposition and fully coupled squeeze film formulation. In the mode superposition method, first, the structure is solved with the imposed boundary conditions and the first n modes of vibration of the structure are extracted. Next, these mode shapes are imposed as velocity on the fluid domain and the squeeze film forces are evaluated for each mode. Finally, the squeeze film forces at any frequency are determined using mode superposition. In the fully coupled formulation, the structure and fluid domains are discretized and both the structural and pressure degrees of freedom are solved together [15]. The simulation tools available to model coupled structure–fluid (film) simulations are discussed in the following section.

Acoustic radiation from a vibrating structure is well-studied and analytical models exist to estimate the acoustic energy radiated from a structure—vibrating with rigid body motion [16], and vibrating in different modes [17]. But due to the complexity of analytically modeling acoustic radiation from a structure with perforations, FEM is

used to estimate the effect of perforations. A fully coupled FEM formulation is used to discretize the structure and the acoustic domain and both the structural displacements and the acoustic pressure are solved simultaneously. The simulation tools able to model coupled structure acoustic radiation are discussed in the following section.

9.2.3 Simulation Tools

Once the structure of the MEMS device is designed, before fabrication, the dynamic response of the structure is simulated to check if the response satisfies the device requirements. During initial stages of design, analytical models based on ideal approximations—rigid body motion of the structure, ideal boundary conditions, symmetric arrangement of perforations, etc.—of the structure are used which might lead to deviation from the expected response of the real structures. Hence, we simulate the structure without these approximations to determine the response of the actual structure. Any complicated MEMS structure can be easily discretized into a finite number of elements and the dynamic characteristics of the structure can be numerically simulated. One can implement FE-based numerical codes to simulate MEMS structures. There are also numerous FE-based software packages commercially available for simulation of MEMS structures under the influence of multi-physics. Due to the slender aspect ratio of most MEMS structural elements, care has to be taken during discretization to avoid skewed elements. We now present some examples of simulations of structures with multi-physics effects.

Figure 9.4 shows a simple Graphical User Interface (GUI) tool implemented in MATLAB to simulate electrostatics using finite difference method. Electric potential is applied on the electrodes (represented in black) and there is dielectric present between the electrodes (represented in blue). Upon discretizing and obtaining the solution, the electric potential is shown in Figure 9.4(b) and the electric field lines are shown in Figure 9.4(c). Figure 9.5(a) shows the simulated potential distribution and displacement of a comb-drive actuator (present on a fixed–fixed beam) due to applied potential. Similarly, Figure 9.5(b) shows the simulated potential and displacement of a suspended gate field effect transistor. These simulations are carried out in COMSOL Multiphysics and involve coupled structure-electrostatic analysis [18].

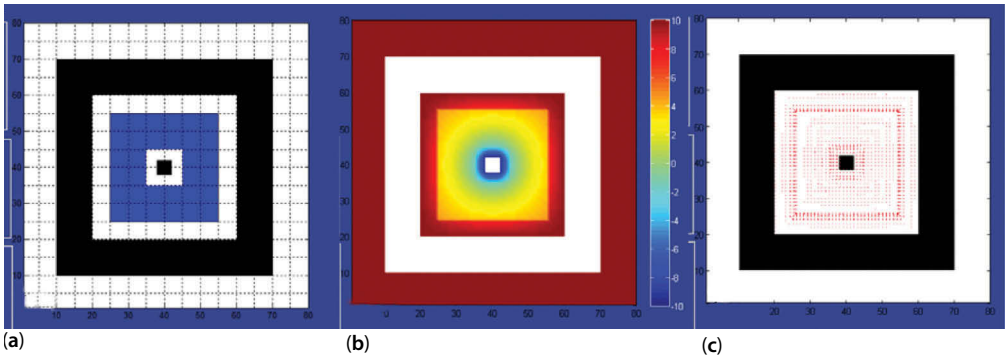

Figure 9.4 Electrostatic simulation: (a) device configuration, (b) simulated electric potential distribution, and (c) simulated electric field line distribution.

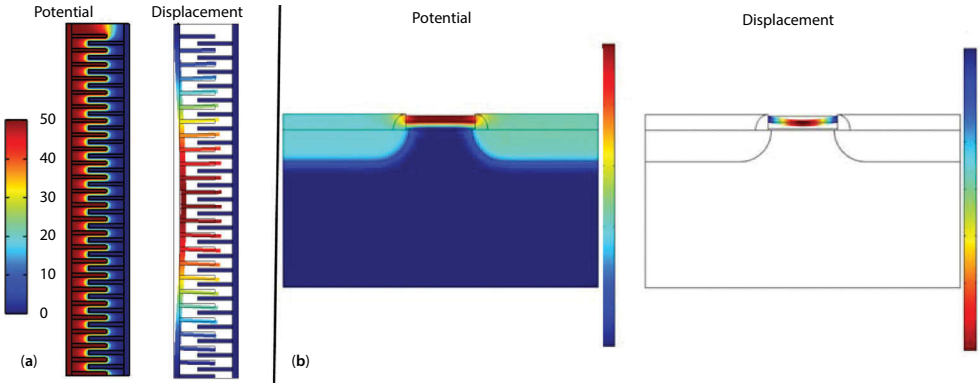

Figure 9.5 Coupled structural-electrostatic simulation: (a) comb-drive actuator and (b) suspended gate field effect transistor.

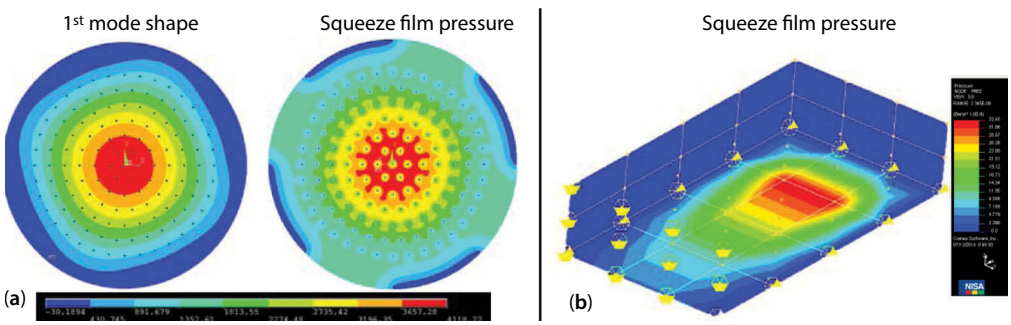

Figure 9.6 Coupled structural–squeeze film simulation: (a) circular plate clamped at every alternate 1/8th sector vibrating in 1st mode (b) cantilever vibrating in 1st mode.

Coupled analysis of a structure and squeeze film is carried out here using the FEM package, ANSYS, using mode superposition method. Figure 9.6(a) shows the first resonant mode of vibration of a circular plate that is clamped at every alternate 1/8th sector (45°). The simulated squeeze film pressure (which is in phase with velocity and causes damping) when the structure vibrates in the first resonant mode is also shown in Figure 9.6(a). The fully coupled (to be implemented as part of the FEM package, NISA) structure–squeeze film analysis is used to simulate the squeeze film pressure due to a cantilever beam vibrating in the first mode of resonance as shown in Figure 9.6(b).

Coupled structure-acoustic analysis is performed using ANSYS to simulate the acoustic radiation from a vibrating circular plate clamped at the circumference. The circular plate is discretized using 2D structural elements (shown in blue) and a hemispherical volume comprising of acoustic elements is created around the structure as shown in Figure 9.7(a). To properly model acoustic radiation into open air, ideally the radius of the acoustic volume should be infinity. But by using infinite elements on the surface of the hemisphere and keeping the radius of this hemisphere greater than R_{min} = (0.2 × largest wavelength + 0.5 × structure length), the infinite boundary

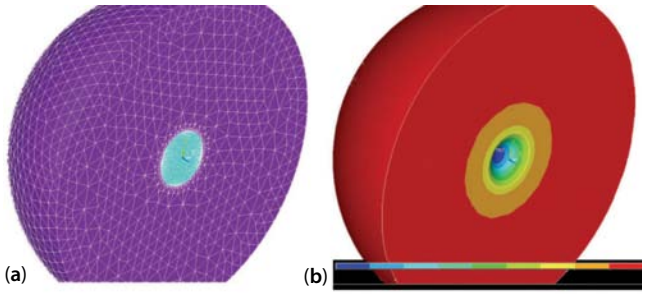

Figure 9.7 Coupled structural-acoustic simulation: (a) acoustic elements surrounding a circular plate clamped on all sides and (b) acoustic pressure radiating from the plate vibrating in the 1st resonant mode.

condition is properly modelled. In order to properly capture the acoustic wave, the element size should be smaller than the smallest wavelength / 20. The simulated acoustic pressure radiating from the circular plate vibrating in its first resonant mode is shown in Figure 9.7(b).

Residual stress is an important side effect of microfabrication that needs to be considered during the design of MEMS structures. Since there is no accurate way to directly quantify the residual stress due to the fabrication processes, the magnitude of stress is estimated indirectly from the effect on the response of the structure. One method of indirect residual stress estimation is from the shift in resonant frequency of different modes of a plate structure. FEM structural analysis is used to determine the stress magnitude that estimates the resonant frequency of all the different modes with minimum error with respect to the experimentally observed frequencies [7].

9.2.4 Process Flow Simulation

After the MEMS structures are simulated and the device design is finalized, depending on the fabrication steps, different photolithography masks need to be designed. These masks are used to pattern the various layers that ultimately result in the designed structure. The process flow with the designed masks is simulated before actually using the masks for fabrication to verify that the final structure will be realized as designed. This verification using process flow simulation is especially important when designing masks for fabrication at commercial foundries using standard processes such as PolyMUMPs, SOIMUMPs, and MetalMUMPs. There are various software packages available to simulate the fabrication process flow such as Coventorware, SEMulator3D, IntelliSuite, and Silvaco-Clever. These software have predefined basic and advanced fabrication process steps that can be used to quickly simulate the fabricated device following the process flow.

We will illustrate the process flow simulation using one of the tools, Coventorware, by simulating the process steps involved in realizing a fixed–fixed beam fabricated using PolyMUMPs. The different process steps simulated to fabricate the beam are listed in Figure 9.8(a). The 3D views of the simulated device at intermediate steps and after the final step are shown in Figure 9.8(b).

nber	Step Name	Layer Name	Material Name	Thickness	Mask Name	Photoresist	Depth	Mask Offset
0	Definition N-type (100) Silcon 1-2 Ohm-cm	Substrate	SILICON	20	GND			
1	LPCVD Deposition 600nm SixNy	Nitride	SIxNy_PolyMUMPs	0.6				
2	LPCVD Deposition 500nm PolySi	Poly0	POLYSILICON0_PolyMUMPs	0.5				
3	Etch RIE 500nm Poly0				L13	+		0
4	Etch RIE 500nm Poly0				Hole0	-		0
5	LPCVD Deposition Phosphosilicate 2000nm	Oxide1	PSG	2				
6	Etch RIE 750nm PSG				L50	-	0.75	0
7	Etch RIE 2000nm PSG				L43	-		0
8	Etch RIE 2000nm PSG				L52	-		0
9	LPCVD Deposition 2000nm Poly1	Poly1	POLYSILICON1_PolyMUMPs	2				
10	Etch RIE 2000nm Poly1				L45	+		0
11	Etch RIE 2000nm Poly1				L0	-		0
12	Etch RIE 2000nm Poly1				L52	-		0
13	LPCVD Deposition Phosphosilicate 750nm	Oxide2	PSG	0.75				
14	Etch RIE 200nm PSG				L47	-		0
15	Etch RIE 200nm PSG				L52	-		0
16	LPCVD Deposition 1500nm Poly2	Poly2	POLYSILICON2_PolyMUMPs	1.5				
17	Etch RIE 1500nm Poly2				L49	+		0
18	Etch RIE 1500nm Poly2				L1	-		0
19	Evaporate 500nm Au	Metal	METAL_PolyMUMPs	0.5				
20	Lift-off Metal Patterning				L51	+		0
21	Lift-off Metal Patterning				L48	-		0
22	HF (49%) Release Etch		PSG					

(a)

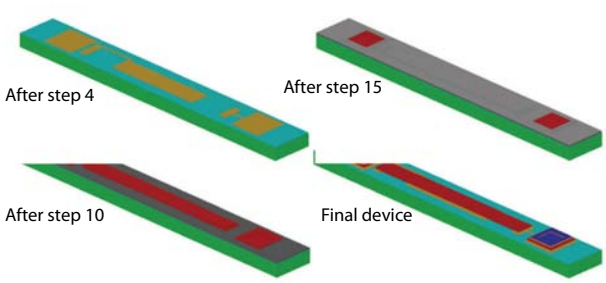

(b)

Figure 9.8 Process flow simulation of a fixed–fixed beam in Coventorware: (a) steps simulated to realize the beam (b) simulated 3D view of the device at different stages.

9.3 Fabrication Methods

There are many ways of fabricating MEMS devices each with their pros and cons [19]. The bottom line is to be able to realize very thin, released micromechanical structures. Since all structures have to have some boundary support, their release typically involves either etching a cavity below the structure with some etching process or creating a cavity by bonding pre-etched and patterned surfaces. Dynamic MEMS structures must vibrate for their intended application and hence, they must have room around them to be able to vibrate. Although, one can fabricate such structures using several processes, here we discuss two popular fabrication methods—surface micromachining and silicon-on-glass bonding—and their respective fabrication failures with examples.

9.3.1 Surface Micromachining

Surface micromachining involves deposition, patterning, and etching of thin layers of material to realize MEMS devices [19]. In this method, materials such as polysilicon, silicon nitride, and metals are generally used as structural layers. Palsma Enhanced Chemical Vapor Deposition (PECVD) oxide is used as the sacrificial layer that is finally etched to release the structure and gold is used to create the electrodes and electrical contacts. Using this method, it is possible to integrate both the MEMS structure and the electronic component fabrication using monolithic fabrication process. There are standard processes such as PolyMUMPs that are used to fabricate

devices using surface micromachining. Devices that can be made using surface micromachining include—microphones, accelerometers, RF switches, mass sensors, micro-fluidic devices, and micro-mirrors for display. Figure 9.2(b) shows a MEMS microphone made of polysilicon and Figure 9.13(a) shows fixed–fixed beams made of silicon nitride that are all realized using surface micromachining.

9.3.1.1 Issues

In surface micromachining, since the material layers are deposited, the thickness of individual layers is limited to a maximum of 2–5 μm. The devices are released by etching the sacrificial layer by using either a wet etching or a dry etching process. In the wet etching release, after the structure is completely released, the etchant is replaced by de-ionized water. As the water dries, the surface tension at the interface between air and water applies a force on the structure. If the structural stiffness is lower than a critical value, this force causes the structure to deform and stick to the bottom substrate resulting in a failure called stiction (e.g., Figure 9.9a) [20]. This problem is avoided by using a process called critical point drying [21] or by using dry etching to release the structure. A release with dry etching does not have stiction issues but based on the device can lead to warping due to large thermal stresses during the etching process as shown in Figure 9.9(b). In some cases, the process parameters during deposition of the structural layer can cause major stress buildup, which will result in structural breakdown after release as shown in Figure 9.9(c). The fixed–fixed beams in Figure 9.13(a) are successfully released using dry etching but with residual stresses created during deposition. Figure 9.9(d) shows a membrane deformed due to non-uniform etching during release.

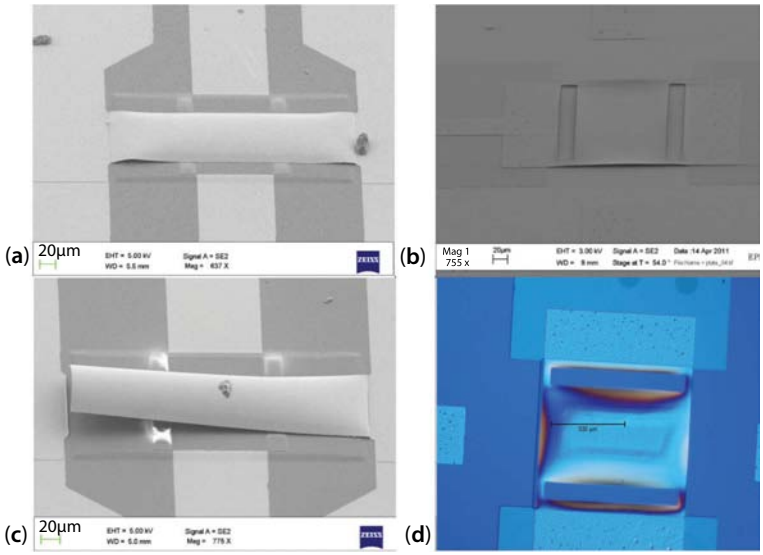

Figure 9.9 Different issues faced during surface micromachining: (a) structure collapse due to stiction, (b) plate structure warped during release, (c) structural fracture due to major stresses, and (d) incomplete release of a plate structure due to non-uniform etching.

9.3.2 Bonding

MEMS devices can also be fabricated by bonding separately patterned wafers. This technique usually get rids of the tricky sacrificial etch process [22] but at the cost of making the device manufacturing a lot more expensive due to dual wafers. Here, we describe an example of silicon and glass wafer bonding to realize some MEMS structures. The fabrication process using bonding of silicon on glass involves two wafers—a silicon on insulator (SOI) wafer and a sodium enriched glass wafer. The structural layer of the SOI wafer is patterned and etched to create dimples. The dimple decides the structural layer thickness and the gap between the structure and the bottom substrate. Bottom electrodes are patterned on the glass substrate using a lift-off process. The two wafers are aligned and bonded with a hybrid bonding process—involving both anodic and eutectic bonding simultaneously [23]. Figure 9.10 shows some structures successfully realized using this hybrid bonding process. In contrast to the surface micromachined process, this does not involve a sacrificial release step and hence does not have the problems associated with release such as stiction and warping. Once the fabrication process is optimized, the released structures are relatively free of residual stresses as seen in the fixed–fixed beam shown in Figure 9.10(a). Only the thickness of structural layer of the SOI wafer limits the thickness of the final structure; hence, it is possible to fabricate 3D MEMS devices with bonding. The MEMS gyroscope shown in Figure 9.1 and the MEMS accelerometer shown Figure 9.2(a) are also realized using bonding process with a structural thickness of 8 μm.

9.3.2.1 Issues

Most of the failures of the fabrication by bonding are during the bonding stage. During bonding, the two wafers are first aligned with respect to each other and kept securely in contact. Then, the wafers are heated to a high temperature (360–400 °C) and electric potential (1000–1500 V) is applied between the two wafers to create the bond. In some cases, due to thermal mismatch between the wafers and the temperature profile during bonding, high intrinsic stresses are created at the wafer-bonding interface (device

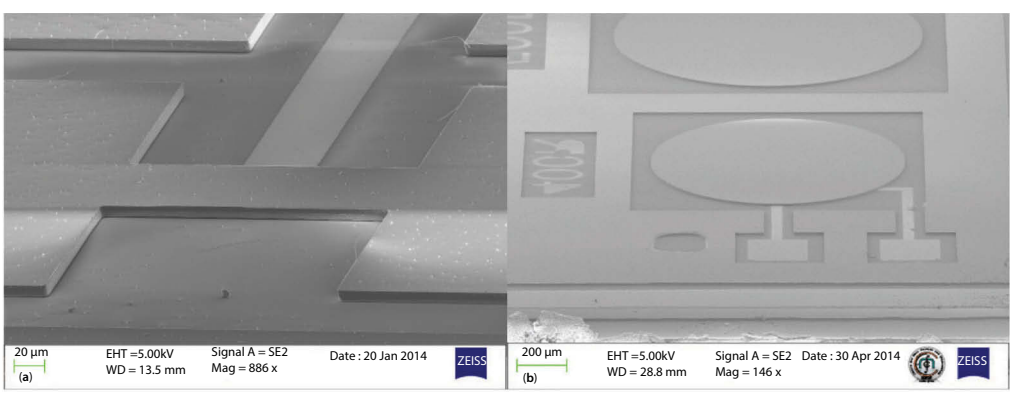

Figure 9.10 Different structures realized using bonding process: (a) fixed–fixed beam and (b) released circumferentially clamped circular plate.

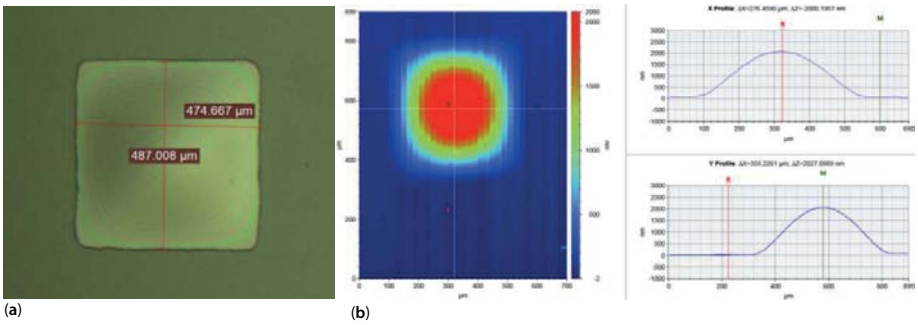

Figure 9.11 Deformation of a membrane due to intrinsic stresses, realized using bonding process: (a) optical image and (b) profile showing the deformed shape of the membrane.

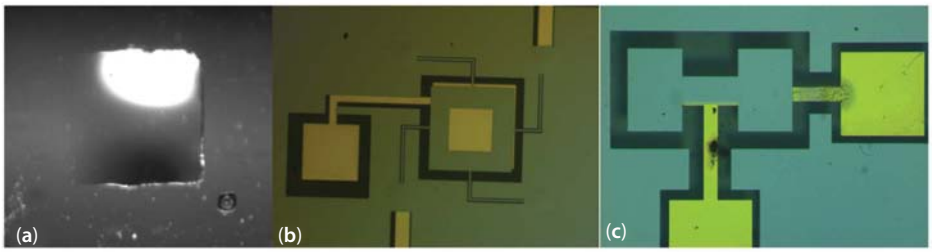

Figure 9.12 Different issues faced during bonding process: (a) broken membrane due to intrinsic stress, (b) misalignment between an electrode and the structure, and (c) electro-migration of the electrode lines during bonding.

anchors) resulting in highly deformed membranes as shown in Figure 9.11 and even broken membranes as seen in Figure 9.12(a). If the alignment of the pattern on the two structures is not properly carried out, it results in the failure of the devices as shown in Figure 9.12(b). In some cases, during the bonding process, when potential is applied between the two wafers, electro-migration can happen at metal electrode lines as seen in Figure 9.12(c).

9.4 Characterization

After the MEMS devices are fabricated, the devices are tested in a systematic manner in order to ascertain if the structures are successfully realized. Most vibratory MEMS devices are characterized in the following ways: visual, electrical, and mechanical. First, the devices are visually inspected using optical microscopes to check for defects and physical dimensions. Next, the devices are electrically characterized using optical microscopes to check if the devices are conducting (for electrostatic actuation) and have the designed base capacitance and dynamic behavior. Finally, the devices are mechanically characterized to verify if the devices are properly released and responding in the desired mode of vibration.

9.4.1 Visual

Visual characterization is the first means of identifying problems during every step of the fabrication process. A person experienced with MEMS fabrication and the various defects can identify many of the defects simply by visual inspection through an optical microscope. The color of the deposited oxide is a rough indicator of the thickness of the deposited layer. With experience, the presence of different gradients across the released structure is used to identify problems such as deformed structure due to pre-stress and stiction of the released structure. Images captured with the optical microscope are used to determine the actual lateral dimensions of the structures. But, optical microscopes have very limited depth of focus and hence a scanning electron microscope (SEM) is used to take images of the cross section of the structures. Cross-sectional images are used to measure the actual thickness of the structure, actual gap between the suspended structure and the bottom substrate, and variations in released dimensions of structures due to undercut during sacrificial release. For structures made up of multiple layers, the difference in contrast of different layers is used to determine the thickness of the individual layers. Another optical technique that is used to determine the out-of-plane dimensions of structures is the optical profiler. The optical profiler works on the principle of interference to detect the difference in height on the surface of the structure. Apart from determining thickness of the structures, optical profiler is used to determine the curvature of deformed beams or plates due to pre-stress and to measure variation in the cross section (such as taper) of the structures. Figure 9.13(a) shows the isometric view, captured using an SEM, of silicon nitride fixed–fixed beams realized using surface micromachining. Deformation due to pre-stress is easily visible on the longest beam. The 3D profile of the beams is captured using optical profiler as shown in Figure 9.13(b). The profile is used to determine that the cross section of the beams is trapezoidal in shape.

9.4.2 Electrical

The devices that are visually free of defects and have electrical contact pads are then tested for their electrical characteristics. An electrical probe station is used to contact the electrodes on the device and a device analyzer is used to perform the tests. For a suspended structure (such as the one in Figure 9.2a), first the current-vs-voltage (I–V)

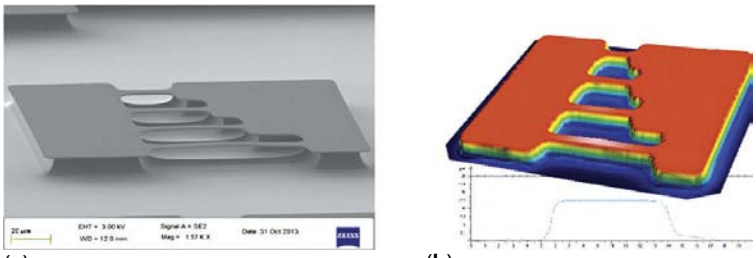

(a) (b)

Figure 9.13 Silicon nitride beams realized using surface micromachining: (a) SEM image and (b) 3D profile of the beams using optical profiler.

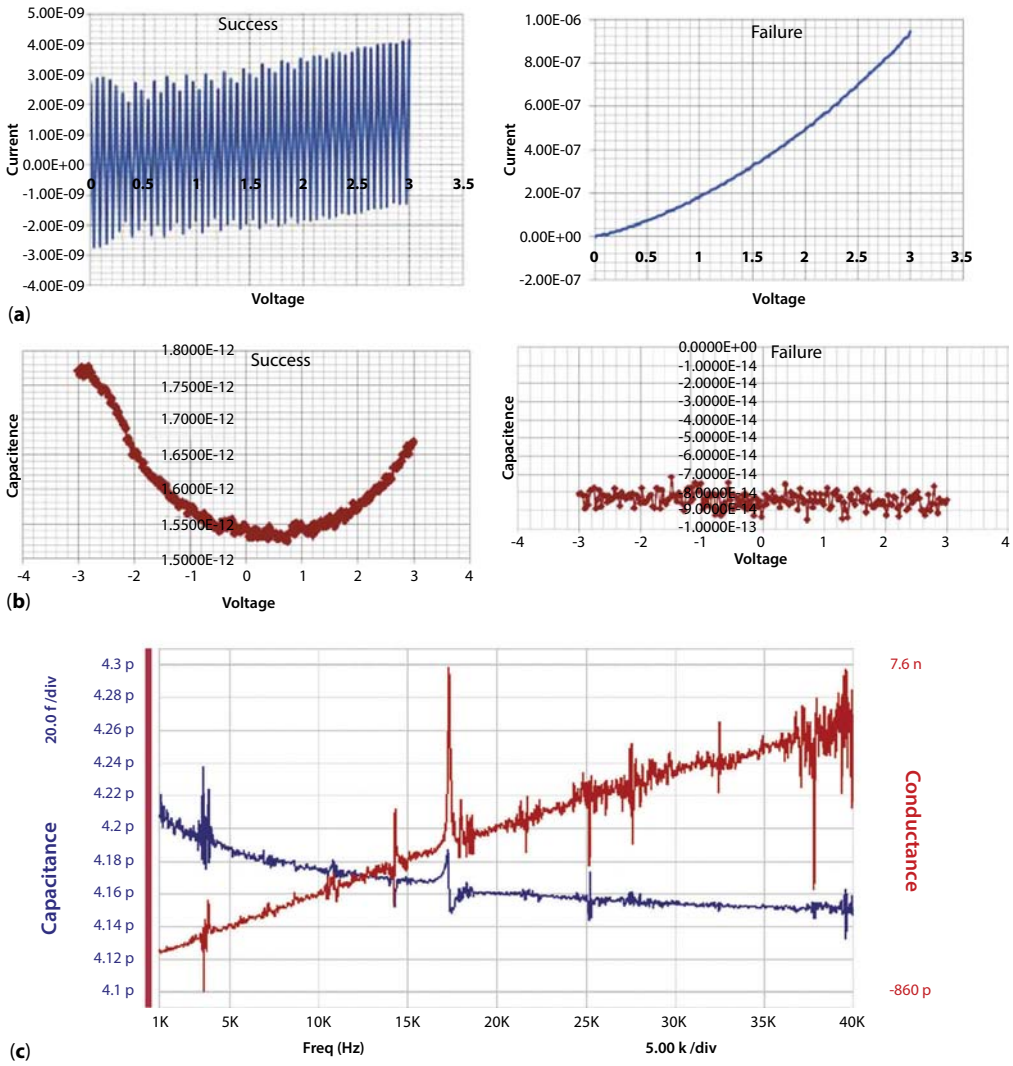

Figure 9.14 Typical electrical measurements of a suspended structure: (a) I–V, (b) C–V, and (c) C–f characteristics.

characteristics across the top and bottom electrodes of the structure are tested. In a successfully released device, the top and bottom electrodes are separated by an air gap, and hence no current should pass though the circuit, but if the structure is not released current should increase with voltage as shown by the typical "Success" and "Failure" I–V graphs in Figure 9.14(a). Next, the capacitance-vs-voltage characteristics of the structure are tested. The capacitance across the top and bottom electrodes of the structure is inversely proportional to the gap, which decreases with increase in voltage due to the electrostatic force of attraction. Hence, for a successfully released device the capacitance increases with increase in the magnitude of applied voltage irrespective of the polarity while for a partially released structure, the capacitance remains constant as

shown by the "Success" and "Failure" C–V graphs in Figure 9.14(b). Finally, the capacitance-vs-frequency (C–f) characteristics of the structure are tested. For a successfully released structure, the capacitance value jumps at resonance since the reduction in gap is higher (for the same applied voltage, deflection of the structure is larger at resonance) as seen in Figure 9.14(c).

9.4.3 Mechanical

The dynamic response of mechanical structures is determined by mounting a sensor—an accelerometer, a strain gauge, etc.—at different points on the structure and measuring the response to a periodic excitation. But for MEMS structures, it is not possible to mount any sensor on the structures and hence a non-contact laser Doppler vibrometer (LDV) is used to measure the displacement and velocity of vibration of the structures. The LDV works on the principle of Doppler's effect. A laser beam is incident on the vibrating structure, and the reflected beam experiences a shift in the laser frequency due to the velocity of the structure. The amplitude of the laser beam gets modulated due to the displacement of the structure. To view and measure vibrations of MEMS structures, a microscope-based LDV consisting of an optical head with different lenses is used (e.g., MSA400 from Polytec GmbH, shown in Figure 9.15a). The LDV has a controller consisting of velocity/displacement decoders to decode the velocity/displacement amplitude of oscillation of the structures. These decoders have a detection limit and maximum frequency of operation, which determine the resolution of the decoder. During testing of the structures, the decoder with the best available resolution (within the range of frequencies being tested) is chosen. The data from the decoder are digitized and stored on a data management system.

Based on the device architecture, the MEMS structures are actuated with either of the following: electrostatic actuation, base actuation, thermal actuation, or acoustic actuation. A probe station is used to contact the electrode pads on the device and provide electrical actuation to the structure. For devices with no electrical pads, base actuation is provided with a piezoelectric actuator. In all the cases, the structure is actuated with a periodic signal. The frequency of the periodic signal is linearly swept with time and the response of the structure at each frequency is captured. *Peak hold* averaging is used to obtain the frequency response function—a plot of the displacement/velocity response of the structure against actuation frequency. The natural frequency and the damping factor are determined from the experimentally measured frequency response function. The LDV also has mirrors inside the optics head to position the laser beam at different points on the structure to obtain frequency response function at pre-selected points. By plotting the response of different points on the structure at a resonant frequency, the corresponding mode shape of vibration is obtained. Figure 9.15(b) shows the experimentally captured frequency response function and the (0,2) mode of vibration of a circumferentially clamped circular plate. The response of the structure at different environmental conditions—pressure, temperature, etc.—can also be determined by actuating the structure in a chamber, with an optical port, where the ambient conditions are controlled.

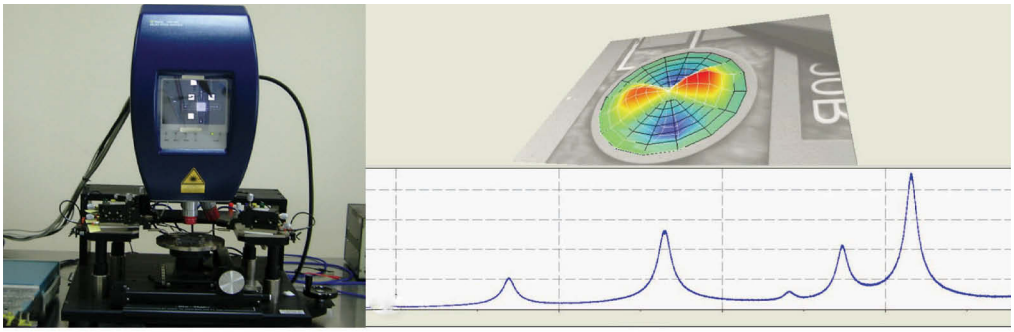

(a) (b)

Figure 9.15 Mechanical response characterization using LDV: (a) microscope-based LDV integrated with a probe station and (b) (0,2) mode shape of a circular plate.

9.5 Device Failures

For dynamic MEMS structures, device failures may results due to various reasons such as frequency shifts, wrong modes, structural defects, and lack of reliability. Most of these failures are a result of the issues faced during fabrication of the device detailed in the fabrication section. Although optimization of fabrication processes is usually carried out in order to minimize fabrication related defects, this optimization is never fool proof especially during lab prototype developments. The commercial production runs are much more reliable and consistent. However, MEMS devices undergo so many steps during packaging and testing that probability of introducing defects cannot be ruled out. Device failures can also occur due to unseen or unplanned operating conditions. Here, we discuss most common defects and failures that one encounter during the prototype development.

9.5.1 Frequency Shifts

The resonant frequency of the final released structure can vary significantly from the designed frequency due to the following causes: over-etching, residual stresses, non-uniform thickness, and squeeze film stiffness. During the sacrificial release of structures, based on the etch rate, the time needed to release the structure is calculated and used for etching. To account for uncertainties in the etch rate, the etching is carried out for a slightly longer time than calculated. This causes over-etching of the anchor resulting in larger dimensions of the released structure. Since the resonant frequency is very sensitive to the change in lateral dimensions over-etching results in a significant shift in resonant frequency of the structures. Residual stresses have the effect of increasing the stiffness, thereby causing an increase in the resonant frequency of the structure. Residual stresses can be accounted for in design (as discussed in the earlier section) or stress engineering, which involves either modifying the deposition parameters to reduce stress in the layer, or depositing layers having opposite residual stresses. This shift in resonant frequency due to residual stress is significant only if the magnitude of stress is high compared to the stiffness of the structure. The rate of deposition is not

always uniform throughout the wafer and this causes thickness variation in the structure across different devices. Since resonant frequency is directly proportional to the thickness of the structure, this causes a shift in resonant frequency across devices. This causes failure when an array of devices is needed with the same resonant frequency. As discussed earlier, the squeeze film affects the structure as an additional frequency dependent stiffness and damping on the structure. If squeeze film effects are unaccounted during the design of the structure, they can lead to a significant shift in the resonant frequency and damping factor of the structure. The designed resonant frequency of the accelerometer structure shown in Figure 9.2(a) is 38 kHz and is seen in the frequency response function (Figure 9.16a) measured in vacuum (no squeeze film). But at atmospheric pressure, the squeeze film effects modify the structural response, as shown in Figure 9.16(b), to a resonant frequency of 210 kHz [24]!

9.5.2 Wrong Modes

Suspended MEMS structures are expected to vibrate as rigid bodies (Figure 9.17a) but due to various issues—asymmetry in the suspended beams, stiction of one corner, etc.—they respond with plate flexural modes resulting in unwanted behavior of the device as shown in Figure 9.17(b). This is a good diagnostic tool for figuring out fabrication failures during device development. Partial release of a large structure is a very common problem

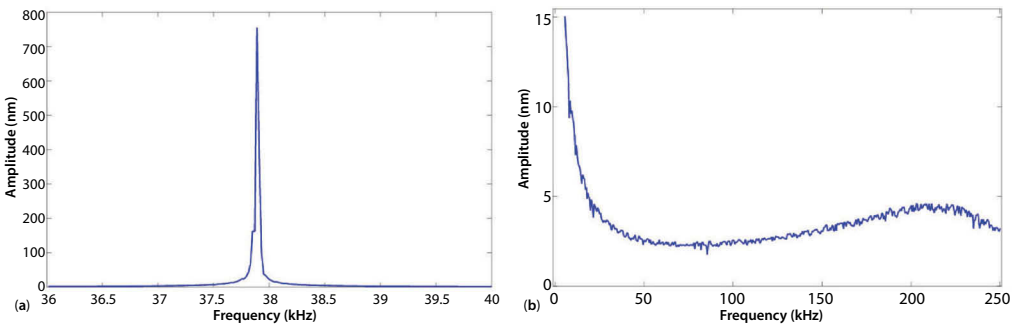

Figure 9.16 Frequency response functions of an accelerometer structure: (a) without squeeze film and (b) with squeeze film.

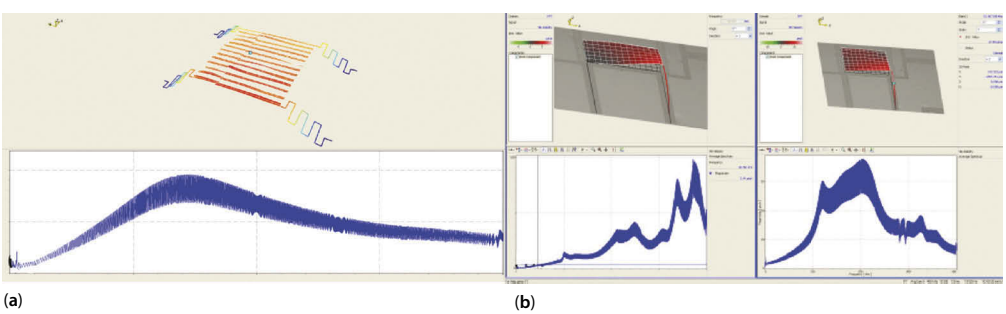

Figure 9.17 Mode shapes of suspended gyroscope structures: (a) rigid body motion and (b) plate flexural modes.

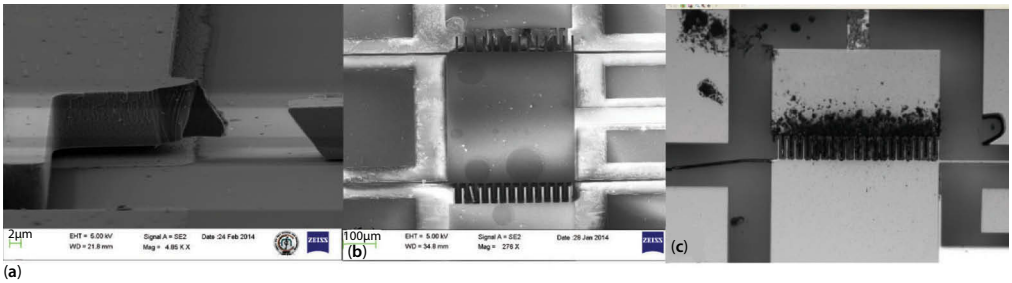

Figure 9.18 Structural failure of suspended gyroscope structures: (a) broken beam, (b) broken comb drive during CPD, and (c) comb drive damaged by high applied voltage.

in MEMS device development. Typically, an FRF of the suspended structure provides very clear evidence of stiction or non uniformity in the thickness of the structure.

9.5.3 Structural Integrity

Structural failure can occur during fabrication due to misalignment of different masks, over-etching, damage during CPD release, etc. Structural failure can also occur during operation due to shock loads to the device, very high actuation voltage, extreme thermal stresses, etc. Some examples of structural failure of a gyroscope structure are shown in Figure 9.18—broken suspending beams and damaged comb drives. Typically, dynamic MEMS structures use electrostatic actuation or sensing, often with the help of comb drives. The comb drives employ very thin fingers, and any defect in their geometry, including some misalignment due to residual stresses, can cause significant variation in the fringe field, changing the intended electrostatic forces considerably and mistuning the actuation to a degree that results in operational failure. In such cases, the structural integrity is not visibly impaired but operationally it is not intact either. The outright failures of structures in terms of breakage, cracks, or missing pieces are usually easy to spot just with optical microscopy.

9.5.4 Reliability Failure

Material degradation can occur due to periodic loading of the structures and due to environmental effects, which results in change in performance of the MEMS devices. A recent report states that micromachined structures made of materials like polysilicon and silicon nitride exhibit an increase in stiffness due to surface oxidation [25]. Also, delamination can occur in structures comprising of multiple layers of thin films after extended usage. High stress and steep stress gradients can cause creep especially in structures made of metallic films where room temperature creep exists. MEMS devices made of silicon and hermetically sealed with vacuum inside, typically exhibit very high reliability. Over a period of operation, however, both the hermetic sealing and the vacuum deteriorate and consequently the reliability degrades. These issues are currently under study and better technologies are continuously being sought to make MEMS devices more reliable than other alternatives.

Acknowledgments

We thank the teams at NNFC and MNCF at Centre for Nano Science and Engineering, Indian Institute of Science, Bengaluru, India for their help during the fabrication and characterization of the MEMS devices. We also thank our fellow research scholars: Dr. Charanjeet Malhi (MEMS microphone and surface micromachining failures), Amruta Ranjan Behara (silicon nitride cantilevers), Vamsi Krishna (surface micromachining failures), and Anish Roychowdhury (squeeze film simulation in NISA) who have helped by sharing data from their research work.

References

1. S. D. Senturia, *Microsystem Design.* Springer, New York, 2000.
2. B. Ilic, Y. Yang, and H. G. Craighead. Virus Detection Using Nanoelectromechanical Devices. *Applied Physics Letters* 85 (13): 2604–6, 2004.
3. C. Malhi. *Studies on the Design of Novel MEMS Microphones* (PhD Thesis). Indian Institute of Science, Bangalore, 2014.
4. S. Timoshenko, and S. Woinowsky-Krieger. *Theory of Plates and Shells.* McGraw-Hill, New York, 1959.
5. R. Pratap, M. Suhas, and A. K. Pandey. Squeeze Film Effects in MEMS Devices. *Journal of the Indian Institute of Science* 87 (1): 75–94, 2007.
6. Vishwakarma, D. Santhosh, A. K. Pandey, J. M. Parpia, D. R. Southworth, H. G. Craighead, and R. Pratap. Evaluation of Mode Dependent Fluid Damping in a High Frequency Drumhead Microresonator. *Journal of Microelectromechanical Systems* 23 (2): 334–46, 2014.
7. Vishwakarma, D. Santhosh. *A Study of Mode Dependent Energy Dissipation in 2D MEMS Resonators* (PhD Thesis). Indian Institute of Science, Bangalore, 2014.
8. D. Elata, and H. Bamberger. On the Dynamic Pull-In of Electrostatic Actuators with Multiple Degrees of Freedom and Multiple Voltage Sources. *Journal of Microelectromechanical Systems* 15 (1): 131–40, 2006.
9. G.K. Ananthasuresh, K. J. Vinoy, S. Gopalakrishnan, K. N. Bhat, and V. K. Aatre. *Micro and Smart Systems*. Wiley-India, New Delhi, 2010.
10. J. J. Blech, On Isothermal Squeeze Films. *Journal of Lubrication Technology 1*05 (4): 615, 1983.
11. R. B. Darling, H. Chris, and X. Jianyang. Compact Analytical Modeling of Squeeze Film Damping with Arbitrary Venting Conditions Using a Green's Function Approach. *Sensors and Actuators A: Physical* 70 (1–2): 32–41, 1998.
12. S. S. Mohite, K. Haneesh, V. R. Sonti, and R. Pratap. Analytical Solutions for the Stiffness and Damping Coefficients of Squeeze Films in MEMS Devices with Perforated Back Plates. *Journal of Micromechanics and Microengineering* 15 (11): 2083–92, 2005.
13. A. K. Pandey, R. Pratap, and S. C. Fook. Influence of Boundary Conditions on the Dynamic Characteristics of Squeeze Films in MEMS Devices. *Journal of Microelectromechanical Systems* 16 (4): 893–903, 2007.
14. A. K. Pandey, R. Pratap. Effect of Flexural Modes on Squeeze Film Damping in MEMS Cantilever Resonators. *Journal of Micromechanics and Microengineering* 17 (12): 2475–84, 2007.

15. A. Roychowdhury, A. Nandy, C. S. Jog, and R. Pratap. A Monolithic, FEM-Based Approach for the Coupled Squeeze Film Problem of an Oscillating Elastic Micro-Plate Using 3D 27-Node Elements. *Journal of Applied Mathematics and Physics* 1 (06): 20–25, 2013.
16. L. E. Kinsler, R. F. Austin, A. B. Coppens, and J. V. Sanders. *Fundamentals of Acoustics.* 4th ed. Wiley India, New Delhi, 2000.
17. F. G. Leppington, E. G. Broadbent, and K. H. Heron. Acoustic Radiation from Rectangular Panels with Constrained Edges. *Proceedings of the Royal Society A: Mathematical, Physical and Engineering Sciences* 393 (1804): 67–84, 1984.
18. R. K. Jayaprakash, K. M. Charanjeet, R. Pratap, and B. Navakanta. Coupled Numerical Analysis of Suspended Gate Field Effect Transistor (SGFET). *In 2012 1st International Symposium on Physics and Technology of Sensors (ISPTS-1),* pp. 141–44, 2012.
19. M. J. Madou, *Fundamentals of Microfabrication: The Science of Miniaturization.* 2nd ed. CRC Press, Boca Raton, 2002.
20. N. Tas, T. Sonnenberg, J. Henri, L. Rob, and E. Miko. Stiction in Surface Micromachining. *Journal of Micromechanics and Microengineering* 6 (4): 385–97, 1996.
21. K. Chang-Jin, Y. K. John, and S. Balaji. Comparative Evaluation of Drying Techniques for Surface Micromachining. *Sensors and Actuators A: Physical* 64 (1): 17–26, 1998.
22. W. D. Sawyer, M. S. Prince, and G. J. Brown. SOI Bonded Wafer Process for High Precision MEMS Inertial Sensors. *Journal of Micromechanics and Microengineering* 15 (8): 1588–93, 2005.
23. R. K. Jayaprakash, K. N. Bhat, and R. Pratap. Stiction Free Fabrication of MEMS Devices with Shallow Cavities Using a Two-Wafer Anodic Bonding Process. *Journal of ISSS* 1 (1): 1–9, 2012.
24. V. Godthi, R. Jayaprakash, and R. Pratap. A Study of Pressure-Dependent Squeeze Film Stiffness as a Resonance Modulator Using Static and Dynamic Measurements. *Journal of Microelectromechanical Systems* 99: 1–1, 2014.
25. C. Marxer, M.-A. Gretillat, N. F. de Rooij, R. Battig, O. Anthamatten, B. Valk, and P. Vogel. Reliability Considerations for Electrostatic Polysilicon Actuators Using as an Example the REMO Component. *Sensors and Actuators A: Physical* 61: 449–454, 1997.

10

Buckling Behaviors and Interfacial Toughness of a Micron-Scale Composite Structure with a Metal Wire on a Flexible Substrate

Qinghua Wang[1], Huimin Xie[2]* and Yanjie Li[3]

[1]*Research Institute for Measurement and Analytical Instrumentation, National Institute of Advanced Industrial Science and Technology, Tsukuba, Ibaraki, Japan*
[2]*Key Laboratory of Applied Mechanics (AML), School of Aerospace, Tsinghua University, Beijing, China*
[3]*School of Civil Engineering and Architecture, University of Jinan, Jinan, China*

Abstract
The buckling behaviors of metal-wire/flexible-substrate structures have gained extensive attentions in both academic and industrial fields. In this chapter, the buckling behaviors of a typical micron-scale constantan-wire/polymer-substrate structure under electrical loading were systematically investigated. Either the constantan wire or the polymer substrate would be subjected to buckling when the geometrical dimensions of the sample varied. The buckling features, the buckling mechanisms, the critical buckling stress, and the residual stress of the constantan wire under electrical loading were analyzed. The electricity-induced buckling method was presented to measure the interfacial toughness of the composite structure, and the applicable conditions of this method were discussed. Besides, four interesting buckling modes of the polymer substrate under restriction of the constantan wire, the occurrence conditions, and the generation mechanisms were studied. This work could offer a reference for the parameter design and the service condition control of the metal-film/flexible-substrate structures.

***Keywords*:** Buckling, constantan wire, polymer, electrical loading, interfacial toughness, mechanism, critical buckling stress, residual stress

10.1 Introduction

The structures made up of metal films and flexible substrates have been universally applied in flexible electronics [1,2], semiconductor integrated circuits [3,4], and micro-electro-mechanical systems [5,6]. During the processes of production and application, these kinds of structures always suffer from various loadings including heat, electricity, forces, etc. Their instability and failure behaviors, which directly affect the reliability of

**Corresponding author*: xiehm@mail.tsinghua.edu.cn

Atul Tiwari and Baldev Raj (eds.), Materials and Failures in MEMS and NEMS, (285–324)
© 2015 Scrivener Publishing LLC

micro-devices, have become the focus of attention [7–9]. In the past few decades, the characteristic dimensions of these structures have reached the micron, the submicron, and even the nanometer levels with the rapid development of miniaturization and integration [10,11]. For the micron/submicron/nano-scale film/substrate structures, there are multifarious instability modes, such as electro-migration [12,13] and buckling [14,15]. The buckling is ubiquitous and has attracted great attentions of researchers in multiple fields such as mechanics, electronics, aerospace, materials science, medical science, and military. Different from the buckling of a film/rigid-substrate structure [16], the buckling of a metal-film/flexible-substrate structure has its uniqueness, which has attracted our intensive interests in this chapter. The current researches related to the buckling modes of the metal-film/flexible-substrate structures mostly focus on the following three aspects.

(1) Simultaneous buckling of the metal film and the flexible substrate. This case happened under the effect of either mechanical loading or thermal loading. As a kind of instability mode, it could also be applied in the processing of flexible electronic devices.

In 1988, Bowden *et al.* [17] firstly reported the simultaneous buckling modes of the polydimethylsiloxane (PDMS) substrate and Ti film or Au film. The PDMS on glass was first heated and then coated by Ti film or Au film by deposition. After cooling, the PDMS would shrink. As the thermal expansion coeffcient of thermal expansion (CTE) of the PDMS was greater than that of the metal, the metal film was subjected to compressive stress, leading to simultaneous buckling of the metal film and the PDMS. When the PDMS was separated from the glass, regular sine-type buckling patterns could be obtained. This technique had been extensively used in extensile interconnects [18,19], expandable electronics [20–22], MEMS [23], phase-adjustable grating [24], piezoelectric films [25], and micron/nano-fabrication [26,27].

There were mainly two ways to induce the simultaneous buckling between a metal film and a flexible substrate. One way was depositing the metal film to the heating-extended flexible substrate on a rigid supporter [17]. The other way was transferring the metal film to the mechanical loading-stretched flexible substrate [20–22]. When the pre-imposed tensile stress or strain of the flexible substrate was released, the flexible substrate tended to recover and the metal films would buckle. Strong bonding force between the metal film and the flexible substrate was necessary for the aforementioned two ways. Some mechanical models had been developed to investigate the relationship between the buckling morphologies and the material constants [28–30].

(2) Buckling of the metal film on the flexible substrate. When the bonding force between the metal film and the flexible substrate was weak somewhere, the partial buckle-driven delamination would happen under the external force (Figure 10.1a). In other words, only the metal film buckled on the thicker flexible substrate. A majority of the buckling-driven delamination in the previous research was induced by mechanical loading or thermal loading.

By adjusting the bonding force, the metal film would buckle regularly on the flexible substrate. Sun *et al.* [31] fabricated regularly distributed low and high-adhesion areas by photolithography on a pre-stretched PDMS substrate. The GaAs and Si nanobelts were then deposited on PDMS. When PDMS recovered, the nanobelts were still connected to PDMS in the high-adhesion areas but delaminated and buckled from PDMS

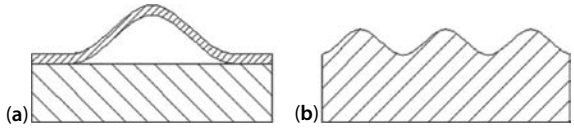

Figure 10.1 Different buckling modes. (a) Buckling of a film on a substrate and (b) surface buckling or wrinkling of a film. Reproduced by permission of The Royal Society of Chemistry, Copyright (2011), from Q.H. Wang, Y.J. Yin, H.M. Xie, *et al. Soft Matter*, Vol. 7, 2888–2894, 2011 [56].

in the low-adhesion areas. The buckling morphologies could be controlled accurately. This method could be used to fabricate electron devices with percentage elongation of 100%, compression ratio of 25%, and curvature radius of 5 mm. Jiang *et al.* [32] proposed a nonlinear buckling model to get the analytical solutions of the buckling wavelength, the buckling deflection and the maximum strain of the metal film. The experimental results from the buckling morphology of GaAs belts on PDMS agreed well with the analytical solutions.

Abdallah *et al.* [33] deposited Si_3N_4 film by chemical vapor deposition on a polyarylester substrate. The Euler buckling and the telephone-line buckling of the Si_3N_4 film were observed under the action of biaxial compression. The round-bubble buckling was found under the uniaxial compressive stress, and the buckling wavelength as well as the deflection grew with the increase of the uniaxial strain. These miscellaneous buckling modes were for large-area metal films. If the metal film was a strip or a wire, the main buckling mode would be the Euler buckling.

George *et al.* [34] and Heinrich *et al.* [35], respectively, investigated the fracture and the buckling behaviors of Ni film and Ta film on a polyimide substrate. The released tensile stress in the tensile direction due to fracture and the compressive stress in the metal films caused by the shrinkage mismatch in the lateral direction were quantitatively analyzed. Frank *et al.* [36] further studied the fracture and the buckling behavior of the Ta film on polyimide under uniaxial tensile stress. The Ta film fractured in the tensile direction, and the fragment after fracture can be considered as several Ta strips. The fracture released the stress in the tensile direction but gave rise to the compressive stress in the lateral direction. The residual stress and the fracture toughness of the Ta film could be determined by treating the main crack spacing as a function of the strain in the tensile direction.

Vella *et al.* [9] symmetrically researched the buckling behaviors of rigid polypropylene film strips on flexible substrates under the uniaxial stress. The thicknesses of the polypropylene film strips range from 15 to 90 μm. The flexible substrates were two types of poly siloxane substrates. One was a pre-stretched thin substrate and the other was a thick substrate without any pre-tension. In allusion to the two cases that the buckling wavelength was much greater and much smaller than the thickness and the width of the film, the relationship among the buckling wavelength, the material constants and the interfacial toughness was acquired from a series of experiments and theoretical derivations.

Xie *et al.* [37] used tensile loading to induce the buckling of an Al film on a PDMS substrate and estimated the interfacial toughness. Feng *et al.* [38] fabricated stretchable ferroelectric ceramics nanoribbons with wavy configurations on elastomeric substrates.

Similar buckling configurations were also used for light emitting diodes [39], stretchable electronics [40], and flexible optoelectronics [41].

Besides mechanical loading, thermal loading could also induce the buckling of the metal film. When the structure temperature changed, the difference of the CTE would create compressive stress in the metal film. If the local bonding force was weak, the buckling-driven delamination would arise. Bowden *et al.* [17] deposited a metal film on a PDMS substrate which was pre-stretched by heating. The metal film would buckle if the bonding force between the metal film and PDMS was weak in a local area. At present, the heat-induced buckling mainly concentrates upon the film/rigid-substrate structures [42].

(3) Buckling of the flexible substrate. The flexible substrate was usually the soft matter. Due to the complexity and the potential for new application characteristics, the buckling mode of the soft matter had gained wide attention from the research scholars. The buckling incentives are still mainly attributed to the action of mechanical loading [43] and thermal loading.

As the flexible substrate was easy to curl, it was usually stuck on a rigid substrate. For the rigid substrate, the flexible substrate could be regarded as a piece of film. A film on a rigid substrate buckled easily, and the buckling mode as well as the buckling mechanism had been well understood. This buckling mode was systematically studied by Hutchinson and Suo [16] from the perspective of fracture mechanics. The round-bubble buckling, the Euler buckling and the telephone-line buckling of a compressed large-area film were found and investigated by Moon *et al.* [44]. Various controllable buckling modes could also be generated on the film [45] when there were multiple defects on the substrate.

On the basis of the Euler buckling of a rectangle plate, three types of secondary buckling modes, i.e., the symmetric bump buckling, the oblique bump buckling, and the anti-symmetric bump buckling, were observed and reported by Audoly *et al.* [14,15]. Two long sides of the elastic plate in his study were fixed under biaxial compression load. It was observed through the numerical simulation and model tests that when Poisson's ratio of the elastic plate was larger than 0.25, it was easier to generate anti-symmetric secondary buckling and when Poisson's ratio was smaller than 0.25, the symmetric secondary buckling was likely to appear. The condition for the oblique secondary buckling was between that for the anti-symmetric secondary buckling and that for the symmetric secondary buckling.

When only the surface of the flexible substrate deformed, it was easy to induce the surface buckling or wrinkling (Figure 10.1b) [46]. In the simultaneous buckling between the metal film and the flexible substrate introduced in the first part of this study, most buckling morphologies of the flexible substrate were the surface buckling. Additionally, the surface wrinkling could be induced on the polymeric [47] and silicate thin films [48] deposited on the flexible substrate. For the free surface flexible substrate, the surface buckling also existed on the dried thin films [49] prepared by the sol–gel method, swollen [50], or dried [51] soft gels placed under geometric confinement, thin-film polymer bilayers under mechanical loading [52], and polymer monolayers depending on the own weight [53]. Moreover, some studies investigated the precise control and spontaneous formation of the aligned wrinkling patterns [54,55].

All the aforementioned buckling modes including the simultaneous buckling of the film wire and the flexible substrate, the buckle-driven delamination of the film wire, and the buckling of the flexible substrate, have been induced by mechanical loading or thermal loading. To the best of the authors' knowledge, there are few reports on the buckling modes of the metal-film/flexible-substrate structures under electrical loading. Moreover, the buckling mode of the flexible substrate restrained by metal film wires is also underreported no matter what the loading form is. In our experiments, two interesting phenomena are observed and analyzed under electrical loading. One is the buckling of a constantan wire on a polymer substrate after electrical loading [57,58]. The other is the buckling of the polymer substrate restricted by the electrified constantan wire [56]. The reason why the sample composed of the constantan wire and the polymer substrate is taken as the object of study lies in that the constantan wire is the major component of resistance strain gauges.

Furthermore, as an important parameter to evaluate the bonding force of the film and the substrate, the interfacial toughness is mainly measured by motivating delamination using mechanical loading currently. However, the traditional buckling incentives such as the indentation method [59] and the four-point bending method [60] are not suitable for flexible substrates. In this chapter, we will present the electricity induced buckling method to measure the interfacial toughness between the constantan wire and the polymer substrate, based on the buckling theory between a rigid film and a flexible substrate raised by Vella *et al.* [9]. This method provides a simple way to overcome the difficulties involving interfacial toughness measurement of flexible substrates.

This chapter mainly includes three parts: the buckling behavior of the constantan wire, the interfacial toughness evaluation, and the buckling behavior of the polymer substrate restrained by the constantan wire. The buckling morphologies, the buckling mechanism, the critical buckling analysis and the post buckling analysis of the constantan wire will be studied. The interfacial toughness of several samples will be evaluated based on the buckling morphologies of the constantan wire, and the applicable conditions of the electricity-induced buckling method will be discussed. Four kinds of interesting buckling modes, the occurrence conditions and the corresponding buckling mechanisms of the polymer substrate restricted by the constantan wire will be summarized and analyzed.

10.2 Buckling Behaviors of Constantan Wire under Electrical Loading

It was observed from this chapter that after electrical loading, the constantan wire delaminated from the polymer substrate due to the thermal mismatch between the constantan wire and the polymer substrate. Moreover, under the coupled electrical–mechanical loading, new instability modes of the constantan wire could be further triggered based on the buckle-driven delamination. This chapter summarized the characteristics of the buckling morphology of the constantan wire from experiments, discussed the buckling formation mechanism, and analyzed the critical buckling stress as well as the residual stress in the buckled constantan wire.

10.2.1 Sample and Experiments

10.2.1.1 Sample Preparation and Characterization

The sample has a composite structure integrated by a micron-scale constantan wire and a polymer substrate. The components of the constantan wire are copper and nickel with mass fractions of 55% and 45%, respectively. The major ingredient of the polymer substrate is polyvinyl formal-acetal (the mass fraction is greater than 90%) and the minor ingredient is epoxy novolac.

The sample fabrication process is illustrated in Figure 10.2 [56]. Before sample preparation, the constantan was in a sheet shape and the polymer was in a liquid form. First, the liquid polymer was coated on the constantan sheet by spin coating, and was heated for 3 h at 190 °C for solidification. The thickness of the polymer was greater than that of the constantan sheet. Then, the polymer and the constantan were turned upside down so that the polymer was used as the substrate. Next, the constantan sheet was covered with a layer of photoresist, and the photoresist was then exposed and developed by photolithography [61] using a grating-like mask. After rinsing, the grating-like photoresist would appear. Finally, the constantan sheet covered with the grating-like photoresist was etched, and the constantan wire would emerge on the polymer substrate.

Figure 10.3(a) and (b) respectively shows the scanning electron microscope (SEM) image and the schematic diagram of the composite structure [57,62]. The whole constantan wire is distributed in the shape of a narrow "S" and all the middle parallel segments are series wound under electrical loading. The thickness, the width, and the length of the parallel segments of the constantan wire are h_c=6 μm, b_c=28 μm, and l_c=3100 μm, respectively. The spacing of the parallel segments is d=108 μm and the number of the parallel segments is 28. The polymer substrate is a film with thickness of h_p=60 μm, width of b_p=5 mm, and length of a_p=7 mm. The aforementioned physical dimensions were measured using a 3D super-depth digital microscope (KEYENCE FE500). Figure 10.3(c) displays an example of the recorded digital microscope image of the constantan wire.

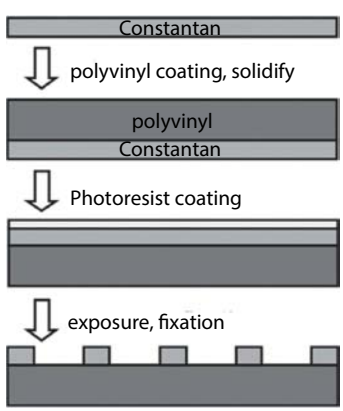

Figure 10.2 Sketch map of the fabrication process of the sample made up of the constantan wire and the polymer substrate. Reproduced by permission of The Royal Society of Chemistry, Copyright (2011), from Q.H. Wang, Y.J. Yin, H.M. Xie, *et al. Soft Matter*, Vol. 7, 2888–2894, 2011 [56].

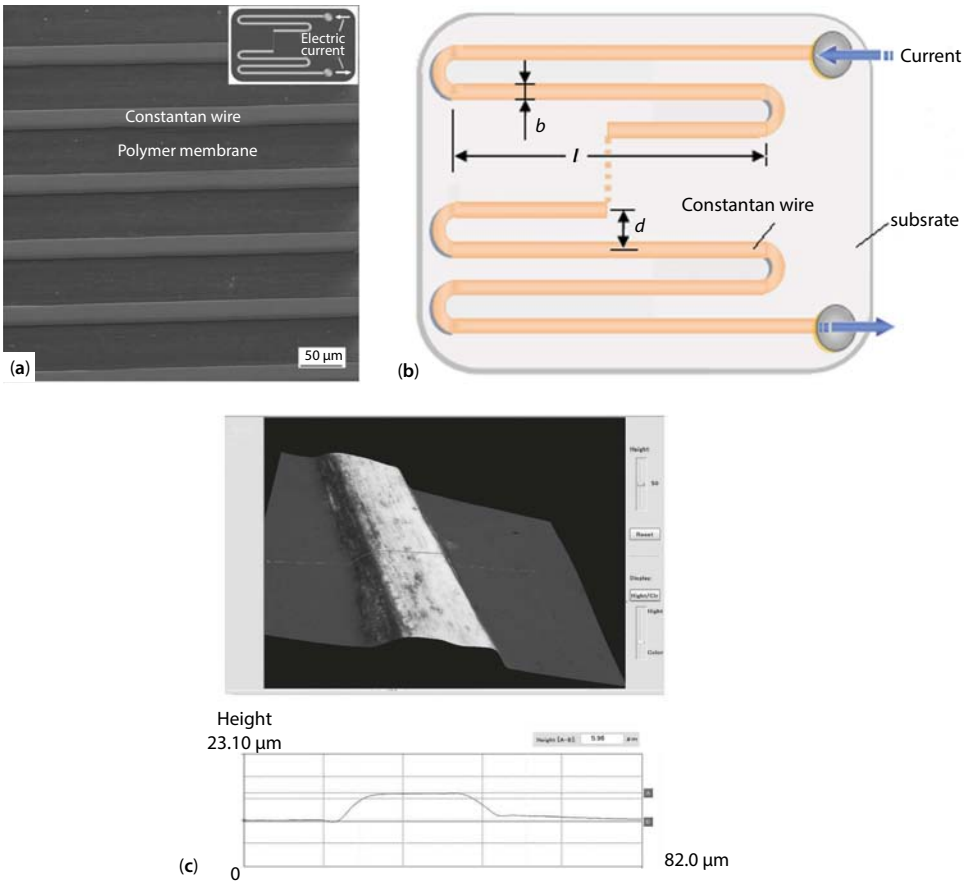

Figure 10.3 The constantan-wire/polymer structure. (a) SEM image of the structure, (b) schematic diagram of the structure, and (c) 3D digital microscope image for measuring the thickness of the constantan wire. (a) and (c) are reprinted, with permission, from Q.H. Wang, S. Kishimoto, H.M. Xie, *et al.*, *Transactions of Nonferrous Metals Society of China*, Vol. 24, 2606–2611, 2014 [62]. (b) Copyright (2009) IEEE. Reprinted, with permission, from Q.H. Wang, H.M. Xie, *et al.*, *Electron Device Letters*, IEEE, Vol. 30, 11–13, 2009 [57].

Young's modulus, Poisson's ratio, and the coefficient of thermal expansion (CTE) of the constantan wire are E_c=160 GPa, ν_c=0.33, and α_c=14.9 × 10^{-6} /K, respectively. For the polymer substrate, these corresponding parameters, respectively, are E_p=3.08 GPa, ν_p=0.31, and α_p=70 × 10^{-6} /K, where Young's modulus and Poisson's ratio are measured by the digital image correlation method. Besides, the glass transition temperature of the polymer substrate is 120.09 °C measured by a differential scanning calorimeter (DSC-60). The relationship between the temperature and the heat flow of the polymer is revealed as Figure 10.4 [58].

10.2.1.2 Electrical Loading Experiments

The experimental setup for electrical loading included a simple closed circuit, the above mentioned 3D super-depth digital microscope (KEYENCEVHX – 500FE), and a

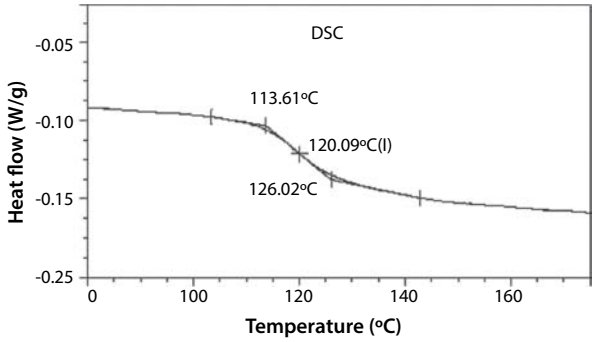

Figure 10.4 The differential scanning calorimetry curve of a polymer substrate. Reprinted from *Journal of Colloid and Interface Science*, Q.H. Wang, H.M. Xie, *et al.*, Measurement of interfacial toughness of metal film wire and polymer membrane through electricity induced buckling method, Vol. 358, 491–496 [58], Copyright (2011), with permission from Elsevier.

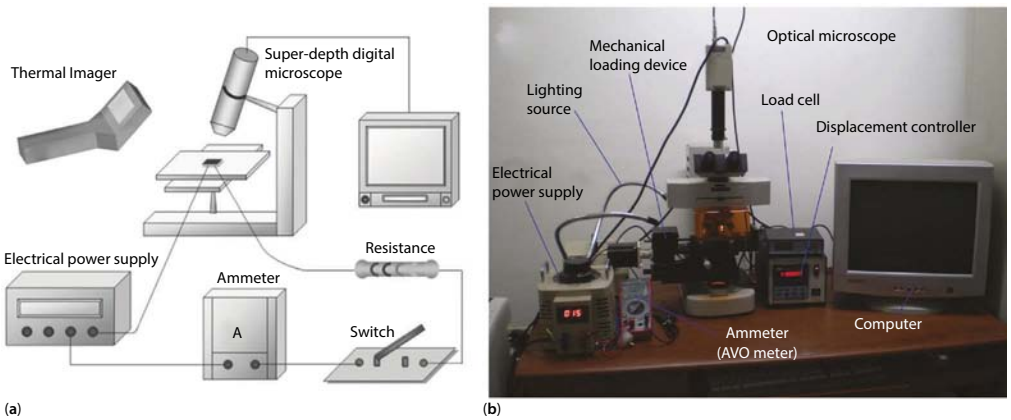

Figure 10.5 Experimental setups: (a) sketch map of the experimental setup for electrical loading and (b) experimental setup for the coupled electrical-mechanical loading, which was applied to a sample by adhering it to a sample supporter. (b) is reprinted, with permission, from Q.H. Wang, S. Kishimoto, H.M. Xie, *et al.*, *Transactions of Nonferrous Metals Society of China*, Vol. 24, 2606–2611, 2014 [62].

thermal infrared imager (ThermaCAM P60) as illustrated in Figure 10.5(a). The closed circuit was made up of a stabilized voltage supply, an ammeter (ampere-volt-ohm meter), a fixed or variable resistor and a switch. The voltage supply could provide either direct current (DC) or alternating current (AC) with frequency of 50 Hz.

The digital microscope was used to observe the surface profile. The buckling morphologies were also observed using a field emission SEM (QUANTA 200 FEG) and a Shimadzu SEM after experiments. The thermal infrared imager was applied to record the surface temperature of the sample. By comparing the sample temperature with the glass-transition temperature during the process of electrification, we could judge whether the glass transition of the polymer takes place or not.

To avoid the curling of the thin polymer substrate under electrical loading, the sample was pasted on organic glass by glue. The electrical loading experiments were carried out at room temperature.

10.2.1.3 Electrical–Mechanical Loading Experiments

In order to realize the combined electrical and mechanical loading, a self-developed mechanical loading device in our laboratory [63] was utilized based on the experimental setup for electrical loading. The experimental setup for the coupled electrical–mechanical loading is presented in Figure 10.5(b) [62]. A 50 Hz AC power supply, an ammeter, a fixed resistor and a switch were used to apply electrical loading. The mechanical loading device composed of a clamping apparatus, a load cell, and a displacement controller was adopted to perform tensile, compressive, and three-point bending tests. The surface topography of the sample was observed by an optical microscope.

Before electrical loading, mechanical loading was first applied to constantan-wire/polymer samples. The electrical-tensile loading could be exerted to a sample by adhering it to an aluminum tensile specimen or an aluminum bending specimen. The electrical-compressive loading could be imposed on a sample by affixing it to a rubber compressive specimen. The tensile and the compressive directions were parallel to the axial direction of the constantan wire segments. When unloading, electrical loading was first stopped prior to mechanical loading. All of the experiments were conducted at room temperature.

10.2.1.4 Temperature Variation under Electrical Loading

The Joule heat generated from the electric current will make the sample temperature increase. Our experiments indicate that the sample temperature rises rapidly at the beginning of the electrical loading regardless of the current form, i.e., DC or AC. The case of electrical loading with current density of $J = 2.21 \times 10^8$ A/m^{2}is taken as an example, where the current density is calculated from the electrical current divided by the cross-sectional area of the constantan wire. The temperature–time curves of the sample under DC and AC are plotted in Figure 10.6 [58]. It can be seen that the sample temperature will reach a stable value almost within 30 s no matter what the current form is.

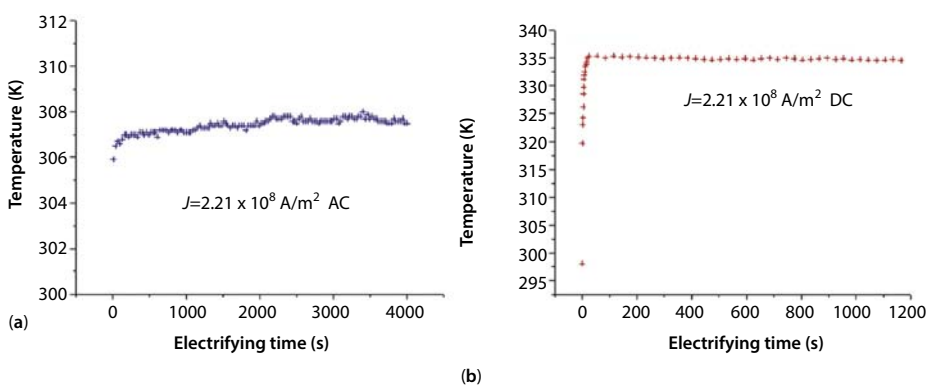

Figure 10.6 The temperature variation with the increase of the electrical loading when the current density is 2.21×10^8 A/m^2. (a) Under AC and (b) under DC. Reprinted from *Journal of Colloid and Interface Science*, Q.H. Wang, H.M. Xie, *et al.*, Measurement of interfacial toughness of metal film wire and polymer membrane through electricity induced buckling method, Vol. 358, 491–496 [58], Copyright (2011), with permission from Elsevier.

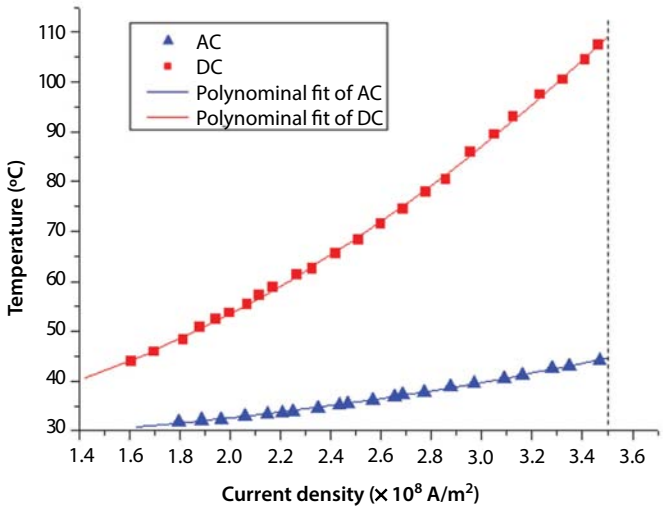

Figure 10.7 The temperature variation of the sample with the increase of the current density. Reprinted from *Journal of Colloid and Interface Science*, Q.H. Wang, H.M. Xie, *et al.*, Measurement of interfacial toughness of metal film wire and polymer membrane through electricity induced buckling method, Vol. 358, 491–496 [58], Copyright (2011), with permission from Elsevier.

The variation of the stable temperature recorded by the thermal imager along with the current density is displayed in Figure 10.7 [58]. The stable temperature on the sample surface monotonously rises with the increase of the current density under both DC and AC. A number of experiments demonstrate that the mean value of the highest current density the sample can bear is 3.5×10^8 A/m^2. The maximum sample temperature under DC and AC corresponding to the highest current density are respectively 112 °C and 45 °C from Figure 10.7. The maximum sample temperature under either DC or AC is lower than the glass transition temperature (120.09 °C) in Figure 10.4, manifesting that the glass transition of the polymer substrate does not take place.

10.2.2 Buckling Morphologies and Characteristics of Constantan Wire

10.2.2.1 Buckling Morphologies under Electrical Loading

During the process of electrification, the surface morphology of the sample does not change. When the current density exceeds a certain critical value, the parallel segments of the constantan wire will buckle from the polymer substrate after cooling for a while.

Figure 10.8 lists several typical buckling morphologies. Figure 10.8(a) is the multi-segment buckling of the constantan wire with buckling wavelength of 400 μm much greater than the width (28 μm) and the thickness (6 μm) of the constantan wire. This type of buckling occurs mostly in our experiments. Figure 10.8(b) shows another type of multi-segment buckling. The buckling wavelength of this type is about 50–100 μm, which is at the initial stage when buckling does not extend. The buckling in Figure 10.8(b) is occasional in the experiments. In Figure 10.8(c), there is only one segment of the constantan wire buckling. The buckling wavelength is about 300 μm that

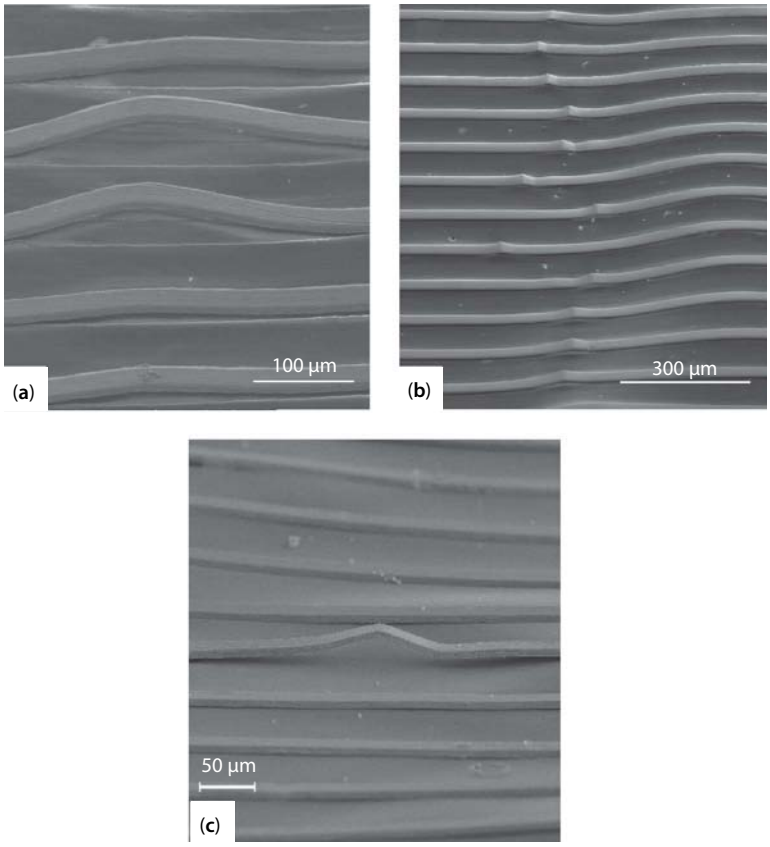

Figure 10.8 SEM images of three typical buckling morphologies of the constantan wire. Multi-segments buckling with (a) large wavelength and (b) small wavelength. (c) Single-segment buckling.

far exceeds the width and thickness of the constantan wire. This type of buckling also appears rarely in our experiments.

The buckling of the constantan wire in Figure 10.9 [57] is a kind of multi-segment buckling with large wavelength of about 300 μm, similar to the buckling morphology in Figure 10.8(a). The fracture of the constantan wire is induced by the electrical loading for the second time. The constantan wire buckled after the electrical loading at the first time and fractured during the electrical loading at the second time.

10.2.2.2 Effects of the Electric Current Form and Current Density

Our repeated experiments demonstrate that the critical current density of AC and DC for buckling are $J_{cr,AC} = 2.38 \times 10^8$ A/m^2 and $J_{cr,DC} = 2.88 \times 10^8$ A/m^2, respectively. In other words, the buckling of the constantan wire can only emerge when the current density is higher than 2.38×10^8 A/m^2 under AC or 2.88×10^8 A/m^2 under DC. We also find from a large number of experiments that the buckling of the constantan wire is easier to come up under AC than under DC. The electrical loading time causing buckling of the constantan wire under DC is much longer that under AC with the same current density. Usually, the former is 100 times the later.

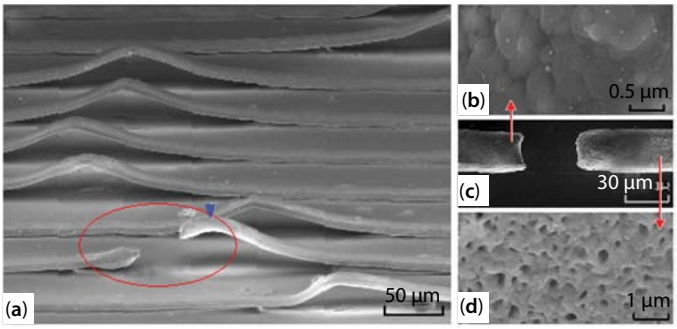

Figure 10.9 Buckling and fracture of the constantan wire. (a) SEM image of the buckling and the fracture after 2.82×10^8 A/m^2 AC for 40 min, and another 160 min after pause for 21.5 h; (c) The top view of the fractured wire, with the microstructures near the fracture area displayed in (b) and (d). Copyright (2009) IEEE. Reprinted, with permission, from Q.H. Wang, H.M. Xie, *et al.*, *Electron Device Letters*, IEEE, Vol. 30, 11–13, 2009 [57].

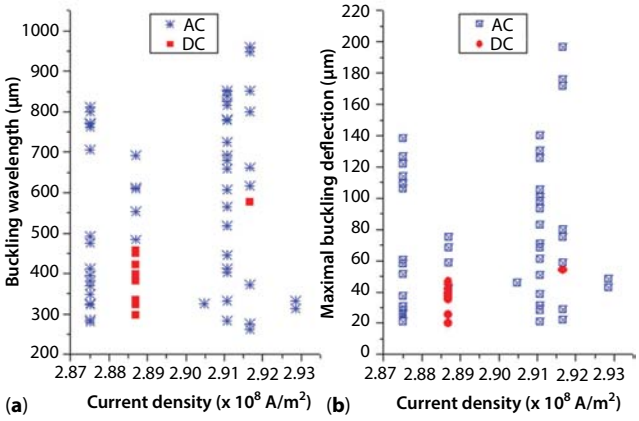

Figure 10.10 Distributions of the buckling wavelengths and the deflections of the buckling wires under different current densities. (a) The buckling wavelength and (b) the maximal buckling deflection. Reprinted from *Journal of Colloid and Interface Science*, Q.H. Wang, H.M. Xie, *et al.*, Measurement of interfacial toughness of metal film wire and polymer membrane through electricity induced buckling method, Vol. 358, 491–496 [58], Copyright (2011), with permission from Elsevier.

With regard to the buckling morphologies when the buckling wavelength is greater than 200 μm, the distributions of the buckling wavelength and the maximum buckling deflection at different current densities are depicted in Figure 10.10 [58]. It is clear that the number of times the buckling appeared under AC is much more than that under DC, indicating that AC is more likely to induce the buckling of the constantan wire than DC. Besides, both the buckling wavelength and the maximum buckling deflection do not present any obvious change rule with the increase of the current density. At a certain current density, either the buckling wavelength or the maximum buckling deflection will range from a small value to a large value. Since the sample temperature monotonously goes up with the increase of the current density, it can be perceived that

both the buckling wavelength and the maximum buckling deflection do not follow any obvious regular patterns with the increase of the sample temperature.

10.2.2.3 Buckling Morphologies under Electrical–Mechanical Loading

In addition to electrical loading, the electrical-tensile loading and the electrical-compressive loading were exerted to samples. Buckling-driven delamination of the constantan wire was also found under electrical–mechanical loading. Besides, some new instability modes based on buckling were observed under the coupled electrical-mechanical loading. The electrical-tensile loading tended to trigger the fracture of the constantan wire after buckling. The electrical-compressive loading was prone to make the constantan wire folded at the top of buckling. Occasionally, the constantan wire would buckle in an opposite direction, i.e., toward the inside of the polymer substrate under electrical-compressive loading.

Figure 10.11 shows three examples of the instability modes of the constantan wire under the combined effect of 2.8×10^8 A/m^2 AC and tensile strain of 0.009, 0.012,

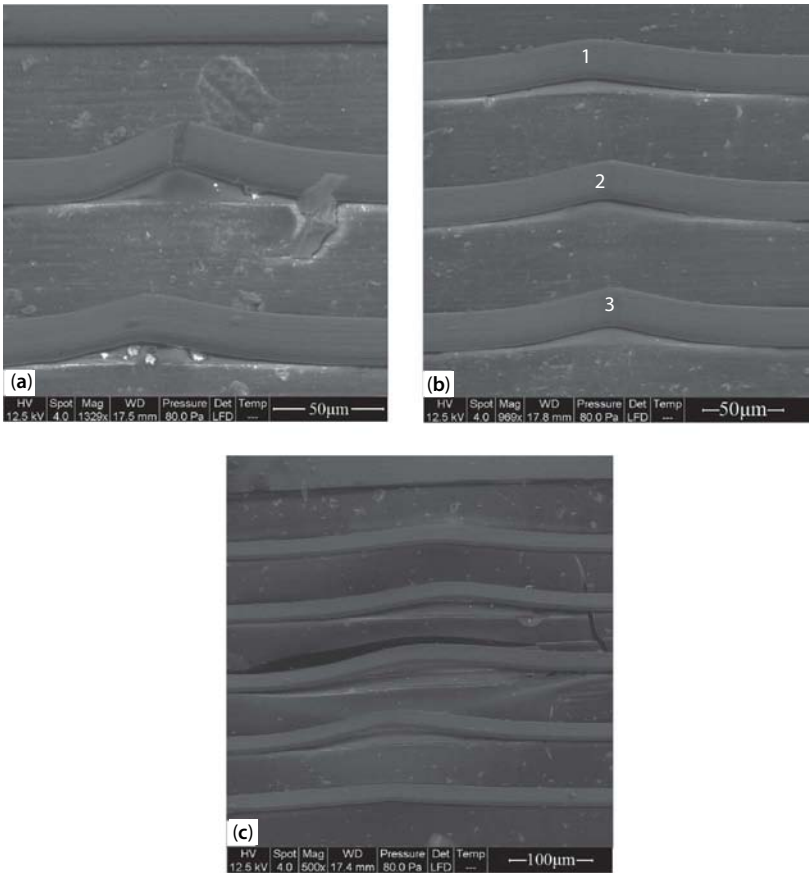

Figure 10.11 Buckling-based instability modes of the constantan wire after the combined action of 2.8×10^8 A/m^2 AC and the tensile strain of (a) 0.009, (b) 0.012, and (c) 0.021. Reprinted, with permission, from Q.H. Wang, S. Kishimoto, H.M. Xie, *et al.*, *Transactions of Nonferrous Metals Society of China*, Vol. 24, 2606–2611, 2014 [62].

and 0.021, respectively [62]. The fracture of the buckled constantan wire in Figure 10.11(a) is caused by the joint effect of the mechanical tensile stress and the bending (buckling)-induced tensile stress. Of course, the buckling plus fracture phenomenon is not common and the frequently appeared phenomenon is buckling only as shown in Figure 10.11(b). The buckling of the constantan wire and the broken of the polymer substrate in Figure 10.11(c) are mainly attributed to the electrical loading and the mechanical tensile loading, respectively.

Figure 10.12 impresses us by giving the typical instability modes of the sample under the combined effect of 2.8×10^8 A/m^2 AC and compressive strain of 0.066, 0.083, and 0.102 [62]. The inward buckling of the constantan wire in Figure 10.12(a) is a very rare phenomenon in our experiments, which may depends on the disturbance effect on the sample. The fracture of the inwardly buckled constantan wire is aroused by the bending-induced tensile stress. The folding of the buckled constantan wires in Figure 12(b) and (c) is owing to the further extrusion by the mechanical compressive stress. Besides, the polymer substrate will buckle from the supporter under a large mechanical compressive force, and the buckling-induced tensile stress will result in the fracture of the polymer substrate in Figure 10.12(c).

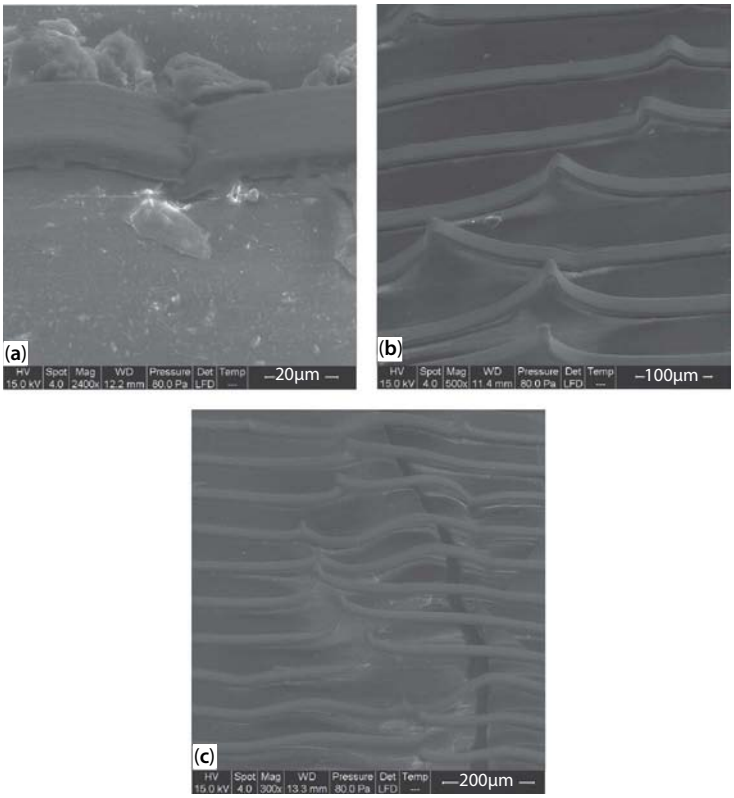

Figure 10.12 Buckling-based instability modes of the constantan wire after the combined loading of 2.8×10^8 A/m^2 AC and compressive strain of (a) 0.066, (b) 0.083, and (c) 0.102. Reprinted, with permission, from Q.H. Wang, S. Kishimoto, H.M. Xie, *et al.*, *Transactions of Nonferrous Metals Society of China*, Vol. 24, 2606–2611, 2014 [62].

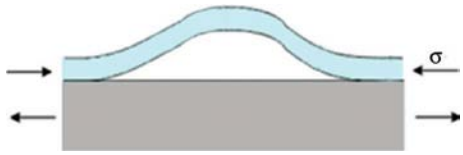

Figure 10.13 Diagram of the buckled constantan wire under compressive stress.

All of the aforementioned instability modes under electrical loading and the electrical–mechanical loading are based on buckling. Selective analysis will be focused on the buckling mechanism of the constantan wire in the following section.

10.2.3 Buckling Mechanism Analysis of Constantan Wire

The buckling of the constantan wire is resulted from thermal mismatch between the constantan wire and the polymer substrate. During the electrical loading process, the sample temperature rises and then almost remains unchanged at a temperature higher than the room temperature from Figures 10.6 and 10.7. The central area of the sample will delaminate from the glass due to higher temperature compared with the edge area. After the electric loading is ceased, the sample temperature gradually drops to the room temperature. As the CTE of the constantan wire ($a_c = 14.9 \times 10^{-6}$/K) is less than that of the polymer substrate ($a_p = 70 \times 10^{-6}$/K), the polymer substrate shrinks faster than the constantan wire, resulting in biaxial compressive loading on the constantan wire. When the compressive force reaches the bond force between the constantan wire and the polymer substrate, the constantan wire will separate from the polymer substrate. If the compressive force continues to increase up to the critical buckling load, the constantan wire will buckle from the polymer substrate as shown in Figure 10.13.

The reason why the constantan wire fractures after buckling under electrical loading twice in Figure 10.8 is analyzed. In the first electrical loading process when the sample temperature rises, the constantan wire bears tensile stress due to the smaller TEC of the constantan wire compared to the polymer substrate. After the first electrical loading is stopped when the sample temperature drops, the constantan wire will withstand compressive stress and then buckle from the polymer substrate. At this time the material resistance already degenerates. During the second electrical loading process, there will be tensile stress inside the constantan wire again. The constantan wire experience a tensile-compressive-tensile stress fatigue, resulting in the fracture of constantan wire under the tensile stress at the second time. The fracture of the buckled constantan wires in Figures 10.11(a) and 10.12(a) is caused by the combined effect of the mechanical stress and the buckling-induced tensile stress, which were already explained in Section 10.2.2 part (3).

Furthermore, AC is more likely to induce buckling of the constantan wire than DC from Figure 10.10, signifying that the buckling of the constantan wire is not only related to the Joule heat but also associated with the electric current form.

The correlation between the buckling occurrence and the electric current form can be explained from the following two aspects. On the one hand, the constantan wire

suffers more disturbances under AC than under DC. The electron wind force, the electric field force and the forced aroused by the stress gradient inside the constantan wire are difficult to achieve the steady-state balance under AC. As a consequence, the constantan wire is always subjected to alternating stress fatigue. The electric current crowding effect and the Joule heat are mutually reinforcing, which will weaken the deformation resistance of the constantan wire. On the other hand, there will be persistent temperature rise phenomenon in a small local area under AC. The constantan wire is easy to buckle in a local area with higher temperature. It is regrettable that the temperature in a small local area was not measured due to the resolution limitation of the used thermal imager.

10.2.4 Critical Buckling Analysis of Constantan Wire

The critical buckling stress is an important parameter for stability assessment of film/substrate structures. Since the thickness of the polymer substrate is much greater than that of the constantan wire, the constantan wire can be regarded as a beam clamped at two ends. The critical buckling stress of the constantan wire will be analyzed using a beam model.

According to the Euler formula [64], the critical buckling force for a two-end clamped beam is

$$F_{cr} = -\frac{\pi E_c I_c}{(0.5l)^2} \tag{10.1}$$

where E_c is Young's modulus, I_c gives the inertia moment of the constantan wire, and l represents the length of the common part between the constantan wire and the polymer substrate. In the critical condition, buckling occurs in the whole common part and l is equal to the crack length λ, i.e., the delaminated length. The half crack length is defined as $a=l/2$. On the basis of the force–stress relationship:

$$\sigma_c = \frac{F_c}{b_c h_c} \tag{10.2}$$

We can get the expression of the critical buckling stress of the constantan wire:

$$\sigma_{cr} = -\frac{\pi^2 E_c h_c^2}{12a^2} \tag{10.3}$$

In the light of the deformation compatibility equation, the relationship between the temperature difference and the force can be represented by

$$\Delta T_{cr} = \left(\frac{1}{A_c E_c} + \frac{1}{A_p E_p}\right) F_{cr} / (\alpha_p - \alpha_c) \tag{10.4}$$

where A is the cross-sectional area; α stands for the CTE; and the subscripts c and p indicate the constantan wire and the polymer substrate, respectively. The critical

buckling temperature difference can be determined by substituting the geometric and the thermal parameters into Equation (10.4).

When the whole constantan wire segment buckles, the half crack length is $a=l_c/2=1550$ μm. The critical buckling stress and the critical buckling temperature difference are respectively calculated to be $\sigma_{cr}=1.97$ MPa and $\Delta T_{cr}=0.52$ °C from Equations (10.3) and (10.4). In our experiments, all the half crack lengths are less than 500 μm. If we suppose $a=500$ μm, the corresponding critical buckling stress and the critical buckling temperature difference are found to be σ_{cr} = 18.95 MPa, ΔT_{cr} = 5.03 °C, respectively. We can see that when the compressive force of the constantan wire reaches the bonding force between the constantan wire and the polymer substrate, a small stress or temperature increment will result in the instability of the constantan wire.

10.2.5 Post-Buckling Analysis of Constantan Wire

The critical buckling stress is the minimum stress which can incur the buckling of the constantan wire; however, it cannot provide the quantitative relation between the residual stress in the constantan wire and the buckling waveform. To obtain the residual stress in the constantan wire from the buckling morphology, we will conduct the post-buckling analysis.

10.2.5.1 Derivation of Residual Stress Calculation Formula

Figure 10.14 illustrates the post buckling of the constantan wire [65]. The relevant symbols are defined as follows: the axial direction is x, the deflection direction is z, the displacement in direction x is u, the displacement in direction z (deflection) is w, the distance from the wire center line in direction z is z', and the half crack length is still a (the crack length $\lambda=2a$). The thickness and Young's modulus of the constantan wire are still h_c and E_c, respectively.

The first step is to get the expression of the displacement u in accordance with the equilibrium equation and the deformation compatibility equation.

The deflection of the constantan wire is defined as a cosine function:

$$w=\frac{1}{2}w_0\left[1+\cos\left(\frac{\pi x}{a}\right)\right] \tag{10.5}$$

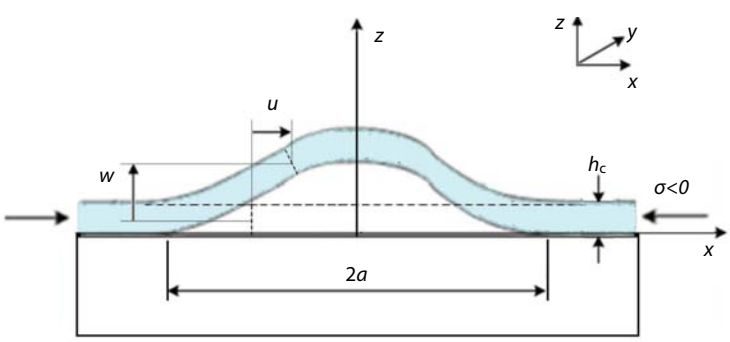

Figure 10.14 Schematic plot of the post-buckling analysis of the buckled constantan wire.

According to the deformation compatibility equation, the axial strain of the constantan wire is

$$\varepsilon_{\text{axial}} = \frac{\partial u}{\partial x} + \frac{1}{2}(w')^2 \tag{10.6}$$

Based on the constitutive relation of materials,

$$\sigma = E_c \varepsilon \tag{10.7}$$

The axial force of the unit width can be obtained.

The equilibrium equation and the uniform nature of the axial force can be displayed in the following equations:

$$E_c I w''' + N w'' = 0 \tag{10.8}$$

$$\frac{dN}{dx} = E_c h_c \frac{d\varepsilon_{\text{axial}}}{dx} = 0 \tag{10.9}$$

The expression of the displacement u in direction x can be elicited by substituting Equations (10.5) and (10.6) into Equations (10.8) and (10.9):

$$u = \frac{\pi w_0^2}{32a} \sin\left(\frac{2\pi x}{a}\right) + \varepsilon_m \cdot x \tag{10.10}$$

where ε_m is the axial mismatch strain of the constantan wire.

The axial strain of the constantan wire can be expressed by substituting Equation (10.10) into Equation (10.6):

$$\varepsilon_{\text{axial}} = \varepsilon_m + \frac{\pi^2 w_0^2}{16a^2} \tag{10.11}$$

The second step is to get the formulas of the residual strain and the residual stress on the basis of the energy minimization principle [64].

The elastic strain energy of the compressed constantan wire in the axial direction is

$$E_{\text{comp}} = h_c \int_{-a}^{a} \frac{1}{2} E_c \, \varepsilon_{\text{axial}}^2 \, dx = h_c E_c a \left(\varepsilon_m + \frac{\pi^2 w_0^2}{16a^2} \right)^2 \tag{10.12}$$

The bending strain energy is

$$E_{\text{bend}} = \int_{-a}^{a} \frac{1}{2} E_c \, I (w'')^2 \, dx = \frac{\pi^4 E_c w_0^2 h_c^3}{96a^3} \tag{10.13}$$

So, the total strain energy is $U_{\text{tot}} = E_{\text{comp}} + E_{\text{bend}}$. The total energy minimization can be realized from the following formula:

$$\frac{\partial U_{\text{tot}}}{\partial w_0}=0 \tag{10.14}$$

The maximum deflection can be acquired by solving the simultaneous equations (10.12–10.14).

$$w_0=4\sqrt{\frac{a^2\,|\,\varepsilon_m\,|}{\pi^2}-\frac{h_c^2}{12}} \tag{10.15}$$

The axial strain and the bending moment can be gained by simultaneously solving Equations (10.5), (10.6), (10.11), and (10.15):

$$\varepsilon_{\text{axial}}=-\frac{\pi^2}{a^2}\frac{h_c^2}{12} \tag{10.16}$$

$$M(x)=E_c I w''=-\frac{\pi^2}{a^2}\frac{E_c h_c^3 w_0}{24}\cos\left(\frac{\pi x}{a}\right) \tag{10.17}$$

As a consequence, the total residual strain becomes

$$\varepsilon=\varepsilon_{\text{axial}}+\varepsilon_{\text{bend}}=-\frac{\pi^2 h_c^2}{12a^2}+\frac{\pi^2 w_0}{2a^2}\cos\left(\frac{\pi x}{a}\right)z' \tag{10.18}$$

Furthermore, the residual stress will be

$$\sigma=-\frac{\pi^2 E_c h_c^2}{12a^2}+\frac{\pi^2 E_c w_0}{2a^2}\cos\left(\frac{\pi x}{a}\right)z' \tag{10.19}$$

10.2.5.2 Calculation of Residual Stress in Constantan Wire

Taking the buckling under AC (Figure 10.15) as an example, the residual strain and the residual stress will be analyzed.

There are 19 buckled constantan wire segments in Figure 10.15(a) and the serial numbers are labeled. The half crack lengths and the maximum buckling deflections are drawn in Figure 10.15(b), declaring the differences in the buckling mode amplitudes of the 19 buckled segments. The axial residual strain, the maximum strain (the upper surface), and the minimum strain (the lower surface) calculated from Equation (10.18) are listed in Figure 10.15(c). The positive sign stands for the tensile strain and the negative sign represents the compressive strain in Figure 10.15(c). It can be seen that the maximum strain and the minimum strain are much greater than the axial strain, demonstrating that the residual strain mainly depends on the bending moment of the constantan wire.

The axial residual stress always attracts extensive attention and is worth to analyze. The axial residual stress of the constantan wire calculated from the first half of Equation (10.19) is displayed in Figure 10.16. Both the axial residual strain and the axial

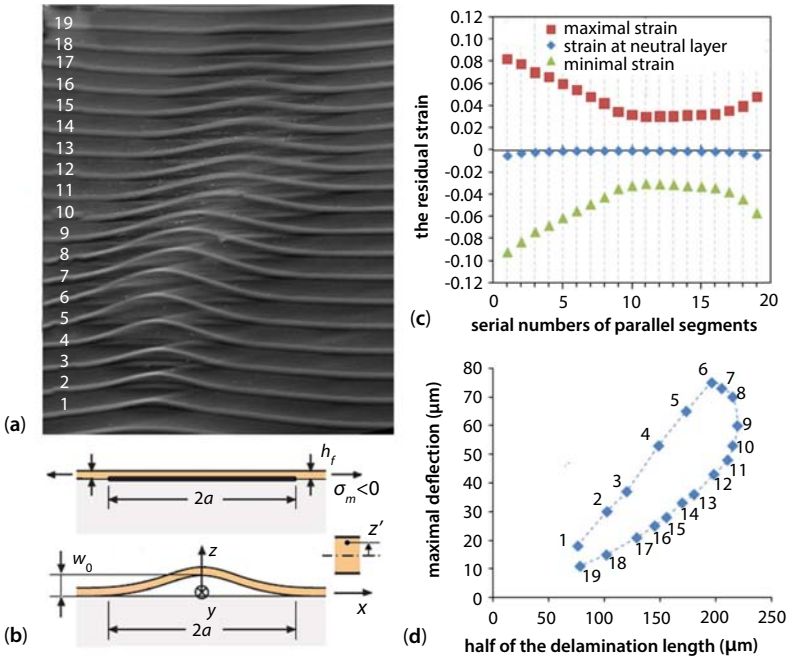

Figure 10.15 Buckling morphology and residual strain of the constantan wire after 3.13×10^8 A/m^{2}AC for 25h. (a) SEM image of the buckling morphology (tilted 45 degrees), (b) sketch maps of a bending beam on an infinitely thick substrate for buckling analysis, (c) the residual strain distribution of the buckled wire segments at positions with maximal deflections, and (d) relation between the maximal deflection and the half crack length of each buckled segment. Copyright (2009) IEEE. Reprinted, with permission, from Q.H. Wang, H.M. Xie, *et al.*, *Electron Device Letters*, IEEE, Vol. 30, 11–13, 2009 [57].

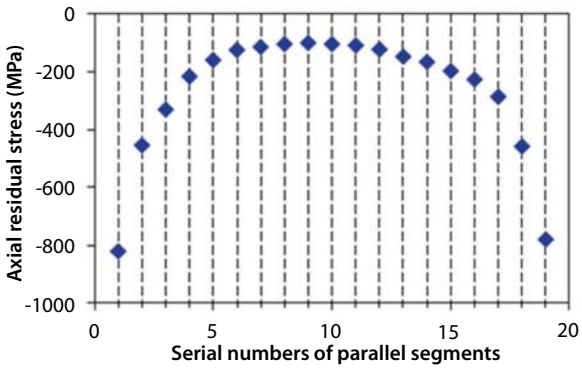

Figure 10.16 The residual stress in the constantan wire after J=3.13 × 10^8 A/m^2 AC.

residual stress are compressive from Figures 10.15(c) and 10.16. The maximum value and the minimum value of the axial residual strain are –0.51% and –0.06%, respectively. The corresponding maximum and minimum values of the axial residual stress are –810 and –96 MPa. The axial residual stress significantly varies when the crack length (known as the buckling wavelength) is small at the ends of the buckling area,

such as segments Nos. 1 and 19, whereas the axial residual stress slightly changes when the crack length is large in the central region of the buckling area, such as segments Nos. 4–16. From Figure 10.15(d), all the half crack lengths of segments Nos. 4–16 are greater than 140 μm, i.e., 5 times the width of the constantan wire (28 μm). Hence, we can see that the derived calculation formulas of the residual strain and the residual stress are more suitable for the case that the half crack length is equal to or greater than 5 times the wire width. In other words, the calculation formulas of the residual strain and stress works better when the buckling wavelength is equal to or greater than 10 times the wire width.

10.3 Interfacial Toughness between Constantan Wire and Polymer Substrate

Based on the buckling theory between the rigid film and the flexible substrate developed by Vella *et al.* [9], we presented the electricity induced buckling method to measure the interfacial toughness between the constantan wire and the polymer substrate.

10.3.1 Interfacial Toughness Formula for Rigid Film and Flexible Substrate

Based on the buckling deflection function in Equation (10.5) and the geometrical relationship for a single buckled film strip, we can obtain the variation of the distance ΔL between the two ends of the film in direction x caused by the buckling

$$\Delta L = \frac{\pi^2}{4}\frac{w_0^2}{\lambda}, \tag{10.20}$$

where w_0 is still the maximum deflection of the film strip. To accommodate the deformation of the buckled film, the deformation of the flexible substrate will be $\varepsilon = \Delta L / \lambda$. For a single buckling film strip, the elastic energy of the film/substrate system can be denoted by

$$U = \pi^4 B \frac{w_0^2}{\lambda^3} b_{\mathrm{f}} + \alpha E_s \varepsilon^2 \lambda^2, \tag{10.21}$$

where $B = E_{\mathrm{f}} h_{\mathrm{f}}^3 / 12$ signifies the bending stiffness of the film; the symbols b, E, and h are the width, Young's modulus, and the thickness, respectively; the subscripts f and s mean the film strip and the substrate, respectively; and α is a function of the substrate thickness [9].

The interfacial toughness $\Delta\gamma$ between the film strip and the flexible substrate can be determined from the energy release rate $-\partial U / \partial \lambda = b_{\mathrm{f}} \Delta\gamma$ [66,67]. Consequently, the buckling wavelength also known as the crack length can be expressed by a function of the interfacial toughness using Equation (10.21):

$$\lambda = 2\pi^{2/3} (B\Delta\lambda / \Delta\gamma)^{1/3}. \tag{10.22}$$

The relationship between the maximum deflection, the interfacial toughness and the buckling wavelength variation can then be expressed by substituting Equation (10.22) into Equation (10.20):

$$w_0 = \frac{2^{3/2}}{\pi^{2/3}} \left(\frac{B}{\Delta\gamma} \right)^{1/6} (\Delta\lambda)^{2/3}. \tag{10.23}$$

Finally, the expression of the interfacial toughness will be simply acquired by solving the simultaneous equations (10.22) and (10.23) and eliminating $\Delta\lambda$

$$\Delta\gamma = 2\pi^4 \frac{Bw_0^2}{\lambda^4}. \tag{10.24}$$

For the given film, if the maximum buckling deflection and the buckling wavelength are known, the interfacial toughness can be easily determined according to this formula.

It is worth noting that the Equation (10.24) can be applied only when the rigid film strip is incompressible compared with the flexible substrate. Whether the requirement is met or not can be judged from the comparison of the product of Young's modulus and the thickness. $E_f h_f >> E_s h_s$ is required when the buckling wavelength is much greater than the thickness as well as the width of the film strip ($\lambda >> h_f$, $\lambda >> b_f$), where f and s, respectively, stand for the rigid film and the flexible substrate.

10.3.2 Interfacial Toughness Measurement and Discussions

In our experiments, the film strip is the constantan wire with $E_c h_c = 160 \times 6 = 960$ Gpa·μm and the flexible substrate is the polymer with $E_p h_p = 3.08 \times 60 = 184.8$ Gpa·μm, respectively. The former is 5.3 times of the latter, and thus $E_c h_c >> E_p h_p$ is basically met. Therefore, the interfacial toughness of the constantan/polymer structure can be analyzed using Equation (10.24) when the buckling wavelength is much greater than the thickness and the width of the constantan wire ($\lambda >> h_c$, $\lambda >> b_c$).

10.3.2.1 Measurement of the Interfacial Toughness

First, the buckling under $J = 2.89 \times 10^8$ A/m^2 DC (Figure 10.17) will be taken as an example to calculate the interfacial toughness between the constantan wire and the polymer substrate.

The serial numbers of the buckled constantan wire segments are labeled in Figure 10.17(a). The buckling wavelength and the maximum deflection are plotted in Figure 10.17(b). The maximum buckling deflection increases with the growth of the buckling wavelength for this kind of buckling morphology. All the buckling wavelength of these 12 segments are greater than 298 μm, 10.6 times greater than the width (28 μm) and 49.7 times greater than the thickness (6 μm) of the constantan wire. Consequently, the interfacial toughness of this structure can be calculated using Equation (10.24) because the conditions $\lambda >> h_c$, $\lambda >> b_c$ and $E_c h_c >> E_p h_p$ are met.

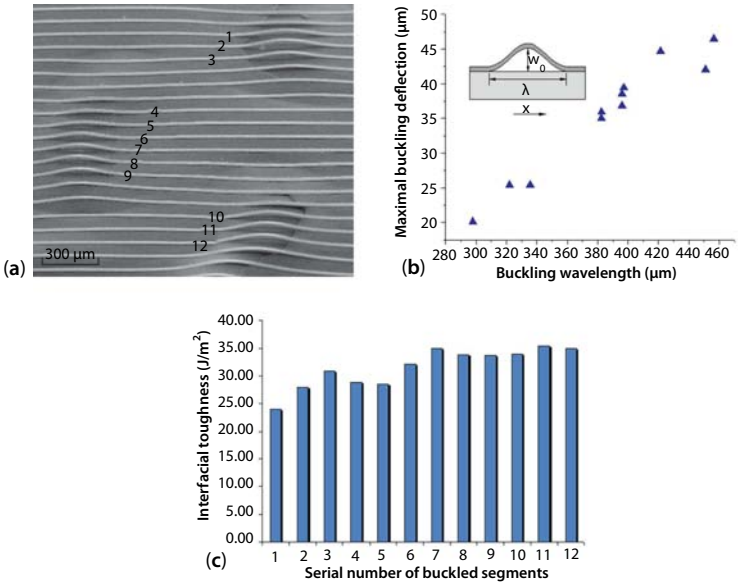

Figure 10.17 Buckling morphology and interfacial toughness of a sample after 2.89×10^8 A/m^2 DC. (a) Buckling morphology of the 12 buckled wire segments, (b) relationship between the buckling wavelengths and the maximal buckling deflections of the buckled wire segments, and (c) distribution of the interfacial toughness between the constantan wire segments and the polymer substrate. Reprinted from *Journal of Colloid and Interface Science*, Q.H. Wang, H.M. Xie, *et al.*, Measurement of interfacial toughness of metal film wire and polymer membrane through electricity induced buckling method, Vol. 358, 491–496 [58], Copyright (2011), with permission from Elsevier.

The measured interfacial toughness between the constantan wire and the polymer substrate in Figure 10.17(a) is shown in Figure 10.17(c). The variation of the interfacial toughness is not regular, and the average interfacial toughness is $\Delta\gamma = 31.6$ J/m^2.

Using the same calculation procedure as the above example, the interfacial toughness of multitudinous samples in our repeated experiments with buckled constantan wires can be measured. As regards the buckling morphologies with buckling wavelength greater than 200 μm listed in Figure 10.10, the relationship between the maximum deflection and the buckling wavelength is revealed in Figure 10.18. The maximum buckling deflection goes up with the increase of the buckling wavelength in overall tendency. The distribution of the interfacial toughness calculated from numerous buckled morphologies using Equation (10.24) is illustrated in Figure 10.19.

The interfacial toughness fluctuates from 10 to 60 J/m^2 in Figure 10.19, and the average value of the whole interfacial toughness under different buckling wavelengths is 27.6 J/m^2. The general trend is that the interfacial toughness decreases slightly with the growth of the buckling wavelength. Since the buckling wavelength does not present any explicit regular rule with electric current density from Figure 10.10, it can be concluded that the interfacial toughness will not have evident varying pattern under different electric current densities.

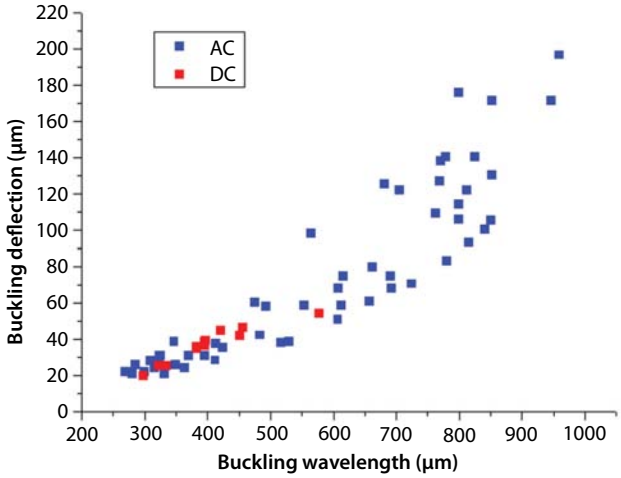

Figure 10.18 Relationship between the maximal buckling deflection and the buckling wavelength. Reprinted from *Journal of Colloid and Interface Science*, Q.H. Wang, H.M. Xie, *et al.*, Measurement of interfacial toughness of metal film wire and polymer membrane through electricity induced buckling method, Vol. 358, 491–496 [58], Copyright (2011), with permission from Elsevier.

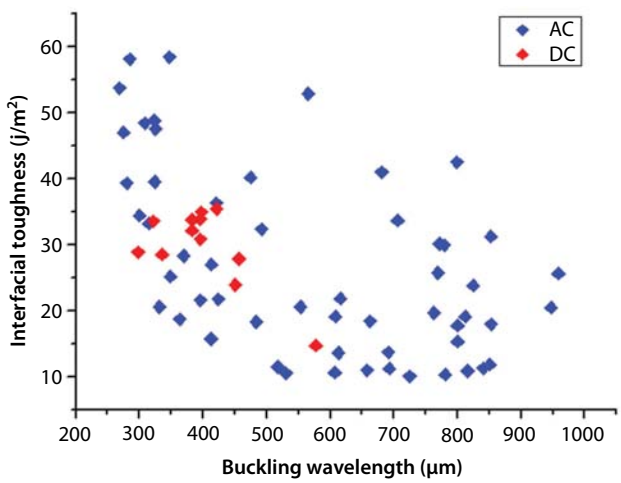

Figure 10.19 Variation of the interfacial toughness between the constantan wire and the polymer substrate along with the buckling wavelength. Reprinted from *Journal of Colloid and Interface Science*, Q.H. Wang, H.M. Xie, *et al.*, Measurement of interfacial toughness of metal film wire and polymer membrane through electricity induced buckling method, Vol. 358, 491–496 [58], Copyright (2011), with permission from Elsevier.

10.3.2.2 Discussions

To the authors' knowledge, the interfacial toughness between the micron-scale constantan wire and the polymer substrate containing polyvinyl formal-acetal and epoxy novolac has not been reported except the authors' work [58]. However, the measurement validity can be verified by comparing with other reported interfacial

toughness values about polymers. The interfacial toughness between a nickel film and a makrolon substrate was reported to be 0.2–3.7 J/m^2 [9]. When it came to the structure made up of a silicon nitride film and a polyimide substrate, the interfacial toughness became 30 J/m^2 [68]. Several interfacial toughness distributions between polymers and glass were also reported as follows [69]: the interfacial toughness value between epoxide resin and glass with surface treatment was within 40–90 J/m^2, the value between polymethylmethacrylate and untreated glass ranged from 1 to 5 J/m^2, and the value between polymethylmethacrylate and glass with surface treatment was in the range of 60–200 J/m^2. The interfacial toughness of the constantan wire and the polymer substrate in our experiments varies from 10 to 60 J/m^2. We can conclude that the measured interfacial toughness in this section is accurate on the order of magnitude.

10.3.3 Applicable Condition of the Electricity-Induced Buckling Method

The electricity induced buckling method for measuring interfacial toughness is not only suitable for the constantan wire and the polymer substrate, but also fit for other rigid films and flexible substrates. In this section, the applicable condition of the electricity induced buckling method will be discussed.

Firstly, the buckling should be able to be induced by electrical loading. For the constantan wire and the polymer substrate, the applied current density should be higher than the critical current density, i.e., 2.38×10^8 A/m^2 under AC and 2.88×10^8 A/m^2 in the case of DC. For other rigid films and flexible substrates, the critical current density can be determined from a large number of experiments. Alternatively, buckling can also occur when the stress is greater than the critical buckling stress expressed in Equation (10.3) or the temperature increment is higher than the critical buckling temperature difference represented in Equation (10.4).

Secondly, the glass transition of the flexible substrate should be avoided when the buckling emerges. The critical condition of sample temperature is that $T_{\text{room}} + \Delta T_{\text{cr}} < T_{\text{gt}}$, where T_{room} is the room temperature, ΔT_{cr} also denotes the critical buckling temperature difference in Equation (10.4), and T_{gt} means the glass transition temperature of the flexible substrate. In line with the expressions of the critical buckling temperature difference in Equation (10.4) and the critical buckling force in Equation (10.1), the critical condition of the sample temperature can be expressed in the following form:

$$\frac{\pi^2 h_f^2}{3l^2}\left(1+\frac{E_{\text{f}} b_{\text{f}} h_{\text{f}}}{E_{\text{s}} b_{\text{s}} h_{\text{s}}}\right)/(a_{\text{s}} - a_{\text{f}}) < T_{\text{gt}} - T_{\text{room}}. \tag{10.25}$$

where l, b, h, E, and a also stand for the length of the common part, the width, the thickness, Young's modulus, and the CTE, respectively. The subscripts f and s, respectively, represent the film and the substrate.

Equation (10.25) is the quantitative expression of the applicable condition of the electricity induced buckling method to measure the interfacial toughness between metal film wires and flexible substrates.

Thirdly, the applying condition of Equation (10.24) should be satisfied. That is to say, the rigid film fire should be incompressible compared with the flexible substrate, i.e., $E_f h_f >> E_s h_s$ when $\lambda >> h_f$, $\lambda >> b_f$.

10.4 Buckling Behaviors of Polymer Substrate Restricted by Constantan Wire

Besides the buckling of constantan wire, the buckling of the polymer substrate was also observed in our experiments. During the usage of the constantan-wire/polymer-substrate structure under electric loading, the buckling of the polymer substrate would also influence the stability of the structure, the operation performance of the metal wire and the reliability of the whole micro device. In this section, we investigated the buckling modes of the polymer substrate restricted by the electrified metal wire, and analyzed the occurrence conditions and the formation mechanisms of various buckling modes.

10.4.1 Sample and Experiments

10.4.1.1 Sample Preparation and Characterization

The sample was prepared by photolithography and the preparation process was the same as in Section 10.2.1. The constantan wire was also distributed in the shape of a narrow "S". But the ingredient of the polymer substrate was changed to 100% polyvinyl formal-acetal. The physical dimensions were also altered. The thickness of the polymer substrate is h_p = 32 μm and the width of the polymer strip ($2b_{ps}$) between two adjacent parallel constantan wire segments is 40 μm. The length a_p and width b_p of the whole polymer substrate are 7 and 5 mm, respectively. For the constantan wire, the width and the thickness are b_c = 20 μm and h_c = 6 μm, respectively. The length of the parallel segments is l_c = 3100 μm.

The elastic constant of the polymer substrate was measured during tensile tests by the digital image correlation method [56]. The elastic (Young's) modulus and Poisson's ratio of the polymer substrate were determined to be E_p=3.08 GPa and ν_p=0.31, respectively.

The glass-transition temperature of this polymer was measured to be 119.72 °C using the DSC-60 differential scanning calorimeter (Figure 10.20). The sample temperature during electrical loading was used to be compared with the glass-transition temperature to determine whether the glass transition of the polymer substrate happens or not.

10.4.1.2 Experiments

The experimental setup was the same as in Figure 10.5(a) in Section 10.2.1. As the polymer substrate was thin, like a membrane, it was easy to curl when it was heated by the electrified constantan wire. To prevent the thermal induced curling of the polymer substrate, the sample was stuck on organic glass by liquid adhesive before electrical loading experiments. At the room temperature, the constantan wire was loaded by 50 Hz AC,

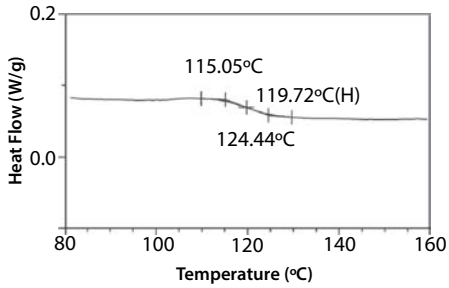

Figure 10.20 The differential scanning calorimetry curve of a polymer substrate (polyvinyl formal-acetal). Reproduced by permission of The Royal Society of Chemistry, Copyright (2011), from Q.H. Wang, Y.J. Yin, H.M. Xie, *et al. Soft Matter*, Vol. 7, 2888–2894, 2011 [56].

and the surface morphology of the sample was under observation at the same time. The phenomena were different from that illustrated in Section 10.2. Due to the decrease in the thickness of the polymer substrate, it was found from experiments that the constantan wire was not easy to buckle. On the contrary, the polymer substrate was not stable and various interesting buckling modes were observed to appear on the polymer substrate. The buckling of the polymer substrate emerged under electrical loading and persisted after cooling to the room temperature.

The geometric dimension of the sample and the buckling morphologies of the polymer substrate were measured using a laser scanning microscope (KEYENCE VK-9700), the aforementioned KEYENCEVHX -500FE 3D super-depth digital microscope and the QUANTA 200 FEG field emission SEM. Since the polymer substrate was non-conductive, the field emission SEM available under a low vacuum environment was used to eliminate the cumbersome gold-spraying process. The height fluctuation of the buckling surface reached up to several microns so that it was very easy to destroy the probe if observed by atomic force microscope (AFM). Therefore, a laser scanning confocal microscope (LSCM, KEYENCE VK-9700) with distinguishability up to hundreds of nanometers in depth was utilized to provide quantitative measurements in three dimensions.

10.4.1.3 Sample Temperature Variations during Experiments

The sample surface temperature during experiments was also determined by the FLUKE Ti55FT thermal infrared imager. This thermal infrared imager with high resolution served to distinguish the temperature of the central area from that of the peripheral one. Our experiments show that the sample temperature in the central area is a little higher than that in the edge area because the heat dissipation rate is lower in the center. The higher temperature in the central region is easier to trigger instability behaviors of the sample. Targeting this point, we set the thermal imager to aim at the central region of the sample to capture the steady-state temperature during experiments. Figure 10.21 gives the steady surface temperature of the sample measured by the thermal imager under AC with the current density of $J = 2.36 \times 10^8$ A/m^2. The steady-state temperature of the central area is determined to be 80.9 °C. The curve of the temperature in the central area changing with the current density is drawn in Figure 10.22.

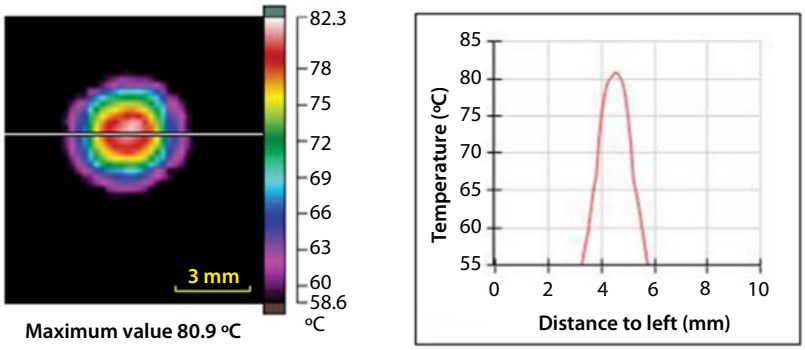

Figure 10.21 Steady-stage temperature on sample surface under J=2.36 × 10^8 A/m^2 AC.

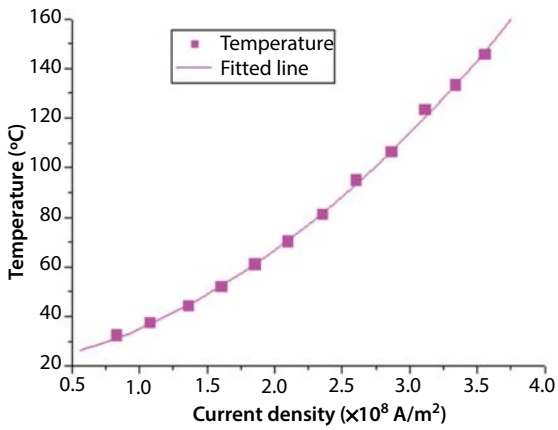

Figure 10.22 The variation of the sample temperature in central region which becomes greater with increase of the current density. Reproduced by permission of The Royal Society of Chemistry, Copyright (2011), from Q.H. Wang, Y.J. Yin, H.M. Xie, *et al. Soft Matter*, Vol. 7, 2888–2894, 2011 [56].

10.4.2 Micron-Scale Buckling Mode of the Polymer Substrate

It is observed from the experiments that three kinds of micron-scale buckling modes appear on the surface of the polymer substrate under electric loading. The buckling wavelength is dozens of micrometers. All the micron-scale buckling modes appear along the axis of the constantan wire (longitudinal). These are the particular instability forms induced by the thermal mismatch of the wire/polymer structure under electrical loading.

10.4.2.1 Orthogonal Wave Buckling

Taking a typical orthogonal wave buckling mode as an example, we will describe the buckling formation process and the morphology features. Before experiments, the polymer substrate is flat (Figure 10.23a). After the constantan wire is loaded by AC the current density was kept stable at J = 2.49 × 10^8 A/m^2 for a while. Meanwhile, the 3D super-depth digital microscope is put to focus on the central area of the sample

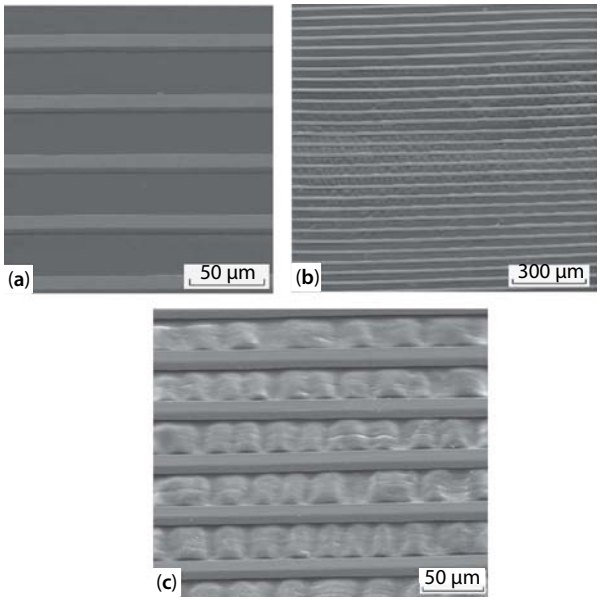

Figure 10.23 SEM images of the orthogonal wave buckling morphology. (a) Before electrical loading and (b) buckling morphologies generated on the central polymer substrate after the constantan wire is loaded by 2.49×10^8 A/m^2 AC. (c) Enlarged image of the buckling in (b). Reproduced by permission of The Royal Society of Chemistry, Copyright (2011), from Q.H. Wang, Y.J. Yin, H.M. Xie, *et al. Soft Matter*, Vol. 7, 2888–2894, 2011 [56].

to observe the deformation of the constantan-wire/polymer-substrate/organic-glass structure. At the primary stage of electrification, there is no significant change observed on the substrate. The constantan wire is kept to be a straight configuration and the polymer substrate remains flat. However, when the electrifying time is up to $t = 30$ min, the periodical buckling suddenly occurs on the polymer substrate along the direction parallel to the constantan wire (Figure 10.23b). As the connection line of the highest point on buckling bump is perpendicular to the axis of the constantan wire, this kind of buckling is named to be orthogonal wave buckling mode. The enlarged SEM image of this type of buckling is shown in Figure 10.23(c).

The morphology of the orthogonal wave buckling is qualitatively revealed through LSCM (Figure 10.24a). Figure 10.24(b) illustrates the measurement process of buckling morphology by the LSCM, displaying the side profile and the metrical data of a buckled polymer strip. The average value of the maximum buckling deflection is w_0=4.7 μm. From the measured data of all the buckling bumps in Figure 10.23(b), it was observed that the buckling wavelength varies from 20 to 54 μm and the average wavelength is $l = 33.1$ μm with mean square error of 7.2 μm (Figure 10.25). The large fluctuation of buckling wavelength in the experiment is induced by the multi-instability of the system, which is an actual feature of the constantan-wire/polymer-substrate/organic-glass structure. After buckling, the width of the polymer strip between two adjacent constantan wires becomes 35 μm with the relative variation of 12.5% compared to the original width of 40 μm. This value is closer to that of the standard confined wrinkles.

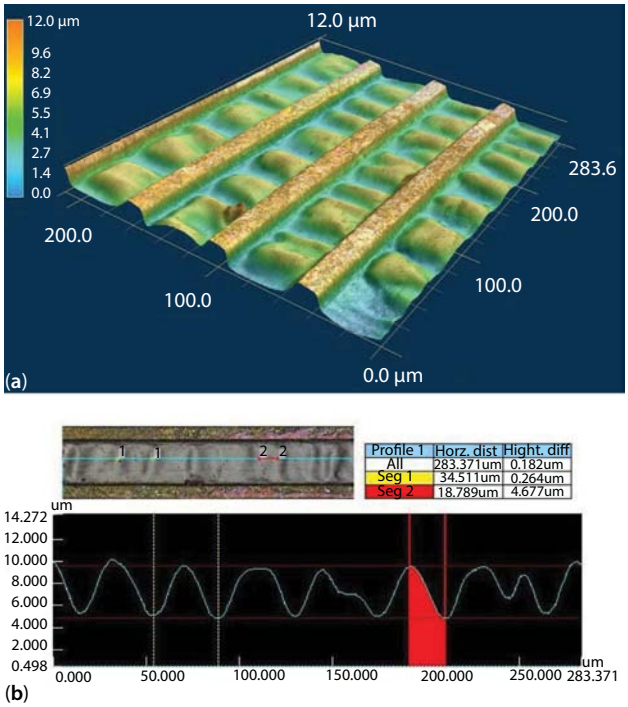

Figure 10.24 Determination of the orthogonal wave buckling wavelength and the buckling deflection. (a) LSCM image of the buckling morphology. (b) An example of the buckling profile. Reproduced by permission of The Royal Society of Chemistry, Copyright (2011), from Q.H. Wang, Y.J. Yin, H.M. Xie, *et al*. *Soft Matter*, Vol. 7, 2888–2894, 2011 [56].

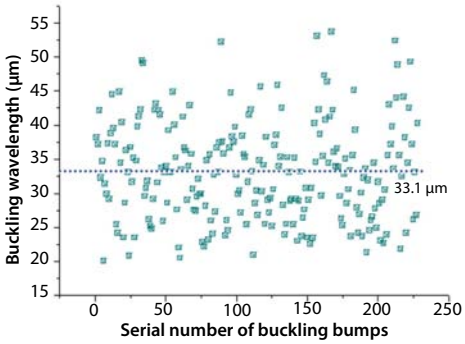

Figure 10.25 Distribution of buckling wavelengths of the orthogonal wave buckling bumps in Figure 10.23(b). Reproduced by permission of The Royal Society of Chemistry, Copyright (2011), from Q.H. Wang, Y.J. Yin, H.M. Xie, *et al*. Soft Matter, Vol. 7, 2888–2894, 2011 [56].

The sample temperature under this electric current density is found to become stable after electrical loading for 2 min. The steady-state sample temperature in the central region is 87 °C, lower than the glass-transition temperature of the polymer substrate. It demonstrates that the glass transition does not occur in the polymer substrate under this current density.

10.4.2.2 Oblique Wave Buckling and Crumpled Wave Buckling

For the constantan-wire/polymer-substrate structure, other two interesting buckling modes of the polymer substrate are observed in our experiments. In one buckling mode, there is an angle between the line connecting the peaks of the buckling bumps and the perpendicular line of the constantan wire. And thus, it is named as the oblique wave buckling (Figure 10.26a and b). As the other buckling shape is similar to a telephone line or a spiral, we call it as the crumpled wave buckling (Figure 10.26c).

The oblique wave buckling has a series of buckling morphologies with different buckling oblique angles. Here the buckling oblique angle means the included angle between

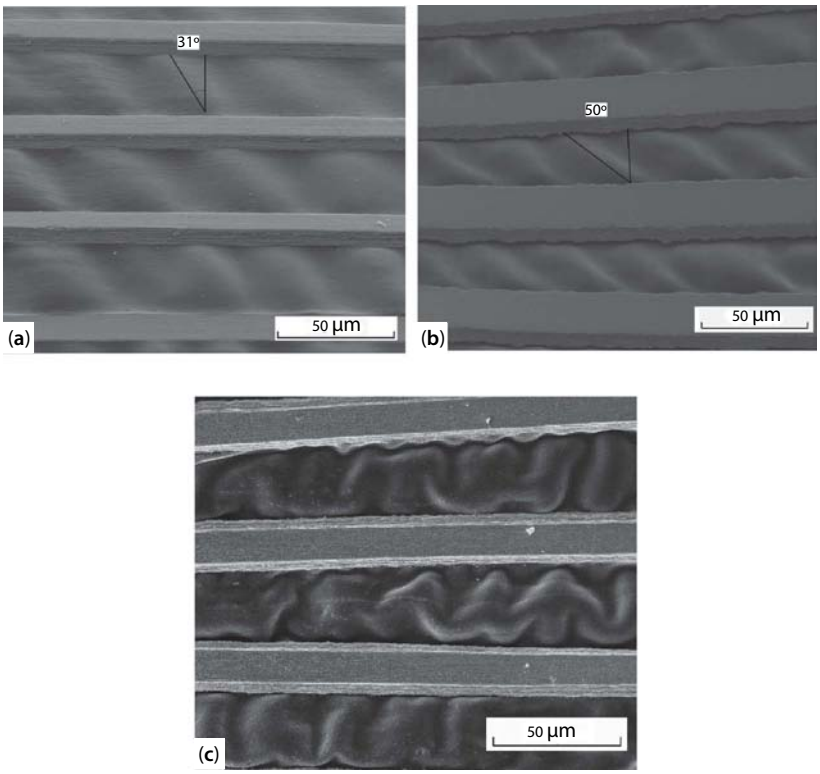

Figure 10.26 Oblique wave buckling and crumpled wave buckling morphologies on the polymer substrate. (a) Oval oblique wave buckling with a smaller oblique angle under 2.57×10^8 A/m^2 AC, (b) slender oblique wave buckling with a greater oblique angle under 3.45×10^8 A/m^2 AC, and (c) the crumpled wave buckling under 2.50×10^8 A/m^2 AC. Reproduced by permission of The Royal Society of Chemistry, Copyright (2011), from Q.H. Wang, Y.J. Yin, H.M. Xie, *et al. Soft Matter*, Vol. 7, 2888–2894, 2011 [56].

the line connecting the buckling bump peaks and the perpendicular line of the constantan wire. Two representative oblique wave buckling morphologies are illustrated in Figure 10.26(a) and (b). The buckling oblique angle of the former is smaller with average value of 30.2° and the buckling bumps are oval. While the buckling oblique angle of the later is greater with average value of 43.1° and the buckling bumps are slender.

The crumpled wave buckling is similar to but different from the telephone line buckling. In the telephone line buckling, the spiral or the helical buckling bumps are mixed with some orthogonal buckling waves. In our experiments, the crumpled wave buckling mode only includes the crumpled or the squirmy buckling bumps. The crumpled wave buckling mode is infrequent, and always accompanied by the orthogonal wave buckling and the oblique wave buckling with a small buckling oblique angle.

10.4.2.3 Occurrence Conditions of Micron-Scale Buckling Modes

The occurrence conditions of the three kinds of micron-scale buckling modes are summarized in Figure 10.27. A large number of repeated experiments demonstrate that, the orthogonal wave buckling mode and the crumpled wave buckling mode will appear when the 50 Hz AC current density is in the range of 2.29×10^8–2.57×10^8 A/m$^{2.}$ The corresponding sample temperature in the central region is within 77.2–93.8 °C from Figure 10.22. All the sample temperatures in this range are lower than the glass transition temperature of the polymer substrate (119.72 °C). The oblique wave buckling mode can appear in a greater range with current density of 2.29×10^8–3.56×10^8 A/m^2. The buckling angle will be different at different current density. The sample temperature scope corresponding to the oblique wave buckling mode is 77.2–145.4 °C. Some sample temperature values are already higher than the polymer glass transition temperature.

The buckling oblique angles of the oblique wave buckling morphologies under different current densities are measured by a MB-ruler software. The average buckling oblique angle and the mean square deviation along with the current density is plotted in Figure 10.28. The overall trend is that the buckling oblique angle monotonously increases with the rise of the current density. The oval buckling bumps with smaller oblique angles are inclined to arise under lower current densities, whereas the slender buckling bumps with greater oblique angles are prone to grow under higher current densities.

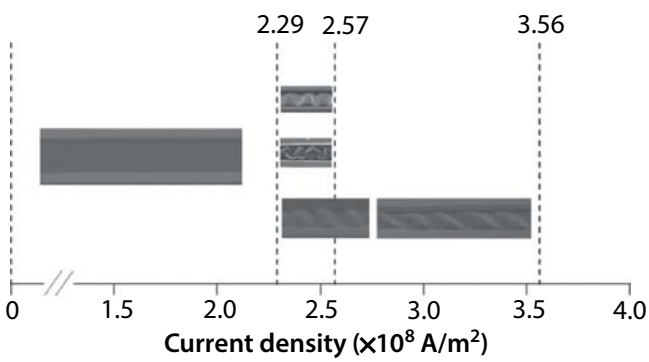

Figure 10.27 The occurrence conditions of the orthogonal wave, the oblique wave and the crumpled wave buckling modes. Reproduced by permission of The Royal Society of Chemistry, Copyright (2011), from Q.H. Wang, Y.J. Yin, H.M. Xie, *et al. Soft Matter*, Vol. 7, 2888–2894, 2011 [56].

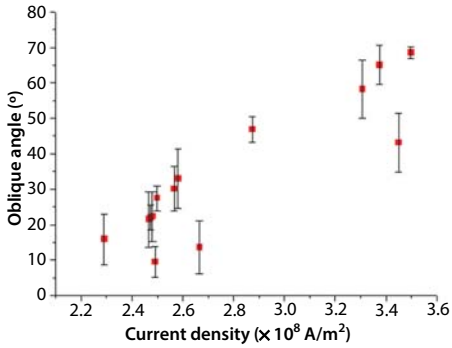

Figure 10.28 Variation of the oblique angle of the oblique wave buckling with the increase of the current density. Reproduced by permission of The Royal Society of Chemistry, Copyright (2011), from Q.H. Wang, Y.J. Yin, H.M. Xie, *et al*. Soft Matter, Vol. 7, 2888–2894, 2011 [56].

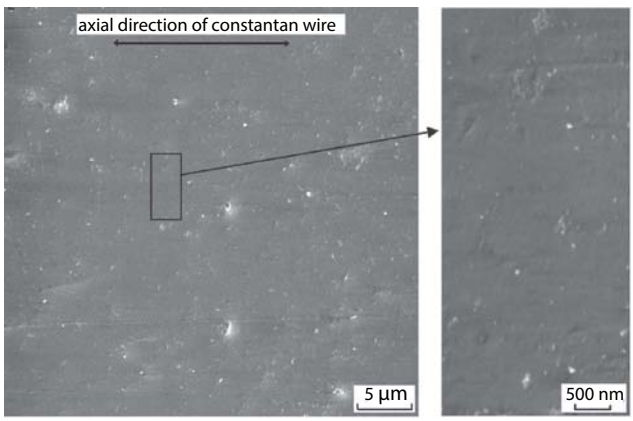

Figure 10.29 Surface morphology of the polymer strip before electrical loading. Reproduced by permission of The Royal Society of Chemistry, Copyright (2011), from Q.H. Wang, Y.J. Yin, H.M. Xie, *et al*. *Soft Matter*, Vol. 7, 2888–2894, 2011 [56].

When the AC current density exceeds 3.07×10^8 A/m^2, the sample temperature in the central region will overtop the glass transition temperature of the polymer substrate from Figure 10.22. Referring to Figure 10.28, we can find that the buckling oblique angle is greater than 40° under a higher current density over 3.07×10^8 A/m^2.

10.4.3 Micron and Submicron Cross-Scale Buckling Modes

Besides the micron-scale buckling modes along the constantan wire axis (longitudinal), our experiments also found submicron-scale buckling wrinkles in the direction perpendicular to the axis of the constantan wire (lateral). The submicron-scale wrinkles emerge on the micron-scale buckling bumps, forming a new cross-scale buckling mode.

Prior to electrical loading, the surface morphology of a polymer strip is shown in Figure 10.29, declaring that no periodical pattern originally exists on the polymer.

Figure 10.30 reveals one kind of cross-scale buckling mode, i.e., the micron-scale orthogonal buckling plus the submicron-scale wrinkles. The follow-up electrical loading after the orthogonal buckling mode turns up under J=2.49 × 10^8 A/m^2 AC, which will motivate a group of small-scale periodical ripples in the lateral direction of the polymer strip. The wavelength of the periodical buckling ripples ranges from 200 to 350 nm, and thus the periodical buckling ripples are called as the submicron-scale wrinkles.

The combination of the micron-scale oblique buckling and the submicron-scale wrinkles is also observed. Figure 10.31 exhibits this kind of cross-scale buckling mode

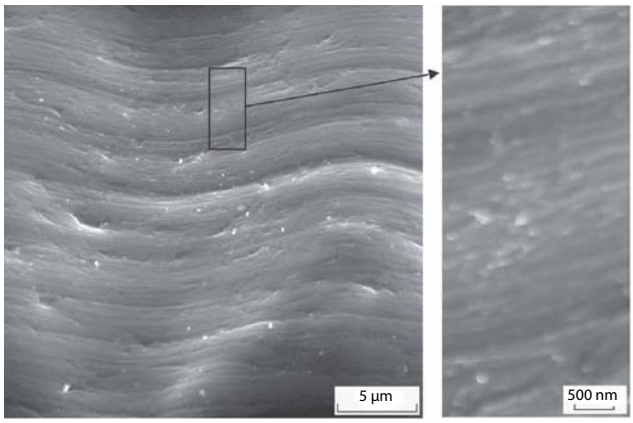

Figure 10.30 Submicron-scale wrinkle on the orthogonal wave buckling under 2.49 × 10^8 A/m^2 in Figure 10.23(c). Reproduced by permission of The Royal Society of Chemistry, Copyright (2011), from Q.H. Wang, Y.J. Yin, H.M. Xie, *et al. Soft Matter*, Vol. 7, 2888–2894, 2011 [56].

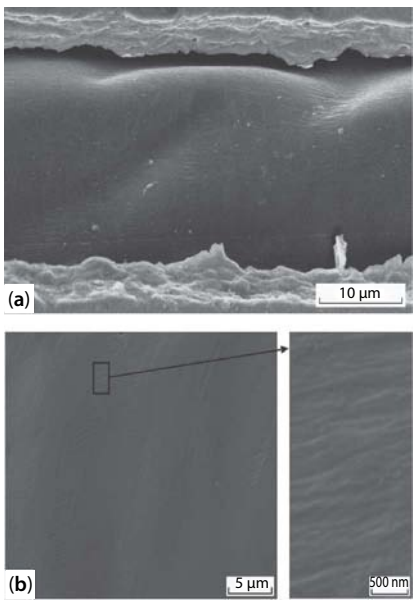

Figure 10.31 Submicron-scale wrinkle on the oblique wave buckling under 3.38 × 10^8 A/m^2, (a) submicron-scale wrinkle on the micron-scale buckling, (b) submicron-scale wrinkle on another site on the same sample. Reproduced by permission of The Royal Society of Chemistry, Copyright (2011), from Q.H. Wang, Y.J. Yin, H.M. Xie, *et al. Soft Matter*, Vol. 7, 2888–2894, 2011 [56].

under $J = 3.38 \times 10^8$ A/m^2 AC. The wavelength of the submicron-scale wrinkles on the oblique buckling bumps is 160–320 nm. Similar phenomena were also found on other samples. It suggests that the cross-scale buckling mode with submicron-scale wrinkles on micron-scale buckling bumps is a pervasive instability form of the polymer strips restricted by metal wires.

The submicron-scale wrinkles can be regarded as an instability mode with a higher order than the micron-scale buckling mode. The micron and submicron cross-scale buckling mode is a new type of instability mode of film/substrate structure, which is seldom reported.

10.4.4 The Buckling Mechanism Analysis of the Polymer Substrate

The micron-scale buckling modes and the submicron-scale winkles of the polymer substrate have different mechanisms. The former is resulted from the thermal mismatch between the polymer substrate and the constantan wire. The latter belongs to a kind of surface buckling wave, related to the uneven distribution of temperature along the thickness direction of the polymer substrate.

10.4.4.1 Formation Mechanisms of Micron-Scale Wave Buckling Modes

The micron-scale wave buckling modes are aroused by the thermal-induced compressive stress of the polymer substrate. Electrical loading to the constantan wire can produce Joule heat which will make the sample temperature rise. Compared to the edge are, it is more difficult for the central area to dissipate heat so that the temperature in the central area is higher than that in the peripheral area. Consequently, the buckling preferentially appears in the central area. The polymer substrate and the glass plate are stuck together through glue line. When the temperature increases, the expansion rate of the polymer substrate is higher than that of the glass plate due to the greater TEC of the polymer (α_p=70 × 10^{-6}/K) compared with the TEC of the glass (α_g=0.55 × 10^{-6}/K). Meanwhile, the deformation of the polymer substrate is restricted, which generates a compressive stress making the polymer substrate like a compressed board. Once partial debonding occurs between the polymer substrate and the glass plate, the interface crack is produced and driven to spread under the action of the compressive stress. Then the polymer substrate gradually separates itself from the glass plate and this is also named as the first buckling.

After the sample is peeled from the glass plate, the polymer substrate will further expand. Because the TEC of the polymer substrate is greater than that of the constantan wire (α_c=14.9 × 10^{-6}/K), the polymer substrate tries to expand faster than the constantan wire. However, the polymer is restricted by several parallel segments of the constantan wire and the deformation of each polymer strip is limited. As a consequence, there will be compressive stress in the polymer generated by the thermal mismatch. In the case that the compressive stress is greater than the critical buckling value, the polymer strips will buckles under the restriction of the constantan wire, which is called as the secondary buckling.

The first buckling between the polymer substrate and glass plate is similar to the common large-area film buckling [16,44,45]. However, the secondary buckling that is

wave buckling in the polymer substrate is different from all the buckling modes ever reported. In this study, since the polymer substrate is restrained by the parallel constantan wire, the buckling can only occur on the slender polymer strip with width of 40 μm between two adjacent metal film wires. In other words, the buckling wave form can only spread in a slender strip and thus the shape is unique.

The polymer strip between two adjacent constantan wire segments can be regarded as a rectangle plate. The orthogonal wave buckling observed in this study is similar to the symmetric secondary buckling reported by Audoly *et al.* but it is also a little different. The rectangle plate studied in Ref. [15] is a free impending film; however, the polymer strip in this study is restricted by the adjacent polymer strip and constantan wire. Moreover, the wave buckling occurs after the polymer substrate delaminated from the glass. Two long sides of the elastic plate in Ref. [15] is fixed while for the polymer strip in this study the two long sides can translate and rotate. The elastic plate in Ref. [15] is thin, but in this study the width of the polymer strip (40 μm) and the thickness (32 μm) are much of a size.

The differences between the orthogonal wave buckling of polymer substrate in this study and the symmetric secondary buckling in Ref. [15] are reflected in the following three aspects. (a) As reported in Ref. [15], when Poisson's ratio of the elastic plate is larger than 0.25, it is easier to generate anti-symmetric secondary buckling. However, in this study, Poisson's ratio of the polymer substrate is 0.31 but it is observed from experiments that the orthogonal wave buckling is easier to appear. (b) When Poisson's ratio is 0.31, in Ref. [15] the ratio of the mean wavelength in symmetric secondary buckling to the half width of the rectangle plate is $l/b = 1.55$ while in this study the ratio of the mean wavelength (33.1 μm) in orthogonal wave buckling and the half width (20 μm) of the polymer substrate is $l/b_{ps} = 1.66$. (c) The occurrence conditions of the symmetric secondary buckling and the anti-symmetric secondary buckling are non-adjacent in Ref. [15]. However, the occurrence conditions of the orthogonal wave buckling (corresponding to symmetric secondary buckling) and the crumpled wave buckling (corresponding to anti-symmetric secondary buckling) are close to each other. Both of the orthogonal and crumpled wave buckling modes come out when the AC current density is between 2.29×10^8 and 2.57×10^8 A/m^2.

Such differences reveal that in comparison to the compressive instability of the metal plate at the millimeter scale, the electro-thermal buckling of the polymer substrate at the micron scale has its own complexities. Therefore, the experimental results in this study can provide necessary parameters for guidance in more systematic theory and simulation study.

10.4.4.2 Formation Mechanisms of Submicron-Scale Wrinkles

The wavelength of the submicron-scale wrinkles (160–350 nm) is much less than the thickness of the polymer substrate (32 μm), indicating that the submicron-scale wrinkles belong to a kind of surface wave [54,70,71]. The submicron-scale wrinkles are caused by the surface compressive stress of the polymer substrate originating from two possible aspects.

On one hand, a temperature gradient exists in the thickness direction of the polymer substrate. The temperature on the surface is different from that at the bottom, creating

the nonuniform temperature field along the thickness. Since the constantan wire is arranged on the polymer surface, the heat flow diffuses from the surface to the bottom of the polymer substrate when the constantan wire bears electrical loading. Hence, the polymer surface temperature is higher than the bottom temperature, and the surface gets greater thermal expansion than the bottom. Restricted by the polymer bottom, the polymer surface is subjected to compressive stress responsible for the submicron-scale wrinkles.

On the other hand, the thermal mismatch between the polymer substrate and the constantan wire needs to be coordinated in a short distance in the lateral direction of the polymer strip. After the micron-scale wave buckling takes place, the polymer continues to expand not only in the longitudinal direction but also in the lateral direction. The lateral expansion of the polymer is restricted by the adjacent constantan wire segments owing to the greater CTE of the polymer substrate. Therefore, the compressive stress of the polymer in the lateral direction gradually accumulates. When the compressive stress reaches the critical buckling value, the lateral buckling mode will grow. As the lateral size of the polymer strip is only 40 μm, the lateral buckling mode is more inclined to spread at the submicron scale.

Furthermore, the submicron-scale wrinkles may come from the surface diffusion. When the local temperature of the sample exceeds the glass transition temperature of the polymer, the polymer begins to soften, and the diffusion of the long-chain organic molecules turns positive. The long-chain organic molecules on the polymer surface are apt to possess higher energy and are easier to break free and move attributed to the higher temperature on the surface. When a stable equilibrium state is reached in the nonlinear dynamic diffusion process on the surface, regular patterns happen frequently. The submicron-scale wrinkles are one possible regular pattern. With respect to the accurate formation mechanism of the submicron-scale wrinkles, more meticulous experimental verification and theoretical analysis has yet to be further conducted.

10.5 Conclusions

In this chapter, we investigated the electricity-induced buckling behaviors of a micron-scale composite structure with a constantan wire on a polymer substrate. The interfacial toughness between the constantan wire and the polymer substrate was evaluated taking advantage of the buckling phenomenon. The research results are the valuable references to the structure parameter design, the instability assessment and the using condition control of metal-wire/flexible-substrate structures.

(1) The buckling behavior of the constantan wire on the polymer substrate was studied. The buckling features and the buckling generation mechanisms under electrical loading and electrical-mechanical loading were discussed. The buckling was caused by the thermal mismatch between the constantan wire and the polymer substrate, and was related to both the electric current form and the current density. The critical buckling stress and the residual stress of the constantan wire were analyzed using a beam model.

(2) The electricity-induced buckling method was presented to measure the interfacial toughness between a metal wire and a flexible substrate. The interfacial toughness

between the constantan wire and the polymer substrate was measured, providing an effective way to evaluate the interface bonding performance

(3) The buckling behavior of the polymer substrate restricted by the constantan wire under electrical loading was researched. The buckling characteristics and the occurrence conditions of three kinds of micron-scale buckling modes, i.e., the orthogonal wave, the oblique wave and the crumpled wave buckling modes, were summarized. A peculiar micron and submicron cross-scale buckling mode was observed. The generation mechanisms of the micron-scale buckling and the submicron-scale wrinkles were analyzed.

Acknowledgments

The authors are grateful to the financial support from the National Basic Research Program of China ("973" Project) (Grant Nos. 2010CB631005 and 2011CB606105), the National Natural Science Foundation of China (Grant Nos. 11232008, 91216301, 11227801, and 11172151), and Tsinghua University Initiative Scientific Research Program.

References

1. W. Wong and A. Salleo, *Flexible electronics: materials and applications*, Springer, New York, 2009.
2. X. Lu and Y. Xia, *Nature Nanotechnology*, Vol. 1, 163–164, 2006.
3. P. Singer, *Semiconductor Internadional*, Vol. 10, 26, 2003.
4. D.-H. Kim, J.-H. Ahn, W.M. Choi, H.-S. Kim, T.-H. Kim, J. Song, Y.Y. Huang, Z. Liu, C. Lu, and J.A. Rogers, *Science*, Vol. 320, 507–511, 2008.
5. T. Hsu, *MEMS & microsystems: design and manufacture*, McGraw-Hill, New York, 2002.
6. H. Cho, S. Bhansali, and C. Ahn, *Journal of Applied Physics*, Vol. 87, 6340–6342, 2009.
7. C. Okoro, K. Vanstreels, R. Labie, O. L¨1hn, B. Vandevelde, B. Verlinden, and D. Vandepitte, *Journal of Micromechanics and Microengineering*, Vol. 20, 045032, 2010.
8. G. Khatibi, M. Lederer, B. Weiss, T. Licht, J. Bernardi, and H. Danninger, *Procedia Engineering*, Vol. 2, 511–519, 2010.
9. D. Vella, J. Bico, A. Boudaoud, B. Roman, and P. Reis, *Proceedings of the National Academy of Sciences*, Vol. 106, 10901, 2009.
10. J. Davis, R. Venkatesan, A. Kaloyeros, M. Beylansky, S. Souri, K. Banerjee, K. Saraswat, A. Rahman, R. Reif, and J. Meindl, *Proceedings of the IEEE*, Vol. 89, 305–324, 2002.
11. K. Bradley, J.-C.P. Gabriel, and G. Grüner, *Nano Letters*, Vol. 3, 1353–1355, 2003.
12. B. Li, C. Christiansen, J. Gill, T. Sullivan, E. Yashchin, and R. Filippi, *Journal of Applied Physics*, Vol. 100, 114516, 2006.
13. K. Tu, *Journal of Applied Physics*, Vol. 94, 5451, 2003.
14. B. Audoly, *Physical Review Letters*, Vol. 83, 4124–4127, 1999.
15. B. Audoly, B. Roman, and A. Pocheau, *The European Physical Journal B*, Vol. 27, 7–10, 2002.
16. J. Hutchinson and Z. Suo, *Advances in Applied Mechanics*, Vol. 29, 63–191, 1992.
17. N. Bowden, S. Brittain, A. Evans, J. Hutchinson, and G. Whitesides, *Nature*, Vol. 393, 146–149, 1998.

18. S. Lacour, J. Jones, Z. Suo, and S. Wagner, *Electron Device Letters, IEEE*, Vol. 25, 179–181, 2004.
19. S. Lacour, S. Wagner, R. Narayan, T. Li, and Z. Suo, *Journal of Applied Physics*, Vol. 100, 014913, 2009.
20. D. Khang, H. Jiang, Y. Huang, and J. Rogers, *Science*, Vol. 311, 208, 2006.
21. W. Choi, J. Song, D. Khang, H. Jiang, Y. Huang, and J. Rogers, *Nano Letters*, Vol. 7, 1655–1663, 2007.
22. H. Jiang, D. Khang, J. Song, Y. Sun, Y. Huang, and J. Rogers, *Proceedings of the National Academy of Sciences*, Vol. 104, 15607, 2007.
23. Y. Fu, S. Sanjabi, Z. Barber, T. Clyne, W. Huang, M. Cai, J. Luo, A. Flewitt, and W. Milne, *Applied Physics Letters*, Vol. 89, 171922, 2006.
24. C. Harrison, C. Stafford, W. Zhang, and A. Karim, *Applied Physics Letters*, Vol. 85, 4016–4018, 2009.
25. Y. Li, B. Fang, J. Zhang, and J. Song, *Journal of Applied Physics*, Vol. 110, 114303, 2011.
26. W. Huck, N. Bowden, P. Onck, T. Pardoen, J. Hutchinson, and G. Whitesides, *Langmuir*, Vol. 16, 3497–3501, 2000.
27. H. Schmid, H. Wolf, R. Allenspach, H. Riel, S. Karg, B. Michel, and E. Delamarche, *Advanced Functional Materials*, Vol. 13, 145–153, 2003.
28. R. Huang, *Journal of the Mechanics and Physics of Solids*, Vol. 53, 63–89, 2005.
29. R. Huang and S. Im, *Physical Review E*, Vol. 74, 26214, 2006.
30. Z. Huang, W. Hong, and Z. Suo, *Journal of the Mechanics and Physics of Solids*, Vol. 53, 2101–2118, 2005.
31. Y. Sun, W. Choi, H. Jiang, Y. Huang, and J. Rogers, *Nature Nanotechnology*, Vol. 1, 201–207, 2006.
32. H. Jiang, Y. Sun, J. Rogers, and Y. Huang, *Applied Physics Letters*, Vol. 90, 133119, 2007.
33. A. Abdallah, D. Kozodaev, P. Bouten, J. Den Toonder, and U. Schubert, *Thin Solid Films*, Vol. 503, 167–176, 2006.
34. M. George, C. Coupeau, J. Colin, and J. Grilh, *Acta Materialia*, Vol. 53, 411–417, 2005.
35. M. Heinrich, P. Gruber, S. Orso, U. Handge, and R. Spolenak, *Nano Letters*, Vol. 6, 2026–2030, 2006.
36. S. Frank, U. Handge, S. Olliges, and R. Spolenak, *Acta Materialia*, Vol. 57, 1442–1453, 2009.
37. D. Wu, H. Xie, Y. Yin, and M. Tang, *Journal of Micromechanics and Microengineering*, Vol. 23, 035040, 2013.
38. X. Feng, B.D. Yang, Y. Liu, Y. Wang, C. Dagdeviren, Z. Liu, A. Carlson, J. Li, Y. Huang, and J.A. Rogers, *ACS Nano*, Vol. 5, 3326–3332, 2011.
39. R.-H. Kim, M.-H. Bae, D.G. Kim, H. Cheng, B.H. Kim, D.-H. Kim, M. Li, J. Wu, F. Du, and H.-S. Kim, *Nano Letters*, Vol. 11, 3881–3886, 2011.
40. Y. Su, J. Wu, Z. Fan, K.-C. Hwang, J. Song, Y. Huang, and J.A. Rogers, *Journal of the Mechanics and Physics of Solids*, Vol. 60, 487–508, 2012.
41. T. Bejitual, N. Morris, D. Cairns, and K. Sierros, *Thin Solid Films*, Vol. 549, 268–275, 2013.
42. S. Goyal, K. Srinivasan, G. Subbarayan, and T. Siegmund, *Thin Solid Films*, Vol. 518, 2056–2064, 2010.
43. A. Milchev, and K. Binder, *EPL (Europhysics Letters)*, Vol. 102, 58003, 2013.
44. M. Moon, H. Jensen, J. Hutchinson, K. Oh, and A. Evans, *Journal of the Mechanics and Physics of Solids*, Vol. 50, 2355–2377, 2002.
45. M. Moon, K. Lee, K. Oh, and J. Hutchinson, *Acta Materialia*, Vol. 52, 3151–3159, 2004.
46. J.-Y. Sun, S. Xia, M.-W. Moon, K.H. Oh, and K.-S. Kim, *Proceedings of the Royal Society A: Mathematical, Physical and Engineering Science*, Vol. 468, 932–953, 2012.

47. C. Stafford, C. Harrison, K. Beers, A. Karim, E. Amis, M. VanLandingham, H. Kim, W. Volksen, R. Miller, and E. Simonyi, *Nature Materials*, Vol. 3, 545–550, 2004.
48. K. Efimenko, M. Rackaitis, E. Manias, A. Vaziri, L. Mahadevan, and J. Genzer, *Nature Materials*, Vol. 4, 293–297, 2005.
49. R. Hayward, B. Chmelka, and E. Kramer, *Macromolecules*, Vol. 38, 7768–7783, 2005.
50. T. Tanaka, S. Sun, Y. Hirokawa, S. Katayama, J. Kucera, Y. Hirose, and T. Amiya, *Nature*, Vol. 325, 796–798, 1987.
51. E. Matsuo and T. Tanaka, , *Nature*, Vol. 358, 482–485, 1992.
52. J. Sharp, K. Thomas, and M. Weir, *Physical Review E*, Vol. 75, 11601, 2007.
53. S. Srivastava and J. Basu, *Physical Review E*, Vol. 79, 41603, 2009.
54. E. Chan and A. Crosby, *Soft Matter*, Vol. 2, 324–328, 2006.
55. J. Chung, A. Nolte, and C. Stafford, *Advanced Materials*, Vol. 21, 1358–1362, 2009.
56. Q. Wang, Y. Yin, H. Xie, J. Liu, W. Yang, P. Chen, and Q. Zhang, *Soft Matter*, Vol. 7, 2888–2894, 2011.
57. Q.-H. Wang, H.-M. Xie, X. Feng, Z. Chen, and F.-L. Dai, *Electron Device Letters, IEEE*, Vol. 30, 11–13, 2009.
58. Q. Wang, H. Xie, J. Lu, P. Chen, and Q. Zhang, *Journal of Colloid and Interface Science*, Vol. 358, 491–496, 2011.
59. B. Yang and A. Volinsky, *Engineering Fracture Mechanics*, Vol. 75, 3121–3130, 2008.
60. Z. Gan, S. Mhaisalkar, Z. Chen, S. Zhang, and K. Prasad, *Surface and Coatings Technology*, Vol. 198, 85–89, 2005.
61. M.D. Levenson, N. Viswanathan, and R.A. Simpson, *Electron Devices, IEEE Transactions on*, Vol. 29, 1828–1836, 1982.
62. Q. Wang, S. Kishimoto, H. Xie, Y. Li, and D. Wu, *Transactions of Nonferrous Metals Society of China*, Vol. 24, 2606–2611, 2014.
63. Z.Q. Guo, H.M. Xie, B.C. Liu, B. Pan, P.W. Chen, Q.M. Zhang, and F.L. Huang, *Key Engineering Materials*, Vol. 326, 155–158, 2006.
64. A.P. Boresi, R.J. Schmidt, and O.M. Sidebottom, *Advanced mechanics of materials*, Wiley, New York, 1993.
65. Q. Wang, H. Xie, J. Liu, X. Feng, and F. Dai, Instability and failure analysis of film-substrate structure under electrical loading, in: *Electronic Packaging Technology & High Density Packaging, 2009. ICEPT-HDP'09. International Conference on, IEEE*, pp. 1027–1029, 2009.
66. A. Volinsky, N. Moody, and W. Gerberich, *Acta Materialia*, Vol. 50, 441–466, 2002.
67. J. Hutchinson and Z. Suo, *Advances in Applied Mechanics*, Vol. 29, 63-191, 1992.
68. S. Tarasovs, J. Andersons, and Y. Leterrier, *Acta Materialia*, Vol. 58, 2948–2956, 2010.
69. F. Caimmi and A. Pavan, *Engineering Fracture Mechanics*, Vol. 76, 2731–2747, 2009.
70. A. Schweikart and A. Fery, *Microchimica Acta*, Vol. 165, 249–263, 2009.
71. D. Breid and A.J. Crosby, *Soft Matter*, Vol. 5, 425–431, 2009.

11

Microcantilever-Based Nano-Electro-Mechanical Sensor Systems: Characterization, Instrumentation, and Applications

Sheetal Patil and V. Ramgopal Rao*

Centre of Excellence in Nanoelectronics, Department of Electrical Engineering, Indian Institute of Technology Bombay (IIT-Bombay), Mumbai, Maharashtra, India

Abstract

There have been spectacular developments in the recent past in the areas of micro-mechanical or micro-electro-mechanical (MEMS) systems, which have enabled the exploration of transduction modes that involve nano-mechanical motion. As a result, innovative applications in chemical and biological domains have emerged. The sensing applications in the areas such as environment monitoring, healthcare, bio-technology, agriculture and food processing demand fast, hand-held, easy-to-use, low-cost, and sensitive methods for the detection of very low levels of gas, chemical, and biological substances. Among a variety of MEMS-based sensors that are under development, microcantilevers modified with sensitive layers have elicited significant interest. The main advantage of this technology is its small size, low power, high sensitivity, and the possibility to integrate multiple sensors in a miniature package. The microcantilever technology offers rapid, label-free, and *in situ* detection of specific bio/chemical analytes. In this chapter, we discuss six important aspects of microcantilever sensors: (1) operation principles; (2) fabrication of Si and polymer microcantilevers; (3) mechanical and electrical characterization; (4) readout principles; (5) applications of microcantilever sensors for vapor-phase chemical/gas detection, biosensing and agriculture applications; and finally (6) nano generators for energy harvesting.

Keywords: Microcantilever, Si micromachining, polymer MEMS, optical/electrical readout, biosensing, vapor-phase detection, soil moisture, energy harvesting

11.1 Introduction

11.1.1 General Definitions and Concepts

A spectacular development has been made in the areas of micro-mechanical or micro-electro-mechanical (MEMS) sensors and actuators. MEMS sensors hold advantages such as low cost of production due to very large production volume, ease of integration with

**Corresponding author*: rrao@ee.iitb.ac.in

Atul Tiwari and Baldev Raj (eds.), Materials and Failures in MEMS and NEMS, (325–360)
© 2015 Scrivener Publishing LLC

the required instrumentation, arraying capability enabling multiplexed measurements, portability, robustness, and low power consumption. As a result, innovative applications in different domains such as chemical, healthcare, environmental monitoring, biomedical technology, agriculture, and food processing have emerged. The sensing applications in such areas demand fast, handheld, easy-to-use, inexpensive, and highly sensitive methods for detection of very low levels of gas, chemical, and biological substances.

MEMS sensors are based on the mechanical property changes on exposure to the target molecules. In particular, the physical, chemical, or biological stimuli affects the mechanical characteristics of the MEMS transducer and the corresponding change is measured using electronic, optical, or other means. Functionality of MEMS sensors is based on the mechanical movements and deformations of their micro machined components, such as microcantilevers (single-clamped suspended beams), micro-bridges (double-clamped suspended beams), and suspended diaphragms.

Among a variety of MEMS sensors that are under development, microcantilevers functionalized with sensitive layers have attracted much attention. They offer numerous advantages including small size, high sensitivity, integrated multiple sensors in a single package, and low power consumption [1–7]. The simple microcantilever-type configurations are known to be especially suitable as transducers of physical, chemical, and biological stimuli. Microcantilevers became available with the invention of the atomic force microscope (AFM) in 1986 [8]. AFM works as a micro phonograph, where the images are obtained by raster scanning the substrate with a probe. This probe consists of a sharp tip mounted on a microcantilever, which deflects due to the forces between tip and sample. These probes need to have micrometer size dimensions (such as 100 μm long, 50 μm wide and 0.5 μm thick) to achieve a high resonant frequency and a low spring constant. The probe with higher resonant frequency and lower spring constant minimizes the effect of external vibrations and improves the force sensitivity. In 1990, microcantilevers with integrated tips were initially reported by Albrecht *et al.* [9] and Wolter *et al.* [10]. Inspired by this work, in 1994, Thundat *et al.* [11] explored the microcantilevers for a possible potential use as a chemical sensor. They demonstrated that an AFM probe, coated one side with a metal layer for improved reflection of the laser beam, can be used as a sensor because of its bimorph effect. The microcantilever sensing based on optical detection emerged in the late 1990s and attracted much attention due to a label-free, cheap, portable, sensitive sensing systems.

An array of polymer-coated silicon cantilevers with a reference (uncoated) cantilever was used to detect the change in surface stress due to molecular adsorption. On the technology side, microcantilevers with integrated readout, i.e., piezoresistive microcantilevers, which can operate in even non-transparent environments, for surface stress sensing were presented. Researchers further demonstrated the possibility of sensor arrays with a compact readout system [11]. On a microcantilever surface, the change in the Gibbs surface free energy induced by surface–analyte interactions leads to a differential stress thereby causing microcantilevers to bend [12].

In this chapter, we discuss six important aspects of microcantilever sensors: (1) operation principles; (2) microfabrication of Si and polymer microcantilevers; (3) mechanical and electrical characterization; (4) readout principles; (5) applications of microcantilever sensors for vapor phase chemical/gas detection, bio-sensing, and agriculture applications; and (6) nano generators for energy harvesting.

11.2 Operation Principle and Fundamental Models

The variety of transduction mechanisms that are involved in the functioning of microcantilever sensors are broadly classified based on the principle of translating the recognition into a nanomechanical motion. Depending on the measured parameter, microcantilever deflection, i.e., mode of microcantilever operation can be referred to as static, dynamic, or heat modes. Each of these modes is associated with different transduction mechanisms as graphically depicted in Figure 11.1. Static cantilever deflections can be caused by either external forces exerted on the cantilever (as in AFM) or intrinsic stresses generated on the cantilever surface or within the cantilever. Microcantilever sensors operating in the dynamic mode are essentially resonance phenomenon characteristics, which depend on the attached mass on microcantilever surface. For instance, adsorption of analyte molecules on a microcantilever results in lowering of its resonance frequency due to the increased suspended mass. In the heat mode of transaction, thermal sensitivity of material (bimetallic or bimorph effect) leads to a bending of a microcantilever when there is a change in temperature.

a) *Static mode*: It has been known that molecular and atomic adsorbents on atomically pure faces tend to induce significant surface stress changes. Before the evolution of the microcantilever technologies, researchers have investigated changes in surface stresses by minute deformation of relatively thin plates up to ~1 mm. This method is further referred as the beam bending technique [13–15]. Kosch *et al.* studied [16, 17] surface stress changes induced by adsorption of atoms on atomically pure surfaces in vacuum. Fundamental studies of adsorption and absorption-induced mechanical phenomena had limited application for chemical sensors until AFM microcantilevers became available. In the static mode of operation, static deflection of the microcantilever is measured. Changes in static deflection are related to a difference in the surface stress of the two surfaces of the microcantilever. This technique can be used to measure changes in surface stress as a sensing mechanism by modifying one surface of the cantilever with a sensitive layer. Microcantilevers coupled with the optical lever readout greatly simplified the real-time measurement of surface stress changes in the low mN m^{-1} range.

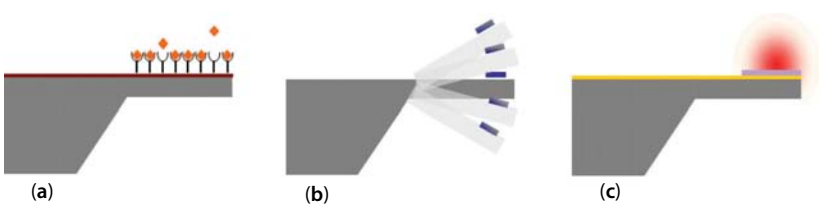

Figure 11.1 Schematic of three modes of microcantilever operation in a cross section view (a) change in surface stress due to molecular adsorption, i.e., static deflection; (b) change in the resonant frequency of microcantilever due to mass, i.e., dynamic mode; and (c) bulk stress changes in the microcantilever material resulting temperature changes caused by a chemical reaction, i.e., heat mode.

The surface stress generated by analyte–surface interaction due to the deformations of thin metal plates is derived by Stoney and von Preissig [18, 19] and given in the following equation:

$$\frac{1}{R} = \frac{6(1-\upsilon)}{Et^2}\Delta\sigma \tag{11.1}$$

where R is the radius of curvature; υ and E are Poisson's ratio and Young's modulus for the substrate, respectively; t is the thickness of the plate; and $\Delta\sigma$ is the differential surface stress. Stoney's equation is further modified for the deflection of rectangular microcantilevers. The differential surface stress at the end point of displacement of microcantilever is given by the following equation [20]:

$$\Delta Z = \frac{1}{2}\frac{L^2}{R} = \frac{3L^2(1-\upsilon)}{Et^2}\Delta\sigma \tag{11.2}$$

where L is length of the microcantilever, and ΔZ is end point of displacement of microcantilever. Microcantilevers used as chemical/gas sensors are surface modified such that one of the sides exhibits high affinity to the targeted analyte while the other side is passivated. The adsorption of target analyte on microcantilever surfaces involves physisorption (weak bonding) or chemisorption (stronger bonding). Physisorption is typically related to van der Waals interactions between the target analyte and the adsorbent substrate and associated with binding energies, which are typically below 0.1 eV. However, in the case of chemisorption, higher binding energies (binding energies >0.3 eV) are typically associated with chemical bonding between the analyte and the surface. In general, changes in surface stresses can be largely attributed to changes in Gibbs free energy associated with adsorption processes. The larger the initial surface free energy of the substrate, greater is the possible change in surface stress resulting from a spontaneous adsorption processes.

The analyte-induced deflections of microcantilevers express the mechanisms of bulk, surface, and inter-surface interactions [21]. These mechanisms further facilitate conversion of the energy of receptor–analyte interactions into a mechanical energy of microcantilever bending. Nano structured coatings substantially increase the number of binding sites on microcantilever surface and hence the sensitivity of the sensor.

b) *Dynamic mode*: The *resonance frequency f0*, of the microcantilever is monitored in the dynamic mode of operation. As mass adsorbs onto the structure, the resonance frequency of the microcantilever decreases. The simplified model of a resonating microcantilever transducer can be based on Hook's law applied to a rectangular leaf spring with an effective

suspended mass m_0 and a spring constant K. Assuming a rectangular microcantilever, the spring constant K is given by [22]

$$K = \frac{Ewt^3}{4L^3} \tag{11.3}$$

where E is the modulus of elasticity for the material composing the cantilever and w width, t thickness, and L length of the cantilever. Assuming a spring constant K and an effective suspended mass m_0, the fundamental resonance frequency f_0 of the microcantilever in the absence of damping is given by

$$f_0 = \frac{1}{2\pi}\sqrt{\frac{K}{m_0}} \tag{11.4}$$

Resonance frequency may change due to changes in mass or changes in spring constant. Hence variation in resonance frequency is a direct indication of mass loading and can be expressed as [23]

$$\Delta m = \frac{K}{4\pi^2}\left\{\frac{1}{F_1^2} - \frac{1}{F_0^2}\right\} \tag{11.5}$$

where F_0 and F_1 are microcantilever resonance frequencies before and after molecular adsorption, respectively. The sensitivity of a resonant mass microcantilever sensor can be defined as a change in resonant frequency due to a change in mass. A high sensitivity of a microcantilever can be achieved by adjusting a high resonant frequency. High resonance frequency depends on a large Young's modulus, low density, and small dimensions. Furthermore, it must have a low mass, requiring a low density and small dimensions. Three mechanisms are involved in resonant operation of microcantilever such as adsorbate induced mass, chemical induced changes, and mechanical damping [24]. The resolution of mass sensing of microcantilevers operating in dynamic mode in liquid medium is expected to get affected by the damping effects, further the damping results in a broadening of the resonant peak which introduces frequency noise. Hence dynamic mode of microcantilevers might not be appropriate for sensing applications with liquid medium.

c) *Heat mode*: Mechanical deformations in microcantilever sensor involve appreciable dissipation of mechanical energy into thermal energy. The deflections of microcantilevers due to analyte/biochemical interactions can be monitored by detecting infra red (IR) photons emitted as a result of an exothermic process. Exposure of IR radiation on an adsorbate covered biomaterial cantilever causes the cantilever to bend more when the

adsorbed molecules absorb IR light [25–28]. A plot of the cantilever bending as a function of illuminating wavelength resembles the traditional IR absorption spectrum of the adsorbate. The sensitivity of the microcantilever-based photo thermal spectroscopy is directly due to the thermal sensitivity of the bi-material cantilever. It has been demonstrated that a bi-material cantilever is extremely sensitive to small changes in temperature. Bi-material microcantilevers consist of two material layers with different thermal expansion coefficients a_1 and a_2. If such a bimorph microcantilever is exposed to a changing influence parameter (i.e., temperature or humidity), the microcantilever bends. The deflection Z of a bi-material microcantilever due to absorbed power P, is given by [25,26]

$$Z = -\frac{3}{4}\left(a_1 - a_2\right)\frac{t_1 + t_2}{t_2{}^2 K}\frac{l^3}{\left(\lambda_1 t_1 + \lambda_2 t_2\right)w}P \tag{11.6}$$

where l length and w the width of the cantilever, a_1 and a_2 are the coefficients of thermal expansion for the two layers, t_1 and t_2 are the layer thicknesses, λ_1 and λ_2 are the layer thermal conductivities (subscript 1 and 2 refer to gold film and silicon nitride substrate, respectively). The parameter K is expressed as [26]

$$K = 4 + 6\left(\frac{t_1}{t_2}\right) + 4\left(\frac{t_1}{t_2}\right)^2 + \frac{E_1}{E_2}\left(\frac{t_1}{t_2}\right)^3 + \frac{E_2}{E_1}\left(\frac{t_2}{t_1}\right) \tag{11.7}$$

where, E_1 and E_2 are Young's moduli for the two layers. As the wavelength of the IR source is changed, the microcantilever bending sensitivity varies as a function of the IR absorption characteristics of the target analyte. The two materials need to have different expansion coefficients with respect to the parameter/analyte to be detected and carefully chosen in order to optimize sensitivity. The best-known application of bi-material microcantilevers is as thermal sensors where two materials with different thermal expansion coefficients are used [29–32]. Bi-material cantilevers can also be used as chemical [33, 34] and humidity sensors [35, 36].

11.3 Microcantilever Sensor Fabrication

Fabrication of microcantilever devices is based on two distinct micromachining strategies: (i) bulk micromachining and (ii) surface micromachining. Bulk micromachining involves removal of substantial portions (i.e., bulk) of the substrate [37–42]. However, in surface micromachining, the original substrate mostly remains intact and is used as a base for the device formed. Microcantilevers can be fabricated in either silicon-based or polymer-based materials. Although the design of the microcantilever sensors

is similar, the fabrication of silicon- and polymer-based microcantilevers is very different and described separately in the following. Microcantilevers design and fabrication are largely defined by the mode of the sensor operation, readout methods, and specific applications. Microcantilever deflection can be measured by external optical readout (laser beam bouncing from the microcantilever tip) and electrical readouts. For optical readout, microcantilever fabrication involves free standing beams with a 50–150 nm metal/reflecting layer deposited on the top side of microcantilever to provide reflectivity and high optical quality. Microcantilevers with electrical readout demand more complex design and device fabrication with integrated functionality. Most commonly used microcantilever structural materials are single crystal silicon, polycrystalline silicon (poly-silicon), silicon nitride, silicon dioxide, and mechanically stable polymers such as SU-8, TOPAS, and Parylene [30, 43–44].

There are following essential requirements for the microcantilever structure (independent of the microcantilever material):

i) Microcantilever should be as thin as possible, to improve the surface stress sensitivity. Precise control on the geometries is crucial to avoid measurement errors.
ii) The microcantilevers should ideally have no initial bending. Initial bending reduces the sensitivity.
iii) For mass sensing, microcantilever should have minimum clamping losses and the material should have low internal damping. Further, microcantilever geometry should allow a high Q factor.

11.3.1 Si Microcantilevers

Silicon microcantilever fabrication is well established and uses technologies initially developed by the IC industry. Low-pressure chemical vapor deposition (LPCVD) and plasma-enhanced chemical vapor deposition (PECVD) techniques are widely used to deposit materials such as silicon dioxide, silicon nitride (structural or sacrificial layers), and poly-silicon layer. Microcantilevers fabricated with these classical materials can be operated over a wide range of temperatures and environmental conditions. Microcantilevers are typically around 1 μm thick and 450–950 μm long. Highly sensitive microcantilevers with thickness h: 500 nm and length L: >100 μm are also commercially available [45, 46]. Si microcantilevers are often realized using bulk micromachining process as described in the following.

11.3.2 Bulk Micromachining

The fabrication process encompasses deposition, patterning, and etching steps that define thickness, lateral sizes, and the encapsulation of the microcantilever. The suspended structures are defined by etching silicon wafer (three dimensionally) from the backside all the way through the wafer. Fabrication is based on single crystal Si wafer with thickness of 300–500 μm. Figure 11.2 illustrates the fabrication process flow of silicon-based microcantilevers by bulk micromachining. The fabrication involves

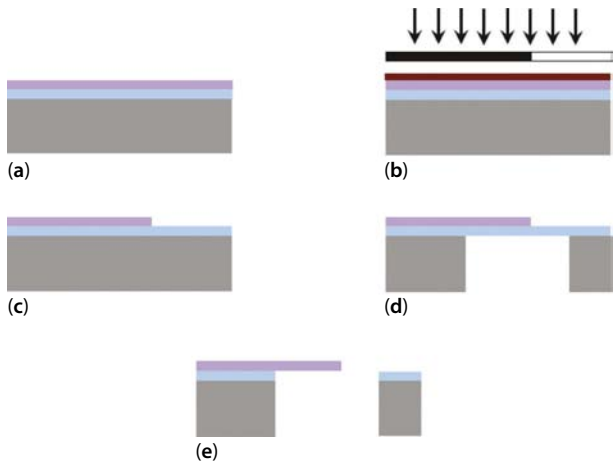

Figure 11.2 Fabrication of silicon-based microcantilevers by bulk micromachining in a cross-section view: (a) substrate preparation by depositing etch stop/sacrificial layer and structural layer (silicon nitride/silicon dioxide, (b) resist spinning and UV lithography to pattern microcantilever structure, (c) pattering of microcantilever structure by etching of structural layer, (d) microcantilever releasing by etching through the bulk wafer from the backside, and (e) etching of etch stop/sacrificial layer.

deposition of a sacrificial/etch stop layer on a substrate. This material protects the actual device layer during the release (in order to secure a thickness and a highly reflecting surface) of the microcantilever. Thin films of the actual structural material layer (such as silicon nitride, silicon dioxide, or a poly-silicon layer) can be deposited by LPCVD or PECVD processes. The stress and stress gradient in the deposited layers can be minimized by varying the deposition conditions, so that suspended structures do not exhibit significant deformation after release. The microcantilever shapes can be defined by UV patterning of the silicon nitride/silicon dioxide film on the top surface using photolithography. This is followed by dry (reactive ion etching, i.e., RIE) or wet chemical etching to remove unwanted material. Photolithographic patterning of the structural material (silicon nitride or silicon oxide) on the bottom surface is used to define mask for anisotropic bulk etch of Si. To produce free-standing microcantilevers, Si etching from the backside is achieved by wet etching using either potassium hydroxide (KOH) [45, 46], or tetramethyl ammonium hydroxide (TMAH). Dry etching of Si can be carried out by deep reactive ion etching (DRIE) [45–48]. As a final step, the etch stop/sacrificial layer is removed to release the microcantilevers. With a similar sequence of processes, single-crystal silicon cantilevers can be created with the difference that doping of silicon. Figure 11.2 shows fabrication of silicon-based microcantilevers by bulk micromachining.

The releasing process results in free-standing microcantilevers, accessible from both sides of the wafer, and can be easily inspected. However, the microcantilevers become fragile and are not well protected. Moreover, etching through the entire silicon wafer is a time-consuming process. In recent years, materials such as silicon carbide [49], graphene [50], and diamond-like carbon [51] have emerged as alternatives to silicon, with unique chemical and mechanical properties.

11.3.3 Polymer Microcantilevers

The microcantilever bending due to surface stress changes is directly proportional to Young's modulus of the microcantilever material. As polymers have Young's modulus typically 40–50X lower than for traditional silicon-based materials they have been considered as attractive candidates for surface stress sensing-based microcantilever applications. The increased sensitivity can be achieved by reducing the stiffness of the microcantilever material by reducing the thickness of the polymer cantilevers down to a few microns. Use of polymers also ensures reduced costs of fabrication and raw material and hence ideally suited for disposable applications.

First polymer microcantilever has been reported by Pechmann *et al.* [52] in 1990s with a Novolak-based photoresist as cantilever material and SU-8, a negative epoxy photo-resist, as a structural layer has been introduced by Genolet *et al.* [53] in 1996. Some well-known polymers such as polyimide, polystyrene (PS), polypropylene, polyethylene terephtalate (PET), and fluoropolymer [54–60] have been reported as a structural material for the fabrication of microcantilevers. New thermoplasts such as parylene and TOPAS® [61–64] were recently introduced as microcantilever materials. Among these polymers reported for microfabrication, for surface stress-based sensing, SU-8 has attracted considerable attention because of its lower Young's modulus (around 4 GPa [65]) compared with silicon and silicon nitride which have Young's modulus values in the range 150–300 GPa [66, 67, 30]. Polymer microcantilevers are realized using the surface micromachining process as described in the following.

11.3.4 Surface Micromachining

In surface micromachining, the freestanding structures are fabricated by building up layers on the surface of a substrate. A sacrificial layer is applied on the substrate, followed by deposition of a thin microcantilever material. In most of the cases, this is achieved by spin-coating of a polymer solution, except parylene, which is deposited by chemical vapor deposition using di-para(xylylene). The standard UV-photolithography method is used to transfer the microcantilever structure. A thin film of photoresist polymer such as SU-8 or polyimide is spin-coated, baked, and exposed to UV light to define the pattern using standard equipments. After defining the microcantilever structure in the actual device layer, an anchor (polymer chip body) can be added on top to facilitate handling of the microcantilevers after device release. In the subsequent steps, SU-8 photolithography has been used to pattern an anchor of thickness ~180 μm with SU-8 2100. The microcantilevers were released by etching the sacrificial layer.

Oxygen plasma etching has been used to pattern microcantilever sensors in parylene [62] and polyimide. The cantilever fabrication of thickness ~4.5 μm was demonstrated by nanoimprint lithography (NIL). Further, patterning methods such as laser ablation and micro-cutting [56, 59] have been also suggested in the literature.

There are many issues that are needed to be solved in order to get robust and stable polymer microcantilevers. Main challenge of polymer microcantilevers for sensing is the stability of the device during measurements. Drift in the output signal [68] and a shift of the resonant frequency of SU-8 microcantilevers due to moisture absorption (due a change in air humidity) is reported by Schmid *et al.* [69]. Further, creep

deformation, ageing can also affect the long-term stability of cantilevers. Process optimization to some extent can minimize the drift and increase stability [70, 71].

11.3.5 Microcantilevers with Integrated Functionality

Microcantilever fabrication becomes a bit more complicated with integrated mechanisms for sensors, when a piezo-resistor, electrodes, or heater elements are integrated. The sensor readout methods are discussed in the next section.

In a piezoresistive microcantilever structure, microcantilever has an integrated resistive layer. The change in the surface stress leads to a change in the resistance of the piezoresistive layer. In silicon microcantilever, resistor is defined with a single-crystal silicon, i.e., polysilicon with silicon nitride as an electrical encapsulation layer. The sensitivity and performance of the silicon microcantilevers depend on crystallinity, doping concentration, and signal-to-noise ratio of polysilicon film.

SU-8 microcantilevers with various strain sensitive layers like gold (Au) and poly silicon have been reported earlier. The gold acts as a low noise piezoresistor, with the signal-to-noise ratio comparable to polysilicon resistors. However, newer materials are being investigated as possible candidates having higher gauge factors compared to gold, in order to improve the surface stress sensitivity. The polymer nanocomposites have been reported as a piezoresistive material by mixing various nanoparticles and polymer. Composites of SU-8 and conducting carbon nanoparticles were used to fabricate microcantilevers with integrated polymer piezoresistors. Figure 11.3 illustrates the fabrication process flow of piezoresistive polymer nanocomposite microcantilevers. Figure 11.4 shows scanning electron microscopic images of released (a) silicon

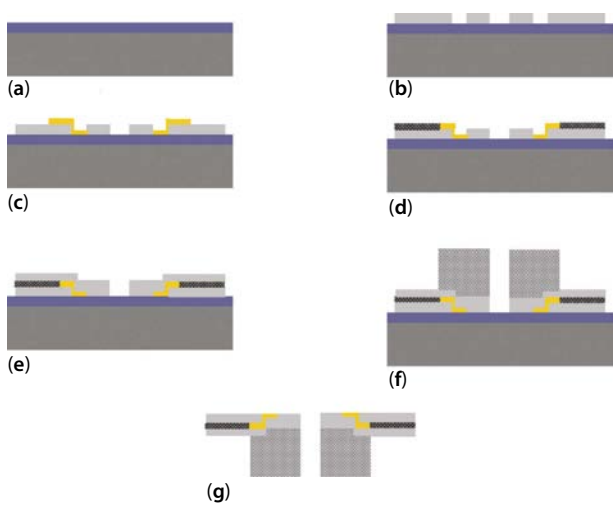

Figure 11.3 Fabrication process flow of piezoresistive polymer nanocomposite microcantilevers: (a) silicon dioxide as a sacrificial layer, (b) first structural layer of SU-8 (spin coated, baked, UV exposed, and developed), (c) sputter deposition and pattering of Cr/Au for contacts, (d) pattering of a piezoresistive SU-8/CB composite layer, (e) encapsulating SU-8 layer (spin coated, baked, UV exposed, and developed), (f) thick SU-8 anchor polymer chip, and (g) release of microcantilever chip from the substrate by etching the sacrificial layer.

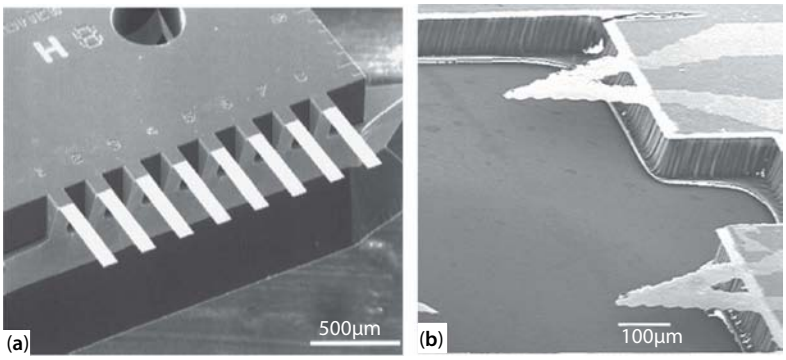

Figure 11.4 Scanning electron microscopic images of released: (a) silicon microcantilevers and (b) piezoresistive SU-8/carbon black polymer nanocomposite microcantilever [7, 46].

microcantilevers and (b) piezoresistive SU-8/carbon black (CB) polymer nanocomposite microcantilever. Conducting polymer materials such as polyaniline [72], 3,4-ethylenedioxythiophene (PEDT) [73] have also been reported as a piezoresistive layer.

11.4 Mechanical and Electrical Characterization of Microcantilevers

11.4.1 Nano-Indentation Techniques

Material characterization plays an important role in the optimization of MEMS system performance. The material properties are process dependent and need to be known for a successful device fabrication. Mechanical material tests such as the uniaxial tension test to measure properties such as Young's modulus and fracture strength are not suitable for the characterization of thin-film materials, as test specimens are very fragile and difficult to handle and align.

Depth-sensing indentation (DIT) is one of the principal methods for mechanical characterization of the materials. In this technique, the penetration of an indenter into the material surface during the application and release of a load is monitored. This technique is also referred to as "nano-indentation" with indentations depths of only a few tens of nanometers. The nano-indentation test includes a loading-hold-unloading cycle. Most commonly, hardness, H, and quasi-static elastic modulus, E, values are derived assuming linear elastic behavior at the onset of unloading. Equations (11.8) and (11.9) are derived by Oliver and Pharr [74] to analyze the unloading part of the load-penetration depth curve in order to extract the hardness and elastic modulus. The reduced modulus is proportional to the contact stiffness, S, at the maximum indentation depth.

$$E_r = \frac{\sqrt{\pi}}{2\beta} \frac{S_{\max}}{\sqrt{A}} \tag{11.8}$$

where E_r, S_{max}, and A are the reduced modulus, the maximum indentation depth, and projected contact area, respectively.

E_r is a function of both, the elastic modulus and Poisson's ratio of material and indenter and defined as Equation (11.9)

$$\frac{1}{E_r} = \frac{\left(1-\nu^2\right)}{E} + \frac{\left(1-\nu_i^2\right)}{E_i} \tag{11.9}$$

Where E and E_i are Young's modulus of material and indenter and μ and μ_i are Poisson's ratios of material and indenter, respectively. The hardness H, of the material is defined as

$$H = \frac{P_{max}}{A} \tag{11.10}$$

where P_{max} is maximum load and A is projected contact area.

Polymer-based composites with nanoscale fillers have attracted much attention over recent years due to their unique mechanical, thermal, and electrical properties [75,76]. The application of DSI technique to polymer nanocomposites (carbon-based, e.g., nanoparticles, nanotubes, graphene, nanodiamond) or inorganic materials (e.g., nanoclays, spherical nanoparticles) nanofillers have gained much interest in recent years. The technique has been proved to be sensitive to filler content, filler dispersion, as well as to the interfacial nanofiller–matrix adhesion [77–79].

The mechanical characterization of SU-8/CB polymer nanocomposites performed by nano-indentation has been determined by Seena *et al.* [6]. They reported that a change in nanoparticle filler loading potentially changes Young's modulus and hardness of the SU-8 nanocomposite. Indentations were carried with maximum load (P_{max}) varying from 80 to 600 μN. Young's moduli and hardness values for different load depth were extracted from loading-hold-unloading cycle (a function of maximum indentation depth). Young's modulus tends to increase for greater depths of indentation and with increasing carbon black (CB) filler loading. Young's modulus of SU-8/CB nanocomposite obtained by nano-indentation was reported to be ~8.5 GPa for 8 vol % CB nano-filler concentration. Further, the hardness values for different samples did not vary much with CB filler concentration. This SU-8/CB nanocomposite filler concentration was further used to fabricate polymer nanocomposite microcantilevers.

Resonant microcantilevers have been used to determine Young's modulus of thin films since 1979 [80]. In 2003, Young's modulus of ultra thin single-crystalline silicon cantilevers was determined by means of the resonance method [81]. The beam thickness was varied from 300 nm down to 12 nm. A steady decrease in Young's modulus for thinner cantilevers was observed with a maximum decrease of 30% for the 12-nm-thick beams compared with the 300-nm-thick beams. At 300 nm, Young's modulus reaches the bulk value of 170 GPa. It is concluded that, for ultrathin single-crystalline silicon, surface effects play an important role in addition to bulk effects. The same size effect of Young's modulus has been reported for sub-100 nm chromium cantilevers determined by static deflection measurements [82,30].

The effective Young's modulus of silicon nitride cantilevers has been determined by Gavan *et al.* [83]. A significant drop of the modulus for cantilevers was observed for

cantilever thickness less than 150 nm. The quality factor, the resonant frequencies and the temperature dependence of Young's modulus of cured SU-8 cantilevers with different lengths have been determined by the group of Hierold [84].

11.4.2 Surface and Resonant Frequency Measurements

The resonance frequency method originally developed by Sader in 1995 [85] and later refined in 1999 [86] utilizes the measurement of the resonance frequency and estimation of the spring constant for a rectangular cantilever. Recently, researchers have reported the high precision of the resonance frequency measurement capability using laser Doppler vibrometry (LDV). LDV is an interferometric technique. The basic concept for LDV measurement involves reflecting a laser beam from the end of a cantilever and measuring the vibrational spectrum. The acquired spectrum is then analyzed using a software package to determine the area under the resonance peak curve. This is then used to extract the spring constant of the cantilever. It is a non contact technique and hence widely used to characterize very small-scale vibrations in devices ranging from MEMS devices such as microcantilevers, rotational oscillators, and silicon nanowires to disk drives. LDVs are well suited for real time measurements of oscillations up to frequencies of tens of megahertz with high frequency resolution, enabling a precise determination of resonant frequencies and quality factors of the different eigenmodes [87–88].

LDV allows the vibrometer laser spot to be focused to a diameter of about 2.5 mm, which is then positioned at the very end of each cantilever. Displacement data are collected at data rates ranging from 256 to 1280 kHz, depending on the resonance frequency of the cantilever being calibrated. Spring constants are calculated according to following equation:

$$k = \frac{0.971 k_B T}{\langle Z^2 \rangle} \tag{11.11}$$

The inherent accuracy and precision of the LDV method for spring constant calibration and resonant frequency measurements performed on commercial cantilevers have been described by R. S. Gates *et al.* [88]. The measurements have been performed on various silicon cantilevers with different lengths ranging from 300 to 600 μm. The average resonant frequency and the spring constant by LDV thermal measurements of these cantilevers have been reported ranging from 20.77 to 5.167 kHz and 0.2098 to 0.0262 Nm^{-1}, respectively. The average spring constants obtained using the LDV method agree with the Euler–Bernoulli values within 3%. A trend of slightly lower resonance frequencies (average 0.7% lower) has been reported for these particular cantilevers. The resonance frequency measurements performed with a LDV on SU-8 polymer nanocomposite microcantilever devices have been reported by V. Seena *et al.* [6]. The microcantilever die was attached to a piezo buzzer which provided the actuation. The laser beam was directed at the cantilever surface. The vibration amplitude and frequency were extracted from the Doppler shift of the laser beam frequency. The measured resonant frequency from the LDV for the polymer nanocomposite microcantilever was 22.6 kHz, which matches well with the analytically calculated value (~20 kHz).

11.4.3 Electrical Characterization

The electrical/electromechanical characterization is an important parameter of integrated piezoresistive of MEMS devices, since it determines the device performance. The aim of the electrical characterization is to understand the conduction behavior of piezoresistive films (such as poly silicon and conductive polymer composites). Recently, Seena V. *et al.* [6] and Sheetal Patil *et al.* [7] reported the electromechanical characterization of SU-8 microcantilevers with integrated piezoresistive (polymer nanocomposite) devices to determine the deflection and surface stress sensitivity. An integrated piezoresistive SU-8 microcantilever is realized using SU-8/CB nanocomposite as a piezo-resistor sandwiched between two SU-8 layers. The electromechanical characterization was performed by deflecting the tip of the microcantilever with a calibrated micromanipulator needle from Suss Microtech with simultaneous measurement of resistance using a Keithley 4200 source measuring unit. The minimum possible vertical deflection using these manipulators was 10 μm. The reported deflection sensitivity and the gauge factor extracted from change in resistance for unit deflection data were 1.1 ppm nm^{-1} and ~90, respectively. Further, the extracted surface stress sensitivity was 7.6×10^{-3} $(Nm^{-1})^{-1}$ which is greater than that of an optimized silicon microcantilever and one order of magnitude higher than that of polymer microcantilevers with Au as the strain gauge.

11.4.4 Noise and Reliability Characterizations

Noise in microcantilever sensors can be divided into intrinsic noise originated during device fabrication process, related to the environmental interactions and from readout systems. Extensive efforts have been made to identify the intrinsic source of noise and the relation between parameters of the mechanical system and its noise level [89]. Microcantilevers, being a mechanical device, there is always a continuous exchange of the mechanical energy and thermal energy of the environment. This energy exchange results in spontaneous oscillation of the microcantilever. The average mechanical energy per mode of cantilever oscillation is defined by thermal energy $k_B T$. Any microcantilever with its thermal environment has a built-in source of noise and this type of noise is referred as white thermal noise $y_{th}(f)$ defined as [90]

$$\psi_{th} = \frac{4m_0 k_B T}{Q} \tag{11.12}$$

The frequencies below the resonance frequency, the amplitude due to thermally induced oscillation of a microcantilever are proportional to the square root of the thermal energy and can be expressed as

$$\left\langle \delta z^2 \right\rangle^{\frac{1}{2}} = \sqrt{\frac{2k_B TB}{\pi k f_0 Q}} \tag{11.13}$$

where k_B is the Boltzmann constant (1.38×10^{-23} J/K), T is the absolute temperature (300 K at room temperature), and B is the bandwidth of measurement. It is observed

from Equation (11.13) that a lower cantilever stiffness corresponds to higher amplitudes of thermal noise.

In case of the dynamic exchange between mechanical energy and the thermal energy, the actual frequency f of thermally induced cantilever oscillations can deviate from the resonance frequency f_0. The amplitude of such frequency fluctuations df_0, is [90]

$$\langle \delta f_0 \rangle = \frac{1}{Z_{\max}} \sqrt{\frac{2\pi f_0 k_B T B}{kQ}} \tag{11.14}$$

For readout systems, the resolution of measurement signal is limited by the noise originating from the piezoresistor layer. The two major and important sources of noise in piezoresistors are (1) Johnson's noise due to thermal fluctuations which is independent of frequency and (2) Hooge's noise also known as $1/f$ noise [91], which is an electrical noise that dominates at lower frequencies and falls off at high frequencies. According to Hooge's model [92], the power spectral density of this noise is inversely proportional to the number of carriers in the resistor and it increases with increase in bias voltage of the resistor. The total noise power spectral density can be obtained by adding all the noise components. The noise level is obtained by integrating the noise power spectral density over the measurement bandwidth.

Noise levels originating from the SU-8 polymer nanocomposite microcantilevers have been estimated by Seena V *et al.* [6] in order to predict the ultimate resolution of these sensors. The noise spectra of these microcantilevers with different CB filler concentrations were recorded by a low noise preamplifier (SR 570) with gain varying from 10^{-3} to 10^{-12} A/V to bias the resistors and to measure and amplify noise levels in current. A spectrum analyser (SR 750) was used to record the noise power spectrum in frequencies ranging from 1 Hz to a few KHz. The noise levels decrease with increase in the filler concentrations that is attributed to the increase in number of charge carriers with CB filler loading. The bias dependence of the noise spectral density indicated that the major component of noise in these SU-8/CB nanocomposite microcantilevers is $1/f$ noise. The noise level for polymer nanocomposite microcantilever (in mV as the product of noise current, assuming a bandwidth 80 Hz) was found to be ~1.89 mV. The noise levels in SU-8/CB nanocomposite microcantilevers were higher compared to those of SU-8 microcantilevers with Au as strain gauge. However, based on these noise levels, the estimated minimum detectable surface stress value reported was ~39 mN m^{-1}, which is higher than that of Au as the strain gauge.

11.5 Readout Principles

The operation of a microcantilever sensor relies on real-time measurements and the resolution of a readout system to monitor changes in mechanical parameters which are directly related to the microcantilever deflection. These mechanical parameters include microcantilever tip position, spatial orientation, radius of curvature, and intrinsic stress. The requirement of a readout system of microcantilever sensors can be dictated by the mode of operation (static or dynamic), cantilever design, materials used

and the magnitude of expected responses. Microcantilever readout schemes can be broadly classified as optical and electrical. There are a variety of electrical transduction schemes such as piezoresistive, piezoelectric, capacitive, electron tunneling technique and embedded MOSFET technique. The principles of operation of these transduction schemes are briefly presented in the following section. The inherent advantages and disadvantages of each transduction scheme are also provided.

11.5.1 Integrated Optical Readout

Optical readout method is most extensively used for measurements of microcantilever deflections in AFM [30, 90] that include optical beam deflection and optical interferometry [90] The optical method proposed for the use in AFM by Meyer and Amer [93] appeared to be simpler and as sensitive as more complex interferometric schemes. In optical beam deflection technique, a laser diode is focused at the free end of the cantilever. A small mirror is attached to a microcantilever (made out of a tungsten) so that a laser beam bounced off this mirror could be monitored using a position-sensitive photodetector (PSD). This optical detection scheme as shown in Figure 11.5 can measure extremely small changes in the cantilever bending. The measurement gives a resolution of 1 nm deflection and even sub-angstrom resolution can be achieved. A most common type of PSD is based on a quadrant photodiode that consists of four cells and each of the cells is coupled to the input of a separate transimpedance amplifier. These normalized differential output voltages are proportional to the illumination of the respective quadrant and depends linearly on the vertical displacement of the light spot projected by the cantilever. The absence of electrical connections to the cantilever, linear response, simplicity, and reliability are some important advantages of the optical lever method.

The optical readout method has been used in the majority of the studies and its limitations are well recognized. For instance, the microcantilever output signal may change due to the interferences in the optical properties and the refractive index of the medium surrounding, ambient light, nonlinear response, and a poorly controllable optical gain. Moreover, applications of cantilever sensors with the optical lever readout are limited to analysis of low opacity and low turbidity media. Another limitation of the optical lever

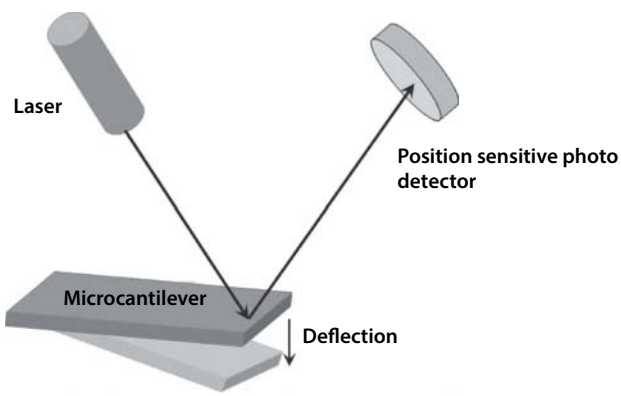

Fig. 11.5 The optical readout commonly used to measure deflection of a microcantilever.

method is related to the bandwidth of PSDs, which typically are in the order of several hundred kilohertz. However, this set-up does not facilitate a simultaneous readout from a reference cantilever.

In order to detect multiple cantilever deflections simultaneously new optical readout schemes have been originally developed at IBM, Zurich [94, 95]. An array of eight commercially available vertical cavity surface emitting lasers (VCSELs) are used to illuminate signal from an array of eight cantilevers spaced with the same pitch (250 μm) as the individual VCSELs. The reflected light is collected by a single photodetector which can track the individual movement of the spots reflected from each respective cantilever. Further, a different approach has been developed in the group of Arun Majumdar, where a two-dimensional array of cantilevers is illuminated simultaneously with an expanded and collimated laser beam. Each cantilever only reflects the light from a mirror placed at the apex and the resulting two-dimensional array of reflected spots are captured by a high-resolution CCD camera [96–98]. However, the optics in its present form tend to be bulky and the resolution is less than that of the optical leverage technique and limited by the resolution of the CCD array.

High-bandwidth optical measurements of cantilever deflections can be carried out using interferometric schemes. This method is based on the interference that occurs between a reference laser beam and the reflected beam from the microcantilever. Differential measurement between two microcantilevers is preferred over single-microcantilever measurements for eliminating the environmental disturbances. Interferometry was revisited as a MEMS readout and as a characterization tool more recently because of its potential for high-bandwidth high-resolution mapping of nanometer scale motions of small cantilevers [99] arranged in large 2D arrays. Rugar et al. [90, 99] used interferometry to measure sub-nanometer deflections of the ultrasensitive cantilevers designed for sensitive force measurements that could ultimately permit single-spin magnetic resonance microscopy.

11.5.2 Piezo-Resistive Readout

Piezoresistive readout is based on the surface stress which changes the resistivity of a piezoresistive material embedded inside the cantilever. Piezoresistivity is the phenomenon of changes in the bulk resistivity with applied stress. The deflection of the cantilever can be determined by an electrical measurement as a resistance change. The ratio of the relative change in resistance per unit strain is called gauge factor, where K is a function of piezoresistive coefficient and Young's modulus of the material. The relation between the strain, ε and the relative change in resistance for a piezoresistor is given as

$$\frac{\Delta R}{R} = K\varepsilon \tag{11.15}$$

$$\frac{\Delta R}{R} = (1+2\nu)\varepsilon + \frac{\Delta\rho}{\rho} \tag{11.16}$$

where R is initial resistance of the piezoresistive material, ν: Poisson's ratio of the material, ε: strain applied, and ρ: resistivity of the piezoresistor. The change in resistance may

also be due to both geometric effects (1+ 2ν) and the fractional change in resistivity ($\Delta\rho/\rho$) of the material with strain and hence can be represented as Equation (11.16) [100].

For a single-layer microcantilever of thickness h, with a thin piezoresistor on top, the surface stress sensitivity can be expressed by Equation (11.17) [101]. Assuming that the piezolayer thickness tends to be zero and neutral axis is placed at the middle of the microcantilever structure:

$$\frac{\Delta R}{R} = 4\left(\frac{K}{Eh}\right)\sigma_s \tag{11.17}$$

where E is Young's modulus of the structural material, h is the thickness of the microcantilever, K is gauge factor of the thin piezoresistor, and σ_s is surface stress. Equation indicates that the surface stress sensitivity depends on the ratio of gauge factor of the piezoresistor and Young's modulus of the structural material. In order to get good sensitivity, it is necessary to keep the piezoresistor away from the neutral axis.

The variation in resistance can be measured by including the cantilever into a dc-biased Wheatstone bridge. A reference and measuring cantilevers are connected with two external resistors to form a Wheatstone bridge configuration [30, 102]. An output signal is recorded when there is a difference in the deflection of the two cantilevers. Typical measuring principle is shown schematically in Figure 11.6.

When a voltage V is applied to the Wheatstone bridge having an initial resistance R, the differential voltage across the bridge can be expressed as

$$V_{out} = \frac{1}{4}\frac{\Delta R}{R}V_{ref} \tag{11.18}$$

Doped single crystal silicon is the most commonly used material as it exhibits strong piezoresistive effect [90]. However, excellent piezoresistivity has been reported for doped poly-silicon microcantilever [90].

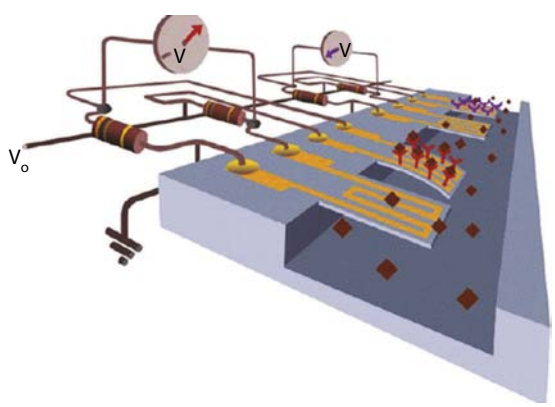

Figure 11.6 Schematic of the microcantilever piezoresistive readout principle commonly used to measure deflection of a microcantilever. Molecular attachment to the microcantilever leads to surface stress and results in the cantilever bending. The bending is detected as a change in the resistance of the resistor embedded inside the microcantilever [30].

The main benefit of piezoresistive method is that it works well in both liquid and gas phase and large arrays can be realized and read out. Also, the technique is applicable for static as well as dynamic measurements. Microcantilever deflection with integrated piezoresistors was originally optimized for AFM and initially reported by Tortonese *et al.* at Stanford University and Rangelow *et al.* at Kassel University [103, 104]. These integrated piezoresistive microcantilevers placed in arrays (either 4 or 16), have been reported for various sensing application such as ethanol and glucose, saccharide, and for gas sensing [105–107]. The piezoresistive microcantilever readout method has also been demonstrated to result in an ultra-sensitive detection of trace-level vapors [6, 7, 108, 109].

Recently, polymers with a much lower Young's modulus than that of silicon using SU-8 (E, ~40 times smaller compared to silicon) have been demonstrated and considered for structural layers. SU-8 microcantilevers with various strain sensitive layers like gold (Au) and polysilicon have been reported earlier. Gold is less sensitive due to the lower gauge factor. Low temperature deposited polysilicon film should be sufficiently thin enough to avoid any contribution to the stiffness of the structure and decreased signal-to-noise ratio [6, 7]. The limitations of using piezoresistive materials can be overcome by integrating polymer nanocomposites as the strain sensitive layer. Subsequently, Gammelgaard *et al.* [110] reported SU-8 microcantilevers integrated with SU-8/CB polymer composite having a gauge factor in the range of 15–20. Recently, an improved performance was achieved by controlling the dispersion parameters of CB in SU-8 and demonstrated polymer nanocomposite piezoresistive microcantilever for various applications such as trace-level detection of explosives and soil moisture detection for agriculture applications [6, 7].

11.5.3 Piezoelectric Readout

Piezoelectric properties of the material have been used for both microcantilever sensing and actuation applications. A mechanical stress due to bending generates an electrical potential across a piezoelectric material and vice versa. In order to achieve high resolution, the microcantilever needs to be operated in the dynamic mode since, in static mode, the electrical potential generated by a static force cannot be sustained by the thin-film piezoelectric material. Therefore, the piezoelectric readout is utilized in resonance mode.

The first piezoelectric readout on microcantilever was introduced in 1993 by Itoh and Suga [111–112]. Various researchers have pursued the use of piezoelectric readout using either zinc oxide or lead zirconate titanate (PZT) [113, 114] thin films deposited on one side of a cantilever used for AFM. The piezoelectric microcantilevers have been used for several sensing applications such as, for the detection of mercury in the ppb range [115], the waterborne parasite "*Giardia lamblia*" (glass cantilevers coated with PZT) [116] and for biosensing (silicon nitride cantilevers with PZT coatings).

Aluminum nitride as a piezoelectric material has been reported by Cleland *et al.* [117]. Aluminum nitride microcantilevers have been realized by sandwiching the aluminum between two electrodes placed at the top and bottom of the cantilever. A single piezoelectric layer has been demonstrated in order to tune the resonant frequency of the microcantilever device with 34 $kHzV^{-1}$ and also for a readout of the signal.

11.5.4 Capacitance Readout

Capacitance readout method is based on measuring the capacitance between two electrodes – one placed on the cantilever and another fixed on the substrate which is separated from the cantilever by a small gap [118]. The capacitance between two conductor plates changes as the gap changes due to cantilever deformation. Since the capacitance is inversely proportional to the separation distance, sensitivity of this method relies on small gap between the cantilever and the substrate. Capacitance readout suffers from interference with variations in the dielectric constant of the medium 201 and electrically conductive media, such as electrolytes, making capacitance readout more challenging. One of the main advantages of capacitance readout is that it can be integrated into MEMS devices and is fully compliant with standard CMOS technology.

The capacitive readout is mainly explored for mass detection in non-liquids. The sensor can be defined on silicon base, the cantilever on the top layer of an SOI wafer and the buried oxide as a sacrificial layer to define the separation [119]. Moreover, the device can be designed in the plane of the wafer using surface micromachining. The electrode and the cantilever are defined in the same layer further the cantilever deflects in the plane of the wafer [120–124].

These cantilever devices reported to have resonant frequencies in the 1 MHz regime and a mass responsivity of 1 ag Hz^{-1} [123]. However, it is reported that polymer walls as resonators with capacitive readout showed resonant frequency of 200 MHz and mass in the order of 0.1 zg Hz^{-1} in air [125]. In the capacitive readout, process parameters such as the surface quality of the cantilever, counter electrode and the spacing between them are crucial and require precise control. Capacitive readout has the advantage that it does not influence the cantilever itself. Further, no additional layers are needed in order to avoid the risk of degrading the cantilever's mechanical performance.

11.6 Application of Microcantilever Sensors

MEMS transducers such as microcantilevers appear to be especially suitable as transducers of physical, chemical, and biological stimuli into readily measurable signals. The physical, chemical, or biological stimuli affect mechanical characteristics of the microcantilever and the change can be measured by electronic, optical, or other means. Adsorption-induced cantilever bending enabled some of the most sensitive detection of trace-level analytes in gases and is a preferred mode of cantilever operation in liquids.

11.6.1 Vapor Phase/Gas/Chemical Detection

Mercury vapor detection was one of the first gas sensor applications of microcantilevers which was reported by Thundat *et al.* [126]. Commercially available delta-shaped silicon nitride AFM cantilevers were used in those studies. An evaporated 50 nm gold coating on one side of the cantilevers provided affinity to mercury. The resonance frequency of the cantilevers increased as a result of exposure to mercury vapors. Static/dynamic mode responses of gold-coated cantilevers were reported for several gaseous

phase analytes, in particular, 2-mercaptoethanol [127]. Detection of mercaptoethanol vapor at concentrations down to 50 part per billion (ppb) have been reported. High sensitivity and selectivity demonstrated using properties of some metals used as active coatings, for instance, gold (being chemically inert metal) has a very high reactivity toward mercaptans (thiols), i.e., compounds with one or more sulfohydryl (–SH) groups. Good sensitivity of Au- and Pd-coated cantilevers for mercury and hydrogen detection were subsequently implemented [128]

Chemically selective organic layer modified microcantilevers have been a subject of more recent studies. Thundat *et al.* [129] described one of the early organic layer-coated microcantilever sensors as a humidity sensor. Silicon nitride AFM microcantilevers coated one side with a 0.1% gelatin solution were exposed to gradually increasing humidity, and an increase in both cantilever deflections and the resonance frequency were observed. The sensor sensitivity measured in the static deflection mode was very high and limited to the dynamic range of relative humidity (RH) 0–60%. Humidity sensitive silicon/silicon oxide microcantilevers, with an integrated piezoresistive readout, were also used as humidity sensors. Theses microcantilevers showed deflection sensitivity $z^{-1}(\Delta R/R)$ of $\sim 10^{-6}$ nm^{-1} [130]. Chemical sensors based on piezoresistive microcantilevers coated with various polymers were studied to distinguish between different volatile organic compounds (VOCs) in air [131]. The concept of multicantilever array with different polymeric coatings is also known as a "chemical nose". Several readily available generic polymers such as polymethylmethacrylate (PMMA), PS, polyurethane, poly-vinyl alcohol (PVA), poly-ethylene imine (PEI), poly-acryl amide (PAAM), and poly-vinyl pyrrolidone (PVP) serve as receptors for gas molecules and they respond differently to various VOCs [131]. Further, it has been shown that the cantilevers with sol–gel coatings exhibited a strong response to vapors of polar VOCs, in particular ethanol.

More recently, microcantilever-based sensors have been applied for trace-level detection of explosives. Development of a miniaturized detector would be highly suitable for use in anti-terror efforts, border control, environmental monitoring, and demining. Different sensing approaches rely on specific receptors for binding of explosives or on specific properties of the explosives such as phase transitions can be used for the detection. Thundat *et al.* demonstrated the detection of explosives such as TNT and RDX in 10–30 parts-per-trillion levels using a gold-coated silicon cantilevers functionalized with a SAM of 4-mercaptobenzoic acid [132]. Zuo *et al.* have reported an increased specificity in the binding of TNT using a silicon oxide piezoresistive cantilevers coated with 6-mercaptonicotinic acid (6-MNA) [133, 134]. V. Seena *et al.* [6] and S. Patil *et al.* [7] demonstrated a compact, low-cost, piezoresistive polymer nanocomposite microcantilever sensor platform for the detection of explosives such as TNT, RDX, and PETN with the limit of detection levels down to a few femto gram.

The microcantilevers being highly sensitive to temperature changes can thus be used for photothermal deflection spectroscopy [135]. When a material absorbs a photon, a fraction of the energy may be transformed into heat. A measurement of photothermal heating as a function of wavelength can provide an absorption spectrum of the material. Bi-material cantilevers can detect local temperature changes associated with a chemical reaction that involves analyte molecules and catalyst on the cantilever surface. This technique was applied in explosives detection [136, 137].

Differential thermal analysis (DTA) is another approach used for the detection of explosives. In DTA technique, the material under study and a reference undergo identical thermal cycles and temperature difference between sample and reference was recorded. Explosives are heated rapidly which undergo decomposition and/or deflagration. This phase transitions is used to achieve a thermal fingerprint of the explosives. Micro structures such as microcantilevers and bridges with integrated heaters have been developed for DTA and used for the detection of explosives such as TNT, PETN, and RDX [138–140].

11.6.2 Biosensors

Bio-sensing applications demand fast detection, easy-to-use, low-cost and high-sensitive methods for the recognition of bio-molecules. All these points can be fulfilled using microcantilever sensors and therefore ideal candidates for biosensing applications. A microcantilever is modified on one side with a suitable receptor that exhibits some affinity for the analyte of interest, whereas the opposite side is relatively "passive". Specific interactions between the analyte and the chemically selective receptor induce a surface stress. This leads to the bending of the microcantilever that can be measured by various readout techniques such as, optical beam deflection, variation in piezoresistivity, piezoelectricity, capacitance, or other means.

In general, a thin gold layer is deposited on one side of the microcantilever. Thiol-based chemistry is used to bind the biomolecules on gold surface. However, the quality of the gold such as surfaces and crystallinity has a high influence on the generated signals. Silane chemistry is used for silicon and the epoxy groups (C–H bonds) on the surface of SU-8 can be utilized [141].

B. Ilic *et al.* [142] demonstrated the mass detection of *E. coli* bacteria using microcantilever technology. A microcantilever resonant frequency was observed to change with the *E. coli* binding. Further, the detection of *Salmonella enterica* was also reported, the change in surface stress upon binding of bacteria [143] was monitored. Piezoelectric microcantilevers made of PZT and glass was used to distinguish between pathogen and *E. coli* [144]. The microcantilever coated with antibodies against pathogen *E. coli*, was seen to be highly selective to the pathogen species upon exposure to both pathogenic and non-pathogenic strains.

Label-free sugar detection using functionalized piezoresistive microcantilevers have been reported by Gary A. Baker *et al.* [145]. The 4-MPBA SAM-modified microcantilevers were exposed to the fructose concentration various values ranging from 2 to 50 mM. Differential surface stress scales linearly with sugar concentration between 2 and 25 mM, with an overall sensitivity of 11.2 mN m^{-1} mM^{-1}. Subramanian *et al.* [146] created a glucose sensor by immobilizing glucose oxidize on gold-coated silicon nitride microcantilevers. The sensor showed the presence of glucose in the aqueous medium due to the enzyme-induced exothermic processes and exhibited a good linearity for glucose concentrations in the range of 5–40 mM. Raiteri *et al.* [147] explored high sensitivity of gold-coated silicon nitride AFM cantilevers as a biosensor for herbicide. They reported bending responses of microcantilevers due to the interaction between the surface-immobilized herbicide (2,4-dichlorophenoxyacetic) and the monoclonal anti-herbicide antibody in an aqueous solution. The cantilever with immobilized herbicide

exhibited partially reversible bending in response to the antiherbicide antibodies at the concentrations of 5 and 25 mg/mL in a phosphate buffer saline. The optical lever method was used to monitor deflections of a cantilever placed in a liquid flow-through cell and the magnitude of the measured responses was about 50 nm.

Moulin *et al.* [148] proposed a microcantilever biosensor for differentiation of low-density lipoproteins (LDL) and their oxidized form (oxLDL) using gold-coated silicon nitride cantilevers modified with heparin. The surface modification included successive incubation of the cantilevers in 2-aminoethanethiol hydrochloride and heparin solutions and saturation of nonspecific binding sites with BSA. The microcantilevers exhibited bending in opposite directions upon exposure to 120 mg/mL of LDL and 10 mg/mL of oxLDL.

A milestone in developing microcantilever-based biosensors was immobilization of single-stranded DNA (ss-DNA) on a microcantilever. The actual hybridization event takes place when a complementary ss-DNA strand is introduced; resulting in a hybridized double-stranded DNA (ds-DNA) bound to the cantilever. In 2000, Fritz *et al.* [149] reported sensitive and specific monitoring of oligonucleotide hybridization using arrays of functionalized (immobilization of thiomodified oligonucleotides) long rectangular gold-coated silicon cantilevers and optical readout of their deflections. Further, they suggested that the surface stress originates from electrostatic, steric and hydrophobic interactions between the hybridized DNA strands on the cantilever. It was observed that the DNA hybridization event causes a compressive surface stress. DNA strands hold a net negative charge. It is argued that the electrostatic interaction changes since ds-DNA has a larger number of charges compared with ss-DNA [149].

Raiteri *et al.* [150] reported the detection of 85 ng/mL myoglobin in an aqueous solution using differential measurements, with one of the cantilevers functionalized with monoclonal anti-myoglobin antibodies.

Microcantilever technology is a promising tool for point of care diagnostics since it is label-free, very sensitive, and offers a possibility to integrate in portable systems. G. Wu *et al.* [151] demonstrated detection of clinically relevant proteins for diagnostics of prostate cancer. Here, antigen against PSA was immobilized using thiol chemistry on gold-coated silicon nitride cantilevers and used to detect two forms of PSA over a wide range of concentrations from 0.2 ng ml^{-1} to 60 μg ml^{-1} in a background of human serum albumin and human plasminogen at 1 $mgml^{-1}$. The methods involved to measure the expression levels of specific genes for diagnostics, for example, fluorescent labeling can achieve pico-molar detection sensitivity, but they are costly, labor intensive and time consuming. In 2006, Zhang *et al.* [151] demonstrated that microcantilever sensors can be used to detect messenger RNA biomarker in a solution of total cellular RNA. The cantilevers were able to detect at the pico-molar level without target amplification, and they were shown to be sensitive to base mismatches.

11.6.3 Agriculture Applications

Soil moisture and temperature are important variables in controlling the exchange of water and heat energy between the land surface and the atmosphere through evaporation and plant transportation. Detection of humidity has become the main concern

in moisture-sensitive domains such as textile manufacturing, high-voltage engineering systems, food processing, storage, and geological soil sample studies [152, 153]. To improve food production efficiency, continuous monitoring of soil moisture and temperature is important. Techniques for detecting soil moisture and temperature such as gamma attenuation, soil heat flux, time-domain reflectometry, and ground penetration radar (GPR) are very expensive, bulky, and mostly limited to surface measurements [154]. These methods, however, suffer from the drawbacks such as inaccuracy or high cost. Further, ease of use for *in situ* applications demands miniaturized, inexpensive, durable, and compact devices, equipped with wireless connectivity.

Accordingly, MEMS sensing devices have matured in the recent years and are being explored as an innovative solution to the requirements of monitoring devices. Conductive polymer poly(3,4-ethylenedioxythiophene–poly(styrene-sulfonate) (PEDOT–PSS)-based microsensors for soil moisture measurement have been reported by Liu *et al.* [155]. The change in electrical characteristics of the PEDOT–PSS polymer film was used to determine the sensitivity and working mechanism when exposed to different levels of moisture content. It is reported that the conductivity of the film decreases when exposed to increasing levels of RH (%RH). Further, PEDOT–PSS thin films were used to detect the gravimetric water content in highly plastic (CH) soil samples (buckshot clay) and change in the output resistance from 2.5 to 4.0 Mohm was observed when exposed to soil samples with 15–35% change in gravimetric water content.

Jackson *et al.* [156] reported development of silicon piezoresistive microcantilever temperature and moisture. The sensors are composed of microcantilevers coated with a water sensitive nanopolymer as a moisture sensor, an on-chip piezoresistive temperature sensor. Both sensors were combined with the wireless sensing node. A good linear relationship between moisture, temperature, and their corresponding microcantilever probe output were observed.

Patil *et al.* [157] recently reported development of a piezoresistive polymer nanocomposite microcantilever platform for humidity and soil moisture detection. A piezoresistive microcantilever is realized using piezoresistive layer (SU-8/CB nanocomposite) embedded between two SU-8 layers. One side of microcantilever was modified by polyaniline (PANI) nanofibers as a water sensing layer and passivating the opposite side. Microcantilever sensor response recorded upon exposure to increasing levels of % RH between 50 (at~0 mV) and 93% exhibits high sensitivity. It was observed that a maximum change of ~28 mV in the output voltage corresponding to a relative change in humidity from 50 to 93% RH, indicating a sensitivity ~ 64mV/0.1% of RH. The sensors revealed small hysteresis (~1–2% RH), with fast response and recovery times of 8 and 10 s, for adsorption and desorption, respectively.

The developed platform for humidity sensing was further used to measure the moisture content of three different soil samples, such as bentonite soil, white clay and sand. PANI nanofiber functionalized microcantilever sensor exhibited detection sensitivity such that 0.1% change in the soil moisture content leads to 43, 275, and 78 mV change in the voltage for bentonite soil, white clay and sand samples, respectively, and provides detection sensitivities approaching ppm (parts per million) levels within a few seconds of exposure. Moreover, microcantilever response toward bentonite soil showed a good linearity between the sensors output and soil gravimetric moisture contents. Further,

for white clay sample, sensor exhibits a good fitting for second order polynomial and the sensor response toward white clay saturates above 60% gravimetric moisture content. The cyclic response of PANI nanofiber-coated piezoresistive microcantilever toward soil gravimetric moisture content exhibited good repeatability and rapid recovery with an average hysteresis of 1% and 2% FS. Authors showed that PANI nanofiber-coated microcantilever-based moisture sensors show a good sensitivity toward RH/soil moisture content and are suited for agriculture applications.

11.7 Energy Harvesting for Sensor Networks

Energy harvesting is a very attractive technique for a wide variety of self-powered microsystems. With the recent progress in wireless and MEMS technologies, the goal is to mount sensors almost anywhere and therefore it is necessary that sensors operate on scavenged power. A significant effort is currently underway to replace batteries with more efficient power sources. The aim is to generate and store power in the sensor node using energy harvesting technologies in order to reduce the size of the wireless sensor systems. The harvesting of energy could be based on solar, vibration, thermal or radio/ microwave frequency conversions [158]. Energy harvesting from ambient vibration by MEMS technology is one of the promising alternatives. The vibration can be converted to electric energy using three types of electromechanical transducers: electromagnetic, electrostatic and piezoelectric [159–164]. Piezoelectric generators show simpler configuration, higher conversion efficiency, and a precise control of the mechanical response [164].

11.7.1 Low-Frequency Vibration Energy Harvesting

The frequency range of common environmental vibration sources is between 60 and 200 Hz; hence, it is necessary to design and fabricate piezoelectric cantilevers having a resonant frequency in the same range. There are two difficulties in the development of MEMS piezoelectric energy harvesting devices: the fabrication of high-quality piezoelectric thin film and the tuning of the resonant frequency of the device suitable for vibration environments.

Initially, ZnO thin film was used as the piezoelectric energy harvesting material due to ease of fabrication, but the low piezoelectric constant obstructed further development. High-quality Pb(Zr,Ti)O3 (PZT) thin films were obtained in energy harvesting device fabrication, due to their high electro-mechanical coupling coefficient. However, the tuning or controlling of the resonant frequency of a piezoelectric energy harvesting device is an issue. Roundy *et al.* [164] reported piezoelectric cantilevers (9–25 mm in length) to generate 375 mW from a vibration source of 2.5 m/s^2 at 120 Hz with a relatively heavy mass on the free end. However, the device size is larger than that of most MEMS devices.

Fang *et al.* [165] reported low-frequency vibrations, a micro piezoelectric power generator which is based on a composite cantilever with nickel metal mass on free end (tip) of the cantilever in order to decrease the structure's natural frequency. The composite cantilever is made up of an upper piezoelectric thick film, sandwiched between a pair of metal (Pt/Ti) electrodes, and with a lower non-piezoelectric element. The

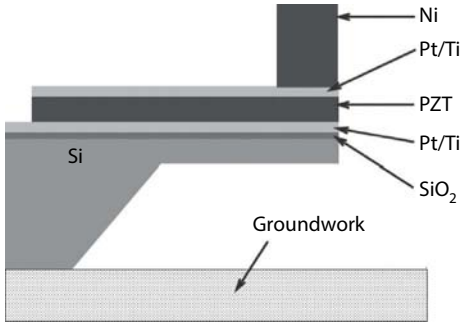

Figure 11.7 Schematic of the schematic of the composite cantilever with nickel metal mass as a piezoelectric power generator.

electrodes are used to exploit d_{31} excitation mode of the PZT material. Techniques such as sol–gel, RIE dry etching, wet chemical etching, UV-LIGA were developed to fabricate the device. The schematic of the composite cantilever with nickel metal mass as a piezoelectric power generator is shown in Figure 11.7. The device performance is measured on a vibration testing setup. The investigation shows that the device operates with a resonant frequency of about 608 Hz and the generator results in about 0.89 V AC peak–peak voltage output and its power output is in 2.16 mW.

Dongna Shen *et al.* [166] investigated a PZT piezoelectric cantilever with an integrated Si proof mass fabricated on a SOI wafer, and a composite Pt/PZT/Pt/ Ti/SiO_2/Si/ SiO_2 multilayer device is generated for low-frequency vibration energy harvesting. The integrated Si proof mass at the free end of the cantilever is used to decrease the resonant frequency of the device. Since, thickness is the most sensitive factor impacting the resonant frequency, the thickness of the silicon supporting layer is precisely controlled by using SiO_2 layer in the SOI wafer. The thin-film PZT generated by sol–gel with a thickness 1.0 μm. The entire effective volume of the fabricated device is about 0.7 mm^3. When excited at 0.75 g (g =9.81 m/s^2) acceleration amplitude at its resonant frequency of 183.8 Hz, the AC output measured across a resistive load of 16 kW has an amplitude of 101 mV. The average power and power density determined are, respectively, 0.32 μW and 416 μW/cm^3.

Muralt *et al.* [167] demonstrated a thin-film PZT laminated cantilever with proof mass and inter-digitated electrodes as micro power generator, which could generate about 1.6 V and 1.4 μW when excited under 2 g at 870 Hz resonant frequency. Elfrink *et al.* [168] reported a MEMS-based AlN piezoelectric cantilever micro-generator, that can generate an output power of 60 μW under 2 g (g = 9.81 m/s^2) acceleration at 572 Hz resonant frequency. Devices with different cantilever beams and mass geometries were produced. Glass wafers were used for the top and bottom covers.

Prashanthi *et al.* and Manoj *et al.* recently demonstrated photo-patternable piezoelectric ZnO SU-8 polymer nanocomposite cantilevers for piezoelectric energy harvesting applications [170, 171]. They have shown for the first time a photo-patternable polymer composite that shows excellent piezoelectric properties. They have shown microcantilever fabrication using these polymer composites and demonstrated energy harvesting from such devices.

11.7.2 Microwave Energy Harvesting

Sood *et al.* [169] presented a piezoelectric micro power generator (PMPG) based on PZT d_{33} mode for conversion of acoustical energy to electrical power. The structure of PMPG is released from the bulk silicon by a way of XeF2 isotropic etch step. Its acoustic operation frequency is set between 20 and 40 kHz, and its power output is about 1 mW. Hagerty *et al.* [170] demonstrated a study of reception and rectification of broadband statistically time-varying low-power-density microwave radiation. A 64-element dual-circularly-polarized spiral rectenna array over a frequency range of 2–18 GHz was designed and characterized with single-tone and multitone incident waves. The integrated design of the antenna and rectifier eliminates matching and filtering circuits. The rectified dc power and efficiency is characterized as a function of dc load and dc circuit topology, RF frequency, polarization, and incidence angle for power densities reported between 10^{-5} and 10^{-1} mW/cm^2.

11.7.3 Photo-Voltaic and Thermal Energy Harvesting

Cuadras *et al.* [173] presented energy harvesting from pyroelectric cells based on screen printed PZT and polyvinylidene fluoride (PVDF) films when subjected to temperature variation. The pyroelectric cell is modeled with current source I_p, capacitor C_p and resistor R_p and defined as

$$I_p = S\lambda \frac{dT}{dt} \tag{11.19}$$

where S is the electrode surface of the cell, l is the pyroelectric coefficient, and T is the temperature. The characteristic of the generated current was measured when temperature changes during heating up and cooling down, and a diode-based full-wave rectifier has been used to store energy. The voltage increases when consecutive heating/cooling cycles were applied to a PZT cell. The output voltage reached a maximum of 21.5 V for the measured cell. Further, it is reported that two parallel cells were able to produce a maximum voltage of 31 V and provide energy of 0.5 mJ and it is possible to power a low power RF transmitter.

Carlson *et al.* [174] presented a switched mode DC–DC boost converter with digital control for thermal source energy harvester. The control is based on turning the pFET off when the inductor current falls to zero. The whole circuit except for an inductance and two filtering capacitors was fabricated with a 0.13 mm CMOS process. The circuit was tested with body heat from a human arm. The converter was allowed to reach a thermal equilibrium over a period of 10 min. At equilibrium, the generator produced 34 mV (unloaded voltage) and the boost converter was able to deliver 34 mW at 1 V.

11.8 Conclusion

As shown in this chapter, microcantilever-based sensing technology is recognized as a promising platform for various sensing applications such as chemical, biological and

for energy harvesting applications. The cantilever technology platform has the capability for development and mass production of extremely sensitive, low-cost, and easily manufacturable sensors suitable for healthcare, homeland security, agriculture, and environmental applications. Further, this technology is also suited for vacuum, gaseous, and liquids measurements. Due to the extremely small thermal masses, cantilevers can be heated and cooled with very low thermal time constants. These phenomena can be used for rapid absorption and regeneration purposes. Responses of cantilever sensors can be measured using readout techniques based on optical, piezoresistance, piezoelectric, and capacitive methods. The work done so far in the area of microcantilever technologies points to a spectacular technology that is on the verge of taking off for a variety of applications that can help improve the quality of life for the mankind.

References

1. L. A. Pinnaduwage, J. E. Hawk, V. Boiadjiev, D. Yi, T. Thundat, Use of microcantilevers for the monitoring of molecular binding to self-assembled monolayers, *Langmuir* 19, 7841, 2003.
2. L. A. Pinnaduwage, D. L. Hedden, A. Gehl, V. I. Boiadjiev, J. E. Hawk, R. H. Farahi, T. Thundat, E. J. Houser, S. Stepnowski, R. A. McGill, L. Deel, R. T. Lareau, A sensitive, handheld vapor sensor based on microcantilevers, *Rev. Sci. Instrum.* 75, 4554, 2004.
3. G. Zuo, X. Li, Z. Zhang, T. Yang, Y. Wang, Z. Cheng, S. Feng, Dual-SAM functionalization on integrated cantilevers for specific trace-explosive sensing and non-specific adsorption suppression, *Nanotechnology*, 18, 255501, 2007.
4. L. Senesac, T. Thundat, Nanosensors for trace explosive detection, *Mater. Today*, 11, 28, 2008.
5. Y. Chen, P. Xu, X. Li, Self-assembling siloxane bilayer directly on SiO_2 surface of microcantilevers for long-term highly repeatable sensing to trace explosives, *Nanotechnology*, 21, 265501, 2010.
6. V. Seena, A. Fernandes, P. Pant, S. Mukherji, V. R. Rao, Polymer nanocomposite nanomechanical cantilever sensors: material characterization, device development and application in explosive vapour detection, *Nanotechnology*, 22, 295501, 2011.
7. S. Patil, N. Duragkar, V. Ramgopal Rao, An ultra-sensitive piezoresistive polymer nanocomposite microcantilever sensor electronic nose platform for explosive vapor detection, *Sens. Actuat. B* 192, 444, 2014.
8. G. Binnig, C. F. Quate, C. Gerber, Atomic force microscope, *Phys. Rev. Lett.* 56, 930, 1986.
9. T. R. Albrecht, S. Akamine, T. E. Carver, C. F. Quate, Microfabrication of cantilever styli for the atomic force microscope, *J. Vac. Sci. Technol. A* 8, 3386, 1990.
10. O. Wolter, T. Bayer, J. Greschner, Micromachined silicon sensors for scanning force microscopy, *J. Vac. Sci. Technol. B* 9, 1353, 1991.
11. A. Boisen, J. Thaysen, H. Jensenius, O. Hansen, Environmental sensors based on micromachined cantilevers with integrated read-out, *Ultramicroscopy* 82, 11, 2000.
12. T. Thundat, R. J. Warmack, G. Y. Chen, D. P. Allison, Thermal and ambient-induced deflections of scanning force microscope cantilevers, *Appl. Phys. Lett.* 64, 2894, 1994.
13. L. J. D. Frink, F van Swol, A common theoretical basis for surface forces apparatus, osmotic stress, and beam bending measurements of surface forces, *Colloids Surf. A* 162, 25, 2000.
14. R. E. Martinez, W. M. Augustyniak, J. A. Golovchenko, Direct measurement of crystal surface stress, *Phys. Rev. Lett.* 64, 1035, 1990.

15. H. Ibach, Adsorbate-induced surface stress, *J. Vac. Sci. Technol. A* 12, 2240, 1994.
16. R. Koch, The intrinsic stress of polycrystalline and epitaxial thin metal films, *J. Phys. Condens. Matter* 6, 9519, 1994.
17. R. Koch, Intrinsic stress of ultrathin epitaxial films, *Appl. Phys. A Mater. Sci. Process.* 69, 529, 1999.
18. G. G. Stoney, The tension of metallic films deposited by electrolysis, *Proc. R. Soc. London A* 82, 172, 1909.
19. FJ von Preissig, Applicability of the classical curvature-stress relation for thin films on plate substrates, *J. Appl. Phys.* 66, 4262, 1989.
20. R. J. Jaccodin, W. A. Schlegel, Measurement of strains at Si–SiO_2 interface, *J. Appl. Phys.* 37, 2429, 1966.
21. J. Israelachvili, *Intermolecular and Surface Forces*, Academic Press, San Diego, 1991.
22. D. Sarid, *Scanning Force Microscopy*, Oxford University Press, New York, 1991.
23. K. M. Hansen, T. Thundat, Microcantilever biosensors, *Methods* 37, 57–64, 2008.
24. S. Y. Yurish, M. T. S. R. Gomes, Smart Sensors and MEMS: Proceedings of the NATO.
25. C. W. Van Neste, L. R. Senesac, D. Yi, T. Thundat, Standoff detection of explosive residues using photothermal microcantilevers, *Appl. Phys. Lett.* 92, 134102, 2008.
26. J. R. Barnes, R. J. Stephenson, C. N. Woodburn, SJ O'Shea, M. E. Welland, T. Rayment, J. K. Gimzewski, Ch Gerber, A femtojoule calorimeter using micromechanical sensors, *Rev. Sci. Instrum.* 65, 3793, 1994; 66, 3083 E, 1995.
27. P. G. Datskos, S. Rajic, M. J. Sepaniak, N. V. Larvick, C. A. Tipple, I. Datskou, Chemical detection based on adsorption-induced and photoinduced stresses in microelectromechanical systems devices, *J. Vac. Sci. Technol. B* 19, 1173, 2001.
28. P. G. Datskos, M. J. Sepaniak, C. A. Tipple, N. Lavrick, Photomechanical chemical microsensors, *Sens. Actuat. B* 76, 393, 2001
29. S. Timoshenko, Analysis of bi-metal thermostats, *J. Opt. Soc. Am.* 11, 233, 1925.
30. A. Boisen, S. Dohn, S. S. Keller, S. Schmid, M. Tenje, Cantilever-like micromechanical sensors, *Rep. Prog. Phys.* 74, 036101, 2011.
31. M. C. LeMieux, M. E. McConney, Y-H. Lin, S. Singamaneni, H. Jiang, T. J. Bunning, V. V. Tsukruk, Polymeric nanolayers as actuators for ultrasensitive thermal bimorphs, *Nano Lett.* 6, 730, 2006.
32. J-H. He *et al.*, A thermal sensor and switch based on a plasma polymer/ZnO suspended nanobelt bimorph structure, *Nanotechnology* 20, 065502, 2009.
33. H. Zhiyu, T. Thundat, R. J. Warmack, Investigation of adsorption and absorption-induced stresses using microcantilever sensors, *J. Appl. Phys.* 90, 427, 2001.
34. J. K. Gimzewski, C. Gerber, E. Meyer, R. R. Schlittler, Observation of a chemical reaction using a micromechanical sensor, *Chem. Phys. Lett.* 217, 589, 1994.
35. S. Singamaneni *et al.,* Bimaterial microcantilevers as a hybrid sensing platform, *Adv. Mater.* 20, 653, 2008.
36. S. Singamaneni, M. E. McConney, M. C. LeMieux, H. Jiang, J. O. Enlow, T. J. Bunning, R. R. Naik, V. V. Tsukruk, Polymer-silicon flexible structures for fast chemical vapor detection, *Adv. Mater.* 19, 4248, 2007.
37. G. T. A. Kovacs, *Micromachined Transducers*, McGraw-Hill, New York, 1998.
38. A. K. Deisingh, *Analyst*, Cambridge, UK, 2003.
39. R. Maboudian, Surface processes in MEMS technology, *Surf. Sci. Rep.* 30, 209, 1998.
40. J. Buhler, E. Fitzer, D. Kehre, Surface micromachining, *J. Electrochem. Soc.* 124, C299, 1977.
41. J. Buhler, F. P. Steiner, H. Baltes, Silicon dioxide sacrificial layer etching in surface micromachining, *J. Micromech. Microeng.* 7, R1, 1997.
42. M. Madou, *Fundamentals of Microfabrication*, CRC. Press, New York, 1997.

43. A. Greve, S. Keller, A. L. Vig, A. Kristensen, D. Larsson, K. Yvind, J. M. Hvam, M. Cerruti, Thermoplastic microcantilevers fabricated by nanoimprint lithography, *J. Micromech. Microeng.* 20, 015009, 2010.
44. R. Katragadda, Z. Wang, W. Khalid, Parylene cantilevers integrated with polycrystalline silicon piezoresistors for surface stress sensing, *Appl. Phys. Lett.* 91, 083505, 2007.
45. www.concentris.ch and www.micromotive.de.
46. M. K. Baller, H. P. Lang, J. Fritz, Ch Gerber, J. K. Gimzewski, U. Drechsler, Rothuizen, M. Despont, P. Vettiger, F. M. Battiston, J. P. Ramseyer, P. Fornaro, E. Meyer, H-J. Guntherodt, A cantilever array-based artificial nose, *Ultramicroscopy* 82, 1, 2000.
47. G. S. May, S. M. Sze, Photolithography, Fundamentals of Semiconductor Fabrication, Wiley, New York, 2004.
48. P. Garrou, C. Bower, P. Ramm, *Handbook of 3D Integration*, Wiley, Weinheim, 2008.
49. A. Bagolini, L. Pakula, T. L. M. Scholtes, H. T. M. Pham, P. J. French, P. M. Sarro, Polyimide sacrificial layer and novel materials for post-processing surface micromachining, *J. Micromech. Microeng.* 12, 385, 2002.
50. A. K. Geim, K. S. Novoselov, The rise of grapheme, *Nat. Mater.* 6, 183, 2007.
51. J. Robertson, Diamond-like amorphous carbon, *Mater. Sci. Eng. R* 37, 129, 2002.
52. R. Pechmann, J. M. Kohler, W. Fritzsche, A. Schaper, T. M. Jovin, The ovolever: a new cantilever for scanning force microscopy microfabricated from polymeric materials, *Rev. Sci. Instrum.* 65, 3702, 1994.
53. G. Genolet, J. Brugger, M. Despont, U. Drechsler, P. Vettiger, NF de Rooij, D. Anselmetti, Soft, entirely photoplastic probes for scanning force microscopy, *Rev. Sci. Instrum.* 70, 2398, 1999.
54. X. Wang, K. S. Ryu, D. A. Bullen, J. Zou, H. Zhang, C. A. Mirkin, C. Liu, Scanning probe contact printing, *Langmuir* 19, 8951, 2003.
55. A. Gaitas, Y. B. Gianchandani, An experimental study of the contact mode AFM scanning capability of polyimide cantilever probes, *Ultramicroscopy* 106, 874, 2006.
56. A. W. McFarland, M. A. Poggi, L. A. Bottomley, J. S. Colton, Production and characterization of polymer microcantilevers, *Rev. Sci. Instrum.* 75, 2756, 2004.
57. A. W. McFarland, M. A. Poggi, L. A. Bottomley, J. S. Colton, Injection moulding of high aspect ratio micron-scale thickness polymeric microcantilevers, *Nanotechnology* 15, 1628, 2004.
58. A. W. McFarland, J. S. Colton, Chemical sensing with micromolded plastic microcantilevers, *J. Microelectromech. Syst.* 14, 1375, 2005.
59. X. R. Zhang, X. Xu, Development of a biosensor based on laser-fabricated polymer microcantilevers, *Appl. Phys. Lett.* 85, 2423, 2004.
60. L. P. Lee, S. A. Berger, D. Liepmann, L. Pruitt, High aspect ratio polymer microstructures and cantilevers for bioMEMS using low energy ion beam and photolithography, *Sens. Actuat. A* 71, 144, 1998.
61. T-J. Yao, X. Yang, Y-C. Tai, BrF_3 dry release technology for large freestanding parylene microstructures and electrostatic actuators, *Sens. Actuat. A* 97/98, 771, 2002.
62. R. Katragadda, Z. Wang, W. Khalid, Y. Li, Y. Xu, Parylene cantilevers integrated with polycrystalline silicon piezoresistors for surface stress sensing, *Appl. Phys. Lett.* 91, 083505, 2007.
63. A. Greve, S. Keller, A. L. Vig, A. Kristensen, D. Larsson, K. Yvind, J. M. Hvam, M. Cerruti, A. Majumdar, A. Boisen, Thermoplastic microcantilevers fabricated by nanoimprint lithography, *J. Micromech. Microeng.* 20, 015009, 2010.
64. www.topas.com.
65. M. Hopcroft, T. Kramer, G. Kim, K. Takashima, Y. Higo, D. Moore, J. Brugger, Micromechanical testing of SU-8 cantilevers, *Fatigue Fract. Eng. Mater. Struct.* 28, 735, 2005.
66. M. Calleja, J. Tamayo, A. Johansson, P. Rasmussen, L. M. Lechuga, A. Boisen, Polymeric cantilever arrays for biosensing applications, *Sens. Lett.* 1, 20, 2003.

67. J. H. T. Ransley, M. Watari, D. Sukumaran, R. A. McKendry, A. A. Seshia, SU8 bio-chemical sensor microarrays, *Microelectron. Eng.* 83, 1621, 2006.
68. M. Tenje, S. Keller, S. Dohn, Z. J. Davis, A. Boisen, Drift study of SU8 cantilevers in liquid and gaseous environments, *Ultramicroscopy* 101, 596, 2010.
69. S. Schmid, S K¨uhne, C. Hierold, Influence of air humidity on polymeric microresonators, *J. Micromech. Microeng.* 19, 065018, 2009.
70. C. Martin, A. Llobera, G. Villanueva, A. Voigt, G. Gruetzner, J. Brugger, F. Perez-Murano, Stress and aging minimization in photoplastic AFM probes, *Microelectron. Eng.* 86, 1226, 2009.
71. S. Keller, D. Haefliger, A. Boisen, Fabrication of thin SU-8 cantilevers: initial bending, release and time-stability, *J. Micromech. Microeng.* 20, 045024, 2010.
72. M. Lillemose, M. Spieser, N. O. Christiansen, A. Christensen, A. Boisen, Intrinsically conductive polymer thin film piezoresistors, Microelectron. Eng. 85, 969, 2008.
73. R. Mateiu, M. Lillemose, T. S. Hansen, A. Boisen, O. Geschke, Reliability of poly 3,4-ethylenedioxythiophene strain gauge, Microelectron. Eng. 84, 1270, 2008,
74. W. C. Oliver, G. M. J. Pharr, An improved technique for determining hardness and elastic modulus using load and displacement sensing indentation experiments, *Mater. Res.* 7, 1564, 1992.
75. E. Manias, Nanocomposites: stiffer by design, *Nat. Mater.* 6, 9–11, 2007.
76. G. Kickelbick, Concepts for the incorporation of inorganic building blocks into organic polymers on a nanoscale, *Prog. Polym. Sci.* 28, 83–114, 2003.
77. T. Liu, I. Y. Phang, L. Shen, S. Y. Chow, W-D. Zhang, Morphology and mechanical properties of multiwalled carbon nanotubes reinforced nylon-6 composites, *Macromolecules* 37, 7214–7222, 2004.
78. B. Das, K. E. Prasad, U. Ramamurty, C. N. R. Rao, Nano-indentation studies on polymer matrix composites reinforced by few layer graphene, *Nanotechnology* 20, 125705–125710, 2009.
79. A. Flores, M. Naffakh, A. M. Díez-Pascual, F. Ania, M. A. Gómez-Fatou, Evaluating the reinforcement of inorganic fullerene-like nanoparticles in thermoplastic matrices by depth-sensing indentation, *J. Phys. Chem. C* 117, 20936–20943, 2013.
80. K. E. Petersen, C. R. Guarnieri, Young's modulus measurements of thin films using micromechanics, *J. Appl. Phys.* 50, 6761, 1979.
81. X. Li, T. Ono, Y. Wang, M. Esashi, Ultrathin single-crystalline-silicon cantilever resonators: fabrication technology and significant specimen size effect on Young's modulus, *Appl. Phys. Lett.* 83, 3081, 2003.
82. S. G. Nilsson, X. Borrise, L. Montelius, Size effect on Young's modulus of thin chromium cantilevers, *Appl. Phys. Lett.* 85, 3555, 2004.
83. K. B. Gavan, H. J. R. Westra, EWJM van der Drift, W. J. Venstra, HSJ van der Zant, Size-dependent effective Young's modulus of silicon nitride cantilevers, *Appl. Phys. Lett.* 94, 233108, 2009.
84. S. Schmid, *Electrostatically Actuated All-Polymer Microbeam Resonators—Characterization and Application*, ed. C. Hierold, Der Andere, Toenning, 2009.
85. J. E. Sader, I. Larson, P. Mulvaney, L. R. White, Method for the calibration of atomic-force microscope cantilevers, *Rev. Sci. Instrum.* 66, 3789–3798, 1995.
86. J. E. Sader, J. W. M. Chon, P. Mulvaney, Calibration of rectangular atomic force microscope cantilevers, *Rev. Sci. Instrum.* 70, 3967–3969, 1999
87. Laura B. Biedermann, Ryan C. Tung, Arvind Raman, Ronald G. Reifenberger, Flexural vibration spectra of carbon nanotubes measured using laser Doppler vibrometry, *Nanotechnology* 20, 035702, 2009.

88. Richard S. Gates, Jon R. Pratt, Accurate and precise calibration of AFM cantilever spring constants using laser Doppler vibrometry, *Nanotechnology* 23, 375702, 2012.
89. A. N. Cleland, M. L. Roukes, Noise processes in nanomechanical resonators, *J. Appl. Phys.* 92, 2758, 2002.
90. Nickolay V. Lavrik, Michael J. Sepaniak, Panos G. Datskos, Cantilever transducers as a platform for chemical and biological sensors, Rev. Sci. Instrum. 75–77, 2229, 2004.
91. B. A. A. Barlian, W-tae Park, J. R. Mallon, A. J. Rastegar, B. L. Pruitt, Review: semiconductor piezoresistance for microsystems, *Proceedings of the IEEE*, 97, 2009.
92. F. N. Hooge, T. G. M. Kleinpenning, L. K. J. Vandamme, Experimental studies on l/f noise, *Rep. Prog. Phys.* 44, 479, 1981.
93. G. Meyer, N. M. Amer, Novel optical approach to atomic force microscopy, *Appl. Phys. Lett.* 53, 1045, 1988.
94. H. P. Lang, M. K. Baller, R. Berger, C. Gerber, J. K. Gimzewski, F. M. Battiston, P. Fornaro, J. P. Ramseyer, E. Meyer, H. J. Guntherodt, An artificial nose based on a micromechanical cantilever array, *Anal. Chim. Acta.* 393, 59, 1999.
95. H. P. Lang *et al.*, Sequential position readout from arrays of micromechanical cantilever sensors, *Appl. Phys. Lett.* 72, 383, 1998.
96. S. H. Lim, D. Raorane, S. Satyanarayana, A. Majumdar, Nano-chemo-mechanical sensor array platform for high-throughput chemical analysis, *Sens. Actuat. B* 119, 466, 2006.
97. M. Yue, J. C. Stachowiak, H. Lin, R. Datar, R. Cote, A. Majumdar, Label-free protein recognition two-dimensional array using nanomechanical sensors, *Nano Lett.* 8, 520, 2008.
98. M. Yue, H. Lin, D. E. Dedrick, S. Satyanarayana, A. Majumdar, A. S. Bedekar, J. W. Jenkins, S. Sundaram, A 2-D microcantilever array for multiplexed biomolecular analysis, *J. Microelectromech. Syst.* 13, 290, 2004.
99. D. Rugar, H. J. Mamin, P. Guethner, Improved fiber-optic interferometer for atomic force microscopy, *Appl. Phys. Lett.* 55, 2588, 1989.
100. A A. Barlian, W-tae Park, J. R. Mallon Jr, A. J. Rastegar, B. L. Pruitt, M. Engineering, Review: semiconductor piezoresistance for microsystems, *Proc. IEEE Inst. Elect. Electron. Eng.* 97, 513–552, 2009.
101. J. Theysen, A. D. Yalcinkaya, P. Vettiger, A. Menon, Polymer-based stress sensor with integrated readout, *J. Phys. D Appl. Phys.* 35, 2698, 2002.
102. J. Thaysen, A. Boisen, O. Hansen, S. Bouwstra, Atomic force microscopy probe with piezoresistive read-out and a highly symmetrical Wheatstone bridge arrangement, *Sens. Actuat. A* 83, 47, 2000.
103. M. Tortonese, R. C. Barrett, C. F. Quate, Atomic resolution with an atomic force microscope using piezoresistive detection, *Appl. Phys. Lett.* 62, 834, 1993.
104. R. Linnemann, T. Gotszalk, L. Hadjiski, I. W. Rangelow, Characterization of a cantilever with an integrated deflection sensor, *Thin Solid Films* 264, 159, 1995.
105. S. Kim, T. Rahman, L. R. Senesac, B. H. Davison, T. Thundat, Piezoresistive cantilever array sensor for consolidated bioprocess monitoring, *Scanning* 31, 204, 2009.
106. G. A. Baker, R. Desikan, T. Thundat, Label-free sugar detection using phenylboronic acid-functionalized piezoresistive microcantilevers, *Anal. Chem.* 80, 4860, 2008.
107. G. Yoshikawa, H. P. Lang, T. Akiyama, L. Aeschimann, U. Staufer, P. Vettiger, M. Aono, T. Sakurai, C. Gerber, Sub-ppm detection of vapors using piezoresistive microcantilever array sensors, *Nanotechnology* 20, 015501, 2009.
108. G. Zuo, X. Li, Z. Zhang, T. Yang, Y. Wang, Z. Cheng, S. Feng, Dual-SAM functionalization on integrated cantilevers for specific trace-explosive sensing and non-specific adsorption suppression, *Nanotechnology* 18, 255501, 2007.

109. Y. Chen, P. Xu, X. Li, Self-assembling siloxane bilayer directly on SiO_2 surface of microcantilevers for long-term highly repeatable sensing to trace explosives, *Nanotechnology* 21, 265501, 2010.
110. L. Gammelgaard, P. A. Rasmussen, M. Calleja, P. Vettiger, A. Boisen, Microfabricated photoplastic cantilever with integrated photoplastic/carbon based piezoresistive strain sensor, *Appl. Phys. Lett.* 88, 113508, 2006.
111. T. Itoh, T. Suga, Development of a force sensor for atomic force microscopy using piezoelectric thin films, *Nanotechnology* 4, 218, 1993.
112. T. Itoh, T. Suga, Piezoelectric force sensor for scanning force microscopy, *Sens. Actuat. A* 43, 305, 1994.
113. S. C. Minne, S. R. Manalis, A. Atalar, C. F. Quate, Contact imaging in the atomic force microscope using a higher order flexural mode combined with a new sensor, *Appl. Phys. Lett.* 68, 1427, 1996.
114. S. Watanabe, T. Fujii, Micro-fabricated piezoelectric cantilever for atomic force microscopy, *Rev. Sci. Instrum.* 67, 3898, 1996.
115. J. D. Adams, B. Rogers, L. Manning, Z. Hu, T. Thundat, H. Cavazos, S. C. Minne, Piezoelectric self-sensing of adsorption-induced microcantilever bending, *Sens. Actuat. A* 121, 457, 2005.
116. S. Xu, R. Mutharasan, Rapid and sensitive detection of *Giardia lamblia* using a piezoelectric cantilever biosensor in finished and source waters, *Environ. Sci. Technol.* 44, 1736, 2010.
117. A. N. Cleland, M. Pophristic, I. Ferguson, Single-crystal aluminum nitride nanomechanical resonators, *Appl. Phys. Lett.* 79, 2070, 2001.
118. C. L. Britton, R. L. Jones, P. I. Oden, Z. Hu, R. J. Warmack, S. F. Smith, W. L. Bryan, J. M. Rochelle, Multiple-input microcantilever sensors, *Ultramicroscopy* 82, 17, 2000.
119. S. J. Kim, T. Ono, M. Esashi, Capacitive resonant mass sensor with frequency demodulation detection based on resonant circuit, *Appl. Phys. Lett.* 88, 053116, 2006.
120. M. Villarroya *et al.,* System on chip mass sensor based on polysilicon cantilevers arrays for multiple detection, *Sens. Actuat. A* 132, 154, 2006.
121. J. Verd *et al.,* Design, fabrication, and characterization of a submicroelectromechanical resonator with monolithically integrated CMOS readout circuit, *J. Microelectromech. Syst.* 14, 508, 2005.
122. Forsen E *et al.,* Fabrication of cantilever based mass sensors integrated with CMOS using direct write laser lithography on resist, *Nanotechnology* 15, S628, 2004.
123. J. Teva, G. Abadal, F. Torres, J. Verd, F. Perez-Murano, N. Barniol, A femtogram resolution mass sensor platform, based on SOI electrostatically driven resonant cantilever: I. Electromechanical model and parameter extraction, *Ultramicroscopy* 106, 800, 2006.
124. J. Arcamone, G. Rius, G. Abadal, J. Teva, N. Barniol, F. Perez-Murano, Micro/nanomechanical resonators for distributed mass sensing with capacitive detection, *Microelectron. Eng.* 83, 1216, 2006.
125. S. Ghatnekar-Nilsson, I. Karlsson, A. Kvennefors, G. Luo, V. Zela, M. Arlelid, T. Parker, L. Montelius, A. Litwin, A new multifunctional platform based on high aspect ratio interdigitated NEMS structures, *Nanotechnology* 20, 175502, 2009.
126. T. Thundat, E. A. Wachter, S. L. Sharp, R. J. Warmack, Detection of mercury vapor using resonating microcantilevers, *Appl. Phys. Lett.* 66, 1695, 1995.
127. P. G. Datskos, I. Sauers, Detection of 2-mercaptoethanol using gold-coated micromachined cantilevers, *Sens. Actuat. B* 61, 75, 1999.
128. C. L. Britton, R. L. Jones, P. I. Oden, Z. Hu, R. J. Warmack, S. F. Smith, W. L. Bryan, J. M. Rochelle, Multiple-input microcantilever sensors, *Ultramicroscopy* 82, 17, 2000.

129. T. Thundat, G. Y. Chen, R. J. Warmack, D. P. Allison, E. A. Wachter, Vapor detection using resonating microcantilevers, *Anal. Chem.* 67, 519, 1995.
130. A. Boisen, J. Thaysen, H. Jensenius, O. Hansen, Environmental sensors based on micromachined cantilevers with integrated read-out, *Ultramicroscopy* 82, 11, 2000.
131. Genki Yoshikawa, Hans-Peter Lang, Terunobu Akiyama, Laure Aeschimann, Urs Staufer, Peter Vettiger, Masakazu Aono, Toshio Sakura,i, Christoph Gerber, Sub-ppm detection of vapors using piezoresistive microcantilever array sensors, *Nanotechnology* 20, 015501, 2009.
132. L. A. Pinnaduwage, V. Boiadjiev, J. E. Hawk, T. Thundat, Sensitive detection of plastic explosives with self-assembled monolayer-coated microcantilevers, *Appl. Phys. Lett.* 83, 1471, 2003.
133. G. Zuo, X. Li, Z. Zhang, T. Yang, Y. Wang, Z. Cheng, S. Feng, Dual-SAM functionalization on integrated cantilevers for specific trace-explosive sensing and non-specific adsorption suppression, *Nanotechnology* 18, 255501, 2007.
134. Y. Chen, P. Xu, X. Li, Self-assembling siloxane bilayer directly on SiO_2 surface of microcantilevers for long-term highly repeatable sensing to trace explosives, *Nanotechnology* 21, 265501, 2010.
135. J. R. Barnes, R. J. Stephenson, M. E. Welland, C. Gerber, J. K. Gimzewski, Photothermal spectroscopy with femtojoule sensitivity using a micromechanical device, *Nature* 372, 79, 1994.
136. P. G. Datskos, S. Rajic, M. J. Sepaniak, N. Lavrik, C. A. Tipple, L. R. Senesac, I. Datskou, Chemical detection based on adsorption-induced and photoinduced stresses in microelectromechanical systems devices, *J. Vac. Sci. Technol. B* 19, 1173, 2001.
137. A. R. Krause, C. Van Neste, L. Senesac, T. Thundat, E. Finot, Trace explosive detection using photothermal deflection spectroscopy, *J. Appl. Phys.* 103, 094906, 2008.
138. D. C. Yi, A. Greve, J. H. Hales, L. R. Senesac, Z. J. Davis, D. M. Nicholson, A. Boisen, T. Thundat, Detection of adsorbed explosive molecules using thermal response of suspended microfabricated bridges, *Appl. Phys. Lett.* 93, 154102, 2008.
139. L. R. Senesac, D. Yi, A. Greve, J. H. Hales, Z. J. Davis, D. M. Nicholson, A. Boisen, T. Thundat, Micro-differential thermal analysis detection of adsorbed explosive molecules using microfabricated bridges, *Rev. Sci. Instrum.* 80, 35102, 2009.
140. A. Greve, J. Olsen, N. Privorotskaya, L. Senesac, T. Thundat, W. P. King, A. Boisen, Microcalorimetric sensor for vapor phase explosive detection with optimized heat profile, *Microelectron. Eng.* 87, 696, 2010.
141. G. Blagoi, S. Keller, A. Johansson, A. Boisen, M. Dufva, Functionalization of SU-8 photoresist surfaces with IgG proteins, *Appl. Surf. Sci.* 255, 2896, 2008.
142. B. Ilic, D. Czaplewski, M. Zalalutdinov, H. G. Craighead, P. Neuzil, C. Campagnolo, C. Batt, Single cell detection with micromechanical oscillators, *J. Vac. Sci. Technol. B* 19, 2825, 2001.
143. B. L. Weeks, J. Camarero, A. Noy, A. E. Miller, L. Stanker, J. J. De Yoreo, A microcantilever-based pathogen detector, *Scanning* 25, 297, 2003.
144. G. A. Campbell, R. Mutharasan, Detection of pathogen *Escherichia coli* O157: H7 using self-excited PZT-glass microcantilevers, *Biosens. Bioelectron.* 21, 462, 2005.
145. Gary A. Baker, Ramya Desikan, Thomas Thundat, Label-free sugar detection using phenylboronic acid-functionalized piezoresistive microcantilevers, *Anal. Chem.* 80, 4860, 2008.
146. A. Subramanian, P. I. Oden, S. J. Kennel, K. B. Jacobson, R. J. Warmack, T. Thundat, M. J. Doktycz, Glucose biosensing using an enzyme-coated microcantilever, *Appl. Phys. Lett.* 81, 385, 2002.
147. R. Raiteri, G. Nelles, H. J. Butt, W. Knoll, P. Skladal, Sensing of biological substances based on the bending of microfabricated cantilevers, *Sens. Actuat. B* 61, 213, 1999.

148. A. M. Moulin, SJ O'Shea, M. E. Welland, Microcantilever-based biosensors, *Ultramicroscopy* 82, 23, 2000.
149. J. Fritz, M. K. Baller, H. P. Lang, H. Rothuizen, P. Vettiger, E. Meyer, H-J G¨untherodt, C. Gerber, J. K. Gimzewski, Translating biomolecular recognition into nanomechanics, *Science* 288, 316, 2000.
150. R. Raiteri, M. Grattarola, H. J. Butt, P. Skladal, Micromechanical cantilever-based biosensors, *Sens. Actuat. B* 79, 115, 2001.
151. J. Zhang, H. P. Lang, F. Huber, A. Bietsch, W. Grange, U. Certa, R. McKendry, H. J. Guntgerodt, M. Hegner, C. Gerber, Rapid and label-free nanomechanical detection of biomarker transcripts in human RNA, *Nat. Nanotechnol.* 1, 214, 2006.
152. T. Maddanimath, I. S. Mulla, S. R. Sainkar, K. Vijayamohanan, K. I. Shaikh, A. S. Patil, S. P. Vernekar, Humidity sensing properties of surface functionalize poly-ethylene and polypropylene films, *Sens. Actuat. B* 81, 141, 2002.
153. S. Jain, S. Chakane, A. B. Samui, V. N. Krishnamurthy, S. V. Bhoraskar, Humiditysensing with weak acid-doped polyaniline and its composites, *Sens. Actuat. B* 96, 124, 2003.
154. T. Nemec, Monitoring of moisture transport in building materials by neutronradiography, in: *7th European Conference on Non-Destructive Testing*, p. 26, ISBN:87-986898, 1998.
155. J. Liu, M. Agarwal, K. Varahramyan, S. B. Ernest IV, W. D. Hodo, Polymer-based microsensor for soil moisture measurement, *Sens. Actuat. B* 129, 599, 2008.
156. T. Jackson, K. Mansfield, M. Saafi, T. Colman, P. Romine, Measuring soil temperature and moisture using wireless MEMS sensors, *Measurement* 41, 381, 2008.
157. S. Patil, A. Adhikari, M. Shojaei Baghini, V. R. Rao, An ultra-sensitive piezoresistive polymer nano-composite microcantilever platform for humidity and soil moisture detection, *Sens. Actuat. B* 203, 165, 2014.
158. N. S. Hudak, G. G. Amatucci, Small-scale energy harvesting through thermoelectric, vibration, and radiofrequency power conversion, *J. Appl. Phys.* 103, 101301, 2008.
159. C. B. Williams, R. B. Yates, Analysis of a micro-electric generator for microsystems, *Sens. Actuat. A* 52, 8–11, 1996.
160. R. Amirtharajah, A. P. Chandrakasan, Self-powered signal processing using vibration-based power generation, *IEEE J. Solid State Circuits* 33, 687–695, 1998.
161. S. Meninger, J. O. Mur-Miranda, R. Amirtharajah, A. P. Chandrakasan, J. H. Lang, Vibration-to-electric energy conversion, *IEEE Trans. Very Large Scale Integr. VLSI Syst.* 9 (1), 64–76, 2001.
162. S. Roundy, P. K. Wright, J. Rabaey, A study of low-level vibrations as a power source for wireless sensor nodes, *Comput. Commun.* 26, 1131–1144, 2003.
163. P. Glynne-Jones *et al.*, Towards a piezoelectric vibration powered microgenerator, *IEEE Sci. Meas. Technol.* 148 (2), 68–72, 2001.
164. S. Roundy, E. S. Leland, J. Baker, E. Carleton, E. Reilly, E. Lai, B. Otis, J. M. Rabaey, P. K. Wright, V. Sundararajan, Improving power output for vibration-based energy scavengers, *IEEE Pervasive Compt.* 4 (1), 28–36, 2005
165. Hua-Bin Fang, Jing-Quan Liu, Zheng-Yi Xu, Lu Dong, Li Wang, Di Chen, Bing-Chu Cai, Yue Liu, Fabrication and performance of MEMS-based piezoelectric power generator for vibration energy harvesting, *Microelectron. J.* 37, 1280–1284, 2006.
166. Dongna Shena, Jung-Hyun Park, Joo Hyon Noh, Song-Yul Choe, Seung-Hyun Kim, Howard C. Wikle III, Dong-Joo Kim, Micromachined PZT cantilever based on SOI structure for low frequency vibration energy harvesting, *Sens. Actuat. A* 154, 103–108, 2009.
167. P. Muralt, M. Marzencki, B. Belgacem, F. Calame, S. Basrour, Vibration energy harvesting with PZT micro device, *Procedia Chem.* 1, 1191–1194, 2009.

168. R. Elfrink, T. M. Kamel, M. Goedbloed, S. Matova, D. Hohlfeld, Y van Andel, R van Schaijk, Vibration energy harvesting with aluminum nitride-based piezoelectric devices, *J. Micromech. Microeng.* 19, 094005, 2009.
169. R. K. Sood, Piezoelectric micro power generator (PMPG): a MEMS based energy scavenger, MIT dissertation, 2003.
170. K. Prashanthi, M. Naresh, V. Seena, T. Thundat, V. Ramgopal Rao, A novel photo-plastic piezoelectric nanocomposite for mems applications, *(IEEE/ASME) J. Microelectromech. Sys. (J-MEMS)* 21 (2), 259, 2012.
171. K. Manoj, S. Chandrashekhar, P. Pankaj, K. P. R. Prashanthi, Apte, V. Ramgopal Rao, Photopattenable nano-composite (SU-8/ZnO) thin films for piezo-electric applications, *Appl. Phys. Lett.* 101 (10), 104102, 2012.
172. J. Hagerty, F. Helmbrecht, W. McCalpin, R. Zane, Z. B. Popovic, Recycling ambient microwave energy with broad-band rectenna arrays, *IEEE Trans. Microwave Theory Tech.* 52(3), 1014, 2004.
173. A. Cuadras, M. Gasulla, V. Ferrari, Thermal energy harvesting through pyroelectricity, Sens, Actuat. A. Phys. 158, 132, 2010.
174. J. Carlson Eric, Strunz Kai, P. Otis Brian, A 20 mV input boost converter with efficient digital control for thermoelectric energy harvesting, IEEE J. Solid State Circuits 45(4), 741, 2010.

12

CMOS MEMS Integration

Thejas and Navakanta Bhat*

Department of Electrical Communication Engineering, Indian Institute of Science, Centre for Nano Science and Engineering (CeNSE), Bangalore, India

Abstract

The inherent challenges faced in CMOS–MEMS integration are elaborated. The possibilities of integration at board level and chip level are discussed. Various circuit architectures popularly used for capacitance detection are listed with a detailed comparison in terms of their merits and demerits. The advantage of continuous time voltage (CTV) scheme for capacitance sensing is shown through a sensitivity of 40 mV/fF, using board-level integration. The same architecture is also implemented as an application-specific integrated circuit (ASIC) solution. Op Amp performance optimization, parameterized circuit tuning through on-chip clock selection, capacitance trimming, bandwidth adjustment, and gain customization features are introduced from an ASIC tunablity stand point. It is shown that the post-fabrication mismatch correction, through various capacitance trims and voltage trims, becomes very essential. Simple packaging techniques for ASIC MEMS interface are proposed. Sensitivity estimates (90 mV/g) through shaker table tests are presented to illustrate the methodologies used in testing/qualifying inertial sensors. Device reliability issues in ASIC MEMS devices are elucidated through possible failure mechanisms. The electrostatic discharge (ESD)-related failures in MEMS devices are also highlighted.

Keywords: CMOS, ASIC, MEMS, CTV, inertial sensing, multichip module, capacitance sensing, electrical reliability, trim capacitance

12.1 Introduction

MEMS devices are widely used in the field of sensing. A wide variety of MEMS devices which span the sensor spectrum include accelerometer, gyroscope, vibrating body Field Effect Transistor (FET), gas sensors, and the like. The displacement sensing mechanism in a broad majority of the MEMS sensors is based on capacitance detection although piezo-resistive, piezo-electric, thermal-based sensors have their due merits. The capacitance detection mechanism has merits in terms of its integration ease with electronics, immunity to thermal variations, ease of fabrication, low-noise floor, reduced leakage, and low-power budget. There is an ever-increasing need for capacitive displacement sensors to respond to changes in nanometer (nm) range. Micro-g accelerometers,

**Corresponding author*: navakant@ece.iisc.ernet.in

Atul Tiwari and Baldev Raj (eds.), Materials and Failures in MEMS and NEMS, (361–380)
© 2015 Scrivener Publishing LLC

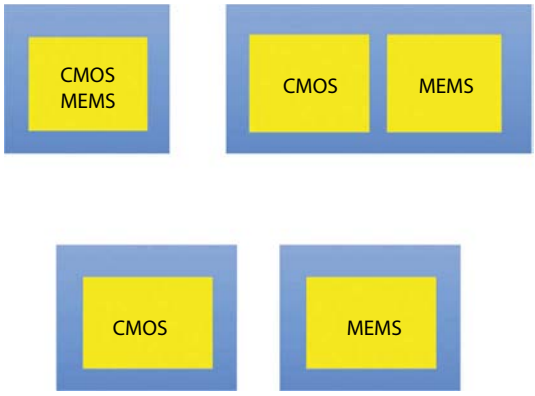

Figure 12.1 Complementary Metal Oxide Semiconductor (CMOS)–MEMS integration options.

milli-deg gyroscope have displacements in nanometer range and the equivalent capacitance change is in the range of femto and atto farads.

In case of nano-electromechanical devices, the equivalent capacitance for the nanometer displacement would be in zepto farads. Capacitance detection in this case would be challenging as the signal-to-noise ratio (SNR) would be very low. Most MEMS sensors are predominantly capacitive in nature and are based on either charge integration, switched capacitor, or sigma delta modulation techniques. These techniques potentially address capacitance values up to a range of few hundred atto farads. The atto-to-zepto-farad regime is extremely challenging with reports of 7 zF over 1 Hz bandwidth reported in Ref. [1] based on complex averaging technique.

There can be three different ways of integrating a MEMS sensor with electronics interface circuit as illustrated in Figure 12.1. While MEMS process technology makes use of similar set of basic semiconductor processes used for CMOS electronics, the exact details of processes are quite different. In most of the cases, integrating MEMS and CMOS electronics on a single die in the same process flow and the fab (Figure 12.1a) results in very low process yield. Hence, typically two dice-single-package (Figure 12.1b) or two-package solution (Figure 12.1c) is followed to obtain high yield, by decoupling the process constraints of MEMS and CMOS. Two dice with three-dimensional package integration on a single package can achieve the same form factor as single die implementation.

12.2 State-of-the-Art inertial Sensor

MEMS inertial sensors are dominating the consumer market with ever-increasing complexity in their design. The degrees of freedom (DOF) offered by these devices has increased from the initial 1 DOF to 6 DOF which comprises of 3-DOF MEMS accelerometer plus 3-DOF gyroscope. The offered range and sensitivity trade-offs are summarized in Table 12.1 specific to sensors made by Analog Devices [2]. The best sensitivity accuracy is about 210 milli-g as in device ADIS16210 over a 3 db bandwidth of 50 Hz. The noise floor increases proportionally with the device bandwidth. The

Table 12.1. Compilation of MEMS inertial sensors and their performance metrics.

Accelerometers										
Part #	**# of axes**	**Accelerometer range in g ± (max)**	**MEMS sensitivity (typ)**	**–3 dB bandwidth (typ)**	**Sensitivity accuracy**	**MEMS output type**	**Noise density**	**Supply**	**Supply current**	**Temp. range**
		(g)		**(Hz)**			**(ug/ sqrt(Hz)**		**(mA)**	
ADIS16210		± 1.7		50 Hz	0.21	SPI	190	3.15–3.6	18	–40 to +85
ADIS16223		± 70	4.768 mg/LSB	14.25 KHz	5	SPI	5000	3.15–3.6	43	–40 to +85
ADXL001	1	± 70	16 mV/g (±70 g)	22 KHz		Analog	4000	3.135–6	5	–40 to +125
ADXL78	1	± 70	27 mV/g	400	5	Analog	1800	4.75–5.25	1.3	–40 to +105
ADXL193	1	± 250	8 mV/g	0.4 kHz	5	Analog	5000	4.75–5.25	1.5	–40 to +125
ADXL180	1	50–500	0.125 g/LSB (50 g)	800		Digital		5–14.5	7.7	–40 to +125
ADXL103	1	± 1.7, ± 18, ± 5	1000 mV/g	2500	4	Analog	110	3–6	0.7	–40 to +125
ADXL213	2	± 1.2	30 %/g	2500	10	PWM	160	3–6	0.7	–40 to +85
ADXL203	2	± 1.7, ± 18, ± 5	1000 mV/g	2500	4	Analog	110	3–6	0.7	–40 to +125
ADXL278	2	± 70	27 mV/g	400	5	Analog	1800	4.75–5.25	2.2	–40 to +105

aforementioned sensors from Analog Devices are mostly integrated with the CMOS process flow. Invensense accelerometers found in the MultiChipModule (MCM) [3] are three axes in nature and support a separate proof mass for each axis of sensing. The sensor has a sigma delta ADC for each axis. The detectable acceleration range in these sensors is ±2, ±4, ±8, and ±16g. The noise power spectral density in these devices is 300mg/$\sqrt{Hz}$. Robert Bosch SMB227 [4] is a dual-axis accelerometer with measurement range in ±3.277g and supports a digital output. These accelerometers are primarily targeted for vehicle dynamics control. Micro-g accelerometer with surface and bulk micro-machining is reported with a measured sensitivity of 2 pF/g [5]. The reported noise floor in this ref is 0.16 mg/$\sqrt{Hz}$. The axis of sensing is in the z-direction with the wafer thickness utilized entirely to enhance the mechanical sensitivity due to mass enhancement. Table 12.1 gives a summary of various accelerometers and their performance metrics.

12.2.1 Hybrid Integration-Based Sensors

The hybrid integration concept has a wire-bonded MEMS device onto a CMOS chip as illustrated in Figure 12.2. Principle of capacitance detection is carried out using an application-specific integrated circuit (ASIC) which converts the charge stored on the MEMS capacitor to voltage or current. The popular ASICs which convert capacitance to voltage are MS3110, AD7747. These ASICs support a generic sensor interface and can be interfaced onto most MEMS devices. MS3110 has an operating bandwidth up to 10 kHz and a reported sensitivity of 300 aF/$\sqrt{Hz}$. The MS3110 [6] circuit block diagram is as in Figure 12.3. The clock frequency of the circuit is 100 kHz and supports a minimum trimmable capacitance of 19 fF on each side of the capacitance bank for offset correction. Charge integration is carried out for a dynamic change in input capacitance values from the MEMS sensor which is then low-pass filtered and passed through a buffer circuit to produce an analog output voltage. Considering second-order low-pass filter as part of circuit architecture, the detectable capacitance in case of MS3110

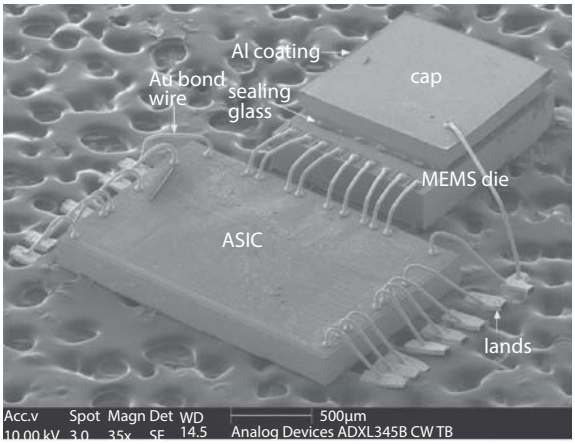

Figure 12.2 Die snap shot of Analog Devices Accelerometer (ADXL) hybrid interface.

considering a bandwidth of 100 Hz, is about 42 aF. Over a bandwidth of 10 kHz, the detectable capacitance limit is about 44 fF. The supply voltage fluctuation and thermal and random vibrations would influence the detectable capacitance limit further.

AD7747 [7] has a limited bandwidth of 70 Hz and supports a single-arm interface. The output noise floor is 11 aF/$\sqrt{Hz}$. The data sheet lists the resolution of this circuit as 20 aF. The accuracy of this ASIC listed as 10 fF and is based on 24-bit Σ-Δ capacitance to digital convertor technique. Here, the analog voltage is transformed into pulse frequencies as in Figure 12.4. Considering third order low-pass filter as part of circuit architecture, the detectable capacitance in case of AD7747 over a 100 Hz bandwidth, is about 112 aF. The supply voltage fluctuation, thermal and random vibrations would in influence the detectable capacitance limit further.

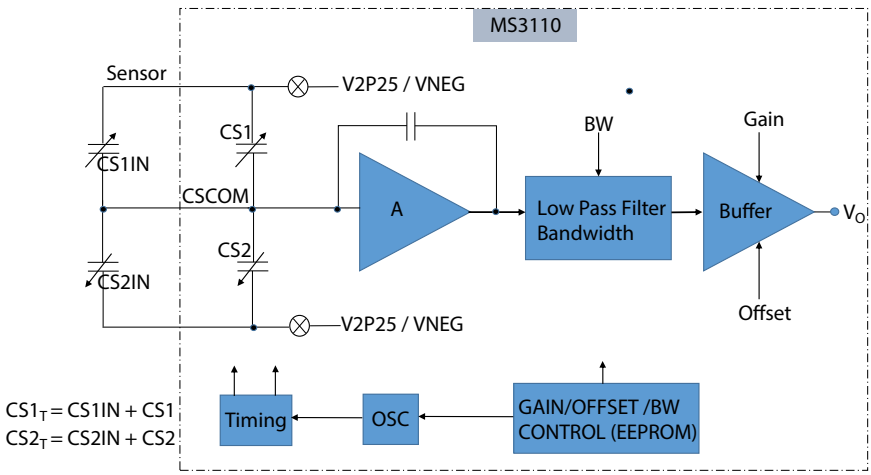

Figure 12.3 MS3110 capacitance sensor circuit block [6].

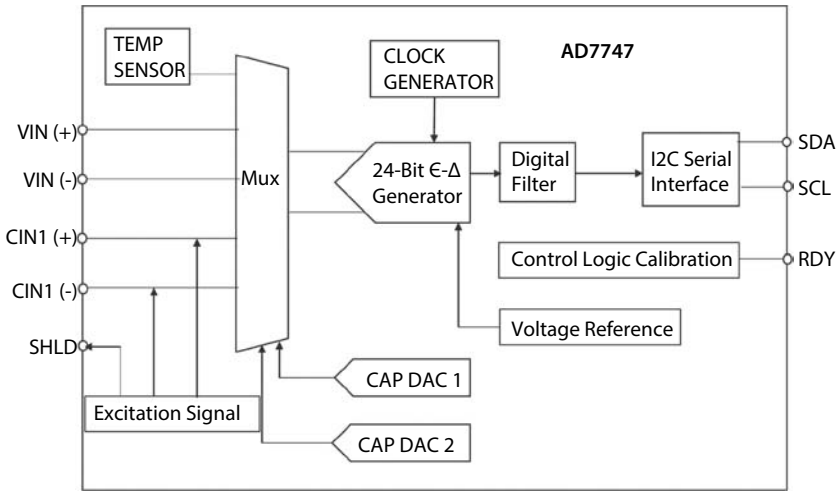

Figure 12.4 AD7747 capacitance sensor circuit block [7].

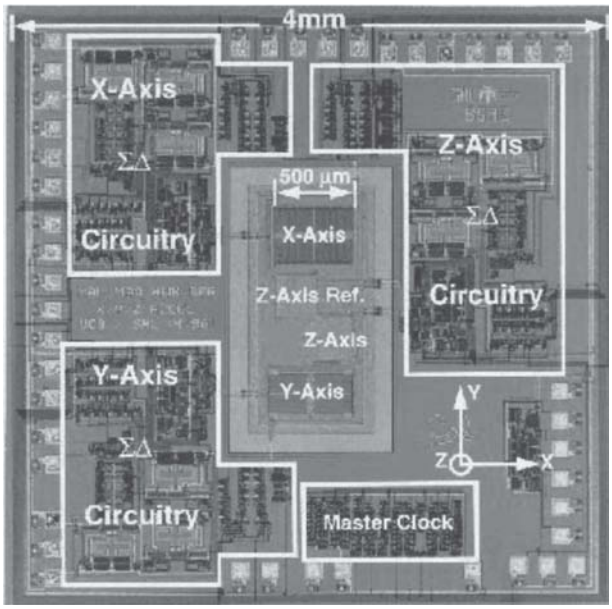

Figure 12.5 Three-axis accelerometer with sigma delta modulation [8].

12.2.2 Monolithic Integration-Based Sensors and Actuators

Analog devices and ST Microelectronics (STM) have a wide variety of MEMS inertial sensors in the market. Most of these sensors are based on Intra CMOS–MEMS fabrication (iMEMS) process techniques. Here, the sensor electronics is placed around the MEMS sensor, and there is a clear isolation between the MEMS and Bi-CMOS structures. A three-axis surface micro-machined sigma delta accelerometer using the iMEMS approach by authors [8] is shown in Figure 12.5. The on-chip electronics offers good parasitic and noise immunity when compared to the hybrid integration approach discussed in the earlier section. Figure 12.1 has a summarized reference to monolithic accelerometers by Analog Devices. While the advantage in terms of low parasitic and ease of integration with CMOS is an obvious merit, the sensitivity offered by these devices does not cater to milli-g or micro-g resolution.

12.3 Capacitance Sensing Techniques

The change of capacitance in a MEMS capacitive sensor is brought about either by the change in gap between the electrodes, by the change in electrode overlap area or by change in the relative permittivity of the dielectric between the plates. The goal of the signal conditioning CMOS electronics is to sense this capacitance change and to convert it to an equivalent voltage. The capacitance change produced by the MEMS sensor with respect to the physical variable being sensed, is very low. Hence, there is a need to develop signal conditioning circuit to convert finer capacitance variations to a measurable voltage signal. The sensitivity of the change in capacitance varies for

different devices like gyroscopes, accelerometers, microphones, and the like. The base capacitance ranges from 1 to 12 pF, with sensitivity requirements of 1 aF to 100 fF over a bandwidth requirement of up to 20 kHz. Numerous sensing methodologies and architectures are reported in literature for the purpose of capacitance sensing. These aspects are compared in the following sections.

Resonance Method: In this method, an Resistor Inductor Capacitor (RLC) tank circuit is driven to resonance. By measuring the resonant frequency and voltage, the value of the unknown capacitance can be estimated. Measurements using this method require several operating steps such as adjusting the resonance frequency, detecting the resonance condition, and calculating the unknown capacitance and loss. The first two steps are often done manually, and therefore, this method is not suitable for continuously monitoring a physical variable and hence currently is not used in online capacitance transducers.

Oscillator Method: In this method, the oscillation frequency of an Inductor Capacitor (LC) or Resistor Capacitor (RC) oscillator depends on the unknown capacitance C. The frequency is measured, either by using a digital counter to obtain a digital output, or by using a frequency-to-voltage converter to obtain an analog output, and then used to determine the unknown capacitance. The RC oscillation method is the most popular method used in general purpose capacitance meters. Generally, these circuits suffer from some common drawbacks—poor immunity to strays, poor sensitivity to small capacitance changes, and poor frequency stability. Therefore, the RC oscillation method generally is not suitable for applications requiring high resolution.

Charge Discharge Method: This method is based on charging time differences between two capacitances. A charging mechanism is used to charge the capacitances: one of them is a reference capacitor, and the other is sensor capacitor. The voltage across the capacitances is compared with a reference voltage using comparators to obtain two time pulses. The difference between the time pulses is a measure of the capacitance change. The capacitors are then discharged and cycle referenced. The time pulses can be detected using a phase detector, and the resulting pulse width modulated wave can be converted to a proportional voltage. The capacitances can be either differential or single ended.

Modulation Demodulation Method: In this method, the two capacitances (differential capacitance) are excited by a carrier wave. The voltage across the capacitance is modulated by the change in capacitance. The modulated waveform can be demodulated, amplified, and passed through a low-pass filter to extract the change in capacitance as a change in voltage. This method is suitable for both high resolution and high bandwidth.

12.4 Capacitance Sensing Architectures

Capacitive sensing is based on motion-induced charge transfer. This charge transfer generates an AC voltage or an AC current. This leads to basically three architectures for capacitance sensing [9]. The three circuit architectures differ in the noise folding process, which has a great influence on overall noise performance.

Continuous Time (CT) Current Sensing: The trans-impedance amplifier (TIA)-based CT sensing is widely used in optical receivers for sensing photo current from photo diodes. In capacitive sensors, the charge transfer generates an AC current which can

be sensed by the TIA. The advantage of TIA architecture is that it provides a virtual ground and robust DC biasing at the sensing node in continuous time. However, it exhibits much high SNR loss because its frequency response is not flat. The TIA is inherently a differentiator and has high-pass frequency response. The high-frequency noise is amplified by the TIA and folded into the signal band. The CT current sensing has the worst noise performance of the three architectures.

Switched Capacitor Circuits: The switched-capacitor readout is the most widely used architecture for capacitive sensing [10]. The Switched Capacitor (SC) circuit provides a virtual ground and robust DC biasing at the sensing node so that the sensed signal is insensitive to parasitic capacitance and undesirable charging. However, despite its popularity, the SC circuit has much higher circuit noise as severe noise folding causes the output noise power to multiply. SC readout circuits have been used extensively in polysilicon MEMS processes. However, with the Metal Oxide Semiconductor (MOS) device size shrinking, the capacitance becomes smaller thus raising the kT/C noise. This added to noise folding has become a major limitation of sensor resolution.

Continuous Time Voltage (CTV) Sensing: It requires a biasing circuit to provide DC bias at the sensing node [10–12]. To avoid attenuating the signal, they must have very large resistance, orders of magnitude higher than the AC impedance of the sensor. With sinusoidal carrier signal, the demodulation in continuous time does not cause noise folding. However, generation of pure Sine wave on chip is much more difficult than generation of square wave. The capacitive feedback continuous-time voltage sensing architecture does not suffer from the amplification of high-frequency noise and is the architecture which has the least-noise floor. The SNR decreases rapidly with increasing bandwidth in the SC charging sensing and CT current sensing. Severe noise folding is inevitable for SC and TIA circuits. The continuous-time voltage sensing approach has the best noise performance.

12.5 Continuous Time Voltage Sensing Circuit

The circuit of the capacitance to voltage converter based on CTV as shown in Figure 12.6 consists of an input stage which acts as Amplitude Modulator (AM) modulator, followed by a demodulating stage and the final instrumentation amplifier stage which provides the gain, as well as rejects common mode signals. The capacitance change is amplitude modulated using a high-frequency carrier and later demodulated and filtered out to obtain a DC voltage. Here, a high-frequency carrier acts as a chopper and reduces the 1/f noise. The input carrier is fed to the common terminal of the differential capacitance to be sensed (C+, C–, and common represent a typical MEMS differential sensor). Unlike in conventional chopper-stabilized circuits, there is no requirement of providing perfect out of phase pulse waveforms to C+ and C– terminals. This simplifies the input stage and also results in better matching and lower noise.

A simple implementation of this circuit can be realized through discrete components on a printed circuit board. This is illustrated through an example. A low-noise precision amplifier OP27GP and instrumentation amplifier INA129 were used. Fast switching diode 1N4148 was chosen to demodulate using envelope detection. The circuit implementation was done on a Printed Circuit Board (PCB) board with 0.2 mm

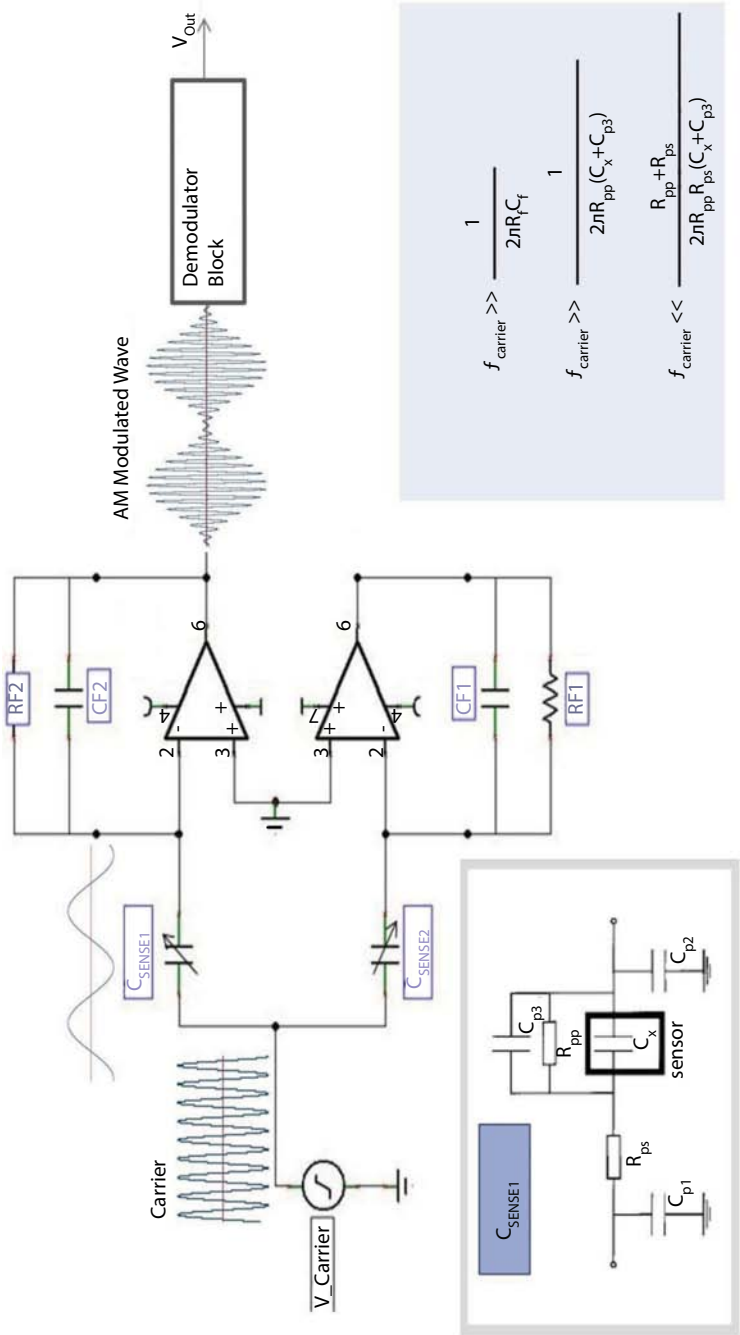

Figure 12.6 CTV-based sensing circuit.

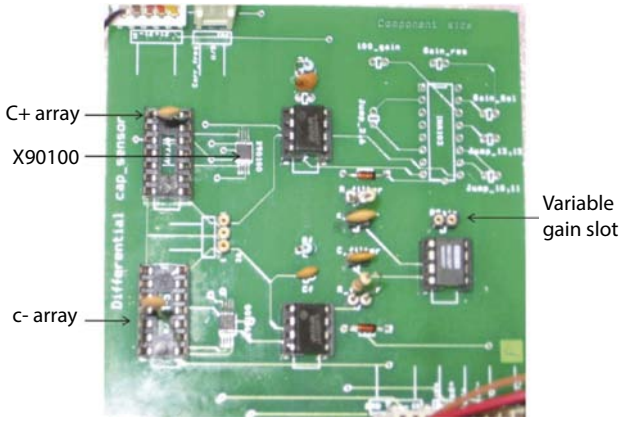

Figure 12.7 PCB circuit board using discrete components.

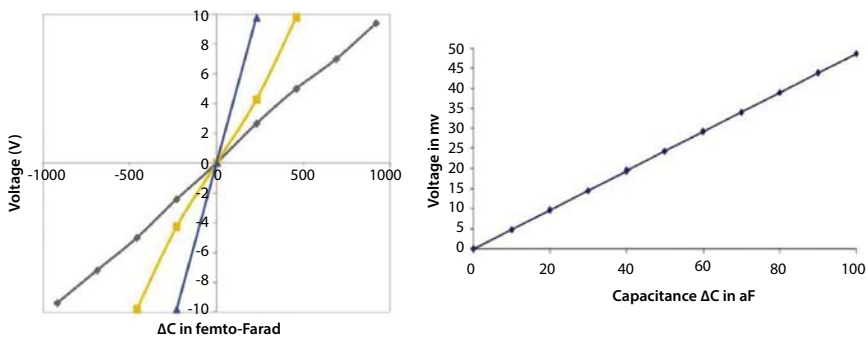

Figure 12.8 (a) Measure response for static capacitance change and (b) simulated response.

track width. Care was taken to ensure that equal track lengths were maintained from the C+ and C– arrays to the input stage. A commercially available digitally programmable capacitance test structure X90100 was also integrated on the PCB which has a minimum step size of 230 fF and a base value of 7 pF. Two different X90100 ICs were connected in parallel to C+ and C– as shown in Figure 12.7.

Figure 12.8(a) represents the graph for a static capacitance variation with the gain adjusted such that the maximum capacitance detection corresponded to an output voltage of 10 Volts. ΔC was varied using the digitally programmable capacitance X90100 in steps of 230 fF. The maximum sensitivity of the circuit obtained is 40 mV/fF. Higher sensitivity can be obtained by increasing the gain, but practical testing is limited, due to non-availability of smaller values of ΔC. Simulation for lower values of ΔC at higher gains was carried out using circuit simulation with spice macro models provided by the vendors. Figure 12.8(b) represents the graph for simulation, for a static capacitance variation in steps of 10 aF, indicating that the circuit is capable of detecting capacitance change down to atto Farad range.

Dynamic change in capacitance was achieved by cyclically varying X90100 digitally programmable capacitance. The response of the circuit for a variation in input

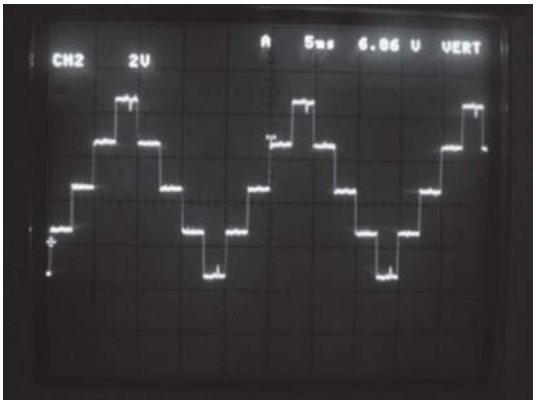

Figure 12.9 Dynamic response of the sensor circuit.

capacitance at a cycle rate of 57 Hz is as seen in Figure 12.9. Here, each step corresponds to 230 fF.

12.6 CMOS ASIC Design

The ASIC design was carried out for two different versions of the sensor for a similar circuit architecture on AMS 0.35-μm CMOS technology node. The first version has on chip demodulator and active filter, and the second version has off chip demodulator and passive filter. The ASIC has various on chip trims for interface customization for a wide variety of sensors, self-test, and calibration. The block diagram of the capacitance sensor along with a die snapshot is given in Figure 12.10.

The circuit consists of a symmetrical input stage which acts as an AM modulator, followed by a demodulator and a symmetrical three-pole low-pass filter. The final stage is an instrumentation amplifier which provides the requisite gain. CS+, CS–, and CMN are the terminals used for interfacing the input MEMS sensor. The CMN terminal is connected to an on chip high-frequency clock for modulation. This arrangement eliminates the need of two perfectly out of phase clocks to be fed to CS+ and CS– terminals. Since the parasitic capacitances come across the voltage source, they have virtually no effect on circuit performance. The feedback resistance R_f provides the necessary DC bias current and along with the feedback capacitor C_f, forms a high-pass filter at the input stage. To ensure that the carrier voltage remains unaffected $f_{carrier} \gg 1/(2\pi R_f C_f)$. The output voltage, when there is no input at the sensor is set at mid rail, i.e., 1.65 V. Positive or negative input transitions are reflected at the output by output voltage moving toward either positive rail or ground. The overall simplified transfer function of the circuit is given by

$$V_{out} = 1.65 + V_{carrier} \times G \times \frac{\Delta C}{C_f} \times \cos\left(2\pi f_{signal} t\right)$$

where $V_{carrier}$ is the excitation voltage, G is the gain of the instrumentation amplifier, ΔC is the change in capacitance of the sensor, and f_{signal} is the rate of change of the capacitance.

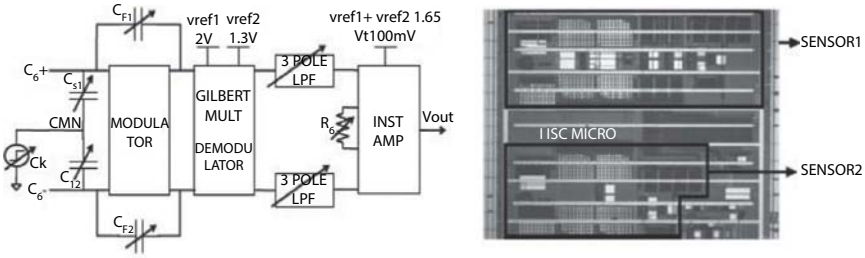

Figure 12.10 (a) CTV architecture and (b) die photograph on 0.35 mm CMOS.

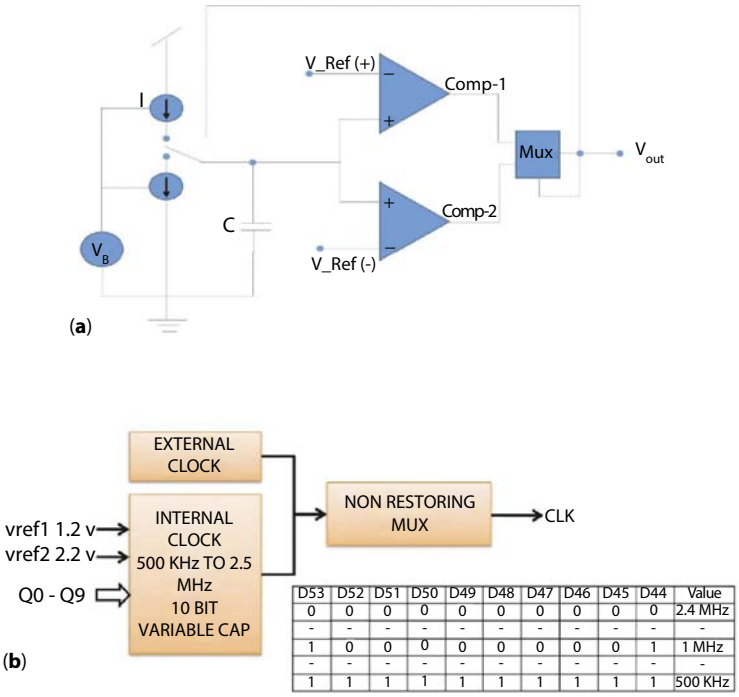

D53	D52	D51	D50	D49	D48	D47	D46	D45	D44	Value
0	0	0	0	0	0	0	0	0	0	2.4 MHz
-	-	-	-	-	-	-	-	-	-	-
1	0	0	0	0	0	0	0	0	1	1 MHz
-	-	-	-	-	-	-	-	-	-	-
1	1	1	1	1	1	1	1	1	1	500 KHz

Figure 12.11 (a) Clock generation circuit and (b) frequency programming sequence.

The sensor has a programmable facility for on chip clock generation as well as a facility to select external clock as shown in Figure 12.11. The external clock enables testing and operation with either a square or a sinusoidal clock and also offers redundancy. The on chip clock generates a square wave and is programmable in 10 bits from 500 kHz to 2.5 MHz. The higher the clock frequency, the lower would be the 1/f noise and lesser the ripple at the output. The internal clock generation is based on the principle of charge and discharge of a 10-bit programmable capacitor against two reference voltages as shown in Figure 12.11.

This oscillator topology gives very low jitter. In this oscillator, the capacitor C is charged and discharged by a constant current I. At start-up, the voltage on the capacitor will be zero, and V_{out} will also be zero. Then the capacitor begins to charge with a

constant current I. Once the voltage on the capacitor reaches the value V_Ref (+), comparator-1 changes state and V_{out} becomes high. The capacitor begins to discharge by the same current I. The reference voltages V_Ref(+)=2.2 V and V_Ref(−)= 1.2 V. Once the capacitor voltage reaches the value V_Ref(−), comparator-2 changes state and capacitor starts charging again. Thus, the capacitor voltage is a triangular waveform between these two voltages with a slope of I/C. The expression for oscillation frequency is given by

$$f = \frac{I}{2C\left(V_{Ref}(+) - V_{Ref}(-)\right)}$$

In this design, the current I is obtained from an on chip programmable current reference, the reference voltages are derived on chip and C is a 10-bit programmable capacitance which is varied to obtain the desired clock frequency. Beta multiplier (Figure 12.12) circuit is used to generate current and bias references used in the ASIC sub-blocks. The targeted current reference is 20 μA with 25% variation chosen based through bit selections. The reference current is given by

$$I = \frac{2}{R^2 \beta_4}\left(1 - \frac{1}{\sqrt{K}}\right)^2$$

Here, $\beta_4 = \mu_n C_{ox} W_4/L_4$ for M4 transistor. The width ratios between M3 and M4 is K = 4, to make it a constant g_m circuit, which is independent of process variations. The reference current has programmability option through four control bits. The trim resistance is realized on-chip using poly-resistance in 0.35-μm CMOS technology. The 4-bit control offers current source range from 15 to 25 μA. The current reference block comprises of M1, M2, M3, and M4. When the gates of M1, M2 FETs are at V_{DD} and the gates of M3, M4 gates at GND the current reference circuit enters a lock state where it can no longer act as a constant current source. To prevent this, lockup-state start-up FETs SU1, SU2, and SU3 are used.

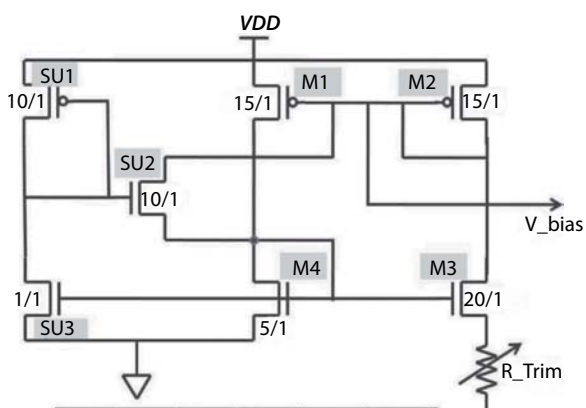

D42	D41	D40	D39	D38	Value
1	0	0	0	0	-25 %
1	1	0	0	0	20μA
1	1	1	1	1	+25 %

Figure 12.12 Beta multiplier circuit for reference current generation.

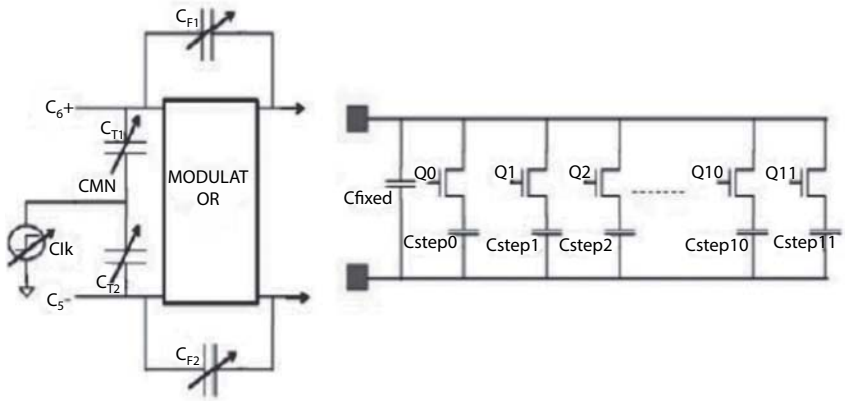

Figure 12.13 Input stage with trim capacitors.

During the lockup state, the gate bias of the start-up circuit FET SU1 (which is either at V_{DD} or at $V_{DD}-V_{thp}$ during the undesirable state) would turn on SU2. The SU2 upon getting weakly turned on allows a current path between the gate of M1, M2 and the gate of M3, M4. Since there is a V_{DD} to ground latch up condition initially between M2 (M1) and M4 (M3) to begin with, the current leaked through SU2 establishes a path and sets the current reference circuit out of the latch-up condition. This would bring back the current reference circuit in action in case of latch-up.

The input stage (Figure 12.13) has CS+ , CS–, and CMN terminals where the input sensor is connected. A programmable on chip clock is connected to the CMN terminal. The input stage has various trims for interface customization depending on the base capacitance of the input MEMS sensor. The various capacitance trims and the schematic illustrating the principle for capacitance trim are shown in Figure 12.13.

CT1 and CT2 are trim capacitances for the two differential arms which are used for self test of the sensor, for tuning the interface for accepting different MEMS sensors and for correcting offset pad capacitance variations. These banks have a 12-bit trim with a range up to 12.5 pF in steps of 3.125 fF.

CF1 and CF2 are feedback capacitances for the two differential arms which are used for self test, tuning of the sensor as per nominal capacitance of the MEMS input sensor to achieve a unity gain transfer function for the input stage. These banks too have a 12-bit trim with a range up to 12.5 pF in steps of 3.125 fF.

Gilbert multiplier is used for demodulation of the amplitude-modulated signal from the input stage. The DC bias levels for the Gilbert multiplier are independently set on chip to enable isolation of DC levels from the input stage as illustrated in Figure 12.14. The output of the Gilbert multiplier is fully differential and fed to two separate three-pole programmable low-pass Bessel filters (Figure 12.15). The low-pass filters are 4-bit programmable up to 20 kHz, to enable bandwidth customization as per type of input MEMS sensor. The low-pass filters have fixed off chip capacitances and programmable on chip resistances R_A, R_B, and R_C.

The low-pass Bessel filters (Figure 12.16) have fixed off chip capacitances and programmable on chip poly resistances. The off-chip capacitance values of C_A, C_B, and C_C

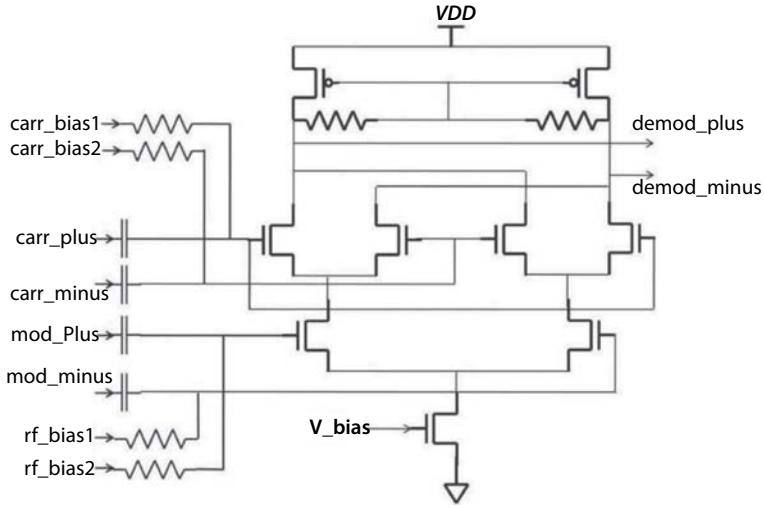

Figure 12.14 Differential Gilbert multiplier.

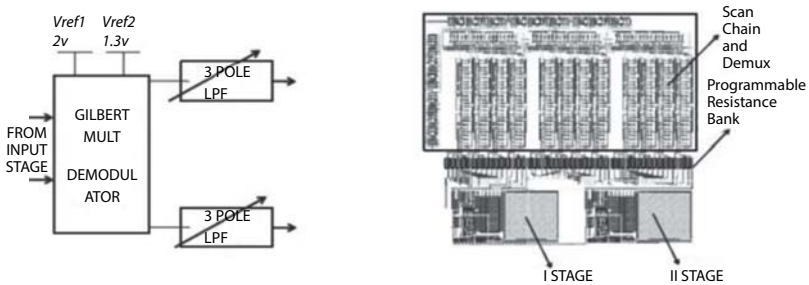

Figure 12.15 (a) Block diagram of Gilbert multiplier and (b) layout of three-pole low-pass filter.

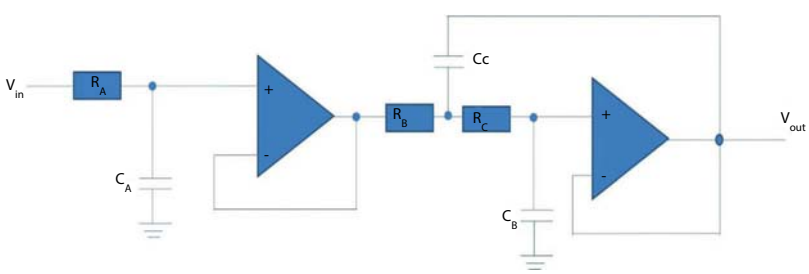

Figure 12.16 Circuit diagram of three-pole low-pass filter.

capacitances are 10, 15, and 39 nF, respectively. There is a separate resistance bank for each of the resistors. The resistance for each block is tapped between R_{top} and R_{bot}. The value of the resistance is selected by turning on the appropriate switch, to cut in desired value of resistance. Each of the depicted switches is an NMOS switch and gets its input from a 4 to 16 demultiplexer which is driven by the output of the scan chain.

The instrumentation amplifier shown in Figure 12.17 is the final stage of the CTV sensing scheme and offers low common mode noise. It is possible to select the gain either on chip or off chip and to trim V_{null} internally or externally. The resistance R_g of the amplification stage can be tuned on chip for achieving different gains ranging from 1 to 100 (4-bit control) as per the sensitivity and range requirements of the input MEMS sensor. An off-chip resistance can also be used to achieve higher gain values up to 1000.

The output voltage at null position of the sensor is required to be 1.65 V (mid rail). This null position can change due to process variations or sensor mismatches between the two differential arms. This offset variation can be corrected on chip by trimming the V_{nul}l voltage in steps of 3.5 mV. With the sensor output at 1.65 V initially, a mismatch tunablity of 100 mV (in fine steps of 3.5 mV) can be adjusted using a 6-bit trim.

The complementary input stage, the low-pass filters, and the final gain stage employing an instrumentation amplifier use operational amplifier (Op Amp) as sub blocks. The Op Amp has a standard design (Figure 12.18) with two stages along with a differential input stage and a miller compensated second gain stage with compensation capacitance of 2.5 pF. The key parameters of the Op Amp are summarized in Figure 12.18.

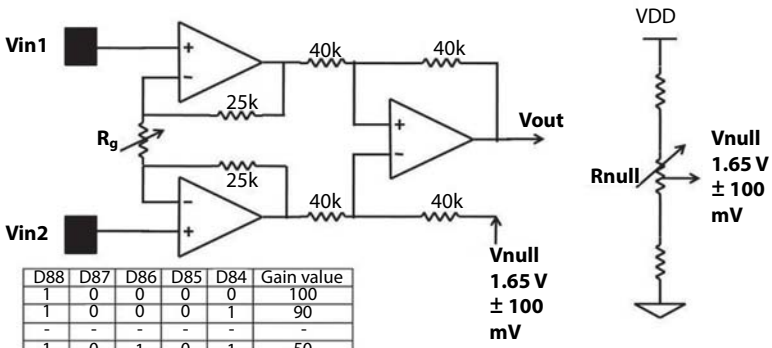

D88	D87	D86	D85	D84	Gain value
1	0	0	0	0	100
1	0	0	0	1	90
-	-	-	-	-	-
1	0	1	0	1	50
1	0	1	1	0	25
1	0	1	1	1	20
1	1	0	0	0	15
1	1	0	0	1	10
1	1	0	1	0	8
1	1	0	1	1	6
1	1	1	0	0	5
1	1	1	0	1	4
1	1	1	1	0	3
1	1	1	1	1	2

D114	D115	D116	D117	D118	D119	Value
0	0	0	0	0	0	1.65V - 100mV
0	1	1	1	1	1	1.65V - 3.5mV
1	0	0	0	0	0	1.65V
1	0	0	0	0	1	1.65V + 3.5mV
1	1	1	1	1	1	1.65V + 100mV

Figure 12.17 Instrumentation amplifier with gain and null control capabilities.

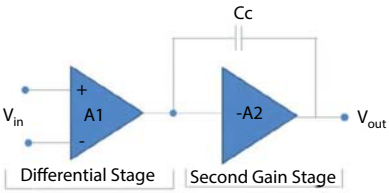

Parameter	Value
Gain	>90dB
Phase Margin	>70°
Unity Gain Bandwidth	>10MHz
I/P Offset Voltage	<2mV
Input Common Mode Range	0.7V-3.25V
Output Common Mode Range	0.05V-3.29V

Figure 12.18 Op Amp used in various circuit blocks, with a summary of key parameters.

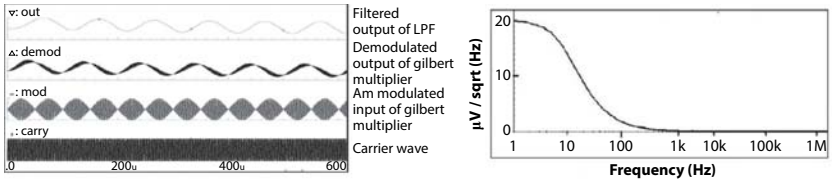

Figure 12.19 Simulated perfromance of capacitance sensing CMOS ASIC.

The CMOS ASIC output response, as simulated in cadence environment, is illustrated in Figure 12.19. The noise response over the frequency range of 1 MHz is also shown. The integrated noise over 100 kHz bandwidth is 80 µV.

12.7 Test Results of CMOS–MEMS Integration

The test results of Sensor 1 with synchronous demodulator, fabricated through AMS 0.35-mm CMOS technology, are detailed in the following. The capacitance bank of C_{T1}^{+} and C_{T2}^{-} are varied sequentially in steps of 12.5 fF to yield a ΔC of 12.5 fF for the self-test operation. The gain of the instrumentation amplifier was set at the minimal value of 2. The offset was seen to be stable at 1.651 Volts. The output response of the sensor for an internal on-chip capacitance variation and corresponding gains of 2, 5, and 10 is as shown in Figure 12.20. The ΔC variation is in steps of 12.5 fF with the clock frequency at 500 kHz, and the low-pass filter bandwidth is limited to 500 Hz.

MEMS accelerometer was interfaced to check the response of the ASIC. The MEMS accelerometer interfaced is a displacement amplification compliant mechanism (DaCM) which amplifies mechanical displacements by a factor of 5 based on compliant action as in Ref. [12]. Packaging of this MEMS DaCM accelerometer was carried out using the PCB approach. The pads on the PCB were electroplated with gold with low surface roughness. The DaCM die was attached on the PCB using silver epoxy heated, and the combo was heated at 1000°C for 5 min. Wedge bonding was carried out subsequently to connect the DaCM pads to the electroplated pads on the PCB. The daughter card (DaCM accelerometer + PCB) is now connected to the capacitance sensing ASIC at the three terminals (C+, C–, and COM), as shown in Figure 12.21. The DaCM accelerometer had a measured sensitivity of 14 fF/g. The ASIC and the DaCM card was mounted on the shaker table. ST microelectronics-integrated MEMS accelerometer chip was also used to calibrate the shaker table and for providing feedback to prevent over-range oscillations on the shaker table.

The response of the CMOS–MEMS-integrated accelerometer for 400 mg acceleration at 20 Hz frequency is as shown in Figure 12.22. The integrated sensor was also evaluated for an acceleration range from 200 mg to 1.8 g (Figure 12.23). The device shows a fairly good linear response, with a sensitivity of 90 mV/g. For comparison purposes, MEMS accelerometer was also interfaced with an off the shelf universal capacitance sensor MS3110 ASIC over the same range of acceleration. The sensitivity in this case was 20 mV/g. It is clear that an optimized implementation of CMOS–MEMS integration is very essential to achieve high sensitivity, as per the needs of a given MEMS sensor design.

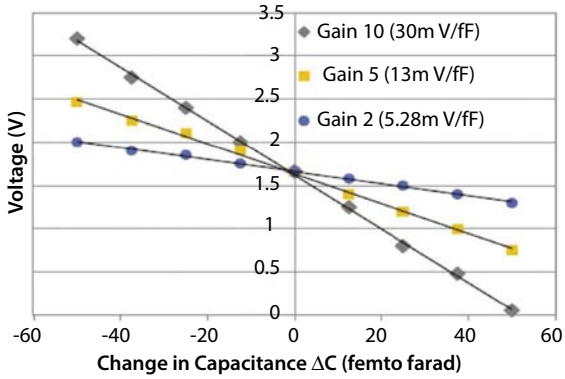

Figure 12.20 Measured results from 0.35-mm CMOS ASIC.

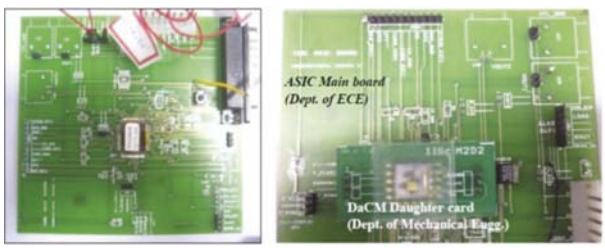

Figure 12.21 DaCM accelerometer daughter card mounted on CMOS ASIC test board.

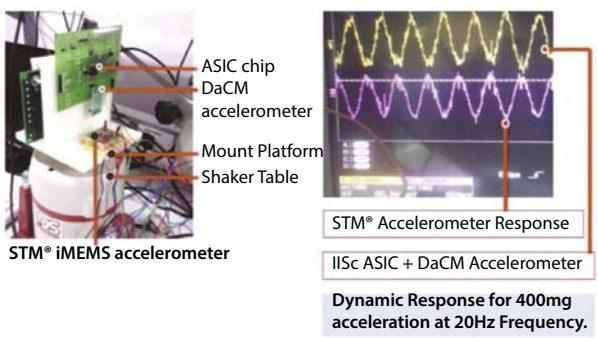

Figure 12.22 Dynamic response of CMOS–MEMS sensor at 20 Hz frequency.

12.8 Electrical Reliability Issues

The reliability and degradation of CMOS–MEMS device depend on electrical stress as well as mechanical stress. The device failure, in turn, is governed by either electrical or mechanical failure in an integrated CMOS–MEMS device. A case study of MEMS digital micromirror device has been reviewed very well in Ref. [13]. All the electrical degradation issues in CMOS circuits [14–15] are also relevant for CMOS–MEMS-integrated device. These include transistor reliability such as hot carrier reliability, time-dependent

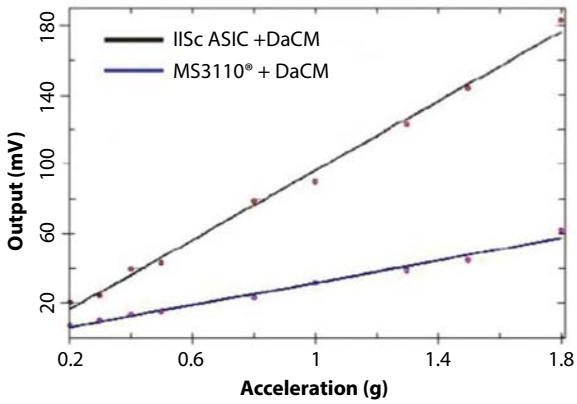

Product	Sensitivity
MS3110® + DaCM	20m V/g
IISc ASIC + DaCM	80m V/g

Figure 12.23 Performance comparison for a customized CMOS–MEMS integration versus a generic integration.

dielectric breakdown, electrostatic discharge (ESD), and interconnect reliability such as electromigration and stress migration. However, the electrical reliability issues could get worse, due to electrical to mechanical interface. For instance, the contact between electrical and mechanical components may wear out over time. This could also influence the noise immunity of the device, even before the catastrophic failure.

Unlike the state-of-the-art digital CMOS circuits made on 22-nm technology and operating at less than 1 V, the CMOS circuits for MEMS interface are typically made on larger dimensions and operate at higher voltages. As illustrated in the capacitance sensing circuit example, 0.35-mm CMOS circuits operate at 3.3 V/5 V supply to interface with MEMS device. Hence, the reliability issues are also very specific to a particular implementation of CMOS–MEMS integration.

The differential paths in the capacitance sensing circuit such as input-stage modulator (Figure 12.10) and instrumentation amplifier (Figure 12.17) should be perfectly balanced during in-use condition, to avoid offset-induced errors. However, the input transistors in the two paths could degrade at different rates, due to hot carrier injection into the gate dielectric. This is further aggravated due to large voltage switching at these transistors. The injected electrons get trapped in the gate dielectric and cause threshold voltage instability. Further, the hot carriers can also create additional trap states at the Si–SiO_2 interface and inside the bulk of the oxide. The different degradation rates at the input transistors can affect the sensitivity of the sensor device. The switching transients at the input-stage transistor can also affect the time-dependent dielectric breakdown, due to the enhanced wear out at high voltage.

The ESD reliability is a transient phenomenon of large discharge of electrical charge, accumulated over an insulating substrate, when it comes in contact with conducting

substrate, such as a silicon-integrated circuit chip. This large discharge results in very high voltages and currents which can destructively breakdown gate dielectric of MOSFETs, p–n junctions of a circuit or electrical interconnects. Typically, ESD is mitigated in CMOS circuits by designing input protection diodes, to bypass the circuitry of the chip. However, ESD protection for a MEMS device is still an emerging research area. The mechanical, suspended structures cannot be protected using conventional input protection diodes [16]. A severe ESD event can result in fusing of the suspended MEMS structure, pull-in instability of a suspended MEMS device. The ESD vulnerability can depend on a variety of MEMS device design parameters, and dictate new design trade-offs. For instance, a smaller air gap in MEMS structure would be desirable to achieve high capacitance value, for ease of measurement. However, smaller air gap also makes the structure more vulnerable to ESD failure, as the pull-in voltage has an inverse relationship with the air gap. Hence, there is a need for developing new insights in reliability aware MEMS design.

References

1. John A. Geen, Steven J. Sherman, John F. Chang, and Stephen R. Lewis, Single-chip surface micromachined integrated gyroscope with 50o/h Allan deviation. *IEEE Journal of Solid State Circuits*, Vol. 37, No. 12, pp. 1860–1866, 2002.
2. http://www.analog.com/en/mems-sensors/mems-accelerometers/products/index.html.
3. http://www.invensense.com/products/motion-tracking/3-axis/
4. http://www.bosch-semiconductors.de/en/ubk_semiconductors/homepage/homepage_1.html
5. N. Yazdi and K. Naja, An all-silicon single-wafer micro-g accelerometer with a combined surface and bulk micromachining process, *Journal of Microelectromechanical System*, Vol. 9, No. 4, pp. 544–550, 2000.
6. Irvine Sensors, MS3110 Datasheet.
7. Analog Devices, AD7747 Datasheet.
8. M. Lemkin, M. Ortiz, N. Wongkomet, B. Boser, and J. Smith, A 3-axis surface micromachined sigma-delta accelerometer, *Proceedings of ISSCC*, pp. 202–203, 1997.
9. Joost C. Lötters, Wouter Olthuis, Peter H. Veltink, A sensitive differential capacitance to voltage converter for sensor applications. *IEEE Transactions on Instrumentation and Measurement*, Vol. 48, No. 1, pp. 89–96, 1999.
10. R. Jacob Baker et al., *CMOS—Circuit Design, Layout and Simulation*, Prentice-Hall, India, 2002.
11. S. Khan, Thejas, G. K. Ananthasuresh, and N. Bhat, Design and characterization of a micromachined accelerometer with mechanical amplifier for intrusion detection. *Proceedings of ISSS*, Vol.3, pp. 1–5, 2011.
12. H. Xie and G.K. Fedder, Vertical comb-finger capacitive actuation and sensing for CMOS-MEMS. *Sensors Actuators A*, Vol. 95, No. 2–3, pp. 212–221, 2002.
13. http://focus.ti.com/pdfs/dlpdmd/153_Reliability_paper.pdf.
14. http://www.analog.com/media/en/technical-documentation/application-notes/AN-397.pdf
15. https://www.mosis.com/files/faqs/tech_cmos_rel.pdf.
16. Jeremy A. Walraven, Failure mechanisms in MEMS. *ITC International Test Conference*, p. 328, 2003.

13

Solving Quality and Reliability Optimization Problems for MEMS with Degradation Data

Yash Lundia[1], Kunal Jain[1], Mamanduru Vamsee Krishna[1], Manoj Kumar Tiwari[1]*, and Baldev Raj[2]

[1]*Department of Industrial & Systems Engineering, Indian Institute of Technology, Kharagpur, India*
[2]*National Institute of Advanced Studies, Bangalore, India*

Abstract
For micro-electro-mechanical systems (MEMS) to be used more widely, it is of extreme importance that they are manufactured in accordance to high-quality standards. So far, only limited mathematical tools are available to deal with issues like reliability modeling and burn-in scheduling. This chapter proposes a mathematical model to determine *strategies* for preventive replacement and inspection for MEMS that are subject to multiple dependent competing failure processes (MDCFP), especially as a result of degradation and/or shock loads. The optimal specification limits for inspection and the replacement interval are determined by optimizing MEMS quality and reliability simultaneously. The model has been formulated to deal with the situation in which the reliability of MEMS is calculated considering both wear degradation and random shocks, which are widely known causes of degradation of MEMS. Based on this reliability model, the optimal replacement time and an upper specification limit for the burn-in process are developed. In order to get optimal specification limit for the burn-in process and the replacement time period, a particle swarm optimization-based optimization method has been proposed to solve the aforementioned model. A numerical example has been presented to illustrate the proposed model.

Keywords: Particle Swarm Optimization, Micro-Electro-Mechanical Systems, Multiple Depeendent Competing Failure Process, System Reliability

Abbreviations

pdf:	probability density function
cdf:	cumulative distribution function
MEMS:	micro-electro-mechanical systems
NDE:	non-destructive evaluation

**Corresponding author*: mkt09@hotmail.com

Atul Tiwari and Baldev Raj (eds.), Materials and Failures in MEMS and NEMS, (381–400)
© 2015 Scrivener Publishing LLC

MDCFP:	multiple dependent competing failure processes
USL:	upper specification limit
i.i.d.:	independent and identically distributed

13.1 Introduction

It is of extreme importance that micro-electro-mechanical systems (MEMS) be extremely reliable and be manufactured to strict quality standards so that they achieve widespread usage. In areas like nuclear, aerospace, medical/biological, and weapons, MEMS technology has great promise for numerous critical applications. Existing products and applications *shall* also greatly *benefit from* improved MEMS technology. Many MEMS devices are being used effectively in commercial products. As the usage of MEMS products is becoming more widespread, many key fabrication/manufacturing issues are *gaining* importance, like reliability modeling and testing, precise dimensional control and inspection, and maintenance strategies. For MEMS to become commercial, influential issues of quality, reliability, and productivity need to be *addressed*. The operational decisions in MEMS manufacturing need to be optimized. *The optimization is enabled by* mathematical tools such that MEMS reliability, quality, and productivity are improved.

Imposed external sources or internal stresses and forces created during the operation of the system are the root causes for the failure of a system. Erosion, corrosion, wear, fatigue, and overload are some of the typical failure mechanisms that may lead to various failure processes. In case of multiple failure processes which compete against one another, the one that occurs first causes the failure of the system. These may be either dependent or independent. In the case that they are dependent, calculating the reliability of the system becomes a challenging situation. This chapter presents a mathematical model which will jointly determine *strategies* for preventive replacement and inspection for systems subject to MDCFP, especially as a result of degradation and/or shock loads. The optimal limits for the above specifications are obtained by optimizing MEMS reliability and quality simultaneously.

Many researchers have studied the reliability optimization problem of MEMS keeping in view the degradation characteristics and also in the presence of random shocks. Degradation modeling *can* provide a greater understanding of the causes of failure and *thus* offer a method to predict reliability *in the context of limited and inadequate* failure data. Hence, it has attracted significant attention from researchers in both statistics and reliability (Lu and Meeker, 1993; Singpurwalla, 1995; Kharoufeh and Cox, 2005). Studies have been done for the purpose of random shock modeling where devices are subjected to external shock environments, like accidental dropping onto hard surfaces, and sudden and unexpected usage loads.

The random shock models can be divided into four categories:

i. Extreme shock: the failure is a result of the value of any shock crossing a particular threshold.
ii. Cumulative shock: the failure is a result of the cumulative damage from shocks crossing a certain critical value.

iii. Run shock: the failure is a result of a run of k shocks beyond a critical magnitude.
iv. δ-Shock: the failure is a result of the time lag between two consecutive shocks being smaller than a threshold δ (Liu *et al.*, 2008; Nakagawa, 2007).
v. Optimal maintenance models have been evolved for different random shock models (Chien *et al.*, 2006; Wang and Zhang, 2005).

An availability model was derived by Klutke and Yang (2002), in which they considered a system which was subject to continuous smooth degradation and shocks that also cause added degradation damage. For a similar failure process, Kharoufeh *et al.* (2006) derived the distribution of system lifetime and also the limiting average availability.

However, there is *scant literature* available involving multiple dependent competing failure process (MDCFP) in analyzing the reliability of systems. Inter-dependence among different failure processes brings forth key issues in the area reliability modeling. A comprehensive mathematical model has been proposed to simultaneously determine policies for preventive replacement and inspection with regard to the surface-micromachined microengines subject to MDCFP. The soft failure process, which is a result of the combination of continuous smooth degradation and additional sudden degradation damages due to a shock process, and hard failures, which are a result of the stress from the same shock process are the two dependent/correlated failure processes considered and reliability model is developed for the same. Due to the competition between the failure processes, any one of these can result in the component or the system failing, based on whichever failure process reaches the critical threshold first. As both failure processes are impacted from the same shock process, the two failure processes are considered to be dependent or correlated. Their failure times are assumed to be dependent, and this dependence is considered in a statistical or probabilistic sense. This does imply physical dependence or link between one failure and the other.

Various maintenance strategies regarding degrading systems are available in the literature (Li and Pham, 2005a; Liao *et al.*, 2006; Tang and Lam, 2006; Zequeira and B´erenguer, 2006; Zhu *et al.*, 2010). The maintenance model developed in this chapter is different from other studies, because in this chapter, a mathematical model is developed which jointly determines parameters for inspection and preventive replacement policies for two dependent competing failure processes which include a sudden failure process and a degrading process.

The developed model is demonstrated on a synthetic example considering a MEMS device. Studies regarding MEMS reliability are of critical importance as the commercialization of MEMS increases. Multiple failure processes are a key *challenging environment* experienced by MEMS in the field, as evidenced by the data collected in reliability tests by the Sandia National Laboratory (Tanner and Dugger, 2003). Studies have been performed by Peng *et al.* (2009a) and Feng and Coit (2010), which include the development of a model specifically for the reliability problem with respect to MEMS. Some vital theoretical arguments and formulae related to reliability were presented by Feng and Coit (2010). However, these theories were not accompanied by mathematical developments, numerical examples, or maintenance models. In this chapter, a reliability model is developed considering a general degradation path and random shock models, and

the chapter also takes into account wear degradation caused by the burn-in process and aims at reducing the warranty cost and repair cost for the equipment. To overcome the non-linearity involved in the model, an evolutionary algorithm, particle swarm optimization (PSO) algorithm (Kennedy and Eberhart, 1995) has been employed as a solution procedure to optimize the proposed model. The reliability model can be readily applied to other cases of dependent competing failures as well, like the changing in degradation rate due to shocks.

13.2 Notations and Assumptions

13.2.1 Notations

The notations are similar to those in Peng *et al.* (2009b, 2010):

t = Number of revolutions till failure,

r = Pin joint radius,

$X(t)$, $X(t;\beta)$ = Material's wear volume at time t,

c = Model parameter which is proportional to wear coefficient, and is inversely proportional to the material's hardness,

t_0 = Burn-in time or number of revolutions till burn-in,

F = Force acting between the contacting surfaces,

η = Upper specification limit,

$L(X(t_0))$ Quality loss function at the end of burn-in,

$C_Q(\eta, t_0)$ Anticipated quality loss at the end of burn-in,

S = Per unit scrap cost,

$C_S = (\eta, t_0)$ Estimated scrap cost,

C_I = Per unit inspection cost,

QC = Anticipated quality-related cost,

f_c = Per unit failure cost,

FC = Anticipated cost of failure,

RC = Cost of Replacement,

τ = Time taken for replacement,

B_τ = Upper limit for the replacement interval,

$\phi(\cdot)$ = pdf of a standard normally distributed variable,

$\Phi(\cdot)$ = cdf of a standard normally distributed variable,

$N(t)$ = number of shock loads that have arrived by time t,

D = threshold or maximal fracture strength for catastrophic failures,

λ = rate of arrival of random shocks,

H = threshold for wear degradation,

W_i = ith shock load's magnitude,

F_W = cdf of W_i,

$X(t)$ = wear volume as a result of continuous degradation at t,

$X_S(t)$ = total wear volume at t comprising of both continual wear and also instantaneous damage,

Y_i = damage size due to the ith shock load,

$S(t)$ = cumulative shock damage size at t,

$G(x,t)$ = cdf of $X(t)$ at time t,

$FX(x,t)$ = cdf of $X_S(t)$ at time t,

$f_y(y)$ = pdf of Y_i,

$f^{(m)}_Y(y)$ = pdf of the sum of i.i.d Y_i variables,

$f_T(t)$ = pdf of the failure time.

13.2.2 Assumptions

The following assumptions *have been made* for the purpose of the model. Each assumption is reasonable and is adequately explained in the section where the model is explained.

1. When the overall degradation, comprising both of continuous degradation over time and sudden damage as a result of random shocks exceeds a threshold value H, soft failure occurs.
2. Catastrophic/hard failure is a result of the extreme shock load exceeding the maximum strength of the material, D.
3. Random shocks are assumed to follow a Poisson process of arrival. Sizes/magnitudes of shock loads are denoted by W_i, and damage sizes which are a result of the ith shock load are denoted by Y_i, both of which are i.i.d. random variables.
4. $G(x, t)$ denotes the cdf for the volume of wear caused by continuous degradation, $X(t)$. In the more specific model, the continuous degradation follows a linear path $X(t) = \rho$, where the initial value ρ is a constant and the degradation rate a follows a normal distribution, $a \sim N(\mu_a, \sigma_a^2)$.

13.3 Reliability Model

For the purpose of our model, the steps followed will be as shown in Figure 13.1. The subsequent sections will elaborate on each step in the model.

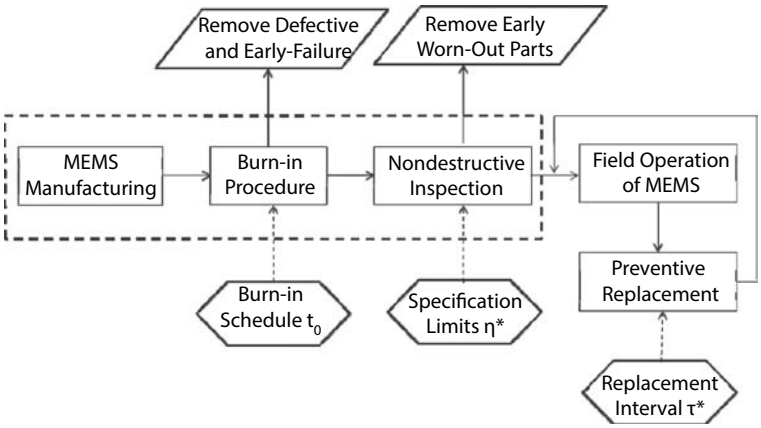

Figure 13.1 Flowchart of entire process

13.3.1 Wear Degradation due to Burn-In Procedure

The occurrence of microengine failures steadily decreases at the initial stages of testing as indicated by experiments which show infant mortality, which is a consequence of the early failures of defective parts (Tanner *et al.*, 1999a). The purpose of a burn in process is to eliminate the unfit devices from the considered population. This process is carried out immediately after the manufacturing processes. To screen out faulty parts, the manufactured units are run for a short period of time. The burn-in time is selected before applying the optimization based on previously available standards. MEMS manufacturers need to balance between the need for shorter production cycles by the reduction of burn-in time and the risk of unacceptable early failures due to incomplete burn-in process as a result of shorter burn-in time. Thus, an appropriate burn-in schedule needs to be predefined where the burn-in process is long enough to induce the defective units to fail, but not too long to impact the required lifetime of engines. The cost of burn-in procedure is inclusive of the failure cost during the burn-in process, the operating cost of the burn-in equipment, and marketing losses which are a consequence of the increased production lead time. But, we need to do further research on the same to incorporate this cost into the model.

In our case, we consider only wear degradation due to the burn-in process. The reason for this is, when the MEMS is exposed to the burn-in process, the type of degradation it experiences over the course of the burn-in type is only of the wear degradation type, and no random shocks are applied in the burn-in process to screen out the defective parts. The evaluation of the wear degradation due to the burn-in process is important, as it is required to find the optimum upper-specification limit for the screening process. For doing that, we develop a degradation path for this time interval.

Let $X(t;\beta)$ represent the actual degradation path of the degrading characteristic over the time t, where β represents the model coefficients as a vector. Apart from specification of the form of the $X(t;\beta)$ function, the degradation model also requires specification of the random and fixed parameters in β (Feng and Coit, 2007). Usually, this model

involves only four parameters. As discussed by Meeker *et al.* (1998), the parameters in β may be random from unit to unit, and one or more parameters could be modeled as constant across all units. The physical theory to quantify the functional relationship between the wear volume, $X(t; \beta)$, and the number of revolutions to failure, t, is the basis for our wear degradation model (Tanner and Dugger, 2003). As discussed previously in Peng *et al.* (2009b), if the radius of the pin joint, r, the coefficient associated with the wear and hardness of the material, c, and force acting between the surfaces in contact, F, the linear degradation path, $X(t;, r, c, F)$ can be expressed as

$$X(t;r,c,F) = 2\pi rcFt \tag{13.1}$$

r is random from unit to unit with mean μ_r and standard deviation σ_r. F varies with the sinusoidal drive frequency as the critical frequency for resonance is approached. For a certain given drive frequency, force applied between rubbing surfaces is random among units with nominal value σ_F and standard deviation μ_F.

It is rational to assume that $X(t)$ is random from unit to unit and follows a S-normal distribution. Various combinations of distributions for r and F will result in a S-normally distributed $X(t)$. Transformations can be applied to achieve the same. Assuming S-independence between r and F, it is demonstrated that

$$\mu_t = 2\pi c\mu_r\mu_F t \tag{13.2}$$

$$\sigma_t = 2\pi ct\sqrt{\sigma_r^2\sigma_F^2 + \sigma_r^2\mu_F^2 + \mu_r^2\sigma_F^2} \tag{13.3}$$

This is indicative of the fact that over time, the mean varies linearly, and the standard deviation increases linearly. Before burn-in, but after the completion of MEMS manufacturing, $X(0) = 0$.

13.3.2 Non-destructive Evaluation

The most serious failure cause for a microengine is the wear. Hence, it is critical to evaluate the wear volume after the burn-in procedure in a proper manner. If the wear volumes are more than a certain specification limit for certain units, they are liable to fail early. Thus, proper screening is essential so as to not reduce the lifetime of units. Systems like focused ion beam systems can provide 100% non-destructive evaluation (NDE) capabilities.

The wear volume after the burn-in procedure is given by $X(t_0) = 2\pi rcFt_0$, which follows a S-normal distribution, $X(t_0) \sim N(\mu_0, \sigma_0^2)$, where $\sigma_0^2 = (2\pi c)^2(\sigma_r^2\sigma_F^2 + \sigma_r^2\mu_F^2 + \mu_r^2\sigma_F^2)t_0^2$ and $\mu_0 = 2\pi c\mu_r\mu_F t_0$, respectively. During the NDE, based on the wear volume, an upper specification limit (USL) needs to be applied for screening the units that which have an excess amount of wear at the end of the burn-in process. By optimizing the quality of a system, the crucial USL is determined (Feng, 2005; Feng and Kapur, 2006). To make sure of maximum efficiency in the case of optimization for the purpose of obtaining specification limits, reliability and quality need to be integrated.

The combination of three quality-related costs is considered during NDE: quality losses as a result of deviating from the ideal value, inspection cost, and rework or scrap (Feng, 2005). The expression of the quality loss function of the wear volume, which is an S-type quality characteristic, is (Peng *et al.*, 2009b)

$$L\left(X\left(t_0\right)\right) = kX\left(t_0\right)^2 \tag{13.4}$$

The transformation of deviation into economic values is done using the coefficient k. $L(X(t_0))$ can be used to arrive at the value of the quality loss. The expected quality loss for the S-type characteristic is derived considering the expected quality loss for the T-type characteristic provided by Feng and Kapur (2006). Therefore, $C_Q(\eta)$ is proven to be

$$\begin{aligned} C_Q(\eta) &= \int_0^{USL} L(x;t_0) f_{X(t_0)}\left(x;t_0\right)dx = \int_0^{\eta} kx^2 f_{X(t_0)}\left(x;t_0\right)dx \\ &= -k\sigma_0\left[\mu_0+\eta\right]\left(\frac{\eta-\mu_0}{\sigma_0}\right)+\sigma_0\mu_0 k\left(\frac{-\mu_0}{\sigma_0}\right)-k\left[\sigma_0^2+\mu_0^2\right] \\ &\left(\frac{-\mu_0}{\sigma_0}\right)+k\left[\sigma_0^2+\mu_0^2\right]\left(\frac{\eta-\mu_0}{\sigma_0}\right) \end{aligned} \tag{13.5}$$

where $f_{X(t_0)}\left(x;t_0\right)$ is the pdf of the wear volume at the end of the burn-in process.

The unit will be scrapped or reworked if a measurement is observed outside the USL. Let $q(\eta)$ denote the fraction of conforming units. The area under the pdf curve bounded by the USL corresponds to this fraction.

$$q(\eta) = \int_0^{\eta} f_{X(t_0)}\left(x;t_0\right)dx = \Phi\left(\frac{\eta-\mu_0}{\sigma_0}\right)-\Phi\left(\frac{-\mu_0}{\sigma_0}\right) \tag{13.6}$$

Considering s to be the scrap/reworked cost per unit, the scrapped portion of $(1-q(\eta))$ causes an expected scrap cost of $(1-q(\eta))s$. This scrap cost can be written as

$$C_s(\eta) = (1-\mathrm{q})s = \left(1-\int_0^{\eta} f_{X(t_0)}\left(x;t_0\right)dx = \Phi\left(\frac{\eta-\mu_0}{\sigma_0}\right)-\Phi\left(\frac{-\mu_0}{\sigma_0}\right)\right)s \tag{13.7}$$

C_I denotes the inspection cost per unit. It is a constant and does not depend on η. Thus, the expression for the total expected quality cost per unit experienced at the manufacturing is

$$QC(\eta) = \mathrm{C}_Q\left(\eta\right)+\mathrm{C}_S\left(\eta\right)+\mathrm{C}_I \tag{13.8}$$

13.3.3 Replacement and Failure Cost

The probability that the wear degradation is less than H after the burn-in process is given by

$$R(t) = P\left(X(t) < H\right) = \int_0^H f_{X(t)}(x;t)dx = \Phi\left(\frac{H-\mu_t}{\sigma_t}\right) \tag{13.9}$$

As discussed by Peng *et al.* (2010), the MDCFP causing the system to fail are

i. Soft failures, which are a result of both continuous wear degradation and additional sudden degradation damages from a random shock process.
ii. Hard/Catastrophic failures, which are a consequence of stress caused by the same random shock process.

During field operations, the continuous wear degradation is an aging process. Apart from this, additional abrupt damages caused by shock loads contribute to this process. Comparatively large-sized wear debris as a result of a shock load is an example of this sort of phenomenon. The occurrence of soft failure is a result of the total wear volume, comprising both of the continuous degradation process and the additional abrupt damages caused by the random shocks, exceeding a critical threshold H. In addition, the crossing of a critical strength level D by a single shock can result in catastrophic/hard failure. The system is considered to be failed when any one of these two competing failure modes occurs. Now, in the following part, we have separately formulated a model for both these cases:

13.3.3.1 Catastrophic Failures as a Result of Random Shocks

Shock loads can be classified with respect to their magnitudes, shapes, locations, and durations. To analyze the reliability of systems which have experienced various types of shocks, the same mathematical framework can be used. A renewal process considering Weibull, exponential, or gamma distributed inter arrival times can be used to show the random arrival of shocks with respect to time intervals. Normal or exponential distributed variable, which are continuous random variables can be used to represent the sizes of shocks. Wear degradation is influenced by shock damage. This may also be modeled as i.i.d. random variables.

An extreme shock model is shown in Figure 13.2(b). The Poisson process $\{N(t), t \geq 0\}$ with a rate λ is considered for the arrival of shocks. W_i denotes the magnitude of the ith shock load which arrives at t_i, for i ranging from 1 to ∞. $F_W(w)$ is considered to be the cdf of W_i, which are i.i.d. considering the stress–strength model demonstrated by Kotz *et al.* (2003), the survival probability at the application of stress due to the ith shock is

$$P(W_i < D) = F_W D \text{ for } i=1,2,\ldots,\infty. \tag{13.10}$$

Based on preceding assumption, it can be considered, $Wi \sim N(\mu_W, \sigma_W^2)$. Thus, the survival probability becomes (Feng and Coit, 2010):

$$P_L = F_W(D) = \Phi\left(\frac{D-\mu_W}{\sigma_W}\right) \text{ for } i=1,2,\ldots,\infty. \tag{13.11}$$

where $\Phi(\cdot)$ is the cdf of a standard normally distributed variable.

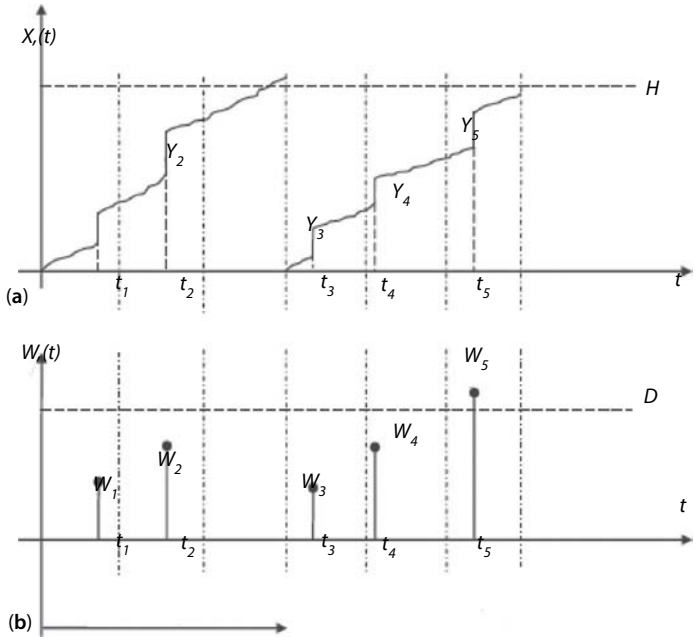

Figure 13.2 Two competing dependent failure processes: (a) soft failure process and (b) hard failure process.

13.3.3.2 Soft Failures as a Result of Shocks and Degradation

The crossing of a threshold level H by the total degradation results in soft failures. Figure 13.2(a) shows the total degradation (Xs (t)) accumulated by the system. It consists of the summation of both the continual wear degradation and the instantaneous damages due to the random shocks. For demonstrating the linear degradation path followed by X (t), a linear degradation path is shown in Figure 13.2(a), $X(t) = \rho + at$, where the initial value ρ and the degradation rate a can either be random variables or constants.

Also, when a shock arrives, shifts or changes in degradation can accumulate instantaneously. Y_i denotes the shock damage sizes for i ranging from 1 to ∞. These are also considered to be i.i.d random variables. The damage size as a result of random shocks until time t, S (t), is given as

$$S(t) = \begin{cases} \sum_{i=1}^{N(t)} Y_i, \; if\, N(t) > 0 \\ 0, \qquad if\, N(t) = 0 \end{cases} \tag{13.12}$$

where N (t) is the total number of shocks that have arrived by time t. A cumulative shock model is implied by this expression. Considering both wear degradation and random shock damages, the overall degradation of the system is expressed as $Xs(t) = X(t) + S(t)$Then, the probability that the total degradation at time t is less than x, F_X (x, t), can be derived as

$$F_X(x,t) = P(X_S(t) < x)$$
$$= \sum_{i=0}^{\infty} P(X(t) + S(t) < x \mid N(t) = i) P(N(t) = i) \tag{13.13}$$

Furthermore, a convolution integral can be used to derive the cdf of $Xs\ (t)$ in Equation (13.13). For doing this, $G\ (x, t)$ is considered to be the cdf of $X\ (t)$ at $t, f_Y\ (y)$ to be the pdf of Y_i, and $f_Y^{(m)}(y)$ to be the pdf of the sum of m i.i.d. Yi variables. The expression now becomes:

$$F_X(x,t) = G(x,t)\exp(-\lambda t) + \sum_{i=1}^{\infty}\left(\int_0^x G(x-u,t) f_Y^{(i)}(u)du\right)\frac{\exp(-\lambda t)(\lambda t)^i}{i!} \tag{13.14}$$

For determining a more specific model based on Equation (13.13), we take into account the earlier made assumptions. The shock damage sizes are i.i.d. normal random variables. Therefore, it is reasonable to assume, $Yi \sim N(\mu_Y, \sigma_Y^2)$. The degradation path is linear with a constant initial value ρ and a normal-distributed degradation rate a, $a \sim N(\mu_a, \sigma_a^2)$. Thus, the expression can be rewritten as (Peng *et al.*, 2009a)

$$F_X(x,t) = \sum_{i=0}^{\infty} \Phi\left(\frac{x - (\mu_a + \varphi + i\mu_Y)}{\sqrt{\sigma_a^2 t^2 + i\sigma_Y^2}}\right)\frac{\exp(-\lambda t)(\lambda t)^i}{i!} \tag{13.15}$$

The probability of no soft failure occurring before time t is denoted by

$$P(X_S(t) < H) = F_X(H,t) \tag{13.16}$$

A non-repairable system is considered for the maintenance policy. The failure due to the wear-out of typical operating units is prevented by employing a preventive periodic replacement policy. The cost of unscheduled maintenance exceeds the cost of a planned replacement. Apart from that, the planned replacement cost is also more economical as once the system ages, its wear increases and it becomes considerably more prone to failure. Hence, a preventive replacement model is used.

The reliability after the burn-in process is essential to calculate the optimal replacement time. Therefore, the system reliability at time t is considered to be the probability that the total degradation is less than the threshold level ($X_s\ (t) < H$) and the system has survived each of the $N(t)$ shock loads ($W_i < D$ for i ranging from 1 to ∞) (Peng *et al.*, 2010)

$$R(t) = P\left(X(t) < H,\ N(t) = 0\right) + \sum_{i=1}^{\infty} \mathrm{P}(W_1 < D, \ldots, W_{N(t)} < D,$$
$$X(t) + \sum_{j=1}^{N(t)} Y_j < H, N(t) = i)$$
$$= P\left(X(t) < H,\ N(t) = 0\right) + \sum_{i=1}^{\infty} F_W(D)^i\, P(X(t) + \sum_{j=1}^{N(t)} Y_j < H|$$
$$N(t) = i) \times P\left(N(t) = i\right) \tag{13.17}$$

For deriving the reliability of the system in the general case, Equations (13.14) and (13.17) can be used. The expression comes out to be

$$R(t) = G(H,t)exp(-\lambda t) + \sum_{i=1}^{\infty} F_W(D)^i \times (\int_0^H G(H-u,t) f_Y^{(i)}(u)du) \frac{exp(-»t)(»t)^i}{i!} \tag{13.18}$$

Using the general case of Equation (13.18), the reliability function for the more specific case with normally distributed W_i, Y_i, and β can be expressed as

$$R(t) = \Phi\left(\frac{H-\mu_a t-\varphi)}{\sigma_a t}\right)\exp(-\lambda t) + \sum_{i=1}^{\infty} P_L{}^i \Phi\left(\frac{H-(\mu_a t+\varphi+i\mu_Y)}{\sqrt{\sigma_a^2 t^2 + i\sigma_Y^2}}\right) \times \frac{\exp(-\lambda t)(\lambda t)^i}{i!} \tag{13.19}$$

where P_L is obtained from Equation (13.11). Then, the pdf of the failure time, $f_T(t)$ for the specific case is derived as

$$\begin{aligned} f_T(t) = -\frac{dR(t)}{dt} &= -\sum_{i=1}^{\infty} P_L{}^i \phi\left(\frac{H-(\mu_a t+\varphi+i\mu_Y)}{\sqrt{\sigma_a^2 t^2 + i\sigma_Y^2}}\right) \\ &\times\left(\frac{-\mu_a(\sigma_a^2 t^2 + i\sigma_Y^2) - \sigma_a^2 t(H-(\mu_a t+\varphi+i\mu_Y))}{(\sigma_a^2 t^2 + i\sigma_Y^2)^{3/2}}\right) \\ &\times\frac{\exp(-\lambda t)(\lambda t)^i}{i!} - \sum_{i=1}^{\infty} P_L{}^i \Phi\left(\frac{H-(\mu_a t+\varphi+i\mu_Y)}{\sqrt{\sigma_a^2 t^2 + i\sigma_Y^2}}\right) \times \frac{\exp(-\lambda t)(\lambda t)^{i-1}(-\lambda t+i)}{i!} \\ &-\phi\left(\frac{H-\mu_a t-\varphi)}{\sigma_a^t}\right) \times \left(\frac{-H+\varphi)}{\sigma_a t^2}\right)\exp(-\lambda t) + \lambda\Phi\left(\frac{H-\mu_a t-\varphi)}{\sigma_a^t}\right)\exp(-\lambda t) \end{aligned} \tag{13.20}$$

where $\phi(\cdot)$ is the pdf of a standard normally distributed variable.

As already stated, the microengine failure is a result of the wear volume of the material exceeding a critical threshold, H. Thus, the reliability of a microengine at any time (or number of cycles) can be calculated by the probability that the wear volume has not exceeded the failure threshold, and catastrophic/hard failure has not occurred, i.e.

$$R(t \mid t_0) = \frac{R(t)}{P(X(t_0) < H)},\ t_0 < t < \tau \tag{13.21}$$

where the numerator is from Equation (13.19) and denominator from Equation (13.9).

We have considered the cost-of-failure approach (Todinov, 2004), to evaluate system reliability and quality in monetary terms. f_c, which is per unit failure cost, is assumed to be constant. It is *s*-independent of the time to failure, and can be projected by either a one-year warranty cost, or a one-time repair cost. At the time of replacement, system reliability is determined with the help of the expected failure cost:

$$FC(\tau) = f_c(1 - \mathrm{R}(\tau \mid \mathrm{t}_0)) \tag{13.22}$$

If the system fails before τ, then it has to be replaced by an operational replacement. The cost for this is *FC* + *RC*, where is *RC* is the cost for replacement. Alternatively, if failure has not occurred by τ, only economic considerations will play a part in the cost of replacement. This cost will just be *RC*. Thus, the expected total failure plus replacement cost at τ is *FC* (τ) + *RC*.

13.3.4 Optimization Model

The optimization model includes minimizing the total cost ranging over the time of usage. We find a comprehensive mathematical model to evaluate the USL for inspection, η, and the interval for replacement, τ.

The estimated total system cost comprises of the failure cost, the expected quality cost, and the replacement cost. This is minimized over the expected time of usage of a microengine. Peng *et al.* (2009b) demonstrated the expected time of usage, τ, to be

$$E[U \mid t_0, \tau] = \int_0^{\tau - t_0} R(t + t_0 \mid t_0)dt \tag{13.23}$$

where $R(t_0)$ is from Equation (13.9) and $R(\tau)$ is from Equation (13.19).

Thus, the expected total system cost per unit expected time of usage is given as

$$TC(\eta, \tau) = \frac{QC(\eta) + FC(\tau) + RC}{E[\mathrm{U} \mid \mathrm{t}_0, \tau]} \tag{13.24}$$

where $QC(\eta)$ is from Equation (13.8), $FC(\eta)$ is from Equation (13.22), *RC* is a constant, and $E\left[U \mid t_o, \tau\right]$ from Equation (13.23).

To obtain the constrained optimization model to minimize the aforementioned function, we take into account the upper bound of the replacement interval, B_τ. Thus, this model can be expressed as

$$\text{Minimise} \quad TC(\eta, t) = \frac{QC(\eta) + FC(\tau) + RC}{E[\mathrm{U} \mid \mathrm{t}_0, \tau]} \tag{13.25}$$

subject to

$$\eta > \mu_0 \tag{13.26}$$

$$t_0 \leq \tau \leq B_\tau \tag{13.27}$$

13.3.5 Solution Methodology—Algorithm Description

PSO algorithm (Kennedy and Eberhart, 1995) is an evolutionary algorithm that has been substantiated to be rigorous one in handling problems with all sorts of complexities. PSO is a random search metaheuristic that guarantees a near optimal solution in all the scenarios irrespective of the nature of problem being unconstrained, linear, non-linear, constrained, continuous, discontinuous, differentiable, non-differentiable, etc. It uses a population of searching agents called particles to explore the search space to arrive at global best position of the particles that optimizes the handling

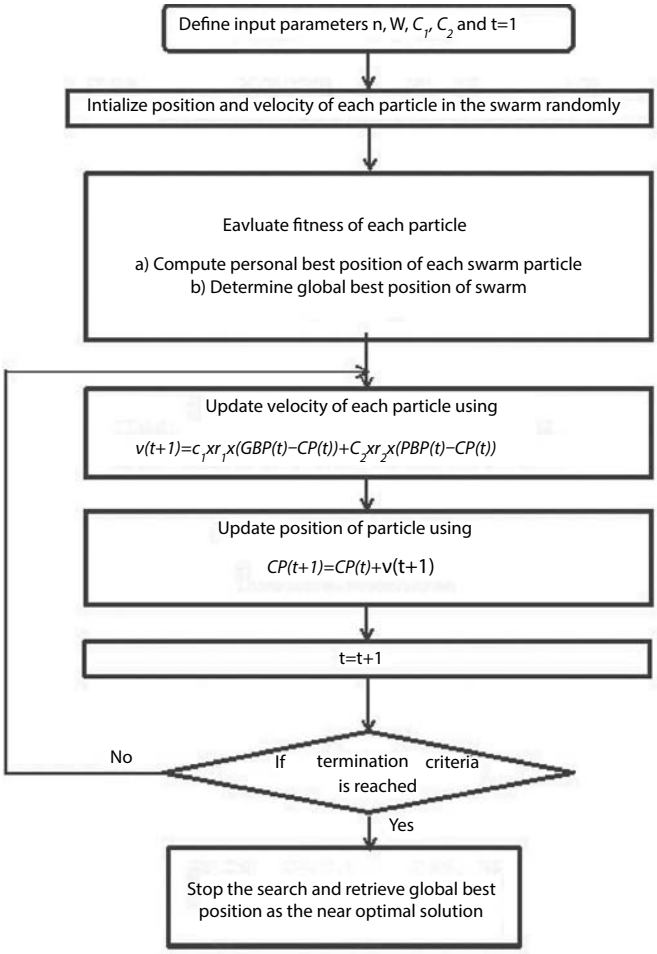

Figure 13.3 Flowchart representing the schematic procedure of PSO algorithm.

situation. The algorithm starts with random initialization of a set of particles called swarm and runs in an iterative manner till the termination criteria gets satisfied. Iterations involve in tracking of personal best for each particle and global best particle among the swarm. The personal best of each particle and global best particles will be used to update the current position of the swarm for the next iteration. The formula used for updating current position drives each particle towards its personal best and global best simultaneously. This in turn facilitates all the particles to travel into the more promising region in the vicinity of near optimal solution after every iteration with effective sharing of information. Finally, the algorithm culminates the search by any one of these two usual ways of terminating criteria, one being, putting the limit on the number of iterations and the other being minimum decimal precision in the convergence value of fitness that can be allowed. The flowchart in Figure 13.3 depicts the schematic representation of the technical procedure involved in the algorithm.

Where notations of the variables used describing algorithm in the Figure 13.3 are as follows

n = number of particles in the swarm
w = inertia weight (weight being given to the velocity of previous iteration)
$c1$, $c2$ = accelerating coefficients
$r1$, $r2$ = random number vectors
t = iteration index
CP(t) = current position of swarm in t^{th} iteration
PBP(t)= personal best position of swarm in t^{th} iteration
GBP(t)= global best position of swarm in t^{th} iteration
$v(t)$ = Velocity of swarm in t^{th} iteration

13.4 Numerical Example

As stated by Tanner and Dugger (2003), orthogonal linear comb drive actuators are mechanically connected to a rotating gear in a microengine. The comb drives are displaced, and this linear displacement is transformed to the gear through a pin joint. The observed wear on rubbing surfaces between the pin joint and the gear, which can result in a broken pin joint, or even a seized microengine, is the dominant failure mechanism. The aging degradation process is the primary cause of the wear volume. Additionally, according to shock tests on microengines, considerable wear debris between the pin joint and the gear, along with the fracturing of springs may be caused by shock loads. Hence, two competing failure processes are experienced by microengines: soft failures due to aging degradation coupled with debris from shock loads, and catastrophic failures due to spring fracture. The failure of the microengine means the failure of the MEMS. We apply the model to find the optimal specification limit and optimal replacement time to enhance the system performance (Table 13.1).

The earlier experimental scenario is solved using MATLAB (2014a) installed in a machine having Intel® Core™ i3 processor, 2.10 GHz CPU with 4GB RAM. The near

Table 13.1. Value of parameters considered for the current scenario.

Parameters	Values	Sources
H	0.00125 μm^3	Tanner and Dugger (2003)
D	1.5 GPa	Tanner and Dugger (2003)
φ	0	Tanner and Dugger (2003)
β	$\sim N\left(\mu_\beta, \sigma_\beta^2\right)$ $\mu_\beta = 8.4823 \times 10^{-9}\ \mu m^3$ $\sigma_\beta = 6.0016 \times 10^{-10}\ \mu m^3$	Tanner and Dugger (2003) Peng *et al.* (2009a)
λ	2.5×10^{-5}	Peng *et al.* (2010)
Y_i	$\sim N\left(\mu_Y, \sigma_Y^2\right)$ *for* $i = 1, 2, \ldots, \infty$ $\mu_Y = 1 \times 10^{-4}\ \mu m^3$ *and* $\sigma_Y = 2 \times 10^{-5}\ \mu m^3$	Peng *et al.* (2010)
W_i	$\sim N(\mu_W, \sigma_W^{2)}$ *for* $i = 1, 2, \ldots, \infty$ $\mu_W = 1.2$ *GPa and* $\sigma_W = 0.2$ *GPa*	Peng *et al.* (2010)
t_0	1000 revolutions	Peng *et al.* (2009b)
μ_0	$8.4823 \times 10^{-6}\ \mu m^3$	Tanner *et al.* (1999a) Peng *et al.* (2009b)
σ_0	$6.0016 \times 10^{-7}\ \mu m^3$	Tanner *et al.* (1999a) Peng *et al.* (2009b)
k (*Quality Coefficient*)	10^{10}	Peng *et al.* (2009b)
C_1	\$0.1 *per unit*	Peng *et al.* (2009b)
S	\$20	Peng *et al.* (2009b)
RC	\$50	Peng *et al.* (2009b)
f_c	\$1000	Peng *et al.* (2009b)

optimal solution has been found at $(\eta^*, \tau^*) = (6.2 \times 10^{-6}, 1.75 \times 10^3)$. The minimum total cost is found to be around $\$2.051 \times 10^{-3}$ per cycle.

Figure 13.4 represents the convergence graph obtained while solving the numerical example using PSO algorithm.

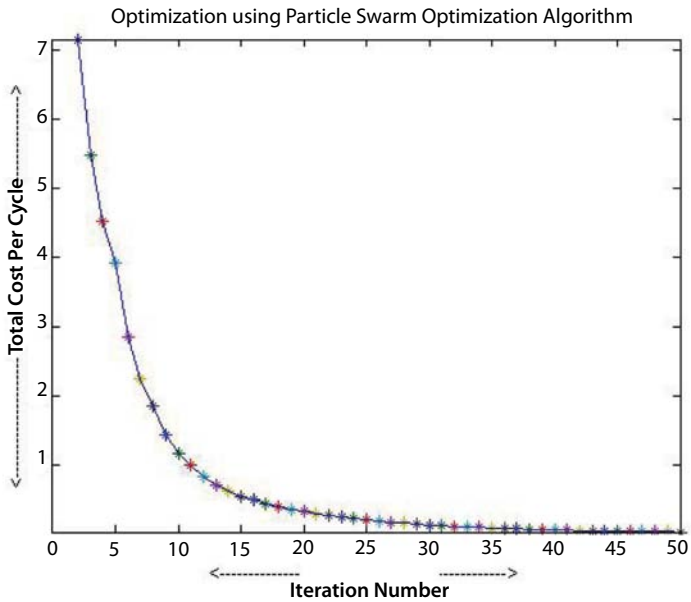

Figure 13.4 Convergence graph of total cost per cycle using PSO.

13.5 Conclusions

In this chapter, we developed a mathematical model to determine policies for preventive replacement and inspection for MEMS that are subject to MDCFPs, especially as a result of degradation and/or shock loads. In the example, the optimal specification limit and the replacement time are determined jointly.

This model can be extended to various other forms of degradation as well. However, the model formation will be challenging if we consider more number of degradation components. Furthermore, to gain an even more accurate reliability model, other issues in MEMS manufacturing and usage, like fabricating, must also be considered. Sensitivity analysis can also be performed on various parameters like failure cost and upper threshold limit to judge the changes in the solution with respect to the changes in these parameters. The present study demonstrates the proposed methodology through an example using simulated data set but does not include experimental data. The absence of independent consideration of some of the factors such as corrosion fatigue, embrittlement due to environment, and complexity of load are a few of the limitations of this chapter.

References

1. Y.-H. Chien, S.-H. Sheu, Z.G. Zhang, and E. Love, An extended optimal replacement model of systems subject to shocks. *European Journal of Operational Research,* 175, 399–412, 2006.

2. Q. Feng, "Integrated Statistical and Optimization Strategies for the Improvement of Six Sigma Methodology," PhD Dissertation, University of Washington, Seattle, WA, 2005.
3. Q. Feng, and D.W. Coit, "Simultaneous quality and reliability optimization for systems composed of degrading components," in Proceed*ings of Industrial Engineering Research Conference, Nashv*ille, TN, May 19–23, 2007.
4. Q. Feng, and Coit, D.W. Short communication: reliability analysis for multiple dependent failure processes: an MEMS application (invited paper). Interna*tional Journal of Performability Engineering, 6(1),* 100–102, 2010.
5. Q. Feng, and K.C. Kapur, Economic development of specifications for 100% inspection based on asymmetric quality loss functions. IIE Tra*nsactions, 38(8)*, 659–669, 2006.
6. J. Kennedy, and R. Eberhart, Particl*e Swarm Optimization, IEEE, Perth, WA, 1942–1948,* 1995.
7. J.P. Kharoufeh, and S.M. Cox, Stochastic models for degradation based reliability. IIE *Transactions,* 37(6), 533–542, 2005.
8. J.P. Kharoufeh, D.E. Finkelstein, and D.G. Mixon, Availability of periodically inspected systems with Markovian wear and shocks. *Journal of Applied Probability,* 43, 303–317, 2006.
9. G.A. Klutke, and Yang, Y. The availability of inspected systems subject to shocks and graceful degradation. *IEEE Transactions on Reliability,* 51, 371–374, 2002.
10. S. Kotz, Y. Lumelskii, and M. Pensky, *The Stress–Strength Model and Its Generalizations: Theory and Applications,* World Scientific, River Edge, NJ, 2003.
11. W. Li, and H. Pham, (2005a) An inspection-maintenance model for systems with multiple competing processes. *IEEE Transactions on Reliability*, 54, 318–327.
12. H. Liao, E.A. Elsayed, and L.Y. Chan, Maintenance of continuously monitored degrading systems. *Proceedings of the European Journal of Operational Research,* 175, 821–835, 2006.
13. Y. Liu, H.-Z. Huang, and H. Pham, Reliability evaluation of systems with degradation and random shocks, in *Proceedings of the Reliability and Maintainability Symposium,* 328–333, 2008.
14. C.J. Lu, and W.Q. Meeker, Using degradation measures to estimate a time-to-failure distribution. *Technometrics,* 35, 161–174, 1993.
15. T. Nakagawa, *Shock and Damage Models in Reliability Theory,* Springer, London, UK, 2007.
16. H. Peng, Q. Feng, and D.W. Coit, (2009a) Reliability modeling for MEMS devices subjected to multiple dependent competing failure processes, Presented at *Industrial Engineering Research Conference*, FL, May 30–June 3, 2009.
17. H. Peng, Q. Feng, and D.W. Coit, (2009b) Simultaneous quality and reliability optimization for microengines subject to degradation. *IEEE Transactions on Reliability*, 58, 98–105.
18. H. Peng, Q. Feng, and D.W. Coit, Reliability and maintenance modeling for systems subject to multiple dependent competing failure processes. *IIE Transactions,* 43(1), 12–22, 2010.
19. S.M. Ross, *Stochastic Processes,* second edition, Wiley, New York, NY, 1996.
20. N.D. Singpurwalla, Survival in dynamic environments. *Statistical Science,* 10, 86–103, 1995.
21. Y. Tang, and Y. Lam, A δ-shock maintenance model for a deteriorating system. *European Journal of Operational Research,* 168(2), 541–556, 2006.
22. D.M. Tanner, W.M. Miller, K.A. Peterson, M.T. Dugger, W.P. Eaton, W.L. Irwin, D.C. Senft, N.F., Smith, P. Tangyunyong, and S.L. Miller, Frequency dependence of the lifetime of a surface micromachined microengine driving a load. *Microelectronics Reliability*, 39, 401–414, 1999a.
23. D.M. Tanner, and M.T. Dugger, Wear mechanisms in a reliability methodology. *Proceedings of the Society of Photo-optical Instrumentation Engineers*, 4980, 22–40, 2003.
24. M.T. Todinov, Reliability analysis and setting reliability requirements based on the cost of failure. *International Journal of Reliability, Quality and Safety Engineering*, 11(3), 273–299.

25. G.J. Wang, and Y.L. Zhang, (2005) A shock model with two-type failures and optimal replacement policy. *International Journal of Systems Science*, 36, 209–214, 2004.
26. R.I. Zequeira, and C. B´erenguer, Periodic imperfect preventive maintenance with two categories. *Reliability Engineering & System Safety*, 91(4), 460–468, 2006.
27. Y. Zhu, E.A. Elsayed, H. Liao, and L.Y. Chan, Availability optimization of systems subject to competing risk. *European Journal of Operational Research*, 202(3), 781–788, 2010.

Index

Accelerometers, 123, 364, 366, 367, 377, 378
Acoustic impedance, 201
Acoustic power, 205
Active switch, 173–174
Actuation,
  acoustic, 279
  base, 279
  electrostatic, 279
  thermal, 279
Adaptive
  controller, 32
  estimation, 38, 39
  estimator, 21, 37
  self-tuning, 54
Alanine aminotransferase (ALT), 153
Aligning, 25
Alternating current (AC), 292–300, 303–304, 308–313, 315–320
Anodic oxidation, 126, 148
Antibody, 132–134, 140, 143, 144, 153, 154
Antigen, 132–134, 143, 153, 154
Applicable condition, 285, 289, 309
Application of microcantilever sensors, 344
  agriculture applications, 347
  biosensors, 346
  vapor phase/gas/chemical detection, 344
Arc-shape, 233
Area Utilization Factor (AUF), 141
Aspartate aminotransferase (AST), 153
Bacteria, 131, 138, 139, 141–143, 152
Bandwidth, 265, 267
Bessel filter, 374
Beta multiplier, 373
Bias T-circuit, 212, 214
Bilirubin, 154
Biochemical adsorbate, 230
Biochips, 122
Biomaterial, 131
Biomolecules, 131, 133, 138
Biosensors, 122, 131, 143, 151, 155, 156
Bi-stable operation, 175–176, 181–183
Buckling behavior, 285, 287, 289, 310, 321–322
Buckling deflection, 287, 296–297, 303, 305–308, 313–314
Buckling feature, 285, 321
Buckling mode, 285–289, 303, 310–313, 315–322
Buckling morphology, 286–289, 292, 294–297, 307, 311, 313, 315–316
Buckling oblique angle, 316–317
Buckling wavelength, 287, 294, 296–297, 304–308, 312–314
Cantilevers, 123, 127, 131–135
Capacitive sensing, 268
Capacitve Micromachined Ultrasonic Transducer (cMUT)
  characterization, 208, 212, 214
  design, 203
  fabrication, 205
  membrane, 203, 204, 209, 210, 214
  principle, 202
  pull-in voltage, 205, 216
  Q-factor, 213
  spring hardening, 214
Capillary, 76
  flow, 76, 93
  force, 76, 93, 95
  Young-Laplace Equation, 77
  pressure, 76, 93, 95, 97
Carbon nanofibers, 4, 6, 16
Carbon nanotubes, 4, 16–18
Carbon precursors, 8
  photoresist, 8/10/2015
Carcinogen, 141
C-f graph, 278–279

Channels
conventional, 65
microchannels, 64–66
minichannels, 65
nanochannels, 65
transitional, 65
Characterization
electrical, 277–278
mechanical,
visual, 276–277, SEM
Charge discharge, 367
Charge drive control, 251
Charge integration, 362, 364
Comb resonator, 27, 33, 36, 44, 49
Composite structure, 285, 290, 321
Compressive stress, 158, 159, 164
Conduction, 78–79, 85–87, 92, 107
Constantan wire, 285, 289–291, 293–313, 315–317, 319–322
Contact resistance, 174, 187, 192–196
Control volume, 67–68, 74–76
Convection, 78–80, 82, 86–95, 107
Copper sulfate, 129
Coriolis acceleration, 264–265
Creep, 282
Critical buckling stress, 285, 289, 300–301, 309, 321
Cross-scale buckling, 317–319, 322
Crumpled wave buckling, 315–316, 320, 322
Current density, 293–296, 307, 309, 311–312, 315–317, 320–321
C-V graph, 278–279
CVD, 2, 4, 6, 8–9, 13, 17
Damping controlled, 266
Damping ratio, 267
Delamination, 282, 286, 288–289, 297, 304
Diagnosis, 21, 29, 31, 32, 41, 49, 51, 54, 59
Diamond-like carbon (DLC), 1, 4, 13
Dielectric breakdown, 379
Dielectric property, 123
Digital image correlation method, 291, 310
Direct current (DC), 292–296, 299–300, 306–309
Discretization, 268
Displacement, 29, 33, 37, 42, 43, 44, 48, 56
encoded, 47
feedback, 46
measurement, 44
monitoring, 46
variation, 52
Displacement amplification, 377
Dissolution, 122, 124–126, 128, 130, 132
DNA
cDNA, 146–148
ncDNA, 146, 147
pDNA, 146–148
Doping, 124, 127, 128
Drying mechanisms, 122, 130
Dynamic device failure,
frequency shift, 280
wrong mode, 280–281
EDL impedance, 145
EISCAP, 148–150
Electrical loading, 285, 289–295, 297–299, 309–313, 315, 317–319, 321–322
Electrical–mechanical loading, 289, 292–293, 297, 299, 321
Electricity-induced buckling method, 285, 289, 309, 321
Electrochemical etching, 121–124, 126, 128, 130–132, 135, 148, 150, 155, 157, 158
Electroluminescence, 122
Electrolyte, 123, 124, 126, 128–131, 138, 141, 143, 145, 148–150, 153, 154, 157
Electropolishing, 121, 125, 126
Electrospinning, 15, 17–18
Electrostatic
attraction, 27
field, 27
force, 27, 29, 33, 37
Electrostatic actuation, 268, 276, 279, 282
Electrostatic discharge, 379
Electrostatic switch, 174, 176, 177, 179, 181, 184, 187, 189, 191, 192, 196
Energy
internal, 68, 111
kinetic, 68
potential, 68
Energy harvesting for sensor betworks, 349
low-frequency vibration energy harvesting, 349
microwave energy harvesting, 351
photovoltaic and thermal energy harvesting, 351
Entrance length, 70, 72–73, 80–82
Epi-Seal process, 188, 190
Equation of motion, 266

Fabrication,
bonding, 273, 275–277
surface micromachining, 273–274, 277
Failure, 28, 30
Failure mechanism, 193–197
Fanning friction factor, 75
Fault,
conditions, 30
diagnosis, 21, 29, 32, 42, 50, 57
less, 30, 32
models, 38, 56
representative, 39, 41, 55
scenario, 43, 51
sequence, 43
tolerant, 31, 32
FEM, 268–272
Filter, 21, 29, 31, 39, 43, 49, 56, 58
Finite Elelment Modelling (FEM), 203
Finite element model, 188
FIPOS, 122
First law, 67–68
Flexible substrate, 285–289, 305–306, 309–310, 321
Fluid mechanics, 70
Fluid–structure interaction damping
acoustic damping, 267–271, 279
squeeze film, 267–269, 271, 280–281
Fluorescent, 133, 134
Focal length, 129
Food toxins
aflatoxin B1 (AfB1), 141
Forgetting-factor, 29, 38, 39, 49, 50, 51, 52, 54, 57, 58
Fracture, 287–288, 295–299
Free vibration, 266
Frequency response, , 266–267, 269, 279, 281
Laser Doppler Vibrometer (LDV), 208
Nano Vibration Analyzer (NVA), 212
Friction factor, 71, 75, 92, 96, 99, 101, 103, 104, 115
Gas damping, 248
Gilbert multiplier, 374, 375, 377
Glass transition, 291–292, 294, 309–310, 315–317, 321
Glassy carbon, 3/4/2015
Glucose, 131, 132
Graphite, 1, 3
Hard failure process, 383, 389
Harsh Environment, 173–174
Heat dissipation rate, 311
Heat flow, 291, 311, 321
Heat pipes, MEMS, 92–101, 104–105
axial, 94
design equations, 97
fluid radius of curvature, 93
heat transfer equations, 98
microchannel use, 100
one-dimensional models, microchannel heat pipes, 102
operation, 92
pressure variation, 95
Heat sinks, MEMS, 65–66, 86–92, 106–108
design equations, 89
models, 90
Heat transfer, 78–80
Heat transfer coefficient, 79–80, 82, 84, 88–89, 91, 109, 113–114
Humidity sensor, 123
Hybrid drive control, 255
Hydraulic diameter, 64–65, 71–73, 77–78, 81–82, 93, 96, 102
Hydrofluoric acid vapor (VHF), 178–179
Hydrophobic, 123
Hysteresis behavior, 175, 181–183, 191
IgG, 153
Immobilization, 131–136, 143, 144, 154
Importance of MEMS, 382
Inertia, 266
inertial sensors
accelerometer, 265
vibratory rate gyroscopes, 264–265
Instability, 285–286, 289, 297–299, 301, 311–313, 319–321
Instrumentation amplifier, 368, 371, 376
Integrated noise, 377
Interfacial toughness, 285, 287, 289, 292–294, 296, 305–309, 321
Inverse problem, 219
I-V graph, 277–278
Jitter, 372
Joule heating, 183, 192, 194–195
Kalman filter, 21, 29, 38, 39, 40, 43, 48, 49, 56, 57, 58, 59
Kinetic energy, 266
Knife effect, 24
Knudsen number (Kn), 77–78
Label free, 138, 141, 143, 152
Laminar flow, 70, 72, 79, 99, 113–114
LDV, 279–280
Lithography, 23, 24

LMTD (Log Mean Temperature Difference), 83, 108–110, 113–114
Low power device, 175, 183–184
LPCVD, 135
Mass sensing, 219–224
Mass sensors, 264
Material growth effect, 22
Mechanical and electrical characterization of microcantilevers, 335
  electrical characterization, 338
  nano-indentation techniques, 335
  noise and reliability characterizations, 338
  surface and resonant frequency measurements, 337
Mechanical elements,
  beam, 264
  membranes, 264
  plate, 263, 265, 266, 268–269, 271–272, 274–275, 277, 279–281,
Mechanical loading, 286, 288–289, 292–293, 297, 299, 321
Mechanism, 285, 288–289, 299, 310, 319–322
MEMS heat exchangers, 64
Metal film, 286–289, 292–294, 296, 307–309, 320
Metal wire, 285, 310, 319, 321
Microcantilever operation principle and fundamental models, 327
  dynamic mode, 328
  heat mode, 329
  static mode, 327
Microcantilever readout principles, 339
  capacitance, 344
  integrated optical, 340
  piezo resistive, 341
  piezoelectric, 343
Microcantilever sensor fabrication, 330
  bulk micromachining, 331
  microcantilevers with integrated functionality, 334
  polymer microcantilevers, 333
  Si microcantilevers, 331
  surface micromachining, 333
Microcrack, 210
Microelectromechanical system (MEMS) switch, 173
Micromachines ultrasonic transducers, 264
Micron-scale buckling, 312, 316–319, 322
Microphone, 263, 265, 268, 274
Microsensors, 123
Misalignment, 276, 282
Model, 21
  based, 21, 29
  matching, 38
  multiple, 37
  parameters, 38
  techniques, 56
  tool, 39
  uncertainty, 31
Modulation demodulation, 367
Momentum, 73–75, 99, 101, 105, 111
Moving
  average, 49
  plate, 35
  shuttle, 33
Multi-physics, 266, 268, 270
Multiple dependent competeing failure process, 383
  failure process, 383
Nanoelectromechanical system (NEMS) switch, 173–175, 187, 197
Nanoporous, 131, 143–145, 155, 160
Natural frequency, 132, 133, 266, 268, 279
Noise
  contaminated, 29
  content, 43
  evaluations, 29
  level, 29
  matrix, 38
  over estimation, 43
  under estimation, 29, 44
Non-destructive evaluation, 387
Non-resonant devices, 264
Non-volatile memory (NVM), 173–174
Nusselt number, 71, 82
Oblique wave buckling, 315, 317–318
Occurrence condition, 285, 289, 310, 316, 320
Optical
  beam, 45
  data, 45, 47, 52
  displacement, 46
  doppler laser, 56
  monitoring, 29
  probing, 44
  signals, 52
  switches, 21
  through wafer, 44
  waveforms, 46
Optical profiler, 277

Optimization, 242, 245–248, 256, 257
Optoelectronics, 122
Orthogonal wave buckling, 312–314, 316, 318, 320
Oscillator method, 367
Overdriving voltage, 187–188
Over-etching, 280, 282
Oxidation, 122, 126, 148, 151, 154, 157, 161
Parameter
  deviation, 31
  estimation, 29, 51
  identification, 38, 41, 44
  identifier, 37
  recognition, 33
  shift, 29
  tolerance, 21
  variation, 22, 29, 36, 39, 46, 51, 54
Parasitic capacitance, 368, 371
Particle-swarm optimization, 394–397
Passive switch, 173
PDMS, 13
Peak hold averaging, 279
PECVD, 149
Photolithography, 286, 290, 310
Photoluminescence, 122,
Piezoresistive co-efficient, 160, 163, 164
Piezoresistors, 156, 157, 160
PNA, 146, 147
Poisson's ratio, 288, 291, 310, 320
Polymer strip, 310, 313, 317–321
Polymer substrate, 285, 289–292, 294, 297–301, 305–313, 315–317, 319–322
Polysilicon, 131, 133, 135, 136, 137, 156, 157, 160
Porosity, 122, 124, 125, 130, 141, 155, 156, 158–162
Porous silicon (PS),
  macro PS, 123, 127–130, 139, 142, 151, 156–159
  meso PS, 123, 127–129, 158,
  micro PS, 123, 127–130, 155–159
Post buckling analysis, 289, 301
Prandtl number, 81–82
Process flow simulation, 266, 272–273
Profiles, 64–65, 70–71, 75, 80, 95, 105–107
Programmable capacitance, 370
Proof mass, 264, 265, 267
Proteins, 131
Pull-in, 268
Pull-in voltage, 175, 181–189, 191
Pull-out voltage, 176, 178, 191
Pumping
  active, 65
  passive, 65
Pure substances, 68–69
Pyrolysis
  e-beam induced pyrolysis, 10
  graphitization, 5, 17–18
  stages, 5
Quality factor, 132, 133, 135
Random shock models, 382
Real Contact Area (RCA), 131
Recursive least square, 38, 49
Reflectivity, 132
Reliability failure, 282
Reliability
  electromigration, 379
  hot carrier, 379
  stress migration, 379
Residual
  deformation, 26
  generation, 29, 55, 56
  signal, 29, 38, 39, 43, 50, 55, 57, 58
  stress, 23
Residual strain, 302–305
Residual stress, 272, 274–275, 280, 282, 285, 287, 289, 301–305, 321
Resistive Damping, 251–256
Resolution, 264, 267, 279
Resonance method, 367
Resonant Devices, 264
Resonant frequency, 224
Resonator, 222, 223, 230
Restriction, 285, 319
Reynolds number (Re), 72–73, 81, 89, 96
RF-MEMS, 239–260
RIVPSE, 135
Sacrificial layer, 206
Sacrificial material, 123
Schottky diode, 126
Secondary buckling, 288, 319–320
Self assembly, 13–16
Self-tuning, 40, 41, 49, 51–59
SEM, 277
Sensitivity, 264–267
Shrinkage,
  drying, 12, 15
  pyrolysis, 5–7, 10, 13
  shrinkage stress, 5, 16

Signature
fault modes, 56
faults, 38, 55
Silicon deep reactive ion etching (DRIE), 178–179, 190
Silicon nanofin (SiNF), 175, 176, 178, 179, 181–184
Silicon-on-Insulator (SOI), 122, 132
Simple harmonic motion, 266
Soft failure process, 383, 389
Soft lithography, 11/13/2015
Soft matter, 288
Spring constant, 133, 138
Spring restoration force, 189, 191–192
S-shape, 233
Stain etching, 131, 132
Stiction, 26, 27, 37, 232, 274–275, 277, 281–282
Stiffness controlled, 266
Stress, 23, 26, 158, 159, 163
Structural damping, 267
Structural failure, 282
Structural modeling, 266
SU-8 photolithography, 6/8/2015
Submicron-scale wrinkles, 317–322
Surface
areas, 27, 36
charge, 37
micromachining, 22
reflecting, 45
roughness, 23
rubbing, 27
Surface adhesion force, 179, 192
Surface asperity, 192, 194, 196
Surface degradation,
bridge formation, 196
delamination, 196
material transfer, 196
micro-welding, 183, 187, 192, 197
Surface elasticity, 228
Surface micromachining, 205
Surface morphology, 209, 210
Surface oxidation, 282
Surface stress, 225, 226
Surface-to-volume ratio, 122, 123, 131, 160, 165
Surfactant, 132, 135
Switched capacitor, 362, 368
Taguchi's optimization, 245, 248, 256
Tailored pulse, 241, 243, 245, 249
Tensile stress, 164
Thermal conductivity, 122, 123
Thermal entrance length, 80–82
Thermal expansion, 286, 291, 321
Thermal mismatch, 289, 299, 312, 319, 321
Thermal resistance, 84–85, 87–88, 90–92, 113
Triglyceride, 131, 133, 135, 136, 149, 150
Turbulent flow, 72, 79, 115
Two-fluid exchanger, 65–67, 106–109, 111
design equations, 109
one-dimensional models, 2-fluid exchanger, 111
temperature profiles, 107
Urea, 131, 149, 154
U-shape nanowire, 184–187
Vacuum encapsulation, 175, 187–188, 192, 194, 197
Van Der Waals force, 175–179, 181
Vapor-phase, 132, 135
Velocity, 68, 70, 73–74, 79–80, 89, 98, 100, 105, 110
Virus, 131
Voltage drive control, 240, 241, 245
Wafer bonding, 205, 207, 211
Wear degradation, 386
Young's modulus, 122, 137, 138, 155, 156, 158–160, 164, 291, 300–301, 305–306, 309–310

Also of Interest

Check out these published and forthcoming books in the Materials Degradation and Failure series

Biobased and Environmentally Benign Coatings
Edited by Atul Tiwari, Anthony Galanis and Mark D. Soucek
Forthcoming 2016. ISBN 978-1-119-18492-8

Fruits and Vegetables: Degradation and Preservation
By Anjali Bishnoi and Sandeep Rai
Forthcoming 2016. ISBN 978-1-118-92584-3

Lifetimes and Compatibility of Synthetic Polymers
Edited by James P. Lewicki and George Overturf
Forthcoming 2016. ISBN 978-1-119-03852-8

Materials and Failures in MEMS and NEMS
Edited by Atul Tiwari and Baldev Raj
Published 2015. ISBN 9781119083603

Reactions and Mechanisms in Thermal Analysis of Advanced Materials
Edited by Atul Tiwari and Baldev Raj
Published 2015. ISBN 9781119117575

Other Scrivener books edited by Atul Tiwari

Concise Encyclopedia of High Performance Silicones
Edited by Atul Tiwari and Mark D. Soucek
Published 2014. ISBN 978-1-118-46965-1

Nanomaterials in Drug Delivery, Imaging, and Tissue Engineering
Edited by Ashutosh Tiwari and Atul Tiwari
Published 2013. ISBN 978-1-118-29032-3

WILEY END USER LICENSE AGREEMENT

Go to www.wiley.com/go/eula to access Wiley’s ebook EULA.